

<b>REPORT DOCUMENTATION PAGE</b>				Form Approved OMB No. 0704-0188	
The public reporting burden for this collection of information is estimated to average 1 hour per response, including the time for reviewing instructions, searching existing data sources, gathering and maintaining the data needed, and completing and reviewing the collection of information. Send comments regarding this burden estimate or any other aspect of this collection of information, including suggestions for reducing the burden, to Department of Defense, Washington Headquarters Services, Directorate for Information Operations and Reports (0704-0188), 1215 Jefferson Davis Highway, Suite 1204, Arlington, VA 22202-4302. Respondents should be aware that notwithstanding any other provision of law, no person shall be subject to any penalty for failing to comply with a collection of information if it does not display a currently valid OMB control number.					
1. REPORT DATE (DD-MM-YYYY) 6/Sep/2001		2. REPORT TYPE THESIS		3. DATES COVERED (From - To)	
4. TITLE AND SUBTITLE EXPLORING PHYSICS BEYOND THE STANDARD MODEL:ASTROPHYSICAL MOTIVATIONS AND ACCELERATOR APPLICATIONS				5a. CONTRACT NUMBER	
				5b. GRANT NUMBER	
				5c. PROGRAM ELEMENT NUMBER	
				5d. PROJECT NUMBER	
6. AUTHOR(S) 2D LT JAVORSEK DANIEL II				5e. TASK NUMBER	
				5f. WORK UNIT NUMBER	
7. PERFORMING ORGANIZATION NAME(S) AND ADDRESS(ES) PURDUE UNIVERSITY				8. PERFORMING ORGANIZATION REPORT NUMBER CI01-215	
9. SPONSORING/MONITORING AGENCY NAME(S) AND ADDRESS(ES) THE DEPARTMENT OF THE AIR FORCE AFIT/CIA, BLDG 125 2950 P STREET WPAFB OH 45433				10. SPONSOR/MONITOR'S ACRONYM(S)	
				11. SPONSOR/MONITOR'S REPORT NUMBER(S)	
12. DISTRIBUTION/AVAILABILITY STATEMENT Unlimited distribution In Accordance With AFI 35-205/AFIT Sup 1					
13. SUPPLEMENTARY NOTES					
14. ABSTRACT          <div style="display: flex; justify-content: space-between; align-items: center;"> <div style="text-align: center;"> <b>DISTRIBUTION STATEMENT A</b>          Approved for Public Release          Distribution Unlimited       </div> <div style="font-size: 2em; font-weight: bold;">20011016 177</div> </div>					
15. SUBJECT TERMS					
16. SECURITY CLASSIFICATION OF:			17. LIMITATION OF ABSTRACT	18. NUMBER OF PAGES 410	19a. NAME OF RESPONSIBLE PERSON
a. REPORT	b. ABSTRACT	c. THIS PAGE			19b. TELEPHONE NUMBER (Include area code)

By Daniel Jarosh II

For the degree of Doctor of Philosophy

Eggarain Fische, chair


Pail Chue

Andrew J. Hinch

James M. Inguah

proved by: Andrew J. Hinch 7/13/01  
Department Head Date

This thesis ☐ is ☒ is not to be regarded as confidential.

  
Major Professor

\_\_\_\_\_ or Stephen M. Durkin  
Chair, Final Examining Committee Thesis Format Adviser

The views expressed in this article are those of the author and do not reflect the official policy or position of the United States Air Force, Department of Defense, or the U.S. Government.

**THE VIEWS EXPRESSED IN THIS ARTICLE  
ARE THOSE OF THE AUTHOR AND DO NOT  
REFLECT THE OFFICIAL POLICY OR  
POSITION OF THE UNITED STATES,  
DEPARTMENT OF DEFENSE, OR THE U.S.  
GOVERNMENT**

JAVORSEK

To my parents Dan and Joyce, for their encouragement and continual support.

## ACKNOWLEDGMENTS

I must begin by thanking my co-advisor Professor Ephraim Fischbach. Without his support and motivation the completion of this degree under the tight time constraints would not have been possible. He was also a source of inspiration beyond just the usual areas of physics and has helped to break the common paradigms typically associated with physics problems. His input in every stage of the thesis was priceless. Also at the top of the list is the entire faculty and staff associated with PRIME Lab. My co-advisor, Professor Dave Elmore was more than generous in allocating accelerator time to two non-funded research projects. Professor Elmore's input on details of accelerator dynamics helped guide my projects through the design stages. His feedback and wide knowledge on accelerator operations was vital to the success of both projects. I am also deeply indebted to Mr. Tom Miller who played an integral role in procedure design, tuning, and accelerator modifications to name just a few. Mr. Tom Miller was phenomenally helpful in minimizing run times since he was able to teach me to perform many of the tasks that would have taken many times longer for me to learn on my own. His vast understanding of the details of accelerator operations made him a valuable asset to both projects.

I also would like to thank the following PRIME Lab staff: Dr. Pankaj Sharma for his diligence and dedication allocating us time in a very full schedule, Dr. George Jackson for his help with data accumulation, Mr. Ken Mueller and Ms. Mary Ann Rounds for performing the swipe tests on the RHIC gold, Mr. Brad Alexander for his assistance in the construction of the gas manifold, Mrs. Susan Ma for her creation of  $\text{TiO}_2$  cathodes. Of course I am also deeply indebted to the Chemistry staff without their input and assistance the entire Be experiment would not have been possible. Dr. Darren Hillegonds was integral in his assistance with creation of the Be

unknown samples including the I/MeOH Be metal solution. Dr. Henry Rohrs, now at Washington University, was also integral in the early stages of the Be experiment and precisely determined the vapor pressure of the  $\text{Be}(\text{C}_5\text{HF}_6\text{O}_2)_2$  used in creating the standards. I also thank Mr. Mike Bourgeois for his novel idea to dissolve the Be metal in I/MeOH solution. Several aspects of this thesis would have been drastically more difficult if it had not been for the computer assistance of Dr. Bob DeBonte with PRIME Lab networking, Dr. Glenn Sembroski with his assistance with PAW, and Dr. Craig Codrington for his extensive knowledge and expertise with LATEX.

I also would like to thank the following people regarding their help with the Be experiment: Professor Graham Cooks for his assistance in the initial stages of this experiment, Professor Don Gaines and Dr. Dovas Saulys of the Chemistry Department, University of Wisconsin for providing us with the sample of  $\text{Be}(\text{C}_5\text{HF}_6\text{O}_2)_2$ , Dr. Jim Marder of the Brush Wellman Corporation for the samples of Be metal and Be ore, Bill Moore of the U.S. Bureau of Mines for providing us with the Bush Dome gas field sample and for determining its chemical composition. I am also indebted to Mike Stohler who assisted with data acquisition along with much of the data analysis for the final Be runs.

Likewise there are several people who have helped to support the Au research: Professor Vigdor Teplitz of the Southern Methodist University for his discussions regarding SIMP interactions, Professor Doug Oliver of the Department of Geological Sciences, Southern Methodist University for acquiring and analyzing the Australian, Arizona and North Carolina gold samples, Dr. Friedrich Horz, Dr. David Lindstrom, Dr. Carl Agee, Dr. William Kinard, and the National Aeronautics and Space Administration Johnson Spaceflight Center for providing gold from the LDEF satellite along with helpful discussions regarding the original LDEF experiment, Dr. Sam Aronson and Dr. Mike Bennett of Brookhaven National Laboratory for providing us with samples Au beam dump from the Relativistic Heavy Ion Collider. I am also indebted to Dave E. Miller who assisted with data acquisition during the final Au run.

I must also thank Colonel Dick Fanjoy for orchestrating my Ph.D. approval and procuring the waiver for my Euro-NATO Joint Jet Pilot Training slot. Also thanks to Colonel Dave Hankins and Major Mike Nunnally for their support and encouragement along the way.

Lastly, I must thank the secretaries of PRIME Lab, theory department and business office, Ms. Linda Paquay, Mrs. Nancy Schnepp and Ms. Coleen Flanagan, and Ms. Sandy Formica. Clearly there were a large number of people who influenced my projects which resulted in this thesis and my degree. Thank you to everyone mentioned above and all of those I am sure I have forgotten in my absentmindedness.

## PREFACE

The following paper is broken into three general parts. The first part is an overview of many of the fundamental principles required to understand the motivations and discussions regarding the physics behind the two experiments found later in the text. It provides a background on quantum mechanics and the standard model and is the basis upon which the experiments are constructed. This first part has been included because of the diversity of the intended audience and was not intended to incur the appearance of excessive length. For those individuals with a good grasp of quantum mechanics and the standard model this part may be skipped without loss of understanding. However, for deeper understanding of future discussion I would still recommend reading the last two chapters of the Introduction (**Chapters 4 and 5**) since they include information specific to the future chapters.

## TABLE OF CONTENTS

	Page
LIST OF TABLES . . . . .	xiv
LIST OF FIGURES . . . . .	xxiii
ABSTRACT . . . . .	xxxv
 <b>I INTRODUCTION AND BACKGROUND</b>	 <b>1</b>
CHAPTER 1. ACCELERATOR MASS SPECTROMETRY . . . . .	2
1.1 Introduction . . . . .	2
1.2 Theoretical Constructs and Accelerator Stages . . . . .	3
1.2.1 Ion Creation and Pre-Acceleration . . . . .	3
1.2.2 Injection . . . . .	7
1.2.3 The Pelletron . . . . .	9
1.2.4 Acceleration . . . . .	11
1.2.5 The Stripper . . . . .	12
1.2.6 High End Magnetic Selection . . . . .	15
1.2.7 Electrostatic Analyzer . . . . .	15
1.2.8 Detection . . . . .	16
1.3 Isotopic Fractionation . . . . .	17
1.4 Contamination, Friend or Foe? . . . . .	19
1.4.1 Guide Beams . . . . .	20
1.4.2 Wien Filter . . . . .	21
1.4.3 Charge State Harmonics . . . . .	22
1.5 Interpreting Results . . . . .	23
1.5.1 Calculating $R/S$ . . . . .	23
1.5.2 Poisson Statistics and a Null Result . . . . .	24

	Page
1.6 Exotic Physics with AMS . . . . .	26
1.6.1 Possible Violations of the Pauli Exclusion Principle . . . . .	26
1.6.2 Strongly Interacting Massive Particles . . . . .	28
1.6.3 Fractionally Charged Particles . . . . .	28
1.6.4 Detection of Solar Neutrinos . . . . .	29
1.6.5 Proton Lifetimes and Proton Decay . . . . .	29
1.6.6 Exotic Radioactivity . . . . .	30
1.6.7 Using PRIME Lab for Exotic Physics in the Future . . . . .	30
1.7 For Further Reference . . . . .	30
CHAPTER 2. THE STANDARD MODEL . . . . .	32
2.1 Elementary Particles . . . . .	32
2.1.1 Fermions . . . . .	34
2.1.2 Hadrons . . . . .	36
2.1.3 Bosons . . . . .	38
2.2 The Forces . . . . .	39
2.2.1 Gravitation . . . . .	40
2.2.2 Electromagnetism . . . . .	43
2.2.3 The Weak Interaction . . . . .	45
2.2.4 The Strong Interaction . . . . .	47
2.3 Noether's Theorem . . . . .	48
2.4 Symmetry Breaking and the Higgs Mechanism . . . . .	50
2.5 For Further Reference . . . . .	52
CHAPTER 3. QUANTUM MECHANICS . . . . .	54
3.1 Basic Principles of Quantum Theory . . . . .	54
3.1.1 Introduction . . . . .	54
3.1.2 The Dirac Notation . . . . .	56
3.1.3 Orbital and Spin Angular Momentum . . . . .	59

	Page
3.2 Schrödinger, Klein-Gordon, and Dirac Equations . . . . .	61
3.2.1 The Schrödinger Equation . . . . .	62
3.2.2 The Klein-Gordon Equation . . . . .	63
3.2.3 The Dirac Equation . . . . .	64
3.3 Review of Quantum Field Theory . . . . .	65
3.3.1 Introduction . . . . .	65
3.3.2 Field Expansion . . . . .	66
3.3.3 Simple Harmonic Motion . . . . .	68
3.4 For Further Reference . . . . .	77
CHAPTER 4. IDENTICAL PARTICLES AND THE PAULI EXCLUSION PRINCIPLE . . . . .	78
4.1 Symmetrization Postulate . . . . .	78
4.1.1 The Permutation Operator . . . . .	78
4.1.2 Permutation Symmetry . . . . .	80
4.2 Spin-Statistics Theorem . . . . .	87
4.3 The Pauli Exclusion Principle . . . . .	89
4.4 Implications of the Symmetrization Postulate . . . . .	90
4.5 For Further Reference . . . . .	91
CHAPTER 5. BEYOND THE STANDARD MODEL . . . . .	93
5.1 Why go beyond the Standard Model? . . . . .	93
5.2 Variation of the Coupling Constants . . . . .	95
5.3 Introduction to Supersymmetry . . . . .	96
5.3.1 Simple Harmonic Motion Revisited . . . . .	98
5.3.2 The SUSY Algebra . . . . .	99
5.4 For Further Reference . . . . .	101

## VOLUME II

Page

<b>II</b>	<b>SEARCHING FOR PARONIC Be</b>	<b>103</b>
CHAPTER 6.	MOTIVATION FOR PARONIC EXPERIMENTS . . . . .	104
6.1	Introduction . . . . .	104
6.2	Pauli Violating Algebras: Trilinear Commutation Relations . . . . .	105
6.3	Pauli Violating Algebras: Quon Algebra and Infinite Statistics . . . . .	111
6.4	Implications of Pauli Principle Violations . . . . .	114
6.4.1	Cosmological Implications . . . . .	114
6.4.2	Solar Neutrino Implications . . . . .	116
6.4.3	Thermodynamical Implications . . . . .	118
6.4.4	Changes to Atomic Excitation Spectrum . . . . .	121
6.5	Possible Apparent Violations of the Pauli Principle . . . . .	121
6.5.1	Electron Substructure . . . . .	121
6.5.2	Violation of Lepton Family Number . . . . .	123
6.5.3	Compactification of Extra Dimensions . . . . .	124
CHAPTER 7.	EARLY EXPERIMENTS TESTING THE SYMMETRIZA- TION POSTULATE . . . . .	126
7.1	Introduction . . . . .	126
7.2	Forbidden Electronic or Nuclear Transitions . . . . .	126
7.2.1	Absorbing Block Experiments . . . . .	127
7.2.2	Decaying Block Experiments . . . . .	127
7.3	Forbidden Electronic or Nuclear States . . . . .	129
7.4	Miscellaneous Tests . . . . .	135
7.4.1	Spectroscopic Tests . . . . .	135
7.4.2	Tests with Photons . . . . .	137
7.4.3	Cosmological Limits . . . . .	137
7.4.4	Limits from Thermodynamic Considerations . . . . .	139

	Page
CHAPTER 8. SEARCHING FOR ANOMALOUS BERYLLIUM . . . . .	140
8.1 The Fischbach, Kirsten and Schaeffer Experiment . . . . .	140
8.2 Underlying Constructs and Assumptions . . . . .	140
8.3 Principle of the Experiment . . . . .	143
8.4 Anomalous Be In the Ion Source . . . . .	145
8.5 Gas Introduction System . . . . .	149
CHAPTER 9. THE SAMPLES . . . . .	155
9.1 The Blank Sample . . . . .	155
9.2 The Standards . . . . .	156
9.3 The Unknowns . . . . .	167
9.3.1 Be Metal . . . . .	168
9.3.2 Beryl . . . . .	176
9.3.3 The Gas Field Sample . . . . .	179
9.3.4 Atmospheric Air . . . . .	183
CHAPTER 10. EXPERIMENTAL RESULTS . . . . .	186
10.1 Introduction . . . . .	186
10.2 Run Be1, Oct 1996: Pre-Tuning and Calculations . . . . .	186
10.3 Run Be2, Oct 1996: Carbon Tuning and Setup . . . . .	188
10.4 Run Be3, Dec 1996: Background Determination and First Results . .	192
10.5 Run Be4, Sep 1997: First Run with Be-Free Source . . . . .	200
10.6 Run Be5, Oct 1997: Surface Tests . . . . .	204
10.7 Run Be6, Feb 1998: First Run with the New Cathode . . . . .	209
10.8 Run Be7, Oct 1998: First Run with the Gas Manifold . . . . .	215
10.9 Run Be8, Jun 1999: Final Results . . . . .	225
10.10 Conclusions . . . . .	232

### III SEARCHING FOR STRONGLY INTERACTING MASSIVE PARTICLES 237

CHAPTER 11. MOTIVATIONS FOR SIMPS . . . . .	238
11.1 Introduction . . . . .	238
11.2 The Dark Matter Problem . . . . .	238
11.2.1 The Robertson-Walker Metric . . . . .	239
11.2.2 Missing Matter . . . . .	249
11.2.3 Particles as Cold Dark Matter . . . . .	253
11.3 Ultra High Energy Cosmic Rays . . . . .	258
11.3.1 The Cosmic Ray Spectrum . . . . .	258
11.3.2 GZK Cutoff . . . . .	261
11.3.3 The Highest Energy Events . . . . .	263
11.4 The Lightest Supersymmetric Particle . . . . .	266
11.5 Current Neutrino Results . . . . .	267
11.6 Conclusions . . . . .	268
CHAPTER 12. SEARCHING FOR SIMPS IN GOLD . . . . .	270
12.1 Introduction . . . . .	270
12.2 SIMPs and Nuclei . . . . .	270
12.3 Previous Experiments . . . . .	274
12.4 Principle of the Experiment . . . . .	275
CHAPTER 13. AU SAMPLES . . . . .	278
13.1 Introduction . . . . .	278
13.2 Geological Samples . . . . .	278
13.2.1 Near-Surface Residency of Au . . . . .	279
13.2.2 Western Australia . . . . .	283
13.2.3 Arizona . . . . .	284
13.2.4 North Carolina . . . . .	286

	Page
13.3 Exotic Samples . . . . .	289
13.3.1 NASA's Long Duration Exposure Facility . . . . .	290
13.3.2 Relativistic Heavy Ion Collider Beam Dump . . . . .	299
13.3.3 Canyon Diablo Meteorite . . . . .	300
CHAPTER 14. EXPERIMENTAL RESULTS . . . . .	304
14.1 Introduction . . . . .	304
14.2 Run Au1, Dec 1999: Initial Tuning and Injector Magnet Scan . . . . .	304
14.3 Run Au2, July 2000: Mass scan from 200-350 amu . . . . .	309
14.4 Run Au3, Oct 2000: Transmission Efficiency Studies . . . . .	318
14.5 Run Au4, January 2001: Mass Scan from 200-688 amu, All Samples . . . . .	323
14.6 Run Au5, May 2001: Final Mass Scan 200-1777 amu . . . . .	337
14.7 Conclusions . . . . .	353
LIST OF REFERENCES . . . . .	361
VITA . . . . .	370

## LIST OF TABLES

Table	Page
1.1 Poisson upper limits for $n$ observed events in the absence of background.	26
2.1 Classification of Fermions (particles whose spin is odd multiples of $\hbar/2$ ) by family. . . . .	35
2.2 Detailed information on the fundamental fermions. Data obtained from the Particle Data Group [1]. . . . .	36
2.3 Detailed information on the hadrons formed from the light quarks, up $u$ , down $d$ , and strange $s$ . Data obtained from the Particle Data Group [1]. . . . .	38
2.4 Properties of the fundamental bosons and the corresponding forces. Data is obtained from the Particle Data Group [1]. . . . .	39
2.5 Summary of the fundamental constants. . . . .	41
2.6 Some symmetries and their respective conservation laws. . . . .	50
3.1 Classification of particles by spin. . . . .	61
8.1 Summary of Be counting rates for several different surfaces. This study resulted in the use of $\text{Sm}_2\text{O}_3$ and $\text{Yb}_2\text{O}_3$ as the oxide surfaces which supply the oxygen needed to create the $\text{BeO}^-$ . An expanded list of the surfaces tested is included in the results section and was taken during Run Be5 in October of 1997. . . . .	147
8.2 Tests performed on the selected oxide surfaces to see if the background was below the 5 ppm standard. Comparison was performed against a plain copper cathode. The counting rates of the oxides when running the blank are much higher than the results reflected in Table 8.1 and are an example of the cross-contamination possible from samples with high Be contamination. The raw data for this is included in the results section and was taken during Run Be5 in October of 1997. . . . .	148

Table	Page
8.3 Impact of newly designed cathode on efficiency of $\text{BeO}^-$ creation. The new cathode introduces the gas by passing it through 6 holes situated around the cathode perimeter. The old gas introduction location was at the opposite end of the source hence requiring a larger quantity of gas to produce only minimal source efficiencies. Introducing the gas directly adjacent to the surface greatly enhances source efficiency by increasing the probability of $\text{BeO}$ formation. These tests were performed in run Be6 which occurred in February of 1998. The raw data for these tests may be found in the Results chapter. . . . .	151
9.1 Vapor pressure measurements for $\text{Be}(\text{C}_5\text{HF}_6\text{O}_2)_2$ . This data was accumulated by Dr. Henry Rohrs and facilitated accurate evaluation of the concentrations for each standard sample. . . . .	158
9.2 Volume calculations for sample vial S1. All pressures are in Torr and volumes are in $\text{cm}^3$ . . . . .	162
9.3 Volume calculations for sample vial S3. All pressures are in Torr and volumes are in $\text{cm}^3$ . . . . .	163
9.4 Volume calculations for sample vial S6. All pressures are in Torr and volumes are in $\text{cm}^3$ . . . . .	163
9.5 Volume calculations for sample vial S7. All pressures are in Torr and volumes are in $\text{cm}^3$ . . . . .	164
9.6 Volume calculations for sample vial S10. All pressures are in Torr and volumes are in $\text{cm}^3$ . . . . .	164
9.7 Summary of volume calculations for the final three standards (S2, S4, and S11). The average masses for each vial is given assuming $\rho_{\text{H}_2\text{O}} = 0.997 \text{ gm/cm}^3$ . . . . .	166
9.8 Summary of the Be concentrations, $[\text{Be}]/[\text{He}]$ , in parts-per-million (ppm) and the corresponding $1\sigma$ errors of the different standard samples. . .	167
9.9 Summary of ore masses consumed during the first etching. The results are broken down by the chunk and crushed versions of the sample each of which was in a separate Teflon beaker of HF. Both of these contributed to the creation of the first ore sample, O1. . . . .	177
9.10 The principle gases of dry air. Notice the presence of helium and methane which were the major topic of the previous section. This table was obtained from Table 1-1 of Ref. [2]. . . . .	184

Table	Page
10.1 Predicted accelerator $^9\text{Be}$ settings based on $^{37}\text{Cl}$ data. Run Be1 was used to perform the necessary calculations for the tandem settings for needed for $^9\text{Be}$ . . . . .	188
10.2 Counting rates of the different surfaces tested during Run Be2. . . . .	189
10.3 Tandem parameter settings following the tune on $^{12}\text{C}$ . It was necessary to tune with C instead of Be to prevent introducing Be source contamination. Use Figure 1.1 to locate the different elements. . . . .	190
10.4 $^9\text{Be}$ Tandem parameter settings for Run Be2. Use Figure 1.1 to locate the different elements. . . . .	191
10.5 $^9\text{Be}$ Tandem parameter settings for Run Be3. Most settings remained the same as for $^{12}\text{C}$ , those which did change in the transition from C to Be are provided with the C values in brackets, for example $V_t = V_t(\text{Be}) [V_t(\text{C})]$ . Use Figure 1.1 to locate the different elements. . . . .	193
10.6 Counting rates on the different surfaces at a range of S9 source pressures. Standard S9 had a concentration of 459 ppm and was clearly visible above the background counting rate of Run Be3. Along the horizontal axis is pressure while the Target is given on the vertical axis. The Table entries are the counting rates in cps measured on the $\Delta E_1$ plate in the detector. . . . .	194
10.7 Counting rates on the different surfaces at a range of He source pressures. Notice the slow decrease in counting rates as a function of source pressure. As in Table 10.6 the Table entries are the corresponding counting rates in cps measured on the $\Delta E_1$ plate in the detector. . . . .	195
10.8 Counting rates on the different surfaces at a range of S5 (the 4.8 ppm standard) source pressures. Like the helium blank notice the slow decrease in counting rates as a function of source pressure. As in Table 10.6 the Table entries are the corresponding counting rates in cps measured on the $\Delta E_1$ plate in the detector. . . . .	196
10.9 Counting rates on the different surfaces at a range of S8 (the 74.2 ppm standard) source pressures. Unlike the helium blank there seems to be a slight indication of an increase in the counting rate as the pressure increases. Again as in Table 10.6 the Table entries are the corresponding counting rates in cps measured on the $\Delta E_1$ plate in the detector. . . . .	197

Table	Page
10.10 Results of rapidly switching the 74 ppm standard on and off. Each time the gas was turned on we took it up to a pressure of $5 \times 10^{-6}$ Torr. This data gives us conclusive evidence that we were observing the standard above background. These tests were run on the graphite surface and helped to establish the contaminating Be concentration of the old source. . . . .	199
10.11 $^9\text{Be}$ Tandem parameter settings for Run Be4, GV. Most settings remained the same as for $^{12}\text{C}$ , those which did change in the transition from C to Be are provided with the C values in brackets, for example $V_t = V_t(\text{Be}) [V_t(\text{C})]$ . Use Figure 1.1 to locate the different elements. .	201
10.12 Counting rates of the different surfaces tested at the start of Run Be4. This time all the rates are reported in counts per minute (cpm) instead of counts per second (cps). . . . .	202
10.13 Counting rates on the different samples at a range of source pressures. All measurements listed here were performed on the 99% pure Ti surface. This time the Table entries are the corresponding counting rates in cpm measured by the computer with mode 5. . . . .	202
10.14 Surface scans performed at the end of Run Be4. These scans were prompted by high Be contamination in Ti surfaces which prevented us from observing the 74 ppm standard above background. These tests were continued in the following run as we searched for an appropriate sputter surface. . . . .	203
10.15 $^9\text{Be}$ Tandem parameter settings for Run Be5, GY. Most settings remained the same as for $^{12}\text{C}$ , those which did change in the transition from C to Be are provided with the C values in brackets, for example $V_t = V_t(\text{Be}) [V_t(\text{C})]$ . Use Figure 1.1 to locate the different elements. .	205
10.16 Elemental surfaces scanned during Run Be5. Each surface possessed a different amount of Be contamination. . . . .	206
10.17 Oxide surfaces scanned during Run Be5. The desired surface would possess oxygen and would provide the amount necessary to create BeO in the ion source. Otherwise we would need to inject a small quantity of $\text{O}_2$ into each sample container. . . . .	207
10.18 Final evaluation of the impact of the new source and the new chosen surfaces. From this table the copper surface (with higher Be contamination) does not show evidence for detection of the 4.8 ppm standard while both oxide surfaces do. From this we may calculate the new background concentration (see Equation (10.6)). These tests were performed at a source pressure of $2.0 \times 10^{-6}$ Torr. . . . .	208

Table	Page
10.19 <sup>9</sup> Be Tandem parameter settings for Run Be6, HJ. Most settings remained the same as for <sup>12</sup> C, those which did change in the transition from C to Be are provided with the C values in brackets, for example $V_t = V_t(\text{Be}) [V_t(\text{C})]$ . Use Figure 1.1 to locate the different elements. .	211
10.20The final data for leading to the selection of the Sm <sub>2</sub> O <sub>3</sub> surface. These tests were performed at a source pressure of $2.4 \times 10^{-6}$ Torr. As before these yield a background limit of 0.016 ppm (or 16 ppb) for the Sm <sub>2</sub> O <sub>3</sub> surface. . . . .	213
10.21Summary of initial tests of the newly designed cathode. Notice the background concentration is reduced by a factor of 4.4 giving us almost half an order of magnitude. . . . .	215
10.22 <sup>9</sup> Be Tandem parameter settings for Run Be7, HY. Most settings remained the same as for <sup>12</sup> C, those which did change in the transition from C to Be are provided with the C values in brackets, for example $V_t = V_t(\text{Be}) [V_t(\text{C})]$ . Use Figure 1.1 to locate the different elements. .	217
10.23First real data taken of the line calibration along with the first of the unknown samples. Sm <sub>2</sub> O <sub>3</sub> was the chosen surface and the data was taken at the standard $2.5 \times 10^{-6}$ Torr. The horizontal lines indicate gas manifold exchanges of a new set of sample tubes (since it can only hold 4 samples at a time). Notice the upward drift of the blank counting rate. This occurred because of running the standards first and initially introducing contamination into the source. This is not quite the actual run order since we frequently monitored the blank while running the unknowns. The actual run order is given in Table 10.26. . . . .	218
10.24Second try with the lower background counting rate after outgassing the wheel and cathode in an oven at 525 K. Again Sm <sub>2</sub> O <sub>3</sub> was the chosen surface and the data was taken at the standard $2.5 \times 10^{-6}$ Torr. As in Table 10.23 this does not reflect the run order since the He Blank was checked between each sample. The actual run order can be found in Table 10.26. . . . .	219
10.25Final concentration calculations for the unknown samples based on the data taken before and after we cooked the wheel in the oven to burn off the Be contamination. The data afterward was scaled based on the change of the He background. . . . .	222

Table	Page
10.26 Raw data taken during Run Be7. The actual data was saved in ursula under the run letters HY and as a result we have included the cycle numbers here in order to retrieve the data if necessary. The surface was $\text{Sm}_2\text{O}_3$ and the source pressure was held constant at $2.5 \times 10^{-6}$ . Each data point was from a 1.9 minute run, which explains the lowest nonzero value of 0.5 (corresponding to 1 count in 1.9 minutes). The horizontal lines indicate gas manifold exchanges of a new set of sample tubes (since it can only hold 4 samples at a time). . . . .	224
10.27 $^9\text{Be}$ Tandem parameter settings for Run Be8, IM. Most settings remained the same as for $^{12}\text{C}$ , those which did change in the transition from C to Be are provided with the C values in brackets, for example $V_t = V_t(\text{Be}) \cdot [V_t(\text{C})]$ . Use Figure 1.1 to locate the different elements. .	226
10.28 Summary of Be counting rates in counts-per-minute (cpm) for standards and blanks. For the blank and each of the seven standards S1-S7, we exhibit the concentration in parts-per-million (ppm), and the corresponding $1\sigma$ errors. . . . .	228
10.29 Summary of Be counting rates in counts-per-minute (cpm) for the unknown samples. Notice several different gas field runs. For each run we tried to see if we could get the Be signal to disappear. Eventually we removed the vial to a different port on the gas manifold and the signal disappeared. When put back to the original port the Be signal did not return. . . . .	229
10.30 Summary of unknown sample concentrations. The first column gives the $\text{Be}'$ concentration, and the second column expresses the $\text{Be}'$ concentration relative to Be or air. All results are at the $1\sigma$ level. . . . .	232
10.31 Page 1 of Raw data for Run Be8. Each entry is the counting rate in cpm for a different 1.9 minute cycle of the designated sample. This time the chosen surface was $\text{Yb}_2\text{O}_3$ and the gas pressure was held constant at $2.5 \times 10^{-6}$ Torr. . . . .	234
10.32 Page 2 of Raw data for Run Be8. Each entry is the counting rate in cpm for a different 1.9 minute cycle of the designated sample. This time the chosen surface was $\text{Yb}_2\text{O}_3$ and the gas pressure was held constant at $2.5 \times 10^{-6}$ Torr. . . . .	235
10.33 Page 3 of Raw data for Run Be8. Each entry is the counting rate in cpm for a different 1.9 minute cycle of the designated sample. This time the chosen surface was $\text{Yb}_2\text{O}_3$ and the gas pressure was held constant at $2.5 \times 10^{-6}$ Torr. . . . .	236

Table	Page
11.1 Non-zero terms of the Affine Connection using the Robertson-Walker metric. . . . .	242
11.2 Comparison of cosmic ray fluxes at $10^{19}$ eV for the major air shower experiments. This data was adapted from Ref. [3]. . . . .	264
11.3 Summary of predicted SIMP masses $M_S$ for several different theories predicting its existence. For a more extensive discussion of SIMP models than that found here see Ref. [4]. . . . .	268
12.1 Abundances of the most abundant nuclei in the Earth's crust as a function of $A_{min}$ . This is a reproduction of Table I of Ref. [5]. . . . .	274
13.1 Relevant estimated ages for Nullagine and Laverton gold nuggets. Three different ages are presented since the actual penetration depth of SIMPs is model dependent. For models in which a SIMP stops in the soil layer of material near the surface the surface age would apply. In contrast, models for which the SIMP penetration depth is much larger than the Earth's crust prompt use of the age of mineralization or even the Au formation from nucleosynthesis. . . . .	284
13.2 Masses of the Australia samples by run. . . . .	284
13.3 Relevant estimated ages for Arizona gold nugget. Three different ages are presented since the actual penetration depth of SIMPs is model dependent. For models in which a SIMP stops in the soil layer of material near the surface the surface age would apply. In contrast, models for which the SIMP penetration depth is much larger than the Earth's crust prompt use of the age of mineralization or even the Au formation from nucleosynthesis. . . . .	286
13.4 Relevant estimated ages for the North Carolina gold samples. The samples were recovered during placer mining of Monkey Bottom/Furnace Mine, Golden Valley/McDowell City, and Black Run Creek. Three different ages are presented since the actual penetration depth of SIMPs is model dependent. For models in which a SIMP stops in the soil layer of material near the surface the surface age would apply. In contrast, models for which the SIMP penetration depth is much larger than the Earth's crust prompt use of the age of mineralization or even the Au formation from nucleosynthesis. . . . .	287
13.5 Masses of the North Carolina samples by run. . . . .	288
13.6 Masses of the LDEF samples by run. Two different types of samples were provided by NASA: exposed and control gold. . . . .	294

Table	Page
14.1 Stripper yield for several charge states using both gas and foil stripping. One may observe from these data that a foil stripper gives much higher efficiencies than the gas. The gas data were taken at a gas pressure of $4 \times 10^{-6}$ Torr. . . . .	307
14.2 Reanalysis of stripper yield for several charge states using both gas and foil stripping. The gas data was taken at a gas pressure of $2.5 \times 10^{-6}$ Torr. The difficulty of short foil lifetimes discussed in the previous section resulted in our choice to run with gas stripping. . . . .	310
14.3 Evaluation of the optimal gas pressure. This data were taken at $q = +6$ and $V_T = 3.217$ MV. These data suggests we should try to run at a pressure of $1 \times 10^{-6}$ Torr. . . . .	311
14.4 Tandem parameter settings following the tune on $q = +7$ . Refer to Figure 1.1 to locate the different elements. . . . .	312
14.5 Tandem parameter settings following the tune on $q = +7$ . These were the settings used for the first scan on the lab and Laverton gold. These are different from Table 14.4 because of the reduced injector energy which was dictated by the desire to reach a maximum mass of 527 amu. Refer to Figure 1.1 to locate the different elements. . . . .	313
14.6 Coefficients for the transmission efficiency curve fit for $q = +7$ and $q = +9$ . The definition of these parameters can be found in Equation (14.8). Notice that $p_3$ is the horizontal shift of the Gaussian. . . . .	320
14.7 Summary of X/Au ratios for the effective SIMP mass $M'_X$ in $\text{GeV}/c^2$ . We define $M'_X \equiv M_X - M_{Au} = M_S -  E_B $ where $ E_B $ is the magnitude of the binding energy of the SIMP to the Au nucleus. See text for further discussion. . . . .	324
14.8 $M_X$ (vertical) in units of $\text{GeV}/c^2$ versus $\sigma_{SN}$ (horizontal) in units of mb. Table entries give the predicted values of $-\log_{10}(\text{X/Au})$ obtained from Ref. [6]. These predictions are obtained under the approximation [7, 6] $\sigma_{SN}^2 \sim \sigma_{SS}\sigma_{NN}$ , which is used to determine the cosmic S abundance. Such baryonic SIMPs fail to saturate halo dark matter for $\sigma_{SN} > 10^{-3}$ mb. The entries in boxes are excluded by the present experimental results at the 95% confidence level. For the sake of comparison to Ref. [6] we assume here that $M'_X \approx M_S$ . . . . .	325
14.9 Sample positions on wheel along with the respective holder numbers (which are stamped on the back of the cathodes). . . . .	327

Table	Page
14.10 Measured parameters used to calibrate the detector. . . . .	330
14.11 Tandem parameter settings following the tune on $q = +9$ . Refer to Figure 1.1 to locate the different elements. . . . .	331
14.12 Coefficients for the transmission efficiency curve fit for Fe in charge state +9. The definition of these parameters can be found in Equation (14.8). Notice that $p_3$ is the horizontal shift of the Gaussian. . . . .	336
14.13 Outline of the variational charge state method which was implemented in Run Au5. Table entries are the mass in amu scanned at each terminal voltage whose units are in MV. Notice that the data wraps to the right column due to the large quantity of points. As a result the $q = +10$ data had to be broken up. This table actually defines an entire phase space with the values shown here corresponding to those actually used in the run. . . . .	339
14.14 Coefficients for the transmission efficiency curve fits through the experimental data plotted in Figures 14.15–14.19. The definition of these parameters can be found in Equation (14.8). Notice that $p_3$ is the horizontal shift of the Gaussian. . . . .	345
14.15 The energies and channels of the Au peak on each detector plate. . .	347
14.16 Run Au5 Guide Beams. These were used to adjust and verify the tune throughout the scan. We also used them to determine the terminal voltage stepsize needed to ensure the half maximum overlap of sequential steps. . . . .	351
14.17 Final experimental results broken down by Sample showing the Run and limit set in the indicated mass range. . . . .	354
14.18 $M_X$ (vertical) in units of $\text{GeV}/c^2$ versus $\sigma_{SN}$ (horizontal) in units of mb. Table entries give the predicted values of $-\log_{10}(X/\text{Au})$ obtained from Ref. [6]. These predictions are obtained under the approximation [7, 6] $\sigma_{SN}^2 \sim \sigma_{SS}\sigma_{NN}$ , which is used to determine the cosmic S abundance. Such baryonic SIMPs fail to saturate halo dark matter for $\sigma_{SN} > 10^{-3}$ mb. The entries in boxes are excluded by the present experimental results at the 95% confidence level. For the sake of comparison to Ref. [6] we assume here that $M'_X \approx M_S$ . . . . .	356

## LIST OF FIGURES

Figure		Page
1.1	Schematic of the PRIME Lab tandem accelerator. The schematic may be used to located different accelerator elements along the beamline. .	4
1.2	Drawing of the PRIME Lab tandem accelerator. . . . .	5
1.3	Source details with rays representing the direction of motion for the cesium ions ( $\text{Cs}^+$ ) and the resulting ion beam. The sample holder on the left is approximately 2 cm long. . . . .	5
1.4	A negative point charge in a uniform electric field undergoes constant acceleration in the direction opposite the field. . . . .	6
1.5	Trajectory of an energetic charged particle in an external magnetic field.	8
1.6	Picture of a typical tank spark. The spark is emanating from the column on the lower left, which houses the pellet chains and discharge tubes, and spreads to the tank wall. Photo courtesy of NEC. . . . .	9
1.7	Schematic of the pelletron charging system. Charge is induced on the pellets in contact with the drive sheave via an external electric field. The pellets then separate from the drive sheave trapping the charge and transferring it to the high voltage terminal using a similar mechanism.	10
1.8	Electron stripping is a function of the incident ion velocity (energy) because of the motion of the ion's electron in the target potential $\phi$ . For low energy ions the electron is able to make many cycles resulting in an averaging of the potential to zero and no stripping occurs. In contrast electrons in high energy ions see a highly asymmetric potential and are stripped away. . . . .	13
1.9	Theoretical prediction of stripper yields as a function of energy for different charge states of $^{197}_{79}\text{Au}$ . . . . .	14
1.10	Trajectory of an energetic charged particle in a transverse electric field.	16
1.11	Schematic cross-section of the PRIME Lab gas ionization detector. Notice the mylar window at the entrance to the detector which prevents the propane gas from getting into the beam pipe. . . . .	17

Figure		Page
1.12	Fractionation $f$ as a function of isotope mass for gold. This discussion is necessary in order to justify neglecting fractionation in the heavy isotope experiment searching for strongly interacting massive particles (SIMPs) in <b>Part III</b> . . . . .	19
2.1	Matter is composed of atoms, which consist of electrons "orbiting" a nucleus made of protons and neutrons. These protons and neutrons are constructed from quarks, the smallest divisible piece of matter in the standard model. . . . .	33
2.2	A particle can be broken up into the classifications shown in this diagram. In general a particle is either a fermion or boson depending on its spin. A hadron is a particle constructed from a composite of quarks and, depending on the number of particles involved, is either spin-1/2 (a fermion and hence called a baryon) or is either spin-1 (a boson and hence a meson). Complex nuclei are then constructed from hadrons and leptons. The other particles are the elementary quarks, leptons, and gauge bosons discussed in the text. . . . .	40
2.3	The gravitational interaction can be represented by (a) classically by lines of force or (b) as the exchange of a virtual graviton in a Feynman diagram. . . . .	43
2.4	As a result of the Heisenberg uncertainty principle, virtual $e^+e^-$ pairs are created from the vacuum with a coupling strength $\sqrt{\alpha}$ . . . . .	44
2.5	The presence of the charged particle introduces polarization of the virtual particle-antiparticle pairs produced in the vacuum. This vacuum polarization "screens" the charge and introduces a dependence on distance in the behavior of the coupling "constant." . . . .	45
2.6	The electromagnetic interaction can be represented by (a) classically by lines of force or (b) as the exchange of a virtual photon in a Feynman diagram. . . . .	46
2.7	The weak interaction is responsible for (a) $\beta$ -decay like that involved in neutron decay $n \rightarrow p + e^- + \bar{\nu}_e$ which involves a $W^-$ or (b) in scattering processes like $\nu_e e^-$ scattering in which a virtual $Z$ is exchanged. . . .	47
2.8	The strong interaction between two quarks is mediated by a virtual gluon with coupling strength $g_s$ and (b) The coupling of two gluons by gluon exchange. . . . .	48

Figure		Page
2.9	Examples of geometrical symmetries. Each object exhibits reflection symmetry about the dashed lines. . . . .	49
2.10	Classical example of spontaneous symmetry breaking. The ball is placed on the top of the 'Mexican hat' surface which has complete rotational symmetry. However, the configuration is unstable and the ball rolls down into the rim of the hat, coming to rest at an arbitrary point. The rotational symmetry is thus broken and the system has traded symmetry for stability. . . . .	51
4.1	In an interaction involving identical particles the particle trajectories in the interaction region are unknown. Thus, the actual paths of the particles could be either Case 1 or Case 2. . . . .	79
4.2	The Fermi-Dirac distribution function goes to 1 for very low-energy states and to 0 for high-energy states. It equals 1/2 for a state with the Fermi energy, $E_f$ , falling off suddenly for low $T$ and gradually for high $T$ . . . . .	89
5.1	A Higgs boson dissociating into a virtual fermion-antifermion pair. . .	94
5.2	The predicted variation of the coupling constants $\alpha_i$ with energy scale. All three interactions seem to converge at a scale of around $E \approx 10^{14} - 10^{15}$ GeV. (This figure is adopted from figure 1 of Ref. [8]) . . . . .	96
5.3	The predicted variation of the coupling constants $\alpha_i$ with energy scale with SUSY corrections. All three interactions seem to converge at a scale of $E \approx 10^{16}$ GeV. (This figure is adopted from figure 2 of Ref. [8])	97
5.4	A Higgs boson dissociating into a virtual sfermion-antisfermion pair. This diagram exactly cancels the one in Figure 5.1. . . . .	101
6.1	Schematic diagram showing the paronic helium states relative to the normal helium reference states. This figure is taken from Figure 1 of Ref. [9]. . . . .	122
7.1	Configurations of atomic electrons for neon (Ne), anomalous neon (Ne'), and fluorine (F). In Ne' there are three electrons in the K-shell thus displaying behavior indicative of a violation of the Pauli exclusion principle. This figure was adapted from Ref. [10, 11, 12]. . . . .	131
7.2	Configurations of atomic electrons for argon (Ar), anomalous argon (Ar'), and chlorine (Cl). In Ar' there are three electrons in the K-shell thus displaying behavior indicative of a violation of the Pauli exclusion principle. This figure was adapted from Ref. [11, 12]. . . . .	133

Figure	Page
7.3 Configurations of nucleons for lithium ( $^4\text{Li}$ , $^5\text{Li}$ ) and anomalous lithium ( $^4\text{Li}'$ , $^5\text{Li}'$ ). This figure was adapted from Ref. [11, 13, 12]. . . . .	134
7.4 Configurations of nucleons for helium ( $^5\text{He}$ ) and anomalous helium ( $^5\text{He}'$ ). This figure was adapted from Ref. [12]. . . . .	134
8.1 The subshells and orbitals of the first two shells. The electronic configuration shown here is that of neutral beryllium. This diagram is adapted from Ref. [14]. . . . .	142
8.2 The configuration of atomic electrons for beryllium (Be), anomalous beryllium (Be') and helium (He). In Be' all of the electrons are crowded into the lowest energy level (the K shell) thus exhibiting bosonic behavior and violating the Pauli exclusion principle. As a result, the beryllium will have the same chemical properties as helium since the 1s shell would be considered to be "filled." . . . . .	144
8.3 Side and top views of the cathode with 6 holes drilled around the perimeter of the oxide surface. Before the introduction of these cathodes the samples were introduced far from the oxide surface. These cathodes increased the efficiency of the Be being converted to $\text{BeO}^-$ which was evidenced in the raw data which saw a 337% increase in the Be counting rate on the 4 ppm standard. Meanwhile the blank saw no noticeable rise in counting rate, as would be expected if contamination resulted from the surface and source and not from the He blank sample.	150
8.4 Gas manifold permitting us to run up to four gas samples at a time. The gas manifold helped reduce the background, monitor source contamination and drift, and greatly reduced run times. . . . .	152
8.5 Front view of the gas manifold. This gives the dimensions of the different tubing used along with the relative size of the apparatus. . . .	153
8.6 The flexible step up adaptor made from aluminum and Tygon tubing which permitted us to tighten the Cajun Ultra-Torr Union connectors without fear of breaking the nozzles of the glass sample holders. . . .	154
9.1 Schematic of experimental setup for the creation of the first known concentration standard. This standard was then diluted and made into the other lower concentration standards. . . . .	159
9.2 (a) Schematic of experimental setup for the dilution of the high concentration standard S8 into standards S1, S3, S6, S7 and S10. This setup was also used to determine the volumes of the sample vials which housed these standards. (b) A picture of the actual apparatus. The top of the helium tank can be seen in the lower right hand corner. . .	162

Figure		Page
9.3	Schematic of experimental setup for the creation of the Be metal sample. The Be cube was completely dissolved by iodine that was placed into solution with MeOH. The reaction went very rapidly and the entire 3.9 gram cube was consumed in 1 hour and 35 minutes. The reaction was highly exothermic and the flask was very hot to the touch and produced a large quantity of $\text{BeI}_2$ . . . . .	170
9.4	Picture of the reaction of the Be metal with the I/MeOH solution. The lighter surface are the bubbles produced in the highly exothermic reaction. . . . .	171
9.5	Pressure time history for the reaction of Be metal in an aqueous solution of iodine and MeOH. The structure of the curve matched the observed quantity of bubbles produced which was so great that it caused the Be cube to float to the surface. . . . .	173
9.6	Profile sketches of the flask containing the Be cube and I aqueous MeOH solution. The dynamics of the MeOH and the observed green fog are represented in (a) by arrows while (b) gives the motion of the MeOH vapor and possible $\text{BeI}_2$ particles. It is believed that the observed green fog is actually suspended $\text{BeI}_2$ particles. Several hours later when the actual sample was extracted, no green fog existed, suggesting the particles were suspended because of the volatility of the reaction. . . . .	174
9.7	Schematic of the experimental setup for the extraction of the Be ore samples. A large ore chunk and several crushed chunks were placed into Teflon containers filled with 48% HF and put into a desiccator. The desiccator was then left for a prolonged period in which the HF etched the surfaces thereby releasing any trapped Be'. . . . .	177
9.8	Picture of the beryl experimental setup whose schematic is given in Figure 9.7. The teflon containers cannot be seen through the glass of the desiccator because of the silicone grease which caused the glass to look a misty white. . . . .	178
9.9	Major U.S. helium-bearing natural gas fields. This figure was adapted from the Helium Statistics paper by David V. Hayes, Jr. produced by the U.S. Geological Survey [15]. . . . .	180
9.10	Oil and natural gas traps. This diagram is a cross-section of the Earth's crust showing the layers of sediment which result in the stratigraphic traps like those of the Panhandle-Hugoton natural gas field of which the Cliffside Field is a part. The gas field sample was taken from one such trap. . . . .	181

Figure	Page
9.11 Experimental setup for the gas field samples. The liquid nitrogen ( $\text{LN}_2$ ) traps lower the temperature of the gas to 77.4 K thus condensing out the hydrocarbons and allowing the He and any Be' to get all the way to the sample vial. . . . .	182
9.12 Picture of the experimental setup in Figure 9.11. The top of the tank holding our original gas field sample is in the left hand corner. . . . .	183
10.1 Counting rate as a function of Standard S9 (459 ppm) source pressure taken in run Be3. Notice the apparent rise and subsequent fall of the counting rate. This structure is from two competing mechanisms effecting the source efficiency. . . . .	194
10.2 Counting rate as a function of He source pressure taken in run Be3. As the pressure increases the gas (in this case He) begins to interfere with the ejected $\text{BeO}^-$ ions. . . . .	195
10.3 Counting rate as a function of S8 (74 ppm standard) source pressure taken in run Be3. In this case we have a slight indication the counting rate is increasing with gas pressure. Following further analysis in the text we confirmed the 74 ppm standard was barely visible above background. This set the limit on the background at just below 74 ppm. As a result vast improvements were needed in order to surpass the Fischbach, Kirsten, and Schaeffer [16] result. . . . .	198
10.4 We may further reduce the minimum detection limit (push the Bkgd Limit to the left) with two different methods: (1) we could lower the background counting rate or (2) we could increase the slope of the calibration line while still constraining it to go through the origin. In either case the intersection point between the calibration line and the background counting rate would decrease and would lower the limit we set (or allow us to discover) Be'. . . . .	210
10.5 Side and top views of the cathode with 6 holes drilled around the perimeter of the oxide surface. The gas flowed from the coolant port in the sample wheel shaft to the aft end of the specially designed screw. . . . .	212
10.6 A picture of the sample changer and gas flow mechanisms leading to the specially designed cathode. The tube entering from the lower right is the inbound sample gas which then flows through the flange and through the tygon tubing wrapped around the sample wheel shaft before entering the cathode. . . . .	213

Figure	Page
10.7 Diagram and picture of the gas manifold as it sat on the high voltage table in the ion source. It allowed us to run up to four gas samples at a time and helped reduce the background, monitor source contamination and drift, and greatly reduced run times. . . . .	216
10.8 Calibration plot derived from the five standards analyzed during Run Be7. The resulting output from the line fit through the data points (with the errors included) provided the equation given on the plot and also in Equation (10.13). This then permitted the determination of the background for the various unknown samples. . . . .	221
10.9 A zoomed in version of Figure 10.8 in which we note the intersection of the background counting rate with the lower $1\sigma$ limit of the calibration line. Although the data shown here is that of the He blank, the concentration limits of each unknown sample were calculated with this same method. Those results are displayed in Table 10.25. . . . .	223
10.10 Calibration of the AMS for gaseous Be. The open circles represent the experimental data for the blank and the seven Be Standards exhibited in Table I. The solid line is the result of the least-squares fit shown in the figure, where the central value is represented by the solid line, and the $1\sigma$ errors by the dashed lines. . . . .	227
10.11 Picture of the ion source showing the direct gas setup for sample G3. Pictured from left to right are Dr. Darren Hillegonds, Prof. Ephraim Fischbach, and Mike Stohler. . . . .	230
10.12 Determination of the Be' concentrations in the beryl and gas field samples. The shaded region is an enlarged version of the lower end of Fig. 10.10 with the $1\sigma$ errors included. The horizontal dashed line is the measured counting rate for Be, which is presumed to arise from the presence of Be' in the samples. The limits on $[Be']/[He]$ for the beryl and gas field samples are identical, as can be seen from Table II, and are obtained from the intersection of the horizontal line and the $1\sigma$ band as shown. The limits from the other samples are obtained in a similar manner. . . . .	231
11.1 The top diagram represents a closed 2-dimensional surface of constant positive curvature, $k = +1$ . A circle with radius $a$ drawn on the sphere has a circumference $C < 2\pi a$ . The middle diagram is a flat 2-dimensional surface with no curvature, $k = 0$ . On this plane $C = 2\pi a$ . Finally, the bottom diagram is an open 2-dimensional surface of negative constant curvature, $k = -1$ . The circle on this surface has $C > 2\pi a$ . . . . .	241

Figure	Page
11.2 A particle of mass $m$ is gravitationally attracted to a uniform sphere of matter with density $\rho$ and radius $R$ . . . . .	246
11.3 The size scale of the universe $R$ versus time $t$ for the three possible values of $k$ . At the present time (marked "NOW") the universe is still expanding but our uncertainty about the deceleration means that we cannot tell which class of curve we are on, only that we are at present very close to the critical $k = 0$ case. . . . .	248
11.4 A typical rotation curve for a galaxy showing the rotational velocity $v$ as a function of the distance $r$ from the galactic center. The dashed line $\sim 1/\sqrt{r}$ is the expected behavior if the actual matter distribution followed that suggested by luminosity measurements which suggest the visible matter is concentrated in the central region. . . . .	251
11.5 The Universe from the Planck time to the present including many of the relevant parameters (namely: size $R$ , density $\rho$ , energy $E$ and temperature of the background radiation $T$ ). We have also included a list of some of the major events along the timeline. This figure was adapted from Figure 15.6 of Ref. [17]. . . . .	254
11.6 A schematic diagram of an air shower produced by a high energy cosmic ray when it hits the atmosphere. . . . .	259
11.7 The cosmic ray energy spectrum. Remarkably, it appears to be a smooth curve over 10 decades of energy with only a few noticeable structures. The most prominent of these are small, abrupt changes in the local spectral index (the power exponent of $\approx 3$ ) just above $10^{15}$ eV and again just above $10^{18}$ eV. In the figure, they appear as small "kinks" in what is otherwise a straight line. Within the Cosmic Ray field, these features are usually referred to as the "knee" and the "ankle", respectively. . . . .	261
11.8 Diagram of resonant pion photo-production. It is this mechanism which dictates the famous GZK cutoff. A high energy proton collides with the 2.7 K cosmic microwave background radiation (CBR) and loses energy via this mechanism. A similar mechanism exists for nuclei whose binding energies are around 8 MeV/nucleon. A high enough energy collision with a CBR photon will dissociate the nucleus. . . . .	262
11.9 Mean energy of protons as a function of propagation distance through the 2.7 K cosmic background radiation. The three different curves correspond to three different initial energies. The sudden drop to $10^{20}$ eV which occurs between 50–100 Mpc is the theoretically predicted GZK cutoff in action. . . . .	263

Figure	Page
11.10 The AGASA energy spectrum multiplied by $E^3$ in order to emphasize details of the steeply falling spectrum. The dashed curve represents the spectrum expected for extragalactic sources distributed uniformly in the Universe, taking account of the energy determination error. This figure is a version of Figure 2 of Ref. [18]. . . . .	264
11.11 Arrival directions of cosmic rays with energies above $4 \times 10^{19}$ eV from the AGASA experiment. The small squares and circles represent cosmic rays with energies of $> 10^{20}$ eV, and $(4 - 10) \times 10^{19}$ eV, respectively. Shaded circles indicate event clustering within $2.5^\circ$ . At (11h 20m, $57^\circ$ ), three $4 \times 10^{19}$ eV cosmic rays are observed against expected 0.06 events. The chance probability of observing such triplet under an isotropic distribution is only 0.9% [19]. This Figure is adapted from Figure 2a of Ref. [19]. . . . .	265
12.1 The results of solving Equation (12.6) for the two different functional forms of $\sigma_{SN}$ discussed in the text (provided in Equation (12.7)). The lines are not continuous but jagged because $A$ is an integer. . . . .	273
13.1 A picture taken of the different geological samples run in our experiment. The largest single nugget was the sample from Arizona. . . . .	278
13.2 Boiling of the deep liquid during ascent causes gold to precipitate in quartz veins, potentially forming a low sulfidation epithermal gold deposit. . . . .	285
13.3 An artists conception of LDEF in orbit about the Earth. Our samples were from one panel which exposed gold the space environment aboard LDEF from 1984 to 1990. Image courtesy of NASA. . . . .	290
13.4 Picture of LDEF taken from the shuttle main cabin during its capture in 1990. Image courtesy of NASA. . . . .	291
13.5 A picture of the gold foil used in our experiment while it was mounted on the LDEF satellite. Image courtesy of NASA. . . . .	292
13.6 Schematic of LDEF showing the Bay and Row assignments along with the overall structure of the spacecraft. Our gold samples were housed on the trailing edge in Bay A Row 3. Image courtesy of NASA. . . .	293
13.7 A picture of our LDEF samples. Their sizes are evident by referencing against the ruler. . . . .	294

Figure	Page
13.8 Result of simple model for nuclear scattering. This is a plot of Equation (13.4) for different SIMP masses which enter into the equation through our choice of the interaction cross-section. These calculations were performed assuming a foil thicknesses of 5 mm and 1.27 m which are the approximate thickness and width of our LDEF samples. . . . .	297
13.9 Distance required to stop 99% of SIMPs with an energy of 14.5 keV. Here we compare our approximate solution for the scattering to the more rigorous solution developed in the previous chapter. . . . .	298
13.10 Picture of the RHIC samples including the radioactive tag which always accompanies the samples. Dr. Sam Aronson and the Brookhaven National Laboratory donated almost 31 grams of Au beam dump to this experiment. . . . .	299
13.11 Picture of 3000 gram Canyon Diablo Meteorite donated by Mrs. Idella Marx. This fragment is a small piece retrieved from an approximately 60,000 ton meteorite which impacted the Earth near Winslow, AZ. However, since most of the meteor shock melted on impact, this fragment is considered rather large and is by far the sample with the highest monetary value since current rates are around \$0.70 per gram. . . . .	301
13.12 Picture of Canyon Diablo Meteor Crater. The crater is about 1.2 km across and 180 meters (570 feet) deep with a rim that rises 200 feet above the plain. . . . .	302
13.13 Result of simple model for nuclear scattering inside the Canyon Diablo meteorite. This is a plot of Equation (13.4) for different SIMP masses which enter into the equation through our choice of the interaction cross-section. These calculations were performed assuming a meteorite whose initial diameter was 30 meters. . . . .	303
14.1 Results of the first scans from 197 to 394 amu. Each noticeable peak is labeled and most peaks were easily identified. Note the presence of AuSm which comes from the $\text{Sm}_2\text{O}_3$ target used in the Be experiment noted earlier. The gold samples for this experiment were made with the same spatula and the contamination is clearly evident. Also notice the presence of Cl which was the isotope run directly before us. . . .	308
14.2 Results of the first scans from 197 to 1002 amu. Again each noticeable peak is labeled and most peaks were easily identified. . . . .	309
14.3 The scan on the laboratory gold before detector energy resolution constraints have been applied. Each noticeable peak is labeled and most peaks were easily identified. . . . .	315

Figure	Page
14.4 The scan on the gold from Laverton Australia before detector energy resolution constraints have been applied. Each noticeable peak is labeled and most peaks were easily identified. . . . .	316
14.5 Raw data from transmission efficiency scan for (a) $q = +7$ and (b) $q = +9$ . Also included are the curve fitted asymmetric Gaussians which are predicted by [20]. . . . .	319
14.6 Dependence of the ratio of the transmission efficiencies $\eta_X/\eta_{Au}$ on the $X$ mass $M_X$ for (a) $q = +7$ and (b) $q = +9$ . The dependence of $\eta$ on $M_X$ arises from its dependence on the particle velocity which is a function of $M_X$ . . . . .	321
14.7 95% confidence limits on the $X/Au$ ratio in Equation (14.12) as a function of $M'_X$ in $\text{GeV}/c^2$ , obtained from the Australia gold sample. As can be seen from Table 14.7, the results for the samples of lab gold and Australian gold are virtually identical. . . . .	323
14.8 Photograph of the sample wheel before the run began. This picture gives a good representation of how the samples are loaded as well as showing their sizes. . . . .	326
14.9 Schematic of bias plate and injector Faraday cup. Each time the cup is inserted into the beam it retracts to a slightly different position between the negatively charged bias plate. The cup then blocks a slightly different fraction of the electric field lines emanating from the plate, thus creating an asymmetric electric field which changes slightly each time the cup is inserted. This had the effect of steering our low energy beam and caused current fluctuations greater than a factor of 2. The problem was solved by removing the bias electric field. . . . .	329
14.10 Beam profile as measured in the detector Faraday cup. This profile allowed us to determine the optimal stepsize to ensure overlap between steps while simultaneously preventing redundancy of the data points. . . . .	332
14.11 Sample currents measured in the detector Faraday cup. These data are used to calculate the $X/Au$ limit for each sample. The Fe data were used only to monitor the sample consumption since the Fe current is needed to evaluate $X/Au$ . . . . .	333
14.12 The final results of the $q = +9$ run on all eight samples. The data for the Fe Meteorite will be discussed in the following pages. . . . .	334

Figure	Page
14.13A comparison of the results for the Laverton data taken during Runs Au2 and Au4. Here we get a glimpse of the tradeoff from one charge state to another. The charge state +7 data gives slightly better limits between 197 and 290; however at 290 the limits from charge state +9 data become more stringent and extend our mass range up to 688 amu. This corresponds to an effective SIMP mass of 491 amu. . . . .	335
14.14(a) The raw data from the efficiency scan on $\text{Fe}^{+9}$ and (b) the normalized efficiency as a function of total mass. . . . .	336
14.15Stripper efficiency data for charge states $q = +5$ and $q = +6$ . Notice that the scales are not the same for each plot. . . . .	340
14.16Stripper efficiency data for charge states $q = +7$ and $q = +8$ . Notice that the scales are not the same for each plot. The $q = +8$ data are new while the $q = +7$ were taken during Run Au3. They are included together here so that the progression with increasing charge states can be visualized. . . . .	341
14.17Stripper efficiency data for charge states $q = +9$ and $q = +10$ . Again the $q = +10$ data are new while the $q = +9$ were taken during Run Au3. They are included together here so that the progression with increasing charge states can be visualized. Also notice that compared to the previous figure for charge states +7 and +8, the peaks have shifted to the right while the data have come from further into the tail of the peak. Also notice the decrease in amplitude. . . . .	342
14.18Stripper efficiency data for charge states $q = +11$ and $q = +12$ . . . .	343
14.19Stripper efficiency data for charge states $q = +13$ and $q = +14$ . Notice that the data are clearly on the flattened portion of the tail and as a result change very little with increasing mass. . . . .	344
14.20Stripper efficiency as a function of energy for the charge states +5 to +14. This is an analogous plot to the output generated by the STRIP program which is given in Figure 1.9. Notice the flatness of the curves in the low energy region for the higher charge states. . . . .	346
14.21Calibration of the detector energy plates. The raw data and equations for the various fit lines can be found in Table 14.15. . . . .	347
14.22Beam profiles for the guide beams listed in Table 14.16. The data in the final column of the table was obtained from these plots. . . . .	350

## Figure

## Page

- 14.23 Stepsize dependence on terminal voltage. Only the portion of the curve relevant to our scan is given here, while the raw data for the higher  $V_T$  data may be found in Table 14.16. . . . . 352
- 14.24 The  $X/Au$  ratios for the 5 different samples. These results effectively search for a 1.48 TeV SIMP. From the bottom right figure we see that they all have very similar limits, their differences result from slightly different beam currents. Notice that the AZ sample produced the lowest beam currents which is reflected by its poorer limit. The small steps in the curve denote the transition to the next higher charge state as indicated in Table 14.13. The steps also increase in size as we increase the charge state which comes from the poorer efficiency along with the lower beam currents. . . . . 353
- 14.25 Limits placed on the SIMP contribution to the cosmological density parameter  $\Omega$ . The small increasing jumps mirror the changes in charge state in the  $X/Au$  data observed in Figure 14.24. The decreasing jumps observed in the  $\sigma_{SN} \equiv 1/M_S^2$  limit are from the shift of  $A_{min}$  from the second to first row of Table 12.1. . . . . 358

## ABSTRACT

Javorsek II, Daniel. Ph.D., Purdue University, August, 2001. Exploring Physics Beyond the Standard Model: Astrophysical Motivations and Accelerator Applications. Major Professors: Dr. Ephraim Fischbach and Dr. David Elmore.

We report the motivation and results of a search for beryllium, Be, with electrons which violate the Pauli exclusion principle. We then present the run by run results of our completed search for the Pauli-forbidden  $1s^4$  state of Be, denoted by Be'. In contrast to most experiments of this type we have obtained unique samples with higher probability of Be' retention. We set limits on the abundance of Be' in metallic Be, Be ore, natural gas, and air with abundances around  $10^{-11}$ . Our results improve on those obtained in a previous search for Be' by a factor of approximately 300.

We also discuss the motivation and results from a search for strongly interacting massive particles (SIMPs) attached to gold (and briefly iron) nuclei. After discussing the cosmological motivations for such a particle we proceed to discuss the details of its interactions with gold before presenting our results. We are able to significantly constrain the existence of such SIMPs with abundances of less than  $10^{-12}$  for low mass SIMPs ( $M_S \approx 3$  amu) to  $10^{-8}$  for superheavy SIMPs ( $M_S \approx 1,578$  amu). We also provide significant constraints on the possible SIMP contribution to the cosmological density parameter and rule out SIMPs with  $M_s < 10$  amu as a possible mechanism to create the desired condition,  $\Omega = 1$ . As in the search for Be', unique Au samples were obtained from a variety of sources with different histories ranging from 40 million year old gold nuggets from Australia to gold foils flown on NASA's LDEF satellite.

## **Part I**

# **INTRODUCTION AND BACKGROUND**

## CHAPTER 1. ACCELERATOR MASS SPECTROMETRY

The basic concepts involved in this chapter are mainly those associated with static electromagnetic fields. Since the subject matter in many contexts is considered well-known when discussing specific equations (Maxwell's equations for instance) no references will be cited. However, a review of these concepts, beyond that provided here may be found in the texts by Serway [21], Reitz, Milford and Christy [22], Heald and Marion [23], Griffiths [24], or Jackson [25]. For more information on the extremely large topic of accelerator physics and accelerator mass spectrometry the reader is referred to the texts by Tuniz *et al.* [26], Conte and MacKay [27], Lee [28], or the books by Wiedemann [29, 30].

### 1.1 Introduction

Accelerator mass spectrometry (AMS) is an ultra-sensitive technique for counting atoms, particularly those with extremely low abundance in nature. Because of the energies (in millions of electron volts, MeV) and methods for ion selection associated with AMS, we may obtain high sensitivity in counting individual atoms with a given mass inside a small sample.

AMS facilities have been developed for a wide range of applications. Most commonly, AMS is used to determine ratios of unstable to stable isotopes of long-lived cosmogenic radionuclides which are produced by interactions with cosmic rays. Carbon dating is one very good example of how AMS is used in this way. Because the half-life of carbon is well known ( $\tau_{1/2} = 5730$  years), we may determine the date when the isotope  $^{14}\text{C}$  ceased being produced.  $^{14}\text{C}$  decays following the usual radioactive decay law

$$N(t) = N(0)e^{-\lambda t}, \quad (1.1)$$

where there are initially  $N(0)$  unstable nuclei present and  $N(t)$  nuclei left after time  $t$ . The constant  $\lambda$  is called the *decay constant* and is related to the half-life through the relation

$$\lambda = \frac{\ln 2}{\tau_{1/2}}. \quad (1.2)$$

By measuring the ratio  $N(t)/N(0)$  we may determine the effective age of the sample. This technique is used extensively in archeology, although determination of cosmogenic radionuclide ratios (the most common being  $^{10}\text{Be}$ ,  $^{14}\text{C}$ ,  $^{26}\text{Al}$ ,  $^{36}\text{Cl}$ ,  $^{41}\text{Ca}$ , and  $^{129}\text{I}$ ) also has applications as tracers and chronometers in geoscience, environmental, and medical research.

AMS also permits the detection of very low concentrations of stable isotopes and may be used to perform particle physics experiments.

## 1.2 Theoretical Constructs and Accelerator Stages

Accelerator mass spectrometry uses electric and magnetic fields for precise isotope selection and mass resolution. In AMS atoms are extracted from a sample where they are ionized and enter a preacceleration and preselection stage before being accelerated to high energies (tens of MeV). They then experience electric and magnetic fields which separate atoms according to their atomic number, mass, momentum, charge, and energy. Finally the ions are detected and counted. A schematic and drawing of PRIME Lab is provided in Figures 1.1 and 1.2.

### 1.2.1 Ion Creation and Pre-Acceleration

Tandem accelerators require negative ions through the preacceleration stage (the reason for this requirement will become apparent shortly). We begin by loading a few milligrams of the sample material to be analyzed into a small copper cathode. This cathode sample holder is then loaded onto a wheel with seven other samples and placed into the ion source. In the source the surface atoms are slowly sputtered off

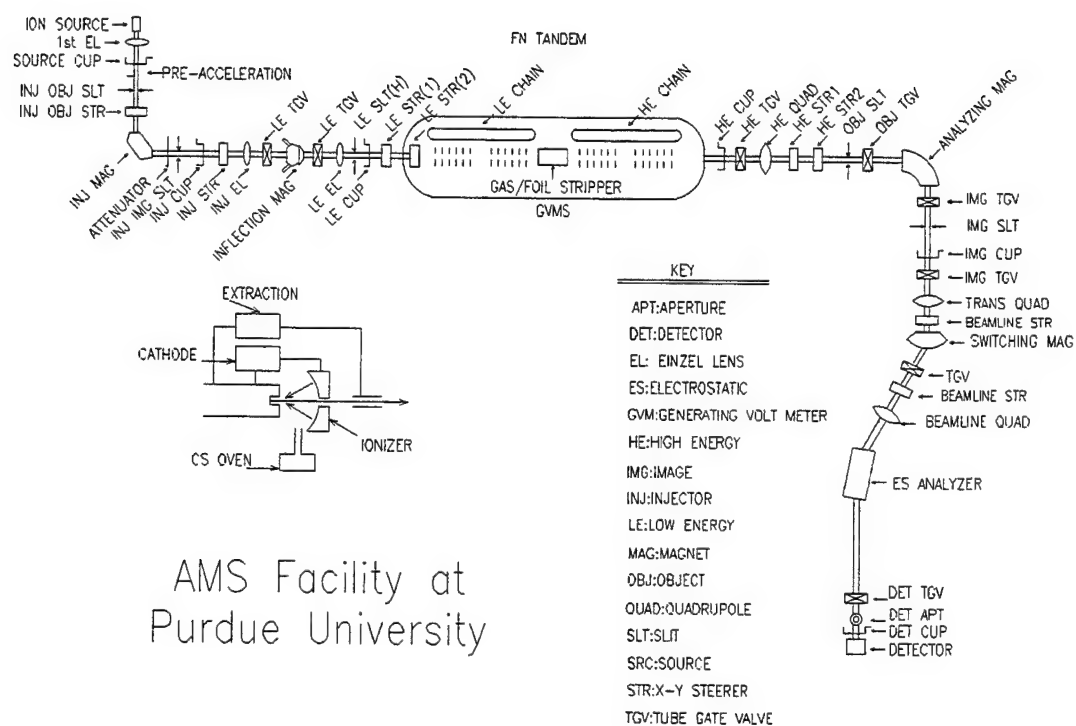


Figure 1.1: Schematic of the PRIME Lab tandem accelerator. The schematic may be used to located different accelerator elements along the beamline.

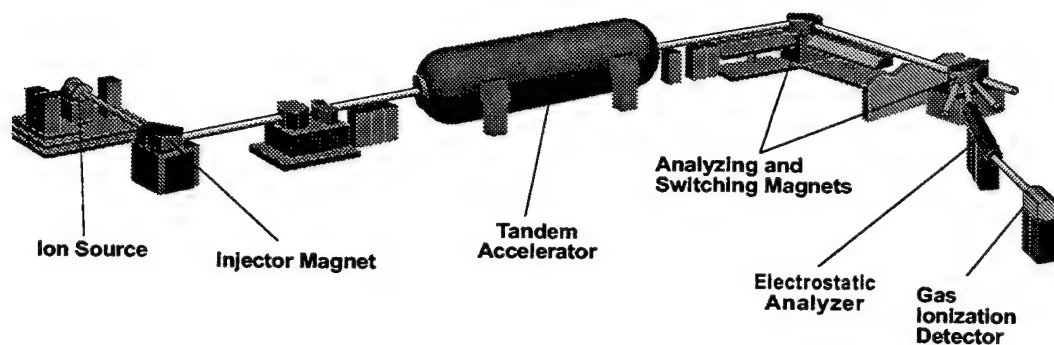


Figure 1.2: Drawing of the PRIME Lab tandem accelerator.

the cathode and ionized through collisions with highly energetic  $\text{Cs}^+$  atoms, which are accelerated to energies on the order of keV (see Figure 1.3). The same field which accelerates the  $\text{Cs}^+$  atoms toward the sample also accelerates the negatively charged ion beam away from the cathode.

### Electrostatics Review I

When a particle of charge  $q$  is placed in an electric field  $\vec{E}$ , the electric force on the charge is  $q\vec{E}$ . Newton's second law then yields

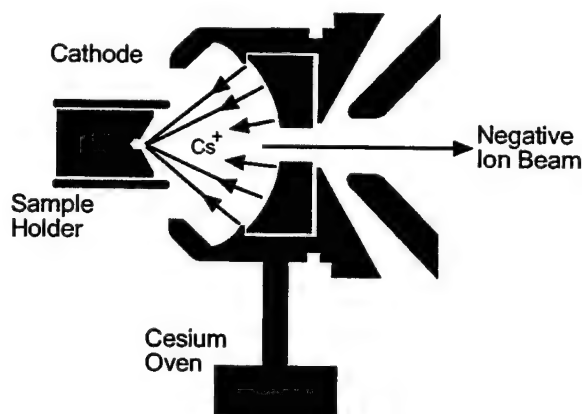


Figure 1.3: Source details with rays representing the direction of motion for the cesium ions ( $\text{Cs}^+$ ) and the resulting ion beam. The sample holder on the left is approximately 2 cm long.

$$\vec{F} = q\vec{\mathcal{E}} = M\vec{a}, \quad (1.3)$$

where  $M$  is the mass of the charged particle, and we assume that the speed is small compared to the speed of light. Figure 1.4 shows the path of the charged particle in the external electric field. Solving the kinematics for a particle under constant acceleration gives

$$\begin{aligned} \vec{a} &= \frac{q\vec{\mathcal{E}}}{M} \\ v &= \frac{q\mathcal{E}}{M}t \end{aligned} \quad (1.4)$$

$$d = \frac{q\mathcal{E}}{M} \frac{t^2}{2}$$

where  $v$  is the velocity of the charged particle and  $d$  is the distance traveled in time  $t$ . Solving for  $t$  and inserting the result into the equation for the velocity we arrive at

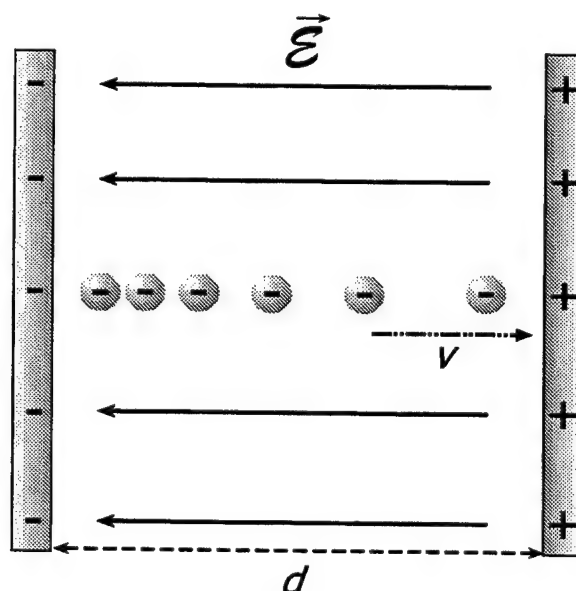


Figure 1.4: A negative point charge in a uniform electric field undergoes constant acceleration in the direction opposite the field.

$$t = \sqrt{\frac{2Md}{q\mathcal{E}}} \quad (1.5)$$

$$\Rightarrow v = \sqrt{\frac{2q\mathcal{E}d}{M}}$$

Assuming that the energy of the charged particle is mainly kinetic, and assuming that the velocity is much less than the speed of light,  $c$ , we may write the energy  $E$  as

$$\begin{aligned} E &= \frac{1}{2}Mv^2 \\ &= \frac{1}{2}M \left( \frac{2q\mathcal{E}d}{M} \right) \\ &= q\mathcal{E}d \\ &= q|V|. \end{aligned} \quad (1.6)$$

For this simple case the potential difference experienced by the charged particle is  $|V| = \mathcal{E}d$ . In this stage of the acceleration process  $V$  is the injection voltage and is a combination of the pre-acceleration and extractor voltages.

### 1.2.2 Injection

The ions are accelerated through a pre-acceleration potential, and obtain an energy on the order of keV. They then enter the injector magnet which is set to accept the desired mass and energy of the atoms we wish to accelerate.

### Magnetostatics Review

The precise dependence of the force on an incident charged particle resulting from a uniform magnetic field may be obtained by starting from the equation for the Lorentz force on the particle and equating with Newton's second law,

$$\begin{aligned} \vec{F} &= q(\vec{v} \times \vec{B}) \\ &= M\vec{a} \\ &= M\frac{v^2}{r}, \end{aligned} \quad (1.7)$$

where  $\vec{B}$  is the magnetic field influencing an ion with charge  $q$ , mass  $M$ , velocity  $\vec{v}$ , and radius of curvature  $r$  experiencing the force  $\vec{F}$  (see Figure 1.5). Again assuming

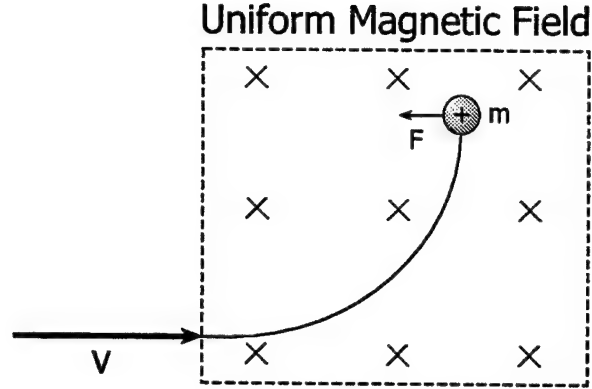


Figure 1.5: Trajectory of an energetic charged particle in an external magnetic field.

the ion's energy is primarily kinetic allows us to solve

$$E = \frac{1}{2} M v^2 \quad (1.8)$$

and Eq. (1.7) for  $v^2$ . Assuming the magnetic field,  $\vec{B}$ , and the velocity,  $\vec{v}$ , are perpendicular we may substitute for their magnitudes,  $B$  and  $v$  respectively. Equating Equations (1.7) and (1.8) we arrive at

$$\begin{aligned} v^2 &= \left( \frac{r q B}{M} \right)^2 = \frac{2E}{M} \\ \Rightarrow \quad \frac{(\tau B)^2}{2} &= \frac{M E}{q^2}. \end{aligned} \quad (1.9)$$

For each magnet, the radius  $r$  is a constant and thus by changing the magnetic field we select for the ion with the desired  $M E / q^2$ .

Here we see one possibility for contamination: If this was all that is used to select the species of interest there would be contamination by species with undesirable mass, energy, and charge but whose  $M E / q^2$  is the same as that of the desired particle. Thus while many of the contaminants have been removed following the injector magnet, there still exist those species which had the correct  $M E / q^2$ . All of these ions (e.g. atoms and/or molecules) will then get accelerated by a large positive potential created

by the Tandem Van de Graaff accelerator. The accelerator produces a potential on the order of several MV (millions of electron volts).

### 1.2.3 The Pelletron

This large potential is produced in much the same way that charge is placed on a conductor using the method of Faraday's ice pail experiment. When a charged conductor is placed in contact with the inside of a hollow conductor, all the charge from the first conductor is transferred to the hollow conductor. In principle, the charge on the hollow conductor and hence its potential can be increased without limit by repeating this process. In the Van de Graaff accelerator specially insulated metal chains deliver this charge to the terminal. Small versions of this method have been used frequently in elementary schools to introduce the concept of static electricity to children. As a demonstration, an ungrounded child is allowed to touch the charged



Figure 1.6: Picture of a typical tank spark. The spark is emanating from the column on the lower left, which houses the pellet chains and discharge tubes, and spreads to the tank wall. Photo courtesy of NEC.

hollow conductor causing his/her hair stand on end.

One might notice that the “breakdown” voltage of air at standard temperature and pressure is equal to about  $3 \times 10^6$  V/m resulting in an upper limit for the potential created with this method. However, the potential of such a system can be increased by increasing the radius of the terminal (hollow conductor) and/or by placing the entire system in a container filled with a high pressure insulating gas like sulfur hexafluoride. Still there are times when something causes a breakdown of the gas and results in a discharge from the terminal to the sides of the tank. This is known as a “tank spark” and results in an awesome transfer of energy in a form of controlled lightning. A picture of a spark is provided in Figure 1.6. Unfortunately, this causes a sudden loss of terminal voltage and requires a somewhat lengthy procedure to recover from. These sparks can significantly increase run times when pushing the machine to its higher terminal voltages.

The charging of the terminal is actually accomplished with a pellet chain or *pel-*

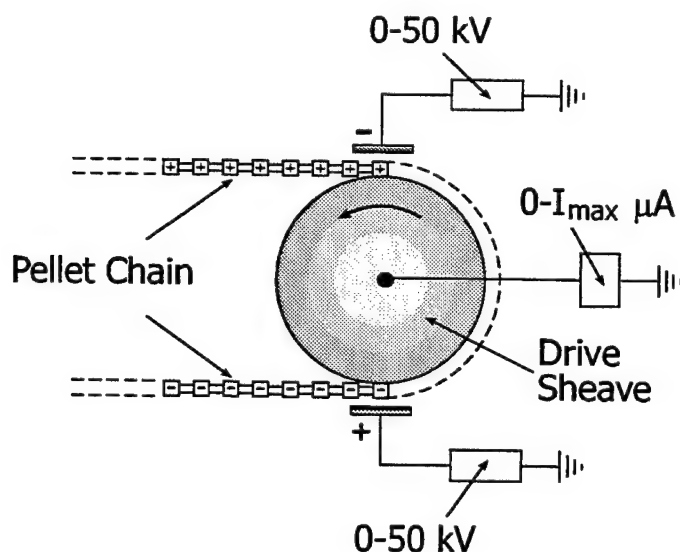


Figure 1.7: Schematic of the pelletron charging system. Charge is induced on the pellets in contact with the drive sheave via an external electric field. The pellets then separate from the drive sheave trapping the charge and transferring it to the high voltage terminal using a similar mechanism.

*lectron*. The charging mechanism is illustrated in Figure 1.7. The chain is made of metallic cylinders joined by insulating links and runs between the driving sheave at the ground end of the accelerator and the driven sheave at the high voltage terminal.

The pellets are charged by induction. Since the wheel and pellet are metal and are in contact in the presence of an electric field, charge is moved to the edges of the metal. The pellet then breaks contact with the drive sheave while still inside the inductor thereby trapping the charge on the pellet (see figure). The charge is delivered to the terminal when the pellet makes contact with the corresponding high voltage sheave in the same manner [31].

#### 1.2.4 Acceleration

At the terminal, many of the electrons are stripped off the ion through collisions with argon gas. The remaining positively charged atomic ions are then accelerated to their final energy. The ion's final energy depends on the terminal voltage  $V_T$  and the number of electrons stripped off and is given by

$$E = \underbrace{\left[ |q_p| (V_p + V_T) \frac{M_p}{M_i} \right]}_{\text{Low End}} + \underbrace{q V_T}_{\text{High End}} |e| \quad (1.10)$$

where  $V_p |e|$  and  $|q_p|$  are the energy and charge of the ions injected into the accelerator (with  $|e|$  the electric charge),  $V_T$  is the terminal voltage, and  $q$  is the charge of the ion leaving the terminal (after the stripping process). In general the positive ion mass  $M_f$  differs from the negative ion mass  $M_p$  if the latter is a molecular ion which dissociates at the stripper; otherwise  $M_f = M_p$  and the energy becomes

$$E = [(|q_p| + q) V_T] |e| + E_p, \quad (1.11)$$

where  $E_p = q_p V_p$  is the initial energy the particle received during the pre-acceleration stage, just after the ion source and is obtained from Eq. (1.6). In usual AMS operations  $q_p = -1$ , however, we have retained this generality because of its relevance in later discussions.

### 1.2.5 The Stripper

The effect of the stripping stage is twofold: All molecular contaminants in the beam with more than 3 electrons stripped during collisions with the Ar gas, dissociate into individual atoms as a result of a "Coulomb explosion," and this has the effect of significantly reducing molecular interference with any putative signal. Secondly by changing the sign of the charge, stripping allows the tandem to accelerate ions both into and out of the accelerator (hence the term "tandem" accelerator). The charge state of a high energy ion moving through a medium fluctuates as a result of electron loss and capture in collisions with the atoms in the medium. After a sufficient number of collisions, an equilibrium distribution of charges is established which depends on the  $Z$  of both interacting particles along with the ion velocity.

In fact the final average charge state an ion ends up in is directly related to its velocity. The analysis of the behavior of the final average charge states of interacting species was pioneered by Bohr [32] and resulted in what Betz [33] calls Bohr's Criterion. To illustrate this behavior let us imagine an incident ion passing a target atom. In the region close to the target atom there exists a potential  $\phi$  shown in Figure 1.8. We also recall that in all atoms the electrons have a distribution of velocities. At low energies (low ion velocities) the ion spends a relatively large amount of time in the region of the target potential  $\phi$ . However, the electrons are also orbiting the ion nucleus at roughly the Bohr velocity,  $\frac{v}{c} = \frac{d}{n} \approx \frac{1}{137 n}$ , where  $n$  is the principle quantum number. Thus they "see" a potential which is constantly changing. If the ion velocity is much lower than the Bohr velocity, the electrons will be able to make many orbits around the ion, and so average out the effects of an external potential. In mathematics this effect is known as the Riemann-Lebesgue Theorem which says that the integration of an oscillating function tends to zero as the frequency of oscillations grows large, namely that

$$\lim_{\omega \rightarrow \infty} \int_a^b f(x) \sin(\omega x) dx = 0. \quad (1.12)$$

Thus the effect of the potential is greatly reduced and few electrons are stripped off

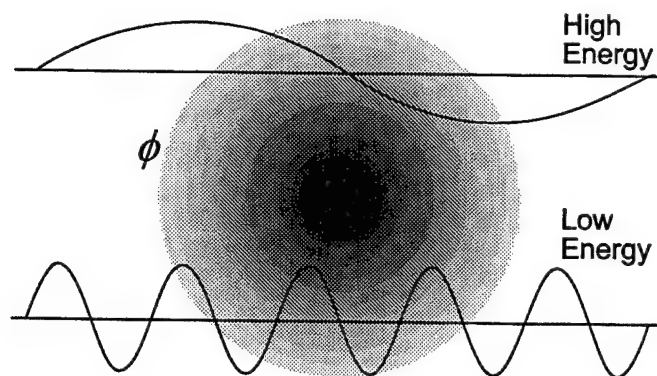


Figure 1.8: Electron stripping is a function of the incident ion velocity (energy) because of the motion of the ion's electron in the target potential  $\phi$ . For low energy ions the electron is able to make many cycles resulting in an averaging of the potential to zero and no stripping occurs. In contrast electrons in high energy ions see a highly asymmetric potential and are stripped away.

the ion because of the apparent symmetry of the potential.

However, at high energies (high ion velocities) the ion spends little time in the target potential  $\phi$  and thus some electrons see a highly asymmetric field. This causes the electron to interact/strip from the ion resulting in a change in the ion's overall charge state. In short, the electrons are unable to complete an entire cycle in the time the ion spends in the potential and thus no averaging occurs. This produces the result that higher energy ions lose their electrons more readily than do lower energy ions. Of course there is a limit to this mechanism, and when the ion velocity is much greater than the Bohr velocity we again have a reduction in the average charge state, but for slightly different reasons. However, in accelerator mass spectrometry we never operate in this regime and thus are concerned more with ion velocities close to the Bohr velocity.

This is not a rigid law simply because of the wide distribution of electron energies, and due to the dependence of stripping on the location of the ion in the target potential.

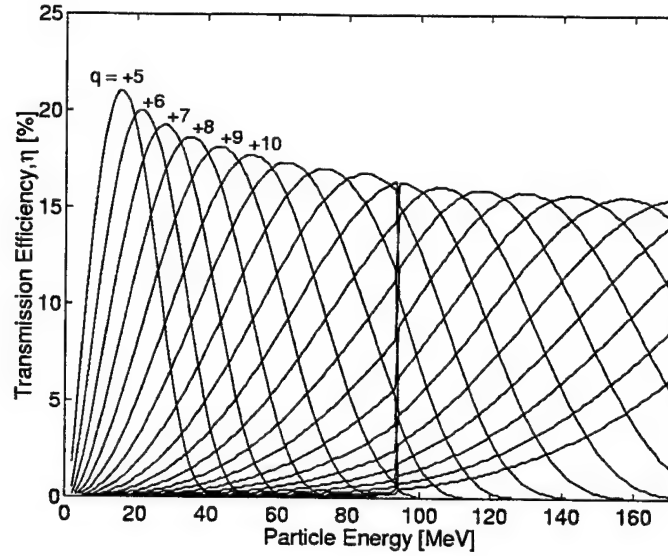


Figure 1.9: Theoretical prediction of stripper yields as a function of energy for different charge states of  ${}_{79}\text{Au}^{197}$ .

In the end the ions exit the stripper in a distribution of charge states, whose yield is best described by an asymmetric Gaussian. For a given energy the stripper yield  $F_q$  function is a function of the charge state  $q$  and is empirically determined to be of the form

$$F_q = F_m e^{-\frac{1}{2} \frac{t^2}{(1+\epsilon t)}} \quad (1.13)$$

where  $F_m$  is the maximum yield,  $t = (q - q_0)/\rho$ , and  $q_0$  is the maximum intensity charge value with  $\epsilon$  and  $\rho$  determined semi-empirically [20].

Thus, the efficiency of the AMS in detecting an isotope depends on the stripper yield at the desired charge state and the ion energy (see Figure 1.9 for sample theoretical stripper yield for multiple charge states). The transmission efficiency is determined experimentally via the relation

$$\eta = \frac{(I_{INJ})100\%}{(I_{IMG})q}, \quad (1.14)$$

where  $I_{INJ}$  and  $I_{IMG}$  are the currents (in nA) detected in the injector and image Faraday cups respectively.

### 1.2.6 High End Magnetic Selection

Ions exiting the terminal thus have a range of masses, energies, and charge states. In order to further discriminate against contamination the ions are introduced to the 90° (analyzing) magnet, and a little further down stream to the switching magnet, each of which selects for the  $ME/q^2$  dependence discussed earlier.

One may observe that there remains possible interference due to the presence of species with the wrong mass but which possess the desired  $ME/q^2$  and hence survived the injector magnet, acceleration, and high end magnets. It is for this reason that we then introduce the particles to an electrostatic analyzer whose electric field selects for a different ratio than do the magnets.

### 1.2.7 Electrostatic Analyzer

The electrostatic analyzer uses a transverse electric field to change the particle's trajectory. This results in different behavior from the electric fields which were previously used for acceleration.

#### Electrostatics Review II

The function of the analyzer can be shown by using a similar argument to that introduced for the pre-acceleration stage. However, this time the field lines are perpendicular to the particle's momentum. Again starting with the Lorentz force and equating with Newton's second law we have,

$$\begin{aligned}\vec{F} &= q\vec{\mathcal{E}} \\ &= M\vec{a} \\ &= M\frac{v^2}{r}\end{aligned}\tag{1.15}$$

where  $\vec{\mathcal{E}}$  is the electric field and  $r$  is the radius of curvature of the ion (see Figure 1.10). Equation (1.15) can then be solved for  $v^2$

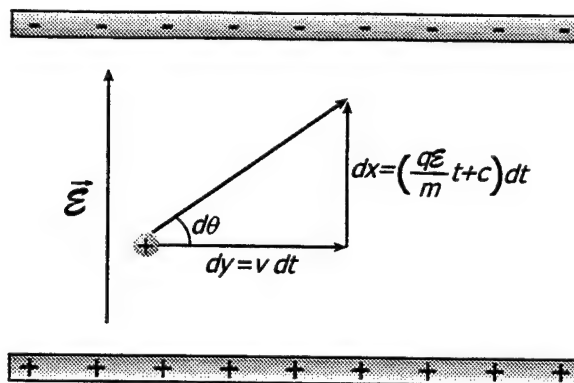


Figure 1.10: Trajectory of an energetic charged particle in a transverse electric field.

$$v^2 = \frac{rq\mathcal{E}}{M} = \frac{2E}{M} \quad (1.16)$$

$$\Rightarrow \frac{r\mathcal{E}}{2} = \frac{E}{q}.$$

From this equation we see that an electrostatic analyzer with a constant radius  $r$  may be used to select the desired  $E/q$  ratio by changing the electric field.

### 1.2.8 Detection

The beam is finally injected into a gas ionization detector [34]. The ions enter the detector through a thin Mylar film and are introduced into a region containing low pressure propane gas and a transverse electric field (see Figure 1.11). The detector has the ability to measure the energy of an incoming particle. This is very useful for selecting out contaminants and guide beams which reach the detector despite all of the mechanisms to select out only those atoms with a specific mass and energy. Part of this selectivity arises from the extreme sensitivity involved; we are looking at roughly one atom in  $10^{15}$  (more on guide beams and contamination later). As the ions travel through the gas they produce electron-ion pairs which separate and induce voltage signals on the cathode and anode inside the detector. These voltage signals are then stored in histograms (broken up by channel) which can later be calibrated to the ion energy through use of beams whose energy is known<sup>1</sup>. The anode is subdivided into

<sup>1</sup>More on this in later sections.

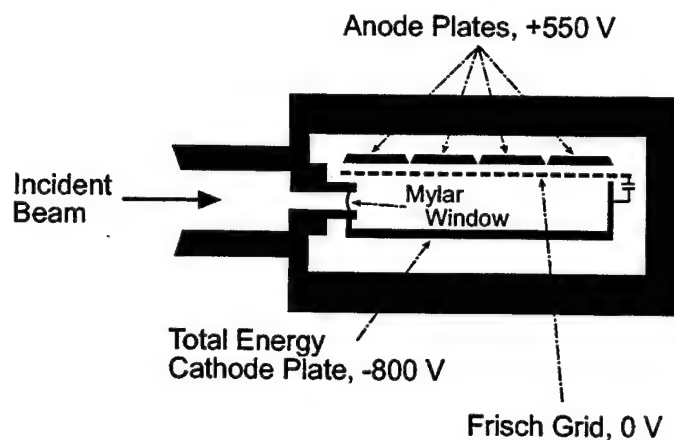


Figure 1.11: Schematic cross-section of the PRIME Lab gas ionization detector. Notice the mylar window at the entrance to the detector which prevents the propane gas from getting into the beam pipe.

segments which determine the energy deposited over a corresponding section of the ion path, while the cathode provides a signal proportional to the total ion energy.

### 1.3 Isotopic Fractionation

One potentially relevant subject for the experiments discussed in future chapters is that of isotopic fractionation. Isotopic fractionation is the observation that different isotopes of the same element have slightly different current yields when extracted from the sample with a high-intensity sputter source. The paper by Middleton, Juenemann and Klein [35] discusses the implications of such fractionation produced by cesium sputter sources. Since sputter rates are mass dependent, we may incorrectly attribute the fractionation to the different sputter rates. However, in high-intensity sources sputter rates are typically several mono-layers per second causing almost instantaneous equilibrium with bulk compositions. This implies that sputter yields of ejected particles will precisely reflect the isotopic composition of the target [35]. The most likely source of the fractionation is the ionization processes occurring either on or close to the sputter surface. In this scenario, the fraction of the ejected particles which emerge ionized depends on the amount of time spent in the Cs vapor region near the surface and thus is related to the average ejected particle velocity. This

average velocity is a function of mass and hence we introduce the observed mass dependence.

In fact, several ionization theories have been proposed which predict such a mass dependence, and a concise review of these theories has been given by Litherland [36]. One representative theory for negative ion formation by secondary-ion emission has been proposed by Nørshov and Lundqvist [37]. In their theory the probability of negative-ion formation,  $P^-$ , is related to the particle velocity by

$$P^- = \frac{2P^0}{\pi} e^{-\left[\frac{\beta(\Phi-A+V_i)}{v \cos \phi}\right]} \quad (1.17)$$

where  $v \cos \phi$  is the velocity of the sputtered ion perpendicular to the surface,  $\Phi$  is the work function of the surface,  $A$  is the electron affinity of the sputtered negative ion, and  $V_i$  is its image charge.  $P^0$  is the number of sputter atoms with energy  $E$  produced per incident particle and is given in terms of the total sputter yield  $Y$ , the angle of emission  $\phi$  (measured with respect to normal), the binding energy  $E_b$  and the energy  $E$  of the sputtered particle

$$P^0 = 2Y \frac{E/E_b}{(1 + E/E_b)^3} \cos \phi. \quad (1.18)$$

The resulting fractionation arises from the different velocity distributions of the ejected sputtered atoms and is given by

$$F^- = \frac{2P^0}{\pi} e^{-\left[\beta(\Phi-A+V_i) \frac{\sqrt{m}-\sqrt{m+1}}{\sqrt{2E}}\right]} - 1, \quad (1.19)$$

which when integrated over all sputtered energies gives the observed fractionation

$$f = \frac{P_m^- - P_{m+1}^-}{P_{m+1}^-}. \quad (1.20)$$

This then was measured experimentally by Middleton, Juenemann and Klein [35] and found to obey the following relationship

$$f = \frac{100}{\Delta m} \left( \sqrt{\frac{M_H}{M_L}} - 1 \right), \quad (1.21)$$

with  $M_H$  and  $M_L$  being the masses of the heavier and lighter isotopes, respectively, and was found to be in striking agreement with the theoretical predictions of Nørskov and Lundqvist [37] for atomic targets. From the above equation we see that the fractionation is roughly inversely proportional to the difference in the masses, since it is the dominating term for large  $M_H - M_L$ . This implies that fractionation actually decreases for larger  $\Delta m$ . Hence in the experiments discussed in the following chapters, particularly those looking for heavy isotopes of ordinary nuclei, fractionation effects will be negligible. For gold,  $^{197}\text{Au}$ , the fractionation is below 0.26 % which is clearly small enough to be negligible for our experiment. A plot displaying the fractionation mass dependence for Au is given in Figure 1.12.

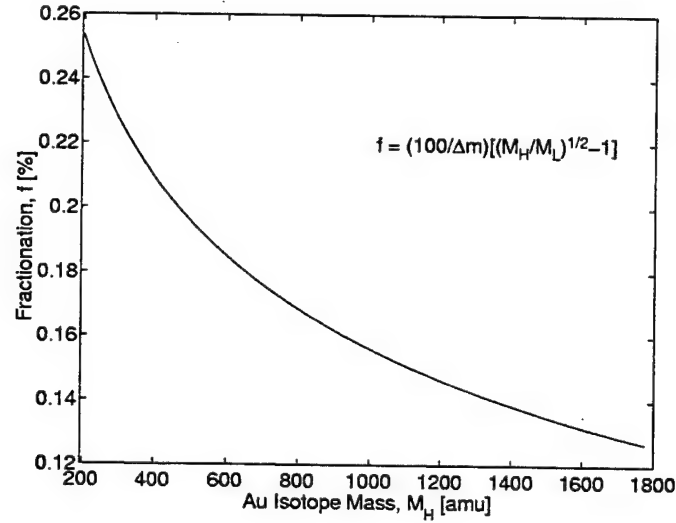


Figure 1.12: Fractionation  $f$  as a function of isotope mass for gold. This discussion is necessary in order to justify neglecting fractionation in the heavy isotope experiment searching for strongly interacting massive particles (SIMPs) in **Part III**.

#### 1.4 Contamination, Friend or Foe?

As mentioned above, even with the many different electrostatic and magnetic elements used in series, we still obtain contamination from species which do not have

the proper mass but passed through the elements discussed above. Any atom which gets through the machine in this manner we will call a guide atom or a *guide beam*.

#### 1.4.1 Guide Beams

The existence of guide beams can be most easily seen by examining the above equations more carefully. For two particles having different masses,  $M_1$  and  $M_2$ , it is still possible for both of them to get all the way to the detector provided  $M_2$  is capable of making a molecule whose mass is that of  $M_1$ . This is necessary in order to get around the injector magnet (more discussion later on including the injector magnet). This can be seen from the two conditions

$$\frac{M_1 E_1}{q_1^2} = \frac{M_2 E_2}{q_2^2}, \quad (1.22)$$

and

$$\frac{E_1}{q_1} = \frac{E_2}{q_2}. \quad (1.23)$$

Substituting Eq. (1.23) into (1.22) leads to

$$\begin{aligned} \frac{M_1}{q_1} \frac{E_1}{q_1} &= \frac{M_2}{q_2} \frac{E_2}{q_2} \\ \Rightarrow \frac{M_1}{q_1} \frac{E_2}{q_2} &= \frac{M_2}{q_2} \frac{E_2}{q_2} \\ \Rightarrow \frac{M_1}{q_1} &= \frac{M_2}{q_2}. \end{aligned} \quad (1.24)$$

Thus any atom or molecule with the same  $M/q$  as the desired isotope will make it into the detector. For example, if we are tuned for  $^{14}\text{C}$  at a charge state of  $q_1 = +4$  we will see a noticeable background from  $^7\text{Li}$  at a charge state of  $q_2 = +2$ . Most of the time this is an extremely undesirable effect, and may be reduced by picking a charge state such that the contaminants are elements which are unstable or of low abundance or  $M_1$  and  $q_1$  are relatively prime<sup>2</sup>.

<sup>2</sup>Two integers are relatively prime if there is no integer greater than one that divides them both

However, this effect may be almost completely removed by adding yet one more constraint on the beam. This comes from a Wien Filter which selects a particle based on its velocity and adds additional  $M/q$  selection.

#### 1.4.2 Wien Filter

The velocity selector ( $\vec{\mathcal{E}} \times \vec{B}$  or Wien filter) uses perpendicular uniform magnetic and electric fields at right angles to the momentum of the incident ions. The magnitudes of these fields can be adjusted to cause zero net deflection only to ions with a specific velocity. The equation governing this selection process is obtained by equating Equations (1.9) and (1.16)

$$v^2 = \left( \frac{rqB}{M} \right)^2 = \frac{rq\xi}{M} \quad (1.25)$$

Other techniques for particle separation and identification include quadrupole mass filtering and time-of-flight analysis.

Thus in normal accelerator mass spectrometry operating with the Wien Filter on reduces the guide beam contamination. However, in one of the experiments, which will be discussed in **Part III**, we were unable to operate with this element of the accelerator on. Fortunately, in this case we are able to use the guide beams to our advantage. In the experiment we scanned to extremely high masses looking for a hypothetical strongly interacting massive particle (SIMP). When running conventional isotopes we tune the accelerator for a given mass by utilizing a known mass that is very near by. For example, to tune for an unstable isotope we tune on a stable isotope of the same element and we have extensive knowledge of how to scale the magnetic components to distinguish between the isotopes. Since the energies are the same (we hold the terminal voltage fixed) we do not need to adjust the electrostatic elements.

In the SIMP experiment this was not the case, and the energy at each mass had to change in order to keep the analyzing magnet at its highest field strength. Since we expected a null result, we needed a way to check if the tune was still accurate, and we also needed a way to check that the electrostatic elements were scaling as (that is, their greatest common divisor is one).

we expected. This was needed since we were pushing the accelerator into regimes in which it had not previously operated. The guide beams allowed us to check/monitor the tune throughout our runs. This behavior of  $M_1/q_1 = M_2/q_2$  lets us use lower masses in lower charge states to check the tune for higher masses in higher charge states.

### 1.4.3 Charge State Harmonics

We also should point out another curious result. If we perform the analysis discussed above for the injector magnet we find it also permits  $M/q$  contamination. To see this we begin with the condition derived from in Equation (1.9) given by the magnetic elements, except with the  $p$  subscript included to denote the pre-acceleration phase,

$$\frac{M_1 E_1}{q_{p1}^2} = \frac{M_2 E_2}{q_{p2}^2} \quad (1.26)$$

We also know that the pre-acceleration energy  $E_p$  of particles is given by

$$E_p = q_p V_p \quad (1.27)$$

where  $q_p$  is the charge the ion acquired in the collisions with the incident cesium ions inside the sputter source.  $V_p$  is the preacceleration potential and is just the sum of the extractor and pre-accelerator voltages. Imposing this constraint on Eq. (1.26) gives

$$\begin{aligned} \frac{M_1 (q_{p1} V_p)}{q_{p1}^2} &= \frac{M_2 (q_{p2} V_p)}{q_{p2}^2} \\ \Rightarrow \quad \frac{M_1}{q_{p1}} &= \frac{M_2}{q_{p2}} \end{aligned} \quad (1.28)$$

This is essentially the same result we obtained for the high-energy end ("high end"). The only difference is that the charges are those from the ion source instead of the stripper. If we then apply the high end condition given by Eq. (1.24) to Eq. (1.28) we find

$$\frac{q_1}{q_2} = \frac{q_{p1}}{q_{p2}} \quad (1.29)$$

This says that different particles with different masses get to the detector provided their masses satisfy Eq. (1.24) if their charge states satisfy Eq. (1.29). This can be checked by observing that the  $E_2$  in Eq. (1.23) is equal to the  $E_2$  calculated using Eq. (1.11). However, usually  $q_{p1} = q_{p2} = -1$  and only works if  $M_1 = M_{p1}$  as is assumed here. Since this behavior is reminiscent of the harmonic nature of strings resulting from the normal modes of a stretched string fixed at both ends, we have called this effect Charge State Harmonics.

## 1.5 Interpreting Results

### 1.5.1 Calculating $R/S$

The quantity of interest is the ratio of the number of rare isotope atoms ( $R$ ) to stable isotope atoms ( $S$ ) in the sample,  $R/S$ . The number of atoms with the rare isotope mass are counted in the detector since they are extremely rare. We actually report a counting rate (in counts per minute) which is given by  $C_R$  below. The number of atoms with the stable isotope mass are measured in the image Faraday cup for conventional AMS and the detector Faraday cup for our SIMP experiment. The Faraday cup is used to determine the current of the stable isotope beam current because the beam is too abundant for the detector itself. Thus we again report a counting rate, this time in nA, denoted by  $I_{det}$ . As a result we can express  $R/S$  in terms of  $I_{det}$ , the charge state  $q$ , and the detector counting rate  $C_R$ ,

$$\begin{aligned} R/S &= \frac{\left[ \frac{C_R \text{ counts}}{\text{min}} \right]}{I_{det} \text{ nA}} \left[ \frac{q(1.602 \times 10^{-19} \text{ C})}{1 \text{ count}} \right] \left[ \frac{1 \text{ min}}{60 \text{ sec}} \right] \left[ \frac{1 \text{ nA}}{1 \times 10^{-9} \text{ C/sec}} \right] \\ &= (2.672 \times 10^{-12}) C_R \frac{q}{I_{det}} \end{aligned} \quad (1.30)$$

The numerical constant is simply that required to convert from counts per minute (cpm) to nanoamps (nA). How this ratio is actually used depends on which application of AMS we are considering.

### 1.5.2 Poisson Statistics and a Null Result

In both experiments we obtain a null result with no detectable background. Thus it is important to understand how we present our results and the confidence limits on them. If we have a large number of events we use Gaussian statistics, and is the method employed by conventional AMS. However, when we have only a few counts we must use Poisson statistics to interpret our results in a meaningful way.

The Poisson distribution is actually quite simple to derive. Recall that we may perform a Taylor series expansion of any exponential, for example

$$e^{\lambda} = 1 + \lambda + \frac{\lambda^2}{2!} + \frac{\lambda^3}{3!} + \dots$$

$$= \sum_{n=0}^{\infty} \frac{\lambda^n}{n!}$$
(1.31)

rearranging the above equation we arrive at the conclusion that

$$1 = \sum_{n=0}^{\infty} e^{-\lambda} \frac{\lambda^n}{n!}$$
(1.32)

The quantity inside the summation is defined as the distribution function for a Poisson distribution and is explicitly given by

$$p(n; \lambda) = \frac{e^{-\lambda} \lambda^n}{n!}$$
(1.33)

The probability distribution function of  $n$  (in this particular case the Poisson distribution) tells us how the total probability ( $=1$ ) is allocated among the various possible values of  $n$ . The Poisson distribution is a valid probability distribution function because it satisfies the following criteria:

$$1) p(n; \lambda) \geq 0$$

$$2) \sum_{\text{all possible } n} p(n; \lambda) = 1$$
(1.34)

In fact we can also see that the Poisson distribution is a limiting case of the binomial distribution whose probability distribution function is

$$b(x; n, p) = \begin{cases} \binom{n}{x} p^x (1-p)^{n-x} & x = 0, 1, 2, \dots, n \\ 0 & \text{otherwise} \end{cases} \quad (1.35)$$

which is used to discuss a set of data with only two possible outcomes (like heads or tails).  $p$  is the probability of success and  $n$  is the distinct number of trials (or number of times we flip the coin). The Poisson distribution is the binomial distribution in the limit as  $p \rightarrow 0$  and  $n \rightarrow \infty$  such that the product  $\lambda = np$  is fixed.

In the Poisson distribution the expectation value and variance are simply  $\lambda$ . Thus for a given  $n$  we can specify a value for  $\lambda$  in order to fix the probability of finding  $n$  again. This concept of fixing the probability for a given  $n$  is called defining a *confidence interval*. Thus we pick a confidence level, CL, and derive the required  $\lambda$  which satisfies this condition. The parameter  $\lambda$  then is the projected upper limit given  $n$  observed events. For example, let us say we want to report a result at a 95% confidence level. If we obtain 0 events, then we insert this information into the equation for the Poisson distribution, solving for  $\lambda$ ,

$$\begin{aligned} p(n=0; \lambda) &= \frac{e^{-\lambda} \lambda^0}{0!} \\ &= e^{-\lambda}. \end{aligned} \quad (1.36)$$

Since  $p(n; \lambda) = 1 - 0.95$  for a 95% CL, we find

$$\begin{aligned} \Rightarrow e^{-\lambda} &= 0.05 \\ \therefore \lambda &= \ln \left( \frac{1}{0.05} \right) = 3.00 \end{aligned} \quad (1.37)$$

This analysis can also be carried out for different  $n$ , although it is slightly more complicated. For  $n \geq 1$  this results in transcendental equations which must be solved numerically. Table 1.1 provides the solutions of these equations for 90% and 95% confidence limits.

Table 1.1: Poisson upper limits for  $n$  observed events in the absence of background.

$n$	90% CL	95% CL	$n$	90% CL	95% CL
0	2.30	3.00	6	10.53	11.84
1	3.89	4.74	7	11.77	13.15
2	5.32	6.30	8	13.00	14.44
3	6.68	7.75	9	14.21	15.71
4	7.99	9.15	10	15.41	16.96
5	9.27	10.51	11	16.60	18.21

Thus we see that the Poisson distribution allows us to project our null result into a reasonable upper limit on each event by simply replacing the actual number of counts  $n$  with the corresponding value for  $\lambda$  provided in Table 1.1.

A good discussion of Poisson and other statistical distributions may be found in most books on statistics [38, 39]. The Particle Data Group also provides a summary of the statistics used frequently in particle physics [40].

## 1.6 Exotic Physics with AMS

Although accelerator mass spectrometry is used primarily for routine measurements of radioisotope ratios, it may also be used to search for particles and test new theoretical developments which push the threshold of physics. Many of the theories beyond the standard model make specific predictions which may be tested with AMS. We will review some of the more salient features of these applications here and will discuss in greater detail (**Parts II and III**) two experiments of this genre.

### 1.6.1 Possible Violations of the Pauli Exclusion Principle

When identical particles interact with each other they interact via a set of rules which are derived from statistical mechanics and field theory. This set of rules is in general different for each type of particle and is called the statistics of the particle. Curiously, the statistics that a particle obeys is related to the intrinsic amount of

spin the particle possesses. The relationship between the statistics and particle spin is known as the spin-statistics theorem.

Based on certain symmetries exhibited by a particle's wave function we are lead to infer the Symmetrization Postulate which says that there are only two kinds of statistics observed in real interactions. Thus there are two fundamental statistics which govern all known processes involving identical particles, Fermi-Dirac statistics and Bose-Einstein statistics.

In order to see this let us recall a few facts about a particle's spin. All of quantum mechanics is based on the quantization of a particle's spin angular momentum. In general, we may differentiate between two classifications of a particle's spin, even and odd multiples of  $\hbar/2$  (where  $\hbar$  is Planck's constant). Particles with half integer spin (odd multiples of  $\hbar/2$ ) are called Fermions since they obey Fermi-Dirac statistics, while particles with an integral amount of spin (even multiples of  $\hbar/2$ ) are called Bosons and obey Bose-Einstein statistics. For example, as a result of the symmetrization postulate, electrons (which are spin-1/2 particles) obey Fermi-Dirac statistics. In Fermi-Dirac statistics no two particles may occupy the same quantum state, and hence no two electrons may be in precisely the same quantum mechanical state simultaneously. This rule is known as the Pauli exclusion principle and is largely responsible for the structure of the periodic table. This is because each energy level in an atom has a limited number of allowable quantum states. Since no two electrons may be in the same state we are led to the Aufbau Principle: Electronic shells sequentially fill from the lowest energy level up to higher levels, giving us the atomic energy level structure evident in the periodic table.

Even though virtually all of chemistry and quantum mechanics relies on the Pauli exclusion principle, until the 1980's it had not been directly tested in an experiment designed for such a purpose. In 1987, a number of theoretical ideas were advanced suggesting that the Pauli principle need not hold rigorously but that small violations of it were permitted in quantum field theory. This motivated a flurry of experiments looking for particles which violate the Pauli principle. Such particles are known as

Parons and their details are a major part of this paper. **Part II** gives a detailed discussion of both the theory and our experiment testing for violations of the Pauli exclusion principle and in turn a test of the fundamental quantum mechanics construct, the symmetrization postulate.

### 1.6.2 Strongly Interacting Massive Particles

Superheavy elements have been theorized for many years and there has always been a fascination with the notion that there is an island of stability just beyond the presently accessible regions of stable nuclei [41]. In fact with the introduction of Big Bang cosmologies [42, 43] it was possible to predict the formation of heavy (10 GeV to 100 TeV) stable particles during the early moments of the universe.

Recently superheavy particles have been introduced as an explanation for a wide array of cosmological questions and inconsistent results seen in astrophysics. One method of searching for such particles would be to identify anomalous isotopes of known heavy nuclei, which can result if a neutral, heavy, stable strongly interacting elementary particle binds with known nuclei. These stable particles, dubbed strongly interacting massive particles (SIMPs), may be present in normal matter.

**Part III** of this thesis goes into the details of the theory behind SIMPs along with a detailed discussion of our experiment searching for such particles. The concepts developed in this chapter, namely the discussions regarding guide beams and charge state harmonics are vital to the understanding of the procedures and data analysis performed on the samples.

### 1.6.3 Fractionally Charged Particles

Four-dimensional string theories predict the existence of fractionally charged particles [44]. In string theory much effort has been invested in attempting to derive a four-dimensional model which leads to the standard model of electroweak and strong interactions at low energies. In these theories the lightest particle with fractional electric charge (FEC) must be stable. Previous searches have placed bounds on their masses and charges including some tests using AMS [45, 46]. There still exists a window in the masses of such FEC particles from 100 GeV to a few TeV. (These

constraints are derived from experiments and cosmological considerations.) This is a ripe possibility for using a system similar to that in our SIMP experiment to search for such particles.

#### 1.6.4 Detection of Solar Neutrinos

The standard model makes clear predictions regarding the flux of solar neutrinos. The average flux of these neutrinos measured over a period of nearly 20 years provides a flux that is more than three times lower than that predicted by the standard model (see reviews by Bahcall *et al.* [47, 48]). This puzzle may be resolved if the neutrinos had mass, allowing them to oscillate, in which case the missing electron neutrinos would arrive as muon or tau neutrinos instead. This problem may be investigated using AMS if one looks at the possibilities of a number of interactions in which the concentrations of the final isotopes is extremely low [49]. Consider, for example, the reaction



According to the standard model, the capture rate of neutrinos in  ${}^7\text{Li}$  corresponds to  $51.8 \pm 0.31$  solar neutrino units (SNU). One hundred tons of lithium would produce only 3,000  ${}^7\text{Be}$  atoms. Such a small number is difficult to measure by counting techniques, but may be easier to measure using AMS.

#### 1.6.5 Proton Lifetimes and Proton Decay

According to Grand Unified Theories, the proton is expected to decay with a lifetime of approximately  $10^{31}$  years [50]. Using geochemical methods one may search for the disappearance of the proton via the decay chain:



where the proton decays in a tellurium mineral of geological age ( $10^9$  years) producing an isotopic anomaly in the  ${}^{129}\text{Xe}$  abundance. We also may be able to detect the  ${}^{129}\text{I}$  directly with AMS.

### 1.6.6 Exotic Radioactivity

An exciting discovery in nuclear physics in recent years was that of exotic radioactivity: the spontaneous emission of heavy ions such as  $^{14}\text{C}$ ,  $^{20}\text{Ne}$ , and  $^{24}\text{Ne}$  from nuclei in the trans-lead region [51]. This discovery was made with nuclear track detectors but may also be detected with AMS looking for  $^{14}\text{C}$  accumulation in uranium and thorium. This accumulation is expected because  $^{14}\text{C}$  clusters are emitted by  $^{223}\text{Pa}$  and  $^{224}\text{Pa}$  in the natural decay series of  $^{235}\text{U}$  and  $^{232}\text{Th}$ , respectively.

### 1.6.7 Using PRIME Lab for Exotic Physics in the Future

While there are currently only two experiments using PRIME Lab to probe exotic questions in particle physics and cosmology, we see from the quick discussions above that there are a number of possible experiments which may be able to utilize the accelerator to help further this blossoming area of physics.

## 1.7 For Further Reference

As mentioned briefly at the beginning of the chapter, the intention here was to provide a brief introduction of the concepts and equipment associated with accelerator mass spectrometry. Good texts for further reference on the fundamentals of electromagnetics are

- Raymond A. Serway, *Physics for Scientists and Engineers*, Saunders College Publishing, 1992.
- John R. Reitz, Frederick J. Milford, and Robert W. Christy, *Foundations of Electromagnetic Theory*, Addison-Wesley Publishing Company, 1993.
- Mark A. Heald and Jerry B. Marion, *Classical Electromagnetic Radiation*, Saunders College Publishing, 1995.
- David J. Griffiths, *Introduction to Electrodynamics*, Prentice-Hall, Inc., 1999.
- John D. Jackson, *Classical Electrodynamics*, John Wiley & Sons, Inc., 1999.

Good texts providing more elaborate details on accelerator physics and accelerator mass spectrometry in general are

- Claudio Tuniz, John R. Bird, David Fink, and Gregory F. Herzog, *Accelerator Mass Spectrometry: Ultrasensitive Analysis for Global Science*, CRC Press LLC, 1998.
- Mario Conte, and William W. MacKay, *An Introduction to the Physics of Particle Accelerators*, World Scientific Publishing Co. Pte. Ltd., 1991.
- Shyn-Yuan Lee, *Accelerator Physics*, World Scientific Publishing Co. Pte. Ltd., 1999.
- Helmut Wiedemann, *Particle Accelerator Physics I: Basic Principles and Linear Beam Dynamics*, Springer Publishing Company, 1999.

## CHAPTER 2. THE STANDARD MODEL

The basic concepts involved in this chapter are mainly those associated with high energy particle physics. As in the previous chapter, the subject matter is considered well-known, and hence when discussing specific equations no references will be cited. However, additional information may be found in the texts by Griffiths [52], Kane [53], Perkins [54], or the book by Collins, Martin and Squires which provides particle physics applications to cosmology [17].

### 2.1 Elementary Particles

To begin let us describe what an elementary particle is according to the standard model of particle physics. It is an observational fact that all matter that we come in contact with may be broken into smaller and smaller constituents. Although Aristotle's four "elements" – fire, earth, air, and water – were accepted by popular opinion for nearly two thousand years, a contradicting theory was briefly proposed by Democritus of Abdera who suggested that, "the only things are atoms and empty space; all else is mere opinion." [55] As such the definition and concept of atoms was set by the Greeks with the Greek word for atom meaning "indivisible" and was used to describe the smallest conceivable bit of matter. The size of an atom is on the order of an angstrom or  $10^{-10}$  meters.

Further inspection of this principle in the 16th and 17th centuries led to the discovery of the different elements whose categorization is evident in the Periodic Table. The elements of the periodic table are chemically different from one another. After probing further it was discovered that each element itself was made of yet smaller constituents. In fact an atom was shown to consist of electrons "orbiting" a charged nucleus whose size is roughly  $10^{-14}$  meters. The nucleus, in turn, is constructed out

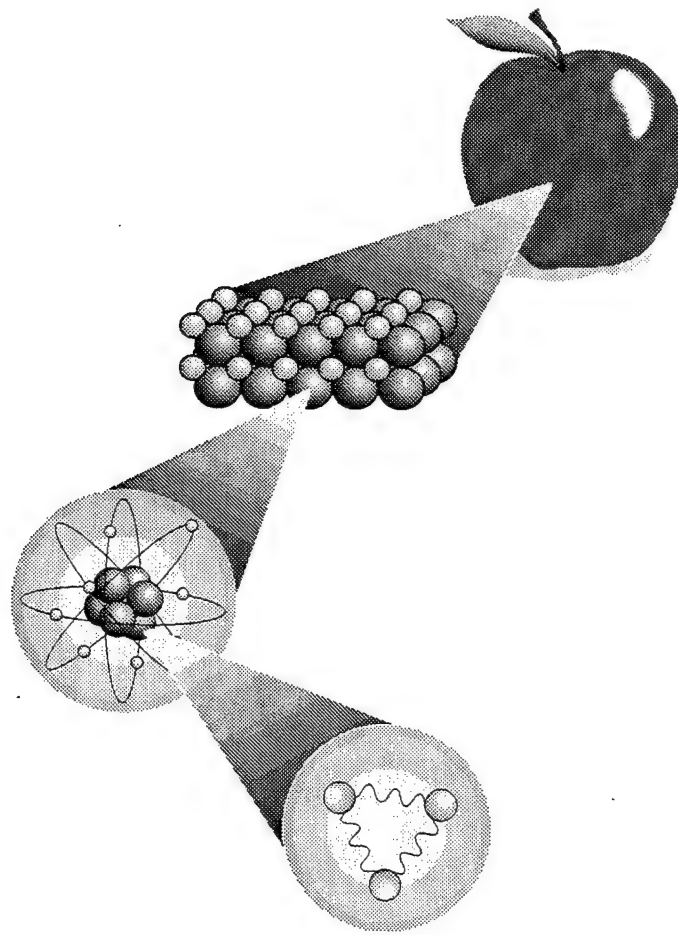


Figure 2.1: Matter is composed of atoms, which consist of electrons “orbiting” a nucleus made of protons and neutrons. These protons and neutrons are constructed from quarks, the smallest divisible piece of matter in the standard model.

of protons and neutrons (whose size is  $\approx 10^{-15}$  m), and it is the number of protons in the nucleus  $Z$  which differentiates one element from another. Eventually it was found that protons and neutrons are composed of even more elementary constituents which Gell-Mann called *quarks* [56].

Before proceeding to discuss the details of the different elementary particles we must draw a distinction between two general classifications of particles – fermions and bosons. From quantum mechanics we find that the spin of a particle (which comes in quantized units of  $\hbar/2$ ) dictates how it behaves in the presence of other particles.

In fact, particles with odd multiples of  $\hbar/2$  obey Fermi-Dirac statistics and are called *fermions*. Fermions obey the Pauli exclusion principle<sup>1</sup>, and no two of them can be in the same quantum state. In contrast, particles with even multiples of  $\hbar/2$ , called *bosons*, obey Bose-Einstein statistics and crowd into the same quantum state. As an example of this classification distinction between fermions and bosons, all matter (which consists of quarks and leptons) is composed of fermions, while particles such as photons (which constitute light) are bosons.

### 2.1.1 Fermions

As mentioned above, electrons and quarks are fermions and are considered to be elementary particles because they have no known substructure. There are actually six different species – down, up, strange, charm, bottom, top (see Table 2.1) – which can be or broken into three types or “flavors”<sup>2</sup> of quark realized in nature – down, up, strange, charm, bottom, top (see Table 2.1). To add yet more complexity, each of the quarks in can exist in three forms distinguished by the “color” quantum number associated with the strong-interaction coupling, which can take the values “red,” “blue,” or “green.” The quarks are also the only known particles to carry fractional charges<sup>3</sup>.

The electron actually belongs to a broader classification of elementary particle called *leptons* which in contrast to quarks, carry integral electric charge. While the electron is the most famous charged lepton it has two heavier cousins, the muon  $\mu$  and the tauon  $\tau$ , which are unstable and rapidly decay into the lighter electron, neutrinos, and other particles. *Neutrinos* are neutral leptons whose masses are very close to zero<sup>4</sup> and are paired with each “family” of charged lepton. The fermions

<sup>1</sup>Much more on this in future chapters.

<sup>2</sup>While particle physicists have been creative with the names of the different flavors, they have nothing to do with how a quark tastes. Flavor is just a label for another intrinsic quantity of the quark, like mass, charge or spin.

<sup>3</sup>As is the theme of this thesis, other elementary particles with fractional charge are predicted by some recent theories beyond the standard model. This will be discussed in greater detail elsewhere.

<sup>4</sup>The possible mass of the neutrino has become a very hot topic in cosmological physics and will be discussed later in the text.

(both the quarks and leptons) can be divided into three natural “generations” or “families” (see Table 2.1).

Table 2.1: Classification of Fermions (particles whose spin is odd multiples of  $\hbar/2$ ) by family.

	Generation		
	First	Second	Third
Quarks	d, u	s, c	b, t
Leptons	$e^-, \nu_e$	$\mu^-, \nu_\mu$	$\tau^-, \nu_\tau$

Thus, each generation contains two flavors of quark and two leptons. The quarks are said to possess “baryon number” of  $B = +1/3$  but zero “lepton number,” while the leptons have lepton number  $L = +1$ , but  $B = 0$ . In the standard model each particle has an associated antiparticle with the same mass but opposite quantum numbers; so there are “antileptons” like the positron  $e^+$  (with  $L = -1$ ) and “antiquarks” like the anti-down quark  $\bar{d}$  (with  $B = -1/3$ ). In all known interactions the net charge, net baryon number and net lepton number are conserved.

The structure of three different generations arises from the observation that the total number of particles in each generation is conserved in all processes. Thus, the familiar  $\mu$  decay process,  $\mu^- \rightarrow e^- \bar{\nu}_e \nu_\mu$ , is allowed, whereas decays like  $\mu^- \rightarrow e^- \bar{\nu}_e \nu_e$  or  $\tau^- \rightarrow e^- \bar{\nu}_e \nu_\mu$  are not. More detailed information on the quarks and leptons is provided in Table 2.2.

Table 2.2: Detailed information on the fundamental fermions. Data obtained from the Particle Data Group [1].

Quarks			Leptons		
Flavor	Charge $ e $	Mass $[\text{GeV}/c^2]$	Lepton	Charge $ e $	Mass $[\text{MeV}/c^2]$
d	-1/3	0.003–0.009	$e^-$	-1	0.511
u	+2/3	0.0015–0.005	$\nu_e$	0	$< 3 \times 10^{-6}$
s	-1/3	0.60–0.17	$\mu^-$	-1	105.658
c	+2/3	1.15–1.35	$\nu_\mu$	0	$< 0.19$
b	-1/3	4.0–4.4	$\tau^-$	-1	1776.77–1777.33
t	+2/3	160.8–179.4	$\nu_\tau$	0	$< 18.2$

### 2.1.2 Hadrons

In the quark model these fundamental fermions may be combined in various ways to create a wide variety of new particles called *hadrons*. Hadrons can be constructed from quarks in two ways, either as three quarks which form together to make a *baryon* or as a quark with its antiquark forming a *meson*.

In a baryon, the quarks must combine so that the resulting hadron is colorless which can only occur if each quark carries a different color. The resulting color wavefunction of the baryon is given by

$$\begin{aligned}
 B &= \frac{1}{\sqrt{6}} (q_1^R q_2^G q_3^B - q_1^G q_2^R q_3^B + \dots) \\
 &= \frac{1}{\sqrt{6}} \varepsilon_{\alpha\beta\gamma} q_1^\alpha q_2^\beta q_3^\gamma
 \end{aligned}
 \tag{2.1}$$

where  $\varepsilon_{\alpha\beta\gamma}$  is the anti-symmetric permutation tensor, and the summation convention of summing over repeated indices is implied. Similarly, the color wave function of a meson can be built from two quarks, one with a given color and the other with the

complementary color (the anti-color so to speak) resulting in a meson wave-function given by

$$\begin{aligned}
 M &= \frac{1}{\sqrt{3}} (q_1^R \overline{q_2^R} + q_1^G \overline{q_2^G} + q_1^B \overline{q_2^B}) \\
 &= \frac{1}{\sqrt{3}} q_1^\alpha \overline{q_2^\alpha}
 \end{aligned}
 \tag{2.2}$$

where here the summation convention is again assumed. A summary of the particles which can be constructed from the light quarks – up, down, and strange – is provided in Table 2.3. A much more exhaustive collection of information on the hadrons can be found in Ref [1]. Notice that there are different particles which seem to result from the same combination of quarks. For example the  $\Delta^+$  and the proton are both composed of two up quarks and a down quark. Just as the hydrogen atom, which consists of an electron plus a proton, has many different energy levels, the quarks in a hadron can bind together in different ways. The main difference arises from magnitude of the difference between the energy states of the bound system. In the hydrogen atom, the energy levels are close together, typically separated by several electron volts. In this case since the spacing in the energy levels is small compared to the rest energy of the system we consider the different states to still be “hydrogen.” In a quark system this is not the case and we typically regard them as different particles.

We should also note that since fermions are spin-1/2 and bosons are spin-1 particles, we can create a boson by creating a bound state of an even number of fermions. Thus, since baryons are made of three fermions they retain the fermion identity whereas, mesons are bosons since the sum of their spins add such that the final result is a spin-1 particle. This observation will be important in later chapters when we discuss the detailed differences between fermions and bosons and the possibility of further substructure of particles which are considered elementary in the standard model.

### 2.1.3 Bosons

As mentioned before a *boson* is a particle whose spin is an even multiple of  $\hbar/2$  and, as dictated by the symmetrization postulate, obeys Bose-Einstein statistics. Bosons

Table 2.3: Detailed information on the hadrons formed from the light quarks, up  $u$ , down  $d$ , and strange  $s$ . Data obtained from the Particle Data Group [1].

#### Baryons

Quark Content	Spin 1/2		Spin 3/2	
	Particle	mass (GeV/ $c^2$ )	Particle	mass (GeV/ $c^2$ )
$uuu$			$\Delta^{++}$	1.232
$uud$	p	0.9383	$\Delta^+$	1.232
$udd$	n	0.9396	$\Delta^0$	1.232
$ddd$			$\Delta^-$	1.232
$uus$	$\Sigma^+$	1.1894	$\Sigma^+(1385)$	1.3828
$uds$	$\Sigma^0$	1.1926	$\Sigma^0(1385)$	1.3837
	$\Lambda$	1.1157		
$dds$	$\Sigma^-$	1.1974	$\Sigma^-(1385)$	1.3872
$uss$	$\Xi^0$	1.3148	$\Xi^0(1530)$	1.5318
$dss$	$\Xi^-$	1.3213	$\Xi^-(1530)$	1.5350
$sss$			$\Omega^-$	1.6725

#### Mesons

Quark Content	Spin 0		Spin 1	
	Particle	mass (GeV/ $c^2$ )	Particle	mass (GeV/ $c^2$ )
$u\bar{d}, d\bar{u}$	$\pi^\pm$	0.13957	$\rho^\pm$	0.7693
$(u\bar{u} - d\bar{d})/\sqrt{2}$	$\pi^0$	0.13498	$\rho^0$	0.7693
$u\bar{s}, s\bar{u}$	$K^\pm$	0.49368	$K^{*\pm}$	0.8917
$d\bar{s}, s\bar{d}$	$K^0, \bar{K}^0$	0.49767	$K^{*0}, \bar{K}^{*0}$	0.8961
$(u\bar{u} + d\bar{d})/\sqrt{2}$	$\eta$	0.5473	$\omega$	0.7826
$s\bar{s}$	$\eta'$	0.9578	$\phi$	1.0194

Table 2.4: Properties of the fundamental bosons and the corresponding forces. Data is obtained from the Particle Data Group [1].

Boson	Symbol	Spin ( $\hbar$ )	Mass (GeV/ $c^2$ )	Corresponding Force
Graviton	G	2	0	Gravitation
Photon	$\gamma$	1	0	Electromagnetism
Charged weak bosons	$W^\pm$	1	80.42	Weak Force
Neutral weak boson	Z	1	91.19	Weak Force
Gluons	$g_1, \dots, g_8$	1	0	Strong Force
Higgs	H	0	$> 95.3$	

may be constructed from fermions (two particles of spin  $1/2$  add up to a particle whose total spin is 1) in which case they create a meson or they may be elementary like the gauge bosons in Table 2.4. Such particles are sometimes referred to as the messenger or force carrying particles because of their relationship to the interactions of the fundamental fermions. Discussion of the bosons is integrally related to the four forces in nature, the gravitational, electromagnetic, weak, and strong forces. In the standard model each of these forces is described by the exchange of a boson. The fundamental bosons are given in Table 2.4 and the details of their properties will be discussed in further detail in the next section.

Thus, there are a large number of different particles which can be constructed from the 12 elementary fermions (6 leptons and 6 quarks) and the 14 elementary bosons. A visual breakdown of the classifications of a particle is provided in Figure 2.2.

## 2.2 The Forces

In the standard model the fundamental fermions experience four known types of gauge interaction: gravitation, electromagnetism, and the weak and strong nuclear forces along with interactions with the Higgs bosons.

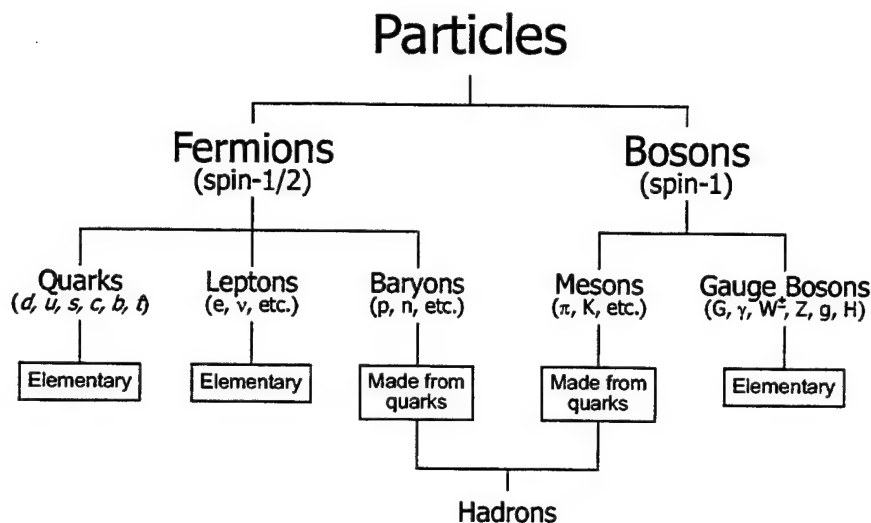


Figure 2.2: A particle can be broken up into the classifications shown in this diagram. In general a particle is either a fermion or boson depending on its spin. A hadron is a particle constructed from a composite of quarks and, depending on the number of particles involved, is either spin-1/2 (a fermion and hence called a baryon) or is either spin-1 (a boson and hence a meson). Complex nuclei are then constructed from hadrons and leptons. The other particles are the elementary quarks, leptons, and gauge bosons discussed in the text.

### 2.2.1 Gravitation

Recall that Newton's nonrelativistic theory of gravitation the potential energy between particles of mass  $m_1$  and  $m_2$  a distance  $r$  apart is given by

$$V(r) = -\frac{G_N m_1 m_2}{r} \quad (2.3)$$

where  $G_N$  is the gravitational constant given in Table 2.5. The usual dimensionless parameter used to determine the strength of the gravitational coupling  $\alpha_G$  is

$$\alpha_G = \frac{G_N m^2}{\hbar c}. \quad (2.4)$$

For an elementary particle like a proton, which is composed of two up quarks and a down quark, we find that the gravitational interaction strength is on the order of

$10^{-40}$ . This interaction is so extraordinarily small compared to the other forces applicable to single elementary particles that it may safely be neglected in most particle physics considerations. However, for macroscopic systems gravity is the dominant force because it has the unique characteristic that there is only one sign for gravitational coupling, namely that there are no negative masses which could make a collection of particles gravitationally neutral as happens with the other forces.

Table 2.5: Summary of the fundamental constants.

Constant	Symbol	Value
Gravitational constant	$G_N$	$6.67259(85) \times 10^{-11} \text{ m}^3 \text{ kg}^{-1} \text{ s}^{-2}$
Speed of light in vacuum	$c$	$2.99792458 \times 10^8 \text{ m/s}$
Planck's constant	$\hbar \equiv \frac{h}{2\pi}$	$\left\{ \begin{array}{l} 1.05457266(63) \times 10^{-34} \text{ J s} \\ 6.5821220(20) \times 10^{-16} \text{ eV s} \end{array} \right.$
Fine structure constant	$\alpha = \frac{e^2}{\hbar c}$	$\frac{1}{137.0359895(61)}$
Fermi constant	$\frac{G_F}{(\hbar c)^3}$	$1.6637(2) \times 10^{-5} \text{ GeV}^{-2}$

As a result of the requirement that mass is only positive, on large distance scales gravity, through the application of Einstein's general relativity, determines the structure of space and time. According to general relativity, gravity actually couples to the total energy which is related to mass via the well known relationship,

$$E = mc^2 \quad (2.5)$$

Putting this into Equation (2.4) we arrive at the gravitational coupling

$$\alpha_G = \frac{G_N m^2}{\hbar c} = \frac{G_N E^2}{\hbar c^5} \quad (2.6)$$

when  $E = E_P \equiv M_P c^2$  the coupling is on the order of unity.  $E_P$  is known as the Planck energy and  $M_P$  is the Planck mass and takes on the numerical value of

$$M_P \equiv \sqrt{\frac{\hbar c}{G_N}} = 1.2 \times 10^{19} \text{ GeV}/c^2 \quad (2.7)$$

where a proton mass is roughly  $1 \text{ GeV}/c^2$ . Thus, at energies close to  $10^{19} \text{ GeV}$  gravity may not be neglected.

To every mass we may attribute a characteristic length scale known as its *Compton wavelength*  $\lambda_C$  and which is given by

$$\lambda_C = \frac{h}{mc} = \frac{hc}{E} \quad (2.8)$$

In this case the Compton wavelength can be transformed into what is commonly known as the Planck length  $l_P$

$$\begin{aligned} l_P \equiv \frac{\lambda_P}{2\pi} &= \frac{h}{2\pi M_P c} \\ &= \frac{\hbar}{M_P c} \\ &= \sqrt{\frac{\hbar G_N}{c^3}} \\ &= 1.6 \times 10^{-35} \text{ m} \end{aligned} \quad (2.9)$$

Thus the Planck length is far smaller than we can observe with today's technology. Coincidentally, theoretical developments suggest that there exists a substructure even smaller than quarks. This new theory, called string or M-theory is not incorporated into the standard model and will be covered in greater detail elsewhere. In this context, M-theory postulates that the elementary particles are small n-dimensional strings (or membranes, hence the M in M-theory) whose length is on the order of the Planck length and whose different "vibrational" modes yield the observed elementary particles.

In quantum field theory, the force a mass feels is carried by the particle quanta of the radiation field in which it is immersed. For gravity, the *graviton*  $G$  is the particle

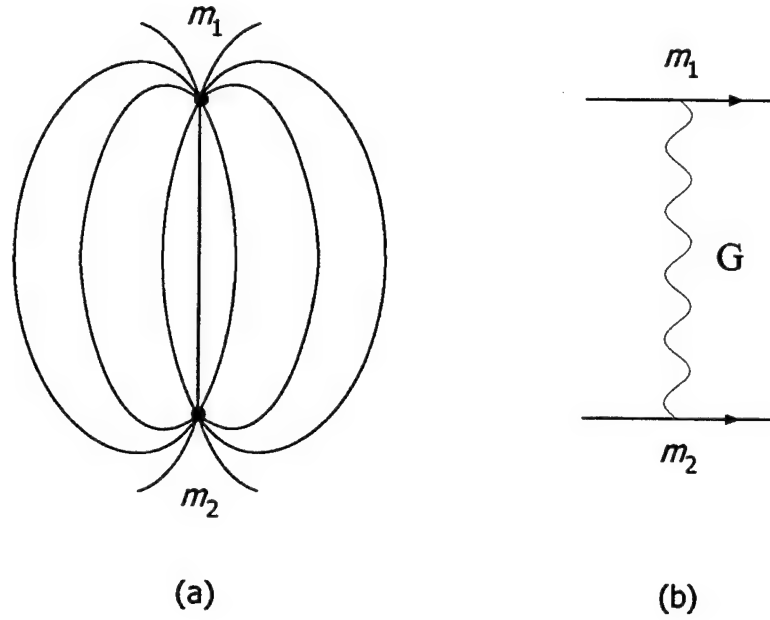


Figure 2.3: The gravitational interaction can be represented by (a) classically by lines of force or (b) as the exchange of a virtual graviton in a Feynman diagram.

which is exchanged between two masses. This interaction can be represented by lines of force as given in Figure 2.3a in the classical representation or as the exchange of a virtual graviton in a Feynman diagram given in Figure 2.3b. In a Feynman diagram time is represented progressing to the right with solid lines representing the particles and the adjoining line representing the exchange of a virtual particle, in this case a graviton. Each virtual particle is distinguished by a different line type. For example, the graviton and photon may be represented by a wiggly line, while the weak interaction bosons ( $W^\pm$  and  $Z$ ) are represented by a dashed line.

Since gravity has infinite range, these gravitons must be massless. Also in general relativity the quantum field represents fluctuations of the metric tensor  $g_{\mu\nu}$  describing space-time, which is a second rank tensor and thus the graviton must have spin 2.

### 2.2.2 Electromagnetism

According to Coulomb's law, the interaction potential between particles with charges  $Q_1$  and  $Q_2$ , separated by a distance  $r$ , is given by

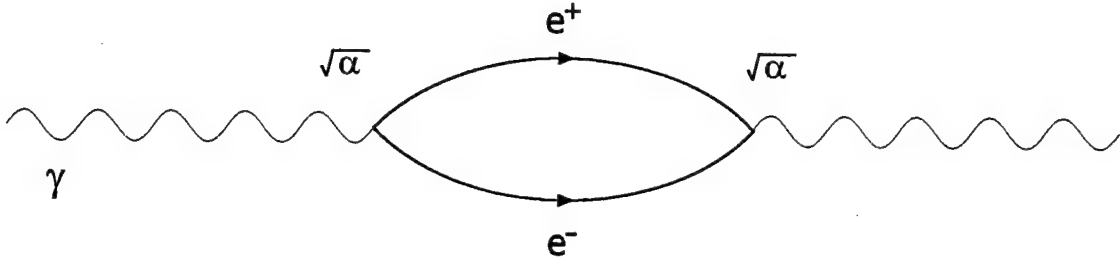


Figure 2.4: As a result of the Heisenberg uncertainty principle, virtual  $e^+e^-$  pairs are created from the vacuum with a coupling strength  $\sqrt{\alpha}$ .

$$V(r) = k \frac{Q_1 Q_2}{r} \quad (2.10)$$

where the constant  $k$  is determined by the choice of units. Just as we had a dimensionless measure of the gravitational coupling, we can express the dimensionless measure of the electromagnetic coupling, known formally as the fine structure constant  $\alpha$ , as

$$\alpha \equiv \frac{e^2}{\hbar c} \approx \frac{1}{137} \quad (2.11)$$

in Gaussian units. Although the QED coupling constant is called a “constant” it is actually depends on the distance from central charge. This effect is a direct consequence of the vacuum polarization discussed in quantum mechanics. *Vacuum Polarization* is a result of the creation of virtual particle-antiparticle pairs from the vacuum. The production of these pairs of particles is permitted by the Heisenberg uncertainty principle<sup>5</sup> for periods  $t$  less than  $\hbar/2mc^2$  (a Feynman diagram of vacuum polarization is provided in Figure 2.4). In the presence of a charged particle these particle-antiparticle pairs are polarized by the electric field due to the charge and result in an effective screening of the actual a charge (see Figure 2.5). The  $e^+e^-$  loop gives

$$\alpha(r) \approx \frac{\alpha}{1 - \frac{\alpha}{3\pi} \log \left( 1 + \frac{\hbar}{m_e r c} \right)} \quad (2.12)$$

<sup>5</sup>More discussion on the Heisenberg uncertainty principle is provided in subsequent chapters.

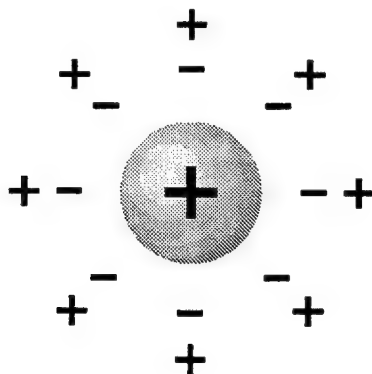


Figure 2.5: The presence of the charged particle introduces polarization of the virtual particle-antiparticle pairs produced in the vacuum. This vacuum polarization “screens” the charge and introduces a dependence on distance in the behavior of the coupling “constant.”

where  $\alpha$  is the value measured at large  $r$  (i.e.,  $r \gg \hbar/m_e c$ , the electron’s Compton wavelength). Thus, the QED coupling constant is not a constant at all<sup>6</sup>.

The quantum of the electromagnetic field is the photon  $\gamma$  which is massless because, like gravity, the electromagnetic field has infinite range. The electromagnetic interaction may also be represented with a Feynman diagram as shown in Figure 2.6. Since the photon actually represents the  $U(1)$  gauge-invariant electromagnetic potential  $A_\mu$ , which is a first rank tensor, its spin is 1. This gauge invariance ensures charge conservation and makes quantum electrodynamics (QED) a renormalizable field theory. A renormalizable theory is one whose finite number of divergences may be subtracted away leaving a finite and sensible set of field equations.

### 2.2.3 The Weak Interaction

The weak interaction is the force responsible for  $\beta$ -decay like  $n \rightarrow p e^- \bar{\nu}_e$  (given in Figure 2.7a) and is very short range. It is unique in that all quarks and leptons have the same overall coupling strength given by

<sup>6</sup>More discussion of the coupling constants will lead to suggestions of theories beyond the standard model discussed in more detail elsewhere.

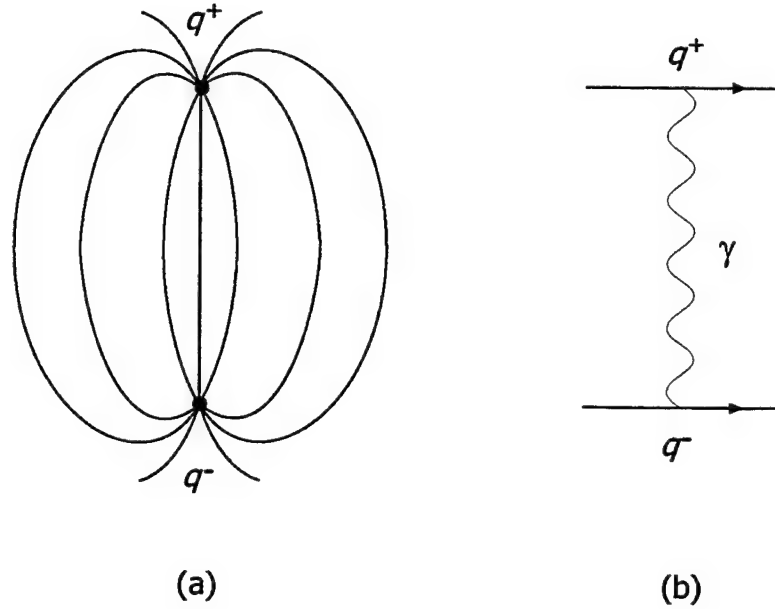


Figure 2.6: The electromagnetic interaction can be represented by (a) classically by lines of force or (b) as the exchange of a virtual photon in a Feynman diagram.

$$\alpha_W = \frac{G_F m^2 c^4}{(\hbar c)^3} \quad (2.13)$$

which is roughly  $1 \times 10^{-5}$  for a typical hadron. In comparison to the electromagnetic coupling given in Equation (2.11) it is clear why it is called the weak force. The theory of Glashow, Weinberg, and Salam states that the limited range of the force results from the fact the weak force is mediated by very massive, spin-1, vector bosons the  $W^+$ ,  $W^-$ , and  $Z$ . The weakness of the interaction is thus a result of the mass of the bosons and not the smallness of the coupling. The weak coupling was later found to be related to the electromagnetic coupling constant with the unification of the two forces – the electromagnetic and weak forces – into the theory of electroweak interactions. The relationship of the dimensionless coupling constants is

$$\alpha_W = \frac{\pi}{\sqrt{2}} \frac{m^2}{M_W^2 \sin^2 \theta_w} \alpha \quad (2.14)$$

where  $\sin^2 \theta_w = 0.230 \pm 0.005$ , and  $\theta_w$  is the Weinberg (weak) mixing angle between the electromagnetic and weak interactions.

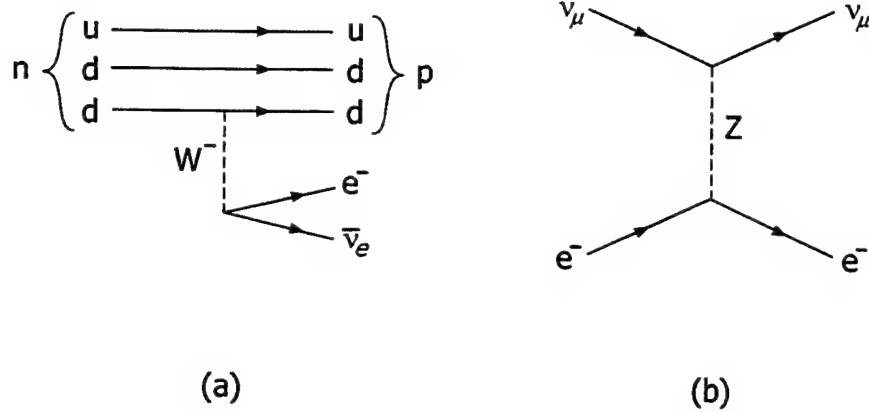


Figure 2.7: The weak interaction is responsible for (a)  $\beta$ -decay like that involved in neutron decay  $n \rightarrow p + e^- + \bar{\nu}_e$  which involves a  $W^-$  or (b) in scattering processes like  $\nu_e e^-$  scattering in which a virtual  $Z$  is exchanged.

#### 2.2.4 The Strong Interaction

The strong force binds quarks together to form hadrons and is associated with color coupling. As mentioned before there are three different color values: “red” (R), “green” (G), and “blue” (B) in the quantum chromodynamic field (QCD). The strong force is carried by gluons  $g$  and is invariant under transformations among the three colors which results in 8 different color combinations of gluon. Unlike the electromagnetic and weak forces, the gluons couple to each other since they carry color. The associated diagrams for the strong interaction are given in Figure 2.8. Like the other forces we may introduce a strong coupling constant  $\alpha_S$  given by

$$\alpha_S^0 \equiv \frac{g_S}{4\pi} \quad (2.15)$$

with coupling strength  $g_S$ . Like the electromagnetic field (QED), this constant is actually a function of distance. In fact, in QCD it actually results in antiscreening. The new strong coupling constant is then

$$\alpha_S = \frac{2\pi}{b \log\left(\frac{\hbar c}{\Lambda_{QCD} r}\right)} \quad (2.16)$$

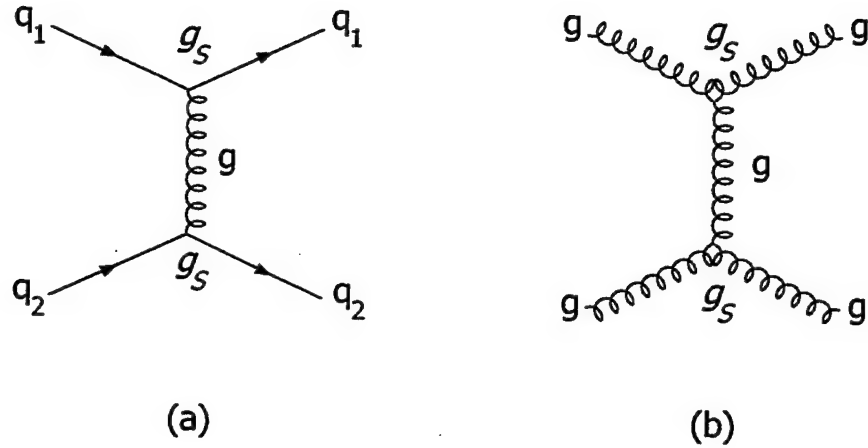


Figure 2.8: The strong interaction between two quarks is mediated by a virtual gluon with coupling strength  $g_s$  and (b) The coupling of two gluons by gluon exchange.

for  $r \ll \hbar c/\Lambda_C$ . Here  $\Lambda_C$  is the hadronic energy scale and has a value 0.2–0.3 GeV. The constant  $b$  is related to the number of colors  $N_c$  and the number of quark flavors  $N_f$  and is defined as

$$b \equiv \frac{11}{3}N_c - \frac{2}{3}N_f \quad (2.17)$$

### 2.3 Noether's Theorem

The implications of symmetries in physics was not fully understood until Noether's theorem was introduced in 1917. *Noether's theorem* states that every symmetry of nature yields a conservation law. This was a profound step providing unique insight into physical systems.

A symmetry is an operation you can perform on a system which leaves it invariant, such that the initial and final configurations are indistinguishable. As a quick example of an operation on a system consider an equilateral triangle, a square, and a circle. Each of these geometrical shapes possesses symmetries which are unique while also sharing other symmetries. Each shape, for example, possesses reflection symmetry about the broken lines shown in Figure 2.9. From the figure we see there are several reflection axes for each object: three for the triangle, four for the square and an infinite

number for the circle. Each also possesses rotation symmetry. Rotating the triangle about an axis perpendicular to the page by multiples of  $120^\circ$  all return the triangle to a configuration that is indistinguishable from the initial one. Likewise, rotating the square by multiples of  $90^\circ$  does the same. In the case of the circle, all rotations about its center leave it invariant. Thus, we see two types of symmetry manifest in this example, discrete (like the triangle and square) and continuous (like the circle). When comparing the geometrical figures we notice that the more distinctive features the figure has the fewer symmetries it possesses. Compared to the square the circle is rather featureless.

These geometrical rotation symmetries can be generalized to physics. In classical mechanics, conservation of energy and momentum arise by considering Lagrange's equation

$$\frac{d}{dt} \left( \frac{\partial L}{\partial \dot{q}_i} \right) - \frac{\partial L}{\partial q_i} = 0 \quad (2.18)$$

where  $L = \sum_i (T_i - V_i)$  is summed over the difference between the particles' kinetic ( $T_i$ ) and potential ( $V_i$ ) energies. If  $L$  is independent of all the position coordinates, or invariant with respect to spatial translations, then we obtain conservation of momentum (or angular momentum, if  $q$  is an angular coordinate). In discrete dynamics

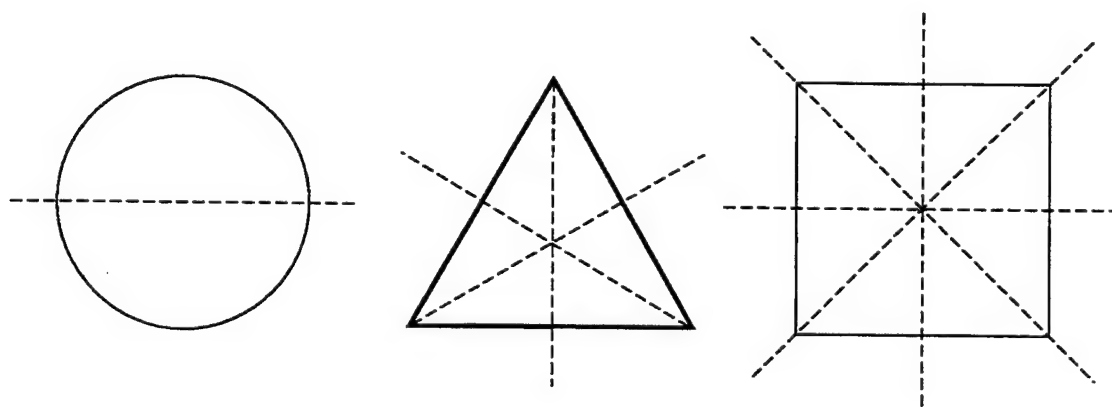


Figure 2.9: Examples of geometrical symmetries. Each object exhibits reflection symmetry about the dashed lines.

this conservation arises directly as a constant of the motion given by

$$p_i \equiv \frac{\partial L}{\partial \dot{q}_i} = \text{constant} \quad (2.19)$$

More realistically, the potential will depend on the  $q_i$ 's, but homogeneity of space dictates that the Lagrangian as a whole will remain invariant under spatial translations. In field dynamics (as opposed to the discrete dynamics example just discussed), the Lagrangian is a density and the result is a conserved current instead of a simple constant of the motion. In such cases the conserved current leads us to the concept of gauge invariance. See Table 2.6 for some of the common symmetries and their respective conservation laws.

Table 2.6: Some symmetries and their respective conservation laws.

Symmetry		Conservation Law
Spatial Translation	$\leftrightarrow$	Momentum
Rotational	$\leftrightarrow$	Angular Momentum
Time Translation	$\leftrightarrow$	Energy
Gauge Transformation	$\leftrightarrow$	Charge

The study of such symmetries is known as group theory. All symmetry operations on any system whose elements possess or include closure, identity, inverse and associative properties comprise a group. Two groups of use here are: the unitary group  $U(n)$  which is a collection of all unitary  $n \times n$  matrices (recall that a unitary matrix is one whose inverse is equal to its transpose conjugate,  $U^{-1} = \tilde{U}^*$ ) and the special unitary group  $SU(n)$  which further constrains the members of the group to unitary matrices with a determinant of 1.

## 2.4 Symmetry Breaking and the Higgs Mechanism

The best way to describe a broken symmetry is to examine a simple example from classical physics. Consider a ball placed on top of a 'Mexican hat' surface provided in Figure 2.10. This sombrero potential has the form

$$V(\phi) = -\mu^2|\phi|^2 + \lambda|\phi|^4 \quad (2.20)$$

where  $\mu$  and  $\lambda$  are arbitrary positive constants. In this position the state of the system is symmetrical under rotations about an axis which passes through the center of the sombrero. Because gravity acts vertically there is no preferred horizontal direction in the system and hence the forces are also rotationally symmetrical. However, with the ball at the top of the hat the system is unstable. When the ball is released it will roll down the surface and will eventually come to rest somewhere in the rim of the hat. The radial position of the ball is predictable while its final azimuthal angle is not. This final system configuration is stable but the rotational symmetry of the initial configuration has been broken. The actual position of the ball in the rim has no deep significance and is purely random. Yet by selecting a particular orientation

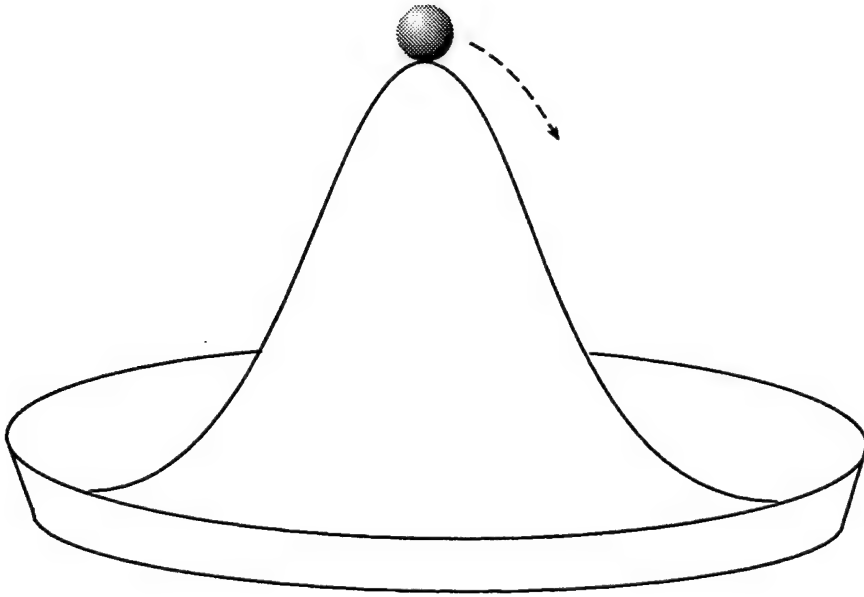


Figure 2.10: Classical example of spontaneous symmetry breaking. The ball is placed on the top of the 'Mexican hat' surface which has complete rotational symmetry. However, the configuration is unstable and the ball rolls down into the rim of the hat, coming to rest at an arbitrary point. The rotational symmetry is thus broken and the system has traded symmetry for stability.

relative to the surface, the ball ensures that the state of the system no longer reflects the symmetry of the underlying forces. This type of symmetry breaking, in which the symmetry of the underlying forces is masked by the lopsided nature of the state, is called spontaneous symmetry breaking.

In the standard model, Weinberg and Salam proposed that the  $W$  and  $Z$  particles acquire their masses through a spontaneous breaking of the underlying gauge symmetry. With this interpretation of the masses the weak force could be placed on the same footing as the electromagnetic force and the two could be given a common description. In order to introduce the masses of the  $W$  and  $Z$  and still keep the photon massless, Weinberg and Salam introduced an additional quantum field, called the Higgs field. The quanta of the Higgs field are massive spinless bosons called Higgs bosons. The effect of coupling between the Higgs field and that of the electromagnetic-weak fields is to introduce a sombrero-like potential from which the system seeks out the lowest energy quantum state corresponding to the  $W$  and  $Z$  acquiring mass.

Thus the electroweak force combines the  $U(1)$  group associated with the electromagnetic force and the  $SU(2)$  group associated with the weak force. The strong force may also be described by a gauge theory and is represented by the group  $SU(3)$ . In all, the standard model, can be summarized by the symmetry

$$\text{Gravity} + \underbrace{U(1)}_{\text{Electromagnetism}} \times \underbrace{SU(2)_L}_{\text{Weak Force}} \times \underbrace{SU(3)_C}_{\text{Strong Force}} . \quad (2.21)$$

After spontaneous breaking due to the Higgs coupling we are left with  $SU(3)_C \times U(1)_{EM}$  as exact gauge symmetries, and the gluons and the photons are massless particles.

## 2.5 For Further Reference

As mentioned briefly at the beginning of the chapter, the intention here was to provide a brief introduction of the concepts and review of the standard model. Good texts for further reference on the fundamentals of particle and high energy physics are

- David J. Griffiths, *Introduction to Elementary Particles*, John Wiley & Sons, Inc., 1987.
- Gordon Kane, *Modern Elementary Particle Physics*, Perseus Books Publishing, L.L.C., 1993.
- Donald H. Perkins, *Introduction to High Energy Physics*, Cambridge University Press, 2000.
- P.D.B Collins, A.D. Martin, and E.J. Squires, *Particle Physics and Cosmology*, John Wiley & Sons, Inc., 1989.

## CHAPTER 3. QUANTUM MECHANICS

Since we will be covering two experiments which test physics beyond the standard model, it is important we get a brief introduction to some of the principles upon which the standard model is built. Quantum mechanics is a tremendously involved and complicated subject area. As such, this chapter is intended to be used only as a quick review of those concepts which we will need in future discussions. I hope it also will provide enough background for those readers who are just being introduced to the details of the subject. Quantum mechanics has been a fundamental part of college curricula and therefore there are many concepts which I will treat as common knowledge in that I will not bother to cite specific proofs but will refer the reader to more detailed texts on the subject in general. Thus, more information or review of the concepts covered in this chapter or those beyond that which is provided here can be found in the texts by Goswami [57], Griffiths [58], Sakurai [59], Itzykson and Zuber [60], Ticiati [61], Weinberg [62, 63, 64], and Ohnuki and Kamefuchi [65].

### 3.1 Basic Principles of Quantum Theory

#### 3.1.1 Introduction

The basic premise behind quantum mechanics is that electromagnetic radiation consists of particle-like discrete bundles of energy called *photons* or *quanta*. The quantization relation for a photon's energy in terms of its angular frequency  $\omega$  is

$$E = \hbar\omega = h\nu = h\frac{c}{\lambda} \quad (3.1)$$

where  $\hbar = \frac{h}{2\pi} = 1.055 \times 10^{-34}$  J·s is *Planck's constant*,  $\nu$  is the frequency of the radiation,  $c = 2.998 \times 10^8$  m/s is the speed of light, and  $\lambda$  is the photon's wavelength. Each photon acts in an all or nothing manner and either gives up all its energy or

none of it. Since photons travel at the speed of light, their energy is entirely kinetic and from relativity we know that  $E = pc$  and thus the momentum  $p$  of each photon is

$$p = \frac{E}{c} = \frac{h\nu}{c} = \frac{h}{\lambda} \quad (3.2)$$

In terms of the wave vector  $\mathbf{k}$  the momentum is

$$\mathbf{p} = \hbar\mathbf{k} \quad (3.3)$$

It had long since been known that light behaved like a wave and this was shown with early diffraction and interference experiments. This new idea of quantization of light suggested that photons also possessed a particle-like quality. This was further supported with experimental observations (e.g. the photoelectric effect, Compton scattering) and lead to the conclusion that electromagnetic radiation exhibits a wave-particle duality. In some situations it behaves like a wave and in others like a particle.

In 1924 Louis de Broglie made a phenomenal proposition. He postulated that if electromagnetic radiation could exhibit this wave-particle duality, material objects (e.g. electrons) may also. In short he proposed that objects which were classically particle-like may also exhibit wave-like behavior. If like de Broglie, we suppose that any wave-like behavior of matter might manifest itself as a plane wave ( $\psi \propto e^{i\mathbf{k}\cdot\mathbf{x}-i\omega t}$ ) and if we guess that the energy-frequency and momentum-wavenumber relations for matter are the same as is observed for photons we arrive at the operator equation

$$P^\mu = i\hbar\partial^\mu \quad (3.4)$$

where here we are using the relativistic (four-vector) form:  $\partial^\mu \equiv \partial/\partial x_\mu = (\partial/\partial ct, -\nabla)$ . Thus,  $\mathbf{p} = -i\hbar\nabla$  and  $E = i\hbar\partial/\partial t$ . The above de Broglie relations predict a group velocity of  $\partial\omega/\partial k = pc^2/E$ , so this procedure makes physical sense if particles are thought of as wave packets.

### 3.1.2 The Dirac Notation

For practical calculations in quantum mechanics the use of Dirac notation is widely used and is extremely valuable in keeping derivations concise. Thus it is worth summarizing a few of the essential elements. The usual wave function is replaced with a state vector, conventionally written as  $\psi(\mathbf{x})$  and in Dirac notation  $|\psi\rangle$ . This state vector includes all the information about the quantum state, from the internal degrees of freedom (such as spin) to the spatial variations in the wave function. The state vectors live in a complex vector space called a *Hilbert Space*.

For state vectors in a Hilbert Space, say  $|\phi\rangle$  and  $|\psi\rangle$ , the quantity  $\eta|\phi\rangle + \xi|\psi\rangle$  is also a state vector for arbitrary complex numbers  $\eta$  and  $\xi$ . In general, state vectors possess the following qualities:

$$\begin{aligned} 1) & (\langle\psi|\phi\rangle)^* = \langle\phi|\psi\rangle \\ 2) & \langle\psi|\eta_1\phi_1 + \eta_2\phi_2\rangle = \eta_1\langle\psi|\phi_1\rangle + \eta_2\langle\psi|\phi_2\rangle \\ 3) & \langle\xi_1\psi_1 + \xi_2\psi_2|\phi\rangle = \xi_1^*\langle\psi_1|\phi\rangle + \xi_2^*\langle\psi_2|\phi\rangle \end{aligned} \tag{3.5}$$

where the  $*$  represents the complex conjugate. Here we have introduced the notion of a *bra*  $\langle\psi|$  and a *ket*  $|\psi\rangle$  (making a bracket when placed together). When placed together in this manner  $\langle\psi|\psi\rangle$  we call it an *inner product*. If the inner product between two kets is zero

$$\langle\phi|\psi\rangle = 0 \tag{3.6}$$

they are said to be orthogonal, in the similar way that the dot product between two orthogonal vectors in Euclidean space is zero. The inner product of a ket with itself generally defines the normalization of the basis. This is generally assumed to be unity, namely that

$$\langle\psi|\psi\rangle = 1 \tag{3.7}$$

In contrast we also have the *outer product* between kets given by

$$(|\psi\rangle) \cdot (\langle\phi|) = |\psi\rangle\langle\phi| \quad (3.8)$$

Whereas the inner product returns a scalar, the outer product is to be regarded as an operator or matrix. An *operator* in Hilbert space, such as  $A$ , represents an observable, like momentum or spin in the usual space. In fact we often build operators from linear combinations of outer products of basis kets. The operator generally acts on the wave function from the left. Particular instances of this are eigenfunctions of operators which return an eigenvalue when operated on. In general they are given by

$$A|\alpha\rangle = a_\alpha|\alpha\rangle \quad (3.9)$$

where  $A$  is an operator and  $a_\alpha$  is the eigenvalue corresponding to the eigenvector  $|\alpha\rangle$ . Often times the eigenvector is represented as a state vector with the eigenvalue ket. For example we usually define the eigenvalue in Equation (3.9) such that  $\alpha \equiv a_\alpha$  resulting in,

$$A|\alpha\rangle = \alpha|\alpha\rangle \quad (3.10)$$

From Equation (3.10) it may be observed that operators behave like matrices acting on a vector. Thus one of the most common calculations performed in quantum mechanics is to evaluate the matrix element for an operator. The expression for this in both Dirac and the usual notation is given by

$$\langle 1|A|2\rangle = \int \psi_1^*(\mathbf{x}) A \psi_2(\mathbf{x}) d^3x \quad (3.11)$$

Here the inner product results in the actual matrix element itself.

Another important definition is that of the Hermitian conjugate of an operator  $A^\dagger$  and is defined easily in Dirac notation as

$$\langle\phi|A|\psi\rangle^* \equiv \langle\psi|A^\dagger|\phi\rangle \quad (3.12)$$

where  $A^*$  denotes the complex conjugate. Using this relation twice displays that we may think of a bracket as arising either from  $A$  operating to the right, or  $A^\dagger$  operating to the left. Basically

$$\langle \phi | A | \psi \rangle = \langle \phi | A \psi \rangle \quad (3.13)$$

or

$$\begin{aligned} \langle \phi | A | \psi \rangle &= \langle \psi | A^\dagger | \phi \rangle^* \\ &= \langle A^\dagger \phi | \psi \rangle \end{aligned} \quad (3.14)$$

A Hermitian operator is also a unique operator and has the property that  $A^\dagger = A$ . Thus

$$\begin{aligned} \langle n | A | n \rangle^* &= \langle n | A | n \rangle \\ \Rightarrow a_n^* &= a_n \end{aligned} \quad (3.15)$$

and the eigenvalues are real. A similar statement can be made if the eigenvalues are non-degenerate

$$\langle n | A | m \rangle^* = \langle m | A | n \rangle \Rightarrow a_m^* \langle m | n \rangle = a_n \langle m | n \rangle \quad (3.16)$$

therefore the eigenfunctions are orthogonal and can thus be defined to be orthonormal,  $\langle m | n \rangle = \delta_{mn}$ . If a set of eigenfunctions are orthonormal they are said to form a complete set since any other state function may be expanded in terms of them. An example would be

$$\begin{aligned} |\psi\rangle &= \sum_{\alpha} c_{\alpha} |\alpha\rangle \\ \langle\psi| &= \sum_{\alpha} c_{\alpha}^* \langle\alpha| \\ c_{\alpha} &= \langle\alpha|\psi\rangle \end{aligned} \quad (3.17)$$

Applying this expansion to two states  $|\psi\rangle = \sum_{\alpha} c_{\alpha} |\alpha\rangle$  and  $|\phi\rangle = \sum_{\alpha} d_{\alpha} |\alpha\rangle$  we can see that the bracket between them is

$$\begin{aligned}
\langle \phi | \psi \rangle &= \sum_{\alpha} d_{\alpha}^* c_{\alpha} \\
&= \sum_{\alpha} \langle \phi | \alpha \rangle \langle \alpha | \psi \rangle
\end{aligned}
\tag{3.18}$$

This equation must be true for all states and thus we deduce the completeness relation

$$\sum_{\alpha} |\alpha\rangle \langle \alpha| = 1 \tag{3.19}$$

which is used widely in solving problems in quantum mechanics.

### 3.1.3 Orbital and Spin Angular Momentum

Starting with a classical picture of angular momentum consider the dynamical motion of the earth in its orbit around the sun. The earth's overall angular momentum may be broken into two general forms: orbital angular momentum (typically given by  $rmv$ ) associated with its annual revolution around the sun, and spin angular momentum (given by  $I\omega$ ) associated with its daily rotation about the north-south axis. In a similar manner the total angular momentum of an electron in a hydrogen atom also possesses both orbital and spin angular momentum but with our distinctive quantum mechanical twist. In the classical (macroscopic) case of the sun-earth system the fundamental distinction between these two kinds of angular momenta is not that profound. In fact, the spin angular momentum of the earth is nothing more than the sum of the "orbital" angular momentum of all the rocks and dirt in their daily "orbit" around the spin axis. In the standard model of particle physics the electron is considered a true point particle and this analogy breaks down. In short the spin angular momentum is an intrinsic property of the particle itself.

Classically there are no restrictions on the values or accuracy to which we measure the components of the orbital angular momentum vector  $\mathbf{L} = \mathbf{r} \times m\mathbf{v}$ . In quantum mechanics this is not the case in part due to the Heisenberg Uncertainty Principle which states that for any pair of observables whose corresponding operators do not commute there exists a quantum uncertainty between the them. For example, the uncertainty principle for the position  $x$  and momentum  $p_x$  is provided by the inequality

$$\Delta x \Delta p_x \geq \frac{\hbar}{2} \quad (3.20)$$

In short, a measurement of  $L_x$  inevitably alters the value of  $L_y$  by an unpredictable amount. We are in fact limited to measurements of the magnitude of  $\mathbf{L}$  (actually in practice we measure its square:  $L^2 = \mathbf{L} \cdot \mathbf{L}$ ), with one of the components (of which, in practice, we take to be the  $z$  component,  $L_z$ ). Because the measurement of an observable like  $L^2$  and  $L_z$  places the system in an eigenstate,  $|\psi(\mathbf{x}, t)\rangle$ , with certain allowed eigenvalues, a measurement of  $L^2$  on the state vector yields

$$L^2|\psi(\mathbf{x}, t)\rangle = l(l+1)\hbar^2|\psi(\mathbf{x}, t)\rangle \quad (3.21)$$

where  $l$  is a nonnegative integer such that

$$l = 0, 1, 2, 3, \dots \quad (3.22)$$

For a given value of  $l$ , a measurement of  $L_z$  always gives a result of the form

$$L_z|\psi(\mathbf{x}, t)\rangle = m_l\hbar|\psi(\mathbf{x}, t)\rangle \quad (3.23)$$

where  $m_l$  is an integer in the range  $[-l, +l]$

$$m_l = -l, -l+1, \dots, -1, 0, +1, \dots, l-1, l \quad (3.24)$$

with  $(2l+1)$  possibilities in all.

The same goes for spin angular momentum: A measurement of  $S^2 = \mathbf{S} \cdot \mathbf{S}$  can only return

$$S^2|\psi(\mathbf{x}, t)\rangle = s(s+1)\hbar^2|\psi(\mathbf{x}, t)\rangle \quad (3.25)$$

In the case of spin, however, the quantum number  $s$  can be a half-integer as well as an integer

$$l = 0, \frac{1}{2}, 1, \frac{3}{2}, 2, \frac{5}{2}, \dots \quad (3.26)$$

Table 3.1: Classification of particles by spin.

Bosons(integer spin)		Fermions(1/2-integer spin)	
Spin 0	Spin 1	Spin 1/2	Spin 3/2
—	Mediators	Quarks, leptons	—
Pseudo-scalar mesons	Vector mesons	Baryon octet	Baryon decuplet

For a given value of  $s$ , a measurement of  $S_z$  always gives a result of the form

$$S_z|\psi(\mathbf{x}, t)\rangle = m_s\hbar|\psi(\mathbf{x}, t)\rangle \quad (3.27)$$

where  $m_s$  is an integer or half integer (which ever  $s$  is) in the range  $[-s, +s]$

$$m_s = -s, -s + 1, \dots, -1, 0, +1, \dots, s - 1, s \quad (3.28)$$

with  $(2s + 1)$  possibilities in all.

Like classical mechanics, a given particle can assume any orbital angular momentum state, however in the standard model the value of  $s$  is fixed for each type of particle. We call  $s$  the “spin” of the particle. Particles with half-integer spin are known as *fermions*—protons, electrons, quarks, etc. are fermions (basically the building blocks for all matter); particles with integer spin are known as *bosons*—the photon, gluon, and mesons are bosons (see Table 3.1).

### 3.2 Schrödinger, Klein-Gordon, and Dirac Equations

We now pause to recall that the equations governing the behavior of a particle is directly related to their spin. As a result we make the following distinctions: In non-relativistic quantum mechanics particles are described by the *Schrödinger* equation whereas in relativistic quantum mechanics particles of spin 0 are described by the *Klein-Gordon* equation, particles of spin 1/2 by the *Dirac* equation, and particles of spin 1 by the *Proca* equation.

### 3.2.1 The Schrödinger Equation

In classical mechanics the sum of the kinetic energy ( $\frac{1}{2}m\mathbf{v}^2 = \mathbf{p}^2/2m$ ) and the potential energy ( $V(\mathbf{x})$ ) is a constant for conservative forces, resulting in a total energy  $E$  given by

$$\frac{\mathbf{p}^2}{2m} + V = E \quad (3.29)$$

As mentioned in the introduction the momentum  $\mathbf{p}$  may be replaced by the *momentum operator*

$$\mathbf{p} \rightarrow \frac{\hbar}{i} \nabla \quad \text{where} \quad \left( p_x \rightarrow \frac{\hbar}{i} \frac{\partial}{\partial x}, p_y \rightarrow \frac{\hbar}{i} \frac{\partial}{\partial y}, p_z \rightarrow \frac{\hbar}{i} \frac{\partial}{\partial z} \right) \quad (3.30)$$

and energy by the operator

$$E \rightarrow i\hbar \frac{\partial}{\partial t} \quad (3.31)$$

Equation (3.29) becomes a collection of derivatives which act on the “wave function”  $\Psi(x, y, z, t)$ :

$$\left( -\frac{\hbar^2}{2m} \nabla^2 + V \right) \Psi = i\hbar \frac{d\Psi}{dt} \quad (3.32)$$

Which is the time-dependent Schrödinger equation. The solution ( $\Psi$ ) describes a particle of mass  $m$  in the presence of a specified potential energy function  $V$ . The wave function is normalized by the condition that the integral over all space of the probability of finding the particle is unity, namely that

$$\int |\Psi|^2 d^3x = 1 \quad (3.33)$$

where  $|\Psi(x, y, z, t)|^2 dx dy dz$  is the probability of finding the particle in the volume element  $d^3x \equiv dx dy dz$ , at time  $t$ .

Notice that the wave function must be complex. This is because the differential operator involved is a mixture of real spatial derivatives and an imaginary time

derivative. For the time-independent version of the above equation the wave function can be real.

### 3.2.2 The Klein-Gordon Equation

The Klein-Gordon equation may be obtained in exactly the same way, except this time we begin with the relativistic energy-momentum relation,  $E^2 - \mathbf{p}^2 c^2 = m^2 c^4$ , or in four-vector notation

$$P^\mu P_\mu - m^2 c^2 = 0 \quad (3.34)$$

To simplify the “derivation” we will assume the particles are *free* and there is no subsequent potential energy term. In four-vector notation Equations (3.30) and (3.31) don’t require any modifications and they become

$$P_\mu \rightarrow i\hbar \partial_\mu \quad (3.35)$$

where we have the following usual definitions

$$\partial_\mu \equiv \frac{\partial}{\partial x^\mu} \text{ where } \partial_0 = \frac{1}{c} \frac{\partial}{\partial t}, \quad \partial_1 = \frac{\partial}{\partial x}, \quad \partial_2 = \frac{\partial}{\partial y}, \quad \partial_3 = \frac{\partial}{\partial z} \quad (3.36)$$

Inserting Equation (3.36) into (3.34), and letting the derivatives act on a wave function  $\Psi$ , we obtain the Klein-Gordon equation

$$\begin{aligned} -\hbar^2 \partial^\mu \partial_\mu \Psi - m^2 c^2 \Psi &= 0 \\ \Rightarrow -\frac{1}{c^2} \frac{\partial^2 \Psi}{\partial t^2} + \nabla^2 \Psi &= \left( \frac{mc}{\hbar} \right)^2 \Psi \end{aligned} \quad (3.37)$$

Schrödinger apparently discovered this equation before the nonrelativistic one that bears his name but rejected it because at the time it was incompatible with the statistical interpretation of  $\Psi$ .

There are a few things to notice about the Klein-Gordon equation. Notice that the equation is second order in time and the conserved quantity associated with  $\Psi$  is no longer constrained to only positive values.

### 3.2.3 The Dirac Equation

Dirac solved the problems associated with the Klein-Gordon equation by insisting that a relativistic wave equation should be linear with time. Relativity also requires that it should be linear in spatial derivatives also leading to the following general form

$$H|\Psi\rangle = i\hbar|\dot{\Psi}\rangle \quad \text{where} \quad H = c(\boldsymbol{\alpha} \cdot \mathbf{p}) + \beta mc^2 \quad (3.38)$$

where  $\alpha$  and  $\beta$  are vector and scalar components. Inserting this Hamiltonian into the relativistic energy-momentum relation gives the following conditions for consistency:

$$\begin{aligned} \beta^2 &= 1 \\ \{\beta, \alpha_i\} &= 0 \\ \{\alpha_i, \alpha_j\} &= 2\delta_{ij} \end{aligned} \quad (3.39)$$

The fact that these relations involve *anticommutators*  $\{a, b\} \equiv ab + ba$  seems bad news from the point of view of obtaining a simple wave equation. As a result,  $\alpha$  and  $\beta$  must be interpreted as operators whose existence reveals a new internal degree of freedom.

We must search for matrices which represent these operators. A simple counting of the number of equations to be satisfied by four Hermitian matrices shows that the smallest viable candidates must be  $4 \times 4$ . The most common is the Dirac representation given by

$$\beta = \begin{pmatrix} I & 0 \\ 0 & -I \end{pmatrix} \quad \alpha_i = \begin{pmatrix} 0 & \sigma_i \\ \sigma_i & 0 \end{pmatrix} \quad (3.40)$$

where we have used the conventional definition of the *Pauli spin matrices*,

$$\sigma_1 = \begin{pmatrix} 0 & 1 \\ 1 & 0 \end{pmatrix}, \quad \sigma_2 = \begin{pmatrix} 0 & -i \\ i & 0 \end{pmatrix}, \quad \sigma_3 = \begin{pmatrix} 1 & 0 \\ 0 & -1 \end{pmatrix} \quad (3.41)$$

These represent the algebra of the  $J = \hbar/2$  angular momentum operator and obey the anticommutation relation  $\{\sigma_i, \sigma_j\} = 2\delta_{ij}$ . To use this matrix representation, the wave function must be represented by a column vector known as a *spinor*.

We may put this into a more compact form by introducing a new set of matrices known as the *gamma matrices* defined by

$$\gamma^0 \equiv \beta, \quad \gamma^i \equiv \beta\alpha_i \quad (3.42)$$

From the anticommutation relations between the  $\alpha$  and  $\beta$  matrices, the gamma matrices obey

$$\{\gamma^\mu, \gamma^\nu\} = 2g^{\mu\nu}. \quad (3.43)$$

where  $g^{\mu\nu}$  is the *metric tensor* given by

$$g = \begin{pmatrix} 1 & 0 & 0 & 0 \\ 0 & -1 & 0 & 0 \\ 0 & 0 & -1 & 0 \\ 0 & 0 & 0 & -1 \end{pmatrix} \quad (3.44)$$

Using the gamma matrices and recalling the de Broglie operator relation  $P_\mu = i\hbar\partial_\mu$ , the Dirac equation becomes

$$(\gamma^\mu P_\mu - mc)\Psi = 0. \quad (3.45)$$

Notice that the wave function  $\Psi$  in the Dirac equation is a four-element column matrix called a Dirac spinor<sup>1</sup>.

### 3.3 Review of Quantum Field Theory

#### 3.3.1 Introduction

Since quantum mechanics was developed from the observed existence of the energy quantization of light and as a good review of the principles associated with gauge

<sup>1</sup>Although a Dirac spinor has four elements it is *not* a four-vector.

fields I will outline the case of electromagnetism from which many points may be generalized to other fields.

### 3.3.2 Field Expansion

We begin by assuming the field may be described by a set of Fourier expansion coefficients

$$\mathbf{A} = \frac{1}{\sqrt{V}} \sum_{\mathbf{k}, \alpha} \left[ c \epsilon^{(\alpha)} e^{i(\mathbf{k} \cdot \mathbf{x} - \omega t)} + c^* \epsilon^{(\alpha)} e^{-i(\mathbf{k} \cdot \mathbf{x} - \omega t)} \right] \quad (3.46)$$

The allowed wave number values are determined by choosing *harmonic boundary conditions* for the expansion. This makes the field periodic on the scale of a box of length  $L$  producing equations of the form  $k_x = 2n\pi/L$ . To arrive at the properties of free space we take the limit  $L \rightarrow \infty$ . The expansion coefficients  $c$  are functions of the wavenumber  $\mathbf{k}$  and  $\alpha$ , the index labeling the polarization, which is described by the two orthogonal unit vectors  $\epsilon^{(1)}$  and  $\epsilon^{(2)}$ . The normalization factor  $1/\sqrt{V}$  (where  $V = L^3$  is the box volume) is chosen for later convenience. The Hamiltonian of the system is

$$\begin{aligned} H &= \frac{1}{2} \int (B^2 + E^2) dV \\ &= \frac{1}{2} \int [(\nabla \times \mathbf{A})^2 + (\dot{\mathbf{A}})^2] dV \end{aligned} \quad (3.47)$$

where we have the following for a representative Fourier term

$$\begin{aligned} (\nabla \times \mathbf{A})_k &= c i \mathbf{k} \times \epsilon^{(\alpha)} e^{i(\mathbf{k} \cdot \mathbf{x} - \omega t)} - c^* i \mathbf{k} \times \epsilon^{(\alpha)} e^{-i(\mathbf{k} \cdot \mathbf{x} - \omega t)} \\ \mathbf{k} \times \epsilon^{(1)} &= k \epsilon^{(2)} \quad \text{etc.} \end{aligned} \quad (3.48)$$

Thus we see most cross terms integrate to zero, either because of the orthogonality of the polarization vectors or because of the harmonic boundary conditions,  $k_x = 2n\pi/L$ , so that  $\int e^{i\Delta \mathbf{k} \cdot \mathbf{x}} dV = 0$  unless  $\Delta \mathbf{k} = 0$ . We then find that each half of the Hamiltonian gives the same result (which we require for radiation), so that the total is

$$H = \sum_{\mathbf{k}, \alpha} \omega^2 (cc^* + c^*c). \quad (3.49)$$

Since the amplitudes  $c$  and  $c^*$  are constants, we have a Hamiltonian that is explicitly independent of time. However, we could equally well have performed the analysis with time-dependent coefficients  $c_{new} = c_{old}e^{-i\omega t}$ , in which we would obtain the same equation for  $H$ , but with a new  $c$ . If we define new variables  $q$  and  $p$  by

$$\begin{aligned} q &= \frac{c + c^*}{\sqrt{m}} \\ p &= -i\omega\sqrt{m}(c - c^*) \end{aligned} \quad (3.50)$$

and the Hamiltonian becomes

$$H = \sum \left( \frac{p^2}{2m} + \frac{1}{2}m\omega^2 q^2 \right). \quad (3.51)$$

Which is the Hamiltonian for a set of simple harmonic oscillators. We can prove this by applying the familiar *Hamiltonian's equations of motion*

$$\begin{aligned} \frac{\partial H}{\partial q} &= -\dot{p} \\ \frac{\partial H}{\partial p} &= \dot{q} \end{aligned} \quad (3.52)$$

These imply the relations  $\dot{p} = -m\omega^2 q$  and  $p = m\dot{q}$ , so that  $p$  and  $q$  look like the momentum and position coordinates for a particle of unit mass in a quadratic potential. In fact, if we consider reinterpreting  $q_i$  and  $p_i$  as quantum-mechanical operators satisfying the *canonical commutation relations*

$$[q_i, p_j] = i\hbar\delta_{ij} \quad (3.53)$$

$$[q_i, q_j] = [p_i, p_j] = 0$$

and combine them with what is known as the *Heisenberg equation of motion*

$$i\hbar \frac{dA}{dt} = [A, H] \quad (3.54)$$

(where  $A$  is some arbitrary observable and  $H$  is the Hamiltonian as previously defined) we arrive at the usual Euler-Lagrange equations of motion that follow from the classical Lagrangian,  $L$ .

### 3.3.3 Simple Harmonic Motion

Often times a field may be represented as a collection of an infinite number of simple harmonic oscillators with different frequencies. We will follow conventional discussion of most text books by analyzing what is known as a bosonic oscillator. The Bosonic oscillator behaves like a classical simple harmonic oscillator and thus provides a good introduction to the Fermionic oscillator.

#### The Bosonic Oscillator

The classical Lagrangian  $L$  for such an oscillator is given by

$$L = \frac{1}{2}m\dot{q}^2 - \frac{1}{2}kq^2 \quad (3.55)$$

Applying the standard substitutions, namely that  $p \equiv m\dot{q}$  and  $\omega = \sqrt{k/m}$  we obtain the Hamiltonian (which we derived in the preceding section from different constructs)

$$H = \frac{p^2}{2m} + \frac{1}{2}m\omega^2 q^2 \quad (3.56)$$

To make the transition to quantum mechanics, we simply invoke the *correspondence principle* which states that any new theory in physics must reduce to the well-established classical theory when it is applied under the circumstances in which the less general theory is known to hold. Thus we first assume the Euler-Lagrange equation and the Hamiltonian are valid in quantum theory. Then, by inserting  $A = q, p$  into the Heisenberg equation of motion (Equation (3.54)), we obtain the following commutation relations

$$\begin{aligned} [q, H] &= ip \\ [p, H] &= -iq \end{aligned} \quad (3.57)$$

It is common to replace  $q$  and  $p$  with the non-hermitian *annihilation* and *creation* operators  $a$  and  $a^\dagger$  respectively

$$a = \sqrt{\frac{m\omega}{2\hbar}} \left( q + \frac{ip}{m\omega} \right) \quad (3.58)$$

$$a^\dagger = \sqrt{\frac{m\omega}{2\hbar}} \left( q - \frac{ip}{m\omega} \right)$$

These operators are often called ladder operators for reasons which will soon become apparent. Rearranging these equations for  $p$  and  $q$  and then plugging into the Hamiltonian defined above (Equation (3.56)) gives us the familiar form

$$\begin{aligned} H &= \frac{\hbar\omega}{2} (aa^\dagger + a^\dagger a) \\ &= \hbar\omega \left( N + \frac{1}{2} \right) \end{aligned} \quad (3.59)$$

We have also introduced the conventional definition of the *number operator*  $N \equiv a^\dagger a$ . The number operator is Hermitian because of the property  $(AB)^\dagger = B^\dagger A^\dagger$  and thus we may label states by the real eigenvalues of  $N$ :

$$N|n\rangle = n|n\rangle \quad (3.60)$$

Using the canonical commutation relations in Equation (3.53) we obtain

$$[a, a^\dagger] = \left( \frac{1}{2\hbar} \right) (-i[q, p] + i[p, q]) = 1 \quad (3.61)$$

The commutator of  $a$  and  $a^\dagger$  gives the following commutators:

$$\begin{aligned} [a, N] &= a \\ [a^\dagger, N] &= -a^\dagger \end{aligned} \quad (3.62)$$

This shows that  $a$  and  $a^\dagger$  may be considered *annihilation* and *creation* operators, which respectively lower or raise  $n$  by one unit

$$\begin{aligned} Na^\dagger|n\rangle &= (n+1)a^\dagger|n\rangle \Rightarrow a^\dagger|n\rangle \propto |n+1\rangle \\ Na|n\rangle &= (n-1)a|n\rangle \Rightarrow a|n\rangle \propto |n-1\rangle \end{aligned} \quad (3.63)$$

We then apply the normalization condition of the wavefunction, namely  $\langle an|an \rangle = 1 = \langle n|N|n \rangle$ , where  $|an \rangle$  stands for  $a|n \rangle$ , and the last step follows from the definition of the Hermitian conjugate,  $\langle m|a|n \rangle^* \equiv \langle n|a^\dagger|m \rangle$ , to obtain the relations for the impact of the lowering and raising operators on the state  $|n \rangle$

$$\begin{aligned} a|n \rangle &= \sqrt{n}|n-1 \rangle \\ a^\dagger|n \rangle &= \sqrt{n+1}|n+1 \rangle \end{aligned} \quad (3.64)$$

which shows us there must be a ground state at  $n=0$ :  $a|0 \rangle$  produces the empty set, and  $n$  cannot be lowered further. The state  $|0 \rangle$  is often referred to as the *vacuum state*. This terminology may be rather misleading since the vacuum is rarely empty, but actually corresponds to a state without excitations in any of the normal modes of the field. This procedure of splitting a wave field into oscillators and quantizing them via a fundamental commutator works for other fields in general.

Finally, as a preview of some of the issues related to possible small violations of the symmetrization postulate (and hence the Pauli exclusion principle) we notice that these bosonic raising and lowering operators also satisfy trilinear commutations. One such example would be

$$aaa^\dagger - a^\dagger aa = 2a \quad (3.65)$$

In order to lead into our discussion of a Fermi-like oscillator we want to now generalize some of the definitions we made above. If we define  $N'$  such that

$$\begin{aligned} H &= \frac{\hbar\omega}{2} (aa^\dagger + a^\dagger a) \\ &\equiv \hbar\omega N' \end{aligned} \quad (3.66)$$

Comparing with Equation (3.59) we see  $N' = N + N_0$  and as there exists a minimum  $N_0$  which was  $1/2$  before. This then implies that the spectrum of  $N'$  is of the form

$$N'_n = n + N_0 \quad (3.67)$$

where  $n = 0, 1, 2, \dots$  and the relations in Equation (3.62) hold as before. Combining Equations (3.66) and (3.67) leads us to the relation

$$n + N_0 = \frac{1}{2} (|a_{n-1,n}|^2 + |a_{n,n+1}|^2) \quad (3.68)$$

We can then solve this starting from  $n = 0$  and proceeding to successively higher  $n$  we find that

$$a_{n,n+1} = a_{n+1,n}^\dagger = \begin{cases} \sqrt{2N_0 + n} & \text{for } n = \text{even} \\ \sqrt{1 + n} & \text{for } n = \text{odd} \end{cases} \quad (3.69)$$

From this we obtain the following general expression for the commutator  $[a, a^\dagger]$  given in Equation (3.61)

$$\langle n|[a, a^\dagger]|m\rangle = \delta_{nm} \times \begin{cases} 2N_0 & \text{for } n = \text{even} \\ 2(1 - N_0) & \text{for } n = \text{odd} \end{cases} \quad (3.70)$$

Thus we see we arrive at the previous result of Equation (3.61) for the case when  $N_0 = 1/2$ .

Let us finally also introduce a set of operators defined by

$$\begin{aligned} J_1 &\equiv \frac{1}{4}(aa + a^\dagger a^\dagger) \\ J_2 &\equiv \frac{1}{4}(aa - a^\dagger a^\dagger) \\ J_3 &\equiv \frac{1}{4}(a^\dagger a + aa^\dagger) = \frac{1}{2}N' \end{aligned} \quad (3.71)$$

Using Equation (3.70) above we can show these operators satisfy the following commutation relations:

$$\begin{aligned} [J_1, J_2] &= -iJ_3, \\ [J_2, J_3] &= iJ_1, \\ [J_3, J_1] &= iJ_2. \end{aligned} \quad (3.72)$$

which are precisely the Lie commutation relations for the generators of the group  $SO(2,1)$ , the three-dimensional Lorentz group.

### The Fermionic Oscillator

Unlike the Bosonic oscillator, there is no classical analog to the Fermionic oscillator and as such we then need to define it. With the Fermi-like oscillator we still retain all of the concepts required to set up the Bose-like oscillator in that Equations (3.55)–(3.58) still hold. What does change however is our functional form of the Hamiltonian

$$\begin{aligned} H &= \frac{\hbar\omega}{2} (a^\dagger a - a a^\dagger) \\ &\equiv \hbar\omega N' \end{aligned} \quad (3.73)$$

In a fashion similar to what was done at the end of the previous section we introduce a set of operators with the following definitions:

$$\begin{aligned} J_1 &\equiv \frac{1}{2}(a^\dagger + a) \\ J_2 &\equiv \frac{1}{2i}(a^\dagger - a) \\ J_3 &\equiv \frac{1}{2}(a^\dagger a - a a^\dagger) = N' \end{aligned} \quad (3.74)$$

and we find from Equations (3.73) and (3.62) that they satisfy

$$\begin{aligned} [J_1, J_2] &= iJ_3, \\ [J_2, J_3] &= iJ_1, \\ [J_3, J_1] &= iJ_2. \end{aligned} \quad (3.75)$$

which are the Lie commutation relations for the generators of the group  $SO(3)$ , the three-dimensional rotation group. In this case, the operator  $N' = J_3$  has  $(p+1)$  eigenvalues like  $-p/2, -p/2+1, \dots, p/2-1, p/2$  (which are those of the irreducible representation  $D_{p/2}$ ). Again the operator  $N$  is defined by

$$N \equiv N' - N_0, \quad \text{with } N_0 = -\frac{p}{2} \leq 0 \quad (3.76)$$

which has the spectrum required of the number operator, namely  $0, 1, 2, \dots, p$ . The matrix representations for  $a$  and  $a^\dagger$  can then be derived from the  $J_i$ 's. Like the case for the Bosonic oscillator, we may choose the appropriate phases of the eigenstates  $|n\rangle$  of  $N$  such that we obtain

$$a_{n,n+1} = a_{n+1,n}^\dagger = \sqrt{(n+1)(p-n)} \quad (3.77)$$

for  $n = 0, 1, 2, \dots, p$ . The resulting commutation relations governing the raising and lowering operators may then be derived from this result. For example,  $p = 0$  leads to the trivial result of  $a = a^\dagger = N' = 0$ . Interestingly,  $p = 1$  leads to the Pauli spin matrices given by Equation (3.41). The corresponding operators  $a$  and  $a^\dagger$  satisfy the familiar anticommutation relations

$$\begin{aligned} \{a, a^\dagger\} &= 1, \\ \{a, a\} &= \{a^\dagger, a^\dagger\} = 0 \end{aligned} \quad (3.78)$$

which correspond to the ordinary Fermionic oscillator. However, the story doesn't end there. For  $p = 2$  the operators  $a$  and  $a^\dagger$  no longer follow the common bilinear commutation relations but rather satisfy tri-linear commutation relations like

$$\begin{aligned} a^3 &= 0, \\ aa^\dagger a &= 2a, \\ aaa^\dagger + a^\dagger aa &= 2a \end{aligned} \quad (3.79)$$

From these relations we may show that  $N \equiv N' + 1$  has the spectrum  $0, 1, 2$ . Thus we see that there is an upper bound on the spectrum for  $N$  which allows us to think of this as a kind of generalization of the ordinary Fermionic oscillator. In fact, the zero-point energy of a Fermi-like oscillator is given by  $\hbar\omega N_0 = -\hbar\omega p/2 \leq 0$ . Also we note the symmetry of the basic relations which remain unchanged under the transformation:  $a \rightarrow a^\dagger, a^\dagger \rightarrow a, N' \rightarrow -N'$ . Bose-like oscillators do not possess this property.

### Simple Harmonic Oscillator Conclusions

The raising and lowering operators greatly simplify our lives. Allow me to provide a brief example. Before the introduction of these operators we would attack a problem by evaluating the Schrödinger equation

$$H\Psi(x, t) = i\hbar \frac{\partial \Psi}{\partial t} \quad (3.80)$$

Breaking up the spatial and time parts of the wave function, we represent the wave function with

$$\Psi(x, t) = \phi(x)e^{-iEt/\hbar} \quad (3.81)$$

which leads us to the time independent equation

$$\left( -\frac{\hbar^2}{2m} \frac{d^2}{dx^2} + \frac{m\omega}{\hbar} x^2 - \frac{2E}{\hbar\omega} \right) \phi(x) = 0 \quad (3.82)$$

which through a change of variables  $\left( \xi = \sqrt{\frac{m\omega}{\hbar}} x \right)$  is made into the Weber equation

$$\frac{d^2\psi}{d\xi^2} + \left( \frac{2E}{\hbar\omega} - \xi^2 \right) \phi(\xi) = 0 \quad (3.83)$$

We solve Weber's Equation with  $\phi(\xi) = e^{-\xi^2/2} V(\xi)$  which leads to the Hermite Equation given by

$$\frac{d^2V(\xi)}{d\xi^2} - 2\xi \frac{dV(\xi)}{d\xi} + 2nV(\xi) = 0 \quad (3.84)$$

The solution to the Hermite Equation above are the Hermite polynomials whose generating function is given by

$$e^{-t^2+2tx} = \sum_{n=0}^{\infty} \frac{H_n(x)t^n}{n!} \quad (3.85)$$

In our solution the  $V(\xi)$  are the Hermite polynomials. We must also exercise the proper orthogonality condition

$$\int_{-\infty}^{+\infty} dx H_n(x) H_m(x) e^{-x^2} = \delta_{nm} \sqrt{\pi} 2^n n! \quad (3.86)$$

to arrive at the final solution for the wave function. The Hermite polynomials are given by

$$\begin{aligned} H_0(\xi) &= 1, \\ H_1(\xi) &= 2\xi, \\ H_2(\xi) &= 4\xi^2 - 2, \\ H_3(\xi) &= 8\xi^3 - 12\xi, \\ H_4(\xi) &= 16\xi^4 - 48\xi^2 + 12, \\ &\vdots \end{aligned} \quad (3.87)$$

Finally, we arrive at the solution for the wave function

$$\begin{aligned} \phi(x) &= C_n H_n(\xi) e^{-\xi^2/2} \\ &= \frac{1}{\pi^{1/4} \sqrt{2^n n!}} \frac{1}{x_0^{n+1/2}} \left( x - x_0^2 \frac{\partial}{\partial x} \right) e^{-x^2/2x_0^2} \end{aligned} \quad (3.88)$$

with  $x_0 = \sqrt{\frac{\hbar}{m\omega}}$  which is known as the characteristic length.

With ladder operators this process is much simpler. We simply start from the idea that  $a|0\rangle = 0 \Rightarrow \langle x|a|0\rangle = 0$  and plug in our expression for  $a$  in terms of  $x$  and  $p$  given in Equation (3.58)

$$\sqrt{\frac{m\omega}{2\hbar}} \langle x| \left( x + \frac{ip}{m\omega} \right) |0\rangle = 0 \quad (3.89)$$

where we have used the usual definition for the momentum  $p = -i\hbar\nabla$ . Expanding and putting in the definition for  $x_0$  we get

$$\begin{aligned} \left( x + x_0^2 \frac{\partial}{\partial x} \right) \langle x|0\rangle &= 0 \\ \Rightarrow \left( x + x_0^2 \frac{\partial}{\partial x} \right) \phi_0(x) &= 0 \end{aligned} \quad (3.90)$$

Which is a first order equation in this formalism! Even though the Schrödinger equation is second order. The solution to this equation is the familiar Gaussian given by

$$\phi_0(x) = Ce^{\frac{1}{2}\left(\frac{x}{x_0}\right)^2} \quad (3.91)$$

To get the constant  $C$  we employ the normalization condition

$$\int_{-\infty}^{+\infty} |Ce^{\frac{1}{2}\left(\frac{x}{x_0}\right)^2}|^2 dx = 1 \quad (3.92)$$

$$\Rightarrow C = \frac{1}{\sqrt{x_0}} \frac{1}{\pi^{1/4}}$$

This leads us to the final equation for  $\phi_0(x)$

$$\phi_0(x) = \frac{1}{\sqrt{x_0}} \frac{1}{\pi^{1/4}} e^{\frac{1}{2}\left(\frac{x}{x_0}\right)^2} \quad (3.93)$$

From here all the other wave functions naturally follow by just allowing the raising operator to operate on the ground state wave function,  $\phi_0(x)$ . For example,

$$\begin{aligned} \phi_1(x) &= \langle x|1\rangle \\ &= \langle x|a^\dagger|0\rangle \\ &= \sqrt{\frac{m\omega}{2\hbar}} \langle x| \left(x - \frac{ip}{m\omega}\right) |0\rangle \\ &= \left(x - x_0^2 \frac{\partial}{\partial x}\right) \langle x|0\rangle \\ &= \text{const} \left[ 2xe^{\frac{1}{2}\left(\frac{x}{x_0}\right)^2} \right] \end{aligned} \quad (3.94)$$

Which gives us the same result as the conventional method of solving the Schrödinger equation but much more quickly and without needing to invoke the use of Hermite polynomials. This method also permits much more conceptual power when generalizing to more complicated systems.

### 3.4 For Further Reference

Clearly this has been a very quick summary of a very wide spread and extensive field. Since these fundamentals can be found in a wide array of textbooks we refer the reader to those with a more detailed account of the materials contained in this chapter. The following books would allow more developed discussions of these topics:

- Amit Goswami, *Quantum Mechanics*, Wm. C. Brown Publishers, 1997.
- David J. Griffiths, *Introduction to Quantum Mechanics*, Prentice-Hall, Inc., 1995.
- Jun John Sakurai, *Modern Quantum Mechanics*, Addison-Wesley Publishing Company, Inc., 1994.
- Claude Itzykson and Jean-Bernard Zuber, *Quantum Field Theory*, McGraw-Hill Inc., 1980.
- Robin Ticciati, *Quantum Field Theory for Mathematicians*, Cambridge University Press, 1999.
- Steven Weinberg, *The Quantum Theory of Fields I: Foundations*, Cambridge University Press, 1995.
- Steven Weinberg, *The Quantum Theory of Fields II: Modern Applications*, Cambridge University Press, 1996.
- Yoshio Ohnuki and Susumu Kamefuchi, *Quantum Field Theory and Parastatistics*, University of Tokyo Press, 1982.

## CHAPTER 4. IDENTICAL PARTICLES AND THE PAULI EXCLUSION PRINCIPLE

### 4.1 Symmetrization Postulate

When quantum mechanics is applied to identical particles we are led to one of the most fundamental concepts of modern physics, the Pauli exclusion principle. In systems of identical particles we observe the unique effects of quantum mechanics applied to such interactions. In classical mechanics we can keep track of identical particles by actually following their trajectories while in quantum mechanics identical particles are indistinguishable from each other. In short, we cannot attach a unique label to each particle.

#### 4.1.1 The Permutation Operator

In quantum mechanics we are unable to follow the particles' trajectories because position measurements would need to be made at every instant in time which disturbs the system. In fact we are unable to distinguish the difference between the two potential trajectories given in Case 1 and 2 of Figure 4.1.

Now consider two particles with wave functions  $|k'\rangle_1$  and  $|k''\rangle_2$  such that their combined wave function  $|\Psi(1, 2)\rangle$  is given by

$$|\Psi(1, 2)\rangle = |k'\rangle_1 |k''\rangle_2 \quad (4.1)$$

where the subscripts 1 and 2 denote which particle the wave function belongs to. As such since they are identical we may interchange their labels resulting in the trivial result that

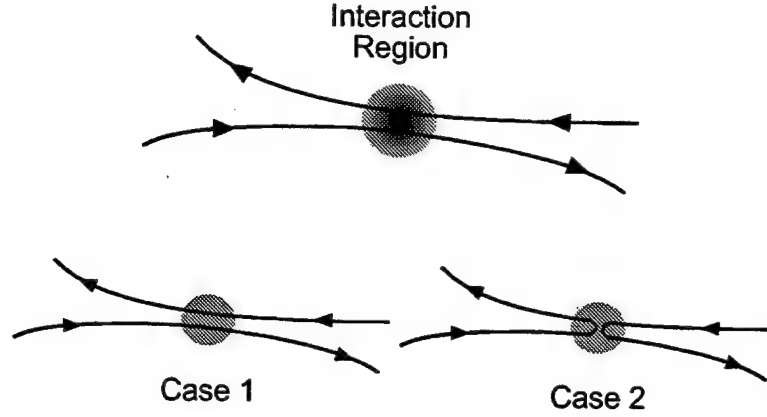


Figure 4.1: In an interaction involving identical particles the particle trajectories in the interaction region are unknown. Thus, the actual paths of the particles could be either Case 1 or Case 2.

$$\begin{aligned} |\Psi(2, 1)\rangle &= |k'\rangle_2 |k''\rangle_1 \\ &= |k''\rangle_1 |k'\rangle_2 \end{aligned} \quad (4.2)$$

We now introduce the Permutation operator such that when it operates on a wave function it effectively interchanges the two particles and is defined as

$$\begin{aligned} P_{12} |k'\rangle_1 |k''\rangle_2 &= |k'\rangle_2 |k''\rangle_1 \\ &= |k''\rangle_1 |k'\rangle_2 \end{aligned} \quad (4.3)$$

The permutation operator also has the property that if it operates twice on the system it returns the system back to its original state and that it also respects the exchange degeneracy that the labels of 1 and 2 are arbitrary. These are summarized by

$$\begin{aligned} 1) \quad &P_{12}^2 = 1 \\ 2) \quad &P_{12} = P_{21} \\ 3) \quad &P_{12}^{-1} P_{12} = 1 \end{aligned} \quad (4.4)$$

The permutation operator has eigenstates given by the following

$$P_{12}|p\rangle = p|p\rangle \quad (4.5)$$

as is usually done in eigenvector equations like this. Using the properties discussed above we solve for the eigenvalues with

$$\begin{aligned} P_{12}^2|p\rangle &= P_{12}(P_{12}|p\rangle) \\ &= P_{12}(p|p\rangle) \\ &= p^2|p\rangle \end{aligned} \quad (4.6)$$

but  $P_{12}^2 = 1$  from Equation (4.4) above

$$\begin{aligned} 1|p\rangle &= p^2|p\rangle \\ \therefore p &= \pm 1 \end{aligned} \quad (4.7)$$

This result that the permutation operator eigenvalues are  $\pm 1$  is very important for future discussions and is one of the most elegant features of this quantum mechanical formulation.

#### 4.1.2 Permutation Symmetry

Lets now consider a wave function  $|\Psi_{\pm}\rangle$  such that

$$|\Psi_{\pm}\rangle = \frac{1}{\sqrt{2}} \{ |k'\rangle_1 |k''\rangle_2 \pm |k''\rangle_1 |k'\rangle_2 \} \quad (4.8)$$

Notice that if we allow the permutation operator operate on  $|\Psi_{+}\rangle$  we get

$$\begin{aligned}
P_{12}|\Psi_+\rangle &= P_{12} \left[ \frac{1}{\sqrt{2}} \{ |k'\rangle_1 |k''\rangle_2 + |k''\rangle_1 |k'\rangle_2 \} \right] \\
&= \frac{1}{\sqrt{2}} \{ P_{12} |k'\rangle_1 |k''\rangle_2 + P_{12} |k''\rangle_1 |k'\rangle_2 \} \\
&= \frac{1}{\sqrt{2}} \{ |k'\rangle_2 |k''\rangle_1 + |k''\rangle_2 |k'\rangle_1 \} \\
&= \frac{1}{\sqrt{2}} \{ |k''\rangle_1 |k'\rangle_2 + |k'\rangle_1 |k''\rangle_2 \} \\
&= |\Psi_+\rangle
\end{aligned} \tag{4.9}$$

A wave function which behaves this way when operated upon by the permutation operator is said to be *symmetric* because it is invariant with respect to the exchange of particles 1 and 2. In contrast, let's consider,

$$\begin{aligned}
P_{12}|\Psi_-\rangle &= P_{12} \left[ \frac{1}{\sqrt{2}} \{ |k'\rangle_1 |k''\rangle_2 - |k''\rangle_1 |k'\rangle_2 \} \right] \\
&= \frac{1}{\sqrt{2}} \{ P_{12} |k'\rangle_1 |k''\rangle_2 - P_{12} |k''\rangle_1 |k'\rangle_2 \} \\
&= \frac{1}{\sqrt{2}} \{ |k'\rangle_2 |k''\rangle_1 - |k''\rangle_2 |k'\rangle_1 \} \\
&= \frac{1}{\sqrt{2}} \{ |k''\rangle_1 |k'\rangle_2 - |k'\rangle_1 |k''\rangle_2 \} \\
&= -|\Psi_-\rangle
\end{aligned} \tag{4.10}$$

A wave function with the characteristic that it changes sign when operated upon by the permutation operator is said to be *antisymmetric* with respect to the exchange of particles 1 and 2. The relevancy of this discussion will be apparent in a few moments.

We also want to emphasize another characteristic of the permutation operator. Let us begin by defining operators  $A_1$  and  $A_2$  which operate only on the part of the wave function pertaining to particle 1 and 2 respectively.

$$A_1|a'\rangle_1|a''\rangle_2 = a'|a'\rangle_1|a''\rangle_2 \quad (4.11)$$

$$A_2|a'\rangle_1|a''\rangle_2 = a''|a'\rangle_1|a''\rangle_2$$

Here the wavefunctions are eigenvectors of the  $A$  operators. Notice that because the  $A$ 's only apply to the corresponding particles  $A_2$  commutes with the eigenvector  $|a\rangle_1$  and thus can effectively be moved past the eigenvector of the first particle leaving it to operate on the second eigenvector only. The primes in these equations allow us to distinguish that the eigenvectors for the two particles do not necessarily have the same eigenvalues. Now lets apply the permutation operator to the  $A_1$  eigenvector equation to arrive at

$$\begin{aligned} P_{12}A_1|a'\rangle_1|a''\rangle_2 &= P_{12}a'|a'\rangle_1|a''\rangle_2 \\ &= a'P_{12}|a'\rangle_1|a''\rangle_2 \\ &= a'|a'\rangle_2|a''\rangle_1 \\ &= a'|a''\rangle_1|a'\rangle_2 \\ &= A_2|a''\rangle_1|a'\rangle_2 \end{aligned} \quad (4.12)$$

However we also notice that if we apply condition 3 of Equation (4.4) this also gives rise to the following

$$\begin{aligned}
P_{12}A_1|a'\rangle_1|a''\rangle_2 &= P_{12}A_1(P_{12}^{-1}P_{12})|a'\rangle_1|a''\rangle_2 \\
&= (P_{12}A_1P_{12}^{-1})P_{12}|a'\rangle_1|a''\rangle_2 \\
&= (P_{12}A_1P_{12}^{-1})|a'\rangle_2|a''\rangle_1 \\
&= (P_{12}A_1P_{12}^{-1})|a''\rangle_1|a'\rangle_2
\end{aligned} \tag{4.13}$$

Thus by equating Equations (4.12) and (4.13) we arrive at the following result

$$A_2 = P_{12}A_1P_{12}^{-1} \tag{4.14}$$

This has profound implications. To check this result consider the simplest non-trivial case, a Helium atom. Since the two electrons in the He atom are identical, the energy of the system (and hence the Hamiltonian) must be invariant under the interchange of the two particles. Basically, the real result cannot depend on how we label the electrons and  $H_{12} = H_{21}$ . Using Equation (4.14) above

$$H_{21} = P_{12}H_{12}P_{12}^{-1} \tag{4.15}$$

Applying the idea that  $H_{12} = H_{21}$  and multiplying through by  $P_{12}$  on the right we obtain the result that

$$\begin{aligned}
H_{12}P_{12} &= P_{12}H_{12} \\
\Rightarrow [P_{12}, H] &= 0
\end{aligned} \tag{4.16}$$

Since the Hamiltonian commutes with the permutation operator then energy eigenstates are also  $P_{12}$  eigenstates. This is an extremely important result.

The arguments have worked thus far for a two particle system. In such a case it is simple to construct both symmetric and antisymmetric wave functions involving both particles but what about more complicated systems? To investigate this concept further lets consider the wave function made up of three particles  $|k'\rangle_1|k''\rangle_2|k'''\rangle_3$ . We

also introduce the 3 particle permutation operator  $P_{123}$  which lets  $1 \rightarrow 2$ ,  $2 \rightarrow 3$ , and  $3 \rightarrow 1$ . Thus

$$\begin{aligned}
 P_{123}|\Psi(123)\rangle &= P_{123}|k'\rangle_1|k''\rangle_2|k'''\rangle_3 \\
 &= |k'\rangle_2|k''\rangle_3|k'''\rangle_1 \\
 &= |k'''\rangle_1|k'\rangle_2|k''\rangle_3 \\
 &= |\Psi(231)\rangle
 \end{aligned} \tag{4.17}$$

We may notice that these permutations form the group  $S_3$  with the following elements:

$$\begin{aligned}
 1) \ I : 1 \rightarrow 1, 2 \rightarrow 2, 3 \rightarrow 3 : I|\Psi(123)\rangle &= |\Psi(123)\rangle \\
 2) \ P_{12} : 1 \rightarrow 2, 2 \rightarrow 1, 3 \rightarrow 3 : P_{12}|\Psi(123)\rangle &= |\Psi(213)\rangle \\
 3) \ P_{13} : 1 \rightarrow 3, 2 \rightarrow 2, 3 \rightarrow 1 : P_{13}|\Psi(123)\rangle &= |\Psi(321)\rangle \\
 4) \ P_{23} : 1 \rightarrow 1, 2 \rightarrow 3, 3 \rightarrow 2 : P_{23}|\Psi(123)\rangle &= |\Psi(132)\rangle \\
 5) \ P_{123} : 1 \rightarrow 2, 2 \rightarrow 3, 3 \rightarrow 1 : P_{123}|\Psi(123)\rangle &= |\Psi(231)\rangle \\
 6) \ P_{132} : 1 \rightarrow 2, 2 \rightarrow 3, 3 \rightarrow 1 : P_{132}|\Psi(123)\rangle &= |\Psi(312)\rangle
 \end{aligned} \tag{4.18}$$

As with any group, elements of the group can be constructed from operations among the elements themselves. For example,

$$\begin{aligned}
 P_{12}P_{23}|\Psi(123)\rangle &= P_{12}|\Psi(132)\rangle \\
 &= |\Psi(231)\rangle \\
 &= P_{123}|\Psi(123)\rangle
 \end{aligned} \tag{4.19}$$

$$\Rightarrow P_{12}P_{23} = P_{123}$$

Because we have the identical particles there exists a sixfold exchange degeneracy and we construct a wavefunction which is in general given by

$$\begin{aligned}
|\Psi_{\pm}\rangle = \frac{1}{\sqrt{6}} \{ & |k'\rangle_1 |k''\rangle_2 |k'''\rangle_3 \pm |k'\rangle_1 |k'''\rangle_2 |k''\rangle_3 \\
& |k''\rangle_1 |k'''\rangle_2 |k'\rangle_3 \pm |k''\rangle_1 |k'\rangle_2 |k'''\rangle_3 \\
& |k'''\rangle_1 |k'\rangle_2 |k''\rangle_3 \pm |k'''\rangle_1 |k''\rangle_2 |k'\rangle_3 \}
\end{aligned} \tag{4.20}$$

These are simultaneous eigenkets of  $P_{12}$ ,  $P_{13}$ , and  $P_{23}$  as shown in the elements of  $S_3$  in Equation (4.18). Only one of these is the symmetric case and one is the antisymmetric one. All the others have no permutation symmetries. We may obtain the symmetric case by inspection recalling that if any of the terms were negative it could not be symmetric and therefore the symmetric case is represented by replacing each  $\pm$  in Equation (4.20) with a  $+$ , we will also prove that  $|\Psi_{-}\rangle$  is the antisymmetric wave function.

In general the antisymmetric case is more complicated. To get the purely antisymmetric case we need to use the *Slater determinant* in which we use the determinant given in terms of the function

$$\bar{f}_1 = (f_{k'}(\bar{x}_1), f_{k''}(\bar{x}_1), f_{k'''}(\bar{x}_1)) \tag{4.21}$$

where similar expressions for  $\bar{f}_2$  and  $\bar{f}_3$  also exist. The Slater determinate [66] is then given by

$$\begin{aligned}
|\Psi(123)\rangle &= \frac{1}{\sqrt{6}} \begin{vmatrix} f_{k'}(\bar{x}_1) & f_{k'}(\bar{x}_2) & f_{k'}(\bar{x}_3) \\ f_{k''}(\bar{x}_1) & f_{k''}(\bar{x}_2) & f_{k''}(\bar{x}_3) \\ f_{k'''}(\bar{x}_1) & f_{k'''}(\bar{x}_2) & f_{k'''}(\bar{x}_3) \end{vmatrix} \\
&= \frac{1}{\sqrt{6}} \bar{f}_1 \cdot (\bar{f}_2 \times \bar{f}_3)
\end{aligned} \tag{4.22}$$

We notice that this result produces an antisymmetric result under the exchange of particles 2 and 3, basically,

$$\begin{aligned}
P_{23}|\Psi(123)\rangle &= P_{23} [\bar{f}_1 \cdot (\bar{f}_2 \times \bar{f}_3)] \\
&= \bar{f}_1 \cdot (\bar{f}_3 \times \bar{f}_2) \\
&= -\bar{f}_1 \cdot (\bar{f}_2 \times \bar{f}_3) \\
&= -|\Psi(123)\rangle
\end{aligned} \tag{4.23}$$

In our case  $f_{k'}(\bar{x}_1) = |k'\rangle_1$  which means that we represent each of the  $f$ s in Equation (4.22) by

$$\begin{aligned}
\bar{f}_1 &= (|k'\rangle_1, |k''\rangle_1, |k'''\rangle_1) \\
\bar{f}_2 &= (|k'\rangle_2, |k''\rangle_2, |k'''\rangle_2) \\
\bar{f}_3 &= (|k'\rangle_3, |k''\rangle_3, |k'''\rangle_3)
\end{aligned} \tag{4.24}$$

Thus we finally arrive at the wave function which is anti-symmetric with respect to the exchange of particles 2 and 3 (as defined by the Slater determinant)

$$\begin{aligned}
|\Psi(123)\rangle_{antisymm} &= \frac{1}{\sqrt{6}} \{ |k'\rangle_1 |k''\rangle_2 |k'''\rangle_3 - |k'\rangle_1 |k'''\rangle_2 |k''\rangle_3 \\
&\quad |k''\rangle_1 |k'''\rangle_2 |k'\rangle_3 - |k''\rangle_1 |k''\rangle_2 |k'''\rangle_3 \\
&\quad |k'''\rangle_1 |k'\rangle_2 |k''\rangle_3 - |k'''\rangle_1 |k''\rangle_2 |k'\rangle_3 \}
\end{aligned} \tag{4.25}$$

Thus we see that this reduces to  $|\Psi_1\rangle$  of Equation (4.20).

In general however, it would be possible to construct a wave function which does not possess any permutation symmetry. In the example of three particles above there is only one completely antisymmetric case and one completely symmetric case. So why is the particular permutation symmetry of the wave function such a big deal?

If the wave function possesses permutation symmetry then it is an eigen function of the permutation operator. For a general wave function this is not necessarily the case as we have seen from the discussion above. However, since we know the permutation operator commutes with the Hamiltonian the wavefunctions we derive must possess permutation symmetry. This observational result that real systems are eigenfunctions of the permutation operator is called the *symmetrization postulate*.

## 4.2 Spin-Statistics Theorem

When identical particles interact with each other they interact via a set of rules which are derived from statistical mechanics. This set of rules is in general different for each type of particle and is called the statistics of the particle. The statistics of a particle is derived by the application of statistics and probability theory to the system of interest. There are many different formulations of statistics which we may derive based on the underlying probability theory of how the particles behave around one another. One common example derived from classical physics is the Maxwell-Boltzmann distribution which is used to describe a large collection of particles (like a gas) and gives you a function which provides you with the ability to calculate the probability of finding a particle in the collection which has a given set of characteristics (speed, energy, etc.). The Maxwell-Boltzmann distribution function, which is proportional to the probability that a particle will be found in the state  $(v_x, v_y, v_z)$ , is given by

$$\begin{aligned} F_{MB} &= N \left( \frac{m}{2\pi kT} \right)^{3/2} e^{-m(v_x^2 + v_y^2 + v_z^2)/2kT} \\ &= N \left( \frac{m}{2\pi kT} \right)^{3/2} e^{-E/kT} \end{aligned} \tag{4.26}$$

where  $N$  is the total number of particles,  $m$  is the mass of each particle,  $k$  is the Boltzmann constant, and  $T$  is the absolute temperature. This area of physics is directly related to thermodynamics and good summaries of this may be found in the books by Wilde and Singh [67] or the recent book by Phillis [68].

In fact there exist a wide range of quantum statistical formulations governing the behavior of identical particles. Some of the more prevalent are the well known Bose-Einstein statistics and Fermi-Dirac statistics, along with the more obscure parastatistics, quon or infinite statistics, orthostatistics, null statistics, or Gentile statistics, to name a few. Curiously, the statistics that a particle obeys is related to the spin of the particle. The relationship between the statistics and particle spin is known as the *Spin-Statistics Connection*.

While there are many different statistics available for us to use in describing particles, the discussion of the symmetrization postulate above shows us that only particles whose wave functions are eigenstates of the permutation operator are realized in nature. These two symmetry states are represented by Bose-Einstein and Fermi-Dirac statistics and govern all known processes involving identical particles.

In order to see this let us observe a few things about a particle's spin. Recalling our discussion of spin, we may differentiate between two classifications – spin which is even or odd multiples of  $\hbar/2$  (where  $\hbar$  is Planck's constant). Particles with an integral amount of spin (even multiples of  $\hbar/2$ ) are called Bosons and obey Bose-Einstein statistics while particles with half-integer spin (odd multiples of  $\hbar/2$ ) are called Fermions since they obey Fermi-Dirac statistics.

Bose-Einstein statistics apply to a system composed of a large number of weakly interacting, identical and indistinguishable particles, each possessing an integral spin. The distribution function  $F_{BE}$  for a system in equilibrium is given by

$$F_{BE} = \frac{1}{e^{\alpha} e^{E_i/kT} - 1} \quad (4.27)$$

and gives the average number of bosons at temperature  $T$  that will be found in a particular state with energy  $E_i$ . Here  $k$  is the Boltzmann constant and for systems of bosons whose numbers are not conserved (like photons)  $\alpha = 0$ .

In contrast, Fermi-Dirac statistics apply to systems of particles whose spin is half-integral. In a system of fermions in equilibrium at the absolute temperature  $T$ , the expected number of particles in a particular state  $i$  with energy  $E_i$  is given by

$$\begin{aligned} F_{FD} &= \frac{1}{e^{\alpha} e^{E_i/kT} + 1} \\ &= \frac{1}{e^{(E_i - E_f)/kT} + 1} \end{aligned} \quad (4.28)$$

where  $E_f = -kT\alpha$  is the Fermi energy and is a characteristic of the system being described. Since all matter we come into contact with on a regular basis is made of fermions and since our experiment on possible violations of the Pauli principle

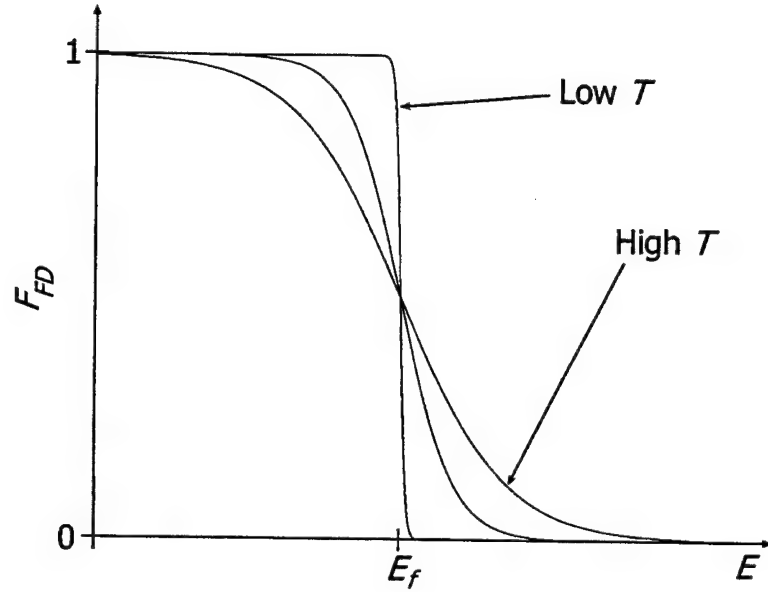


Figure 4.2: The Fermi-Dirac distribution function goes to 1 for very low-energy states and to 0 for high-energy states. It equals  $1/2$  for a state with the Fermi energy,  $E_f$ , falling off suddenly for low  $T$  and gradually for high  $T$ .

also deals with fermions it is useful to observe a plot of the Fermi-Dirac distribution function (see Figure 4.2). Notice the sharp cutoff in the distribution at the Fermi energy. In each case –  $F_{MB}$ ,  $F_{BE}$ , and  $F_{FD}$  – the distribution function does not give the number of particles with energy  $E_i$  but rather the number of particles occupying the state  $i$  which has an energy  $E_i$ .

### 4.3 The Pauli Exclusion Principle

Thus, as a result of the symmetrization postulate as applied to the spin-statistics connection, electrons (which are spin- $1/2$  particles) obey Fermi-Dirac statistics. In Fermi-Dirac statistics no two particles may occupy the same quantum state which results in the law that no two electrons may be in precisely the same quantum mechanical state simultaneously. For example if we let the two electrons be in the same state then  $|k'\rangle = |k''\rangle = |k\rangle$  in Equation (4.8) and for the antisymmetric case

$$|\Psi(12)\rangle = \frac{1}{\sqrt{2}} \{ |k\rangle_1 |k\rangle_2 - |k\rangle_1 |k\rangle_2 \} = 0 \quad (4.29)$$

resulting in a zero probability that they will both be in the same quantum state. This rule that no two electrons may be in the same quantum state is known as the *Pauli exclusion principle* and is responsible for the entire structure of the periodic table. This is because each energy level in an atom has a limited number of allowable quantum states. Since no two electrons may be in the same state we are led to the Aufbau Principle and are forced to sequentially fill from the lowest energy level up to higher levels, giving us the atomic energy level structure evident in the periodic table.

#### 4.4 Implications of the Symmetrization Postulate

Thus, the application of the symmetrization postulate to the spin-statistics connection yields the famous Pauli exclusion principle. This whole discussion on permutation symmetry can be summed up in the following

$$\begin{aligned} P_{ij}|N \text{ identical bosons}\rangle &= +|N \text{ identical bosons}\rangle \\ P_{ij}|N \text{ identical fermions}\rangle &= -|N \text{ identical fermions}\rangle \end{aligned} \quad (4.30)$$

where  $P_{ij}$  is the permutation operator that interchanges the  $i$ th and  $j$ th particles where  $i$  and  $j$  are arbitrary. It is an empirical fact that a mixed symmetry does not occur and further discussion of an experiment proving this fact is described in **Part II**.

Now is an appropriate time to comment on a result which came to the forefront of theoretical discussions in the early 1980s. We notice from the result that the Hamiltonian and permutation operator commute we may write

$$\begin{aligned} P_{12}(H|\Psi_{\pm}) &= H(P_{12}|\Psi_{\pm}) \\ &= H(\pm|\Psi_{\pm}) \\ &= \pm(H|\Psi_{\pm}) \end{aligned} \quad (4.31)$$

If we recall from our previous chapter on quantum mechanics that

$$H|\Psi_{\pm}\rangle = i\hbar \frac{\partial}{\partial t} |\Psi_{\pm}\rangle \quad (4.32)$$

Thus,  $H$  cannot change the permutation symmetry of the wave function  $|\Psi_{\pm}\rangle$  because it doesn't change the sign of the wave function like the permutation operator does. This is ultimately because the Hamiltonian is invariant under the interchange of the particles (namely  $H_{12} = H_{21}$ ). This was precisely the argument brought up by Amado and Primakoff [69] which discredited experiments claiming to test the symmetrization postulate by simply watching for decays of Pauli obeying electrons spontaneously dropping to the ground state of the atom releasing a photon. This transition from a Pauli-obeying to a Pauli-violating quantum state is not allowed in the theoretical constructs of quantum mechanics.

#### 4.5 For Further Reference

Unlike the preceding chapters this was devoted more intensely to providing some more of the details behind the formulation and development of the symmetrization postulate and its implications to the Pauli exclusion principle through the spin-statistics theorem. Of course there are more detailed discussions on this subject and while every basic book on chemistry or physics undoubtedly mentions the Pauli principle few provide the formalism behind its derivation or fundamental understanding. In fact in Feynman's famous lectures on physics he stated the following about the spin-statistics theorem [70]:

Why is it that particles with half-integral spin are Fermi particles ..., whereas particles with integral spin are Bose particles ... ? We apologize for the fact that we cannot give you an elementary explanation. An explanation has been worked out by Pauli from complicated arguments of quantum field theory and relativity. He has shown that the two must go together, but we have not been able to find a way of reproducing his arguments on an elementary level. It appears to be one of the few places

in physics where there is a rule which can be stated very simply, but for which no one has found a simple and easy explanation. The explanation is deep down in relativistic quantum mechanics. This probably means that we do not have a complete understanding of the fundamental principle involved. For the moment, you will just have to take it as one of the rules of the world.

While Sakurai [59] provides a nice chapter on identical particles, the most extensive collection of proofs of the spin-statistics theorem is provided by Duck and Sudarshan [71]. This text is solely focused on the different proofs of the spin-statistics connection along with providing a compilation of the notable works themselves and a pleasant historical summary. It is a must for anyone seriously interested in the details and fundamental foundations of the Pauli exclusion principle.

- Ian Duck and E.C.G. Sudarshan, *Pauli and the Spin-Statistics Theorem*, World Scientific Publishing Co. Pte. Ltd., 1997.

## CHAPTER 5. BEYOND THE STANDARD MODEL

Good summaries of the concepts and arguments presented in this chapter may be found in the books by Peacock [72] and the text by Collins, Martin, and Squires [17]. Of course much of the subject matter briefly covered in this chapter (e.g. supersymmetry) is extensively covered in existing texts. For the books on supersymmetry and string theories see Jacob's compilation of papers [73], also books by Müller-Kirsten and Wiedemann [74], Duff [75], Kaku [76], and the excellent book providing a less technical summary by Kane [77].

### 5.1 Why go beyond the Standard Model?

The standard model of particle physics is one of the twentieth century's most significant achievements, but few if any physicists would say that it is the last word in the understanding of fundamental processes. In fact, no confirmed experimental results blatantly contradict it. So why are we convinced it cannot be the final theory?

Gravity is probably the most compelling motivation for work in this area. The gravitational field is not included in the calculational apparatus of field theory. Although much work has been done in the area of quantum gravity – an attempt to quantize general relativity – we have yet to arrive at a renormalizable field theory. The only hope is to somehow try to unify it with the other forces which may equalize the divergences.

Another motivation suggesting the standard model is incomplete is known as the Higgs divergence problem. As mentioned in Chapter 2 the Higgs boson gives the particles their masses. Figure 5.1 is one of many Feynman diagrams which contribute to the mass of the Higgs boson itself. There are an infinite number of these diagrams which can be drawn and each involving more than one such fermion loop. The result

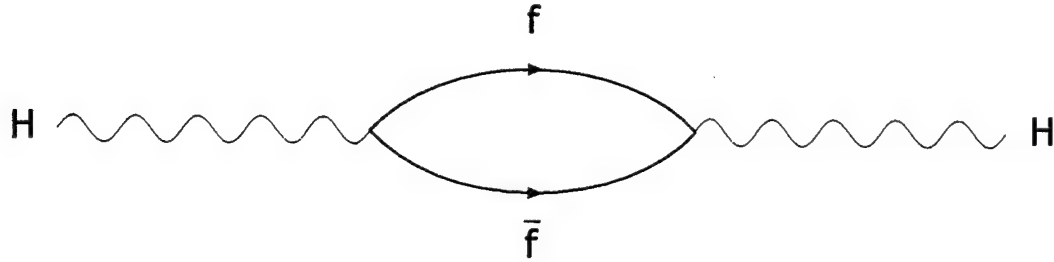


Figure 5.1: A Higgs boson dissociating into a virtual fermion-antifermion pair.

of trying to calculate the Higgs mass correction with an infinite number of these diagrams, diverges to infinity.

Many physicists feel that there are also aesthetic reasons suggesting the standard model, although experimentally well-confirmed, cannot be the final story. The standard model fails to explain the 'why' behind the structure of the theory itself. For example; Why are there three distinct coupling constants, and what defines their relative strengths? Why are there three generations of quarks and leptons when any number are possible? Why are the charges of quarks and leptons related, why the quantization of charge? On top of this the Higgs spontaneous symmetry breakdown mechanism, which is absolutely crucial to the success of the standard model, requires an inelegant and arbitrary addition to the Lagrangian.

Finally, the goal of any theory is to be able to make successful predictions with the fewest number of free parameters which must be set by hand. In the standard model there are 19 free parameters! The nine fermion masses ( $m_e$ ,  $m_u$ ,  $m_d$ ;  $m_\mu$ ,  $m_s$ ,  $m_c$ ;  $m_\tau$ ,  $m_b$ ,  $m_t$ ) the four quark mixing parameters (which arise in the Cabbibo-Kobayashi-Maskawa matrix included in the QCD quark current), the three coupling parameters ( $\alpha$ ,  $\theta_w$ , and  $\Lambda_{QCD}$ ), the two Higgs potential parameters ( $M_H$  and  $\lambda$ ), and the QCD  $\theta$ . So many arbitrary parameters seems to be screaming at a hidden underlying meaning. It may be that the standard model is only the low-energy manifestation of some

deeper and simpler theory. This statement is justified by looking at the variation of the different coupling constants.

## 5.2 Variation of the Coupling Constants

Recall from the review of the standard model that the coupling constants are not really constants at all. In fact, each can be made to be a function of energy which are logarithmically varying and whose renormalization group equations are of the form

$$\frac{1}{\alpha(E_1)} = \frac{1}{\alpha(E_2)} + \frac{b}{2\pi} \ln \left( \frac{E_2}{E_1} \right) \quad (5.1)$$

where  $\alpha$  carries the definition

$$\alpha \equiv \frac{g^2}{4\pi} \quad (5.2)$$

based on the strength of the given interaction  $g$ .

For laboratory energies near  $M_W$  the values of the coupling constants are quite different:  $\alpha_{EM} \approx 1/137$ ,  $\alpha_W \approx 1/25$ , and  $\alpha_S \approx 1/10$ . However, their energy dependences are also different. The electromagnetic coupling increases with energy, while the strong and weak couplings decrease with energy. In fact, their  $b$  coefficients are given by Equation (2.17) which is

$$b[U(1)] = -\frac{4}{3}N_f \quad (5.3)$$

$$b[SU(N)] = \frac{11}{3}N - \frac{2}{3}N_f$$

where  $N_f$  is the number of distinct families (which is three in the standard model). Thus Equation (5.1) implies a linear dependence of  $1/\alpha$  on  $\ln(\text{energy})$ , whose slope around  $E \leq M_W$  is known from the low-energy structure of the theory. Extending the initial values to higher energies shows that they coincidentally almost intersect (see Figure 5.2). In fact at the energy  $E_U \approx 10^{14} - 10^{15}$  the coupling constants of the three forces have the value  $\alpha_i(E_U) \approx 1/40$ .

This is a radical prediction and suggests that new physics may be at stake. In fact, the story gets even more interesting with the introduction of a new kind of symmetry,

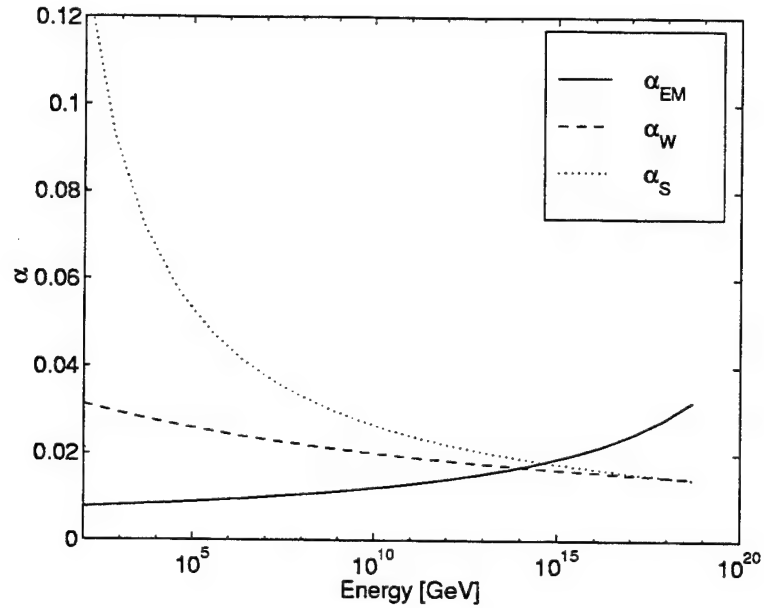


Figure 5.2: The predicted variation of the coupling constants  $\alpha_i$  with energy scale. All three interactions seem to converge at a scale of around  $E \approx 10^{14} - 10^{15}$  GeV. (This figure is adopted from figure 1 of Ref. [8])

called supersymmetry. When this symmetry is applied it has the effect of causing the coupling constants to intersect exactly as shown in Figure 5.3.

### 5.3 Introduction to Supersymmetry

In supersymmetry (SUSY) we introduce an operator that can transform between fermions and bosons

$$\begin{aligned} Q|\text{fermion}\rangle &= |\text{boson}\rangle \\ Q|\text{boson}\rangle &= |\text{fermion}\rangle \end{aligned} \tag{5.4}$$

As a result any supersymmetric multiplet must contain equal numbers of bosons and fermions of the same mass. Since we know that the particles do not group into mass-degenerate pairs we conclude that nature is not supersymmetric at the energy scales we have tested. Detailed modeling efforts only make progress if there are no pairings between known particles. Thus, supersymmetry predicts the introduction of

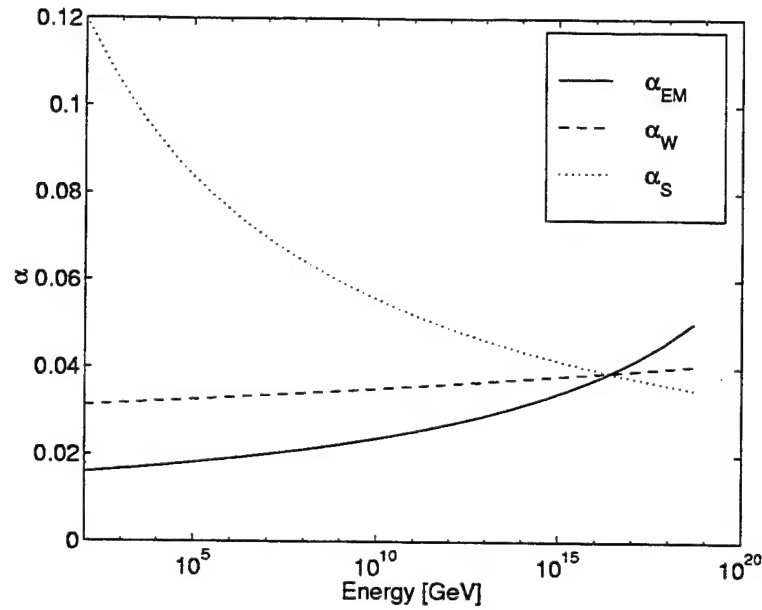


Figure 5.3: The predicted variation of the coupling constants  $\alpha_i$  with energy scale with SUSY corrections. All three interactions seem to converge at a scale of  $E \approx 10^{16}$  GeV. (This figure is adopted from figure 2 of Ref. [8])

new particles. Each known particle must have a *superpartner*: boson A implies the fermion A-ino and fermion B implies the boson s-B, populating the universe with novel ‘sparticles’ such as ‘sqarks’, and ‘gluinos’. The superpartners are typically denoted by a tilde:  $\tilde{q}$ ,  $\tilde{g}$ , etc.

Most supersymmetric particles will be unstable, but supersymmetric theories forbid processes in which a sparticle decays to normal particles only. Thus there should be a lightest supersymmetric particle (LSP) which is stable. So far such a particle has gone undetected which is suggestive that it is very massive and must be greater than  $6.3 \text{ GeV}/c^2$  [78].

Since verifiable experimental evidence for supersymmetry is lacking (with a few recent exceptions [79]) the first evidence for SUSY it will be as a broken symmetry. The scale of such breaking is dependant upon the particular SUSY breaking mechanism which is assumed.

### 5.3.1 Simple Harmonic Motion Revisited

In order to illustrate how supersymmetry works we begin with an example which includes many of the important features of the SUSY formalism. Consider a simple harmonic oscillator with both bosonic and fermionic degrees of freedom. The creation and annihilation operators of the boson ( $a^\dagger$  and  $a$ , respectively) satisfy the commutation relations given in Equation (3.61) which are

$$\begin{aligned} [a, a^\dagger] &= 1 \\ [a, a] &= [a^\dagger, a^\dagger] = 0 \end{aligned} \tag{5.5}$$

while those of the fermion satisfy the anticommutation relations given by Equation (3.78) and which will be represented here by the  $b$ 's

$$\begin{aligned} \{b, b^\dagger\} &= 1, \\ \{b, b\} &= \{b^\dagger, b^\dagger\} = 0 \end{aligned} \tag{5.6}$$

Recall that since  $b^\dagger b^\dagger |0\rangle = 0$ , no two fermions may occupy the same state. In terms of these operators, the Hamiltonian takes the form

$$H = \frac{1}{2}\omega_B \{a^\dagger, a\} + \frac{1}{2}\omega_F [b^\dagger, b] \tag{5.7}$$

where  $\omega_B$  and  $\omega_F$  are the classical frequencies of the bosonic and fermionic oscillators, respectively, and the allowed energies are

$$\begin{aligned} E &= \omega_B \left( n_B + \frac{1}{2} \right) + \omega_F \left( n_F - \frac{1}{2} \right) \\ &= \omega(n_B + n_F) \end{aligned} \tag{5.8}$$

if  $\omega_B = \omega_F = \omega$ . In this symmetry limit we have exact cancellation of the zero-point energies. The only allowed eigenvalues of the fermion number operator  $b^\dagger b$  are  $n_F = 0, 1$  and so all the energy levels except the ground state ( $n_B = n_F = 0$ ) are doubly degenerate. The system thus contains equal numbers of bosonic and fermionic degrees of freedom.

This degeneracy indicates that there must exist some (super)symmetry of the Hamiltonian. In fact, it is easy to check that the operators

$$\begin{aligned} Q &\equiv \sqrt{2\omega} a^\dagger b \\ Q^\dagger &\equiv \sqrt{2\omega} b^\dagger a \end{aligned} \tag{5.9}$$

commute with the Hamiltonian, i.e.,

$$[Q, H] = [Q^\dagger, H] = 0 \tag{5.10}$$

where  $\sqrt{2\omega}$  is just a normalization factor. The operators  $Q$  and  $Q^\dagger$  have the effect of replacing a fermion by a boson, and vice versa as dictated in Equation (5.4) and so they are supersymmetry generators. Furthermore, we find that

$$\{Q, Q^\dagger\} = 2H \tag{5.11}$$

and so the algebra of  $Q$ ,  $Q^\dagger$ , and  $H$  closes if we include anticommutation relations as well. This anticommutator is the essence of SUSY.

### 5.3.2 The SUSY Algebra

We introduce four generators  $Q_\alpha$  ( $\alpha = 1, \dots, 4$ ), which form a four component Majorana spinor. Majorana spinors are the simplest type of spinor possible. They are self-conjugate in that

$$\begin{aligned} Q &= Q^c \\ &= C \bar{Q}^T \\ &= C \gamma_0^T Q^* \end{aligned} \tag{5.12}$$

where  $C$  is the charge conjugation matrix and  $\gamma^\mu$  are the set of  $4 \times 4$  matrices given by Equation (3.42) and introduced by Dirac. Here we have also introduced the adjoint spinor where

$$\bar{Q} \equiv Q^\dagger \gamma^0 \tag{5.13}$$

As a result of the condition provided in Equation (5.12) a Majorana spinor has only half as many degrees of freedom as a Dirac spinor. Any Dirac spinor  $\psi$  may be written as

$$\psi = \frac{1}{\sqrt{2}}(\psi_1 + i\psi_2) \quad (5.14)$$

where

$$\psi_1 = \frac{1}{\sqrt{2}}(\psi + \psi^c) \quad \text{and} \quad \psi_2 = -\frac{i}{\sqrt{2}}(\psi - \psi^c) \quad (5.15)$$

are two independent Majorana spinors that satisfy  $\psi_i = \psi_i^c$ .

Since  $Q_\alpha$  is a spinor, it must satisfy

$$[Q_\alpha, M_{\mu\nu}] = \frac{1}{2}(\sigma_{\mu\nu})_{\alpha\beta} Q_\beta \quad (5.16)$$

where  $M_{\mu\nu}$  is the antisymmetric tensor which generates space-time rotations and  $\sigma_{\mu\nu}$  is defined as

$$\sigma^{\mu\nu} \equiv \frac{1}{2}i[\gamma^\mu, \gamma^\nu] \quad (5.17)$$

and which transforms as an antisymmetric tensor when sandwiched between two spinors. Thus Equation (5.16) reflects that the  $Q_\alpha$ 's transform as a spinor under the rotations generated by  $M_{\mu\nu}$ .

The Jacobi identity of commutators for the four-momentum  $P_\mu$  is

$$[[Q_\alpha, P_\mu], P_\nu] + [[P_\nu, Q_\alpha], P_\mu] + [[P_\mu, P_\nu], Q_\alpha] = 0 \quad (5.18)$$

and requires that the  $Q_\alpha$ 's be translationally invariant, or basically that

$$[Q_\alpha, P_\mu] = 0 \quad (5.19)$$

In order to close the algebra, just like the classical example, we introduce the anticommutation relation given by

$$\{Q_\alpha, \bar{Q}_\beta\} = 2(\gamma^\mu)_{\alpha\beta} P_\mu \quad (5.20)$$

It is this anticommutation relation which leads to the most interesting consequences.

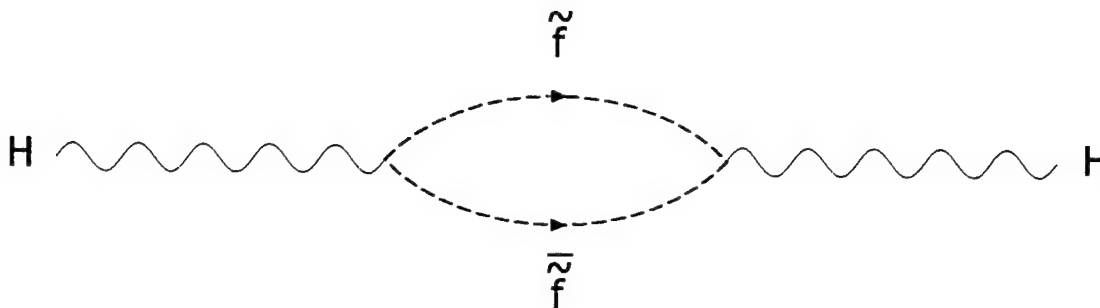


Figure 5.4: A Higgs boson dissociating into a virtual sfermion-antisfermion pair. This diagram exactly cancels the one in Figure 5.1.

So supersymmetry coincidentally causes the coupling constants to converge to a single point at very high energy. It also solves the Higgs divergence problem discussed above. The existence of the superpartners, particles with exactly the same properties as the standard model particles, except for different spins introduce diagrams like that in Figure 5.4 which cancel diagrams like those in Figure 5.1. Both diagrams have the same vertices and coupling constants and thus the same magnitude for the amplitude. However, since the particle spins are different, the amplitudes have opposite signs such that when calculating the cross section their amplitudes cancel yielding a finite interaction probability.

#### 5.4 For Further Reference

As mentioned briefly at the beginning of the chapter, the intention here was to provide a brief introduction of the concepts and review of the problems with the standard model. Good texts for further reference on such topics are

- Maurice Jacob, *Supersymmetry and Supergravity*, Elsevier Science Publishers, 1986.
- H.J.W Müller-Kirsten and A. Wiedemann, *Supersymmetry: An Introduction with Conceptual and Computational Details*, World Scientific Publishing Co. Pte. Ltd., 1987.

- M.J. Duff, *The World in Eleven Dimensions: Supergravity, Supermembranes and M-theory*, Institute of Physics Publishing Ltd, 1999.
- Michio Kaku, *Introduction to Superstrings and M-Theory*, Springer-Verlag New York, Inc., 1999.
- Steven Weinberg, *The Quantum Theory of Fields Volume III: Supersymmetry*, Cambridge University Press, 2000.
- Gordon Kane, *Supersymmetry: Unveiling the Ultimate Laws of Nature*, Perseus Books Publishing, L.L.C., 2000.

EXPLORING PHYSICS BEYOND THE STANDARD MODEL:  
ASTROPHYSICAL MOTIVATIONS AND ACCELERATOR APPLICATIONS  
VOLUME II

A Thesis  
Submitted to the Faculty  
of  
Purdue University  
by  
Daniel Javorsek II

In Partial Fulfillment of the  
Requirements for the Degree  
of  
Doctor of Philosophy

August 2001

## Part II

# SEARCHING FOR PARONIC Be

## CHAPTER 6. MOTIVATION FOR PARONIC EXPERIMENTS

An in-depth discussion of the derivations behind the Pauli principle along with background material required to understand the details of possible violations of the Pauli principle were provided in Chapter 4. The reader should refer to the background chapters when further explanation is needed.

Of course much progress has been made in the area of possible violations of the symmetrization postulate and the Pauli exclusion principle. The best collection of papers on the subject can be found in the conference proceedings on *Spin-Statistics Connection and Commutation Relations: Experimental Tests and Theoretical Implications* edited by Hilborn and Tino [80].

### 6.1 Introduction

The Pauli exclusion principle has played a central role in quantum mechanics since its formulation in 1925 [81]. With its roots in quantum mechanics, the Pauli principle arises from the application of the symmetrization postulate to the spin-statistics connection. In general, the exclusion principle is a statement that no two fermions may occupy the same quantum state, and is expressed by a wave function that is completely anti-symmetric with respect to the exchange of two identical fermions. Even though the Pauli exclusion principle plays an integral role in our understanding of the structure and properties of atoms and nuclei, by the late 1980s few direct experiments testing its validity had been performed.

In fact, in 1987 Okun' stated "The special place enjoyed by the Pauli principle in modern theoretical physics does not mean that this principle does not require further and exhaustive experimental tests. On the contrary, it is specifically the fundamental nature of the Pauli principle which would make such tests, *over the entire periodic*

*table*, of special interest.” [82] Of course, its considerable success in explaining a wide range of phenomenon is indicative of its high degree of validity.

However, the question of possible small violations of the Pauli principle arose with the introduction of what was believed to be a consistent quantum field theory permitting such violations. With the introduction of this formalism, a great deal of theoretical and experimental progress has been made. This chapter summarizes the theories including their strengths and weaknesses, and concludes with a discussion of the implications of such a violation.

## 6.2 Pauli Violating Algebras: Trilinear Commutation Relations

Greenberg and Mohapatra [83], using the trilinear commutation relations developed by Green [84] and building on the field-theory analysis of a single oscillator performed by Ignat’ev and Kuz’min (IK) [85], developed a construction which mainly obeys Fermi statistics but which allows double occupancy with a small amplitude  $\beta$ . In the IK single oscillator formalism  $\beta$  is a dimensionless parameter such that when  $\beta = 0$  the Pauli principle is satisfied exactly, and when  $\beta \neq 0$  processes which violate this principle are possible but are suppressed by some power of  $\beta$ . An example of this is the existence of more than one electron occupying the same quantum state (as in the case of our experiment).

The Pauli principle follows automatically from the form of the commutation relations among the creation and annihilation operators  $a_{k\sigma}$ ,  $a_{k\sigma}^\dagger$ ,  $b_{k\sigma}$ ,  $b_{k\sigma}^\dagger$  for electrons and positrons. Thus for theories describing a violation of the Pauli principle the corresponding commutation relations must be changed. Because it is very difficult to solve for the new relations while holding that they still satisfy the principles of quantum field theory (positivity of energy, Lorentz invariance, relativistic causality, C-parity, and conservation of electric charge or fermion number), IK begin by attempting to construct a representation of this algebra with the required properties, and then find the commutation relations themselves.

IK begin with the familiar electron creation and annihilation operators  $a, a^\dagger$

$$a = \begin{pmatrix} 0 & 1 \\ 0 & 0 \end{pmatrix} \quad a^\dagger = \begin{pmatrix} 0 & 0 \\ 1 & 0 \end{pmatrix} \quad (6.1)$$

and choosing as an orthonormal basis the vacuum  $|0\rangle$ , the one-particle  $|1\rangle$ , and two-particle  $|2\rangle$  states. The resulting effect of the creation and annihilation operators are as follows (note that in the limit  $\beta \rightarrow 0$  their effect reduces to the usual results):

$$\begin{aligned} a^\dagger|0\rangle &= |1\rangle, & a|0\rangle &= 0, \\ a^\dagger|1\rangle &= \beta|2\rangle, & a|1\rangle &= |0\rangle, \\ a^\dagger|2\rangle &= 0, & a|2\rangle &= \beta|1\rangle. \end{aligned} \quad (6.2)$$

Ignat'ev and Kuz'min then proceed to find the commutation relations (or algebra) satisfied by the operators  $a, a^\dagger$ . To develop the commutation relations and number operator associated with the IK model it is necessary to calculate all possible products of the operators (i.e.  $a^2, a^\dagger a, aa^\dagger, a^3, \dots$ ) and the relations among them. It can be shown that products of the second degree and lower are linearly independent thus their model excludes all bilinear commutation relations.

This set of all possible operator products defines a linear nine-dimensional space,  $L$ , of the  $3 \times 3$  matrices and can be decomposed into the direct sum of a three-dimensional space,  $L_d$  (diagonal matrices), and a six-dimensional space,  $L_0$  (matrices with zero diagonal elements).  $L_d$  contains two of the independent operators  $a^\dagger a$  and  $aa^\dagger$  while  $L_0$  contains the ten operators ( $a, a^2, a^2 a^\dagger, aa^\dagger a, a^\dagger a^2$ , along with their Hermitian conjugates). Thus, four independent linear relations exist among the operators in the space  $L_0$ . These relations can be written in the form,

$$a^2 a^\dagger + \beta^2 a^\dagger a^2 = \beta^2 a \quad (6.3)$$

$$a^2 a^\dagger + \beta^4 a^\dagger a^2 = \beta^2 aa^\dagger a \quad (6.4)$$

plus their Hermitian conjugates. Also, it is necessary to have

$$a^3 = 0, \quad (a^\dagger)^3 = 0 \quad (6.5)$$

Thus, IK have developed commutation relations described by Equations (6.3) through (6.5) that are satisfied by the newly defined creation and annihilation operators. Using these new relations we can construct the number operator,  $N$ , to be

$$N = \begin{pmatrix} 0 & 0 & 0 \\ 0 & 1 & 0 \\ 0 & 0 & 2 \end{pmatrix} \quad (6.6)$$

where the usual commutation relations are satisfied:

$$[N, a] = -a, \quad [N, a^\dagger] = a^\dagger \quad (6.7)$$

Expressing  $N$  in terms of the creation and annihilation operators yields a trilinear equation of the form:

$$N = A_1 a^\dagger a + A_2 a a^\dagger + A_3 \quad (6.8)$$

with the coefficients  $A_1$ ,  $A_2$ , and  $A_3$  given by

$$A_1 = \frac{-1 + 2\beta^2}{1 - \beta^2 + \beta^4}, \quad A_2 = \frac{-2 + \beta^2}{1 - \beta^2 + \beta^4}, \quad A_3 = \frac{2 - \beta^2}{1 - \beta^2 + \beta^4}. \quad (6.9)$$

However, because the IK model is that of a single oscillator, it is impossible to apply it to experimental data. This motivated Greenberg and Mohapatra (GM) to generalize the IK model into a local quantum field theory [83]. GM begin with Green's parastatistics [84] which uses the trilinear commutation relations

$$\begin{aligned} [[b_k^\dagger, b_l]_\pm, b_m]_- &= -2\delta_{km}b_l, \\ [[b_k, b_l]_\pm, b_m]_- &= 0, \\ [b_i, b_j]_\pm &= b_i b_j \pm b_j b_i, \end{aligned} \quad (6.10)$$

where  $[ ]_{\pm}$  designates the commutation (-) and anti-commutation (+) relations. (For future reference throughout the paper when a specific relation is used instead of the general statements given in Equations (6.10) we will represent the commutation relation as  $[ ]_- = [ ]$  and the anti-commutation relation as  $[ ]_+ = \{ \}$ .) Green then gave a representation of the operators obeying these rules with “Green’s *Ansatz*”:

$$b_k = \sum_{\alpha=1}^p b_k^{(\alpha)}, \quad (6.11)$$

where for equal values of  $\alpha$  (the “Green index”) the operators obey the usual commutation relations, but for different values of the Green index, the operators have abnormal relative commutation relations,

$$\begin{aligned} [b_k^{(\alpha)}, b_l^{(\alpha)\dagger}]_{\mp} &= \delta_{kl}, \\ [b_k^{(\alpha)}, b_l^{(\gamma)\dagger}]_{\pm} &= 0, \quad \alpha \neq \gamma. \end{aligned} \quad (6.12)$$

The number  $p$  of values over which the Green index runs is the “order” of the parastatistics. For parabosons (parafermions) of order  $p$ , at most  $p$  particles can be in an antisymmetric (symmetric) state. For  $p = 1$ , parabosons (parafermions) reduce to bosons (fermions). Greenberg and Messiah [86] later derived the selection rules for paraparticles, and proved that there is no case in which a single paraparticle can decay into normal particles, nor can a paraparticle mix (i.e., form a linear superposition) with a normal particle. Thus a validation of Amado and Primakoff’s [69] statement that a symmetric Hamiltonian forbids transition from a normal antisymmetric atomic state to a forbidden state with mixed symmetry.

For Fock-type representations, the trilinear commutation relations of parastatistics are supplemented by a no-particle and a single-particle condition. The analogs of these conditions for the IK model are

$$\begin{aligned} a|0\rangle &= 0, \\ aa^{\dagger}|0\rangle &= 0. \end{aligned} \quad (6.13)$$

Thus, with the use of Equation (6.13), Equation (6.3) implies Equations (6.4) and (6.5). To see the connection to the parafermi theory, use parafermi operators,  $b$

and  $b^\dagger$ , of order 2 (since they will have a maximum occupancy of two). For a single oscillator, the only terms which can occur are  $b$  and  $b^\dagger b^2$ . A simple calculation shows that the IK oscillator can be expressed with a Green-type *Ansatz* by,

$$\begin{aligned} a^\dagger &= \frac{1}{2}\sqrt{2}[b^\dagger + (\beta - 1)b^{\dagger 2}b] \\ &= \frac{1}{2}\sqrt{2}b^\dagger[1 + (\beta - 1)N_0], \end{aligned} \quad (6.14)$$

$$b = b^{(1)} + b^{(2)}, \quad (6.15)$$

$$\begin{aligned} N_0 &= \frac{1}{2}[b^\dagger, b] + 1 \\ &= b^{(1)\dagger}b^{(1)} + b^{(2)\dagger}b^{(2)}, \end{aligned} \quad (6.16)$$

where  $b^{(\alpha)}$  obeys the Green component relations (6.12). This representation makes it clear that  $a^2 \rightarrow 0$ ,  $\beta \rightarrow 0$ . Then we see that  $a$  is a parafermi operator of order 2 which has been modified by the factor  $1 - N_0$  which prevents double occupancy. This is then combined with the term  $\beta N_0$  which allows double occupancy proportional to  $\beta$ . Thus Equation (6.14) shows that for  $\beta = 1$  ( $\beta = 0$ ), we can recover a parafermi oscillator of order 2 (an operator which behaves like a Fermi oscillator). Greenberg and Mohapatra [83] call this construction a “hindered parafermion” or, for short, a “paron” of order 2. They call an electron which obeys these statistics a “paronic electron.”

To discuss the field theory based on the IK oscillator, GM derive the trilinear commutation relations for an arbitrary set of momentum-dependent operators. They do this in two steps. First, they replace the operators  $a$  and  $a^\dagger$  in Equations (6.3) and (6.4) with

$$a = \frac{\kappa a_k + \lambda a_l + \mu a_m}{[\kappa^2 + \lambda^2 + \mu^2 + 2(\kappa\lambda\delta_{kl} + \lambda\mu\delta_{lm} + \mu\kappa\delta_{mk})]^{1/2}} \quad (6.17)$$

and the corresponding formula for  $a^\dagger$ . After collecting all terms with the coefficient  $\kappa\lambda\mu$  and transforming we arrive at equations with terms that create or annihilate

different net amounts of momentum. Thus the equations can be separated into three equivalent equations free of cyclic permutations. They are

$$\{a_k, a_l\}a_m^\dagger + \beta^2 a_m^\dagger \{a_k, a_l\} = \beta^2 (\delta_{lm} a_k + \delta_{mk} a_l), \quad (6.18)$$

$$\{a_k, a_l\}a_m^\dagger + \beta^4 a_m^\dagger \{a_k, a_l\} = \beta^2 (a_l a_m^\dagger a_l + a_k a_m^\dagger a_l). \quad (6.19)$$

Here the Kronecker deltas are used as shorthand for the Dirac deltas. The analogs of Equations (6.13) are

$$\begin{aligned} a_k |0\rangle &= 0, \\ a_k a_l^\dagger |0\rangle &= \delta_{kl} |0\rangle > 0. \end{aligned} \quad (6.20)$$

After imposing local commutivity on the theory, and requiring that the charge density be bilinear in the spinor field, GM arrive at the final commutation relations for the paronic Fermi fields of order 2. They are as follows:

$$\begin{aligned} (2 - \beta^2)[a_k, a_l]a_m^\dagger + (1 - 2\beta^2)a_m^\dagger[a_k, a_l] = \\ (1 - \beta^2 + \beta^4)(\delta_{lm} a_k - \delta_{km} a_l) + 3(1 - \beta^2)(a_l a_m^\dagger a_k - a_k a_m^\dagger a_l), \end{aligned} \quad (6.21)$$

$$\begin{aligned} (2 - \beta^2)\{a_k, a_l\}a_m^\dagger - (1 - 2\beta^2)a_m^\dagger\{a_k, a_l\} = \\ - (1 - \beta^2 + \beta^4)(\delta_{km} a_l + \delta_{lm} a_k) + (1 + \beta^2)(a_k a_m^\dagger a_l + a_l a_m^\dagger a_k). \end{aligned} \quad (6.22)$$

In effect, this construction allows for small violations of the exclusion principle and introduces a state that obeys para-Fermi statistics of order 2. However, there were difficulties with this new formalism allowing small violations of the Pauli exclusion principle.

An earlier proof by Govorkov [87] when applied to their new model leads to states with negative norms (resulting in a negative Hilbert space). Govorkov's results actually rule out trilinear commutation rules as a way of producing a theory in which the Pauli principle is violated by a small amount [88].

Thus, while *integral* parastatistics can be realized as local field theories, in a positive definite Hilbert space the case of non-integral  $p$  at the heart of the GM model leads to negative norm states and cannot as originally developed lead to a complete local field theory.

### 6.3 Pauli Violating Algebras: Quon Algebra and Infinite Statistics

In an attempt to search for an alternate method of formulating a complete theory of possible Pauli principle violation, Mohapatra [89] and Greenberg [90, 91] both introduce quon (or  $q$ -mutator) algebra of which “infinite statistics” is a special case and which was not treated by Govorkov.

The quon algebra is a deformation of the Bose and Fermi algebras which interpolates between these algebras as  $q$  goes from 1 to -1 on the real axis and is described by

$$a_k a_l^\dagger - q a_l^\dagger a_k = \delta_{kl} \quad (6.23)$$

The quon algebra, supplemented by the vacuum condition

$$a_k |0\rangle = 0, \quad (6.24)$$

determines a (Fock-like) representation in a linear vector space. For  $-1 \leq q \leq 1$ , the squared norms of all vectors made by limits of polynomials of the creation operators  $a_k^\dagger$  are strictly positive, thus solving the problem of a negative Hilbert space. For  $q = \pm 1$  the squared norms of all such vectors are never negative; vectors which are not totally antisymmetric (symmetric) under permutations have zero norms. Any relation of the form

$$c_1 A_k A_l^\dagger - c_2 A_l^\dagger A_k = c_3 \delta_{kl} \quad (6.25)$$

can be brought into the form of Equation (6.23) by the change of normalization

$$\begin{aligned} a_k &= \sqrt{\frac{c_1}{c_3}} A_k, \\ a_k^\dagger &= \sqrt{\frac{c_1}{c_3}} A_k^\dagger, \end{aligned} \quad (6.26)$$

with  $q = c_2/c_1$ , provided  $c_1/c_3 > 0$  and  $c_3 \neq 0$ . The choice made in Equation (6.23) is particularly convenient for the interpolation between Bose and Fermi statistics. The choice

$$a_k a_l^\dagger - q a_l^\dagger a_k = q^{-N} \delta_{kl}, \quad (6.27)$$

(where  $N$  is the number operator discussed before) studied by some authors [89], does not have a convenient interpolation. The Bose ( $q = 1$ ), Fermi ( $q = -1$ ), and infinite ( $q = 0$ ) statistics are special cases of this formalism. The range  $-1 \leq q \leq 1$  share with the case of  $q = 0$  the property of having positive norm vectors belonging to all representations of the symmetric (i.e., the permutation) group. Also, as in the case of  $q = 0$ , Equations (6.23) and (6.24) allow the calculation of the vacuum-to-vacuum matrix element of any polynomial in the  $a$ 's and  $a^\dagger$ 's.

All vacuum matrix elements can be calculated by moving annihilation operators to the right using Equation (6.23), until they annihilate the vacuum according to Equation (6.24), or by moving creation operators to the left again using Equation (6.23) until they annihilate the vacuum on the left according to the adjoint of Equation (6.24). The relation

$$a_k a_l - q a_l a_k = 0 \quad (6.28)$$

between to  $a$ 's which one might guess in analogy with the Bose and Fermi commutation rules holds only when  $q^2 = 1$ ; and requires that  $q = \pm 1$  in Equation (6.23) (i.e. Equation (6.28) only holds in the Bose and Fermi cases). For  $q = 0$ , all states formed by monomials in  $a^\dagger$ 's acting on the vacuum have norm one, regardless of whether the  $a^\dagger$ 's have the same or distinct labels. Monomial states are orthogonal unless the same set of  $a^\dagger$ 's occur in the same order. It can be shown that this space of states is a

Hilbert space and thus has a positive-definite metric. To construct the operators for the energy, momentum, angular momentum, etc. in terms of the creation and annihilation operators, it suffices to construct a set of number operators,  $n_i$ , and transition operators,  $n_{ij}$ , which obey the commutation relations

$$[n_i, a_j] = -\delta_{ij}a_j \quad (6.29)$$

$$[n_{ij}, a_k] = -\delta_{ik}a_j \quad (6.30)$$

where the number operator  $n_k = n_{kk}$ . The transition operator  $n_{ij}$  annihilates a particle in state  $j$  and creates a particle in the state  $i$ .

Operators which obey Equations (6.29) and (6.30) are composite Bose operators whose eigenvalues are additive for product states. The condition that observables must be composite Bose operators leads to conservation of statistics which states that all interactions *must involve an even number of fermions or parafermions* and an even number of paraparticles. This statement is very important as all AMS experiments done prior to ours have *odd* numbers of parafermions and fermions.

While this new algebra validates the motivation for our experiment it can also shown to be an inconsistent theory. Fredenhagen [92] showed that a theory which has neither para-Bose (including Bose) nor para-Fermi (including Fermi) statistics cannot be local. Here local means both (a) that the observables are pointlike functionals of the fields and (b) that the observables commute at spacelike separation [i.e., satisfy local commutativity (LC)]. For the  $q = 0$  case, Greenberg showed [90] that the fields associated with infinite statistics are not local. Thus by replacing the original non-integral formulation of Greenberg and Mohapatra with the quon algebra we have traded the problem of negative norms for that of non-locality.

## 6.4 Implications of Pauli Principle Violations

### 6.4.1 Cosmological Implications

While the Pauli exclusion principle is responsible for nearly all of atomic physics and chemistry on the low energy level, one place where it is tested at more extreme energies is in stellar collapse.

Stars are fueled by nuclear fusion which creates a radiation pressure that balances the force of gravity. When the rate of nuclear fusion reactions decreases, the radiation pressure drops and the star collapses. If the star's mass is between 0.5–1.4 solar masses ( $1.4M_{\odot}$  is called the Chandrasekhar limit), the collapse will be halted by the electron pressure generated by the Pauli exclusion principle. In effect, the star has become so dense, about  $10^9 \text{ kg/m}^3$ , that the electron repulsion due to the Pauli principle has become the main cause of resistance against further contraction. The star has become a white dwarf with a radius roughly that of the earth and a surface temperature of about  $10^4 \text{ K}$ . In the degenerate electron gas of a white dwarf, the electrons are distributed relatively uniformly throughout the medium surrounding the nuclei. The nuclei themselves are regularly spaced and become more tightly constrained as the pressures increase. Eventually they are so tightly packed that they resemble a crystalline lattice. Under these conditions, the material is more like a solid than a gas. From the equation of state for a degenerate gas we obtain the relation between a white dwarf's mass and radius

$$R = \frac{4\pi K}{G_N(4/3\pi)^{5/3} M^{1/3}}, \quad (6.31)$$

where  $K$  is the constant arising from the relationship between pressure  $P$  and density  $\rho$  for a nonrelativistic degenerate gas

$$P = K\rho^{5/3}. \quad (6.32)$$

This shows that as the mass increases, the radius decreases. The white dwarf mass-radius relation of Equation (6.31) is often taken to be

$$\begin{aligned}
 R &= \frac{f}{M^{1/3}} \\
 &= \frac{\frac{2}{G_N} \left(\frac{3}{8\pi}\right)^{4/3} h^2}{2^{1/3} (\mu_e m_p)^{5/3} m_e} \frac{1}{M^{1/3}} \\
 &\approx \frac{9.03 \times 10^{19} \text{ cm g}^{1/3}}{M^{1/3}}
 \end{aligned} \tag{6.33}$$

in the literature [93]. Here  $\mu_e$  is the mean molecular weight per electron. The constant  $K$  in Equation (6.31) is related to  $f$  through the relation

$$K = \frac{G_N (4/3\pi)^{5/3} f}{4\pi}. \tag{6.34}$$

If the exclusion principle were violated by some small fraction, electron degeneracy pressure would be less effective at a given mass, since a higher fraction of electrons would be allowed to stay in lower energy levels. Thus gravity would be more effective, and the radius would be smaller for a given mass than you would expect from the conventional theory. Interestingly, the recent data on the white dwarf mass-radius relation [94, 95, 96] notes systematically smaller radii than one would expect from the conventional theory. Of course, the exact stellar mechanisms are not rigorously understood and most attempts to explain this discrepancy invoke a core composition of heavier elements. However, we simply note that at first approximation a violation of the Pauli principle would possess such features.

If we introduce the customary parameter  $\beta$  but let it be equal to the ratio of the number of electrons violating the Pauli principle to those obeying it we notice that the mass-radius relation provided by Equation (6.33) would be changed slightly. This follows by noting that the pressure will be re-adjusted due to the  $\beta n_e$  electrons not contributing to the pressure. In order to devise a more complete test more work must be done to introduce a Pauli violating parameter into the equation of state for the degenerate gas.

Probably the most sensitive test would involve Type Ia supernovae, which are white dwarfs that explode after exceeding the Chandrasekhar mass limit, calculated to be 1.4 solar masses. Type Ia are supernovae with an absence of hydrogen lines and the presence of a specific Si II line in their spectra. This limit is generally obtained when a white dwarf star is in a binary star system. In such a case, the mass of the white dwarf grows as it accretes material from its companion. The high accretion rates permit stable H and He shell burning and lead to a growing white dwarf star which is made primarily of carbon and oxygen (thus the lack of hydrogen lines observed in the subsequent supernova). When the white dwarf mass grows to the Chandrasekhar mass, contraction sets in and the central density becomes high enough to ignite carbon fusion under degenerate conditions. The environment of the degenerate gas provides a pressure which depends only on the density (as given in Equation (6.32)). Thus, the initial heat generation does not lead to pressure increase and expansion, which would result in controlled and stable burning. Instead, a thermonuclear runaway reaction occurs with a burning front that propagates through the whole star, causing complete disruption without a remnant [97].

If the exclusion principle were allowed to be violated slightly, the mass could exceed the Chandrasekhar limit slightly, and one would predict the possible existence of a white dwarf with a mass exceeding 1.4 solar masses. The most massive white dwarf currently known is below the theoretical limit, but it may be interesting to question the consequences of higher mass progenitors on the supernova explosions. It may also be possible to set a limit on Pauli principle violations from the observation that no white dwarfs have been observed with masses which exceed the Chandrasekhar limit.

#### **6.4.2 Solar Neutrino Implications**

One big cloud in our understanding the sun is something known as the solar neutrino problem [48]. The limits placed on Pauli principle violation with data from interactions from the solar interior along with a more detailed discussion of how a violation of the Pauli principle could solve the solar neutrino problem is provided by Plaga [98].

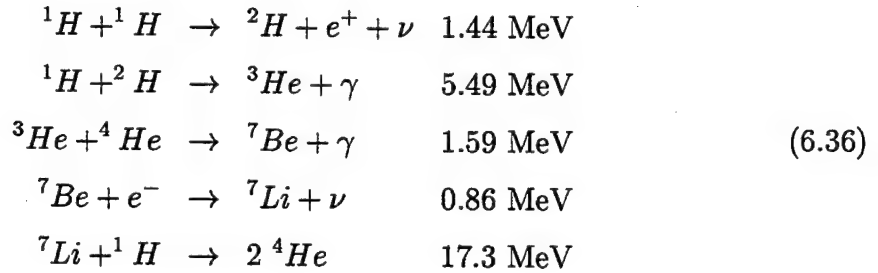
Theory predicts that the solar neutrino rate should be 9.3 SNU [48, 3] while experiments on  $^{37}\text{Cl}$  give  $2.55 \pm 0.25$  SNU [47] where SNU is a solar neutrino unit  $\equiv 10^{-36}$  interactions per second per Cl atom. This discrepancy between standard theory and observation has persisted for over two decades and is known as the solar neutrino problem.

Increasing the astrophysical  $S$ -factor, which is related to the cross section, in the basic p-p reaction, leads to a reduction of the sun's central temperature [99]. The  $S$ -factor is related to the interaction cross section through

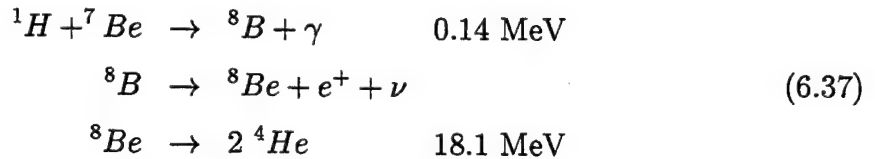
$$S(0) = \sigma_{th} \sqrt{E_{th} E_c} \left( \frac{E_{\gamma 1}}{E_{\gamma 2}} \right)^3 e^{4 \frac{E_c}{\gamma}}, \quad (6.35)$$

where  $\sigma_{th}$  denotes the thermal neutron capture cross section,  $E_{th}$  the maximum of the thermal energy distribution,  $E_c$  the Coulomb barrier energy and  $\gamma^2$  the Wigner limit  $\hbar^2/(2m_{\text{red}}R^2)$  with the interaction radius  $R$  and the reduced mass  $m_{\text{red}}$  of the interacting particles.  $E_{\gamma 1,2}$  stands for the  $\gamma$  energy in the reactions  $p(p, \gamma)^4\text{He}$ , and  $p(n, \gamma)D$  respectively.

The lower temperature discriminates against the PP II and PP III fusion processes. The PP II chain consists of the following set of reactions



and the PP III chain is given by



This lower temperature thus lowers the flux of high energy neutrinos. If we set  $\beta$ , which is a purely phenomenological parameter (since the GM theory was shown to be

inconsistent with a positive metric Hilbert space), to be near  $7.9 \times 10^{-9}$  it may yield the enhancement of the  $S$ -factor needed to solve the solar neutrino problem [98].

#### 6.4.3 Thermodynamical Implications

Because of the reliance of statistical mechanics on the assumption that particles obey the Fermi-Dirac or Bose-Einstein distributions, Pauli principle violations will have an effect on thermodynamical systems. Some of the thermodynamical implications of Pauli principle violations were discussed in detail by Rahal and Campa [100].

Recall that statistical mechanics provides a link between the thermodynamic (macroscopic) and quantum mechanical (microscopic) descriptions of a system via the partition function. The partition function  $Z$  is the normalization constant for the probability  $P$  of finding the system in some state  $i$  with energy  $E_i$

$$P_i = \frac{e^{-E_i/kT}}{Z}, \quad (6.38)$$

where, in general the partition function may be given by

$$Z = \sum_i e^{-E_i/kT}. \quad (6.39)$$

More information on the partition function for different ensembles is provided in nearly every book on statistical mechanics, (see Schroeder [101] or Wilde and Singh [67] for more information on different partition functions). For a two electron system with a probability  $\beta$  that they will occupy the same state, we can derive the partition function

$$Z = e^{-(E_a+E_b)/kT} + \beta e^{-2E_a/kT} + \beta e^{-2E_b/kT}, \quad (6.40)$$

where  $E_a$  and  $E_b$  are the two available energy levels. Generalizing to more electrons we may derive the grand partition function for a free-electron gas [102] like that in a metal which is given by

$$\ln Z = \sum_i \ln [1 + e^{-(E_i - \mu)/kT} + \beta e^{-2(E_i - \mu)/kT}] \quad (6.41)$$

where  $\mu$  is the chemical potential (sometimes referred to as the Fermi energy), and the sum is performed over the one-particle levels  $E_i$ . Notice that the above equation reduces to that of a Fermi gas for  $\beta = 0$ . The average occupation number  $N_i$  is the number of atoms in the state  $E_i$  and is given by

$$N_i = \frac{1 + 2\beta e^{-(E_i - \mu)/kT}}{1 + e^{(E_i - \mu)/kT} + \beta e^{-(E_i - \mu)/kT}} \quad (6.42)$$

notice that again when  $\beta \rightarrow 0$  we arrive at the usual equation for the occupation number of the Fermi-Dirac distribution and we recover the Fermi statistics. We notice that the inclusion of the nonvanishing  $\beta$  does not change the system much if the metal is in thermodynamical equilibrium [100]. However, the time required to reach equilibrium is much larger than usual. Thus, the observation that metals are in equilibrium allows Rahal and Campa to place a bound on the Pauli violating parameter of  $\beta \ll 10^{-23}$ .

We also notice that the presence of these anomalous statistics affects the Fermi energy and transport phenomena like electrical conductivity at extremely low energies along with anomalous contributions to the free electron specific heat. These observations were first made by Wolf [103] in 1997. Building on the work of Wu [104], he introduces the parameter  $\epsilon$  which is similar in nature to the parameter  $q$  in the quon algebra mentioned above. We then write the relative probability of partition (which is the number of ways of placing  $N_i$  particles in  $g_i$  cells) as

$$W_i = \frac{[g_i + \epsilon(N_i - 1)]!}{N_i! [g_i - (1 - \epsilon)N_i - \epsilon]!} \quad (6.43)$$

Here we see that  $\epsilon = 1$  returns us to the relative probability of partition for Bose-Einstein statistics and  $\epsilon = 0$  gives the usual Fermi-Dirac representation. This results in a Fermi energy which is dependant on  $\epsilon$  given by

$$E_F = \frac{1}{2m} \left( \frac{3Nh^3}{(1+\epsilon)8\pi V} \right)^{2/3}, \quad (6.44)$$

where  $V$  is the spatial volume. Thus as we diverge further from Fermi-Dirac statistics,  $\epsilon$  increases and the Fermi energy decreases. This also applies to the electric current, which we define as

$$J_x = \int_{-\infty}^{+\infty} \int_{-\infty}^{+\infty} \int_{-\infty}^{+\infty} \left( -\frac{\mathcal{E}e^2}{m} \right) \tau_r V_x \frac{\partial f_0}{\partial V_x} dV_x dV_y dV_z. \quad (6.45)$$

Here  $\mathcal{E}$  is the electric field,  $\tau_r$  is the relaxation time, and the distribution function  $f_0$  depends on  $\epsilon$  through

$$f_0 = \left[ 2(1+\epsilon)m^3 - \frac{2\epsilon m^3 e^{(E-\mu)/\tau}}{e^{(E-\mu)/\tau} + 1} \right] \frac{1}{(e^{(E-\mu)/\tau} + 1)h^3}. \quad (6.46)$$

Inserting this into Equation (6.45) gives the electric current in terms of the Pauli violating parameter  $\epsilon$

$$J_x = \frac{16\pi\sqrt{2m}\mathcal{E}e^2\tau_r(E_{F0})^{3/2}}{3h^3}(1-2\epsilon) \quad (6.47)$$

$E_{F0}$  is the Fermi energy without anomalous statistics. Thus, like the Fermi energy, the electric current drops as the violation of the Pauli principle increases and the system gets farther from the ideal Fermi-Dirac case.

The specific heat  $C_v$  of a free electron gas is given by

$$\begin{aligned} C_v &= \frac{dU}{dT} \\ &= \int_0^{+\infty} (E - E_F) \frac{df(E)}{dT} D(E) dE \end{aligned} \quad (6.48)$$

with  $D(E)$  is the density of states. After some algebra the specific heat as a function of  $\epsilon$  is

$$C_v = kTD(E_F) \left[ \frac{\pi^2}{3} + \frac{\epsilon}{9} \left( \frac{4}{3} - \pi^2 \right) \right] \quad (6.49)$$

Thus, like the Fermi energy and the electric current, the specific heat decreases with increasing  $\epsilon$ . The essential reason for the diminished values with the introduction of the Pauli-violating statistics is that, as a result of the small violations of the Pauli exclusion principle by the electrons in the metal, more electrons may be placed in lower energy levels, thus producing the diminished Fermi energy and a diminished free electron total energy and free electron current [103].

#### 6.4.4 Changes to Atomic Excitation Spectrum

Kelleher *et al.* [105] proposed that the excitation spectrum of helium would be sensitive to small violations of the Pauli principle, and proposed an experiment to test and bound such theories. Drake [9] proceeded to calculate the theoretical values for the transition frequencies of paronic helium.

The concept of the experiment may be quickly summarized by considering the nonrelativistic *LS* coupling approximation. In this approximation the wave functions for anomalous helium are different from those of normal helium in that the singlet and triplet spin functions are interchanged so that they form a completely symmetric wave function. This relationship is best viewed by a schematic diagram comparing the energy levels of anomalous He to normal He. A reproduction of Figure 1 in Ref [9] is provided in Figure 6.1. These shifts can then be detected with an experiment and used to place a limit on Pauli principle violations.

### 6.5 Possible Apparent Violations of the Pauli Principle

With the introduction of the theory of Greenberg and Mohapatra and the sudden burst of experiments which followed several studies were performed about how to deal with a positive signal suggesting Pauli principle violation.

#### 6.5.1 Electron Substructure

Akama *et al.* [106] show that a superficial violation of the Pauli principle will occur if the electron is a composite particle of finite size. They emphasize that such superficial violation of the Pauli principle *must* exist, no matter how small it is, if the electron has any substructure at all. This possible substructure of the electron is

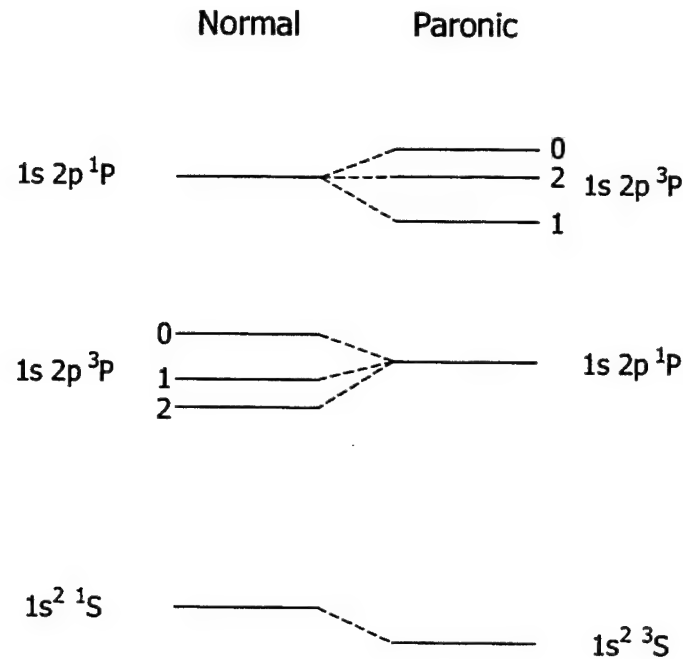


Figure 6.1: Schematic diagram showing the paronic helium states relative to the normal helium reference states. This figure is taken from Figure 1 of Ref. [9].

a natural extension of familiar effects at various levels of atoms, nuclei, and hadrons (see Figure 2.1). In order to see how this substructure could have masked detection let us look at a few examples of systems which have different behaviors at different distance scales.

The hydrogen atom consists of the proton and the electron and on distance scales that are large compared to the Bohr radius obeys Bose-Einstein statistics. This is because the spin of the system, which consists of an even number of fermions, adds up to that of a spin-1 particle, or boson. Thus in a low density hydrogen gas where the space between atoms is large compared to the atomic size, hydrogen behaves like a collection of bosons. However, as the density increases the average distance between atoms decreases until the gas is so dense that the hydrogen atoms overlap each other. When this occurs, the bosonic property of each hydrogen becomes meaningless and, instead, the fermionic property of the constituent protons and electrons becomes apparent.

This also occurs at smaller distance scales. Suppose that two helium atoms are so close that their nuclei are overlapping each other. Then, the genuine bosonic characteristics of each helium nucleus is meaningless and only fermionic statistics of the constituent nucleons is valid.

An apparent violation of the Pauli principle may then be present when two electrons in the system are so close together that they overlap and it is the nature of their substructure which becomes evident. Thus, violations will seem to occur when two electrons are virtually on top of each other: this “di-electron” which has charge  $2e$ , mass  $2m$ , and total spin  $\hbar$  will be unstable and will transition to a new  $1S$  orbit with about one-fourth the radius [106].

### 6.5.2 Violation of Lepton Family Number

Biedenharn, Truini, and van Dam [107] introduce a unique angle to possible Pauli principle violations. After introducing the an algebra based on Jordan pairs they show that it is possible to construct the same algebra of Ignatiev and Kuzmin [85] and Greenberg and Mohapatra [83] without ever violating the Pauli exclusion principle.

Recall that there are two different kinds of symmetries we are faced with in nature<sup>1</sup>. Continuous symmetries like the reflection symmetry about any diameter of the circle (see Figure 2.9) or discrete symmetries like the reflection symmetries of the square or triangle. The Pauli principle is a discrete symmetry because it pertains to the exchange of identical particles.

Jordan pairs are an algebra which provide a framework for structures which do not assume the bilinear commutation relations usually encountered in quantum mechanics. Their model ascribes a new degree of freedom to the electron permitting it to have different states  $e$  and  $\mu$ . Taken literally, their model introduces a quantum number which is the family label, and the mixing needed to obtain the IK and GM algebras introduces a violation of the usual conservation of lepton family number instead of a violation of the Pauli principle. If muons did mix into electron states it

<sup>1</sup>Recall the discussion of symmetries from the section on Noether’s theorem in Chapter 2 covering the standard model.

would lead to a triplet spin component in the helium atom ground state which would look like a violation of the Pauli principle but would actually be due to the mixing in the lepton family number.

Current developments in neutrino physics postulate a possible mixing of this type in order to solve several experimental inconsistencies including the Solar Neutrino Problem discussed in previous chapters. It would be interesting if such mixing occurred between the neutrinos, and it may also occur between the charged leptons and would introduce a (Cabbibo-Kobayahi-Maskawa)-like mixing matrix. Of course, there are no known violations of lepton family number, and thus if observed this apparent Pauli principle violation would imply interesting new physics beyond that described in the preceding chapters.

### 6.5.3 Compactification of Extra Dimensions

Lets assume that the wave function of two identical fermions is given by

$$\psi(\mathbf{x}_1, \theta_1; \mathbf{x}_2, \theta_2) = \psi(\mathbf{x}_1, \theta_1)\psi(\mathbf{x}_2, \theta_2) \quad (6.50)$$

which in  $3 + d$  space dimensions is completely antisymmetric under the interchange of both the  $\mathbf{x}$  and  $\theta$  variables. Here  $\mathbf{x}$  denotes the usual three space coordinates and  $\theta$  denotes the  $d$  extra space dimensions. According to Greenberg and Mohapatra [108], if there is a small excitation of antisymmetric states in the two-particle state of the  $d$  extra dimensions, then after the  $\theta$ 's are compactified, the projected 3-dimensional state (which depends on the  $x$ 's) must have a small symmetric part. The size of this symmetric component will depend on the compactification scales of the extra dimensions and on the amplitude of the antisymmetric excitation in the compactified space.

Another way to see this would be to imagine that while we do live in a  $3 + d$  space, a given 3-dimensional state labeled by momentum and spin can correspond to many states in the big space each with different values of the compactified momenta. Multiple occupancy of states labeled by 3-dimensional momenta and spin which seem to violate the Pauli principle do not necessarily directly correspond to multiple oc-

cupancy of states labeled by the  $(3 + d)$ -dimensional momenta and spin and thus do not necessarily violate the Pauli principle [108].

However, if the usual cyclic boundary conditions are assumed  $\psi(\phi) = \psi(\phi + 2\pi)$  for the wave function in the extra dimensions an apparent violation of the Pauli principle would not occur since the energy level spacing in the extra dimensions is large. An example would be the energy levels of a particle in a box whose length is  $a$ . The energy levels for this case are given by

$$E_n = \frac{n^2 \pi^2 \hbar^2}{2ma^2} \quad (6.51)$$

If the compactified dimensions are small (on the order of the Plank length defined by Equation (2.9)), then the separation between the levels is large. However, if the boundary conditions are instead twisted such that the wave function is no longer cyclic  $\psi(\phi) \neq \psi(\phi + 2\pi)$  it may be possible to have degeneracy in the extra dimensions. In fact, it may be possible to use the experimental results of the following chapters to limit the existence of such boundary conditions since no apparent violation has been observed.

Electrons may only move in the compactified dimension if the dimension is larger than the size of the electron which may allow us to set a limit on the size of such extra dimensions given knowledge about the electron and the experimental results in the following chapter [109].

This new degree of freedom introduced by the compactified spatial dimensions is similar in context to the discussion of possible violation of lepton family number discussed in Ref. [107] and provided in the previous section.

## CHAPTER 7. EARLY EXPERIMENTS TESTING THE SYMMETRIZATION POSTULATE

As mentioned in the previous chapter, probably the best collection of papers both on the theory of possible violations of the symmetrization postulate and the Pauli exclusion principle along with reviews of the different experiments can be found in the conference proceedings on *Spin-Statistics Connection and Commutation Relations: Experimental Tests and Theoretical Implications* edited by Hilborn and Tino [80].

### 7.1 Introduction

Generally speaking, tests of the symmetrization postulate (SP) and the Pauli exclusion principle (PEP) fall into one of five classes: Searches for PEP-forbidden electronic or nuclear transitions, or for PEP-forbidden electronic or nuclear states. The fifth miscellaneous class of experiments includes bounds placed on such violations by spectroscopy, observational data or cosmological constraints.

### 7.2 Forbidden Electronic or Nuclear Transitions

We may further break up the category of forbidden transitions by observing that there are generally two different kinds of experiments which have been performed in this genre. In such experiments what is often experimentally observed are photons which result from the transition of the particle from a state in which the Pauli principle is not violated to one that is. For example, if the ground state of an atom is filled then the Pauli principle says that no additional electrons will be allowed to occupy this state. If a photon, which would result from an electron transitioning to the filled ground state, is observed this would be an indication that the Pauli principle had been violated. In general there are two ways this transition may occur. It could be from new electrons which are introduced to the system, which Gillaspay has called

Absorbing Block Experiments, or from electrons already present in the atom which he has dubbed Decaying Block Experiments.

### 7.2.1 Absorbing Block Experiments

The first data directly testing the Pauli principle was actually reanalysis of results from older experiments. The experiment performed by Goldhaber and Scharff-Goldhaber [110] in 1948 originally investigated if beta-rays were, in fact, electrons. Now it is known that beta rays are electrons and thus their experiment may be reinterpreted as a test of the Pauli principle, since they used the idea of the Pauli principle to verify that the new electrons (beta-rays) did not cascade to the ground state releasing K shell x-rays.

A similar experiment was later performed by Ramberg and Snow [111]. By passing a current through a copper, Cu, strip Ramberg and Snow ensured that new electrons were introduced to the copper. They simultaneously watched for the K shell x-rays that would be emitted if one of the electrons was captured by a Cu atom and cascaded down to the filled 1S level. The experiment concluded that the probability a new electron introduced into the copper would form a mixed symmetry state with respect to the electrons already present in the sample, thus violating the Pauli exclusion principle, was less than  $1.7 \times 10^{-26}$ .

### 7.2.2 Decaying Block Experiments

In 1974 Reines and Sobel [112] reinterpreted the experiment performed by Moe and Reines [113] (MR) in 1965 in which they originally were setting limits on the lifetime of the electron. In the original experiment MR looked for the transition of an *L*-shell electron to the *K*-shell, which as mentioned before emits a 33.2 keV x-ray. In their original experiment the premise was that this transition would occur if one of the ground state (*K*-shell) electrons decayed leaving a state with which another electron could occupy. This data was thus reinterpreted as a test of the Pauli exclusion principle and the background present in the apparatus was used to set a limit of greater than  $\tau > 2 \times 10^{27}$  seconds for the Pauli violating transition.

An experiment of this type was also performed for nucleons by Logan and Ljubičić [114]. In this experiment they searched for 20 MeV  $\gamma$  rays which would be emitted if a nucleon in the  $p$ -shell of  $^{12}\text{C}$  fell into the fully occupied  $1s_{1/2}$  shell. The mean lifetime  $\tau$  against  $p$ -shell nucleons in  $^{12}\text{C}$  falling into the fully occupied  $1s_{1/2}$  shell was shown to be  $\tau > 6 \times 10^{27}$  seconds with a 99.7% confidence limit.

Another such experiment on nucleons was performed by Kishimoto *et al.* [115] in which holes appear in the ground state of lead following a violation of the Pauli principle. The presence of these holes results in the formation of a compound nuclear state which subsequently decays emitting nucleons. In their experiment Kishimoto *et al.* watched for neutrons emitted from the system as opposed to the  $\gamma$  ray emission tests of Logan and Ljubičić. Neutrons from natural lead were found to be less than  $1.6 \times 10^{-3}$  neutrons/s kg which gives a lifetime of  $\tau > 3.2 \times 10^{27}$  seconds.

Another experiment of this type was proposed and executed by Ejiri and Toki [116] in which they searched for non-fermionic statistics by observing the energy spectrum from stable Na and I in a large NaI detector. In this case their detector was also their experiment since NaI is a scintillator and they watched for protons and  $\gamma$ -rays emitted from a nuclear decay with eight of twenty NaI detector-modules of ELEGANTS V at the Kamioka underground laboratory. This experiment set the amazingly small upper bound of  $\leq 1.4 \times 10^{-53}$  for such violations of the Pauli principle. The experiment was repeated by Bernabei *et al.* [117] several years later at the Gran Sasso National Laboratory. Their result expanded the range of energies observed and set limits as low as  $1.9 \times 10^{-55}$  for such transitions in Na and I.

Another test of violations of the Pauli principle by nucleons was performed with the underground water Cherenkov detector Kamiokande [118]. Their experiment set limits on the branching ratios for the Pauli forbidden decays  $n \rightarrow \nu_e \nu_e \bar{\nu}_e$ ,  $n \rightarrow \nu_\mu \nu_\mu \bar{\nu}_\mu$ , and  $n \rightarrow \nu_\tau \nu_\tau \bar{\nu}_\tau$ . This experiment reports the most stringent limits to date on Pauli principle violations and suggests that if violated the relative strength of such transitions is less than  $2.3 \times 10^{-57}$  with a 90% confidence limit. Of course pending a consistent theory, there is no way to show that such transitions are not suppressed

over other experiments and thus experiments have continued to be performed in light of this stringent result provided in 1993.

The most recent test of the Pauli exclusion principle for nucleons comes from an experiment using the NEMO-2 detector [119] which was designed for double beta decay studies and was operated in the Fréjus Underground Laboratory from 1991 to 1997. The concept for using such liquid scintillation detectors to look for the probable non-paulian transitions  $2p \rightarrow 1s\beta^-(\beta^+)$  of  $^{12}\text{C}$  to  $^{12}\text{N}(^{12}\text{B})$  was first discussed by Kekez, Ljubić, and Logan [120]. The NEMO-2 detector was used to place limits on the violation of the Pauli principle for p-shell nucleons in carbon. Transitions to the fully occupied  $1s_{1/2}$ -shell yielded a lifetime of  $1.3 \times 10^{32}$  seconds for the process with emission of a  $\gamma$ -quantum. Similarly, limits of  $9.8 \times 10^{31}$  seconds for the emission of a  $\beta^-$  and of  $8.2 \times 10^{31}$  seconds for the emission of a  $\beta^+$  in the Pauli-forbidden transition of  $^{12}\text{C} \rightarrow ^{12}\text{N}'(^{12}\text{B}')$ .

This type of experiment (namely the Reines and Sobel [112] reanalysis of the Moe and Reines [113] experiment) came under some scrutiny when Amado and Primakoff [69] pointed out that such a transition from a Pauli-obeying state to a Pauli-violating state is not permitted in the constructs of quantum mechanics. This arises from the fact that the Hamiltonian is invariant under the interchange of two particles. More discussion of this is provided surrounding Equations (4.31) and (4.32).

### 7.3 Forbidden Electronic or Nuclear States

Like forbidden transitions, the first data on forbidden nuclear states comes from an experiment which was not intended to test for violations of the Pauli exclusion principle but which could be reinterpreted as such a test. Fischbach, Kirsten, and Schaeffer [16] originally searched for anomalous electrons which differed from the usual electrons by some conserved internal quantum number (this concept is not unlike that presented by Biedenharn, Truini, and van Dam [107] in which they predicted lepton mixing would produce apparent violations of the Pauli principle). Since the original experiment investigated the possibility of an additional quantum number, more electrons could fit in a shell than was previously believed since the Pauli principle

says that no two electrons may have the same quantum numbers. This meant that beryllium which usually has two electrons in the  $1s$  shell and two electrons in the  $2s$  shell would have an additional shell (called the  $1s'$  shell) for the electrons to reside. This anomalous beryllium  $Be'$  would have the same chemical properties as an ideal gas and would behave chemically like helium. In the experiment Fischbach, Kirsten, and Schaeffer set limits on the existence of such electrons and hence limited the proposed conserved internal quantum number with mass spectrometry. This was later interpreted as a test of the Pauli principle because the experiment looked for all four electrons to exist in the ground state, namely  $1s^4$  instead of the usual configuration  $1s^2 2s^2$ . This experiment reported a  $Be'$  concentration in He of

$$\frac{[Be']}{[He]} < 9.1 \times 10^{-7} \quad (7.1)$$

in an atmospheric sample. This experiment was then performed again using the accelerator mass spectrometer at Purdue and which is the subject of future chapters.

The idea of forbidden electronic states seems to have originated in the paper by Gavrin, Ignatiev, and Kuzmin [121] and Novikov and Pomanskii [122] followed the idea up with the possibility of using nucleosynthesis to bolster an experimental ratio of PEP violating atoms to PEP obeying ones. This was later used in the papers produced by their collaboration [10, 11, 12, 13, 123]. Each of these papers were produced on the same experiment in which the collaboration looked at possible Pauli principle violations by both electrons and nuclei. Unlike the experiments discussed previously which looked for a transition of an electron/nucleon to a forbidden state, the Nolte experiments searched for the existence of the final forbidden state.

To test the Pauli principle for electrons they looked for Neon, Ne, which was violating the Pauli principle and behaving chemically like fluorine, F. In this experiment one of the electrons in usually filled valence shell of Ne transitions into the ground state leaving a whole in the valence shell. Thus the anomalous neon, denoted  $Ne'$ , is electrically neutral but has a valence shell which is like that of fluorine. Thus, the only difference between the  $Ne'$  and F is the mass of the nucleus (see Figure 7.1). Of

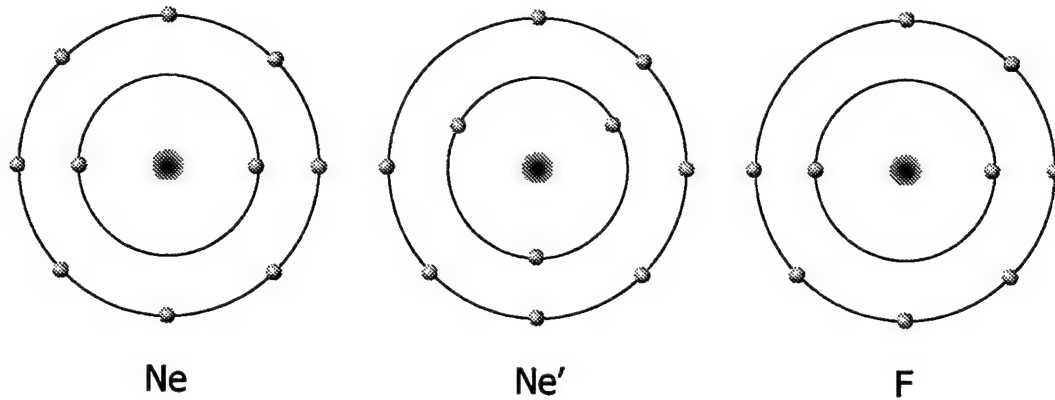


Figure 7.1: Configurations of atomic electrons for neon (Ne), anomalous neon (Ne'), and fluorine (F). In Ne' there are three electrons in the K-shell thus displaying behavior indicative of a violation of the Pauli exclusion principle. This figure was adapted from Ref. [10, 11, 12].

course as discovered in Chapter 1, accelerator mass spectrometry is ideally suited for finding trace amounts of a specific mass and differentiating one mass from another. The Ne' concentration in F was measured to be

$$\frac{[Ne']}{[F]} < 6 \times 10^{-18} \quad (7.2)$$

In order to transform this ratio into the number of anomalous neon to neon they employ the nucleosynthesis arguments discussed by Novikov and Pomanskiĭ [122] which includes the ratio of the cosmic abundances of each particle species

$$\frac{[Z']}{[Z]} = \frac{[Z']}{[Z-1]} \frac{P(Z-1)}{P(Z)P(A,Z)} \quad (7.3)$$

where  $[Z']/[Z-1]$  is the measured parameter and  $P(A, Z)$  is the cosmic isotopic abundance of the isotope with mass  $A$  of element  $Z$ . For application to their neon experiment Nolte *et al.* [10, 11, 12, 13, 123] observe that

$$\frac{P(Ne)}{P(F)} = 3300 \quad \text{and} \quad P(^{20}Ne) = 90\% \quad (7.4)$$

Thus, plugging the results from Equations (7.2) and (7.4) into Equation (7.3) gives

$$\frac{[Ne']}{[Ne]} < 2 \times 10^{-21} \quad (7.5)$$

This experiment provided a nice limit on the existence of Pauli principle violations with accelerator mass spectrometry. In the experiment there was no contamination from regular neon because its filled valence shell inhibits it from reacting to form a solid. However, the anomalous neon would behave chemically like fluorine and thus could form the calcium compound  $CaF_2$  used in their experiment.

There is one problem with this experiment. The anomalous neon would be expected to coexist with regular neon and not necessarily with fluorine. Thus the  $CaF_2$  they tested may not have contained anomalous neon because the anomalous neon was not present at the formation of the  $CaF_2$ . Ideally, the  $CaF_2$  should have been created in a neon rich environment. In such a scenario, the anomalous neon would be present and available to form  $CaNe_2$ . If this had been done there would not have been the need to introduce the cosmic abundance arguments to turn their  $[Z']/[Z - 1]$  ratio into  $[Z']/[Z]$ .

We may also observe that if the anomalous neon resulted from some kind of decay of Ne to Ne' their experiment would not have been sensitive to the effect unless such a lifetime was much shorter than the age of the universe and such that a transition occurred in sufficient abundance in nucleosynthesis.

Nolte *et al.* [10, 11, 12, 13, 123] performed a similar test with anomalous argon, Ar', in chlorine, Cl, samples (see Figure 7.2). The Ar' concentration in Cl was measured to be

$$\frac{[Ar']}{[Cl]} < 8 \times 10^{-16} \quad (7.6)$$

Again plugging in for the ratio of the cosmic abundances

$$\frac{P(Ar)}{P(Cl)} = 22 \quad \text{and} \quad P(^{36}Ar) = 84\% \quad (7.7)$$

yields

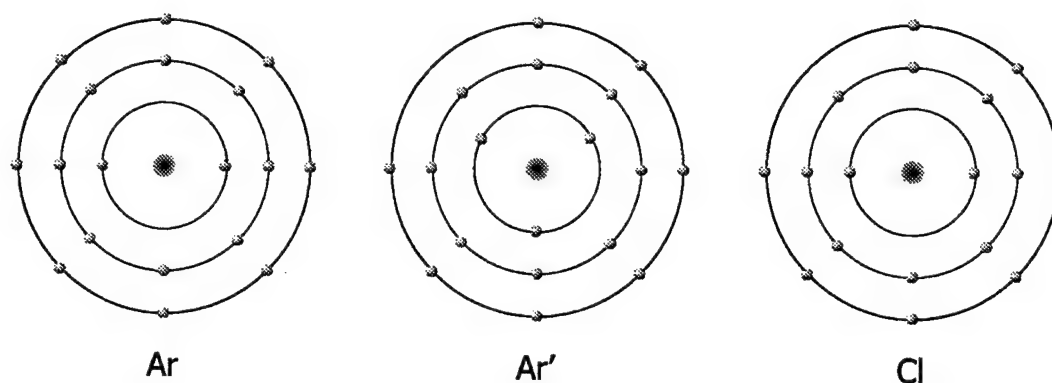


Figure 7.2: Configurations of atomic electrons for argon (Ar), anomalous argon (Ar'), and chlorine (Cl). In Ar' there are three electrons in the K-shell thus displaying behavior indicative of a violation of the Pauli exclusion principle. This figure was adapted from Ref. [11, 12].

$$\frac{[Ar']}{[Ar]} < 4 \times 10^{-17} \quad (7.8)$$

Like the  $\text{CaF}_2$  of their previous experiment, the solid was silver chloride,  $\text{AgCl}$  and again the possibility of  $\text{AgAr}$  formation would need to be considered. In both of these experiments the role of shielding of the nucleus is not understood. In the experiment searching for anomalous neon this does not play an important role since the  $1s$  shell is the only level involved and thus only 2 electrons are “shielding” the nucleus. However, as is evident from a comparison between Figures 7.1 and 7.2 there are 10 electrons involved in the shielding in the anomalous argon experiment.

Finally the Nolte collaboration [11, 12, 13] also produced results looking for nuclear states which are not permitted by the Pauli principle. They searched for stable  $^4\text{Li}$ ,  $^5\text{Li}$ , and  $^5\text{He}$  atoms. Since these atoms decay no such background should exist. The energy levels of lithium,  $\text{Li}$ , are provided in Figure 7.3 while those of helium,  $\text{He}$ , are shown in Figure 7.4.

Another experiment of this genre was performed by Barabash *et al.* [124] and Tsipenyuk *et al.* [125]. In this experiment, a search was made for anomalous carbon atoms in boron. Like the searches mentioned above the anomalous carbon contains

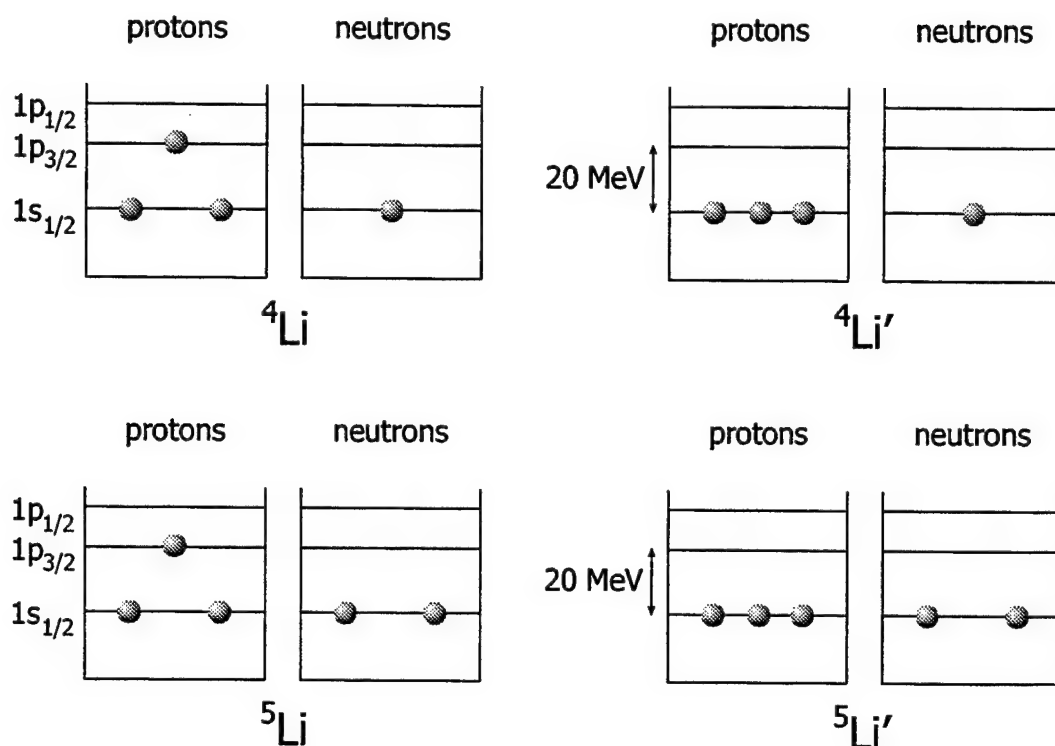


Figure 7.3: Configurations of nucleons for lithium ( ${}^4\text{Li}$ ,  ${}^5\text{Li}$ ) and anomalous lithium ( ${}^4\text{Li}'$ ,  ${}^5\text{Li}'$ ). This figure was adapted from Ref. [11, 13, 12].

three  $K$ -shell electrons and thus behaves chemically like boron. Unlike the previously mentioned experiments, accelerator mass spectrometry is essentially rendered useless in this instance because of the large quantity of “ordinary” carbon as a trace element

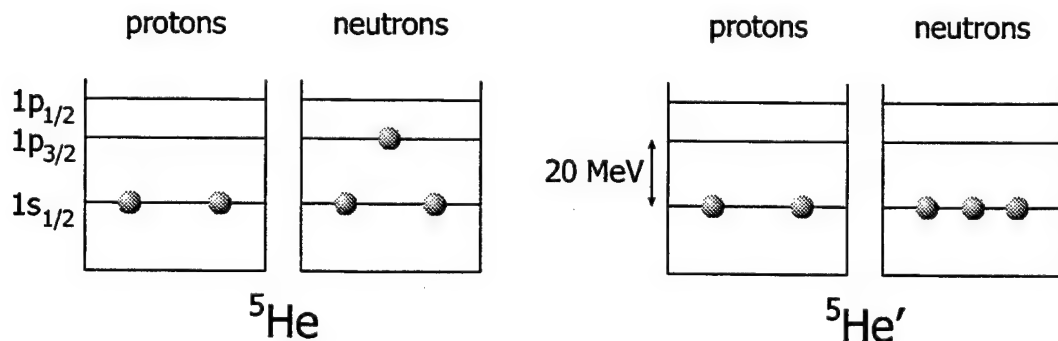


Figure 7.4: Configurations of nucleons for helium ( ${}^5\text{He}$ ) and anomalous helium ( ${}^5\text{He}'$ ): This figure was adapted from Ref. [12].

in boron. The idea of this experiment was to first remove carbon atoms chemically from a boron sample and then to measure the content of carbon nuclei in it. The search for anomalous carbon atoms was then performed by  $\gamma$ -activation analysis of different boron samples. Boron is an ideal object for the  $\gamma$ -activation method since irradiation with  $\gamma$  rays does not produce any radioactive isotopes in it and the entire induced activity is thereby completely determined by the impurities alone. This experiment reported a concentration of anomalous carbon,  $C'$ , in boron,  $B$ , to be

$$\frac{[C']}{[B]} \leq 5 \times 10^{-6} \frac{\text{g}}{\text{g}} \quad (7.9)$$

Using the cosmic abundance arguments of Novikov and Pomanskii [122] this led them to conclude

$$\frac{[C']}{[C]} \leq 2.5 \times 10^{-12} \quad (7.10)$$

## 7.4 Miscellaneous Tests

### 7.4.1 Spectroscopic Tests

Recall from the previous chapter that Drake [9] published precise calculations of the paronic energy shifts that would exist if small violations of the Pauli principle existed (for a diagram of the shifts see Figure 6.1). In fact, helium is the only system of fermions for which such detailed calculations are available and can be experimentally verified since zeroth order spatial wave functions are identical in both cases [126]. Deilamian, Gillaspay and Kelleher [127] carried out such an experiment. Their experiment set a limit on the existence of the predicted spectral line with no signal above a background which was  $2 \times 10^5$  below the peak signal of the Pauli principle allowed line. This led them to infer a limit on the dimensionless PEP/SP violation coefficient introduced by Greenberg and Mohapatra [83] to be  $\beta^2/2 < (0.2 \pm 5.0) \times 10^{-6}$ .

Until now, all experiments have been tests of the Pauli exclusion principle in that they have tested only fermions. However, some tests were proposed which tested the

symmetrization postulate for bosons [128, 129]. These suggestions were to search for forbidden exchange-antisymmetric states in molecules containing two oxygen, O, nuclei which are spin-0 bosons. Two independent tests on  $^{16}\text{O}_2$  set bounds on such violations. De Angelis *et al.* [130] investigated the spectrum of the  $^{16}\text{O}_2$  molecule by high-sensitivity laser spectroscopy and searched for transitions involving states which were antisymmetric under the exchange of the nuclei. Unlike fermion systems in which a violation of the Pauli principle can be detected as a signal on a zero background, the effects of a small violation for particles obeying Bose-Einstein statistics would usually manifest themselves as a small change in the properties of a many-particle system. This arises from the difference between the behavioral characteristics of fermions and bosons. The basic idea behind these experiments is analogous to that of Deilamian, Gillaspy and Kelleher [127] discussed above.

De Angelis *et al.* [130] were the first to perform such an experiment testing the symmetrization postulate for integer-spin particles and set an upper limit of  $5 \times 10^{-7}$  to a possible violation of this postulate. Hilborn and Yuca [131] published an adjacent paper to de Angelis *et al.* in the Physical Review Letters on another experiment of this genre. Hilborn and Yuca used diode laser absorption spectroscopy of the "A" band of molecular oxygen to provide an upper limit of  $(0.8 \pm 1.3) \times 10^{-6}$  on the probability of finding two identical  $^{16}\text{O}$  nuclei in an antisymmetric spin state.

This experiment was improved upon by Modugno, Inguscio, and Tino [132]. The carbon dioxide molecule possesses the same symmetry properties as oxygen but, since it is triatomic, it has strong active vibrational bands in the infrared, which are lacking in the biatomic  $\text{O}_2$ . Thus, by looking for transitions in the  $\text{CO}_2$  spectra involving states which are antisymmetric in the exchange of the nuclei, they lowered the limit on violations of the symmetrization postulate by spin-0 nuclei. Using high-sensitivity laser spectroscopy, Modugno, Inguscio and Tino [132] lowered the limit by two orders of magnitude setting a limit of  $2.1 \times 10^{-9}$  on such SP violating transitions.

The most recent reduction of the limit on such transitions was reported by Mazzotti *et al.* [133]. Like the previous experiment, the authors investigate the  $\text{CO}_2$

spectrum. Unlike previous references [132] which used the  $12^0_1 - 00^0_0$  band, Mazzotti *et al.* used the  $00^0_1 - 00^0_0$  fundamental band which is nearly 2000 times stronger and thus allowed them to reach an even lower limit of  $1.7 \times 10^{-11}$  for the probability that the two spin-0 oxygen nuclei are in forbidden exchange-antisymmetric states.

#### 7.4.2 Tests with Photons

While the first proposed experimental test of the symmetrization postulate using photons was provided by Gerry and Hilborn [134] DeMille *et al.* [135] provided the first experimental limits for photons. If photons do not obey Bose-Einstein statistics, there would be a nonzero probability that two photons are in an exchange-antisymmetric state like that of the oxygen discussed above. DeMille *et al.* studied transitions in atomic Ba and set a limit of  $\nu < 1.2 \times 10^{-7}$  with a 90% confidence limit on the probability that photons are in such exchange-antisymmetric states. Their experiment searches for the forbidden states based on a selection rule derived by some of the authors [136] which forbids two-photon transitions between atomic states with  $J = 0$  and  $J' = 1$  for degenerate photons.

#### 7.4.3 Cosmological Limits

Following the theoretical developments discussed in the previous chapter several limits were placed on violations of the Pauli principle using less than conventional methods. The use of cosmological observations and our understanding of cosmological processes are among the most interesting limits imposed upon PEP violations.

The first astrophysical limits on possible violations of the Pauli principle came from Plaga [98]. One of the ideas introduced in Ref. [98] was that violations of the Pauli principle may be used to solve the longstanding solar neutrino problem discussed in the previous chapter. In the same paper Plaga describes the details of a calculation of the limits on Pauli principle violation in the interior of the sun.

Plaga shows that inside the sun  $^2\text{He}_s$ , a symmetric helium-2 may be formed from the reaction  $p(p, \gamma) ^2\text{He}_s$ . Using the reaction  $p(n, \gamma) D$  as a guide Plaga calculates the  $S$ -factor which is given by Equation (6.35) and gives

$$S(0) = 6.5 \times 10^{-6} \cdot \varepsilon^2 \text{ keV} - \text{b} \quad (7.11)$$

where  $\varepsilon^2/2$  is the probability for the formation of an anomalous state with a totally symmetric wavefunction in a nucleon-nucleon collision. Thus the measured value for the  $S$ -factor provides a limit of  $\varepsilon^2/2 < 1.6 \times 10^{-15}$ .

Another astrophysical limit on possible violations of the Pauli principle comes from Thoma and Nolte [137]. They investigate the hypothetical consequences of Pauli principle violation on primordial nucleosynthesis. Since the abundances of anomalous nuclei (like  $\text{Li}'$  and  $\text{He}'$ ) can be estimated by incorporating anomalous reactions and nuclei during primordial nucleosynthesis (PNS) Thoma and Nolte derive

$$\frac{N(Z')}{N(^4\text{He})_{\text{PNS}}} > \frac{N(Z')_{\text{PNS}}}{N(^4\text{He})_{\text{PNS}}} \quad (7.12)$$

which, if interpreted as a function of  $\beta^2/2$ , provides a limit on the parameter. Here  $Z'$  is the anomalous nuclei of investigated. This assumption on the abundances of such nuclei from primordial nucleosynthesis is given by,

$$\frac{N(Z')_{\text{PNS}}}{N(^4\text{He})_{\text{PNS}}} \approx e^{\Delta/kT} \frac{\gamma(Z')}{\gamma(^4\text{He})} \frac{\beta^2}{2} \quad (7.13)$$

where  $\Delta$  is the binding energy per nucleon with respect to  $^4\text{He}$

$$\Delta = \frac{1}{A}B(Z') - \frac{1}{4}B(^4\text{He}) \quad (7.14)$$

$$\gamma(Z, A) = e^{\frac{-2.83(Z-1)^{2/3}(A-1)^{1/3}}{(AT_9)^{1/3}}}$$

These definitions can be found in Claytons book "Principles of Stellar Evolution and Nucleosynthesis" [99].

The application of these equations yield the following limits on the Pauli violating parameter  $\beta^2/2$  for two of the anomalous nuclei tested in the Nolte experiments [11, 12, 13]  $\text{Li}'$  (in which protons are violating the Pauli principle, see Figure 7.3) and  $\text{He}'$  (in which neutrons are violating the Pauli principle, see Figure 7.4),

$$\text{For protons : } \text{Li}' \quad \frac{\beta^2}{2} < 5 \times 10^{-33} \quad (7.15)$$

$$\text{For neutrons : } \text{He}' \quad \frac{\beta^2}{2} < 3 \times 10^{-15}$$

#### 7.4.4 Limits from Thermodynamic Considerations

As mentioned in the previous chapter there are thermodynamic implications of PEP violations. Rahal and Campus [100] consider a metal box of  $1 \text{ cm}^{-3}$  with energy level spacing on the order of  $10^{-8} \text{ eV}$ . Transitions between these levels is roughly  $h/10^{-8} \approx 10^{-7}$  seconds. If there is an inhibition  $\beta^2$ , then the average time for PEP-violating transitions would be  $10^{-7}\beta^{-2}$  seconds. If the metal is  $10^9$  years old and limit the average transition time to be greater than its age, this sets an upper limit of  $\beta^2 \ll 10^{-23}$  on the Pauli violating parameter  $\beta$ .

## CHAPTER 8. SEARCHING FOR ANOMALOUS BERYLLIUM

### 8.1 The Fischbach, Kirsten and Schaeffer Experiment

As mentioned in the previous chapter, the first data constraining violations of the Pauli exclusion principle by searching for forbidden electronic states comes from an experiment searching for anomalous electrons performed by Fischbach, Kirsten, and Schaeffer (FKS) [16] in 1968. In this experiment, atmospheric air was analyzed with a mass spectrometer to search for anomalous beryllium  $\text{Be}'$ .  $\text{Be}'$  is beryllium with the PEP-forbidden electronic configuration  $1s^4$  instead the usual configuration  $1s^2 2s^2$ .

This experiment failed to detect any anomalous beryllium above background and set the following limits on the existence of  $\text{Be}'$  in air.

$$\rho' = \frac{[\text{Be}']}{[\text{air}]} < 5 \times 10^{-12} \quad (8.1)$$

While the results from the FKS experiment were originally interpreted as a test for the existence of anomalous electrons and positrons which differ from ordinary electrons and positrons by an unspecified conserved quantum number, they also provided a direct test of the validity of the Pauli exclusion principle.

This experiment was then rerun with several notable improvements and novel changes which led to several publications and is the subject of Part II of this thesis.

### 8.2 Underlying Constructs and Assumptions

Like the experiments described in the preceding chapter this experiment searches for electronic states which are forbidden by the Pauli exclusion principle. If the Pauli principle is not violated, electrons fill from the ground state up as they are introduced to the atom. For  ${}^9_4\text{Be}$ , whose nucleus consists of 4 protons,  $Z = 4$ , and 5 neutrons,  $N = 5$  ( $A = Z + N = 4 + 5 = 9$ ), the first electron falls into the lowest energy level

(called the K shell) and may have its spin orientation either “up” or “down” (see Figure 8.1 for the electron spin orientations and energy levels of neutral Be). The K shell has only one subshell called the  $1s$  shell with only one orbital and the electronic configuration of the Be atom is given by

$$\text{Be}(Z = 4) : \frac{\uparrow}{1s} \quad (8.2)$$

written in shorthand spectroscopic notation as  $\text{Be}:1s^1$ .

The second electron to be added to Be will also cascade down to the K shell but will orient its spin so that it is opposite that of the existing electron thus obeying the Pauli exclusion principle. With two electrons the Be now has the configuration  $\text{Be}:1s^2$  which written longhand is

$$\text{Be}(Z = 4) : \frac{\uparrow\downarrow}{1s} \quad (8.3)$$

Since each orbital may hold a total of two electrons (one spin up and another spin down) the  $1s$  shell is said to be filled forcing the next electrons to be placed in a higher energy level denoted the L shell. Unlike the K shell which only possessed one subshell, the L shell has two subshells the  $2s$  subshell which has one orbital and the  $2p$  subshell which has three orbitals (see Figure 8.1). Neutral Be has the electronic configuration

$$\text{Be}(Z = 4) : \frac{\uparrow\downarrow}{1s} \left| \frac{\uparrow\downarrow}{2s} \right. \quad (8.4)$$

The electrons fill the energy levels according to the Aufbau principle. If the Pauli principle were violated electrons would not be constrained to fill the energy levels in this manner. Since a consistent theory for Pauli principle violation does not exist we are left with an open experimental question. All of the experiments of the previous chapter (except the FKS experiment) assume that when the Pauli principle is violated it does so with only one electron. In such experiments, one of the electrons is “caught” violating the Pauli principle while it is assumed that the other electrons continue to

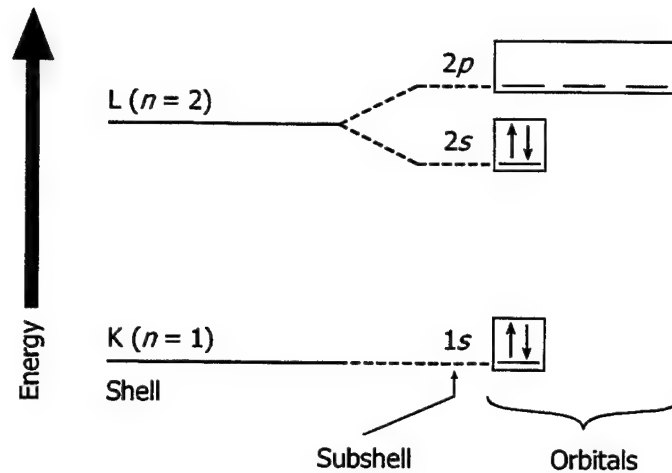


Figure 8.1: The subshells and orbitals of the first two shells. The electronic configuration shown here is that of neutral beryllium. This diagram is adapted from Ref. [14].

obey Fermi-Dirac statistics. However, this may not be the case. Without a consistent theoretical framework to guide the experiments we cannot conclude that this would be the case. For example, how do we know which electrons are actually violating the Pauli principle? In the case of the Nolte *et al.* experiments [10, 11, 12, 13, 123] there were three electrons occupying the K shell. Without a theory of PEP violation we cannot tell which electron is doing the violating and which is obeying. Since the mechanism for such a violation is not known it may be that violations never occur to single particles but must occur in pairs or that all the electrons of the atom must be Pauli violating.

Thus, without a theory for Pauli principle violation we cannot predict what a Pauli violating atom would look like. It may be that the beryllium would behave chemically like either lithium ( $\text{Be}' : 1s^3 2s^1$ ) or like helium ( $\text{Be}' : 1s^4$ ). As mentioned before each of the previous experiments searched for the violation of the Pauli principle by only one electron and thus searching for lithium-like  $\text{Be}'$  would only set limits on such a species but would most definitely would not produce the most stringent results available (since Susuki *et al.* [118] have set limits on the order of  $10^{-57}$ ).

Thus to provide more stringent limits in a regime that has only one known previous experiment would be to look for helium-like anomalous Be whose limits were derived from a reanalysis of the FKS experiment from the previous section.

To recapitulate, in contrast to previous experiments in which the PEP is violated by a single additional fermion in a forbidden state, a search for Be' probes for a PEP violation by two electrons. Although such a violation may appear at first sight to be suppressed relative to that for a single fermion, in the absence of a consistent fundamental theory of PEP violation one cannot exclude the possibility that the reverse may be true.

A comparison of the atomic electron configurations of Be, Be' and He is provided in Figure 8.2. Since the 1s (valence) shell is "filled" to external Pauli-obeying electrons, the Be' is assumed to have the same chemical properties as the helium<sup>1</sup>. As a result, we expect Be' to be a gas at standard temperatures and pressures. Since normal Be does not readily combine to form compounds which are gases at STP, it is easy to separate Be from Be'. This fact will prove to be one of the major hurdles of the experiment.

### 8.3 Principle of the Experiment

The concept behind the experiment was thus straightforward. First we make up several gas samples of helium derived from different sources. Since normal Be is not a gas at standard temperatures and pressures only <sup>9</sup>Be' and He will be present in the sample. Thus if the Pauli principle were obeyed nothing of mass  $A = 9$  (which is the mass of beryllium <sup>9</sup>Be) would exist in the samples. Thus we tune the accelerator for mass  $A = 9$  and watch for counts in the detector.

While simple to explain the concept was much harder to implement. In order to set a limit on violations of the Pauli principle we had to know the sensitivity of the accelerator to Be concentration. This is done by creating gas samples with varying Be concentration. As mentioned before, Be does not readily make gaseous compounds which introduced one of several problems. The major problems were:

<sup>1</sup>Since chemical properties are dictated by the valence shell characteristics.

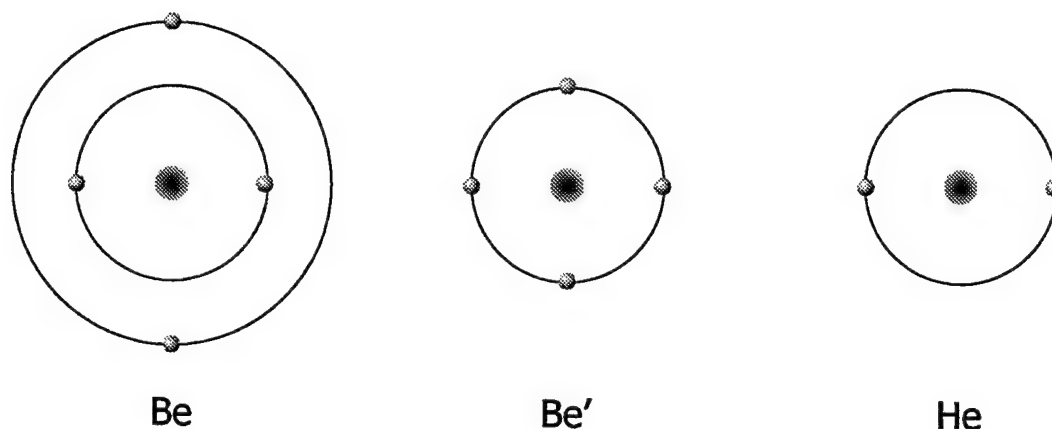


Figure 8.2: The configuration of atomic electrons for beryllium (Be), anomalous beryllium (Be') and helium (He). In Be' all of the electrons are crowded into the lowest energy level (the K shell) thus exhibiting bosonic behavior and violating the Pauli exclusion principle. As a result, the beryllium will have the same chemical properties as helium since the  $1s$  shell would be considered to be "filled."

1. Be does not readily make gaseous compounds.
2. The samples are gases. This is a problem because the accelerator is only designed to accept solid samples. Thus a new gas manifold had to be designed, tested, and added to the ion source in order to efficiently introduce gas samples to the accelerator.
3. The ion source was grossly contaminated with Be. Since  $^{10}\text{Be}$  is one of the cosmogenic radioisotopes run regularly on the PRIME Lab accelerator, Be contamination was everywhere inside the source. This contamination was so great that the experiment would not have been possible without construction of a new Be-free source.
4. Releasing Be' from the samples. One of the novelties of the experiment was that unlike previous AMS tests, which used fuzzy cosmological considerations to obtain the ratio of  $[Z']/[Z]$ , we obtained the Be' directly from samples of Be. In so doing this we increased the complexity of the experiment tremendously.

The difficulty arose from how to safely extract the Be' gas from each sample. A different solution was discovered for each sample.

5. Volatility of Be. To top all of this, Be is a hazardous element causing bronchitis, pneumonia and in some cases death. Beryllium causes scarring of the lungs and other organs which may result in heart failure. It has also been categorized as a carcinogen (a cancer causing agent) and may cause reproductive damage. Needless to say Be and its compounds must be handled with extreme caution.

#### 8.4 Anomalous Be In the Ion Source

As a quick review the sample is given a negative charge by the  $\text{Cs}^+$  ion beam (which has been accelerated through a potential difference of 5 keV) sputtering on a cathode containing a solid sample. Since we searched for Be it was necessary to extract negative ions of Be from the ion source. However, since Be has a low electron affinity (only 0.195 eV) it does not readily form negative ions. In fact, the study by Middleton [138] shows that  $\text{Be}^-$  beam currents produced at the University of Pennsylvania ion source were only about  $0.2 \mu\text{A}$ . In order to obtain larger beam currents we used  $\text{BeO}^-$  which produces much larger beam currents. In Middleton's study they were able to produce  $\text{BeO}^-$  currents on the order of  $10 \mu\text{A}$ . This procedure of using molecular ion beams is common in accelerator mass spectrometry when elements do not form negative ions. However, there are a few disadvantages of such molecular ion beams. First, they reduce the energy of the element of interest in the terminal since the energy is shared by each of the constituents of the molecule (see Equation (1.10) for the implications of the molecular mass on the ion energy). This is relevant because often higher stripping efficiencies may be obtained with high energy ions. Secondly, if more than three electrons are stripped from the molecule it undergoes coulomb explosion in which the two atoms push each other apart as they travel down the beamline. The contaminating atom (in our case oxygen) will get selected out by the high energy magnetic and electrostatic elements but has the effect of degrading the

quality of the final Be beam. In the case of BeO the advantage of the 2 orders of magnitude gained in the beam current significantly outweighs the disadvantages.

Since our samples consisted primarily of helium with possibly some Be' we needed to introduce oxygen so that if any Be' did exist in our samples there would be oxygen present to create BeO<sup>-</sup>. As a result the solid samples needed to be an oxide. After trying several different oxides, we picked two primary cathode surfaces, Sm<sub>2</sub>O<sub>3</sub> and Yb<sub>2</sub>O<sub>3</sub>. Each surface we tested exhibited different characteristics such as packing ability, quantity with our main concern being the level of Be contamination in each compound (see Table 8.1 for details of Be concentration of several different surfaces). Since we were looking for the presence of Be' in the sample we needed surfaces with the lowest possible Be contamination so that our background counting rate (the counting rate present when the He blank sample was being run) was minimized. The surfaces Sm<sub>2</sub>O<sub>3</sub> and Yb<sub>2</sub>O<sub>3</sub> possessed the lowest Be counting rates of all the surfaces tested and since we had a large quantity it was deemed best suited for our experiment.

Following the decision to use the Sm<sub>2</sub>O<sub>3</sub> and Yb<sub>2</sub>O<sub>3</sub> as the oxide surfaces some tests were run to see if this lowered the background so that the 4 ppm standard was noticeable above background. The results for this study for three different surfaces is given in Table 8.2. By comparing the two Sm and Yb oxide surfaces to the plain Cu cathode we see that with the Cu cathode there is no noticeable difference between the counting rates with the blank and 5 ppm standard (which means that the background is above this 5 ppm Be concentration). However with the Sm<sub>2</sub>O<sub>3</sub> and Yb<sub>2</sub>O<sub>3</sub> surfaces there is a noticeable difference. From this data we realized that use of these apparently Be-free oxides achieved a significantly lower background. The Cu cathode had counting rates lower than the TiO<sub>2</sub> which was used as the oxide in previous runs. With the introduction of the new ion source we decided not to introduce samples with unusually high Be counting rates. Certainly the Be contamination of the TiO<sub>2</sub> added to the high backgrounds realized in earlier runs.

The actual choice of which surface changed from run to run and depended upon which was producing the lowest Be counting rates at that time. As will be evidenced

Table 8.1: Summary of Be counting rates for several different surfaces. This study resulted in the use of  $\text{Sm}_2\text{O}_3$  and  $\text{Yb}_2\text{O}_3$  as the oxide surfaces which supply the oxygen needed to create the  $\text{BeO}^-$ . An expanded list of the surfaces tested is included in the results section and was taken during Run Be5 in October of 1997.

Surface Type	Material	Be Counting Rate [CPS]
Metals	Stainless Steel	91
	Ni	$3 \times 10^3$
	Cu	$8.645 \times 10^2$
	Ag	$3.2 \times 10^4$
	Pt	$1.464 \times 10^4$
Oxides	$\text{Fe}_3\text{O}_4$	$1 \times 10^5$
	$\text{TiO}_2$	$> 5.7 \times 10^4$
	$\text{SnO}_2$	$2.227 \times 10^3$
	$\text{Yb}_2\text{O}_3$	$< 1$
	$\text{Sm}_2\text{O}_3$	$< 1$

in later chapters the data from two separate runs (run Be7 in October of 1998 used  $\text{Yb}_2\text{O}_3$  while run Be8 in June of 1999 used  $\text{Sm}_2\text{O}_3$ ) agree with each other on the machine calibration line produced from the standards. Of course the choice to use these samples was not made until run Be5 in October of 1997 before that time  $\text{TiO}_2$  was used which was one factor contributing to the higher background counting rates observed in earlier runs.

We also point out the interesting notion regarding cross-contamination. In the sputtering process the sample is ablated away but only a few atoms actually get ionized and accelerated. Thus many atoms which are not ionized are deposited on the various surfaces inside the ion source and only slowly may be burned off with time. Unfortunately, this cross-contamination effect means that a sample with high Be concentration will deposit Be onto its nearest neighbors on the sample wheel and

Table 8.2: Tests performed on the selected oxide surfaces to see if the background was below the 5 ppm standard. Comparison was performed against a plain copper cathode. The counting rates of the oxides when running the blank are much higher than the results reflected in Table 8.1 and are an example of the cross-contamination possible from samples with high Be contamination. The raw data for this is included in the results section and was taken during Run Be5 in October of 1997.

Surface	Sample	Counting Rate [CPM]
Cu	Blank	27,943
	Standard, S5 (4.8 ppm)	27,196
Sm <sub>2</sub> O <sub>3</sub>	Blank	211
	Standard, S5 (4.8 ppm)	1,559
Yb <sub>2</sub> O <sub>3</sub>	Blank	99
	Standard, S5 (4.8 ppm)	506

hence will cause a rise in the background which is proportional to the concentration of the contamination. In fact, the data for the Sm<sub>2</sub>O<sub>3</sub> and Yb<sub>2</sub>O<sub>3</sub> surfaces in Table 8.1 were on a low Be concentration wheel, whereas for the data given in Table 8.2 the oxides were on the wheel with the Cu cathode which possessed a high counting rate. It is also important to note that a silver, Ag, sample was run on the preceding wheel which had an extremely high counting rate (the highest counting rate we ever noticed in all the tests and which was over the maximum readable rate from the interference meter and was greater than 60,000 cps with the attenuator in). This very contaminated sample may also be responsible for the rise in the Cu cathode counting rate.

This concept of cross-contamination was so noticeable in our most precise measurements that the standards even caused the background to rise. Thus in order to minimize the background for our unknown samples we ran them first and followed with the samples ordered by increasing Be concentrations. We monitored the upward drift of the background by interspersing the blank to evaluate this drift. This would

not have been possible without the gas manifold which is discussed in the following sections.

Another concern related to the source, is that Be' which is assumed to have the chemical properties of He would not bind to oxygen under normal conditions because of its filled valence shell. However, this problem is overcome in the source when the Be' atoms are bombarded by high energy Cs atoms. Since the potential which produces the Cs<sup>+</sup> beam (on the order of keV) is much greater than the typical binding energies of atomic electrons (on the order of eV) we may make the assumption that the Pauli-violating electrons are knocked off the Be' and new Pauli-obeying electrons take their place forming usual Be. This normal Be is then free to combine with the oxygen atoms supplied by the Sm<sub>2</sub>O<sub>3</sub> or Yb<sub>2</sub>O<sub>3</sub> surfaces and create the BeO<sup>-</sup> ions which are fed into the accelerator. Thus, it can be presumed that any Be' atoms initially present in the sample were first converted to Be through collisions with Cs<sup>+</sup>. In the results we report we are assuming that the probability  $P$  for the Cs<sup>+</sup> beam to convert Be' to Be is  $\approx 1$ , while in principle it could be possible that  $P < 1$ . However, since we cannot perform such tests on Be' which is the unknown, this is one assumption that the experimental results are reliant upon.

Because of this assumption that  $P \approx 1$ , the counting rate at the detector is a result of Be' in the samples and any small fraction of regular Be from contamination. Thus, any Be atoms detected above background can then be identified as having come from the gas samples, and hence are candidates for Be'.

## 8.5 Gas Introduction System

As mentioned above one of the difficulties with this experiment was that it utilized gas samples while typical AMS procedures call for solid cathodes. In the first several runs the gas samples were introduced to the ion source through a port far from the wheel location. Unfortunately this did not efficiently deliver the Be from the standards and any possible Be' in the unknowns to the cathode surface where it could interact with the Cs and O in order to create the necessary BeO<sup>-</sup>. In the early runs much of the samples were lost simply because the Be was forced to permeate the entire source

with only a small fraction of the gas sample close enough to the surface to obtain the acceleration required to get around the injector magnet and into the accelerator.

We changed the gas introduction location in run Be6 when we exhibited a specially designed cathode. The new cathode had was designed to allow the gas to enter the ion source directly adjacent to the oxide surface. This was accomplished by drilling 6 holes around the rim of the cathode. The oxide was then packed in the area just inside the holes. A diagram of the cathode is given in Figure 8.3. From the data which is provided in the section on run Be6 we notice that this greatly increased the efficiency of converting the gaseous Be in the standards to  $\text{BeO}^-$ . Evidence of this comes from the 337.4% rise in the Be/He ratio of the 4 ppm standard (see Table 8.3). This higher ratio means that this new cathode increased our efficiency of detecting gaseous Be and hence increased the slope of the line calibration. By increasing the

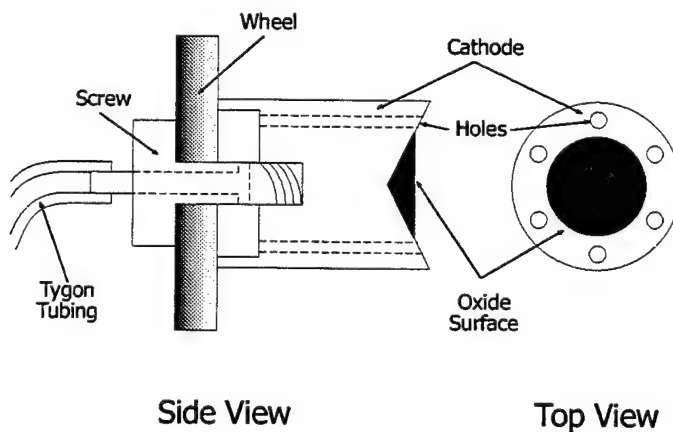


Figure 8.3: Side and top views of the cathode with 6 holes drilled around the perimeter of the oxide surface. Before the introduction of these cathodes the samples were introduced far from the oxide surface. These cathodes increased the efficiency of the Be being converted to  $\text{BeO}^-$  which was evidenced in the raw data which saw a 337% increase in the Be counting rate on the 4 ppm standard. Meanwhile the blank saw no noticeable rise in counting rate, as would be expected if contamination resulted from the surface and source and not from the He blank sample.

Table 8.3: Impact of newly designed cathode on efficiency of  $\text{BeO}^-$  creation. The new cathode introduces the gas by passing it through 6 holes situated around the cathode perimeter. The old gas introduction location was at the opposite end of the source hence requiring a larger quantity of gas to produce only minimal source efficiencies. Introducing the gas directly adjacent to the surface greatly enhances source efficiency by increasing the probability of  $\text{BeO}$  formation. These tests were performed in run Be6 which occurred in February of 1998. The raw data for these tests may be found in the Results chapter.

Cathode	Sample	Average Counting Rate [CPM]
Regular	Blank	13.2
	Standard, S5 (4.8 ppm)	4024.3
	$R_{\text{old}} = \frac{\text{Std}}{\text{Blank}}$	304.9
6 Holes	Blank	5.2
	Standard, S5 (4.8 ppm)	6968.0
	$R_6 = \frac{\text{Std}}{\text{Blank}}$	1333.6
Summary	$\% \text{ Difference} = \frac{R_6 - R_{\text{old}}}{R_{\text{old}}}$	337.4 %

slope we raise the intersection point with the background and decrease the limit we are able to set on such Pauli principle violations.

Another modification which was implemented in run Be5 was the construction of the gas manifold which permitted rapid switching among multiple samples. Prior to this we had to go into the source cage to change a sample out. This procedure took on average 15-30 minutes depending on whether the high speed roughing vacuum pump was used. Thus there was up to a 30 minute down time between taking data points or counting rates of different samples. This added uncertainties into the system since the machine parameters do drift slowly over time. With such long change times it was impossible to monitor such drifting without nearly quadrupling the total run times.

The gas manifold which was constructed and tested in the summer of 1998 and permitted us to run 4 samples simultaneously with a 30 second change time between samples. Thus, we were able to always have the blank sample connected to the source and used this to monitor changing conditions and the characteristic drift and cross contamination of the source from the Be standards. This manifold greatly reduced run times and increased efficiencies.

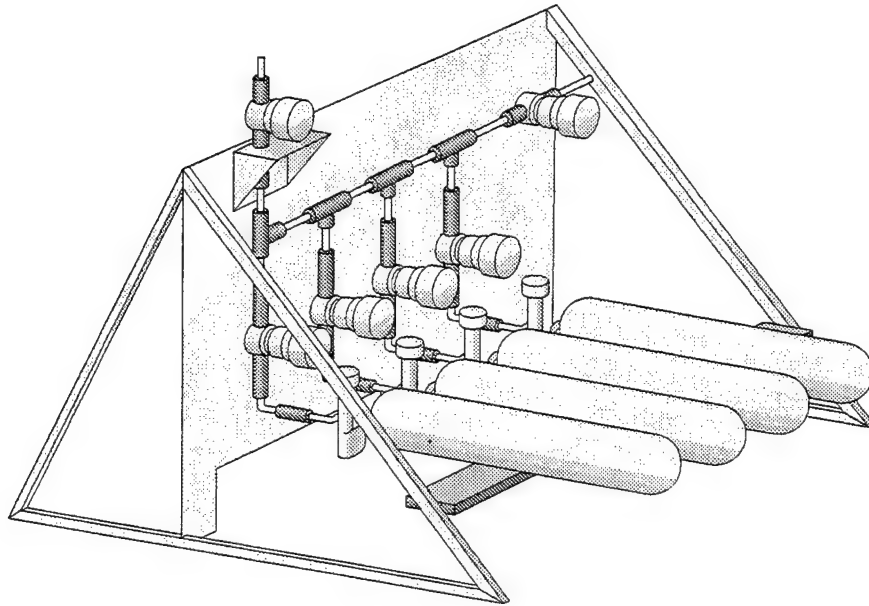


Figure 8.4: Gas manifold permitting us to run up to four gas samples at a time. The gas manifold helped reduce the background, monitor source contamination and drift, and greatly reduced run times.

The manifold was designed to sit on the high voltage table inside the source cage and a diagram of it is provided in Figure 8.4 with a front view with dimensions provided in 8.5. It consisted of a gas line with 5 NUPRO air operated 1/4 inch VCR valves (SS-4BK, VCR-1C) – one for each of the 4 samples and one for the turbo pump – on the high voltage panel. These were operated by 5 NUPRO solenoid valves (MS-SOL-2K) on the ground panel outside the source cage. Since the valves were air operated we could run the poly-flo tubing (#44-P) through the cage without grounding the source or sparking across the high voltage table.

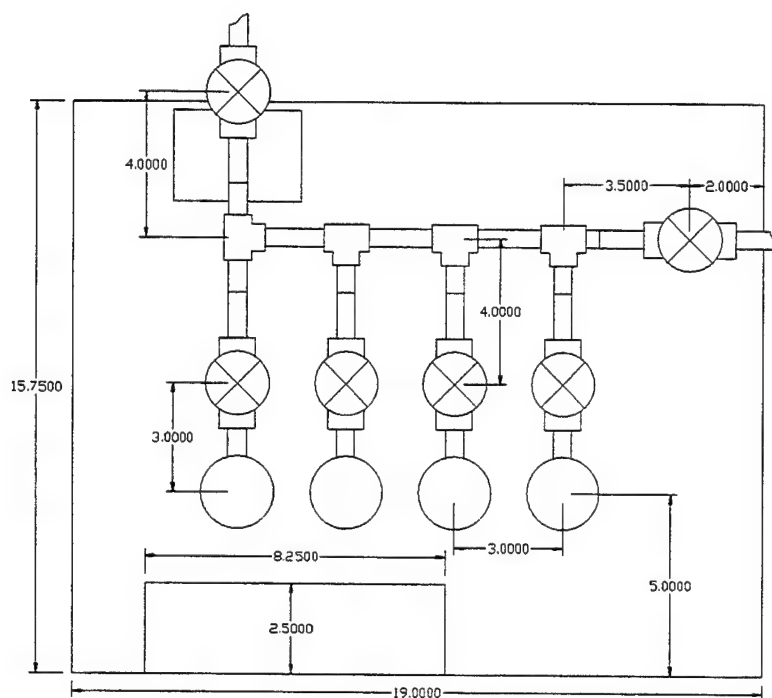


Figure 8.5: Front view of the gas manifold. This gives the dimensions of the different tubing used along with the relative size of the apparatus.

The vacuum line itself was made from 1/4 inch aluminum tubing and Cajun 1/4 inch tube socket weld Union tees (SS-4-TSW-3) on the high voltage panel and brass swagelok tees (B-400-3) and brass Sure-Lok instant tube fittings (#10-32 UNF  $\times$  1/4 inch O.D. tube #51025K324). In order to connect to the sample vials we used Cajon 1/4 inch ultra-torr Union connectors (SS-4-UT-6).

However, it was often difficult to determine how tightly we needed to secure the connectors to obtain a seal but not break the glass nozzle of the sample bottles. We of course learned the hard way during run Be7 when we broke the end of the nozzle of the 4 ppm standard and had to have it glass blown and fixed. This prompted us to design and weld a connection joint from aluminum which would insure proper tightening and seal of the samples. This then was connected to a short tygon tube which lead to the sample nozzle. Since under a vacuum the tygon would flex and

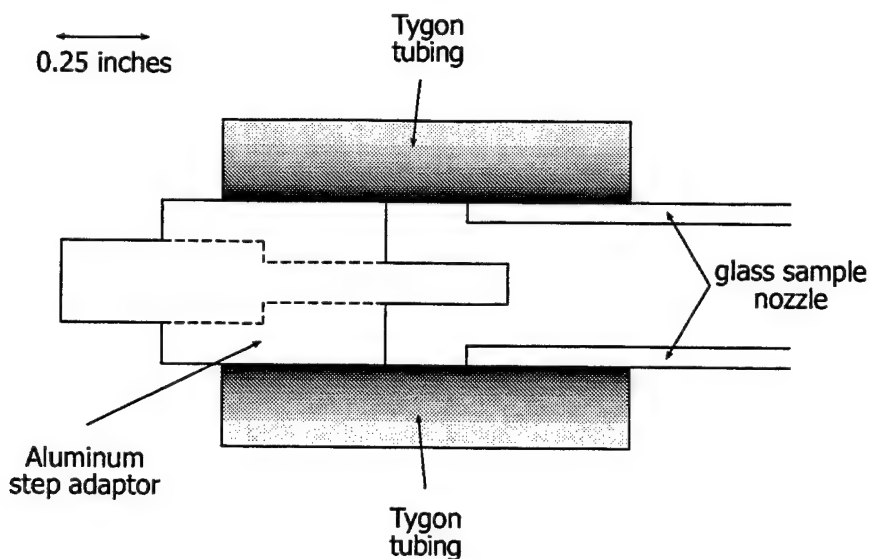


Figure 8.6: The flexible step up adaptor made from aluminum and Tygon tubing which permitted us to tighten the Cajun Ultra-Torr Union connectors without fear of breaking the nozzles of the glass sample holders.

potentially close off the supply from the sample we added a small aluminum tube which ran down the center of the step up connection joint and was set just inside the sample tube nozzle. A diagram of this flexible connection is given in Figure 8.6.

The gas manifold helped lower the run times while also reducing uncertainties associated with the inability to rapidly cycle between samples. This whole gas introduction system is an example of pushing the machine to new limits as normal AMS operations do not accommodate samples in the gas phase. A significant amount of work and effort went into this system and as is evident from the above discussion it was difficult to plan ahead to predict potential problems. Each was solved until we had a system that worked efficiently to increase the efficiency of the source in creating BeO.

## CHAPTER 9. THE SAMPLES

In general there were three different kinds of samples which were run during the experiment: the Blank, Standards, and Unknowns. The blank sample did not contain any Be and thus was used to set our background counting rate. The blank was used in conjunction with seven standards, which had known concentrations of Be, to calibrate the detector counting rate with the sample concentration. This calibration allowed us to determine the sensitivity of the accelerator to various concentrations of Be and allowed us to extrapolate the minimum observable concentration above background. Once the calibration was performed the unknowns were run against this calibration to determine their respective Be concentrations.

### 9.1 The Blank Sample

The blank sample was made of pure helium and contained no known Be concentration. Since this was the same helium injected into the unknown samples (to bring them up to the same relative pressure as the standards), this sample represented an evaluation of the background. Any Be contamination in the blank would also be present in each of our samples and thus through the comparison with the samples would be appropriately subtracted away and would not impact the final counting rates.

While one might think that the background could be determined by simply running the accelerator without a sample, it is impossible to emulate the conditions inside the ion source which is run at a predetermined optimal pressure of  $2.4 - 2.6 \times 10^{-6}$  Torr (where  $1 \text{ atm} = 760.0 \text{ Torr}$ ) without a gas sample connected to the ion source. It was also important to test the background with the gas manifold attached in order to best represent the conditions of the standards and unknowns.

## 9.2 The Standards

In general, the efficiency of the machine may be broken into several smaller pieces, the stripping efficiency  $\eta_{strip}$  (which was mentioned in Chapter 1), the transmission efficiency  $\eta_{trans}$  of beam through the beamline (i.e. how much of the beam is lost going through different apertures and slits) and the efficiency of producing the ion from the sample  $\eta_{prod}$ . Thus the total efficiency is given by

$$\eta = (\eta_{prod})(\eta_{strip})(\eta_{trans}) \quad (9.1)$$

When dealing with the same species as is done in usual AMS (when ratios are always that of the radioactive to stable isotope), these efficiencies all cancel because one is comparing the radioactive to stable isotopes which have the same  $Z^1$ . This is one of the elegant aspects of AMS, because we make measurements of *relative* counting rates and beam currents we may obtain a result without the need for complete and detailed understanding of the complicated mechanisms in the source or at the stripper.

In our case this is not so and the effect of these efficiencies must be evaluated. Our first instinct would be to try to obtain a He beam current and produce the usual R/S ratio given in Equation (1.30). However, in this equation is built the assumption that such terms cancel. Since the ratio of He production efficiency to that of Be is unknown and since He does not readily form negative ions (Middleton obtained a current of only  $10^4$  cps [138]), the procedure needed to be changed from the way that AMS is usually run. This called for the need to calibrate the machine to see its sensitivity in evaluating Be concentrations.

As mentioned above, to set a limit on the presence of Be' in each of the unknown samples, it was necessary to determine the efficiency of the AMS in detecting a known concentration of Be in a gaseous sample. The needed calibrations were carried out by preparing gaseous samples of a volatile Be compound containing a known concentration of Be. The compound was beryllium bis-1,1,1,6,6,6-hexafluoroacetylacetonate,

<sup>1</sup>There is in actuality a small impact which results from isotopic fractionation. This concept is discussed in Chapter 1 in greater detail.

$\text{Be}(\text{C}_5\text{HF}_6\text{O}_2)_2$ , with a molecular weight of 423. An approximately 150 mg sample of this compound was obtained from Prof. Don Gaines and Dr. Dovas Saulys of the University of Wisconsin Chemistry Department, and analyzed via a conventional mass spectrometer to verify its composition.

Much work went into the evaluation of this pressure which was done extremely precisely by Dr. Henry Rohrs of Washington University in St. Louis. The vapor pressure is the dynamic equilibrium pressure which results from the two opposing processes, evaporation and condensation, occur at exactly the same rate. This means that  $\text{Be}(\text{C}_5\text{HF}_6\text{O}_2)_2$  in an isolated vial will be in both the liquid and gas phase. The gas phase will exert a vapor pressure which is both a function of the volume and temperature of the vial<sup>2</sup>. Knowledge of this vapor pressure and the precise evaluation of the volumes of each of the standard sample containers is necessary to determining the concentration in each sample.

Since the vapor pressure of  $\text{Be}(\text{C}_5\text{HF}_6\text{O}_2)_2$  was originally unknown, we needed to first evaluate it by letting in some of the  $\text{Be}(\text{C}_5\text{HF}_6\text{O}_2)_2$  gas into a region of known volume. While geometry will give us a good estimate of the volume of the region a more precise evaluation of the volume may be obtained by first introducing a gas whose partial pressure is already known and measuring the pressure and temperature of the system. We then may deduce the volume via the ideal gas law,

$$\begin{aligned} PV &= nRT \\ \Rightarrow V &= \frac{nRT}{P} \end{aligned} \tag{9.2}$$

where  $n$  is the quantity (or total mass) of the gas, usually measured in moles and  $R$  is the ideal gas constant and is  $8.314 \text{ dm}^3\text{kPa K}^{-1}\text{mol}^{-1}$  ( $0.0624 \text{ m}^3\text{Torr K}^{-1}\text{mol}^{-1}$  in the units we dealt with in the experiment). However, sometimes this method may also be cumbersome because of the need to evaluate  $n$  so an alternate method is to fill the volume with a substance whose density is known (like water) and weigh the filled

<sup>2</sup>Vapor pressures are a common concept in chemistry and more information on the idea (which is responsible for boiling, etc.) may be found in any chemistry textbook. See pages 349–400 of Ref [14] for a more detailed discussion.

Table 9.1: Vapor pressure measurements for  $\text{Be}(\text{C}_5\text{HF}_6\text{O}_2)_2$ . This data was accumulated by Dr. Henry Rohrs and facilitated accurate evaluation of the concentrations for each standard sample.

Measured Pressure [Torr]	Temperature [°C]	Corrected Pressure at 298.15 K [Torr]
0.576	21.5	0.583
0.571	21.5	0.578
0.565	21.5	0.572
0.567	21.5	0.574
0.599	21.5	0.606
0.585	21.5	0.592
0.571	21.0	0.579
0.572	21.5	0.579
0.588	21.5	0.595
0.568	22.0	0.574
0.578	22.0	0.584
Range		0.572–0.606 (–0.011, +0.023)
Average		$0.583 \pm 0.003$ Torr

container. After subtracting off the dry weight we obtain the mass of the water in the container. The volume follows naturally from the definition of the density  $\rho = M/V$ .

The vapor pressure of  $\text{Be}(\text{C}_5\text{HF}_6\text{O}_2)_2$  was finally determined to be  $(0.583 \pm 0.003)$  Torr at 298.15°K. A summary of the raw data from the measurement of the vapor pressure is given in Table 9.1 with the absolute measured pressures with their corresponding temperatures. Since the temperature varied slowly from measurement to measurement, we needed to correct the absolute pressure to a standard temperature which was chosen to be 298.15 K.

We then created two high concentration standard samples by adding known amounts

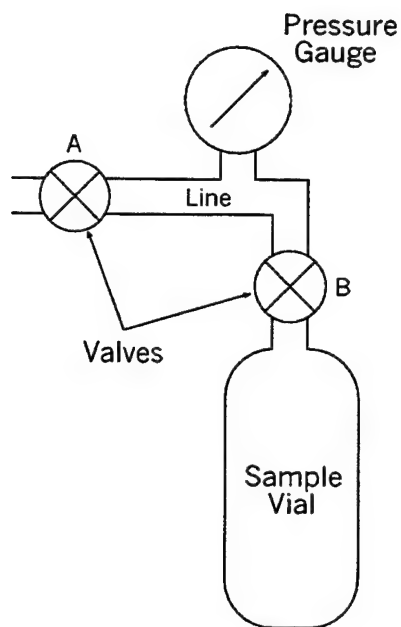


Figure 9.1: Schematic of experimental setup for the creation of the first known concentration standard. This standard was then diluted and made into the other lower concentration standards.

of the Be compound and He to a sample vial whose volume was known ( $523 \text{ cm}^3$ ). Here the calculation of the volume was slightly more complicated because the volume of the line containing the pressure gauge was unknown. The experimental setup for the first standard sample creation is shown in Figure 9.1.

Before creating the sample we evacuate the line and sample vial. After obtaining a base vacuum of 450 mTorr we close both valves and connect any gas to the left of valve A. We then proceed to open valve A and allow the gas to fill the line. After closing valve A the pressure in the line was 795 Torr, we then open valve B and allow the vapor to diffuse into the sample vial. Once equilibrium is established we measured the pressure to be 60.4 Torr. This reduction in pressure allows us to determine the volume of the line from

$$P_L V_L + P_S V_S = P(V_L + V_S) \quad (9.3)$$

$$\Rightarrow V_L = V_S \frac{P - P_S}{P_L - P}$$

Using our numbers the volume of the line was determined to be only 43 cm<sup>3</sup>.

$$\begin{aligned} V_L &= V_S \frac{P - P_S}{P_L - P} \\ &= 523 \text{ cm}^3 \frac{60.4 - 0.45 \text{ Torr}}{795 - 60.4 \text{ Torr}} \end{aligned} \quad (9.4)$$

$$= 42.7 \text{ cm}^3$$

We then closed valve B and pumped the line back down to the base vacuum. Now that the volume of the line is known we may proceed to create the first standard. We begin by introducing the Be(C<sub>5</sub>HF<sub>6</sub>O<sub>2</sub>)<sub>2</sub> to the sample vial and line together which register a pressure of 160 mTorr. We then close valve B and pump down the line before moving helium to the left of valve A. After introducing helium to valve A we filled the line with 494 Torr of He. With valve A closed we then opened valve B and allowed the He to enter the sample vial. This process of adding He to the line and then the vial was performed 6 times until the final pressure in the vial was 269 Torr. Since each time the He was added a small amount of the Be compound flowed into the line and was pumped away the Be pressure was reduced based on the number of times  $n$  that this procedure was performed

$$\begin{aligned} P_{Be} &= P_0 \left( \frac{V_S}{V_S + V_L} \right)^n \\ &= 197.9 \text{ mTorr} \left[ \frac{523 \text{ cm}^3}{(523 + 42.7) \text{ cm}^3} \right]^6 \\ &= 0.1236 \text{ Torr} \end{aligned} \quad (9.5)$$

The resulting concentration is then calculated by the ratio of the partial pressures of the Be to He and is given by

$$\begin{aligned}
 \frac{[Be]}{[He]} &= \frac{P_{Be}}{P_f - P_{Be}} \\
 &= \frac{0.1236 \text{ Torr}}{(269 - 0.1236) \text{ Torr}} \quad (9.6) \\
 &= 4.59 \times 10^{-4} \\
 &= 459 \text{ ppm}
 \end{aligned}$$

In a similar manner to the 459 ppm standard above we created 74.2 ppm and 4.84 ppm standards. These were created in the fall 1996 prior to run Be3 which was the first run that data was actually taken on the experiment. Once introducing the Be-free source we decided the 459 ppm and 74.2 ppm standards would contaminate the source so it was necessary to make up several more low concentration standard samples. Four new low concentration samples were created in May of 1998 and were analyzed in Run Be7. These samples were created by making dilutions from S8 the 74.2 ppm standard.

As with the higher concentration standards, the volumes of the sample vials had to first be determined. This time we used the method described above in which He and a vial whose volume was known provided the necessary reference data to determine the volumes of the other vials. The diagram representing the experimental setup for the volume calculations and the dilutions is shown in Figure 9.2.

When calculating the volumes of the vials 5 different measurements were made on the entire system. Volume A was the reference volume and was calculated using the water density method discussed before. The reference volume was calculated to be 28.8 cm<sup>3</sup> and was placed at position A while the unknown volumes were placed at position B in the diagram. The series of tables below are the calculations of the volumes for the different standard samples including the raw data from each trial. You can see that it was necessary to calculate the volume of the line for each case also since conditions change slightly from vial to vial.

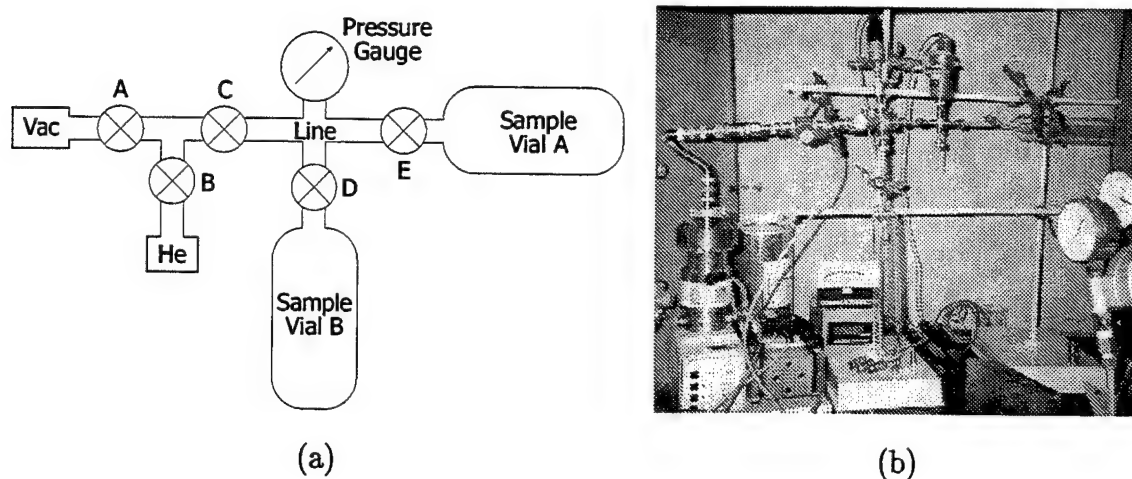


Figure 9.2: (a) Schematic of experimental setup for the dilution of the high concentration standard S8 into standards S1, S3, S6, S7 and S10. This setup was also used to determine the volumes of the sample vials which housed these standards. (b) A picture of the actual apparatus. The top of the helium tank can be seen in the lower right hand corner.

Table 9.2: Volume calculations for sample vial S1. All pressures are in Torr and volumes are in  $\text{cm}^3$ .

Trial	P(A)	P(AL)	P(ABL)	V(C)	V(B)
1	20.32	12.65	1.15	17.4	462.1
2	25.36	15.78	1.43	17.5	464.0
3	19.93	12.41	1.13	17.4	461.2
4	21.89	13.63	1.24	17.4	461.7
5	19.54	12.16	1.09	17.5	469.5
Avg	21.41	13.33	1.21	17.4	463.7
St Dev	2.38	1.48	0.14	0.0	3.4

Table 9.3: Volume calculations for sample vial S3. All pressures are in Torr and volumes are in  $\text{cm}^3$ .

Trial	P(A)	P(AL)	P(ABL)	V(C)	V(B)
1	19.98	12.41	1.11	17.5	471.5
2	20.88	12.95	1.17	17.6	467.0
3	21.01	13.03	1.17	17.6	470.2
4	20.28	12.58	1.13	17.6	470.0
5	20.53	12.75	1.15	17.6	467.3
Avg	20.54	12.74	1.15	17.6	469.2
St Dev	0.42	0.26	0.02	0.0	2.0

Table 9.4: Volume calculations for sample vial S6. All pressures are in Torr and volumes are in  $\text{cm}^3$ .

Trial	P(A)	P(AL)	P(ABL)	V(C)	V(B)
1	20.47	12.79	1.15	17.3	466.1
2	20.42	12.77	1.15	17.2	464.9
3	20.30	12.70	1.15	17.2	461.9
4	21.41	13.37	1.20	17.3	467.2
5	20.64	12.92	1.16	17.2	465.9
Avg	20.65	12.91	1.16	17.2	465.2
St Dev	0.44	0.27	0.02	0.0	2.0

Table 9.5: Volume calculations for sample vial S7. All pressures are in Torr and volumes are in  $\text{cm}^3$ .

Trial	P(A)	P(AL)	P(ABL)	V(C)	V(B)
1	20.47	12.71	1.12	17.6	479.5
2	20.22	12.52	1.11	17.7	477.6
3	21.37	13.24	1.18	17.7	474.6
4	20.58	12.77	1.14	17.6	473.0
5	22.00	13.63	1.22	17.7	472.4
Avg	20.93	12.97	1.15	17.6	475.4
St Dev	0.74	0.45	0.05	0.1	3.0

Table 9.6: Volume calculations for sample vial S10. All pressures are in Torr and volumes are in  $\text{cm}^3$ .

Trial	P(A)	P(AL)	P(ABL)	V(C)	V(B)
1	21.10	13.10	1.19	17.6	463.8
2	20.16	12.54	1.14	17.5	462.5
3	21.34	13.27	1.20	17.5	465.4
4	20.06	12.47	1.13	17.5	464.4
5	20.14	12.52	1.13	17.5	466.5
Avg	20.56	12.78	1.16	17.5	464.5
St Dev	0.61	0.38	0.03	0.0	1.5

Once these volumes are obtained we begin the dilutions by hooking up S8 to position A and the new container to position B in Figure 9.2. After evacuating the container we inject vial B with He at roughly the same pressure that exists in S8 (3.09 psia). We then allow the two vials to come to equilibrium, hence introducing more He atoms to the overall mixture. This has the effect of diluting the standard since the two vials then contain the same partial pressures of Be and He following equilibrium. Doing this only once does not lower the Be concentration to the desired value so when creating S7 we then discarded the gas in S7 and repeated this procedure, all the while keeping the overall pressure relatively constant.

From the knowledge of the initial S8 concentration we are able to apply the ideal gas law and determine the number of  $\text{Be}(\text{C}_5\text{HF}_6\text{O}_2)_2$  molecules present in the sample. By following the number of dilutions and knowing the three volumes (vial A, vial B, and the line) we are able to determine the number of Be molecules present in each vial. We then divide the number of Be molecules in a particular vial by the number of He atoms whose number is determined from the ideal gas law. After obtaining the desired S7 concentration, we removed S7 from position B and replaced it with S6 and again repeated the procedure of injecting He to 3.09 psia and allowing it to equalize with S8 in position A. After only one dilution the desired concentration was obtained and we again repeated the procedure for standards S3, S10, and S1.

Unfortunately the valve on S10 failed which left us with only one ultra-low-level-concentration standard in Run Be7. Because we wanted more low level standards we created the last three standards (S2, S4, and S11) in June of 1999. This time we calculated the volumes based on the water density method. Table 9.7 gives the results from these calculations. The density of the purified de-ionized water was taken to be  $0.997 \text{ grams/cm}^3$ .

Again the same method of dilutions was performed using the ideal gas law to determine the number of Be molecules in each container. The standard procedure of filling the sample in position B with He and then allowing the two to come into

Table 9.7: Summary of volume calculations for the final three standards (S2, S4, and S11). The average masses for each vial is given assuming  $\rho_{H_2O} = 0.997 \text{ gm/cm}^3$ .

Sample	Dry Mass [gm]	Wet Mass [gm]	H <sub>2</sub> O Mass [gm]	Volume [cm <sup>3</sup> ]
Standard, S2	215.25	688.10	472.85	474.27
Standard, S4	224.40	721.10	496.70	498.19
Standard, S11	221.60	690.40	468.80	470.21

equilibrium in order to decrease the number of Be molecules in each sample was used. Standard S11 was created from the high concentration standard S9 in order to preserve the ability to create more dilutions should they be needed at a later time. Since the last series of dilutions cannibalized standard S8 we decided to preserve some of the remaining Be with the creation of S11 from S9 which was used to create the new standards S2 and S4.

The final concentrations of all 11 standard samples is given in Table 9.8 and each was prepared by mixing the  $\text{Be}(\text{C}_5\text{HF}_6\text{O}_2)_2$  with He to produce mixtures with known Be/He concentrations. As mentioned above S10 had a broken valve, S8 and S9 were cannibalized in the creation of the lower concentration standards thus after all the dilutions were completed only S1-S7 and S11 remained. Standards S1-S7 were used in the final results while S11 was kept as a reference and had a concentration so high that it would most definitely contaminate the Be-free source. In fact all of the standards produced noticeable rises in the background counting rate due to the cross-contamination effects previously discussed. This cross-contamination effect is what dictated a run procedure with ran samples in order of increasing Be concentration so as to limit the contamination and decrease its impact on the final limits set on the existence of Pauli principle violating (paronic) Be.

Throughout the paper we will loosely use the term parts-per-million (ppm) or parts-per-billion (ppb) to represent ratios whose exponent is  $1 \times 10^{-6}$  and  $1 \times 10^{-9}$  respectively. These ratios are taken and calculated as the number of Be or Be' atoms

Table 9.8: Summary of the Be concentrations,  $[\text{Be}]/[\text{He}]$ , in parts-per-million (ppm) and the corresponding  $1\sigma$  errors of the different standard samples.

Sample	Be Concentration [ $\times 10^{-6}$ ]
Standard, S1	$0.24 \pm 0.05$
Standard, S2	$0.54 \pm 0.05$
Standard, S3	$0.97 \pm 0.10$
Standard, S4	$2.49 \pm 0.10$
Standard, S5	$4.84 \pm 0.10$
Standard, S6	$8.47 \pm 0.20$
Standard, S7	$16.94 \pm 0.20$
Standard, S8	$74.2 \pm 0.20$
Standard, S9	$459.4 \pm 0.40$
Standard, S10	$0.51 \pm 0.05$
Standard, S11	$225.99 \pm 0.30$

to the number of He atoms in the sample and give no reference to the volume or mass of the samples outside of their considerations in determining the raw number of atoms present.

### 9.3 The Unknowns

As briefly mentioned in the previous chapter on different experiments testing the validity of the Pauli exclusion principle, experiments searching for forbidden electronic and nuclear states failed to consider the history of the analyzed samples. In contrast in this experiment we have gone to great lengths to obtain samples where the probability of Be' retention is highest. In fact, we have obtained several different samples from different locations and with widely varying histories. In addition to a sample of laboratory air, which we used to compare to the previous result of Ref. [16], we ran samples of pure Be metal, Be ore, and a sample of natural gas containing He.

It will soon become evident that while extracting any anomalous Be is trivial to discuss in principle this is an extremely challenging task to perform. This mainly results from the toxicity of Be along with the challenge associated with isolating the trapped gas while not producing excessive quantities of undesired reaction byproducts.<sup>3</sup> These byproducts are frequently highly reactive and volatile themselves. As a result several ingenious methods of sample extraction were devised the most unique of which was the dissolution of the Be metal.

### 9.3.1 Be Metal

To test for the presence of Be' in a pure metal sample we began with a 3.9 gram Be cube that was produced in 1967. The metal was provided by Jim Marder of the Brush-Wellman corporation which was one of the leading beryllium manufacturers in the latter half of the century. This weapons grade (high purity) Be was manufactured with extremely stringent tolerances for the United States government.

Since it was necessary to decompose the metal in such a way as to liberate and collect any Be' gas trapped inside, a number of methods for decomposing the metal were considered. These included melting the sample, dissolving it in acid, and mechanically breaking it apart. However, each of these methods presented difficulties given the expectation that Be' would be present in at most trace amounts.

Since common soda-lime glass (that is cooled quickly) melts at around 823 K beryllium melts at 1,560 K it would be necessary to construct the sample container out of something other than glass as was used in all the other samples. Unfortunately the container would need to be constructed of something with a melting point higher than that of Be which can be quite expensive to construct (due to the difficulty in creating the sample container possibly because of the high melting point). We then would need to find a furnace which can reach temperatures high enough to melt the Be inside the container. Unfortunately, there would be no way to determine how much of the Be was actually melted since opening the container would release any Be' that

---

<sup>3</sup>Hydrogen is a common byproduct which results from etching and dissolving surfaces. Hydrogen is often created in extremely large quantities and is difficult to dispose of due to its extreme volatility (in fact it is frequently used as a rocket propellant as a result).

may be trapped inside. Thus, melting was reduced to a last resort option. In contrast dissolving the metal sample in acid seemed much more reasonable with the exception that such a reaction would produce large volumes of  $H_2$  gas which would sweep away any  $Be'$ . We also investigated the possibility of grinding the sample into a fine powder with a "shatter box." A typical shatter box is around  $100,000\text{ cm}^3$  and contains a hockey puck like disk along with the sample to be pulverized. It then violently shakes the entire system allowing the puck to repeatedly smash the sample into ever smaller pieces. Shatter boxes are used regularly in Mineralogy and Metallurgy to pulverize rock samples, ores, and alloys into tiny pieces. Unfortunately, it would be difficult to trap any released  $Be'$  gas which would result from the mechanical breakup of the sample. Because the Be would be ground into a fine powder it would be easy to accidentally inhale and thus the high safety risk would require stringent laboratory techniques.

Following a discussion of the dissolving properties of chlorine we performed a few tests on the possible reaction of chlorine gas with Be metal. After these attempts produced no effect we moved to other elements in column VIIB of the periodic table and finally centered on iodine. We began by dropping several iodine crystals onto the Be metal and alloy surfaces and noticed that they had begun to etch the surface in the places where direct contact was made. Mike Bourgeois then suggested dissolving the iodine in methanol ( $CH_3OH$ , or typically denoted  $MeOH$ ) to increase the contact area. This worked beautifully and the Be metal cube began a highly exothermic reaction as the surface was slowly etched away.

After performing these tests we then proceeded to devise an experimental setup which would allow the reaction to proceed unimpeded but also allow us to collect the  $Be'$  gas released when the sample dissolved. To reduce the byproducts of the reaction (and  $MeOH$  vapor), the extracted gases were passed through a conventional cold water condenser and a liquid nitrogen ( $LN_2$ ) trap. A schematic of the experimental setup is provided in Figure 9.3. Any gas passing through the condenser and trap

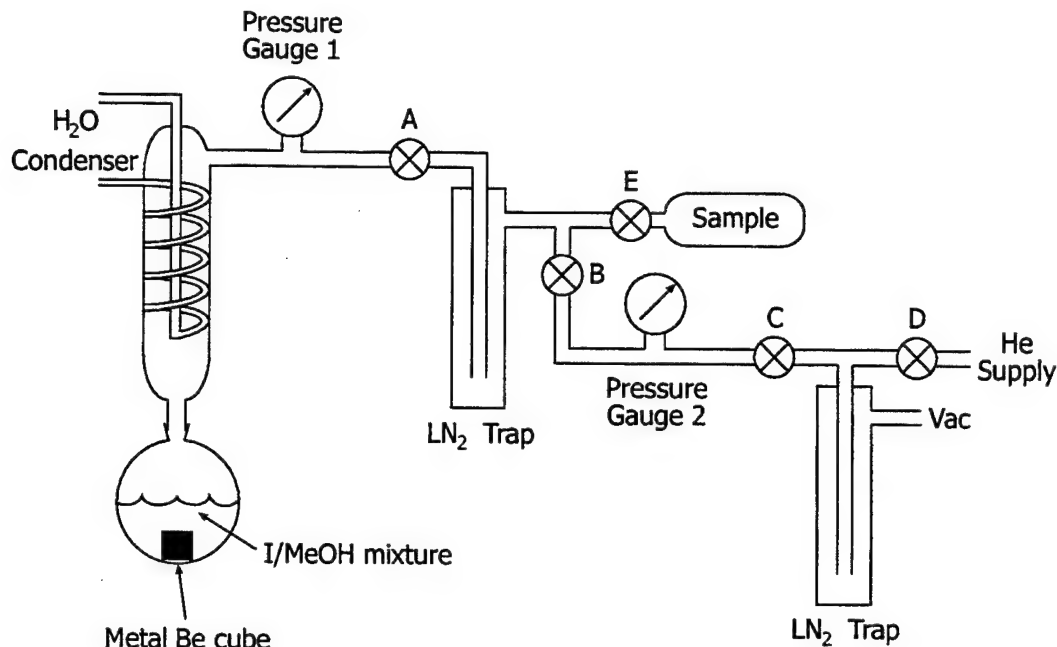


Figure 9.3: Schematic of experimental setup for the creation of the Be metal sample. The Be cube was completely dissolved by iodine that was placed into solution with MeOH. The reaction went very rapidly and the entire 3.9 gram cube was consumed in 1 hour and 35 minutes. The reaction was highly exothermic and the flask was very hot to the touch and produced a large quantity of BeI<sub>2</sub>.

(including Be' if present), was collected in a sample tube where it was mixed with He to produce a gas sample at 528.5 Torr.

Because Be has two valence electrons and I has seven valence electrons the Be will want to donate its 2s electrons to the I atoms which each want to accept the electrons. In this case the Be (Be: 1s<sup>2</sup>2s<sup>2</sup>) and I (I: 1s<sup>2</sup>2s<sup>2</sup>2p<sup>6</sup>3s<sup>2</sup>3p<sup>6</sup>4s<sup>2</sup>3d<sup>10</sup>4p<sup>6</sup>5s<sup>2</sup>4d<sup>10</sup>5p<sup>5</sup> = [Kr]5s<sup>2</sup>4d<sup>10</sup>5p<sup>5</sup>) are both striving to obtain filled valence shells – the Be will need to donate its two 2s electrons to still have a filled 1s shell while the much more aggressive I atoms only require one additional electron to have filled 5p shells. This exchange of the electrons from the Be to the I atoms results in the formation of BeI<sub>2</sub> via an ionic bond. The bond is actually formed because of the electrostatic force between the Be<sup>+2</sup> with each I<sup>-1</sup> atom (here their charge results from the electron exchange).



As a result, for the reaction to go to completion we need more than twice the number of moles of iodine than we have of Be. Since a 3.9 gram cube of Be translates into  $3.9 \text{ gm} \left( \frac{1 \text{ mol}}{9.01 \text{ gm}} \right) = 0.433 \text{ moles}$  we need at least  $0.866 \text{ mol} \left( \frac{126.9 \text{ gm}}{1 \text{ mol}} \right) = 109.86 \text{ grams}$  of I to complete the reaction. However there are several other possible species which may result and may include:  $\text{BeI}^+$ ,  $\text{I}^-$ ,  $\text{I}_2$ ,  $\text{I}_2^-$ ,  $\text{H}^+$ ,  $\text{HI}$ ,  $\text{HO}^-$ ,  $\text{H}_2\text{O}$ ,  $\text{MeO}^-$ ,  $\text{MeOH}_2$  and other possible combinations of these like  $\text{BeI MeO}$ . Since there are other possible products we added 150.9 grams of iodine to 800 ml of MeOH.



Figure 9.4: Picture of the reaction of the Be metal with the I/MeOH solution. The lighter surface are the bubbles produced in the highly exothermic reaction.

We began the reaction at 1705 on 27 May 1999 and immediately the flask heated dramatically as bubbles began to emerge from near the surface of the cube. Originally the Be cube rested at the bottom of the flask. However, after only 5 minutes the cube was producing enough bubbles to cause it to become bouyant and float to the surface in much the same manner that a straw will float in a glass of soda (see Figure 9.4

for a picture of the reaction in progress). Throughout the reaction, the pressure was monitored with Pressure Gauge 1 with valve A closed and only the cold water condenser to cool the emitted gas (MeOH in its vapor phase which results from the increase in heating in the solution near the surface of the metal where the reaction is occurring). As expected the pressure seemed to be related to the number of bubbles produced during the reaction. In addition we were able to observe the purplish I/MeOH gas condensing on the bottom surface of the cold water condenser creating a nearly constant stream of liquid I/MeOH which fell back to the surface verifying that the condenser was working properly.

The pressure peaked at just over 0.75 psig above atmospheric pressure after nearly 20 minutes elapsed time. A plot of the pressure as a function of time is given in Figure 9.5. The sharp rise in the pressure is indicative of the reaction rate increasing while the dropoff is what would be expected since the surface area is decreasing as the cube is consumed.

One very curious observation was the presence of a relatively dense green fog approximately 1-1.5 cm thick which was resting on the surface of the MeOH. This observation was made only after roughly 50 minutes of elapsed time since things finally began to calm and some sort of equilibrium was apparently established. The dynamics of the fog was dictated by the escaping MeOH vapor and is depicted in Figure 9.6a. When the reaction was finally calming down the bubbles would rise to the surface in the center but drifted to the outside before popping causing the rotational motion described in the figure. The MeOH vapor rising from the outer rim caused the fog to rotate inward. The flow of the bubbles and thus the MeOH vapor is given by the arrow in Figure 9.6b.

While the actual composition of the green fog is undetermined it is possible that it is actually  $\text{BeI}_2$  which may be taken out with the bubbles that drift to the sides of the flask before popping thus causing the observed counter-rotation. This behavior is indicated in Figure 9.6b and shows the path of some of the  $\text{BeI}_2$  molecules. This may also describe the greenish tint to the fog, since Be ore is slightly greenish in color.

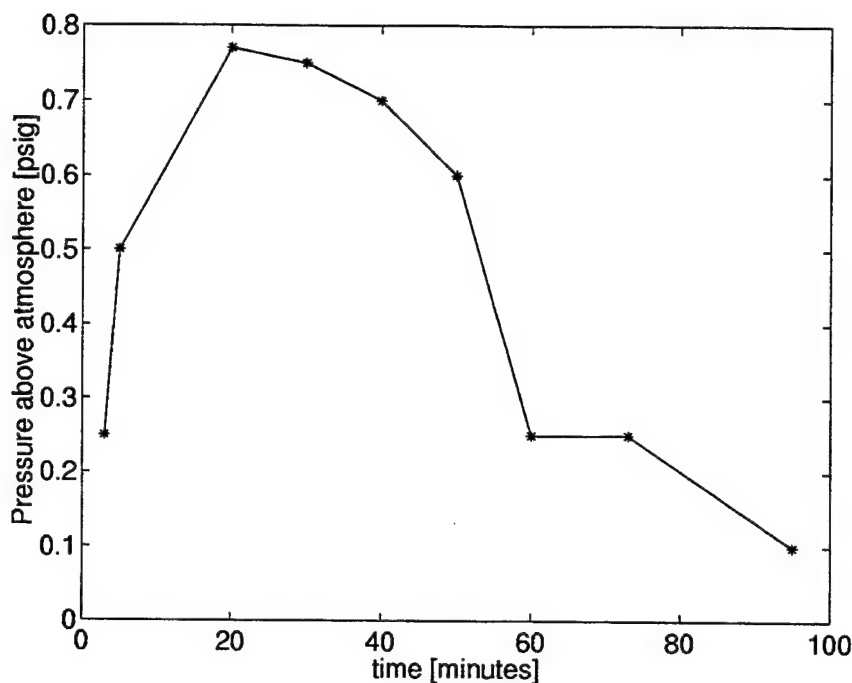


Figure 9.5: Pressure time history for the reaction of Be metal in an aqueous solution of iodine and MeOH. The structure of the curve matched the observed quantity of bubbles produced which was so great that it caused the Be cube to float to the surface.

We waited several hours to allow the temperature to drop back to its original value. This wait also ensured that the reaction went to completion. Before extracting the sample we visually confirmed that the Be cube was nonexistent while a large quantity of  $\text{BeI}_2$  sat at the bottom of the flask. We also noted that no green fog remained which seems to confirm our belief that it was in fact,  $\text{BeI}_2$  molecules suspended in the region above the surface because of the volatility of the reaction. Allowing the system to settle permitted the molecules to drop back down into the liquid.

However, to be completely sure no  $\text{BeI}_2$  molecules were still in suspension and to remove any unwanted MeOH vapor the sample was first sent through a liquid nitrogen ( $\text{LN}_2$ ) trap before entering the sample container and becoming sample M1. From the diagram given in Figure 9.3 we also placed a liquid nitrogen trap before the vacuum

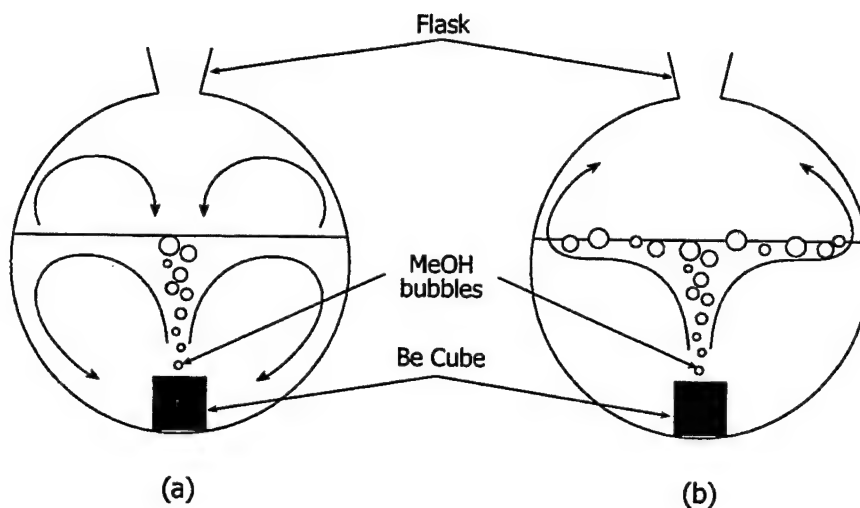


Figure 9.6: Profile sketches of the flask containing the Be cube and I aqueous MeOH solution. The dynamics of the MeOH and the observed green fog are represented in (a) by arrows while (b) gives the motion of the MeOH vapor and possible  $\text{BeI}_2$  particles. It is believed that the observed green fog is actually suspended  $\text{BeI}_2$  particles. Several hours later when the actual sample was extracted, no green fog existed, suggesting the particles were suspended because of the volatility of the reaction.

pump and as is customary with each of the unknown samples we added He carrier to increase the sample pressure to that of the standards and blank.

Since we know the total number of Be atoms sampled (dissolved) along with the final He pressure (10.1 Torr) we may calculate the factor which allows us to transform the result obtained following the accelerator run, namely the  $[\text{Be}']/[\text{He}]$  ratio, into the more meaningful  $[\text{Be}']/[\text{Be}]$  ratio. This is done by first converting the mass of the metal Be cube into the number of atoms via the following calculation:

$$\begin{aligned}
 N_{\text{Be}} &= 3.9 \text{ gm} \left( \frac{1 \text{ mol}}{9.012 \text{ gm}} \right) \left( \frac{6.022 \times 10^{23} \text{ atoms}}{1 \text{ mol}} \right) \\
 &= 2.606 \times 10^{23} \text{ atoms}
 \end{aligned}
 \tag{9.8}$$

We then compute the number of He atoms present in the sample with the ideal gas law since we know the volume ( $438.19 \text{ cm}^3$ ), temperature ( $294.26 \text{ K}$ ), and pressure ( $10.1 \text{ Torr}$ ) of the He carrier,

$$\begin{aligned}
 N_{\text{He}} &= \frac{PV}{RT} \\
 &= \frac{(10.1 \text{ Torr}) \left( \frac{133.322 \text{ N/m}^2}{1 \text{ Torr}} \right) (438.19 \text{ cm}^3) \left( \frac{1 \text{ m}}{100 \text{ cm}} \right)^3}{\left( 8.314 \frac{\text{Nm}}{\text{mol K}} \right) \left( \frac{1 \text{ mol}}{6.022 \times 10^{23} \text{ atoms}} \right) (294.26 \text{ K})} \quad (9.9) \\
 &= 1.45 \times 10^{20} \text{ atoms}
 \end{aligned}$$

We then multiply the ratio of the number of Be atoms to He atoms sampled (which is effectively the concentration of the sampled Be cube) to the accelerator result to obtain the true number of Be' atoms present per Be atom,

$$\begin{aligned}
 \frac{[\text{Be}']}{[\text{Be}]} &= \frac{[\text{He}][\text{Be}']}{[\text{Be}][\text{He}]} \\
 &= \frac{N_{\text{He}}[\text{Be}']}{N_{\text{Be}}[\text{He}]} \quad (9.10) \\
 &= (5.57 \times 10^{-4}) \frac{[\text{Be}']}{[\text{He}]}
 \end{aligned}$$

which is the final quantity of interest. Notice that no assumptions regarding the cosmological abundances had to be made in order to obtain the result which is one of the big improvements of this experiment over previous ones of this type. If we had 100% transmission through the machine and 100% efficiency in detecting the anomalous Be we would set a limit which is on the order of  $4 \times 10^{-24}$ . However, the standards are needed to determine the actual impact of the machine efficiencies and as will be shown in the following chapter on the results the limit we set is significantly less – at  $9 \times 10^{-12}$  the limit is nearly 12 orders of magnitude smaller!

### 9.3.2 Beryl

The search for the presence of Be' in Be ore presented a number of problems similar to those encountered with the metal sample, and again a number of alternatives were considered for decomposing the ore. Be is extracted from the mineral beryl which has a nominal chemical formula  $3\text{BeO} \cdot \text{Al}_2\text{O}_3 \cdot 6\text{SiO}_2$ . Beryl dissolves in hydrofluoric acid (HF), albeit slowly and as a result creation of the beryl samples took a long period of time while we waited for the surfaces to etch. In the first ore sample, we placed two different ore fragments into two separate Teflon containers each filled with an excess quantity (453 grams) of 48% HF. In the first Teflon container we placed a single 115.6 gram chunk. For the second container we first crushed a larger chunk into several smaller ones in order to increase the surface area exposed to the HF and possibly increase the quantity of ore etched away. In the second container held the 246.4 grams of ore chunks in 453 grams of 48% HF. Thus in the first ore sample we placed the two different Teflon containers full of HF into a sealed glass desiccator that was previously coated with silicone grease to retard etching by the HF. The dessicator was then connected to a manometer which monitored the internal pressure and the entire apparatus was left undisturbed from 18 June 1997 until 22 October 1997. The sample was then extracted for Run Be5. Although data on it was not taken until Run Be7. The experimental setup for the extraction of the ore samples is shown in Figure 9.7 and a picture is provided in Figure 9.8.

The rocks did not completely etch away while some of the Be ore was etched off and was deposited into the HF solution. Table 9.9 gives a summary of the original and final masses of the ore chunks following the etching along with a summary of the analysis performed on the HF to see the amount in solution. This analysis was facilitated by Darren Hillegonds and the actual analysis of the HF was performed by Jon Friedrich.

From the table we see that a total of 32.5 grams of beryl was etched in the first attempt and thus we sampled nearly 10 times more material than in the pure metal

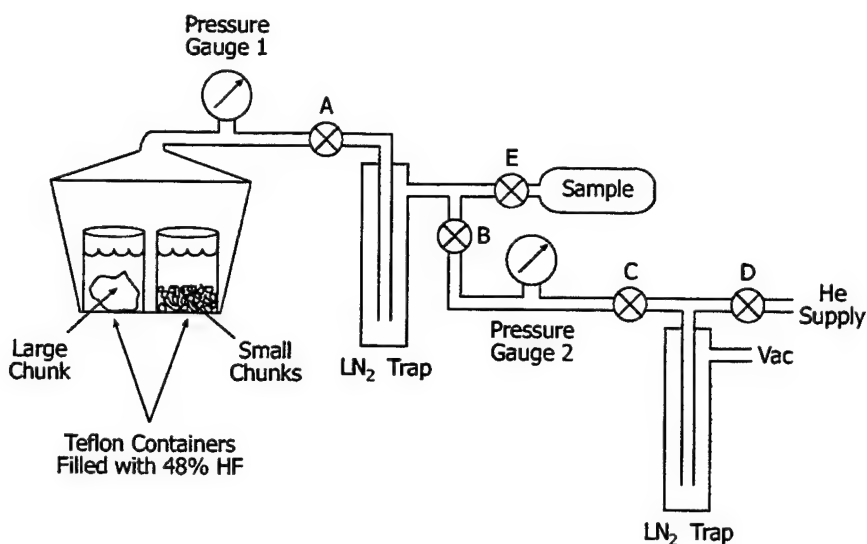


Figure 9.7: Schematic of the experimental setup for the extraction of the Be ore samples. A large ore chunk and several crushed chunks were placed into Teflon containers filled with 48% HF and put into a desiccator. The desiccator was then left for a prolonged period in which the HF etched the surfaces thereby releasing any trapped Be'.

case. This larger quantity however came at the cost of extremely long exposure times to the HF. Since this was so successful we decided to repeat the procedure with the same chunks and the entire process was repeated. This time they were placed into

Table 9.9: Summary of ore masses consumed during the first etching. The results are broken down by the chunk and crushed versions of the sample each of which was in a separate Teflon beaker of HF. Both of these contributed to the creation of the first ore sample, O1.

Mass	Chunk	Crushed
Before Etching	115.6 gm	246.4 gm
After Etching	101.3 gm	228.2 gm
Etched Mass	14.3 gm	18.2 gm
% by weight of Be in HF	0.155 %	0.148 %

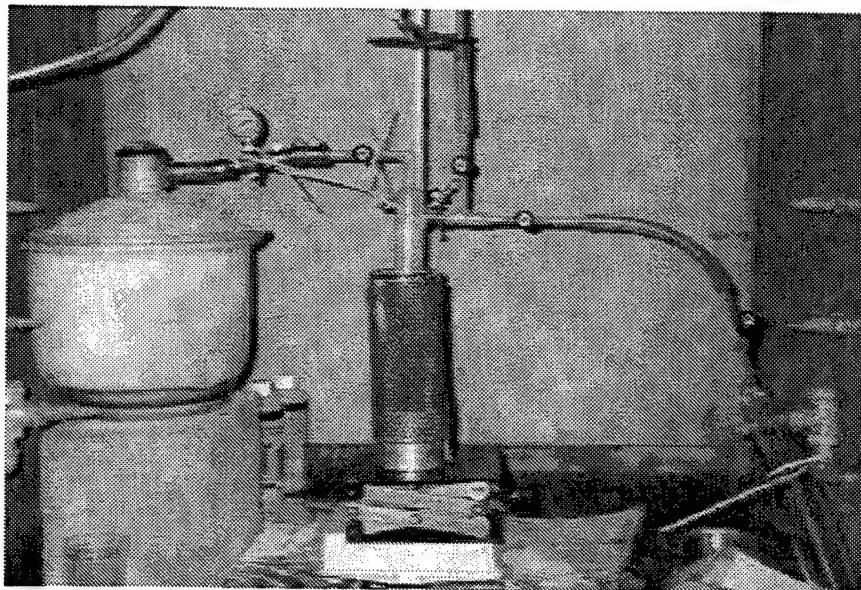


Figure 9.8: Picture of the beryl experimental setup whose schematic is given in Figure 9.7. The teflon containers cannot be seen through the glass of the desiccator because of the silicone grease which caused the glass to look a misty white.

solution on 11 February 1999 and removed 25 May 1999. This time a total of 81.4 grams of beryl was etched bringing the total to 113.9 grams of beryl. However, this is grams of beryl sampled which translates into 5.81 grams of Be since the Be/beryl = 0.051.

This may then be turned into the pure  $[Be']/[Be]$  ratio as an adjustment to the accelerator ratio ( $[Be']/[He]$ ) using the same procedure as was developed for the metal sample discussed above. For the beryl the mass of Be sampled turns into

$$\begin{aligned}
 N_{Be} &= 5.81 \text{ gm} \left( \frac{1 \text{ mol}}{9.012 \text{ gm}} \right) \left( \frac{6.022 \times 10^{23} \text{ atoms}}{1 \text{ mol}} \right) \\
 &= 3.88 \times 10^{23} \text{ atoms}
 \end{aligned}
 \tag{9.11}$$

Again we compute the number of He atoms present in the sample with the ideal gas law since we know the volume ( $470.21 \text{ cm}^3$ ), temperature ( $294.26 \text{ K}$ ), and pressure ( $1.01 \text{ psi}$ ) of the He carrier,

$$\begin{aligned}
N_{He} &= \frac{PV}{RT} \\
&= \frac{(1.01 \text{ psi}) \left( \frac{6894.8 \text{ N/m}^2}{1 \text{ psi}} \right) (470.21 \text{ cm}^3) \left( \frac{1 \text{ m}}{100 \text{ cm}} \right)^3}{\left( 8.314 \frac{\text{Nm}}{\text{mol K}} \right) \left( \frac{1 \text{ mol}}{6.022 \times 10^{23} \text{ atoms}} \right) (294.26 \text{ K})} \quad (9.12) \\
&= 8.06 \times 10^{20} \text{ atoms}
\end{aligned}$$

We then multiply the ratio of the number of Be atoms to He atoms sampled (which is effectively the concentration of the beryl sampled) to the accelerator result to obtain the true number of Be' atoms present per Be atom,

$$\begin{aligned}
\frac{[Be']}{[Be]} &= \frac{[He] [Be']}{[Be] [He]} \\
&= \frac{N_{He} [Be']}{N_{Be} [He]} \quad (9.13) \\
&= (2.07 \times 10^{-3}) \frac{[Be']}{[He]}
\end{aligned}$$

Thus we now have the necessary correction required to transform our raw accelerator result into a meaningful one that evaluates the ratio of Pauli-violating Be atoms to Pauli-abiding ones.

### 9.3.3 The Gas Field Sample

One unique sample is the gas field sample which was obtained from the Bush Dome Bivins A-11 site in the Cliffside natural gas field located five miles northwest of Amarillo, Texas. The Cliffside natural gas field is actually part of the much larger Panhandle-Hugoton gas field which spans from North Texas through the Oklahoma panhandle and into central Kansas (see Figure 9.9). The Panhandle-Hugoton Field is a classic carbonate stratigraphic trap.

Hydrocarbons (like natural gas and petroleum) form from the remains of microscopic organisms that exist in seas and large lakes. When the organisms die, their remains settle to the sea or lake floor where little oxygen is present to decompose

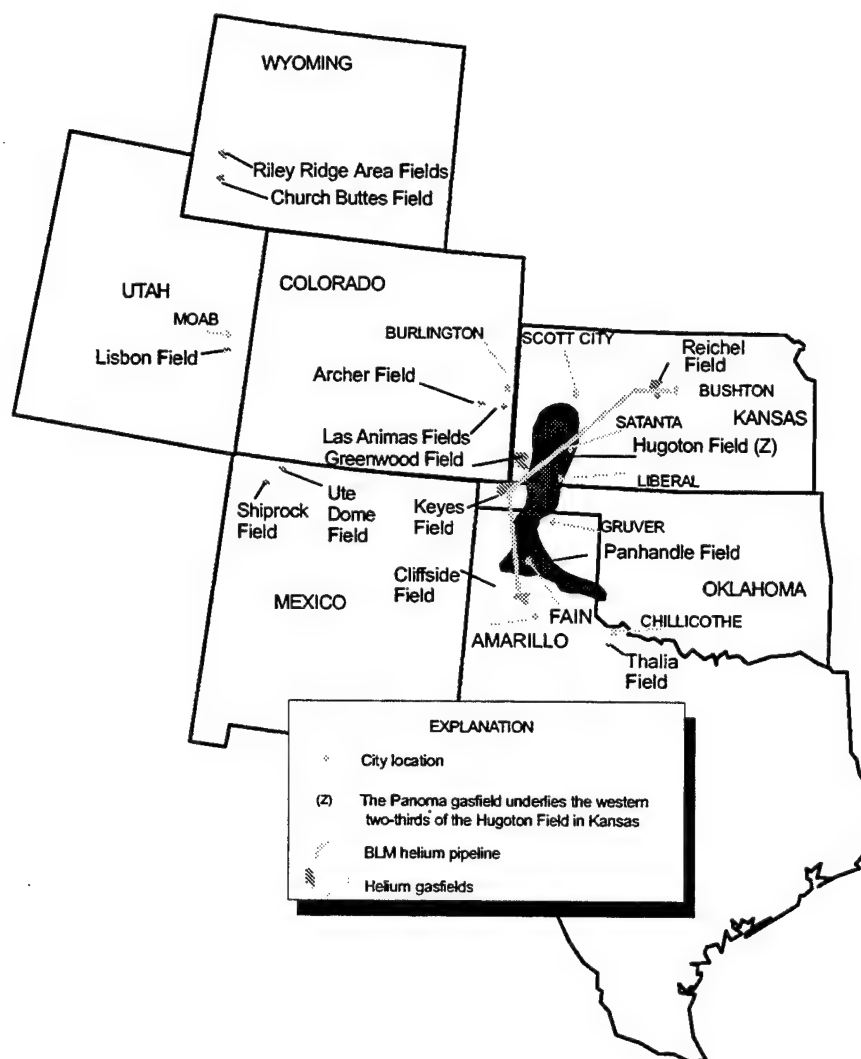


Figure 9.9: Major U.S. helium-bearing natural gas fields. This figure was adapted from the Helium Statistics paper by David V. Hayes, Jr. produced by the U.S. Geological Survey [15].

them. As a result they remain long enough to be buried by layers of sediment. As the depth at which they are buried increases they are heated and transformed into hydrocarbons. The hydrocarbons then migrate through the layers until they eventually seep out at the surface. However, sometimes the hydrocarbons get trapped and accumulate in a reservoir rock. Such rocks contain a considerable amount of pore space

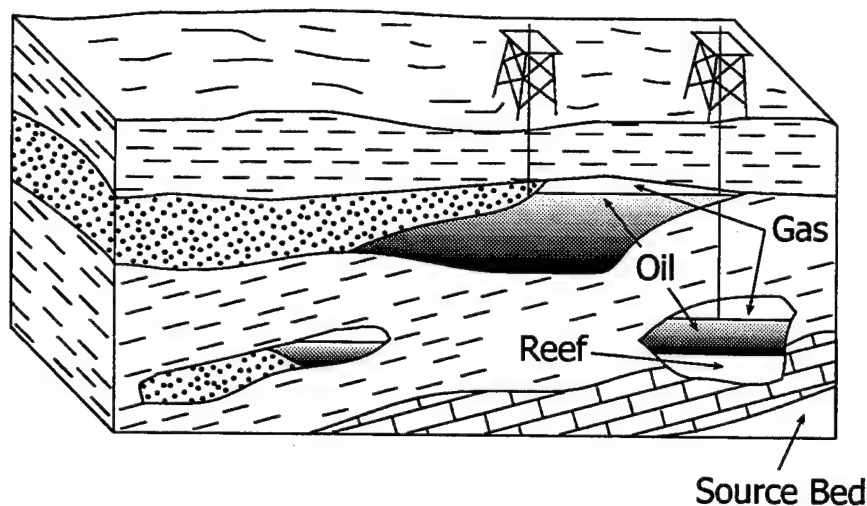


Figure 9.10: Oil and natural gas traps. This diagram is a cross-section of the Earth's crust showing the layers of sediment which result in the stratigraphic traps like those of the Panhandle-Hugoton natural gas field of which the Cliffside Field is a part. The gas field sample was taken from one such trap.

so that appreciable quantities of the hydrocarbons may accumulate. To prevent further migration of the hydrocarbons there must exist a layer of impermeable cap rock to contain the hydrocarbons. Stratigraphic traps are hydrocarbon reservoirs which consist of near-shore marine sandstones in proximity with fine-grained, organic-rich source rock [139]. Figure 9.10 is a diagram of several stratigraphic traps. Because of the properties of the stratigraphic traps they also trap other gases produced in the Earth's interior. In our case it is significant that the field also trap helium and possibly Be'. However, helium is not universally present in natural gas fields. Most helium found in the Earth's crust is a result of radioactive decay of uranium and thorium which emit an abundance of alpha particles. Thus, only natural gas reservoirs near large uranium and thorium deposits will have large He concentration.

The gas field sample was extracted on 3 April 1996 and analysis of the sample gave the following composition:  $>93\%$   $\text{CH}_4$ ,  $2.9\%$  He,  $< 4\%$   $\text{C}_2\text{H}_6$ ,  $< 1\%$   $\text{C}_3\text{H}_8$ ,  $< 0.4\%$   $\text{C}_4\text{H}_{10}$ ,  $< 0.7\%$   $\text{CO}_2$ ,  $< 0.6\%$   $\text{N}_2$ , and  $(2 \pm 1)$  ppm  $\text{O}_2$ . As a result of the high He content the sample may be thought of as primarily natural gas with a high

He contamination. In fact, when the Panhandle-Hugoton Field was first discovered by entrepreneurs in search of oil reserves, its high helium content was considered a contaminate because of its inert properties which decreased the BTU per cubic meter. However with the advent of WWI and the large rise in the demand for He made the field famous by producing the highest He yield in the world.

In 1927 the U.S. Bureau of Mines was tasked with creating the Federal Helium Reserve which pertains to the crude helium gas which currently resides in the Bush Dome reservoir in the Cliffside natural gas field. The Bush Dome originally contained one of the early helium-rich natural gas deposits discussed above. The formation is approximately 3,500 feet deep and 300 feet thick and has a 10 % porosity. The Dome has a total capacity of approximately 45 billion scf and currently contains approximately 30.5 billion scf of government-owned crude helium. The pure helium is extracted from the natural gas after the gas temperature is reduced to about 88.7 K ( $-300^{\circ}\text{F}$ ). Since the He boiling point is at 20.3 K it remains a gas and is subsequently drawn off.

We used a similar method in extracting the He for our gas field samples – G1, G2, and G3. The unprocessed gas field sample passed through two  $\text{LN}_2$  traps which

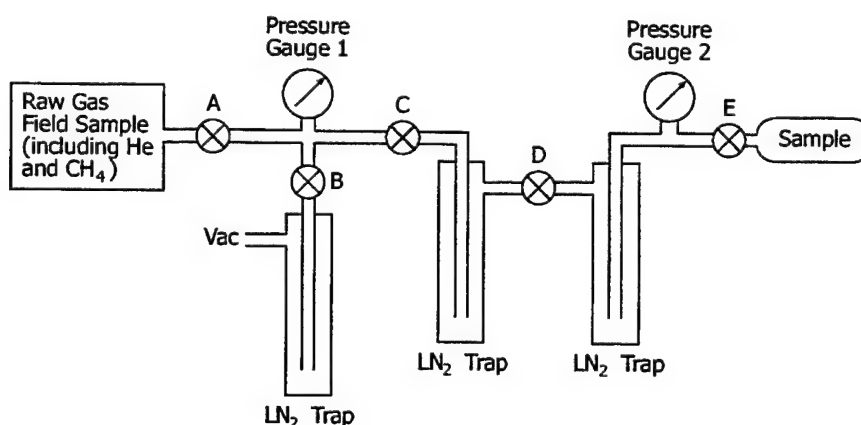


Figure 9.11: Experimental setup for the gas field samples. The liquid nitrogen ( $\text{LN}_2$ ) traps lower the temperature of the gas to 77.4 K thus condensing out the hydrocarbons and allowing the He and any Be' to get all the way to the sample vial.

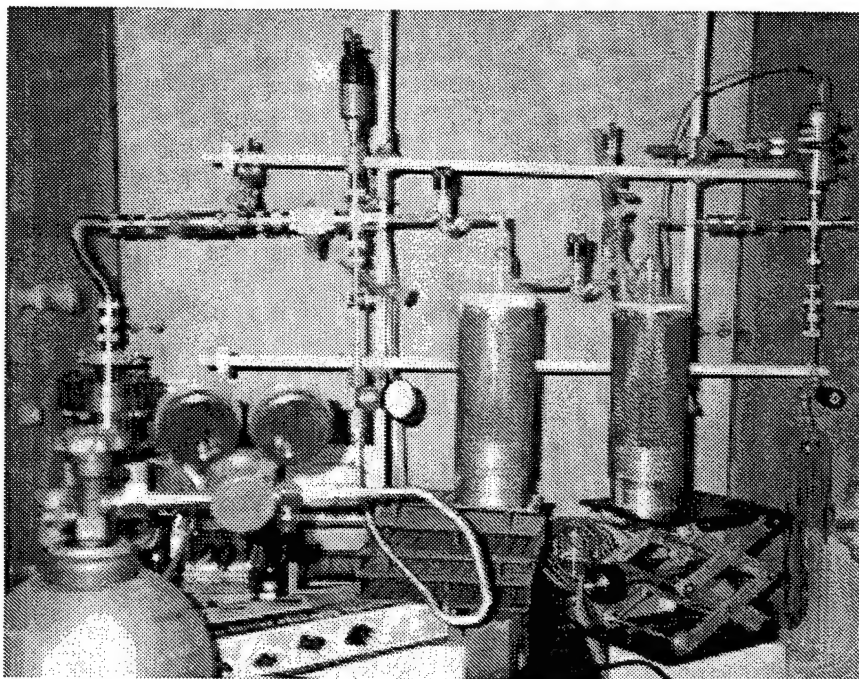


Figure 9.12: Picture of the experimental setup in Figure 9.11. The top of the tank holding our original gas field sample is in the left hand corner.

reduced the gas temperature to 77.4 K and condensed out the  $\text{CO}_2$ ,  $\text{O}_2$ , and the hydrocarbons. The remaining gas was collected in a glass sample flask which had been evacuated to  $10^{-5}$  Torr, and which was maintained at  $19^\circ\text{C}$ . When the cylinder containing the original gas field sample was shut off, the pressure in the gas sample flask stabilized at 495 Torr as measured by an MKS Baratron Capacitance Manometer. A diagram of the experimental setup is given in Figure 9.11 with a picture of the setup in Figure 9.12.

Again we reiterate the importance that the sample contained a significant amount of He was critical since, as noted above, this justified the assumption that  $\text{Be}'$  could also be trapped at the same site.

### 9.3.4 Atmospheric Air

In addition to the gas field sample, we also ran a sample of laboratory air. This was done for two reasons; first it allowed us to compare our result to the previous results set by Fischbach, Kirsten, and Schaeffer which set limits on air only. Second, the air

was easy to run and did not add any complexity to the mechanism, in fact it was obtained by simply opening an intake port of the gas manifold to the atmosphere. The air sample was subsequently run under the same conditions of pressure and temperature as were the other samples.

The atmosphere is a mixture of many discrete gases and is not constant but varies depending on the location time and amount of suspended particles that are present. As a reference however, we may use clean dry air (following the removal of suspended particles and water vapor) which is composed primarily of nitrogen and oxygen. Table 9.10 gives the principle gases found in common air. Of importance is the presence of helium and methane (which were also present in the gas field sample). These low concentrations of each is a result from seepage mentioned above. In fact, prior to its discovery in natural gas deposits He was extracted from the atmosphere where it is incredibly scarce with a concentration of only 5.24 ppm [2]. This low atmospheric He concentration results from the observation that it is seven times lighter than air and

Table 9.10: The principle gases of dry air. Notice the presence of helium and methane which were the major topic of the previous section. This table was obtained from Table 1-1 of Ref. [2].

Constituent	Percent by Volume	Concentration [ppm]
Nitrogen (N <sub>2</sub> )	78.084	—
Oxygen (O <sub>2</sub> )	20.946	—
Argon (Ar)	0.934	—
Carbon dioxide (CO <sub>2</sub> )	0.035	—
Neon (Ne)	0.00182	18.2
Helium (He)	0.000524	5.24
Methane (CH <sub>4</sub> )	0.00015	1.5
Krypton (Kr)	0.000114	1.14
Hydrogen (H <sub>2</sub> )	0.00005	0.5

thus the same property which makes it popular for birthday balloons also causes it to escape the Earth's gravity and be lost into space.

Thus, like the previous samples we may make the necessary correction for anomalous Be in air instead of just in He. This comes from simple application of the data contained in Table 9.10 to the  $[Be']/[He]$  ratio measured by the accelerator. The equation for converting the ratio with respect to He to that of air  $\rho'$  is

$$\begin{aligned}
 \rho' &= \frac{[Be']}{[air]} \\
 &= \frac{[He]}{[air]} \frac{[Be']}{[He]} \\
 &= \frac{N_{He}}{N_{air}} \frac{[Be']}{[He]} \\
 &= (5.24 \times 10^{-6}) \frac{[Be']}{[He]}
 \end{aligned}
 \tag{9.14}$$

## CHAPTER 10. EXPERIMENTAL RESULTS

### 10.1 Introduction

Now that we understand the overarching concepts of how we were planning to look for possible violations of the Pauli principle we may proceed to discuss the experimental results. However, before proceeding lets summarize the chapters leading up to these results.

Paronic beryllium is Be with all of its electrons crowded into the 1s shell. As a result its valence electrons cause it to possess the same chemical properties as He and thus would be a gas at standard temperatures and pressures. Since He beam currents are extremely low (because it has the highest ionization potential of all the elements) we need to first calibrate the accelerator by preparing standard samples whose Be concentrations are known and then running them to determine the relationship between counting rate and concentration. This then allows us to infer the Be concentration of the unknown samples based on the counting rates we obtain.

### 10.2 Run Be1, Oct 1996: Pre-Tuning and Calculations

In the beginning our understanding of the mechanism and procedure was still under development. Many of the subsequent developments, like the new cathode or the gas manifold were designed to account for problems encountered in the earlier runs.

This first run was not really a run at all but used to calculate the necessary field settings and predict difficulties of tuning on carbon instead of beryllium to reduce potential contamination. This was when many of the original decisions were made about charge states, energies, and ion source settings. As is customarily done in such cases where we are unsure of proper tune settings to expect, we begin with the known

detector settings for a known mass (in this case  $^{37}\text{Cl}$ ). We then scale all the magnetic and electrostatic elements based on the formulas and concepts covered in great detail in Chapter 1. As a quick review recall that since the magnetic elements obey the relationship given in Equation (1.9) and reproduced here

$$B = \frac{\sqrt{2ME}}{rq} \quad (10.1)$$

Since the magnets radii are constant we calculate the new B-field,  $B_2$  from

$$\begin{aligned} \frac{B_2}{B_1} &= \frac{\sqrt{2M_2E_2}/rq_2}{\sqrt{2M_1E_1}/rq_1} \\ &= \frac{q_1}{q_2} \sqrt{\frac{M_2E_2}{M_1E_1}} \end{aligned} \quad (10.2)$$

$$\Rightarrow B_2 = B_1 \left( \frac{q_1}{q_2} \sqrt{\frac{M_2E_2}{M_1E_1}} \right)$$

which are all known quantities once the charge state and terminal voltage are picked. Similarly, we may calculate the electrostatic field  $\mathcal{E}$  settings using Equation (1.16) and which is reproduced here

$$\mathcal{E} = \frac{2E}{rq} \quad (10.3)$$

Just like the magnets, the radius is constant for the electrostatic elements and the new settings are derived from existing data via the relationship

$$\begin{aligned} \frac{\mathcal{E}_2}{\mathcal{E}_1} &= \frac{2E_2/rq_2}{2E_1/rq_1} \\ &= \frac{q_1}{q_2} \frac{E_2}{E_1} \end{aligned} \quad (10.4)$$

$$\Rightarrow \mathcal{E}_2 = \mathcal{E}_1 \left( \frac{q_1}{q_2} \frac{E_2}{E_1} \right)$$

Table 10.1: Predicted accelerator  $^9\text{Be}$  settings based on  $^{37}\text{Cl}$  data. Run Be1 was used to perform the necessary calculations for the tandem settings for needed for  $^9\text{Be}$ .

Stage	Setting	Value
Ion Source	Cathode =	5 kV
	Pre-Acc =	65 kV
	Extractor =	20 kV
	Injection Energy =	0.085 MeV
	Injector B-field =	-0.32811 T
Terminal	Stripping =	Foil
	Charge State, $q$ =	+4
	Terminal Voltage, $V_t$ =	6 MV
	Be Energy =	26.191 MeV
High End	Analyzing B-field =	-0.54811 T
	Switching B-field =	-0.36727 T
	Electrostatic Analyzer, ESA =	68.83 kV

which again are all known quantities. In this case the subscript 1 quantities are those from the  $^{37}\text{Cl}$  data.

We begin by accelerating  $\text{BeO}^-$  whose mass is  $^9\text{Be} + ^{16}\text{O} = 25$  amu. This molecule is then broken apart at the stripper and the resulting  $^9\text{Be}$  in charge state +4 is selected down the high end elements to the detector. To save the tedium of writing out all the calculations, we will assume that Chapter 1 was more than adequate in providing justification/proof of the necessary calculations and we will only report the final predicted numbers for all the settings in Table 10.1.

### 10.3 Run Be2, Oct 1996: Carbon Tuning and Setup

In this run we actually put beam through the accelerator to test our tuning method. Originally we might wonder why this needed to be tested since Be is regularly run on the accelerator and such a tune would normally be commonplace. However,

we already were predicting the presence of high Be contamination levels inside the ion source itself. In fact we were already working on having the Be-free source constructed (which was later implemented in Run Be4). The concept of the Be-free source was to never introduce it to Be measurements to minimize ion source contamination effects. Thus, we needed to find a way to tune the Be beam without Be.

This was accomplished by tuning with  $^{12}\text{C}$  and adjusting the settings for Be using the above mentioned relationships (namely Equations (10.2) and (10.4)). Since typical AMS operations regularly runs  $^{12}\text{C}$  it was possible to simply look up the values and just check them with the calculations mentioned above. The settings for the  $^{12}\text{C}$  following the tune are given in Table 10.3.

The terminal voltage and electromagnetic settings were then adjusted to the Be settings given in Table 10.1. As is evident by the much larger Table 10.3 we are unable to predict specific tune settings (like the steerers and lenses) however for the small shift from mass 12 to 9, we may assume that these are roughly constant. We then were able to put Be into the detector. The source of this Be is the naturally occurring abundance in the  $^{12}\text{C}$  blank along with the Be produced inherently by the source. Moving to position 5, which held an empty copper cathode, produced a Be counting rate of 20 counts per second (cps) with the attenuator in. Thus with an attenuation factor of 22 the actual counting rate was 440 cps. The counting rates for the different surfaces Cu, Ag, and  $\text{Al}_2\text{O}_3$  are given in Table 10.2.

This quick test of the beam currents for the different surfaces shows their varying amounts of Be contamination. In the cases of the elemental surface in which no oxygen

Table 10.2: Counting rates of the different surfaces tested during Run Be2.

Surface Target	Counting Rate [cps]
Graphite	330
Copper	440
Silver	5,170
$\text{Al}_2\text{O}_3$	50

Table 10.3: Tandem parameter settings following the tune on  $^{12}\text{C}$ . It was necessary to tune with C instead of Be to prevent introducing Be source contamination. Use Figure 1.1 to locate the different elements.

Stage	Setting	Value
Ion Source	Oven =	0.5 A
	Ionizer =	14 A
	Cathode =	5 kV
	Extractor =	20 kV
	Pre-Acc =	66 kV
	Injection Energy =	0.086 MeV
	1st Einzel Lens =	7 kV
	Injector B-field =	-0.22732 T
	Einzel Lens =	802
Low End	X/Y Steerers =	18L, 13R, 14D, 11U
Terminal	Stripping =	Foil # 55
	Charge State, $q$ =	+4
	Terminal Voltage, $V_t$ =	3.888 MV
	C Energy =	19.526 MeV
	Corona Current =	40 $\mu\text{A}$
High End	Points =	12.6 inches
	Analyzing B-field =	-0.54811 T
	X/Y Steerers =	0L, 0R, 15D, 8D
	Trans Quad A/B =	319/337
	BL Quad A/B =	191/191
	Switching B-field =	-0.36740 T
	Electrostatic Analyzer, ESA =	51.37 kV
Final Transmission	Injector Faraday Cup (FC) Current =	215 nA
	Image FC Current =	230 nA
	Transmission, $\eta$ =	26.7 %

was present the currents decreased as the oxygen on the surface from its exposure to air was used up. This was verified by opening the source to allow atmosphere to get back in contact with the surfaces and replenish the oxygen in the source. The  $\text{Al}_2\text{O}_3$  did not seem to have such a dependence but its low beam current in relation to the others caused us to suspect an overwhelming oxygen  $\text{O}_2$  current was reducing the impact of the BeO. However, after changing the injector magnetic field setting to  $\text{O}_2$  only a small current was realized suggesting the low counting rate of the  $\text{Al}_2\text{O}_3$  was just a lower contamination level and not from an overwhelming oxygen beam. This test was performed again in Run Be5 with similar results.

This variability of the beam current from oxygen consumption would prove to be the motivation for the surface studies performed in Run Be5 as we searched for

surfaces with low Be contamination and preferably searched for oxides which would provide the oxygen inside the source, saving us the trouble of adding the necessary oxygen to each of the samples. These beam currents are even high enough to touch up the Be tune whose final values are provided in Table 10.4.

Table 10.4:  $^9\text{Be}$  Tandem parameter settings for Run Be2. Use Figure 1.1 to locate the different elements.

Stage	Setting	Value
Ion Source	Oven =	0.55 A
	Ionizer =	14 A
	Cathode =	5 kV
	Extractor =	19.8 kV
	Pre-Acc =	66 kV
	Injection Energy =	0.0858 MeV
	1st Einzel Lens =	7 kV
Low End	Injector B-field =	-0.32811 T
	Object X/Y Steerers =	0.50/0.49
	Image X/Y Steerers =	0.57/0.48
	Image Einzel Lens =	41.2 kV
	Beamline Einzel Lens =	790
Terminal	Gridded Lens =	0.0
	X/Y Steerers =	13L, 13R, 15D, 11U
	LE Chains =	12 kV
	HE Chains =	22 kV
	Stripping =	Foil # 55
	Charge State, $q$ =	+4
	Terminal Voltage, $V_t$ =	5.943 MV
	Control =	Varian GVM
	Be Energy =	25.942 MeV
	Corona Current =	40 $\mu\text{A}$
High End	Points =	12.6 inches
	HE Quad A/B =	297/292
	X/Y Steerers =	0L, 0R, 15D, 8D
	Analyzing B-field =	-0.54815 T
	Trans Quad A/B =	319/337
	BL Quad A/B =	191/191
	Switching B-field =	-0.36745 T
	Electrostatic Analyzer, ESA =	68.50 kV
Final Transmission	Injector FC Current =	7.17 nA
	Image FC Current =	0.18 nA
	Detector FC Current =	0.175 nA
	Transmission, $\eta$ =	0.63 % with tight slits

#### 10.4 Run Be3, Dec 1996: Background Determination and First Results

Now that we had gained valuable experience tuning and running solid surfaces we needed to introduce the concept of gas samples. This had never been attempted on the Purdue facility and as a result we were dabbling in unknown regions of the operational phase space of the accelerator.

The tune proceeded as in Run Be2 with a pre-tune being performed with carbon with the usual adjustments made to obtain the Be values. The tandem parameter settings for this tune are given in Table 10.5. All the settings were the same with only a few exceptions, in the cases where such differences existed the  $^{12}\text{C}$  values are provided in brackets [ ].

We introduced the gas on the only available opening which was located across from the ion source from the cathode. Initially we were unsure of how much gas to leak into the source so measurements were taken at different ranges of source pressures in our initial attempt to evaluate the background counting rate present in the source. The background was determined by introducing the different concentration standards to the source and evaluating if there was a noticeable rise in the counting rate. We also decided to try a few different surfaces a graphite blank, a  $\text{TiO}_2 + \text{Ag}$  mixture, and  $\text{TiO}_2$ . The Ag would contain a large amount of Be concentration as noticed from the previous run and we were optimistic that it would give a good calibration.

We began by running the highest concentration standard S9 at 459 ppm this sample was clearly visible on all surfaces since the counting rate climbed with the pressure as would be expected. The results from S9 are given in Table 10.6 and are plotted in Figure 10.1.

From this table we see the decrease in counting rate reflected by the increase in the pressure. Thus we are already beginning to see the trade off between low Be quantities and higher pressures. More discussion on this later.

Unfortunately these extremely high counting rates persisted after S9 was removed from the source indicating that we had contaminated the source. As a result, the source was run overnight to burn off the contamination. The following morning we

Table 10.5:  $^9\text{Be}$  Tandem parameter settings for Run Be3. Most settings remained the same as for  $^{12}\text{C}$ , those which did change in the transition from C to Be are provided with the C values in brackets, for example  $V_t = V_t(\text{Be}) [V_t(\text{C})]$ . Use Figure 1.1 to locate the different elements.

Stage	Setting	Value
Ion Source	Oven =	0.55 A
	Ionizer =	16.5 A
	Cathode =	5 kV
	Extractor =	20 kV
	Pre-Acc =	65.5 kV
	Injection Energy =	0.0855 MeV
	1st Einzel Lens =	5 kV
	2nd Einzel Lens =	3.5 kV
	Injector B-field =	-0.32811 [-0.22733] T
	Object X/Y Steerers =	0.1/0.0 mA
Low End	Image X/Y Steerers =	0.5/0.38 mA
	Image Einzel Lens =	40.0 kV
	Beamline Einzel Lens =	449
	Gridded Lens =	0.0
	X/Y Steerers =	5L, 3R, 9D, 0U
Terminal	LE Chains =	13 kV
	HE Chains =	13 kV
	Stripping =	Foil # 10
	Charge State, q =	+4
	Terminal Voltage, $V_t$ =	5.945 [3.896] MV
High End	Control =	Varian GVM
	Corona Current =	42 $\mu\text{A}$
	Points =	12.8 inches
	HE Quad A/B =	300/292
	X/Y Steerers =	0L, 0R, 25D, 9U
	Analyzing B-field =	-.54813 T
	Trans Quad A/B =	311/335
	BL Quad A/B =	203/200
	Switching B-field =	-0.36790 T
	Electrostatic Analyzer, ESA =	68.40 [51.10] kV
Final Transmission	Injector FC Current =	[217] nA
	Image FC Current =	[320] nA
	Detector FC Current =	[325] nA
	Transmission, $\eta$ =	[36.9] %

added fresh C, Ag+TiO<sub>2</sub>, and TiO<sub>2</sub> samples to the wheel. We then proceeded to perform the tests on samples ordered with increasing Be concentration. Thus we began with the He blank sample and as expected observed the source efficiency

Table 10.6: Counting rates on the different surfaces at a range of S9 source pressures. Standard S9 had a concentration of 459 ppm and was clearly visible above the background counting rate of Run Be3. Along the horizontal axis is pressure while the Target is given on the vertical axis. The Table entries are the counting rates in cps measured on the  $\Delta E_1$  plate in the detector.

Surface Target	Pressure [Torr]			
	$1.1 \times 10^{-6}$	$1.4 \times 10^{-6}$	$2.6 \times 10^{-6}$	$4.9 \times 10^{-6}$
C	60	60	2800	420
Ag+TiO <sub>2</sub>	700	900	79200	72600
TiO <sub>2</sub>	0	2	9	4

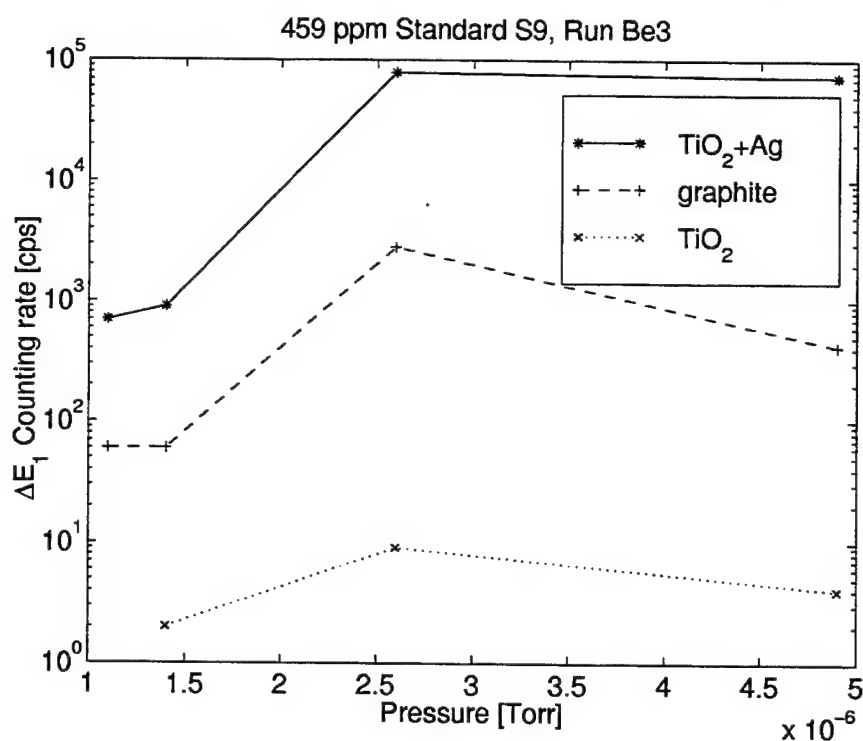


Figure 10.1: Counting rate as a function of Standard S9 (459 ppm) source pressure taken in run Be3. Notice the apparent rise and subsequent fall of the counting rate. This structure is from two competing mechanisms effecting the source efficiency.

decrease with increasing pressure. This is reflected in Table 10.7 and is also plotted

Table 10.7: Counting rates on the different surfaces at a range of He source pressures. Notice the slow decrease in counting rates as a function of source pressure. As in Table 10.6 the Table entries are the corresponding counting rates in cps measured on the  $\Delta E_1$  plate in the detector.

Surface Target	Pressure [Torr]				
	vac = $6.7 \times 10^{-7}$	$1.2 \times 10^{-6}$	$1.5 \times 10^{-6}$	$2.6 \times 10^{-6}$	$4.8 \times 10^{-6}$
C	600	700	320	250	190
Ag+TiO <sub>2</sub>	8800	4000	3400	2900	2200
TiO <sub>2</sub>	0	0	0	0	0

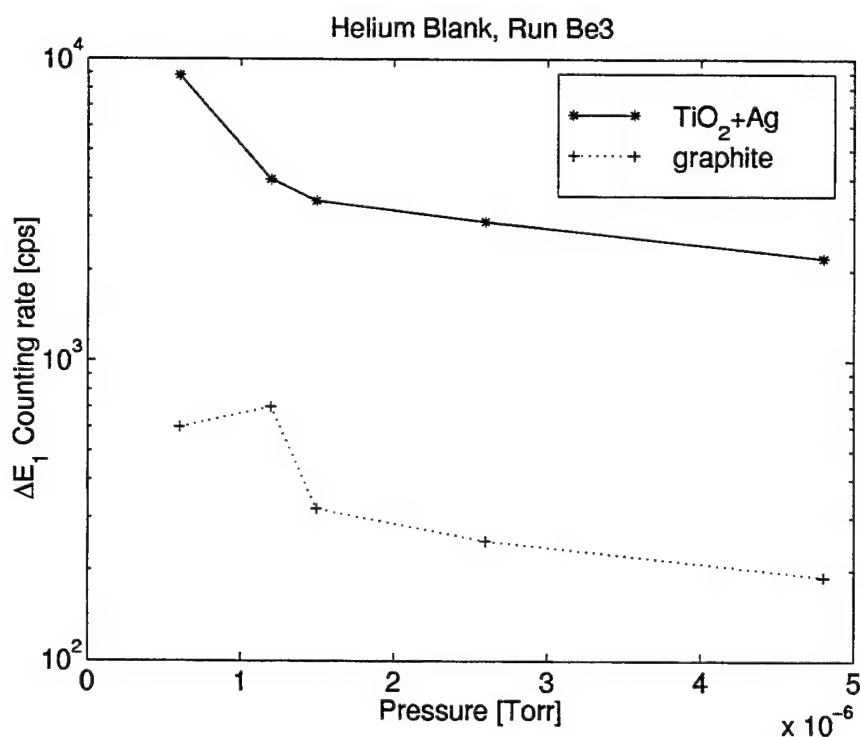


Figure 10.2: Counting rate as a function of He source pressure taken in run Be3. As the pressure increases the gas (in this case He) begins to interfere with the ejected BeO<sup>-</sup> ions.

in Figure 10.2.

This same procedure was repeated for the 4.8 ppm standard, S5, which executed

Table 10.8: Counting rates on the different surfaces at a range of S5 (the 4.8 ppm standard) source pressures. Like the helium blank notice the slow decrease in counting rates as a function of source pressure. As in Table 10.6 the Table entries are the corresponding counting rates in cps measured on the  $\Delta E_1$  plate in the detector.

Surface Target	Pressure [Torr]			
	vac = $9.6 \times 10^{-7}$	$1.5 \times 10^{-6}$	$2.5 \times 10^{-6}$	$4.8 \times 10^{-6}$
C	300	160	120	120
Ag+TiO <sub>2</sub>	2300	2000	1700	1600
TiO <sub>2</sub>	0	0	0	0

the same basic behavior as the helium with just a slow decline as the pressure increased. The data from this run is provided in Table 10.8 and is not plotted because of its striking similarity in nature to the helium blank. This result was the first evidence that we were dealing with significant Be contamination. We also notice that because of long sample change times we are unable to relate the different samples to each other very reliably. This is because the time required to switch samples was on the order of 30 minutes. As we are changing samples the surface is slowly being sputtered away by the Cs and as a result the focus is slowly changing. Not to mention that we sometimes spend more time on one surface than another which causes them to change their focus in different ways. Finally, each surface sputters at a different rate causing comparison between the surfaces to be unreliable since the focus can be drastically different resulting in non-optimized beam currents. These are the first naive indications for the need of the gas manifold which was constructed in the summer of 1998.

This was finally repeated with the 74 ppm standard, S8. In this case the current seemed to slowly rise with pressure but was very subtle. The data, provided in Table 10.9, suggests that the 74 ppm standard is just barely visible above the background. Because of the importance of this data in determining the initial background we have plotted it in Figure 10.3. In this case the C data and the TiO<sub>2</sub> show indications of small rise in the current while the TiO<sub>2</sub>+Ag data is inconclusive.

Table 10.9: Counting rates on the different surfaces at a range of S8 (the 74.2 ppm standard) source pressures. Unlike the helium blank there seems to be a slight indication of an increase in the counting rate as the pressure increases. Again as in Table 10.6 the Table entries are the corresponding counting rates in cps measured on the  $\Delta E_1$  plate in the detector.

Surface Target	Pressure [Torr]			
	vac = $8.2 \times 10^{-7}$	$1.5 \times 10^{-6}$	$2.5 \times 10^{-6}$	$4.7 \times 10^{-6}$
C	300	200	250	320
Ag+TiO <sub>2</sub>	5000	3700	3500	4600
TiO <sub>2</sub>	0	0.5	0.5	1

Comparing Figure 10.3 representing S8 with Figure 10.2 the helium blank data we notice that it does not follow this same trend. In fact, the data begins a slight turn upward suggesting the tandem is sensitive to it. To qualify the statement we alternately opened and shut the valve at a pressure of  $5 \times 10^{-6}$  Torr and watched the graphite surface for noticeable fluctuations. This study made it clear that we were in fact observing the presence of the 74 ppm standard. The results from this study are provided in Table 10.10. The data seems much more decisive in this case because we are not spending the time to change samples and are getting more or less immediate feedback. Here we notice the counting rate is almost doubling and is showing a result which is much higher than the 1 cps fluctuations in the meter.

From this we may determine an incredibly crude estimate for the background and residual Be concentration found in the existing source. If we assume that the calibration goes through the origin we may use the data in Table 10.10 to determine the background concentration. With this assumption we know that a linear calibration may be created which goes through the origin and the data point (74 ppm, 210 cps). If we then assume that the background counting rate at  $5 \times 10^{-6}$  is 32 % the counting rate with the gas off (which is the % decrease realized by the Helium blank) we obtain a background concentration of

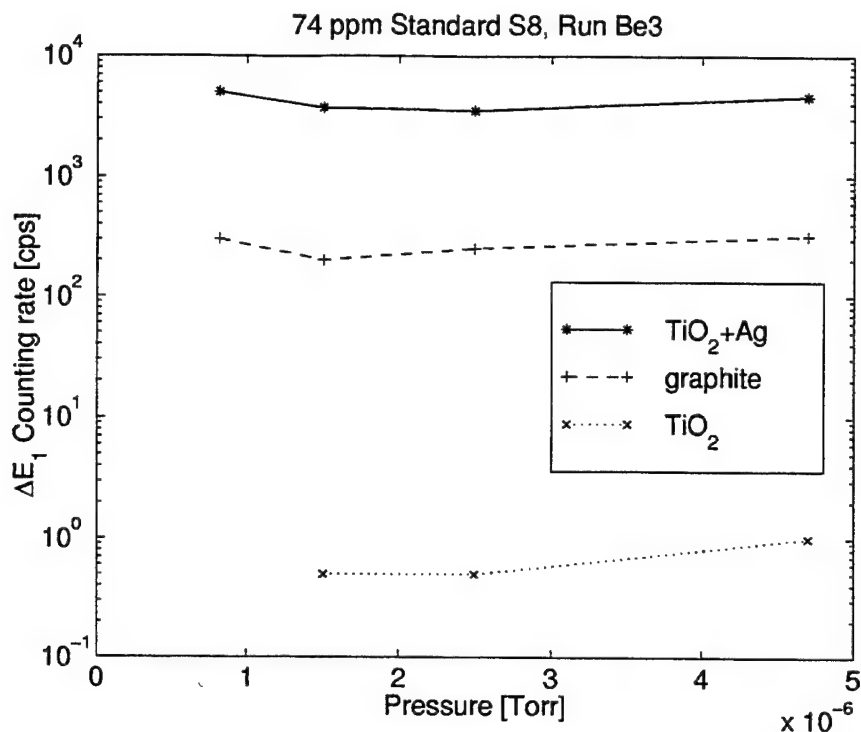


Figure 10.3: Counting rate as a function of S8 (74 ppm standard) source pressure taken in run Be3. In this case we have a slight indication the counting rate is increasing with gas pressure. Following further analysis in the text we confirmed the 74 ppm standard was barely visible above background. This set the limit on the background at just below 74 ppm. As a result vast improvements were needed in order to surpass the Fischbach, Kirsten, and Schaeffer [16] result.

$$\begin{aligned} \frac{[Be]}{[He]_{bgd}} &\approx \left( \frac{74 \text{ ppm}}{210 \text{ cps}} \right) (32\%) 130 \text{ cps} \\ &= 14.6 \text{ ppm} \end{aligned} \tag{10.5}$$

This result explains why the 4.8 ppm standard was not noticeable above background. Of course, this is an extremely approximate solution since the actual value of the He was not run following S8 and this makes the tremendous assumption that there is no y-intercept to the calibration line. Unfortunately, because of our skepticism about running high concentration standards this assumption carries into several

Table 10.10: Results of rapidly switching the 74 ppm standard on and off. Each time the gas was turned on we took it up to a pressure of  $5 \times 10^{-6}$  Torr. This data gives us conclusive evidence that we were observing the standard above background. These tests were run on the graphite surface and helped to establish the contaminating Be concentration of the old source.

Valve Position	Counting Rate [cps]
Closed	130
Open	210
Closed	130
Open	220
Closed	130

of the future runs until more low concentration standards are created.

The result did provide us with hope that we could obtain better data since we already had a Be-free source in the construction stage. However, the most major lesson learned from this run was the identification of future obstacles and provided us with a game plan for future runs.

First, we realized the need to determine a single operating pressure so that we could eliminate that as a variable. The data seemed to suggest an optimal pressure of around  $2.5 \times 10^{-6}$  Torr. This optimal pressure exists because while low pressures do not impede the ejected BeO ions they do mean fewer Be atoms are available for combination into BeO. Thus at first we would expect higher pressures to give better efficiencies since we increase the quantity of Be in the source but the competing mechanism in which the gas begins to degrade the exiting beam (which occurs because the ejected molecules interact with the higher pressure gas) will take over at higher pressures. The beam degradation due to higher pressures is evident in the He blank and the 4.8 ppm standard data while the overall structure was identifiable in the 459 ppm data.

We also identified the need to pick a standard surface which has potential to greatly impact the background Be concentration. The goal was to find a surface which registered the presence of the standards while simultaneously showing minimal

counts when running the blank. This topic is one of extensive review in Run Be5. Our first goal though was to determine the effect of the new source.

### 10.5 Run Be4, Sep 1997: First Run with Be-Free Source

As with prior runs the beam was tuned with carbon first before adjusting the parameters to the Be settings. At the beginning of the run we tried to tune with oxygen but the beam was too weak to get a substantial distance through the beamline and we had difficulty seeing the beam spot on the viewers. The final machine settings resulting from the tune are provided in Table 10.11.

As mentioned in the summary of Be3, one of the ways the background was reduced was by constructing a new source which had not previously been exposed to Be. We also tried a few new components this run. First off we used the new terminal voltage regulating system designed and built by Prof. Paul Simms. Second we added some complexity and sent the beam into the detector to use the computer to get more precise counting rates than just reading the numbers from the red interference meter as was done in Run Be3. This was done with a relatively simple mode sequence of (2, 5, 20) which permitted us to use the BR table and get an accurate measurement. The gas pressure in the detector was set so that the beam stopped in the  $\Delta E_3$  plate.

This time with the more precise output we repeated the results we obtained from the first run. This time we began with the He blank and worked our way to higher concentrations. We also tried some new surfaces, with air bleeding in at  $4.3 \times 10^{-6}$  we obtained the results provided in Table 10.12. This time we introduced primarily purely elemental surfaces with the exception of the Ti with which we mixed an astonishingly small amount of  $\text{TiO}_2$ . Unfortunately, these each possessed serious Be contamination which thwarted our efforts throughout this run.

The contamination was much higher in this run although we believed the contamination to be a result of the chosen surfaces and not the source itself. For example, the He blank measured the similar trend as last time with the counting rate dropping as the pressure increased. Like last time the 4.8 ppm standard was not observed above background. The unfortunate circumstance came from our inability to see the 74 ppm

Table 10.11:  $^9\text{Be}$  Tandem parameter settings for Run Be4, GV. Most settings remained the same as for  $^{12}\text{C}$ , those which did change in the transition from C to Be are provided with the C values in brackets, for example  $V_t = V_t(\text{Be}) [V_t(\text{C})]$ . Use Figure 1.1 to locate the different elements.

Stage	Setting	Value
Ion Source	Oven =	0.6 A
	Ionizer =	16.0 A
	Cathode =	5 kV
	Extractor =	20 kV
	Pre-Acc =	65.5 kV
	Injection Energy =	0.0855 MeV
	1st Einzel Lens =	6 kV
	2nd Einzel Lens =	7 kV
	Injector B-field =	-0.32811 [-0.22733] T
Low End	Object X/Y Steerers =	2.1/2.2 mA
	Image X/Y Steerers =	0.52/0.42 mA
	Image Einzel Lens =	38.5 kV
	X/Y Steerers =	10L, 1L, 6U, 15D
Terminal	LE Chains =	23 kV
	HE Chains =	23 kV
	Stripping =	Foil # 9
	Charge State, q =	+4
	Terminal Voltage, $V_t$ =	5.950 [3.889] MV
	Control =	Varian GVM
	Corona Current =	40 $\mu\text{A}$
	Points =	8 inches
	HE Quad A/B =	291/292
High End	X/Y Steerers =	0L, 0R, 16D, 7D
	Analyzing B-field =	-0.54813 T
	Trans Quad A/B =	317/335
	BL Quad A/B =	177/162
	Switching B-field =	-0.36670 T
	Electrostatic Analyzer, ESA =	67.97 [51.10] kV
	Injector FC Current =	[8.47] nA
	Image FC Current =	[13.53] nA
	Detector FC Current =	[13.53] nA
Final Transmission	Transmission, $\eta$ =	[39.94] %

standard above the background. The results are given in Table 10.13. One of the biggest differences in this case was the extremely high counting rates exhibited by the pure Ti target which was used to perform the tests. In the last run the background rate for the graphite was around 130 cps = 7800 cpm with the attenuator out. This time it ran at 6084 with the attenuator in! The attenuation factor is between 20 to

Table 10.12: Counting rates of the different surfaces tested at the start of Run Be4. This time all the rates are reported in counts per minute (cpm) instead of counts per second (cps).

Surface Target	Counting Rate [cpm]
Graphite	$1.3 \times 10^5$
99% Pure Ti	$2.4 \times 10^5$
99.99% Pure Ag	$6.6 \times 10^7$
Ti+TiO <sub>2</sub>	$3.2 \times 10^6$

Table 10.13: Counting rates on the different samples at a range of source pressures. All measurements listed here were performed on the 99% pure Ti surface. This time the Table entries are the corresponding counting rates in cpm measured by the computer with mode 5.

Sample	Pressure [Torr]			
	vac = $8 \times 10^{-7}$	$1.5 \times 10^{-6}$	$2.5 \times 10^{-6}$	$4.7 \times 10^{-6}$
He Blank	$2.70 \times 10^5$	$2.22 \times 10^5$	$2.19 \times 10^5$	$1.67 \times 10^5$
Standard S5, 4.8 ppm	$2.75 \times 10^5$	$2.29 \times 10^5$	$1.96 \times 10^5$	$1.62 \times 10^5$
Standard S8, 74 ppm	$2.19 \times 10^5$	$2.29 \times 10^5$	$2.09 \times 10^5$	$1.56 \times 10^5$

22 which means that the contamination coming from the samples is nearly 20 times worse. If this were true than we would expect the machine sensitivity to also decrease by a factor of 20 and the 14.6 ppm from the last run turns into 292 ppm! This time we also chose to use Ti to perform the tests on which had a contamination that was worse than the graphite. If this estimation of 292 ppm is correct then we would not expect to see the 74 ppm standard.

As a result, we learned an extremely important lesson from this run: The surface contamination is one of the major contributors of a high background. This led us to start our search for the best surface<sup>1</sup>. We were able to get started on the surface

<sup>1</sup>We even discussed the possible use of palladium which is supposed to have an amazing affinity for attracting gases (and was at the heart of the cold fusion fiasco in the 1980s).

Table 10.14: Surface scans performed at the end of Run Be4. These scans were prompted by high Be contamination in Ti surfaces which prevented us from observing the 74 ppm standard above background. These tests were continued in the following run as we searched for an appropriate sputter surface.

Surface	Avg. Counting Rate [cpm]	Run Time [min]
Ag+TiO <sub>2</sub>	59550	5
Au	1468	5
Al #1	$8.14 \times 10^5$	< 1
Al #2	60505	5
C	$1.3 \times 10^5$	5
Cu #1	5544	5
Cu #2	3328	5
Cu #3	5813	5
Cu #4	6543	5
Ionizer Casing #1	$1.76 \times 10^6$	< 1
Ionizer Casing #2	$2.2 \times 10^6$	< 1
Ionizer Casing #3	$7.92 \times 10^5$	< 1
Sc <sub>2</sub> O <sub>3</sub>	0.2	5
Stainless Steel #1	732.4	10
Stainless Steel #2	6547	5
Ti	$2.4 \times 10^5$	5
TiO <sub>2</sub> #1	2.8	5
TiO <sub>2</sub> #2	72701	5

search but had to abandon it to create a large catalog of surfaces to test. We did get a few scanned before we had to turn the machine back over to PRIME Lab. The results from this initial scan are provided in Table 10.14.

As is evident from the table several surfaces were tested all yielding high Be contaminations. However, we notice the reduced contamination of the oxides as opposed to the pure surfaces. However, we notice that TiO<sub>2</sub> #2 has an uncharacteristically

high contamination and was created following the creation of the Ti+TiO<sub>2</sub> mixture of Table 10.12. In fact, following the creation of the mixture the TiO<sub>2</sub> vial suddenly began giving anomalously high counting rates which suggests to us that it was somehow contaminated during the mixture procedure. Unfortunately this was our only supply of TiO<sub>2</sub>. We also proceeded to check the contamination in parts of the source which were not replaced when the new Be-free source was introduced. We took several shavings from different parts of the ionizer each of which produced extremely high Be contamination. The ionizer was run once before in PO# 3830319.

Of course more work needed to be performed on the possible surfaces and as a result we needed time to create the spread of different surfaces to check. Thus we ended Run Be4 with prospects of a quick return to the tandem once our surface samples had been prepared. In the interim we raided the green cabinets just outside the tank room which housed the collection of chemical substances left over from the nuclear physics days.

#### **10.6 Run Be5, Oct 1997: Surface Tests**

As noted in the summary of Run Be4, PRIME Lab gave us time to create a catalog of surfaces to test which would help us to choose a surface with low Be contamination and which would permit us to see the low ppm standard above that background. The tune was again performed as usual with carbon as a guide tune with parameters shifted to the Be settings and the final results are given in Table 10.15.

The main objective of this run was to solidify a surface on which to do our future runs and as a result we scanned over 50 different surfaces. These surfaces can be broken down into two general categories, elemental and oxide surfaces. The elemental surfaces are summarized in Table 10.16.

The elemental surfaces displayed a wide range of Be counting rates from I with 0 cps to Zr with  $1.54 \times 10^5$  cps. However the average contamination was on the order of 22491 cps. Thus once we determine the machine calibration to concentration we could transform this rate into a residual Be concentration and could give estimates of Be as a trace element in all metals.

Table 10.15:  $^9\text{Be}$  Tandem parameter settings for Run Be5, GY. Most settings remained the same as for  $^{12}\text{C}$ , those which did change in the transition from C to Be are provided with the C values in brackets, for example  $V_t = V_t(\text{Be}) [V_t(\text{C})]$ . Use Figure 1.1 to locate the different elements.

Stage	Setting	Value
Ion Source	Oven =	0.6 A
	Ionizer =	16.0 A
	Cathode =	5 kV
	Extractor =	20 kV
	Pre-Acc =	66 kV
	Injection Energy =	0.086 MeV
	1st Einzel Lens =	6 kV
	2nd Einzel Lens =	6 kV
Low End	Injector B-field =	-0.32811 [-0.22733] T
	Object X/Y Steerers =	0.1/0.2 mA
	Image X/Y Steerers =	0.5/0.42 mA
	Image Einzel Lens =	39.0 kV
	LE Einzel Lens =	29.5 kV
Terminal	X/Y Steerers =	15L, 9D, 0, 0
	LE Chains =	18 kV
	HE Chains =	18 kV
	Stripping =	Foil # 21
	Charge State, q =	+4
	Terminal Voltage, $V_t$ =	5.880 [3.841] MV
	Control =	Varian GVM
	Corona Current =	40 $\mu\text{A}$
	Points =	8 inches
	HE Quad A/B =	28/29.5 mA
High End	X/Y Steerers =	0, 29D, 0, 11U
	Analyzing B-field =	-.54813 T
	Trans Quad A/B =	340/358
	Switching B-field =	-0.36690 T
	BL Quad A/B =	220/205
	Electrostatic Analyzer, ESA =	67.81 [51.10] kV
Final Transmission	Injector FC Current =	[37] nA
	Image FC Current =	[52] nA
	Detector FC Current =	[52] nA
	Transmission, $\eta$ =	[35.1] %

Since the actual surface of interest was an oxide and naturally we also ran tests on them. The oxides are necessary to provide the oxygen required to create BeO in the ion source. This is one of the causes for the decrease in the rates with run time as observed in Runs Be2, Be3, and Be4. A summary of the surfaces scanned is given in Table 10.17.

Table 10.16: Elemental surfaces scanned during Run Be5. Each surface possessed a different amount of Be contamination.

Surface	Description	Counting Rate [cps]
Ag	Silver Sponge, 99.99% Pure	35200
Bi	Metallic Shards	514
Bi	Bismuth Clumps, 99.999% Pure	11000
Bi	Bismuth Merck chunks, 99.5-100% Pure	300
Ce	Cerium, green powder	11946
Co	Cobalt, gray powder, very pure	5911
Cu	Copper Cathode	864.5
Cu	Purified Cu metal	1228
Cu	Purified Cu metal	390
Gd	Gadolinium powder, 99.9% Pure	5720
Ge	Germanium clumps, 99.99% Pure	1000
Hf	Halfnium powder, reactor grade	1100
I	Iodine crystals in metallic flakes	0
Ni	Nickel powder, 99.99% Pure	3000
Os	Osmium powder, gray	54846
Pt	Platinum powder, gray, 99.99% Pure	16104
Se	Selenium Clumps, 99.99% Pure	100
Si	Silicon, shiny metallic chunks	1172
Th	Thorium powder, 99.99% Pure	1900
Tl	Thallium metal, black chunks with white coating	82500
Yb	Ytterbium, white powder	$1.06 \times 10^5$
Zr	Zirconium, gray/gold powder, 98.5% Pure	$1.54 \times 10^5$
Ba <sub>3</sub> N <sub>2</sub>	Barium nitrate, white crystals	174

Although the average for the oxides is actually higher than the elemental surfaces at  $1.95 \times 10^5$  we have three surfaces which produce minimal counting rates. As mentioned before the TiO<sub>2</sub> was contaminated and the data given in this table is of a sample which was rerun from Run Be2. We may say that the high Be counting

Table 10.17: Oxide surfaces scanned during Run Be5. The desired surface would possess oxygen and would provide the amount necessary to create BeO in the ion source. Otherwise we would need to inject a small quantity of O<sub>2</sub> into each sample container.

Surface	Description	Counting Rate [cps]
Fe <sub>3</sub> O <sub>4</sub>	Shiny, black, brittle chunks	$1.1 \times 10^5$
Sm <sub>2</sub> O <sub>3</sub>	Samarium Oxide powder, pure	1
SnO <sub>2</sub>	Grey powder, 99.99% Pure	2227
TiO <sub>2</sub>	Titanium Dioxide, pure	1
TiO <sub>2</sub> +Ag	95% Ag, 5% TiO <sub>2</sub>	$1.25 \times 10^6$
Yb <sub>2</sub> O <sub>3</sub>	Ytterbium oxide, pure	1

rates in the Fe and Sn molecules are from the contamination of the metal. When we compare the Yb<sub>2</sub>O<sub>3</sub> data in Table 10.17 to the Yb data in Table 10.16 we notice a large discrepancy. This originally led us to suspect an overwhelming oxygen beam was present but as in Run Be3 shifting the injector magnet did not yield this result. In fact, we were unable to tune with O<sub>2</sub> at the beginning of Be4 due to insufficient beam currents. One possible explanation for this effect is that in the Be contamination in the Yb may be significantly reduced in the chemistry preparation procedures which create the high quality Yb<sub>2</sub>O<sub>3</sub>. Whatever the cause for this result, the answer is clear: The oxide does not possess the high Be contamination of the elemental substance. The true test of how this effects our results is to run the different samples and see if a noticeable rise in the counting rate is observed.

The Helium blank and the 4.8 ppm standard were then run against each other for the Cu metal, the Yb<sub>2</sub>O<sub>3</sub> and Sm<sub>2</sub>O<sub>3</sub> surfaces. The results of this run suggests that the 4.8 ppm standard is clearly visible above background and suggests that we have indeed found two surfaces with low enough Be contamination to notice the standard above background. The data from these tests are given in Table 10.18.

Here we see the striking results of this study. The copper sample which possesses a high Be counting rate does not show the presence of the 4.8 ppm standard while the

Table 10.18: Final evaluation of the impact of the new source and the new chosen surfaces. From this table the copper surface (with higher Be contamination) does not show evidence for detection of the 4.8 ppm standard while both oxide surfaces do. From this we may calculate the new background concentration (see Equation (10.6)). These tests were performed at a source pressure of  $2.0 \times 10^{-6}$  Torr.

Surface	Sample	Counting Rate [cpm]
Cu	Blank, He	27943.7
	Standard S5, 4.8 ppm	27196.3
Sm <sub>2</sub> O <sub>3</sub>	Blank, He	211.6
	Standard S5, 4.8 ppm	1558.9
Yb <sub>2</sub> O <sub>3</sub>	Blank, He	52.1
	Standard S5, 4.8 ppm	506.0

oxide surfaces certainly do. As a result we may calculate the respective background Be concentration for each of the oxide surfaces and evaluate the impact of the new source and different surface choice.

Since we only have data from the lowest concentration standard we proceed with the calculation assuming the line calibration is linear and includes the origin. This result is still an approximation since only one standard is being used but is a better method than that calculated at the conclusion of Run Be3. Improvement of this method will have to wait until Run Be7 when more low concentration standards were created. Using this method we simply scale the 4.8 ppm concentration with the counting rates. As a result the following Be background concentrations were determined for each surface:

$$\begin{aligned}
 \text{Sm}_2\text{O}_3 : \frac{[Be]}{[He]_{bgd}} &= \left( \frac{4.8 \text{ ppm}}{1558.9 \text{ cpm}} \right) 211.6 \text{ cpm} \\
 &= 0.65 \text{ ppm} \\
 \text{Yb}_2\text{O}_3 : \frac{[Be]}{[He]_{bgd}} &= \left( \frac{4.8 \text{ ppm}}{506.0 \text{ cpm}} \right) 52.1 \text{ cpm} \\
 &= 0.49 \text{ ppm}
 \end{aligned} \tag{10.6}$$

Here we see that the two are very close in their amount of Be contamination and are probably well within the errors associated with our initial assumption. Thus we decided to retain both surfaces for use in the later runs. The particular surface of use was then determined at the beginning of the run based on which gave the slightly lower background concentration.

These results also suggest that the background has been lowered by nearly a factor of 30. Thus replacing the old ion source which was contaminated with Be by the new Be-free one we effectively have gained an order of magnitude in the possible limit set on the existence of Be' in our samples. This is a little less than a factor of 2 lower than the earlier Fischbach, Kirsten, and Schaeffer [16] result quoted at 0.9 ppm.

### 10.7 Run Be6, Feb 1998: First Run with the New Cathode

The design of this run was to introduce a new method of introducing the gas into the ion source. Now that we have a good concept of how the process of setting a limit on (or detecting) Be' is undertaken we realize that we may make two changes to the current system to increase the sensitivity. First we could lower the background still further or second we could increase the slope of the calibration line causing it to intersect the background line at a lower concentration (see Figure 10.4). During the first several runs we were accomplishing the first task and were minimizing the background by introducing the new Be-free ion source and by choosing surfaces with low Be contamination.

Now it was time to work on increasing the slope of the resulting calibration line. The slope of the calibration line is an indication of the machine's efficiency, a higher slope means that we get more counts for a given concentration. Thus by increasing the efficiency of the machine in converting the Be standards into counts we increase the slope and decrease the background limit. The first step in accomplishing this task was to design a new cathode which would introduce the gas directly adjacent to the surface instead of on the opposite end of the source. This increases the number of Be molecules that exist in the region near the surface in increases the ion source efficiency of converting the Be atoms into  $\text{BeO}^-$  ions.

However, before we could test our idea we had to tune up the machine using the now standard procedure of starting with carbon. As usual the results from the tune are provided in Table 10.19.

The newly designed cathode (see Figure 10.5) allowed us to bleed the gas through

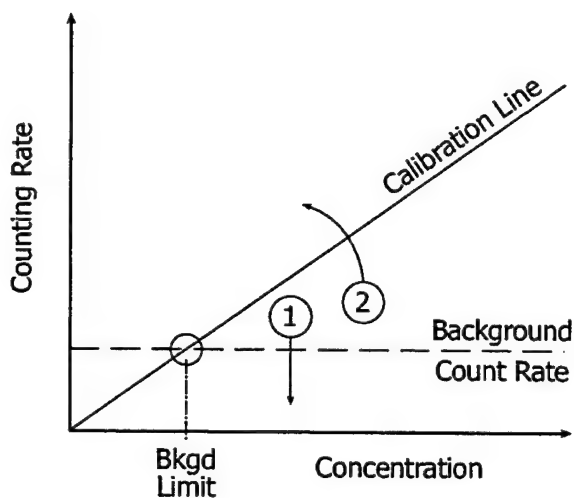


Figure 10.4: We may further reduce the minimum detection limit (push the Bkgd Limit to the left) with two different methods: (1) we could lower the background counting rate or (2) we could increase the slope of the calibration line while still constraining it to go through the origin. In either case the intersection point between the calibration line and the background counting rate would decrease and would lower the limit we set (or allow us to discover) Be'.

Table 10.19:  $^9\text{Be}$  Tandem parameter settings for Run Be6, HJ. Most settings remained the same as for  $^{12}\text{C}$ , those which did change in the transition from C to Be are provided with the C values in brackets, for example  $V_t = V_t(\text{Be}) [V_t(\text{C})]$ . Use Figure 1.1 to locate the different elements.

Stage	Setting	Value
Ion Source	Oven =	0.65 A
	Ionizer =	11.0 A
	Cathode =	5 kV
	Extractor =	20 kV
	Pre-Acc =	66 kV
	Injection Energy =	0.086 MeV
	1st Einzel Lens =	6 kV
	2nd Einzel Lens =	6 kV
	Injector B-field =	-0.32811 [-0.22733] T
	Object X/Y Steerers =	0.08/0.18 mA
Low End	Image X/Y Steerers =	0.48/0.38 mA
	Injector Einzel Lens =	39.0 kV
	LE Einzel Lens =	31.8 kV
	X/Y Steerers =	17L, 9D, 0, 0
Terminal	LE Chains =	18 kV
	HE Chains =	18 kV
	Stripping =	Foil # 67
	Charge State, q =	+4
High End	Terminal Voltage, $V_t$ =	5.947 [3.892] MV
	Control =	Varian GVM
	Corona Current =	40 $\mu\text{A}$
	Points =	9.1 inches
	HE ES Quad A/B =	27.4/30.40 mA
	X/Y Steerers =	21R, 50D, 0, 0
	Analyzing B-field =	-0.54813 T
	Trans Quad A/B =	330/345
	Switching B-field =	-0.36730 T
	BL Quad A/B =	195/189
Final Transmission	Electrostatic Analyzer, ESA =	68.08 [51.28] kV
	Injector FC Current =	[35] nA
	Image FC Current =	[40] nA
	Detector FC Current =	[40] nA
	Transmission, $\eta$ =	[28.6] %

a specially designed flange which had an aluminum tube welded into it. This flange replaced the alignment window located just below the sample wheel shaft. We then ran the tygon tubing from the flange to the aft end of the screw holding the cathode to the wheel. Because of the tygon tubing we were unable to rotate the wheel more than the one time needed in the change wheel procedure. However since we have already

derived a method for choosing the surface we only needed the one sample position. The center of the screw which holds the cathode to the wheel had a hollow center which permitted the gas to flow through the screw (see Figure 10.5). The back end of the cathode was then countersunk so that the gas could flow out of two adjacent holes in the sides of the screw to the space between the cathode and the wheel. Finally the cathode then had 6 holes drilled around its perimeter which connected the back region between the wheel and cathode to the front of the cathode where the surface had been applied.

This addition effectively moved the gas introduction location from nearly 6 inches away from the surface to directly onto it thereby increasing the probability of BeO formation mentioned above. A picture of the ion source with the specially designed cathode is provided in Figure 10.6. This picture shows the flow of the incoming gas which arrives via the thick tubing inbound from the lower right corner of the picture. It then enters the flange on the lower side of the sample wheel shaft housing where it is sent through the Tygon tubing loosely wrapped around the sample wheel shaft. It then connects onto the back of the specially designed screw which holds the cathode to the wheel as discussed above. The rest of the gas flow can be traced using Figure 10.5.

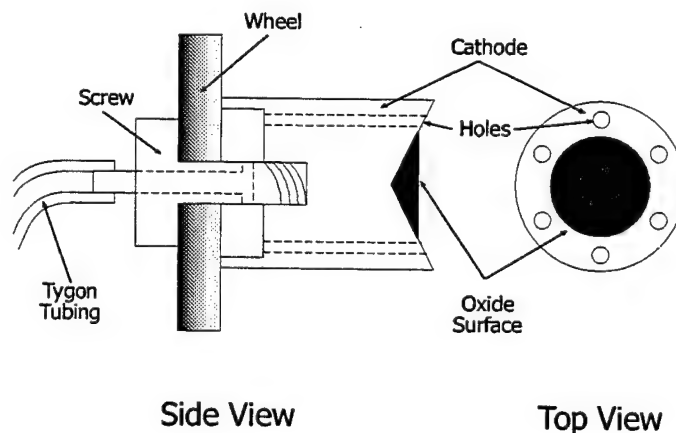


Figure 10.5: Side and top views of the cathode with 6 holes drilled around the perimeter of the oxide surface. The gas flowed from the coolant port in the sample wheel shaft to the aft end of the specially designed screw.

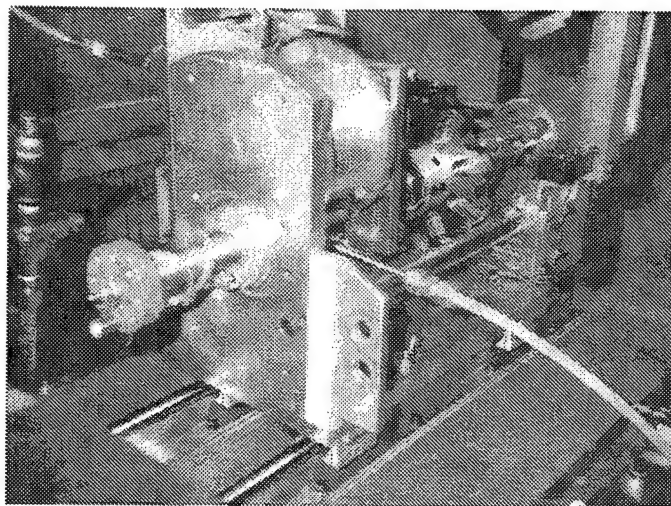


Figure 10.6: A picture of the sample changer and gas flow mechanisms leading to the specially designed cathode. The tube entering from the lower right is the inbound sample gas which then flows through the flange and through the tygon tubing wrapped around the sample wheel shaft before entering the cathode.

The initial check for which surface to use suggested that  $\text{Sm}_2\text{O}_3$  was the optimal choice for this particular run. The resulting data for the  $\text{Sm}_2\text{O}_3$  is given in Table 10.20. This time we compared the  $\text{Sm}_2\text{O}_3$  to the  $\text{TiO}_2$  since the  $\text{Yb}_2\text{O}_3$  surface did not seem to register the standard as well.

Table 10.20: The final data for leading to the selection of the  $\text{Sm}_2\text{O}_3$  surface. These tests were performed at a source pressure of  $2.4 \times 10^{-6}$  Torr. As before these yield a background limit of 0.016 ppm (or 16 ppb) for the  $\text{Sm}_2\text{O}_3$  surface.

Surface	Sample	Counting Rate [cpm]
$\text{Sm}_2\text{O}_3$ :	Blank, He	13.2
	Standard S5, 4.8 ppm	4024.3
$\text{TiO}_2$ :	Blank, He	3189.5
	Standard S5, 4.8 ppm	7668.7

From this data we may calculate the background limit based on the usual assumption that the calibration is linear and that it goes through the origin (this assumption

is still our biggest and is causing rather generous concentrations, as we will see in the last two runs). This data then suggests that with the old system the source background concentration is

$$\begin{aligned} \text{Sm}_2\text{O}_3 : \frac{[\text{Be}]}{[\text{He}]_{\text{bkgd}}} &= \left( \frac{4.8 \text{ ppm}}{4024.3 \text{ cpm}} \right) 13.2 \text{ cpm} \\ &= 0.0157 \text{ ppm} \\ &= 15.7 \text{ ppb} \end{aligned} \tag{10.7}$$

$$\begin{aligned} \text{TiO}_2 : \frac{[\text{Be}]}{[\text{He}]_{\text{bkgd}}} &= \left( \frac{4.8 \text{ ppm}}{7668.7 \text{ cpm}} \right) 3189.5 \text{ cpm} \\ &= 1.996 \text{ ppm} \end{aligned}$$

Here we may notice that this is a factor of 40 lower than the value calculated at the end of the previous run and is a good indication on how the tune impacts the final result. We also note that the data from Be5 was taken after we had effectively contaminated the source by running all the surfaces in the scan so it makes sense that a clean source would give a lower background.

We then proceeded to hook up the new cathode in order to determine its effects on the counting rate for the standard. We would expect that the He counting rate should not change since there is no Be in the He Blank. The test was performed on the  $\text{Sm}_2\text{O}_3$  surface in order to see find out the new background concentration limit set with the new cathode. The results are provided in Table 10.21.

Thus we see that the background concentration dropped by a factor of 4.4 or a half an order of magnitude. As is probably becoming evident as we progressed through the runs more improvements were made which continue to lower the limit of the calculated background concentration. Of course as mentioned before the absolute values reported are misleading since we make some generous assumptions in their derivations. Nonetheless, the relative magnitudes are what is important, while the ratio of the Standard to Blank grew by 4.4 the background concentration decreased by its inverse 0.23 resulting in a value that is 23% of its original.

Table 10.21: Summary of initial tests of the newly designed cathode. Notice the background concentration is reduced by a factor of 4.4 giving us almost half an order of magnitude.

Cathode	Sample	Average Counting Rate [CPM]
Regular	He Blank	13.2
	Standard, S5 (4.8 ppm)	4024.3
	Background Concentration	15.7 ppb
6 Holes	He Blank	5.225
	Standard, S5 (4.8 ppm)	6968.0
	Background Concentration	3.6 ppb

Just to give a slight hint, the final results set limits of 5.8 ppb so we can see that while the assumption of the calibration line including the origin seems naive it makes the remarkably close prediction of 3.6 ppb. Of course the final number is much more rigorously tested and proven but it is somewhat interesting to note that if we had stopped here we would have been astonishingly close to the "right" answer.

#### 10.8 Run Be7, Oct 1998: First Run with the Gas Manifold

One additional problem still plaguing us was the difficulty of changing from one sample to another. With the desire to add more standards this would prove to be a difficult task and would probably add more uncertainty than help it would give since each time we change the settings by a small amount all the while allowing the surface focus to change. We circumvented this problem with the construction of the gas manifold in the summer of 1998.

The gas manifold (see Figure 10.7) allowed us to run 4 samples at a time without going into the source cage to change them out. The details of the manifold have already been discussed in Chapter 8.5 so we will save some time and just discuss the results. We also introduced 4 new low-concentration standards which helped refine the calibration line and allowed us to remove the assumption that the calibration went through the origin.

We also finally ran the first of the unknown samples namely the gas field, the ore, and atmospheric air. The metal sample had not yet been built and would see its debut in the final run Be8. However, as a result this run was a landmark run because it included all the accelerator upgrades along with almost all the samples (definitely enough to have made good results and a solid paper). However, before we could get to taking the data we had to tune up the machine. As before the tune was performed with graphite before shifting to the Be settings and as usual the final tandem settings are given in Table 10.22.

Since the only real way to test the gas manifold is to use it we exhibited it along with our new standards. These were standards S7 (16.9 ppm), S6 (8.5 ppm), S3 (0.97 ppm), and S1 (0.24 ppm) which we ran along with S5 (4.8 ppm standard) and the first gas field G1, the first ore sample O1, and atmospheric air. We also tried to run standard S10 (0.51 ppm) standard but unfortunately the valve was closed too tightly and sheared shut making the sample inaccessible and destroying one of our specially made sample vials.

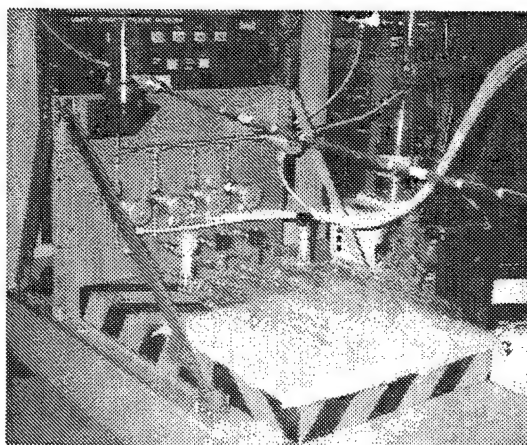
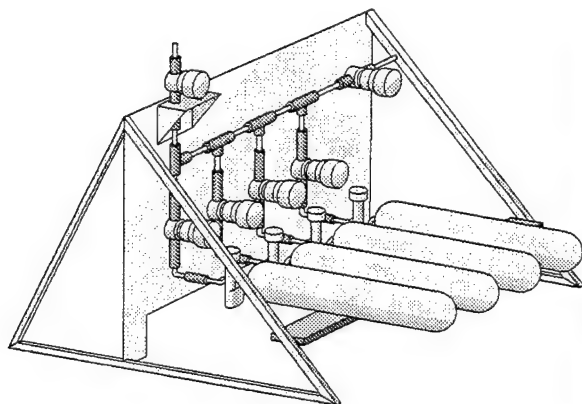


Figure 10.7: Diagram and picture of the gas manifold as it sat on the high voltage table in the ion source. It allowed us to run up to four gas samples at a time and helped reduce the background, monitor source contamination and drift, and greatly reduced run times.

Table 10.22:  $^9\text{Be}$  Tandem parameter settings for Run Be7, HY. Most settings remained the same as for  $^{12}\text{C}$ , those which did change in the transition from C to Be are provided with the C values in brackets, for example  $V_t = V_t(\text{Be}) [V_t(\text{C})]$ . Use Figure 1.1 to locate the different elements.

Stage	Setting	Value
Ion Source	Oven =	0.65 A
	Ionizer =	17.0 A
	Cathode =	5 kV
	Extractor =	20 kV
	Pre-Acc =	66 kV
	Injection Energy =	0.086 MeV
	1st Einzel Lens =	5 kV
	2nd Einzel Lens =	5 kV
	Injector B-field =	-0.32811 [-0.22733] T
	Object X/Y Steerers =	0.0/0.1 mA
Low End	Image X/Y Steerers =	0.48/0.38 mA
	Injector Einzel Lens =	38.0 kV
	X/Y Steerers =	12L, 8D, 0, 0
Terminal	LE Chains =	19 kV
	HE Chains =	19 kV
	Stripping =	Foil # 29
	Charge State, q =	+4
	Terminal Voltage, $V_t$ =	5.945 [3.887] MV
	Control =	Varian GVM
	Corona Current =	38 $\mu\text{A}$
	Points =	9.0 inches
	HE ES Quad A/B =	27.34/30.05 kV
	X/Y Steerers =	14R, 55D, 0, 16U
High End	Analyzing B-field =	-0.54813 T
	Trans Quad A/B =	311.5/330
	Switching B-field =	-0.36710 T
	BL Quad A/B =	200/205
	Electrostatic Analyzer, ESA =	67.98 [51.06] kV
	Injector FC Current =	[58.5] nA
	Image FC Current =	[63] nA
	Detector FC Current =	[60] nA
Final Transmission	Transmission, $\eta$ =	[26.9] %

Throughout the run we also interspersed the He blank sample so that we could continue to go back to it in order to check the background at all times. This turned out to be a very good idea and allowed us to learn an important lesson about cross-contamination. The first time we ran the data we started with the highest

concentration standard (S7) and worked our way down as is shown in Table 10.23 which contains the results from this first attempt.

Table 10.23: First real data taken of the line calibration along with the first of the unknown samples.  $\text{Sm}_2\text{O}_3$  was the chosen surface and the data was taken at the standard  $2.5 \times 10^{-6}$  Torr. The horizontal lines indicate gas manifold exchanges of a new set of sample tubes (since it can only hold 4 samples at a time). Notice the upward drift of the blank counting rate. This occurred because of running the standards first and initially introducing contamination into the source. This is not quite the actual run order since we frequently monitored the blank while running the unknowns. The actual run order is given in Table 10.26.

Sample	Counting Rate [CPM]
Standard, S5 (4.84 ppm)	$143.58 \pm 10.10$
Standard, S6 (8.47 ppm)	$253.58 \pm 8.74$
Standard, S7 (16.94 ppm)	$468.45 \pm 19.30$
He Blank	$17.18 \pm 0.95$
He Blank	$29.4 \pm 1.82$
Standard, S3 (0.97 ppm)	$54.95 \pm 2.22$
Standard, S1 (0.24 ppm)	$60.0 \pm 1.36$
He Blank	$48.37 \pm 1.86$
Gas Field, G1	$59.05 \pm 1.33$
Beryl Ore, O1	$45.04 \pm 1.10$
Atmosphere, A1	$49.05 \pm 1.22$

Since this is the first time that errors have been introduced to the reported measurements we will quickly discuss how they were derived. We begin by calculating the variance  $\sigma^2$  which results from measurement error. In terms of  $N$  unbiased independent measurements  $y_i$  the average and variance are calculated by the following

$$\hat{\mu} = \frac{1}{N} \sum_{i=1}^N y_i \quad (10.8)$$

$$\hat{\sigma}^2 = \frac{1}{N-1} \sum_{i=1}^N (y_i - \hat{\mu})^2 \quad (10.9)$$

which are unbiased. The resulting error is finally given by the standard deviation of the mean  $\sigma$  divided by the square root of the number of data points or  $\sigma/N$ . This method is quite standard and is discussed thoroughly in many statistics books [38] while this particular notation is that used by the Particle Data Group [1].

As will be evident shortly the sample order makes a large impact on the final result. This is because we unknowingly contaminated the source right off with our 17 ppm standard (S7) which caused us to have a higher than usual background. Notice that the background started at 17 cpm and ended at 48. As a result, we placed the wheel in an oven at 525 K for one hour to try to outgas the cathode and burn off any residual Be. We then retook the unknown data but since we also had the blank data from both days we could introduce the appropriate scaling factor to use the data obtained on the previous run. The results from the second try with after outgassing lowered the background considerably as is evident from Table 10.24.

Table 10.24: Second try with the lower background counting rate after outgassing the wheel and cathode in an oven at 525 K. Again  $\text{Sm}_2\text{O}_3$  was the chosen surface and the data was taken at the standard  $2.5 \times 10^{-6}$  Torr. As in Table 10.23 this does not reflect the run order since the He Blank was checked between each sample. The actual run order can be found in Table 10.26.

Sample	Counting Rate [CPM]
He Blank	$0.2563 \pm 0.0171$
Gas Field, G1	$0.5250 \pm 0.0232$
Beryl Ore, O1	$0.0625 \pm 0.0109$
Atmosphere, A1	$0.0938 \pm 0.0130$

First notice the drastic reduction of the background from 48 cpm to 0.26 cpm. This implies that running the standards in inverse order increases the background by a factor of 185 or nearly two orders of magnitude. This is an incredibly large effect that is only evident since the background has been reduced to such a low level.

We also point out another curious effect. The gas field sample produced a counting rate that was slightly higher than background both times. With the high background G1 was only 23 % higher with a value nearly identical to the 0.24 ppm standard. However, in the case where the background had been reduced by the outgassing, G1 is over twice as large in magnitude. This is precisely the behavior we would expect if sample G1 was exhibiting evidence of possible Be'. Unfortunately this deviation was just small enough to not be noticed until the analysis performed after the run was complete.

The final calibration plot derived from this data is given in Figure 10.8. While the points give the average values of the data the line was fit through the raw data whose spread was determined by the standard deviation of the mean, which is the standard deviation divided by the square root of the number of data points. The raw data used in this line calibration is given in Table 10.26. The previous tables (Tables 10.23 and 10.24) can be thought of as summaries of the average values represented in this table.

We then used the program PAW++ to perform the necessary curve fit. While at first glance this would seem to be trivial it is more complicated than the simple least squares fit we are all used to. Because the error bars exist in both the x and y directions we must use an iterative method to solve the equations. As a quick outline of the process PAW uses lets assume the more general form for the equation to fit. If we wish to fit data points  $(x_i, \sigma_{xi}; y_i, \sigma_{yi})$  to the function  $y = f(x; \alpha)$  where  $x_i$  and  $y_i$  are independent Gaussian variates with parameters  $\alpha$  and  $x_{0i}$  the Likelihood function is

$$L = \prod_i \left( \frac{e^{-\left[\frac{(x_i - x_{0i})^2}{2\sigma_{xi}^2}\right]}}{\sqrt{2\pi}\sigma_{xi}} \right) \left( \frac{e^{-\left[\frac{(y_i - f(x_i; \alpha))^2}{2\sigma_{yi}^2}\right]}}{\sqrt{2\pi}\sigma_{yi}} \right) \quad (10.10)$$

$$w = \ln L = - \sum_i \left[ \frac{(x_i - x_{0i})^2}{2\sigma_{xi}^2} + \frac{(y_i - f(x_i; \alpha))^2}{2\sigma_{yi}^2} \right] + \text{constants}$$

Extremizing, we have:

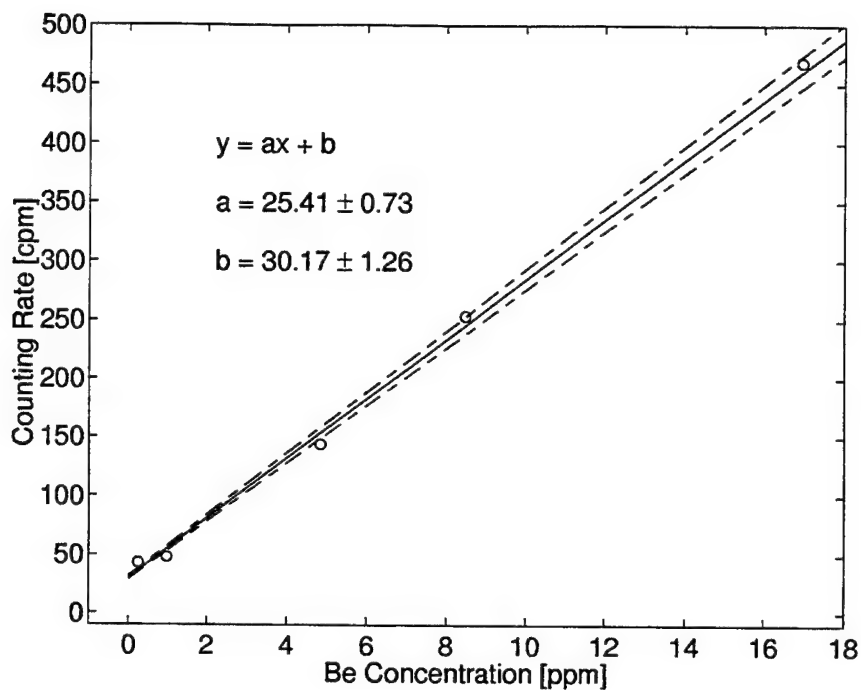


Figure 10.8: Calibration plot derived from the five standards analyzed during Run Be7. The resulting output from the line fit through the data points (with the errors included) provided the equation given on the plot and also in Equation (10.13). This then permitted the determination of the background for the various unknown samples.

$$\frac{dw}{dx_{0i}} = \frac{x_i - x_{0i}}{\sigma_{xi}^2} + \frac{y_i - f(x_i; \alpha)}{\sigma_{yi}^2} = 0 \quad (10.11)$$

which yields an expression  $x_{0i} = x_{0i}(x_i, \sigma_{xi}; y_i, \sigma_{yi}; \alpha)$  and

$$\frac{dw}{d\alpha_j} = \sum_i \left[ \frac{y_i - f(x_i; \alpha)}{\sigma_{yi}^2} \right] \left[ \frac{df(x_{0i}; \alpha)}{d\alpha_j} \right] = 0 \quad (10.12)$$

which results in the usual least-squares equations but containing the parameters  $x_{0i}$  instead of the usual  $x_i$ . These equations can then be solved iteratively:

1. Find  $\alpha = \alpha(x_i, y_i, \sigma_{yi})$  using Equation (10.11).
2. Find  $x_{0i} = x_{0i}(x_i, \sigma_{xi}, y_i, \sigma_{yi}, \alpha)$  using Equation (10.12).
3. Repeat until convergence is obtained.

In our case the PAW did all this work for us and yielded an output equation of

$$y = (25.41 \pm 0.73)x + (30.17 \pm 1.26) \quad (10.13)$$

Notice first off that the calibration is remarkably linear as we expected. This also explains why our initial assumptions in previous runs turned up results which were remarkably close to their actual values even though we were using only one measured data point to create the approximate calibration. With this calibration determined, we were able to calculate the concentration of the background counting rates for the different samples by setting their lower  $1\sigma$  counting rates equal to  $y$  in Equation (10.13) above. As an example Figure 10.9 shows this calculation performed on the He blank. From the plot we see that the blank represents a concentration limit of 19.85 ppb. The results for the different unknown samples is given in Table 10.25.

Table 10.25: Final concentration calculations for the unknown samples based on the data taken before and after we cooked the wheel in the oven to burn off the Be contamination. The data afterward was scaled based on the change of the He background.

Sample	$\frac{[\text{Be}']}{[\text{He}]}$ Concentration	
	Before Oven [ppm]	After Oven [ppb]
He Blank	$0.788 \pm 0.030$	$4.24 \pm 0.16$
Gas Field, G1	$1.221 \pm 0.028$	$6.56 \pm 0.15$
Beryl Ore, O1	$0.653 \pm 0.016$	$3.51 \pm 0.09$
Atmosphere, A1	$0.816 \pm 0.020$	$4.39 \pm 0.11$

In this table we notice that the average value for the gas field sample actually lies outside the  $1\sigma$  errors for the background. This was definitely worth investigating further and was one of the major goals of the final run. We can see that the background is now to the ppb range all that is needed is to refine the calibration line and armed with our new knowledge of the cross-contamination effects we may adjust the sequence so that the highest concentration standards are run last.

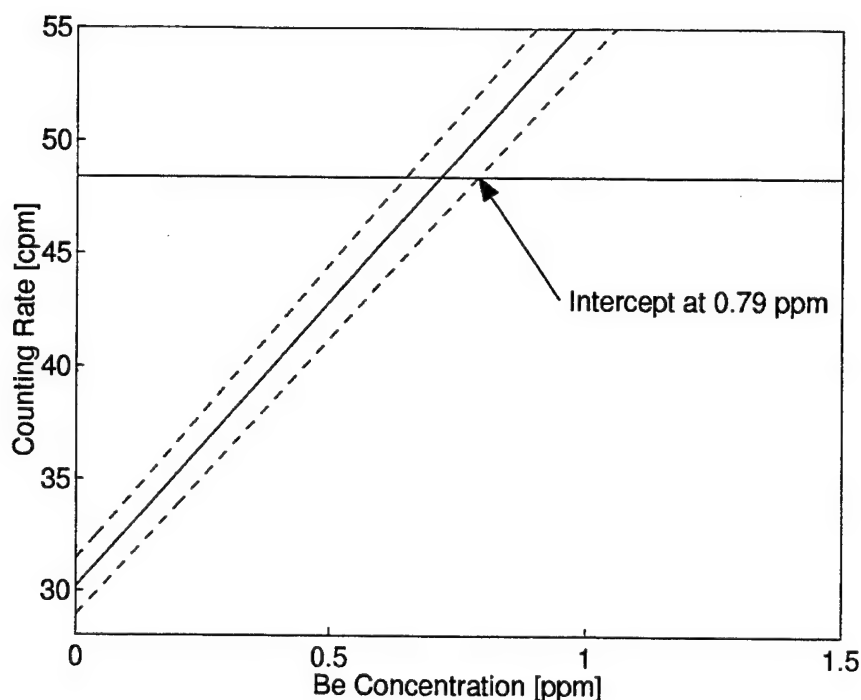


Figure 10.9: A zoomed in version of Figure 10.8 in which we note the intersection of the background counting rate with the lower  $1\sigma$  limit of the calibration line. Although the data shown here is that of the He blank, the concentration limits of each unknown sample were calculated with this same method. Those results are displayed in Table 10.25.

Finally, since this is the first real set of data that was taken we have included the raw data in Table 10.26. This is primarily done in case future analysis is warranted. From this table we may observe why each sample has the errors it does since we did not run a standard number of times on each sample. For instance, the blank was run far more times which drives its error down.

All in all each improvement made along the way has had a significant impact on the final result. Recall that the rough calculations following Run Be3 of 14.6 ppm have been reduced to around 6 ppb or over 3 orders of magnitude better.

Table 10.26: Raw data taken during Run Be7. The actual data was saved in ursula under the run letters HY and as a result we have included the cycle numbers here in order to retrieve the data if necessary. The surface was  $\text{Sm}_2\text{O}_3$  and the source pressure was held constant at  $2.5 \times 10^{-6}$ . Each data point was from a 1.9 minute run, which explains the lowest nonzero value of 0.5 (corresponding to 1 count in 1.9 minutes). The horizontal lines indicate gas manifold exchanges of a new set of sample tubes (since it can only hold 4 samples at a time).

Sample	Counting Rate Before Oven [cpm]							
	Cycle	Rate	Cycle	Rate	Cycle	Rate	Cycle	Rate
Standard S5	31	130.1	32	128.4	33	143.7	34	172.1
Standard S6	36	264.4	37	253.9	38	228.8	39	267.2
Standard S7	41	433.1	42	453.2	43	464.5	44	523.0
He Blank	46	15.0	47	16.8	48	17.3	49	19.6
He Blank	52	24.3	53	29.2	54	31.7	55	32.3
Standard S3	58	48.5	59	57.9	60	55.5	61	57.9
Standard S1	65	58.3	66	65.9	67	61.1	68	54.7
He Blank	70	40.2	71	37.2	72	50.4	73	42.9
Gas Field G1	75	58.3	76	60.2	77	53.3	78	64.4
He Blank	80	50.0	81	43.4	82	50.9	83	46.1
Beryl Ore O1	85	57.3	86	54.6	87	45.4	88	43.0
He Blank	90	57.8	91	48.6	92	56.0	93	55.3
Beryl Ore O1	96	30.9	97	45.4	98	39.7	99	44.0
Atmosphere A1	101	52.3	102	48.1	103	43.5	104	52.3
After Oven								
He Blank	115	0.0	116	0.5	117	0.5	118	0.5
	119	0.5	120	2.8	121	0.9	122	0.5
Gas Field G1	124	0.9	125	0.5	126	0.9	127	0.9
	128	0.5	129	0.9	130	0.0	131	0.9
	132	0.5	133	0.5	134	0.5	135	0.9
	136	0.0	137	0.5	138	0.0	139	0.0
Atmosphere A2	141	0.0	142	0.5	143	0.0	144	0.0
	145	0.0	146	0.5	147	0.0	148	0.0
	149	0.0	150	0.0	151	0.0	152	0.0
	153	0.0	154	0.5	155	0.0	156	0.0
Beryl Ore O1	159	0.0	160	0.0	161	0.0	162	0.0
	163	0.0	164	0.0	165	0.0	166	0.0
	167	0.0	168	0.0	169	0.0	170	0.5
	171	0.5	172	0.0	173	0.0	174	0.0
He Blank	176	0.0	177	0.0	178	0.0	179	0.0
	180	0.0	181	0.0	182	0.0	183	0.0
	184	0.5	185	0.0	186	0.5	187	0.0
	188	0.0	189	0.0	190	0.5	191	0.0
	192	0.0	193	0.0	194	0.0	195	0.0
	196	0.0	197	0.0	198	0.0	199	0.5

### 10.9 Run Be8, Jun 1999: Final Results

Thus the seven preceding runs all culminated in Run Be8 during which we had incorporated all of the improvements and were ready to refine the data taken in Run Be7. Run Be7 was a nice preparation run and allowed us to work out small details of the run procedure along with giving us the indication that the gas field sample may be producing interesting results. Again the tune was first performed with carbon and the machine settings for the final run, whose data was recorded with run letters IM, is given in Table 10.27. Notice that this tune has given the highest transmission efficiency ever which also helps to slightly boost our final results.

This time we ran with  $\text{Yb}_2\text{O}_3$  as the surface target and held a constant source pressure of  $2.5 \times 10^{-6}$ . As usual the standard samples were then used to calibrate the sensitivity of the AMS to Be by carrying out a least-squares fit to the data in Table 10.28 (see Fig. 10.10). The estimated error in the concentrations of the standards and the standard deviation of the mean for the corresponding counting rates were used in the iterative procedure discussed in Run Be7 to determine a best-fit line relating the counting rates and concentrations. Again the Be counting rate in the detector varied linearly with the concentration, and as evident from the equation on the figure possessed nearly the same qualities (see Figure 10.10). This equation, which was again derived with PAW++ was found to be

$$y = (24.70 \pm 0.71)x + (0.12 \pm 0.08) \quad (10.14)$$

This time the data was taken in order of increasing Be concentration in order to minimize the contamination effects. As a monitor of this contamination the blank was interspersed throughout the run to monitor its effects and allow us to correct for the upward drift of the background.

The data and counting rates for the unknown samples is given in Table 10.29. We also added another metal sample, M2, which was a Be/Al alloy we tried to melt in an oven. The alloy was provided by Jim Marder of Brush Wellmann but unfortunately, we do not know to what extent the sample melted, if at all. Data was taken on it

Table 10.27:  $^9\text{Be}$  Tandem parameter settings for Run Be8, IM. Most settings remained the same as for  $^{12}\text{C}$ , those which did change in the transition from C to Be are provided with the C values in brackets, for example  $V_t = V_t(\text{Be}) [V_t(\text{C})]$ . Use Figure 1.1 to locate the different elements.

Stage	Setting	Value
Ion Source	Oven =	0.65 A
	Ionizer =	17.0 A
	Cathode =	5 kV
	Extractor =	20 kV
	Pre-Acc =	66.5 kV
	Injection Energy =	0.0865 MeV
	1st Einzel Lens =	5 kV
	2nd Einzel Lens =	5 kV
	Injector B-field =	-0.32811 [-0.22733] T
	Object X/Y Steerers =	20/140
Low End	Image X/Y Steerers =	0.50/0.50 mA
	Injector Einzel Lens =	38.0 kV
	LE Einzel Lens =	34 kV
	X/Y Steerers =	10L, 6D, 0, 0
Terminal	LE Chains =	12 kV
	HE Chains =	12 kV
	Stripping =	Foil # 30
	Charge State, $q$ =	+4
	Terminal Voltage, $V_t$ =	5.925 [3.885] MV
	Control =	Varian GVM
High End	Corona Current =	35 $\mu\text{A}$
	Points =	8.1 inches
	HE ES Quad A/B =	27.38/24.37 kV
	X/Y Steerers =	23L, 29D, 0, 0
	Analyzing B-field =	-0.56713 T
	Trans Quad A/B =	64/327
	Switching B-field =	-0.36430 T
	BL Quad A/B =	174/192
	Electrostatic Analyzer, ESA =	65.24 [49.08] kV
	Injector FC Current =	[206] nA
Final Transmission	Image FC Current =	[332] nA
	Detector FC Current =	[285] nA
	Transmission, $\eta$ =	[40.29] %

regardless of this fact. From the data below we see that no signal was observed above background.

One extremely puzzling result was that of the gas field. We ran the same sample that indicated a Be concentration from Run Be7 and this time the counting rate was

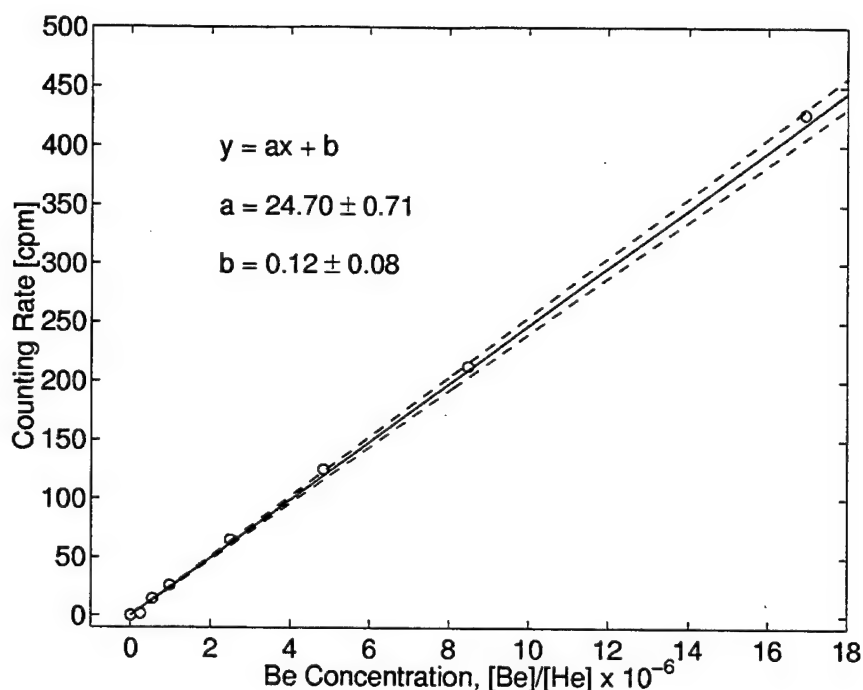


Figure 10.10: Calibration of the AMS for gaseous Be. The open circles represent the experimental data for the blank and the seven Be Standards exhibited in Table I. The solid line is the result of the least-squares fit shown in the figure, where the central value is represented by the solid line, and the  $1\sigma$  errors by the dashed lines.

at background. So the signal which was apparent in G1 during the last run was not indicating a Be signal this run. Still, in preparation for this run we created a second gas field sample, G2, which we ran following G1. To our surprise the newly created gas field sample was showing a very distinctive Be signal.

As with any experiment it was then our task to determine if there was a mistake that was giving us an erroneous Be signal. After checking tandem settings the first check we performed was to see if we had used up the surface and were observing the Be contamination in the copper cathode beneath the now possibly consumed surface. If this were the case then the He blank sample would also indicate this background. Unfortunately this was not the case and the signal was back in fact this time with an even higher counting rate. We now had a discrepancy of data from the two gas field samples. It was postulated that the anomalous Be may possess a lifetime which causes

Table 10.28: Summary of Be counting rates in counts-per-minute (cpm) for standards and blanks. For the blank and each of the seven standards S1-S7, we exhibit the concentration in parts-per-million (ppm), and the corresponding  $1\sigma$  errors.

Sample	Concentration	Counting Rate [cpm]
Blank	$0.00 \pm 0.05$	$0.18 \pm 0.08$
Standard, S1	$0.24 \pm 0.05$	$1.77 \pm 0.14$
Standard, S2	$0.54 \pm 0.05$	$14.56 \pm 0.47$
Standard, S3	$0.97 \pm 0.10$	$26.14 \pm 0.32$
Standard, S4	$2.49 \pm 0.10$	$65.02 \pm 0.47$
Standard, S5	$4.84 \pm 0.10$	$124.91 \pm 0.82$
Standard, S6	$8.47 \pm 0.20$	$212.81 \pm 0.56$
Standard, S7	$16.94 \pm 0.20$	$426.84 \pm 0.56$

it to decay at some given rate. Since G1 showed a signal in Run Be7 which was just barely above the detection limits of the machine, it may be possible that eight months later in Run Be8, the Be' has decayed enough to drop below the detection limits of the machine. In contrast G2, which was created 9 days prior to Run Be8, would possibly show a concentration above background. This was an intriguing notion and in order to test it we would need to make yet another gas field sample. However, this time instead of making up a sample we decided to bring the entire line (like that shown in Figure 9.11) down to the ion source. Thus unlike the figure which has a sample vial, the gas was fed directly into the ion source. Figure 10.11 shows part of this setup on the ion source.

This sample did not show any indication of Be concentration above background which suggested that G2 had somehow become contaminated with Be. We later ran it for a prolonged period and found that the rate eventually disappeared and arrived at background like the others. In retrospect we noticed that the same vacuum line which was used to make the standards S2, S4, and S11 was used to create G2. It may be that some of the Be molecules were somehow transferred to the nozzle of the sample vial. After prolonged exposure to atmosphere (basically just sitting out) the concentration was dropping as the Be molecules were slowly released from the nozzle. This is the

Table 10.29: Summary of Be counting rates in counts-per-minute (cpm) for the unknown samples. Notice several different gas field runs. For each run we tried to see if we could get the Be signal to disappear. Eventually we removed the vial to a different port on the gas manifold and the signal disappeared. When put back to the original port the Be signal did not return.

Sample	Counting Rate [cpm]
Blank	$0.18 \pm 0.08$
Gas Field, G1	0.0
Gas Field, G2 #1	$2.47 \pm 0.41$
Gas Field, G2 #2	$18.98 \pm 1.60$
Gas Field, G2 #3	$21.58 \pm 0.77$
Gas Field, G3	$0.07 \pm 0.01$
Gas Field, G2 #4	$0.07 \pm 0.01$
Gas Field, G2 #5	$0.05 \pm 0.006$
Gas Field, G2 #6	0.0
Gas Field, G2 #7	0.0
Beryl Ore, O1	0.0
Beryl Ore, O2	0.0
Dissolved Metal, M1	$0.18 \pm 0.08$
Melted Metal, M2	$0.14 \pm 0.08$
Atmosphere	0.0

only plausible cause of the contamination and of the resulting disappearance of the Be contamination in sample G2. Nonetheless, there were several days of excitement during Run Be8 when the possibility of a violation of the Pauli principle seemed to be indicated by the data. So with that glitch explained the rest of the data turned out as expected.

The data was then combined with Equation (10.14) to obtain their final concentration limits. As in Run Be7, the intersection of the resulting line calibration and the horizontal band corresponding to the Be counting rate in the unknown sample determined the minimum detectable Be concentration, as illustrated in Fig. 10.12.

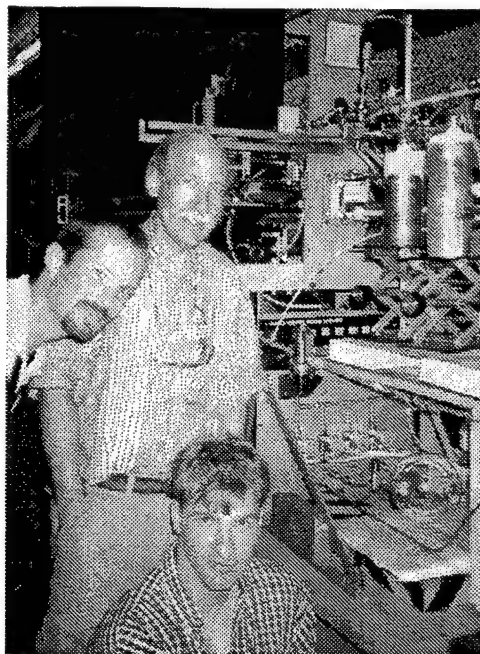


Figure 10.11: Picture of the ion source showing the direct gas setup for sample G3. Pictured from left to right are Dr. Darren Hillegonds, Prof. Ephraim Fischbach, and Mike Stohler.

This method combined with the data from Table 10.29 led us to the results provided in Table 10.30. For the samples without a band the He blank adjustment data was used in order to determine the limit. Since this adjustment was at 0.18 cpm it was a more conservative estimate than that made by Poisson statistics<sup>2</sup> which would dictate 3 counts for a 95% confidence limit. When run for 30 minutes these three counts would have given a counting rate of 0.1 cpm. Thus our use of 0.18 background drift is more conservative and actually corresponds to a 99.55% confidence limit.

The final ratios reported in Table 10.30 are obtained based on the derivations at the conclusion of the discussion section on each of the samples. These are one of the strongest aspects of this experiment since these ratios are measured quantities instead of using the cosmological abundances discussed by previous authors.

As observed before the extreme sensitivity of the AMS led to a minor problem in determining the background and calibration. The effect of running a Be standard was

<sup>2</sup>For more info on Poisson statistics see Chapter 1.

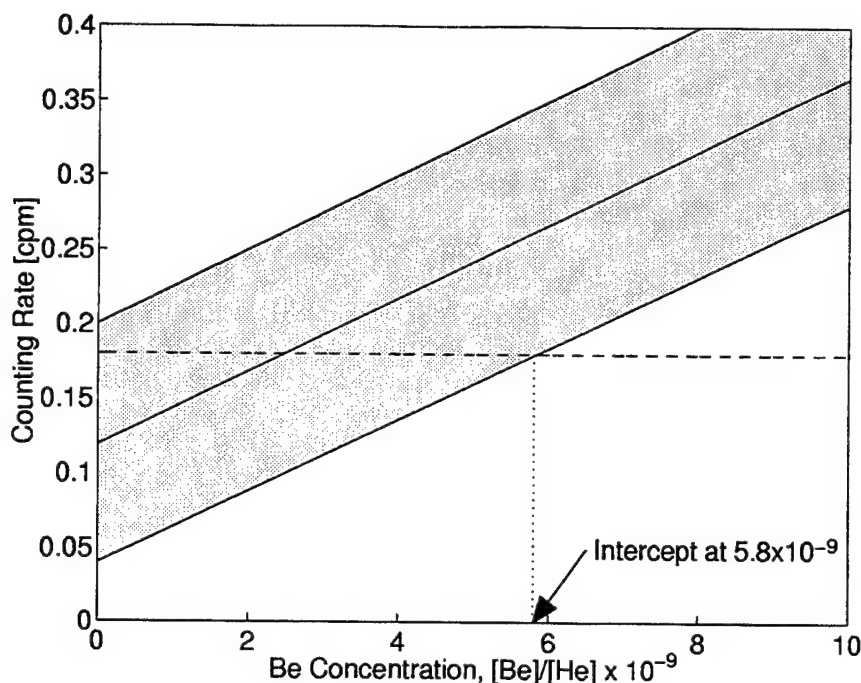


Figure 10.12: Determination of the Be' concentrations in the beryl and gas field samples. The shaded region is an enlarged version of the lower end of Fig. 10.10 with the  $1\sigma$  errors included. The horizontal dashed line is the measured counting rate for Be, which is presumed to arise from the presence of Be' in the samples. The limits on  $[\text{Be}']/[\text{He}]$  for the beryl and gas field samples are identical, as can be seen from Table II, and are obtained from the intersection of the horizontal line and the  $1\sigma$  band as shown. The limits from the other samples are obtained in a similar manner.

to produce a small but detectable increase in the subsequent Be background counting rate. This produced a slow upward drift in the background from 0.18 cpm to 4.8 cpm. To minimize the effects of this drift, the unknown samples (presumably containing no Be) were run first, followed by the standards in order of increasing concentration. These samples were interspersed with blanks which continually monitored the drift of the background. Thus the run consisted of the sequence blank-unknown sample-low standard-blank-high standard-blank. The gas manifold (see Fig. 10.7) was designed which allowed the AMS to cycle on a 5 minute time scale among the standards, the unknown samples, and the blank, and this helped to further reduce the effects of the

Table 10.30: Summary of unknown sample concentrations. The first column gives the Be' concentration, and the second column expresses the Be' concentration relative to Be or air. All results are at the  $1\sigma$  level.

Sample	Concentration	Final Ratio
Be Metal	$< (1.67 \pm 0.74) \times 10^{-8}$	$\frac{[Be']}{[Be]} < (9.30 \pm 4.13) \times 10^{-12}$
Be Alloy	$< (1.50 \pm 0.86) \times 10^{-8}$	—
Beryl	$< (5.81 \pm 2.61) \times 10^{-9}$	$\frac{[Be']}{[Be]} < (1.20 \pm 0.53) \times 10^{-11}$
Gas Field	$< (5.81 \pm 2.61) \times 10^{-9}$	—
Air	$< (5.45 \pm 2.42) \times 10^{-9}$	$\rho' = \frac{[Be']}{[air]} < (2.86 \pm 1.27) \times 10^{-14}$

drift in the background. The measured drift was then used to correct the counting rates for the Be standards. Adhering to the protocol of starting with the most dilute samples minimized the Be background to the extent that no signal for Be above background was detected in any of the unknown samples (Be metal, ore, gas field, and laboratory air).

Finally, as with Run Be7 we will present the Raw data here. Tables 10.31 to 10.32 give the raw data used to create the plots and tables given in this chapter. Each table entry is the counting rate measured for the designated sample.

### 10.10 Conclusions

Our final results are shown in Table 10.30. We see from Figure 10.12 that since no signal for Be' was detected above background, this translates into a  $1\sigma$  limit on the concentration of Be' relative to He in each of the samples, as shown in Table 10.30. Finally, to compare to the Fischbach, Kirsten, and Schaeffer [16], we obtain a limit

on the Be' concentration,  $\rho'$ , in air of  $\rho' < 2.86 \times 10^{-14}$ , which improves on that reported in Ref. [16] by a factor of almost 300.

The more significant results are those from the Be metal, beryl, and gas field sample, since these were obtained from sources where Be' was more likely to be found than in air. In the absence of a rigorous fundamental theory of PEP violation, it is unclear how to convert the results from these specific samples into meaningful limits on the PEP-violating parameter  $\beta^2$  often quoted in the literature [88]. For this reason we list only the quantities directly measured by our experiment and defer the interpretation of these results to a future complete theory. That theory could, of course, indicate that PEP violation would not be expected to arise in some or all of the systems studied to date, in which case a new class of experiments may be required.

Table 10.31: Page 1 of Raw data for Run Be8. Each entry is the counting rate in cpm for a different 1.9 minute cycle of the designated sample. This time the chosen surface was  $\text{Yb}_2\text{O}_3$  and the gas pressure was held constant at  $2.5 \times 10^{-6}$  Torr.

Sample	Counting rate [cpm]									
He	0.0	0.0	0.0	0.0	0.0	0.0	0.0	0.0	0.0	0.0
	0.0	0.0	0.0	0.0	0.0	0.0	0.0	0.0	0.0	0.0
	0.0	0.0	0.0	0.0	0.0	0.0	0.0	0.0	0.0	0.0
	0.0	0.0	0.0	0.0	0.0	0.0	0.0	0.0	0.0	0.53
	0.0	0.0	0.0	0.0	0.0	0.0	0.0	0.0	0.0	0.53
	0.0	0.53	0.0	0.0	0.0	0.0	0.0	0.0	0.0	0.0
G1	0.0	0.0	0.0	0.0	0.0	0.0	0.0	0.0	0.0	0.0
G2	0.0	0.0	0.0	0.0	0.0					
	0.53	0.0	0.0	1.05	0.0	1.05	0.53	1.05	0.53	0.0
	0.53	0.0	2.11	1.58	2.63	2.11	2.63	2.11	3.16	5.79
O1	3.16	4.74	2.63	3.68	4.21	5.79	6.32	2.11	5.79	
	0.0	0.0	0.0	0.0	0.0	0.0	0.0	0.0	0.0	0.0
	0.0	0.0								
He	0.53	0.0	0.0	0.0	0.0	0.0	0.0	0.0	0.53	0.0
	0.0	0.0	0.53	0.0	1.05					
G2	6.32	10.00	11.05	15.79	22.63	17.89	20.53	20.53	15.26	21.05
	25.79	23.16	27.37	21.50	25.79					
He	0.53	1.05	2.11	1.05	2.11	1.58	0.53	0.53	1.11	0.53
	2.11	1.58	1.11	0.0	2.63					
O2	0.0	0.0	0.0	0.0	0.0	0.0	0.0	0.0	0.0	0.0
	0.0	0.0	0.0	0.0	0.0					
M1	1.05	0.0	0.53	0.0	0.0	0.0	0.0	0.53	0.0	0.53
	0.0	0.0	0.0	0.0	0.0					
M2	0.0	0.0	0.0	0.0	0.53	0.0	0.0	0.0	0.0	0.53
	0.0	0.0	0.0	1.05	0.0					
He	1.05	3.15	1.05	1.05	1.05	1.05	1.05	2.63	2.22	1.05
	3.16	4.21	3.68	4.21	1.58					
He	0.0	0.0	0.0	0.0	0.0	0.0	0.0	0.0	0.0	0.0
	0.0	0.0	0.0	0.0	0.0	0.0	0.0	0.0	0.0	0.0
	0.0	0.0	0.0	0.0	0.0	0.0	0.0	0.0	0.0	0.0
	0.0	0.0	0.0	0.0	0.0	0.0	0.0	0.0	0.0	0.0
	0.0	0.0	0.0	0.0	0.0	0.0	0.0	0.0	0.0	0.0
	0.0	0.0	0.0	0.0	0.0	0.0	0.0	0.0	0.53	0.0
Air	0.0	0.0	0.0	0.0	0.0	0.0	0.0	0.0	0.0	0.0
	0.0	0.0	0.0	0.0	0.0					
G2	13.16	26.84	19.47	24.21	21.05	23.16	20.00	21.58	21.05	22.63
	23.16	21.05	20.53	23.68	22.11					

Table 10.32: Page 2 of Raw data for Run Be8. Each entry is the counting rate in cpm for a different 1.9 minute cycle of the designated sample. This time the chosen surface was  $\text{Yb}_2\text{O}_3$  and the gas pressure was held constant at  $2.5 \times 10^{-6}$  Torr.

Sample	Counting rate [cpm]							
S1	3.16	1.05	2.11	1.05	0.53	1.67	3.16	1.05
	2.11	0.53	1.05	3.16	1.05	0.53	2.11	1.67
	2.11	1.05	0.53	0.0	2.11	3.16	4.21	2.11
	1.67	0.53	1.67	1.05	2.11	1.67	2.11	1.67
	2.11	3.16	2.63	2.11	1.05	0.53	1.67	2.63
	2.11	3.16	2.11	1.05	2.11			
S2	6.32	10.53	14.74	18.42	15.79	12.63	11.58	
	14.74	17.37	15.26	14.74	17.89	17.37	15.26	14.74
	14.74	15.26	13.68	14.74	11.58	10.53	12.63	14.74
	13.68	15.26	11.58	13.16	10.53	12.63		
S3	24.74	23.68	25.26	26.32	27.37	26.32	25.26	28.95
	26.32	26.32	27.37	25.79	25.26	26.32	26.84	
S4	63.16	65.79	68.42	67.37	62.11	65.79	64.21	63.16
	64.74	66.32	64.21	65.26	67.37	63.16	64.21	
He	0.0	0.0	0.53	0.0	0.0	0.0	0.53	0.0
	1.05	0.0	0.0	0.0	0.53	0.0	0.0	
S5	121.05	118.42	123.68	122.63	126.32	127.37	129.47	128.95
	127.89	126.32	125.26	126.84	123.68	124.74	122.05	
S6	209.47	213.16	215.26	210.53	211.58	213.68	212.63	210.53
	211.58	214.74	215.79	216.32	214.74	210.53	211.58	
S7	423.68	426.84	427.37	422.11	426.32	424.74	428.95	430.00
	427.37	426.32	426.32	427.89	428.95	429.47	426.32	
He	3.16	3.16	5.79	1.05	5.26	2.63	4.74	1.58
	5.26	7.37	7.37	3.16	10.53	4.21	6.32	

Table 10.33: Page 3 of Raw data for Run Be8. Each entry is the counting rate in cpm for a different 1.9 minute cycle of the designated sample. This time the chosen surface was  $\text{Yb}_2\text{O}_3$  and the gas pressure was held constant at  $2.5 \times 10^{-6}$  Torr.

Sample	Counting rate [cpm]							
He	0.0	0.0	0.0	0.0	0.0	0.0	0.0	0.0
	0.0	0.0	0.0	0.0	0.0	0.0	0.0	
He	0.0	0.53	0.0	0.53	0.0	0.0	0.0	0.0
	0.0	0.0	0.0	0.0	0.0	0.0	0.0	
He	1.05	1.05	1.67	7.22	3.68	3.16	4.21	5.79
	2.63	2.11	4.74	6.32	2.63	5.79	7.89	
He	0.0	0.0	0.0	0.0	0.0	0.0	0.53	0.0
	0.0	0.0	0.0	0.0	0.0	0.0	0.0	
He	0.0	0.0	0.0	0.0	0.0	0.0	0.0	0.0
	0.0	0.0	0.0	0.0	0.0	0.0	0.0	
G2	0.0	0.0	0.0	0.0	0.0	0.0	0.53	0.0
	0.0	0.0	0.0	0.0	0.0	0.0	0.0	
G2	0.0	0.0	0.0	0.0	0.0	0.0	0.0	0.0
	0.0	0.0	0.0	0.0	0.0	0.0	0.0	
G2	0.0	0.0	0.0	0.0	0.0	0.0	0.0	0.0
	0.0	0.0	0.0	0.0	0.0	0.0	0.0	
G2	0.0	0.0	0.0	0.0	0.0	0.0	0.0	0.0
	0.0	0.0	0.0	0.53	0.0	0.0	0.0	
G2	0.0	0.0	0.0	0.0	0.0			
S1	2.11	3.16	0.95	3.16	2.38	4.21	0.48	2.11
	1.43	2.11	0.95	3.16	3.81	2.11	2.86	
S2	15.79	11.43	15.71	14.74	17.62	13.16	13.81	21.05
	15.71	13.68	12.86	16.32	11.43	17.37	14.29	
G3	0.0	0.0	0.0	0.0	0.0	0.0	0.0	0.0
	0.0	0.0	0.0	0.0	0.0	0.53	0.0	
He	0.0	0.0	0.0	0.0	0.0	0.0	0.0	0.0
	0.0	0.0	0.0	0.53	0.0	0.0	0.0	

## **Part III**

# **SEARCHING FOR STRONGLY INTERACTING MASSIVE PARTICLES**

## CHAPTER 11. MOTIVATIONS FOR SIMPS

### 11.1 Introduction

The concept of superheavy elements is not a new one as they have been theorized for many years. There has always been a fascination with the notion that there is an island of stability just beyond the presently accessible regions of stable nuclei [41]. In fact with the introduction of Big Bang cosmologies [42, 43] it was possible to predict the formation of heavy (10 GeV to 100 TeV) stable particles during the early moments of the universe.

Recently superheavy particles have been introduced as an explanation to a wide array of cosmological questions and inconsistent results seen in astrophysics. One method of searching for such particles would be to identify anomalous isotopes of known heavy nuclei, which can result if a neutral, heavy, stable strongly interacting elementary particle binds with known nuclei. These stable particles, dubbed strongly interacting massive particles (SIMPs), may be present in normal matter.

There are both particle physics and cosmological motivations for the existence of heavy nuclei and stable heavy hadrons. These include the dark matter problem [140, 4, 141, 142, 7], predictions of gauge mediated supersymmetry (SUSY) models [143, 144, 145, 146, 147], predictions of models that explain current neutrino results [148, 149, 150], and predictions of models that explain perplexing ultra high energy cosmic ray events [151, 146, 152, 153].

### 11.2 The Dark Matter Problem

One of the fundamental problems in cosmology is to compile a census of the contents of the universe. Material at a range of different densities and temperatures can be detected by emission or absorption somewhere in the electromagnetic spectrum. Gravity, however, detects mass quite independently of its equation of state. In an ideal world, these two results of the total density of the universe would coincide.

However, in practice, the gravitational method detects up to a factor of ten more mass that can be detected in any other way. SIMPs may constitute a solution to this dark matter problem [72].

It was recently shown that, given their annihilation cross section SIMPs can appear in sufficient abundance to saturate either the cosmic density or the galactic halo [146]. In order to saturate the cosmic density their mass  $M_X$  must satisfy  $M_X \geq 10^{3.5}$  GeV [7]. However, if in the process of cosmological evolution, SIMPs formed the gravitational potential well and became halo dark matter, Mohapatra and Teplitz [7] predict  $M_X \leq 100$  GeV.

SIMP models that predict saturation of the upper bound on (galactic halo) dark matter are restricted by a number of experiments as reviewed by Starkman *et. al.* [4]. The relic SIMP abundance is roughly proportional to  $(\sigma_{\bar{S}S}M_S)^{-1}$  where  $M_S$  is the SIMP mass and  $\sigma$  is the particle-antiparticle annihilation cross section [154]. As  $\sigma_{\bar{S}S}$  moves beyond  $\sigma_{\bar{S}S}^{min} \sim 10^{-36} \text{ cm}^2$ , the bound is not saturated and the limits of Ref. [4] do not apply. Thus such heavy, strongly interacting particles, may form bound states with nuclei that have observable abundances [7] and could therefore be detected in experiments that search for anomalous nuclei in nature.

### 11.2.1 The Robertson-Walker Metric

In Einstein's general theory of relativity the invariant interval between two points is given by

$$ds^2 = g_{\mu\nu}(x)dx^\mu dx^\nu \quad (11.1)$$

where the metric tensor  $g_{\mu\nu}(x)$  reflects the distribution of matter and energy. For large distances this invariant may be written as

$$ds^2 = c^2 dt^2 - g_{ij}(\mathbf{x}, t)dx^i dx^j \quad (11.2)$$

where  $i, j = 1, 2, 3$  run over the spatial coordinates only, and  $\mathbf{x}$  is a spatial vector.

On large distance scales the universe appears to be homogenous and isotropic. As a result the curvature of space must also be the same everywhere. The equation for a surface of constant curvature is

$$x_1^2 + x_2^2 + x_3^2 + \frac{x_4^2}{k} = \frac{R(t)^2}{k} \quad (11.3)$$

where  $k$  represents the sign of the curvature. The sign can be one of three values  $k = 0, \pm 1$ :  $k = +1$  corresponds to a closed hyperspace,  $k = 0$  to a flat surface with zero curvature, and  $k = -1$  to an open surface of negative curvature (two-dimensional surfaces of these types are provided in Figure 11.1). The actual curvature is given by

$$K = \frac{k}{R(t)^2} \quad (11.4)$$

As a result  $R(t)$  determines the magnitude of the curvature.

Thus the universe is a closed 3-dimensional hyperspace of volume  $V = 2\pi^2 R(t)^2$  in 4-dimensional space-time if  $k = +1$ . In contrast, if  $k = 0$  ( $k = -1$ ) the universe is flat (closed) with an infinite volume.

On the surface given in Equation (11.3) we can transform to polar coordinates

$$\begin{aligned} x_1 &= Rr \sin \theta \cos \phi \\ x_2 &= Rr \sin \theta \sin \phi \\ x_3 &= Rr \cos \theta \\ x_4 &= R\sqrt{1 - kr^2} \end{aligned} \quad (11.5)$$

A line element on the space-time surface is then given by

$$\begin{aligned} ds^2 &= c^2 dt^2 - \left( dx_1^2 + dx_2^2 + dx_3^2 + \frac{dx_4^2}{k} \right) \\ &= c^2 dt^2 - R(t)^2 \left[ \frac{dr^2}{1 - kr^2} + r^2 (d\theta^2 + \sin^2 \theta d\phi^2) \right] \end{aligned} \quad (11.6)$$

$R(t)$  is the time-dependent cosmic scale factor, which determines the length scale and increases as the universe expands, thus breaking Lorentz invariance. Here  $r$ ,  $\theta$ , and  $\phi$  are co-moving (non-inertial) coordinates.

Comparing Equation (11.6) to the general form represented in Equation (11.1) gives us the nonvanishing terms of the metric tensor

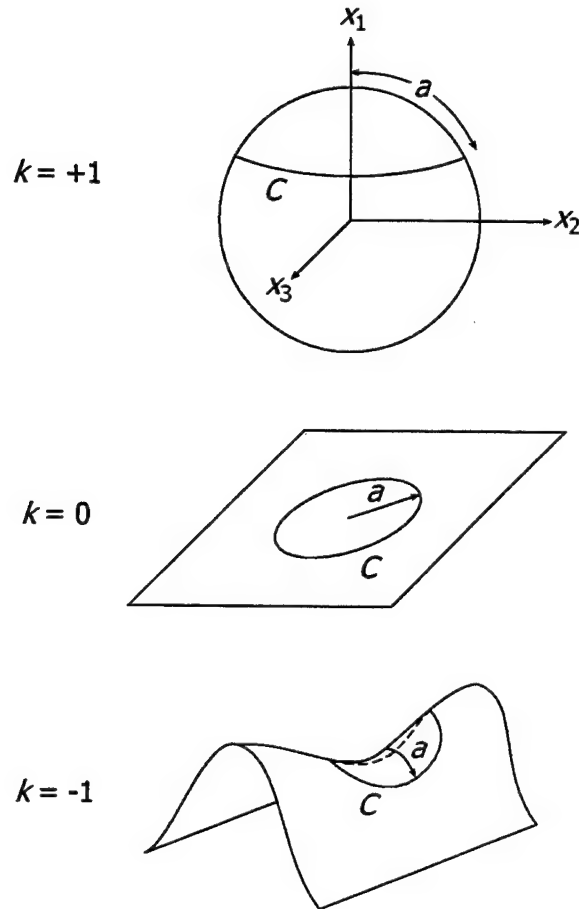


Figure 11.1: The top diagram represents a closed 2-dimensional surface of constant positive curvature,  $k = +1$ . A circle with radius  $a$  drawn on the sphere has a circumference  $C < 2\pi a$ . The middle diagram is a flat 2-dimensional surface with no curvature,  $k = 0$ . On this plane  $C = 2\pi a$ . Finally, the bottom diagram is an open 2-dimensional surface of negative constant curvature,  $k = -1$ . The circle on this surface has  $C > 2\pi a$ .

$$g_{rr} = -\frac{R^2}{1 - kr^2} \quad g_{\theta\theta} = -R^2 r^2 \quad (11.7)$$

$$g_{\phi\phi} = -R^2 r^2 \sin^2 \theta \quad g_{00} = 1$$

This metric is known as the Robertson-Walker metric [17]. We would like to calculate the solution of Einstein's equation

Table 11.1: Non-zero terms of the Affine Connection using the Robertson-Walker metric.

	$\Gamma_{r\nu}^\lambda$	$\Gamma_{\theta\nu}^\lambda$	$\Gamma_{\phi\nu}^\lambda$	$\Gamma_{0\nu}^\lambda$
$\Gamma_{\mu\nu}^r$	$\Gamma_{rr}^r = \frac{r}{1-kr^2}$	$\Gamma_{\theta\theta}^r = -r(1-kr^2)$	$\Gamma_{\phi\phi}^r = -r(1-kr^2)\sin^2\theta$	$\Gamma_{0r}^r = \frac{1}{c}\frac{\dot{R}}{R}$
$\Gamma_{\mu\nu}^\theta$	$\Gamma_{r\theta}^\theta = \frac{1}{r}$	$\Gamma_{\phi\phi}^\theta = -\sin\theta\cos\theta$		$\Gamma_{0\theta}^\theta = \frac{1}{c}\frac{\dot{R}}{R}$
$\Gamma_{\mu\nu}^\phi$	$\Gamma_{r\phi}^\phi = \frac{1}{r}$	$\Gamma_{\theta\phi}^\phi = \cot\theta$		$\Gamma_{0\phi}^\phi = \frac{1}{c}\frac{\dot{R}}{R}$
$\Gamma_{\mu\nu}^0$	$\Gamma_{rr}^0 = \frac{R\dot{R}}{c(1-kr^2)}$	$\Gamma_{\theta\theta}^0 = \frac{R\dot{R}r^2}{c}$	$\Gamma_{\phi\phi}^0 = \frac{R\dot{R}r^2\sin^2\theta}{c}$	

$$R_{\mu\nu} - \frac{1}{2}Rg_{\mu\nu} + \frac{\Lambda}{c^2}g_{\mu\nu} = -\frac{8\pi G_N}{c^4}T_{\mu\nu} \quad (11.8)$$

with this metric. Since we have  $g_{\mu\nu}$  we may calculate the non-vanishing terms in the Affine Connection with

$$\Gamma_{\mu\nu}^\lambda = \frac{1}{2}g^{\lambda\rho} \left[ \frac{\partial g_{\nu\rho}}{\partial x^\mu} + \frac{\partial g_{\mu\rho}}{\partial x^\nu} - \frac{\partial g_{\mu\nu}}{\partial x^\rho} \right] \quad (11.9)$$

Applying this to Equation (11.7) yields the nonzero Affine Connection terms provided in Table 11.1.

From the Affine Connection we may then derive the nonzero components of the Riemann-Christoffel tensor whose components are given by

$$R_{\mu\nu\rho\sigma} = \frac{1}{2} \left[ \frac{\partial^2 g_{\mu\sigma}}{\partial x^\nu \partial x^\rho} - \frac{\partial^2 g_{\nu\sigma}}{\partial x^\mu \partial x^\rho} - \frac{\partial^2 g_{\mu\rho}}{\partial x^\nu \partial x^\sigma} + \frac{\partial^2 g_{\nu\rho}}{\partial x^\mu \partial x^\sigma} \right] \quad (11.10)$$

$$+\Gamma_{\lambda\mu\sigma}\Gamma_{\nu\rho}^\lambda - \Gamma_{\lambda\mu\rho}\Gamma_{\nu\sigma}^\lambda$$

which, following a contraction, can be simplified to the Ricci tensor and is given by the usual expression

$$R_{\mu\nu} = \frac{\partial \Gamma_{\mu\lambda}^\lambda}{\partial x^\nu} - \frac{\partial \Gamma_{\mu\nu}^\lambda}{\partial x^\lambda} - \Gamma_{\mu\nu}^\rho \Gamma_{\rho\sigma}^\sigma + \Gamma_{\mu\sigma}^\rho \Gamma_{\nu\rho}^\sigma \quad (11.11)$$

Thus we arrive at the nonzero components of the Ricci tensor for polar coordinates

$$R_{ii} = \frac{R\ddot{R} + 2\dot{R}^2 + 2kc^2}{c^2 R^2} \quad \text{for } i = r, \theta, \phi \quad (11.12)$$

$$R_{00} = \frac{3\ddot{R}}{c^2 R}$$

The Ricci scalar also appears in Einstein's field equations (given in Equation (11.8)) and is a contraction of the Ricci tensor given by

$$R = g^{\mu\nu} R_{\mu\nu} = R^\mu_\mu \quad (11.13)$$

In terms of this metric (in polar coordinates) the Ricci scalar is

$$R = \frac{6}{c^2 R^2} (\ddot{R}R + \dot{R}^2 + kc^2) \quad (11.14)$$

Now that all the terms on the left hand side of Einstein's field equations have been determined all that is needed is for us to include the effects of matter and radiation. These come into play via the energy-momentum tensor  $T_{\mu\nu}$  which is given by

$$T_{\mu\nu} = m \int d\tau \frac{\dot{x}_\mu \dot{x}_\nu}{\sqrt{g_{\rho\sigma} \dot{x}_\rho \dot{x}_\sigma}} \delta^4(x^\mu - x^\mu(\tau)) \quad (11.15)$$

for a single particle of mass  $m$ . If we momentarily set  $g^{\mu\nu} = \eta^{\mu\nu}$  in the above equation, the energy-momentum tensor for matter with density  $\rho$  moving with velocity  $v$  reduces to

$$T_{\mu\nu} = \rho c^2 U_\mu U_\nu \quad (11.16)$$

where

$$U_\mu \equiv \frac{dx_\mu}{d\tau} \quad (11.17)$$

is the velocity 4-vector with the usual components

$$U = \frac{dx}{d\tau} = \gamma v \quad (11.18)$$

$$U_0 = \frac{dt}{d\tau} = \gamma$$

where  $\tau$  is the proper time and  $\gamma = 1/\sqrt{1 - v^2/c^2}$ . Thus for bulk matter at rest, the only nonzero component is

$$T_{00} = \rho c^2 \quad (11.19)$$

In contrast for a nonviscous fluid that is at rest but which has random nonrelativistic internal motion, we have

$$\begin{aligned} T_{ii} &= \frac{1}{3} \sum_a m_a v_a^2 = p & \text{for } i = 1, 2, 3 \\ T_{00} &= \sum_a m_a c^2 = \rho c^2 \end{aligned} \quad (11.20)$$

where the sums run over all the particles  $a$ , with mass  $m_a$ , in a unit volume. The factor of  $\frac{1}{3}$  arises from averaging over the three spatial dimensions and  $p$  is the magnitude of the pressure. In any other Lorentz frame we get

$$T_{\mu\nu} = (p + \rho c^2) U_\mu U_\nu - p \eta_{\mu\nu} \quad (11.21)$$

Similarly, for radiation (which are highly relativistic particles with  $E^2 = |\mathbf{p}|^2 c^2 + m^2 c^4 \simeq |\mathbf{p}|^2 c^2$ ), we have instead

$$\begin{aligned} T_{ii} &= \frac{1}{3} \sum \frac{|\mathbf{p}|^2 c^2}{E} \\ &= \frac{1}{3} \sum E \end{aligned} \quad (11.22)$$

$$= \frac{1}{3} \rho c^2$$

$$\begin{aligned} T_{00} &= \sum E \\ &= \rho c^2 \end{aligned} \quad (11.23)$$

and again in any frame the energy-momentum tensor is given by Equation (11.21) but with  $\rho c^2$  interpreted as the energy density and  $p = \frac{1}{3}\rho c^2$ .

On large distance scales we may assume that matter and radiation are homogeneous and are effectively smeared out uniformly into a perfect fluid. For a co-moving observer in the presence of gravity, the total energy-momentum tensor has only diagonal nonvanishing components

$$\begin{aligned} T_{ii} &= pg_{ii} & \text{for } i = 1, 2, 3 \\ T_{00} &= \rho c^2 \end{aligned} \quad (11.24)$$

Substituting into Einstein's field equations (11.8) gives the following differential equations

$$\begin{aligned} \frac{\ddot{R}}{R} &= -\frac{4\pi G_N}{3} \left( \rho + 3\frac{p}{c^2} \right) + \frac{\Lambda}{3} \\ \left( \frac{\dot{R}}{R} \right)^2 &= \frac{8\pi G_N \rho}{3} - \frac{kc^2}{R^2} + \frac{\Lambda}{3} \end{aligned} \quad (11.25)$$

In the present time, the matter (which does not exert pressure) determines the dynamics of the universe, and, assuming  $\Lambda$  is small (or at least very close to 0), these equations reduce to the Friedmann equations

$$\frac{\ddot{R}}{R} = -\frac{4\pi G_N \rho}{3} \quad (11.26)$$

$$H^2 \equiv \left( \frac{\dot{R}}{R} \right)^2 = \frac{8\pi G_N \rho}{3} - \frac{kc^2}{R^2} \quad (11.27)$$

where  $H$  is Hubble's constant. More detailed derivations of the Friedmann equations are provided in a number of texts including the books by Longair (see Chapter 1 of [155]), Collins, Martin and Squires (see Chapter 15 of Ref. [17]) and of Weinberg (see Chapter 15 of [156]). Since the total amount of matter in a given co-moving volume is fixed (namely,  $\rho R^3$  which is a constant) and is independent of time, Equation (11.27) can be written as

$$\dot{R}^2 = \frac{8\pi G_N}{3} (\rho R^3) \frac{1}{R} - kc^2 \quad (11.28)$$

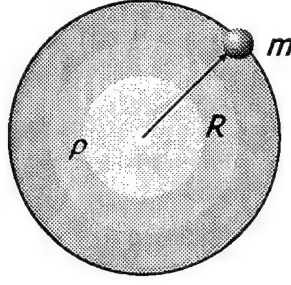


Figure 11.2: A particle of mass  $m$  is gravitationally attracted to a uniform sphere of matter with density  $\rho$  and radius  $R$ .

which, when differentiated with respect to  $t$ , gives

$$2\dot{R}\ddot{R} = -\frac{8\pi G_N}{3}(\rho R^3) \left( \frac{\dot{R}}{R^2} \right) \quad (11.29)$$

which after dividing by  $2\dot{R}$  is identical to Equation (11.26) and thus the two equations are equivalent. These are easy to understand from nonrelativistic Newtonian gravity. A particle of mass  $m$  gravitationally attracted by a sphere of matter with density  $\rho$  and radius  $R$  (see Figure 11.2) experiences a force given by

$$\begin{aligned} F &= m\ddot{R} \\ &= -\frac{G_N M m}{R^2} \\ &= -\frac{G_N \rho \left( \frac{4}{3}\pi R^3 \right) m}{R^2} \end{aligned} \quad (11.30)$$

$$\Rightarrow -\frac{G_N \rho \left( \frac{4}{3}\pi R^3 \right) m}{R^2} = m\ddot{R}$$

$$\Rightarrow \frac{\ddot{R}}{R} = -\frac{4\pi G_N \rho}{3}$$

which is the same as Equation (11.26). Conservation of energy requires

$$\begin{aligned}
E_{TOT} &= T + V \\
&= \frac{1}{2}m\dot{R}^2 - \frac{G_N\rho(\frac{4}{3}\pi R^3)m}{R} \\
&= \text{constant} \\
&\equiv -\frac{1}{2}mc^2k
\end{aligned} \tag{11.31}$$

which gives Equation (11.27). Thus, the Friedmann equations may be derived from classical physics assuming a particle is gravitationally attracted by a uniform sphere of matter. Notice in this analogy that  $k$  gives the sign of the total energy. However, general relativity is still needed to give meaning to  $k$  and to justify neglecting matter outside the sphere. We also notice that the velocities are not necessarily always  $\ll c$ .

Since  $\rho \sim R^{-3}$ , if  $k = -1$  the solution of Equation (11.27) for large  $R$  is determined by the curvature, and we find  $R \rightarrow ct$ , so that ultimately the universe will expand with the speed of light. If  $k = 0$  then

$$\begin{aligned}
\left(\frac{\dot{R}}{R}\right)^2 &= \frac{8\pi G_N\rho}{3} \sim \frac{1}{R^3} \\
\Rightarrow R &\sim t^{2/3}
\end{aligned} \tag{11.32}$$

while if  $k = +1$  then  $\dot{R}$  vanishes for some finite

$$R_{\max} = \frac{4G_N M}{3\pi c^2} \tag{11.33}$$

where  $M = 2\pi^2 R^3 \rho$  is the total mass of the universe, and after this the universe will contract again and eventually the big bang will be followed by the big “crunch.” These three possibilities are illustrated in Figure 11.3 and are discussed in great detail in nearly every book on cosmology. A few good references are the books by Peacock [72], Bahcall and Ostriker [3], Kolb and Turner [154], Collins, Martin and Squires [17], and the texts by Longair [157, 155].

A major step in the development of cosmology was the observation by Hubble in 1929 that the universe is expanding and that the velocity at which galaxies are receding from us is proportional to their distance,  $\dot{R} = HR$ . Current estimates give Hubble’s constant

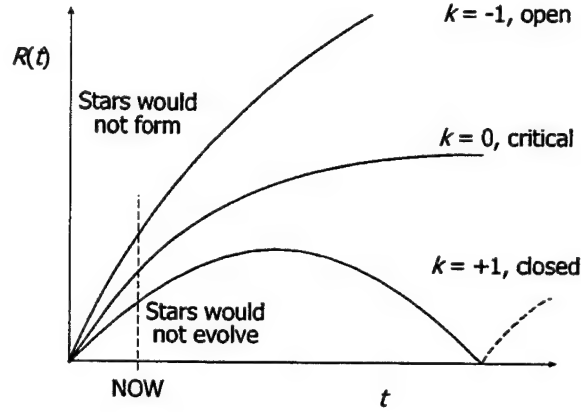


Figure 11.3: The size scale of the universe  $R$  versus time  $t$  for the three possible values of  $k$ . At the present time (marked “NOW”) the universe is still expanding but our uncertainty about the deceleration means that we cannot tell which class of curve we are on, only that we are at present very close to the critical  $k = 0$  case.

$$\begin{aligned}
 H_0 &\equiv \left( \frac{\dot{R}}{R} \right)_0 \\
 &= h_0 \times 100 \text{ km s}^{-1} \text{Mpc}^{-1} \\
 &\approx \frac{h_0}{10^{10}} \text{ years}
 \end{aligned}
 \tag{11.34}$$

where 1 parsec  $\equiv 3.09 \times 10^{16}$  m and  $h_0$  is in the range 0.5–1 and incorporates observational uncertainties. The zero subscript is frequently used to denote the present value, since we see from Equation (11.27) that Hubble’s “constant”  $H$  is actually dependent on the time scale of the universe. The current age of the universe,  $t_0$ , is somewhat less than  $1/H_0$  because of the deceleration illustrated in Figure 11.3. If  $k = 0$ , for example, then

$$\frac{1}{H_0} = \frac{3}{2} t_0
 \tag{11.35}$$

from Equation (11.32).

The magnitude of the deceleration,  $-\ddot{R}$ , is scale-dependent and it is customary to introduce the dimensionless deceleration parameter

$$q \equiv -\frac{R\ddot{R}}{\dot{R}^2} = \frac{4\pi G_N \rho}{3H^2}
 \tag{11.36}$$

from the Friedmann Equations (11.26) and (11.27). Hence from Equation (11.27)

$$k = \frac{R^2 H^2}{c^2} (2q - 1) \quad (11.37)$$

and so  $q > 1/2$  for  $k = +1$  and  $q < 1/2$  for  $k = -1$ . Since observations to date only yield  $-1 < q_0 < 2$  the sign of  $k$  is unknown. If the universe is flat and  $k = 0$  then  $q = 1/2$  and the average density of the universe is known as the "critical density"

$$\begin{aligned} \rho_c &\equiv \frac{3H_0^2}{8\pi G_N} = h_0^2 \times 1.88 \times 10^{-29} \text{ gm cm}^{-3} \\ &= h_0^2 \times 1.05 \times 10^{-5} \text{ GeV cm}^{-3} \end{aligned} \quad (11.38)$$

It is often convenient to introduce the density parameter

$$\Omega \equiv \frac{\rho}{\rho_c} = 1 + \frac{kc^2}{R^2 H^2} = 2q \quad (11.39)$$

where  $0.01 \leq \Omega \leq 4$  with the lower limit arising from observational bounds on the amount of luminous matter and the upper limit from the bound on the deceleration parameter.

The observed baryonic matter density  $\rho_B$  is much less than the critical density, namely

$$\rho_B \approx (0.01 - 0.15)\rho_c \quad (11.40)$$

But the matter density must be close to  $\rho_c$ . Otherwise if  $\rho \gg \rho_c$  then the deceleration would be so great that the universe would have contracted again before stars had time to evolve while if  $\rho \ll \rho_c$  the universe would have expanded so fast that matter would not have condensed into galaxies and stars.

### 11.2.2 Missing Matter

As mentioned above one of the fundamental problems in astrophysics today is to compile a census of the contents of the universe. We may detect mass either electromagnetically or gravitationally. By observing emission or absorption somewhere in the electromagnetic spectrum we detect material at a range of different densities and temperatures. However, unlike electromagnetic means, gravity detects mass independently of its equation of state. Ideally these two methods would predict the

same amount of mass since they measure mass independently. Unfortunately, this is not the case. In fact, measurements suggest that there exists nearly 10-50 times more mass present in large scale systems than would be inferred from their visible light. This disagreement has been called the Dark Matter Problem [72, 155].

While there are several motivations for why we believe dark matter (matter we are unable to detect electromagnetically) exists, the most dramatic evidence comes from the observed flat rotation curves many galaxies exhibit. From Newtonian gravity an object of mass  $m$  in a circular orbit a distance  $r$  from the center of a galaxy whose total mass within  $r$  is  $M(r)$  yields the relationship

$$\frac{mv^2}{r} = \frac{G_N m M(r)}{r^2} \quad (11.41)$$

where  $v$  is the object's velocity. Luminosity measurements suggest that the mass falls off exponentially such that we may assume that  $M(r) \simeq M = \text{constant}$  far from the galaxy nucleus. As a result, the velocity is given by

$$v = \sqrt{\frac{G_N M}{r}} \quad (11.42)$$

Thus we expect the velocities of stars outside the galactic center to follow the above relation and exhibit behavior shown by the dashed line in Figure 11.4.

Instead however, it is found that the velocity is roughly constant with distance outside the galactic center with the actual data following the solid curve in Figure 11.4 [158]. We notice that if we superimpose a spherically symmetric mass distribution we obtain the added contribution from what is known as the galactic halo. This addition causes the rotation curve described by Equation (11.42) to flatten and gives us the observed results. Thus, there seems to be a spherically symmetric distribution of additional mass surrounding the galaxy. Because the additional mass is not observed visually it has been given the name dark matter.

Another important point is that this additional mass does not possess the characteristic disk shape of the galaxy but rather is spherically symmetric. This may be explained by our current model of how large objects form from massive dust clouds. If the temperature of the cloud is greater than that of the cosmic background radiation the cloud will radiate electromagnetically and begin to collapse to form the

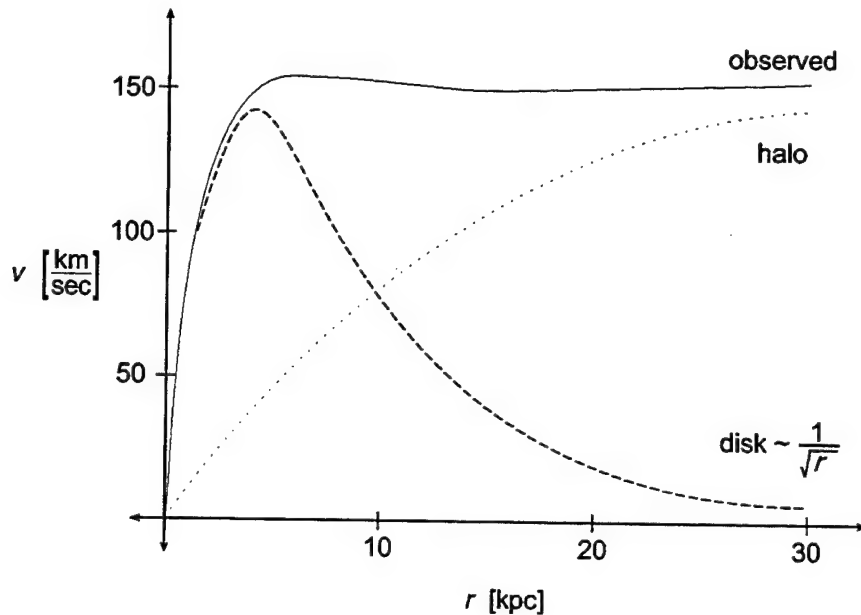


Figure 11.4: A typical rotation curve for a galaxy showing the rotational velocity  $v$  as a function of the distance  $r$  from the galactic center. The dashed line  $\sim 1/\sqrt{r}$  is the expected behavior if the actual matter distribution followed that suggested by luminosity measurements which suggest the visible matter is concentrated in the central region.

typical nucleus and disk shape (which results from conservation of angular momentum). However, the dark matter is unable to radiate the energy electromagnetically (because it is dark) and hence retains its spherically symmetric shape.

The reason for the spherical nature of the hypothetical dark matter arises from its particular behavior. Recall that a cloud of interstellar gas and dust becomes bound gravitationally because it radiates away its energy electromagnetically since it is warmer than the 2.7 K cosmic background radiation. Thus in a nascent galaxy, while all the matter which interacts electromagnetically begins to contract due to this radiative energy loss, the dark matter retains its spherically symmetric shape since it is unable to radiate energy electromagnetically (which is why it is dark to begin with). As the ordinary matter collapses it begins to rotate in order to conserve angular momentum and the flat disk is born. Of course this is an extreme oversimplification of the process but it allows us to make sense of the results. This new distribution

of the matter then exerts more gravitational force to the spherically symmetric dark matter and establishes a density which is roughly proportional to  $1/r$ . This then produces the parabolic shape for the halo contribution shown in Figure 11.4.

There are of course many different dark matter candidates. Since the only generic restriction on the particle is that it is unable to interact electromagnetically. In general we can break the dark matter into two categories: baryonic and nonbaryonic dark matter. Baryonic dark matter would consist of mainly dust clouds, planets, or dead stellar remnants (like white dwarfs, neutron stars, or black holes). However, the baryonic dark matter cannot constitute the majority of dark matter simply because their parent stars would have greatly increased the amount of high- $Z$  matter which would have prevented the formation of stars with a low metal content. Due to the absence of large numbers of stars with masses just large enough for hydrogen burning ( $\sim 0.08M_{\odot}$ ) we do not expect a large number of substellar objects with masses just below this threshold for stellar formation. Still recent searches for these massive compact halo objects (MACHOs) were performed by watching for their gravitational “microlensing” of background stars. Proposed by Paczynski [159, 160] microlensing is an indirect technique that does not depend on emitted light and several groups have begun to report results of MACHO searches [161, 162, 163, 164, 165]. However, accounting for baryonic dark matter the range of allowed values for cosmological density parameter are

$$0.2 \leq \Omega \leq 4 \quad (11.43)$$

From primordial nucleosynthesis, we obtain estimates on the baryonic contribution to the density parameter of  $\Omega_B h_0^2 \simeq 0.0125$ . Including baryonic dark matter takes us to  $\Omega_B \simeq 0.2$  which is the lower limit in Equation (11.43). Thus, the majority of dark matter is probably nonbaryonic. Within nonbaryonic dark matter we distinguish the difference between hot and cold dark matter. This distinction arises from whether the dark matter is relativistic or not, since the average energy for massless thermal quanta is roughly  $\langle E \rangle \approx 3kT$ . Since a relativistic particle has a high velocity it would correspond to a higher temperature and thus would be “hot” compared to the “cold” nonrelativistic dark matter. The most promising example of hot dark matter

(HDM) are low mass neutrinos. Originally thought to be massless the idea of massive neutrinos has become the subject of renewed investigation both theoretically and experimentally. The dependence of the cosmological density parameter on neutrino mass is given by

$$\Omega_{HDM} = \frac{\sum_i m_i}{(93.5 \text{ eV}) h_0^2} \quad (11.44)$$

where the sum is taken over the neutrino species. For a low Hubble parameter  $h \simeq 0.5$  an average neutrino mass of only 8 MeV would produce  $\Omega = 1$  and give the critical density. Current limits on the neutrino masses do not rule out this as a possibility since

$$\begin{aligned} \nu_e &\leq 3 \text{ eV} \\ \nu_\mu &\leq 0.19 \text{ MeV} \\ \nu_\tau &\leq 18.2 \text{ MeV} \end{aligned} \quad (11.45)$$

These values were taken from the Particle Data Group [1]. Since the current limits on neutrino masses do not exclude them from solving the dark matter problem they are of course a real possibility. However, while massive neutrinos could provide the needed dark-matter density,  $N$ -body simulations of structure formation in a neutrino-dominated Universe do a poor job of reproducing the observed structure of the Universe [166]. It is also difficult to see (from phase-space arguments) how such a neutrino could make up the dark matter in galaxy halos [166, 167]. More on the possibility of massive neutrinos later. For now let's focus on other particle dark matter candidates.

### 11.2.3 Particles as Cold Dark Matter

Cold dark matter is often described as relic particles which theoretically may have condensed out of the high energy particle "soup" as the Universe cooled following the big bang. When the temperature was high and the Universe was still young (see Figure 11.5) all particles existed in thermal equilibrium through reversible processes in which heavy relic particles  $X$  and antiparticles  $\bar{X}$  annihilate into lighter particles  $L$  and antiparticles  $\bar{L}$  such that  $X\bar{X} \leftrightarrow L\bar{L}$ . However as the temperature drops below the mass of the heavy particle the equilibrium abundance drops exponentially

and only light particles survive in thermal equilibrium (like photons). The equilibrium abundance of the relic particle drops until the rate for the annihilation reaction ( $X\bar{X} \rightarrow L\bar{L}$ ) falls below the Hubble expansion rate  $H$  at which point a cosmological abundance for the relic particle “freezes in” [154, 72, 17, 166].

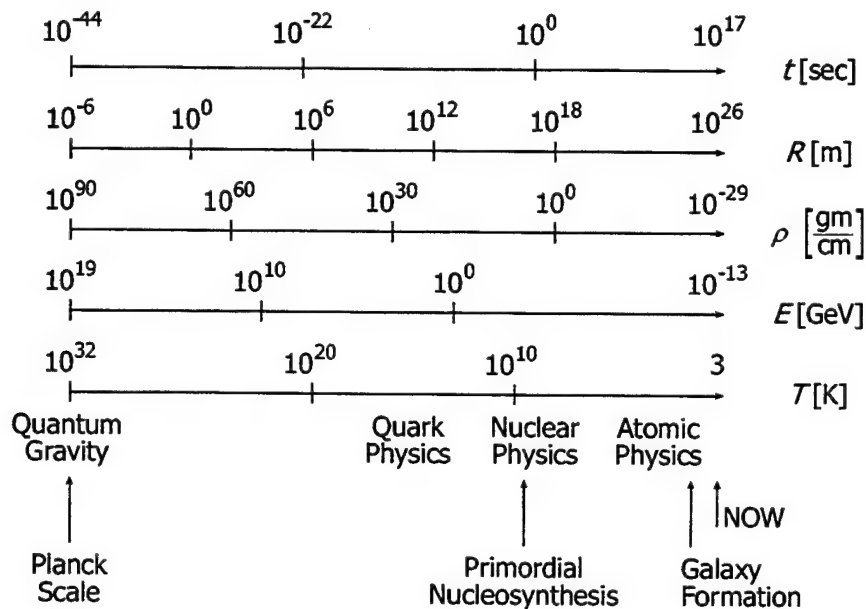


Figure 11.5: The Universe from the Planck time to the present including many of the relevant parameters (namely: size  $R$ , density  $\rho$ , energy  $E$  and temperature of the background radiation  $T$ ). We have also included a list of some of the major events along the timeline. This figure was adapted from Figure 15.6 of Ref. [17].

Thus, as time progressed and the temperature dropped, particles whose reactions were reversible suddenly began to decouple and condense out. This decoupling occurs if the interaction timescales are larger than the local Hubble time, leaving behind abundances of particles frozen at the values they had when last in thermal equilibrium. The relic cosmological abundance of particle  $X$  is set shortly after  $T$  drops below  $M_X$  at which time the number density  $n_X$  drops exponentially and the annihilation rate  $\Gamma$  drops below the expansion rate ( $\Gamma \leq H$ ) thus halting  $X\bar{X}$  annihilation. The annihilation rate is described by

$$\Gamma \equiv \frac{1}{n_X} \frac{dn_X}{dt} \quad (11.46)$$

$$= \langle \sigma_{X\bar{X}} v \rangle n_X$$

where  $\langle \sigma_{X\bar{X}} v \rangle$  is the thermally averaged total annihilation cross section times the relative velocity  $v$ . The time evolution of the number density is given by

$$\frac{dn_X}{dt} + 3Hn_X = -\langle \sigma_{X\bar{X}} v \rangle [(n_X)^2 - (n_X^{\text{EQ}})^2] \quad (11.47)$$

where the equilibrium number density  $n_X^{\text{EQ}}$  is determined by the Boltzmann distribution

$$n_X^{\text{EQ}} \simeq g_X \left( \frac{M_X T}{2\pi} \right)^{2/3} e^{-M_X/T} \quad (11.48)$$

where  $g_X$  is the number of internal degrees of freedom of the particle. In the early universe the Hubble-expansion rate falls with temperature

$$H(T) = \frac{1.66\sqrt{g^*}T^2}{M_P} \quad (11.49)$$

where  $g^*$  is the effective number of relativistic degrees of freedom and  $M_P \simeq 10^{19}$  GeV is the Planck mass. The quantity  $g^*$  is approximately equal to the number of bosonic relativistic degrees of freedom plus 7/8 times the number of fermionic relativistic degrees of freedom. Thus, instead of solving Equation (11.47) we may assume the freezeout condition that  $\Gamma(T_f) = H(T_f)$ .

### Weakly Interacting Massive Particles

At this point we must notice that in general there exist two different types of relic particles, those that interact via the weak force and those that interact via the strong force. For weakly interacting massive particles (or WIMPs) the freeze out temperature is roughly  $T_f \simeq M_X/20$  which results in a WIMP density of

$$\begin{aligned}
\rho_{\text{WIMP}} &= M_X n_X \\
&= \frac{1.66\sqrt{g^*}}{20^2 M_P} \frac{M_X^3}{\langle \sigma_{X\bar{X}} v \rangle} \\
&= \frac{3 \times 10^{-32} \text{ cm}^3/\text{sec}}{\langle \sigma_{X\bar{X}} v \rangle}
\end{aligned} \tag{11.50}$$

The application of the final coefficient comes from the idea that  $n_X/s$  is constant and  $s \simeq 0.4g^*T^3$  is the entropy density. Making the assumption that the annihilation cross section decreases with increasing mass we conclude that the cosmological density parameter for WIMPs is given by

$$\begin{aligned}
\Omega_{\text{WIMP}} &= \frac{\rho_{\text{WIMP}}}{\rho_c} \\
&\simeq \frac{3 \times 10^{-27} \text{ cm}^3/\text{sec}}{\langle \sigma_{X\bar{X}} v \rangle h_0^2} \\
&\geq \frac{M_X^2}{(300 \text{ TeV})^2 h_0^2}
\end{aligned} \tag{11.51}$$

The concepts behind this derivation can be found in a large number of places and while the text by Kolb and Turner [154] is probably cited the most, many other references contain summaries of such calculations [17, 72, 166, 146].

### Strongly Interacting Massive Particles

For strongly interacting massive particles (SIMPs) the problem is slightly different. Explicit discussion of the relic density for strongly interacting particles was derived by Mohapatra and Nussinov [146] and follows closely the derivation presented above. This then motivated several papers which calculated in detail the interactions of strongly interacting relic particles with ordinary matter [7, 5]. Because the relic particles are strongly interacting it was possible to construct models that predicted bound states of SIMPs with ordinary nuclei. Although several experiments [168, 4] provided significant constraints to such binding in low- $Z$  nuclei, Mohapatra *et al.* showed that binding will not occur below a mass cutoff for ordinary nuclei. This minimum mass (denoted  $A_{\min}$  for the minimum atomic number) is a function of the

SIMP mass  $M_S$  (where the subscript  $S$  denotes a SIMP property). Following the discussion in Ref. [5], we find the above dependence by assuming the SIMP binding energy is given by

$$n_S = \frac{1}{vt} \left( \frac{C_M \tilde{A}^{1/3}}{\sigma_{SN} A_M^{1/3} A_N^{2/3} \left[ 1 - \left( \frac{M_S}{M_S + A m_{nuc}} \right)^2 \right]} \right) \left( \frac{X}{Au} \right) \quad (11.52)$$

Here  $n_S$  is the resulting SIMP number density  $n_S$  and is then calculated from the experimentally determined fraction of anomalous gold (nuclei that captured a SIMP) to ordinary gold,  $X/Au$ , which is a function of the SIMP mass. The interaction cross section  $\sigma_{SN}$  is also a function of mass in certain models. The other variables are constants whose definitions are

$v \equiv$  galactic virial velocity ( $\approx 300$  km/sec)

$t \equiv$  sample exposure time to SIMP bombardment

$C_M \equiv$  concentration by weight of the most abundant element  $A_M$  in the Earth's crust with a nucleus heavier than  $A_{min}$

$A_N \equiv$  mass of the nucleus in amu

$\tilde{A} \equiv$  the  $A$  of an "average nucleus,"  $\tilde{A} \sim 20$

$m_{nuc} \equiv$  mass of an ordinary nucleon ( $m_{nuc} = (m_p + m_n)/2$ )

In the usual manner we then define the density as  $\rho_{SIMP} = n_S M_S$  so that the SIMP contribution to the cosmological density parameter becomes

$$\begin{aligned} \Omega_{SIMP} &= \frac{\rho_{SIMP}}{\rho_c} \\ &= \frac{n_S M_S}{\rho_c} \end{aligned} \quad (11.53)$$

The details of this derivation are provided in the following chapter. What is important here is that the experimental results regarding the SIMP abundance in ordinary nuclei can be transformed into a bound on the cosmological density parameter. In future chapters we will discuss how the results from our experiment measure up and constrain the cosmological density parameter.

### 11.3 Ultra High Energy Cosmic Rays

Another reason for considering heavy strongly interacting particles comes from recent theoretical attempts to understand several ultra high energy cosmic ray (UHECR) events. Nearly thirty years ago it was pointed out that sufficiently energetic cosmic rays will lose energy scattering with the cosmic microwave background or radio wavelength background radiation. Greisen [169] and Zatsepin and Kuzmin [170] noticed that above the threshold for pion production a cosmic-ray proton will lose energy by pion photoproduction. Sufficiently energetic nuclei also have a limited range before facing photodissociation. The resulting mean-free-path for a proton with energy above the pion production threshold is less than a dozen Mpc, while the mean-free-path for a nucleus above the threshold for photodissociation is even shorter [153].

With the assumption that very high energy cosmic rays originate from sources more distant than this, Greisen and Zatsepin and Kuzmin predicted that there should be a maximum observed energy in the cosmic-ray spectrum. This maximum energy, known as the GZK cutoff, is usually taken to be around  $5 \times 10^{19}$  eV. Surprisingly, today there are more than 20 events observed with energies above the Greisen-Zatsepin-Kuzmin bound and may be originating from cosmological distances greater than 5 - 10 Mpc.

All known particles fail to provide any satisfactory mechanism for understanding these events, and this has led some [152, 153] to consider new strongly interacting particles with masses in the 20 to 50 GeV range with nuclear cross sections near  $10^{-3}$  barns. These particles would also fall into the category we are considering and as shown by Teplitz and Mohapatra [7], will lead to anomalous isotopes of heavy nuclei.

#### 11.3.1 The Cosmic Ray Spectrum

The term "Cosmic Rays" refers to elementary particles, nuclei, and electro-magnetic radiation of extra-terrestrial origin. These may include exotic, short-lived particles such as muons, pi-mesons or lambda baryons. In the energy range of  $10^{12} - 10^{15}$  eV, cosmic rays arriving at the edge of the Earth's atmosphere have been measured to consist of:

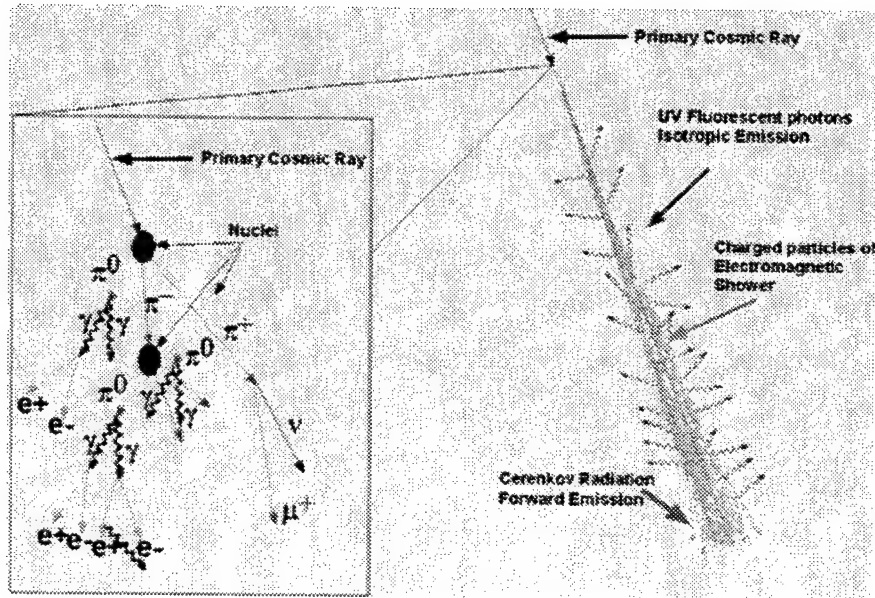


Figure 11.6: A schematic diagram of an air shower produced by a high energy cosmic ray when it hits the atmosphere.

- $\approx 50\%$  protons
- $\approx 25\%$  alpha particles
- $\approx 13\%$  C/N/O nuclei
- $< 1\%$  electrons
- $< 0.1\%$  gamma rays

Above  $10^{14}$  eV, direct observation of primary cosmic rays with balloon and satellite-born detectors becomes exceedingly difficult. As a result they are observed instead by the extensive air showers (see Figure 11.6) they produce when they interact with the atmosphere. This technique takes advantage of the fact that interaction between high-energy cosmic rays and the air produces a correlated cascade of secondary particles. The process begins with the collision of the primary cosmic ray with a nucleus near the top of the atmosphere. This first collision typically produces more than 50 secondary particles, a majority of which are pions.

The charged pions are relatively long-lived and will most probably collide with another nucleus before decaying. The subsequent collisions are similar in nature to the primary collision and this process then leads to a cascade of particles which is

referred to as a "hadronic shower." The neutral pions are very short-lived and will almost all decay into a pair of gamma rays before interacting with nuclei in the atmosphere. The photons interact with the nuclei in the air to produce electron-positron pairs, which in turn will produce photons via the "bremsstrahlung" process. This cascading process leads to the formation of an "electromagnetic shower". The hadronic shower itself is continuously producing neutral pions and thus initiating secondary electromagnetic showers along its path. For example, a cosmic ray with an energy of  $10^{14}$  eV generates an air shower which spreads charged particles over a diameter of 100 meters. At  $10^{20}$  eV the shower is even larger and can have a diameter of over 5 km. Thus, by creating large arrays of detectors which spread over a vast area, we may detect the presence of an extensive air shower. The energy of the shower can then be inferred by measuring the particle density distribution. To give a feel for the numbers involved, a  $10^{19}$  eV primary cosmic ray will produce around  $10^{10}$  charged particles at the shower maximum which usually occurs at an atmospheric depth of  $800 \text{ gm/cm}^2$  [3].

Another way that air showers are detected is by fluorescence. This technique relies on the fact that charged particles passing through the atmosphere excite nitrogen fluorescence. Even though only about 3 photons are typically produced for every meter of the charged particle track, the large number of charged particles discussed above can yield enough light to be detected by a photomultiplier more than 10 km away. It is actually the fluorescence technique which has been instrumental in analyzing the cosmic ray spectrum above  $10^{17}$  eV.

These techniques combine to give the cosmic ray spectrum (plotted in Figure 11.7) which behaves the power law  $E^{-2.7}$  up to an energy of  $5 \times 10^{15}$  and then steepens to  $E^{-3.0}$ . This kink in the spectrum is the famous knee whose energy is predicted by supernova shock acceleration in the galaxy [3]. A good review of the upper end of this spectrum is provided by James Cronin in his article, "The Highest Energy Cosmic Rays," included in the book by Bahcall and Ostriker [3]. Other useful reviews are provided in the papers by Watson [171], Rubakov [172], and the Physics Reports article by Bhattacharjee and Sigl [173].

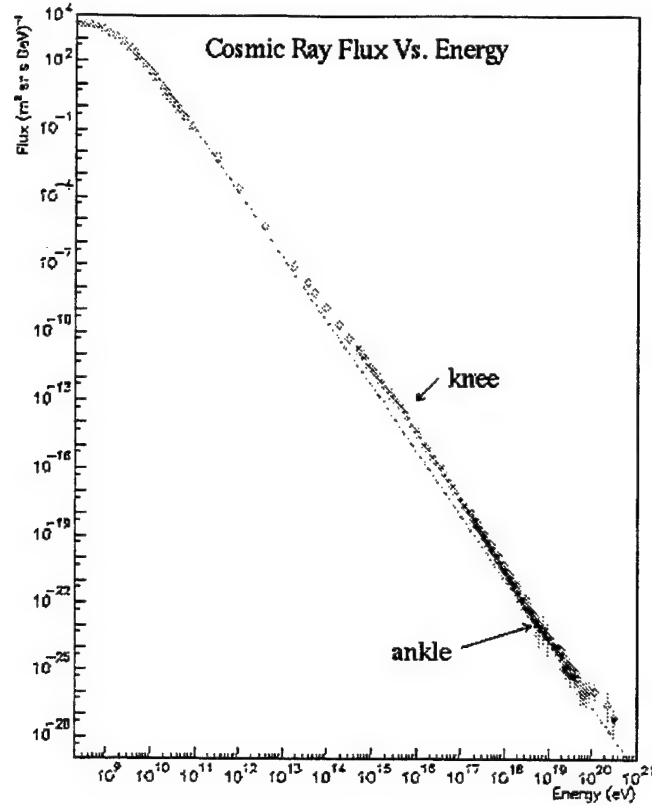


Figure 11.7: The cosmic ray energy spectrum. Remarkably, it appears to be a smooth curve over 10 decades of energy with only a few noticeable structures. The most prominent of these are small, abrupt changes in the local spectral index (the power exponent of  $\approx 3$ ) just above  $10^{15}$  eV and again just above  $10^{18}$  eV. In the figure, they appear as small “kinks” in what is otherwise a straight line. Within the Cosmic Ray field, these features are usually referred to as the “knee” and the “ankle”, respectively.

### 11.3.2 GZK Cutoff

Acceleration aside, the curious effects relevant to our experiment is in the transport of the highest energy cosmic rays. In fact, the lifetime of a high energy cosmic ray is strongly affected by the presence of the 2.7 K cosmic microwave background radiation (CBR). Cosmic protons lose energy by photo-pion production (see Figure 11.8). This occurs because the CBR photons are blue shifted by a factor of  $10^{11}$  in the rest frame of a cosmic ray with an energy of  $10^{20}$  eV. As a result several hundred MeV is available in a collision between the proton and the CBR photon. Thus a substantial fraction

of the CBR photons appear as gamma rays whose energy is above the threshold for photo-pion production

$$E_{\gamma}^{th} = m_{\pi} + \frac{m_{\pi}^2}{2m_N} \simeq 160 \text{ MeV} \quad (11.54)$$

For a background photon energy  $\varepsilon$  of  $10^{-3}$  eV the threshold energy translates into a corresponding threshold for the nucleon energy,

$$E_{th} = \frac{m_{\pi}(m_N + m_{\pi}/2)}{\varepsilon} \simeq 6.8 \times 10^{19} \quad (11.55)$$

which is often rounded to  $5 \times 10^{19}$  and is known as the GZK cutoff since it was originally theorized by Greisen [169] and Zatsepin and Kuzmin [170]. A similar mechanism exists for nuclei whose binding energies are around 8 MeV/nucleon. A high enough energy collision with a CBR photon will dissociate the nucleus.

As a result of this behavior, there exists a mean-free path for such an interaction to occur. This mean-free path is usually quoted at  $\approx 50$ – $100$  Mpc and is quite close to us in cosmological terms. Figure 11.9 is a plot of this theoretical mean-free path for three different energies and we see the rapid decrease in the energy for distances less than 50–100 Mpc. Thus, UHECRs above the GZK cutoff must either be within

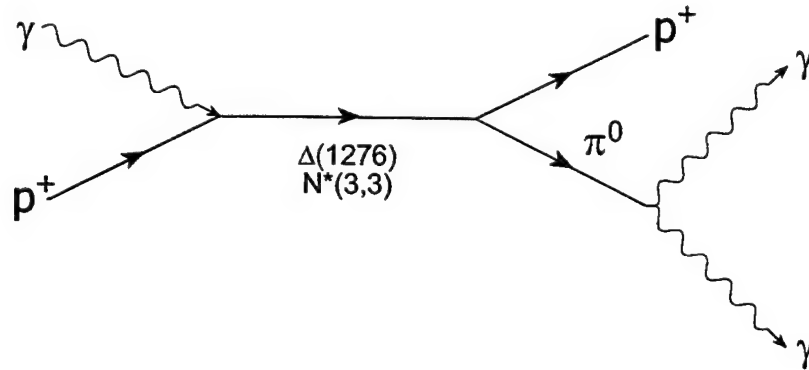


Figure 11.8: Diagram of resonant pion photo-production. It is this mechanism which dictates the famous GZK cutoff. A high energy proton collides with the 2.7 K cosmic microwave background radiation (CBR) and loses energy via this mechanism. A similar mechanism exists for nuclei whose binding energies are around 8 MeV/nucleon. A high enough energy collision with a CBR photon will dissociate the nucleus.

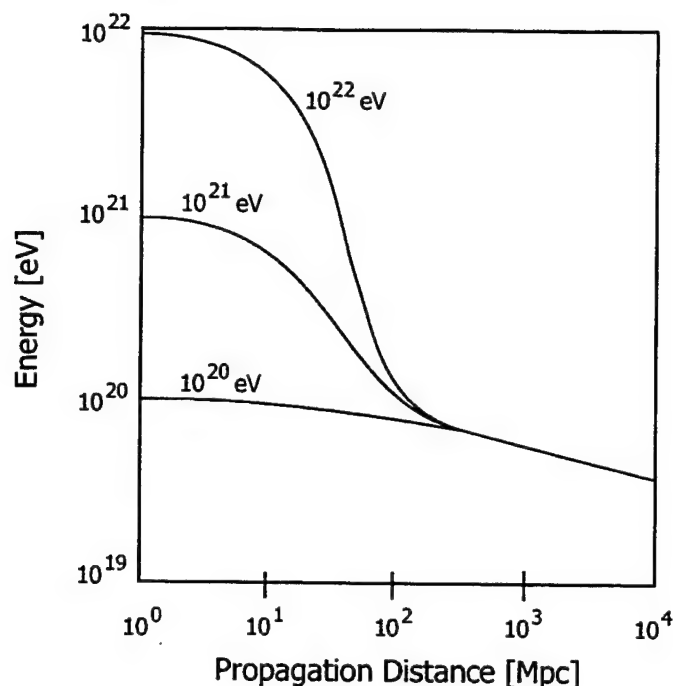


Figure 11.9: Mean energy of protons as a function of propagation distance through the 2.7 K cosmic background radiation. The three different curves correspond to three different initial energies. The sudden drop to  $10^{20}$  eV which occurs between 50–100 Mpc is the theoretically predicted GZK cutoff in action.

50 Mpc of us or not be subject to the mechanism described above. We have several confirmed events above this GZK cutoff but have no potential sources within this 50–100 Mpc sphere leading us to the puzzling result and difficulty explaining the highest energy events.

### 11.3.3 The Highest Energy Events

Several events have been recorded by different detectors. The results from these events provide a flux at  $10^{19}$  eV of roughly  $10^{-33}$ . Comparison of the data from four of the major air shower experiments is provided in Table 11.2 and they are all in close agreement with each other.

At the high end of the spectrum the data seem to suggest a deviation from the featureless power law discussed above. This behavior has been displayed in each of the different experiments but has large errors due to the lack of an adequate flux to

Table 11.2: Comparison of cosmic ray fluxes at  $10^{19}$  eV for the major air shower experiments. This data was adapted from Ref. [3].

Experiment	Flux at $10^{19}$ eV ( $\text{m}^{-2}\text{s}^{-1}\text{sr}^{-1}\text{eV}^{-1}$ )
AGASA	$3.2 \times 10^{-33}$
Fly's Eye	$2.3 \times 10^{-33}$
Haverah Park	$2.2 \times 10^{-33}$
Yakutsk	$3.4 \times 10^{-33}$

give reliable measurements. Figure 11.10 is a plot of this high end of the cosmic ray spectrum as measured by the Akeno Giant Air Shower Array (AGASA). In this figure we also see the ankle which is the observed flattening of the spectrum above  $10^{19}$  eV.

If these ultra high energy cosmic rays are protons, they will point to their source given the distance due to the GZK cutoff. If the cosmic rays are heavier and are

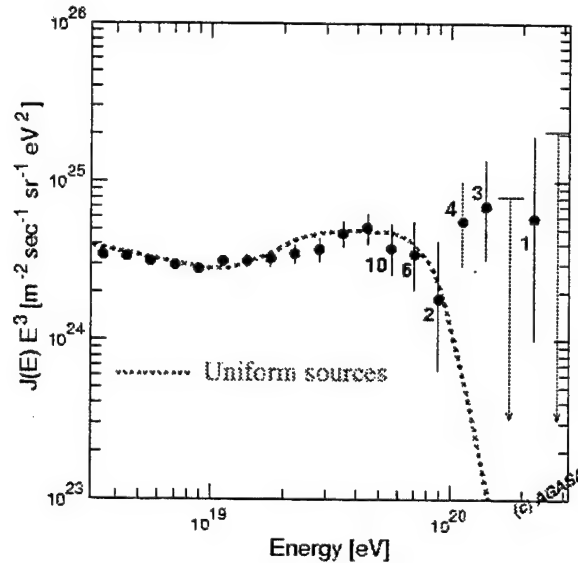


Figure 11.10: The AGASA energy spectrum multiplied by  $E^3$  in order to emphasize details of the steeply falling spectrum. The dashed curve represents the spectrum expected for extragalactic sources distributed uniformly in the Universe, taking account of the energy determination error. This figure is a version of Figure 2 of Ref. [18].

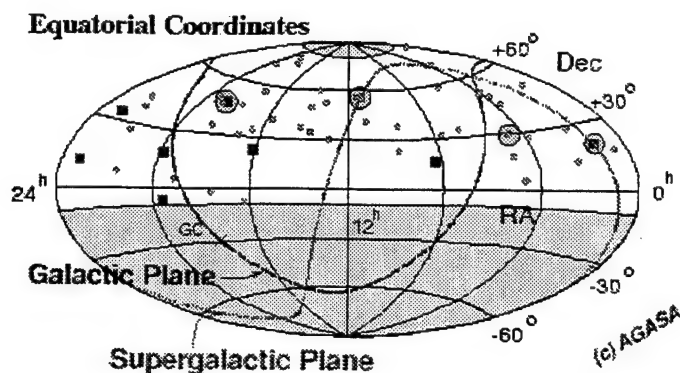


Figure 11.11: Arrival directions of cosmic rays with energies above  $4 \times 10^{19}$  eV from the AGASA experiment. The small squares and circles represent cosmic rays with energies of  $> 10^{20}$  eV, and  $(4 - 10) \times 10^{19}$  eV, respectively. Shaded circles indicate event clustering within  $2.5^\circ$ . At (11h 20m,  $57^\circ$ ), three  $4 \times 10^{19}$  eV cosmic rays are observed against expected 0.06 events. The chance probability of observing such triplet under an isotropic distribution is only 0.9% [19]. This Figure is adapted from Figure 2a of Ref. [19].

charged, they will be influenced by the galactic magnetic field. In the northern hemisphere the deflections are essentially perpendicular to the galactic plane for cosmic rays entering from the galactic anticenter. Heavy neutral particles on the other hand, like protons, will point to the source. Because of the lack of possible acceleration mechanisms within the GZK defined 100 Mpc radius in the same directions as any of the observed events (see Figure 11.11), it is unlikely that these events are from cosmic protons. One of the most attractive aspects of strongly interacting massive particles is that since they are a new elementary particle they are not subject to the GZK mechanisms for either protons or nuclei. Thus a SIMP will not have this short mean free path which rules out the aforementioned particles. Certainly the solution to this puzzle will be in the form of new physics beyond the standard model.

Thus we have observed several ultra high energy cosmic ray events whose energy is above the established GZK cutoff. Of course the sources for these high energy particles may be closer than 50 Mpc although this is highly unlikely since no mechanism exists within that distance which could produce the necessary accelerations. Thus we are left to postulate the possibility of a neutral strongly interacting relic particle which is not

subject to the electromagnetic interactions governing the GZK cutoff [152, 153]. Such a particle would also be subject to the binding discussions outlined by Mohapatra *et al.* [5] and given in the following chapter. While the acceleration mechanism for such a particle is difficult to devise one possible paradigm shift is that the high energies are not a result of an acceleration but rather a decay of an extremely massive supersymmetric particle.

#### 11.4 The Lightest Supersymmetric Particle

Recall from the discussion of Chapter 5 that we mentioned supersymmetric theories forbid processes in which a sparticle decays to normal particles only. This constraint arises from the conservation of  $R$ -parity.  $R$ -parity is defined for each particle as

$$R = (-1)^{(3B+L+2S)} \quad (11.56)$$

where  $B$ ,  $L$ , and  $S$  are the baryon number, lepton number, and spin of each particle. This works out to be a much simpler notation that all standard model particles have  $R = +1$  while their supersymmetric partners have  $R = -1$ . If  $R$ -parity is conserved it means that the decay of a massive SUSY particle must always include another SUSY particle with a smaller mass. This results in the concept of a lightest supersymmetric particle (LSP) which halts further SUSY decay. This also means that the LSP must be stable since  $R$ -parity prevents further decay.

Mafi and Raby of the Ohio State University have devised a scenario in which the gluino is the lightest SUSY particle with a mass in the range 25–35 GeV [174, 175]. This possibility has also been investigated by several different groups. Raby [144, 78] has proposed a class of SUSY models in which the gluino is the lightest supersymmetric particle (LSP), and predicts a mass range from 6.3 GeV/c<sup>2</sup> to 100 GeV/c<sup>2</sup>. In contrast, Berezhinsky and Kachelreiß [147] suggest the gluino is disfavored below 150 GeV/c<sup>2</sup> and predict a range for the gluino mass to be 150–9000 GeV/c<sup>2</sup>. Another recent interesting class of models on which strongly interacting particles may provide insight, are gauge mediated supersymmetry (SUSY) breaking models [145].

There are many compelling reasons to believe nature is supersymmetric at short distances. However, because the observed spectrum of fermions and gauge bosons

does not exhibit any trace of supersymmetry, it must be broken at a scale of greater than 100 GeV. Recently, it has been argued that to create a realistic model with broken supersymmetry we must assume the breaking takes place in a hidden sector which is completely separate from the visible sector of the standard model [143]. This effect is then transmitted to the quarks and leptons through the messenger sector.

Different classes of SUSY models may be distinguished by the way the messengers transmit supersymmetry breaking from the hidden sector to the visible one, and recent discoveries suggest the standard model gauge interactions of the messenger fields are the ones that transmit SUSY breaking to the visible sector [145]. This class of models provides a new way to understand the characteristics of supersymmetry breaking in nature and suggests SUSY breaking information is transmitted via the known forces of the standard model rather than via gravity as other models propose. This suggests the gluino rather than the photino has mass (which breaks SUSY) and is the lightest supersymmetric particle [176]. In some supergravity theories SUSY breaking in the observable sector is set by the graviton mass [144].

Clearly there are several supersymmetric models suggesting the strongly interacting gluino may be the LSP. If so it would be capable of binding to ordinary nuclei if the appropriate nuclear parameters are chosen. In each model different predictions are made with the gluino mass ranging from as low as 6 GeV to as high as 9 TeV. If the gluino is the LSP and  $R$ -parity is conserved requiring it to be stable we have a candidate for a potentially undiscovered neutral strongly interacting massive particle which could form anomalous nuclei. Failure to find such nuclei would provide significant constraints on these models.

### 11.5 Current Neutrino Results

There is another class of particle physics models motivated by recent discoveries in neutrino physics, which under certain circumstances may lead to stable strongly interacting particles. The basic idea is that if the three indications for neutrino oscillations (i.e. solar, atmospheric neutrino data, and the latest observations from the Liquid Scintillation Neutrino Detector) are accepted at face value, then one needs to postulate a fourth sterile neutrino [150] which has mass in the milli-eV range.

In order to understand its ultralightness, it has been suggested [148, 149] there may be a parallel standard model duplicating the fermion and force content of the known standard model. Since the strongly interacting sector of this model is not constrained by neutrino data, one may identify the two colors as has been done in Barr's paper [177]. In this model, weak symmetry breaking in the mirror sector can be heavier, leading to heavy mirror quarks. The lightest of these would be stable and could form bound states with known nuclei.

## 11.6 Conclusions

From this chapter we see that there are several motivations for the possible presence of SIMPs both theoretically and experimentally. This is by far not an exhaustive list of possibilities although it constitutes the largest fraction and in our opinion those which seem to produce consistent coherent predictions for the existence of SIMPs. In fact, each theory does make explicit predictions on the mass range for the SIMP each of which is given and compared in Table 11.3.

Table 11.3: Summary of predicted SIMP masses  $M_S$  for several different theories predicting its existence. For a more extensive discussion of SIMP models than that found here see Ref. [4].

Reference	Predicted SIMP Masses
Mohapatra [7]	$M_S < 100 \text{ GeV}/c^2$
Mafi [174, 175]	$25 \text{ GeV}/c^2 < M_S < 35 \text{ GeV}/c^2$
Raby [144, 78]	$6.3 \text{ GeV}/c^2 < M_S < 100 \text{ GeV}/c^2$
Berezinsky [147]	$150 \text{ GeV}/c^2 < M_S < 9 \text{ TeV}/c^2$
Albuquerque [153]	$10 \text{ GeV}/c^2 < M_S < 50 \text{ GeV}/c^2$
Starkman [4]	$3 \text{ GeV}/c^2 < M_S < 10 \text{ TeV}/c^2$

One might naturally ask how such a massive particle could have escaped detection. While each of the theories has their own explanation to this question one of the most straight forward is that the mass may be above the detection limits of current generation accelerators and be at an abundance that is so low it has escaped detection

in more conventional means. For the SIMP to be produced in a particle accelerator the coincident collision must have a center of mass energy that is greater than the mass of the SIMP. As a result, a SIMP's subsequent creation in today's particle accelerators is reliant upon the maximum center of mass energy available for the process to occur. The other problem is that of low abundances which is why AMS is perfect for the job. Since AMS can detect extremely minute quantities of material, we are able to set stringent limits on the existence of SIMPs over a broad mass range.

Finally, these theories are really all interconnected. For example, in some SUSY models the gluino is the lightest supersymmetric particle. All the superpartners then decay into several known particles and the gluino. Since this particle is a relic of the Big Bang, it could be present today with abundance levels which are too low to have been detected yet but are high enough to constitute the Dark Matter observed gravitationally in the universe. We may already have evidence for these gluinos in the form of the unexplained ultra high energy cosmic ray results. Since the gluino is strongly interacting it is possible for it to bind with known nuclei provided it follows the restrictions discussed in the preceding sections. As a result, over the last several million years gluinos have been slowly trapped by high- $Z$  nuclei in the Earth's crust. Analyzing some of those nuclei for anomalously high mass isotopes will provide us with data on this possibility. This is the basis of our experiment.

## CHAPTER 12. SEARCHING FOR SIMPS IN GOLD

### 12.1 Introduction

As with the Paronic Be experiment discussed in **PART II**, there exists a single assumption upon which the entire SIMP experiment rests. In the Be experiment we relied on the speculation that Pauli-violating beryllium would possess approximately the same chemical properties as helium. This time we have another pivotal assumption which is that SIMPs will bind to ordinary nuclei. Of course this is not an arbitrary assumption, and the details of it will be outlined shortly.

We also point out another similarity to the Paronic Be experiment. In each of the experiments we had to operate the PRIME Lab accelerator mass spectrometer in untested regions of its operational phase space. In the Be experiment we had to design and construct the new source, special cathode, and the gas manifold, but were running all of the elements of the tandem within ranges which were well understood. With the SIMP experiment we did not have to construct any additional hardware, but were operating each element to its extreme limits. As a result, several of the problems we encountered were a result of beam and operating conditions that the machine had never experienced.

### 12.2 SIMPs and Nuclei

In order to justify the statement that SIMPs will bind preferentially to high- $Z$  nuclei we must derive the relations governing its interactions with ordinary nuclei. As a model, our derivations follow closely those performed in the searches for weakly interacting massive particles (WIMPs) along with the  $\Lambda$ -hypernucleon as a guide.

Explicit discussion of the relic density for strongly interacting particles was derived by Mohapatra and Nussinov [146]. This then motivated several papers which calculated in detail the interactions of strongly interacting relic particles with ordinary matter [7, 5]. Because the relic particles are strongly interacting it was possible

to construct models that predicted bound states of SIMPs with ordinary nuclei. Although several experiments [168, 4] provided significant constraints to such binding in low- $Z$  nuclei, Mohapatra *et al.* showed that binding will not occur below a mass cut-off for ordinary nuclei. This minimum mass (denoted  $A_{min}$  for the minimum atomic number) is a function of the SIMP mass  $M_S$  (where the subscript  $S$  denotes a SIMP property). Following the discussion in Ref. [5], we find the above dependence by assuming the SIMP binding energy is given by

$$B_S = V_{SN} - \frac{\pi^2}{2\mu R^2}, \quad (12.1)$$

where  $V_{SN}$  is the average  $S - N$  potential at rest and is given by,

$$V_{SN} = V_{NN} \sqrt{\frac{\sigma_{SN}}{\sigma_{NN}}}. \quad (12.2)$$

$R$  is the size of the nucleus in which the SIMP is bound, and  $\mu$  is the reduced mass of the  $S - A$  system whose definition is

$$\frac{1}{\mu} = \frac{1}{M_A} + \frac{1}{M_S}. \quad (12.3)$$

If we make the assumption that the density of the nuclear matter is constant, then the volume of the nucleus will be directly proportional to the number of nucleons  $A$  in it. For spherical symmetry we have  $V = \left(\frac{4}{3}\pi r_0^3\right) A$  giving the usual relationship for the nuclear radius

$$R = r_0 A^{1/3}, \quad (12.4)$$

where  $r_0$  is usually taken to be  $1.4 \times 10^{-15}$  meters. Inserting these definitions into Eq. (12.1) gives us the relation

$$B_S = V_{NN} \sqrt{\frac{\sigma_{SN}}{\sigma_{NN}}} - \frac{\pi^2}{2r_0^2 A^{2/3}} \left[ \frac{1}{M_A} + \frac{1}{M_S} \right] \quad (12.5)$$

If we then assume that  $B_S \ll V_{SN}$ ,  $V_{NN} \simeq 50$  MeV, and that the low energy  $N - N$  scattering cross section  $\sigma_{NN}$  is on the order of 1 barn, we obtain the following functional form for  $A_{min}$

$$A_{min} = \left[ \frac{2 \text{ GeV}}{\sqrt{\sigma_{SN}}} \left( \frac{1}{M_A} + \frac{1}{M_S} \right) \right]^{3/2} \quad (12.6)$$

which is a function of both the SIMP mass  $M_S$  and the  $S - N$  interaction cross section. However noticing that  $M_A = Zm_P + Nm_N \simeq Am_P$  means that this is a transcendental equation. We consider two different functional forms for  $\sigma_{SN}$

$$(1) \sigma_{S\bar{S}} \simeq \frac{1}{M_S^2} \Rightarrow \sigma_{SN} \simeq \frac{0.4 \text{ mb}}{M_S \text{ GeV}}, \quad (12.7)$$

$$(2) \sigma_{SN} \simeq 0.1 \sigma_{\pi N} \simeq 2 \text{ mb},$$

where we have used the approximate factorization hypothesis introduced by Mohapatra and Teplitz [7]

$$\beta \sigma_{S\bar{S}} \sigma_{NN} \simeq \sigma_{SN}^2 \quad (12.8)$$

with  $\beta \sim 1$ . These two functional forms for  $\sigma_{SN}$  were summarized in Ref. [5]: (1) was introduced by Mohapatra and Nussinov [143] and utilized in greater detail by Mohapatra and Teplitz [7] and (2) was estimated in Refs. [152, 153]. The functional dependence of  $A_{min}$  on the SIMP mass  $M_X$  for these two different cross sections is given in Figure 12.1.

The expected fraction of SIMPs captured by gold,  $f_{Au}$ , depends on  $A_M$  which is the most abundant element in the Earth's crust with a nucleus heavier than  $A_{min}$ . This fraction is given by

$$f_{Au} = \frac{C_{Au}}{C_M} \left( \frac{A_M}{A_{Au}} \right)^{1/3}, \quad (12.9)$$

where the  $C$ 's are the concentrations by weight in the Earth's crust. The values for  $A_M$  and  $C_M$  for different ranges of  $A_{min}$  are provided in Table 12.1.

As alluded to above, the SIMPs bind to gold nuclei forming a new anomalously massive isotope of  $^{79}\text{Au}$  denoted by  $^{79}X$  with mass  $M_X$ . The resulting SIMP number density  $n_S$  is then calculated from the experimentally determined fraction of anomalous gold (nuclei that captured a SIMP) to ordinary gold,  $X/Au$ , which is a function of the SIMP mass. We thus arrive at the following relationship

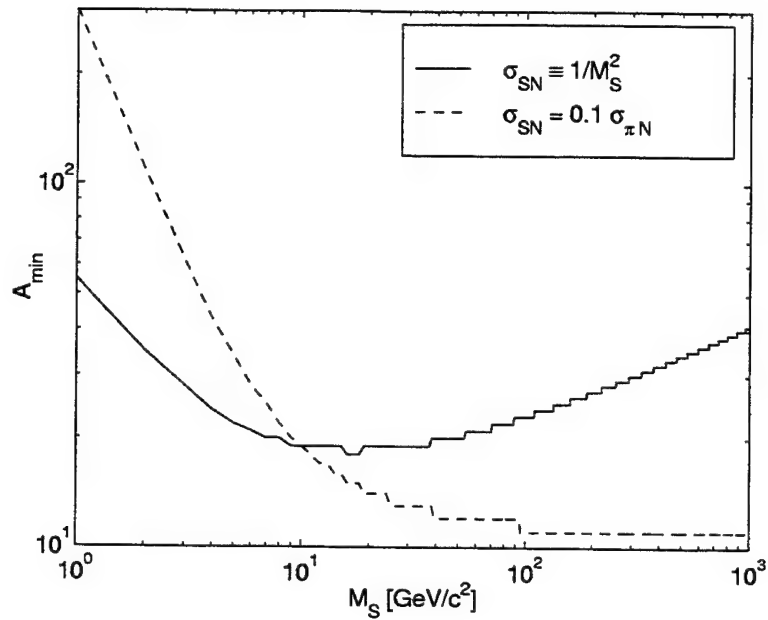


Figure 12.1: The results of solving Equation (12.6) for the two different functional forms of  $\sigma_{SN}$  discussed in the text (provided in Equation (12.7)). The lines are not continuous but jagged because  $A$  is an integer.

$$n_S = \frac{1}{vt} \frac{N_{Au}}{f_{Au}} \left( \frac{X}{Au} \right), \quad (12.10)$$

where  $v$  is the galactic virial velocity (300 km/sec),  $t$  is the exposure time, and  $N_{Au}$  is the number of Au nuclei (per  $\text{cm}^2$ ) in the stopping length  $\lambda_S$  of the SIMP. This stopping length is given by

$$N_{Au} = \lambda_S \frac{\rho_E}{m_{nuc}} \frac{C_{Au}}{A_{Au}}, \quad (12.11)$$

where  $\rho_E$  is the density of the Earth's crust and  $m_{nuc}$  is the mass of an ordinary nucleon ( $m_{nuc} = (m_p + m_n)/2$ ). The stopping length  $\lambda_S$  is taken to be

$$\lambda_S = \frac{\tilde{A}^{1/3} m_{nuc}}{\rho_E \sigma_{SN} \left[ 1 - \left( \frac{M_S}{M_S + A m_{nuc}} \right)^2 \right]}, \quad (12.12)$$

Table 12.1: Abundances of the most abundant nuclei in the Earth’s crust as a function of  $A_{min}$ . This is a reproduction of Table I of Ref. [5].

Range of $A_{min}$	Element	$A_M$	$C_M$ in ( $\mu\text{g/g}$ )
$A_{min} \leq 20$	Ne	20	$5 \times 10^5$
$20 \leq A_{min} \leq 26$	Al	26	$8.3 \times 10^4$
$26 \leq A_{min} \leq 137$	Ba	137	425
$137 \leq A_{min} \leq 207$	Pb	207	12.5

where  $\tilde{A} \sim 20$  is the  $A$  of an “average nucleus,” and we assume that  $S - A$  scattering in the center of mass is isotropic. Putting these definitions into Equation (12.10) gives

$$n_S = \frac{1}{vt} \left( \frac{C_M \tilde{A}^{1/3}}{\sigma_{SN} A_M^{1/3} A_{Au}^{2/3} \left[ 1 - \left( \frac{M_S}{M_S + \tilde{A} m_{nuc}} \right)^2 \right]} \right) \left( \frac{X}{Au} \right). \quad (12.13)$$

This equation can then be used to define the density as  $\rho_{SIMP} = n_S M_S$  so that the SIMP contribution to the cosmological density parameter discussed in the previous chapter becomes

$$\begin{aligned} \Omega_{SIMP} &= \frac{\rho_{SIMP}}{\rho_c} \\ &= \frac{n_S M_S}{\rho_c}. \end{aligned} \quad (12.14)$$

In future chapters we will discuss how the results from our experiment constrain the cosmological density parameter. What is important is that there exists a minimum nuclear mass for which SIMP-nucleon binding is possible and which is dependent on the SIMP mass,  $M_S$ . Again we point the reader to Figure 12.1 to see this relationship for two different likely forms for the interaction cross-section  $\sigma_{SN}$ .

### 12.3 Previous Experiments

While experiments performed by Middleton *et al.* [178] and Hemmick *et al.* [168] set stringent constraints on the existence of SIMPs when bound to low- $Z$  nuclei,

no experiments have been performed on high- $Z$  nuclei. The preceding arguments (originally put forth by Mohapatra *et al.* [5]) suggest that binding is more likely in the more massive high- $Z$  nuclei than in low- $Z$  nuclei. In short this is due to the Heisenberg uncertainty principle, since there is less kinetic energy for the SIMP in the high- $Z$  nucleus which creates a larger potential well. If their strong interaction parameters are chosen correctly, namely the interaction cross-section, SIMPs may exist despite the existence of significant previous constraints [178, 168, 142, 141, 7].

#### 12.4 Principle of the Experiment

As a result of the derivation provided in the preceding sections we postulate that SIMPs may manifest themselves as heavy isotopes of common heavy nuclei such as gold or uranium. The accelerator is well suited for such purposes, and we thus look for anomalously heavy isotopes of gold. Since gold readily forms negative ions, and has little isotope interference, we have chosen it as our first sample. We begin by accelerating negative gold ions,  $\text{Au}^-$ , which are readily produced by our ion source.

The gold samples are placed in normal copper cathodes attached to a wheel, which allows each sample in turn to be rotated into the path of the  $\text{Cs}^+$  beam. The accelerator is then tuned to select for a particular mass, and after all samples are counted at this mass for 1 minute the injector magnetic field is increased, while the terminal voltage and the electric fields in the electrostatic analyzer and high energy electrostatic quadrupoles are decreased, to select for the next isotope mass. As a result the fields in the analyzing magnets following the accelerator are held constant at their maximum values and the mass is selected by lowering the ion energy.

As discussed in Chapter 1, all magnetic components of the AMS select for a particle with a predetermined value of  $ME/q^2$ , while electrostatic components select for  $E/q$ , where  $M$ ,  $E$ , and  $q$  are the ion mass, energy, and charge respectively. It then follows that the combination of the magnetic and electric components selects particles on the basis of  $M/q$ , so that all particles with (approximately) the same  $M/q$  will reach the detector. This observation allows us to use atomic or molecular ions in appropriate charge states as "guide beams" to tune the optics of the AMS. For example, gold ( $M = 197$  u) in charge state  $q = +5$  would be a guide beam to test the tune of the AMS at  $M_X = 276$  u running at charge state  $q = +7$ . Since

each Au beam has a different total energy, we can distinguish the guide beams from any anomalously heavy gold nuclei by using the energy measurements made by the detector.

Using only one charge state we are limited in the mass range that we can cover during a mass scan. This limitation arises because of several competing constraints which affect the detection of potential SIMPs. First, we have the limitation imposed by a minimum terminal voltage (roughly 0.9 MV) which can be effectively controlled. Although lower voltages may be obtained by running only one chain or dropping the charge to zero, we do not have the corona current or balance that is necessary for GVM control. As a result we see large fluctuations in the terminal voltage. This problem could partially be solved if we could somehow extend the corona points past their maximum of 32 inches, but we would then run the risk of contact with the terminal, and this could cause more problems than such a modification would be worth. The other competing constraint is that of the detector window.

The gas ionization detector functions based on the electrons knocked off the propane gas inside<sup>1</sup>. Since the beamline is held at a low vacuum, a window at the entrance to the detector is necessary to contain the propane within the detector while still allowing for the vacuum on the other side. For normal AMS operations this is not a problem since beam energies are typically on the order of 50 MeV. In our experiment, at the initial stages of the scan the energies are in this same range and the energy lost as the ion traverses the window is insignificant when compared with the total energy of the beam. However, in order to increase the mass and hold  $ME/q^2$  constant the energy must be reduced. As a result, as the mass increases the energy decreases and approaches the critical energy such that the window (which is made of polyethylene terephthalate,  $H_8C_{10}O_4$ , commonly called mylar) removes a substantial fraction of the ion's energy. In fact, an incident beam of particles may be stopped given enough target material. This stopping range is generally much lower than typical beam energies, and usually has the characteristic of simply degrading the beam energy and spreading out the beam's energy peak in the detector. In our experiment, however, the energy may drop lower than that required to stop the incident beam

<sup>1</sup>See Chapter 1 for more information on the detector and other accelerator elements.

and we could have a very high concentration of ions hitting the window, but with insufficient energy to penetrate into the detector. Thus our mass scan is limited by the lowest beam energy that can reliably penetrate into the detector. One solution to this problem would be to find a thinner window while another would be to find a way to increase the beam energy for a given mass while still holding  $ME/q^2$  constant.

Since our limiting factor in each run was the window constraint, we purchased the thinnest window that is manufactured. The new window was made of Ultra-Polyester and was 1.5 microns ( $\mu\text{m}$ ) thick and was 1 micron thinner than the 2.5 micron window used in normal AMS operations. However, this window was never run since testing would have required a substantial amount of development when time was not a luxury. As a result, we found another way to overcome this obstacle. This is accomplished by running at a higher charge state. Of course this was not without its drawbacks, since higher charge states produce lower stripper yields and reduced sensitivity. In the end a method of charge state optimization (called the variational charge state method) was designed to maximize the yield at a particular mass setting while still maintaining a beam energy above that of the window penetration. Before presenting our results we will discuss our unique samples.

## CHAPTER 13. AU SAMPLES

### 13.1 Introduction

As in the search for paronic beryllium, we have obtained a number of unique samples which add to the novelty of this experiment. In addition to ordinary reagent (lab) gold which we utilized for all our tuning and testing of the tandem, we have a range of different sample types, each with a unique history of cosmic ray or other exotic exposures.

### 13.2 Geological Samples

In an effort to analyze gold with even longer galactic cosmic ray exposure times, we have obtained gold nuggets from a variety of geological regions around the Earth. In the following pages we will outline the characteristics of the different samples. As a reference please use Figure 13.1 to compare the different nuggets found in the various regions. Before proceeding to discuss the samples themselves we present a more quantitative evaluation of the surface residency provided for each of the samples.

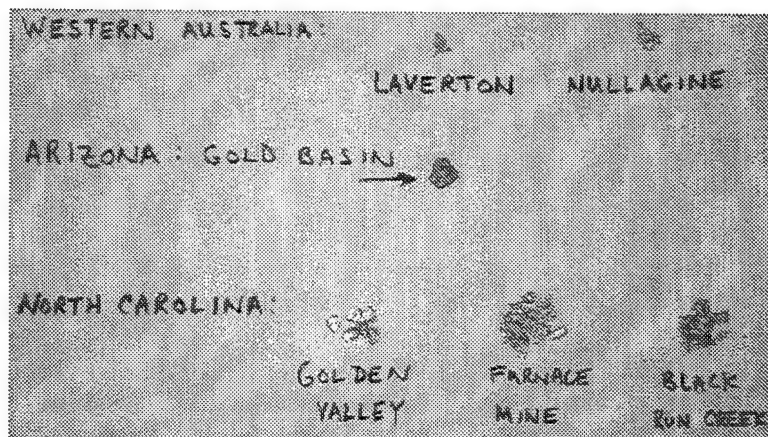


Figure 13.1: A picture taken of the different geological samples run in our experiment. The largest single nugget was the sample from Arizona.

### 13.2.1 Near-Surface Residency of Au

Dr. Doug Oliver of the Southern Methodist University in Dallas, TX not only obtained the geological samples but was also responsible for estimating their near-surface residencies. We are deeply indebted to him for his efforts and willingness to accommodate us in this regard.

#### The Criteria for Near-Surface Residency

To begin with, the occurrence of gold at the lithosphere/atmosphere interface is a transient condition and does not guarantee long near-surface residency<sup>1</sup>. This is because the majority of the earth's surface undergoes either erosion or deposition<sup>2</sup> and as a result bedrock is either being exhumed or buried. For those areas undergoing exhumation, surface exposure times are typically short. Bedrock brought to the Earth's surface by weathering and erosion tends to be either physically or chemically removed [179]. However, in rare instances exhumed material can be left behind. Material properties favoring such *in situ* (on location) increases in concentration are high specific gravity<sup>3</sup>, physical durability and resistance to chemical weathering. These are all properties that typically characterize gold and are one of the factors which lead to the use of gold for this experiment. Materials with these properties are either retained in the soil overlying the bedrock that originally contained them, or are partially transported as particles and concentrated in active stream channels – so-called placer deposits. The potential for materials with these properties to have long near-surface residency times (measured in thousands or millions of years) is quite good [179].

The factor most affecting the duration of near-surface residency is the erosion rate [179]. High erosion rates cause the rapid exhumation of gold contained in the bedrock. However, this gold tends to be physically removed or quickly re-buried and is unlikely to reside close to the surface for any significant length of time. The reverse is true for areas where low erosion rates equate to slower exhumation. Gold in such areas is more likely to be concentrated in the soil or in placer deposits. Low erosion

<sup>1</sup>In general, the earth may be divided into three major parts: the solid earth or lithosphere; the water portion called the hydrosphere; and the earth's gaseous envelope, the atmosphere [2].

<sup>2</sup>Deposition occurs when sediment accumulates over bedrock or underlying sediment.

<sup>3</sup>The specific gravity of a mineral is the ratio of its weight to the weight of an equal volume of water [139].

rates also make it less likely that the gold will be re-buried, and will increase the time spent in the near-surface bedrock prior to exhumation [139, 179].

Key factors influencing erosion rates include:

1. *Climate* - Precipitation affects both the erosion and transportation of particulate matter as well as the rate of near-surface chemical weathering. In general, areas with low annual precipitation experience lower erosion rates than areas with abundant rainfall [139]. Deserts, which are defined as areas receiving less than 250 mm of precipitation per year, typically have very low erosion rates. Several factors determine where deserts form although latitude is the most important since subsiding air masses at 30° N and 30° S are the primary cause for many of the Earth's most extensive deserts [2, 139]. Since desert erosion rates are typically quite low they are good places to look for materials with long near-surface residency times [179].

In contrast, glaciers cause some of the highest erosion rates observed on Earth. Glaciers are currently restricted to mountainous regions and/or high latitudes. However, during the Ice Age glaciers covered broad areas in the mid-latitudes in North America and around the world [139]. Gold contained in soils or active stream channels of regions covered by glaciers during the Ice Age experienced rapid erosion and are unlikely to have long near-surface residency times [179].

As a result it is important to try to understand to what extent the present climate may be used as a basis for understanding past climatic uncertainties. Paleoclimatic data suggest that the key features of the Earth's present climate date back only 12,000 years ago to when the Ice Age ended. Excluding the tropics, this involved all of the Earth's climatic zones, with the mid-latitude regions particularly affected [139]. Precipitation in mid-latitude regions during the Ice Age was much more abundant relative to the present and many of today's deserts were forested. Climate changes associated with the encroachment of deserts are particularly rapid and significant climate changes are possible even over relatively short time periods ( $\approx 1,000$  years). Finally, plate tectonics can result in long-term ( $\approx 10,000,000$  years) climate changes as continents drift

across climate zones. As an example, the northward drift of Australia is the primary factor responsible for its transformation to the present continent-wide desert from the cool, temperate forest that existed when Australia was closer to the South Pole [139, 179].

2. *Topography* - Running water is the principle agent of erosion and material transport on Earth (even in deserts where it is often incorrectly assumed that wind is primarily responsible for erosion) [139]. Ice is the primary agent only in glaciated regions and wind is a secondary factor in all but the most severe deserts. The effectiveness of running water as an erosive agent is a function of the water velocity which is directly related to the stream gradient. In general, areas with subdued topography have slower erosion rates than areas with strong relief<sup>4</sup>. Because precipitation is often also more abundant in mountainous areas, this also increases the erosion rates in those areas. For these reasons, surficial material in areas with flat topography tend to have much longer near-surface residency times than in mountainous regions [179].

Topography uncertainties involve the possibility of sequential reburial of surficial materials. Sediments in mountainous areas are quickly removed because there is no place to store them for extended periods of time. In contrast, temporary redeposition of eroded sediments is more likely in areas with subdued topography. For example, dune fields in desert regions can migrate and bury surficial materials making it difficult or impossible to quantify the extent to which local redeposition of sediments has affected near-surface residency times [139, 179].

3. *Tectonics* - Plate tectonics renew topography by providing structural uplift. Unless there is a mechanism like this which may rejuvenate the topography, erosion will flatten even mountainous areas. Tectonics can even be passive like the isostatic rebound<sup>5</sup> of the crust induced by erosion. More typically, though,

<sup>4</sup>Relief is the difference in elevation between high and low points in a region [139].

<sup>5</sup>Like a ship in water, the Earth's crust sinks into the mantle. As a result, heavily loaded crust (like that below a mountain range) will sink deeper into the mantle. If there is widespread erosion causes unloading of the crust it will respond by rising upward until equilibrium is again attained. This

tectonics involve active plate boundaries such as convergent boundaries in the Andes, Japan, and Indonesia, divergent boundaries like those found in the Red Sea and East Africa, or transform boundaries<sup>6</sup> like the famous San Andreas Fault [139, 179].

Tectonically inactive areas typically have lower erosion rates and longer near-surface residencies. In contrast, the higher erosion rates found in tectonically active regions suggest shorter near-surface residency times [179].

### Estimation of Near-Surface Residency

Since the actual penetration depth of SIMPs is heavily model dependent, we have chosen to represent three distinct ages for a gold nugget. First, we represent the approximate time it spent in the top meter of the surface. This calculated age follows from simple estimates involving erosion rates for the region of interest. These rates are subject to the elaborate discussion of the preceding section which gives some support for why rates may show large variability even within a single region. This seemingly simplistic method of determining surface residency times is used regularly to provide reliable approximations to the actual values [180]. We also are making the rather common assumption that the soil layer of material is roughly one meter thick which allows us to directly apply the more rigorously determined erosion rates for each region (a concise summary of representative erosion rates for several different regions is provided by Granger, Fabel, and Palmer [181]).

We also introduce the age of mineralization, which often times results in the Au forming in quartz deposits. Finally, we estimate the age of nucleosynthesis as an upper bound on the age of an Au sample. This is set at a value larger than the estimated age of the Earth (which is usually quoted at roughly  $4.54 \pm 0.04$  billion years ago [182]), and instead the estimated age at which the first heavy elements formed and is taken to be around 10 billion years ago, since most authors postulate that such elements formed between 8.6 and 15.7 billion years ago [182].

---

phenomenon is known as *isostatic rebound* [139].

<sup>6</sup>The tectonic plate boundaries are characterized by the motion of the two plates relative to each other. Convergent and divergent boundaries are ones in which the plates collide or separate respectively, whereas a transform boundary exists then the plates slide past each other [139]. Of course all these definitions may be found in any basic geology textbook.

### 13.2.2 Western Australia

Our oldest near surface samples come from two different areas of the Leanora District of western Australia (Laverton and Nullagine). Laverton (Lat:  $28^{\circ} 37.5' \text{ S}$ , Long:  $122^{\circ} 24.0' \text{ E}$ ) and Nullagine (Lat:  $28^{\circ} 53.2' \text{ S}$ , Long:  $122^{\circ} 19.8' \text{ E}$ ) are from an epithermal vein/submarine hydrothermal vent deposit. Hydrothermal vents occur near spreading ridges where seawater seeps down into the oceanic crust through cracks and fissures. The seawater is then heated to as much as  $400^{\circ} \text{ C}$  by the hot rocks. The water then reacts with the crust and is transformed into a metal bearing solution. As it rises rapidly to the seafloor it cools precipitating out the minerals it transported from deeper in the crust and creating chimney-like vent [139].

These nuggets were found in the upper few centimeters of soil with a metal detector. Both of the above locations are within the Yilgarn block of Archean age and are characterized by low relief with playa lakes and poorly defined drainage. Although the sample sites are on the western edge of the Great Victorian Desert, the sample areas do not contain sand dunes. This region of Australia is tectonically inactive with a rift margin at approximately 150 My. Because of its arid climate, low topographic relief, and tectonic quiescence, samples from western Australia have one of the longest near-surface exposures of any gold on Earth. The age of mineralization of these samples has been estimated at 3 Gy. The data supporting the mean near-surface residency are provided in Table 13.1 and excludes any time spent at the seawater/sediment interface following initial gold deposition. Alternatively, it discounts any possible re-burial by sand dunes or playa lake sediments.

Of all our samples, Laverton has been run the most number of times and is the subject of our first SIMP paper on our results [184]. Since AMS requires only a small quantity of each sample we were able to save quantities for later runs. The quantities of each Au sample for each Run are given in Table 13.2. A new Laverton sample needed to be created for Run Au5 while inspection of the Nullagine sample did not so we were able to spare the Australian samples from further destruction by re-running the Nullagine sample. Since gold is quite malleable we were able to simply re-pound the same cathode so that the outlying gold that was missed by the Cs was pushed into the Cs sputter hole from the previous run. As is evident from the table we still

Table 13.1: Relevant estimated ages for Nullagine and Laverton gold nuggets. Three different ages are presented since the actual penetration depth of SIMPs is model dependent. For models in which a SIMP stops in the soil layer of material near the surface the surface age would apply. In contrast, models for which the SIMP penetration depth is much larger than the Earth's crust prompt use of the age of mineralization or even the Au formation from nucleosynthesis.

Type	Assumed Erosion Rate	Age
Surface (within top meter)	0.8 m/My [183]	1.25 My
Mineralization		3 Gy
Formation		10 Gy

have 0.7395 grams of the Laverton sample and 0.8887 grams of the Nullagine sample which we may decide to run at a future time in some other experiment of this genre.

Table 13.2: Masses of the Australia samples by run.

Sample	Run	Mass [gm]
Laverton	Total	$0.9385 \pm 0.0001$
	Au4	$0.1106 \pm 0.0001$
	Au5	$0.0884 \pm 0.0001$
Nullagine	Total	$1.0777 \pm 0.0001$
	Au4	$0.1890 \pm 0.0001$
	Au5	Same Cathode

### 13.2.3 Arizona

Similarly we have obtained a sample from the Mineral Park District of northwestern Arizona (Gold Basin) that was also found using metal detectors. The nugget was found in the upper few centimeters of the soil and was on the crest of a small hill. The sample includes vein quartz indicating that it was not transported. The sample's discovery location (Lat:  $35^{\circ} 47.2'$  N, Long:  $114^{\circ} 10.7'$  W) was in the transition region from the tectonically active Basin and Range to the inactive Colorado Plateau. This

sample came from an epithermal vein type gold deposit in a region with moderate topographic relief. Epithermal gold deposits form in hydrothermal systems related to volcanic activity. These systems, while active, discharge to the surface as hot springs or via gas vents called fumaroles. Epithermal gold deposits (see Figure 13.2) occur largely in volcano-plutonic arcs (island arcs as well as continental arcs) associated with subduction zones, with ages similar to those of volcanism. The deposits form at shallow depth, < 1 km, and are hosted mainly by volcanic rocks [139].

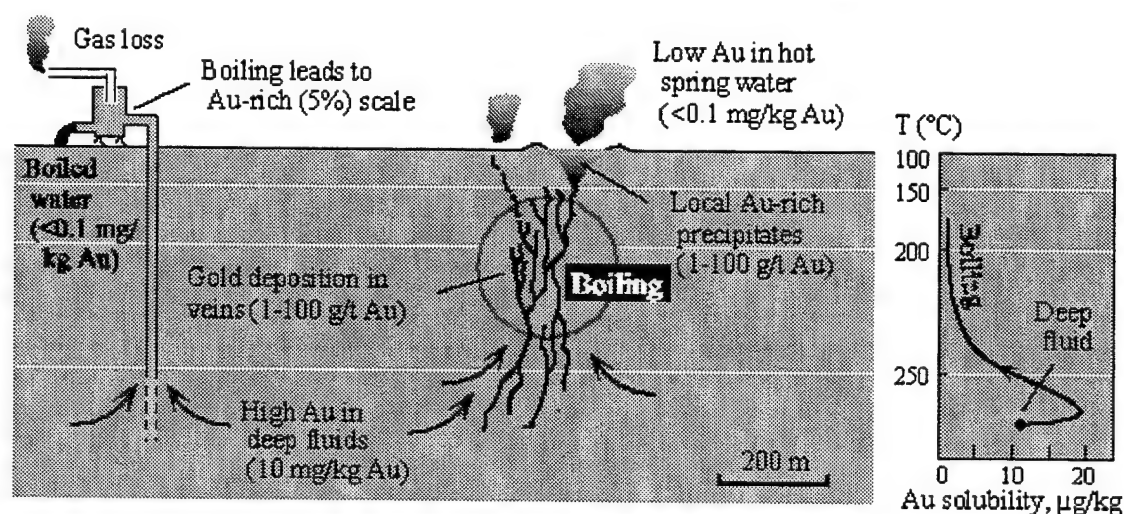


Figure 13.2: Boiling of the deep liquid during ascent causes gold to precipitate in quartz veins, potentially forming a low sulfidation epithermal gold deposit.

The climate in this region is semi-arid and has approximately 8 inches of annual precipitation. This region of the southwest United States is considered a semi-active tectonic region, with an age of mineralization estimated at 100 My. The final data for this sample are given in Table 13.3.

Compared to the Australian samples, the Arizona one, as with all North American samples, is likely to have a much shorter near-surface residency. However, this is probably the best that can be expected from North America and reflects both the recent tectonic activity and high rates of erosion.

Like the Nullagine sample, the Arizona sample was quite large (at  $1.4300 \pm 0.0001$  grams). In order to make the sample for run Au4 we removed a  $0.3767 \pm 0.0001$  gram

Table 13.3: Relevant estimated ages for Arizona gold nugget. Three different ages are presented since the actual penetration depth of SIMPs is model dependent. For models in which a SIMP stops in the soil layer of material near the surface the surface age would apply. In contrast, models for which the SIMP penetration depth is much larger than the Earth's crust prompt use of the age of mineralization or even the Au formation from nucleosynthesis.

Type	Assumed erosion rate	Age
Surface (within top meter)	2.5 m/My [179]	0.4 My
Mineralization		100 My
Formation		10 Gy

chunk of the nugget. Following the completion of Au4 we noticed that very little of the nugget had been consumed and we were able to reuse the sample for our final run Au5, thus conserving the sample for future use. As a result we still have 1.0533 grams of the sample left.

One other point to note is that the AZ nugget has a dirty appearance. This apparent abundance of contaminants was later confirmed by the observation of many contaminating peaks in the total energy spectra. In fact the contamination in the AZ sample helped to confirm our tune, since whenever an interference guide beam was going to come through we could always rely on the AZ sample to produce the largest contaminating beam of all the samples.

#### 13.2.4 North Carolina

Three samples have also been collected from streams in western North Carolina. The samples were recovered during placer mining from Monkey Bottom/Furnace Mine, Golden Valley/McDowell City, and Black Run Creek, all of which were extracted from (Lat: 35° 47' N, Long: 82° 20' W). The samples range from fine to course gold nuggets which were recovered within the active or recent stream channels. These streams drain disseminated gold deposits that were formed about 570 million years ago. The deposits were subsequently buried but were since exposed after the Appalachian Mountains formed about 300 million years ago. The region to-

Table 13.4: Relevant estimated ages for the North Carolina gold samples. The samples were recovered during placer mining of Monkey Bottom/Furnace Mine, Golden Valley/McDowell City, and Black Run Creek. Three different ages are presented since the actual penetration depth of SIMPs is model dependent. For models in which a SIMP stops in the soil layer of material near the surface the surface age would apply. In contrast, models for which the SIMP penetration depth is much larger than the Earth's crust prompt use of the age of mineralization or even the Au formation from nucleosynthesis.

Type	Assumed erosion rate	Age
Surface (within top meter)	6.25 m/My [185]	0.2 My
Mineralization		570 My
Formation		10 Gy

pography is classified as moderate relief with a climate which receives approximately 45 inches of precipitation annually. As a positive note, the rates of erosion are low in the Appalachian foothills since they are tectonically quiet and were south of the glaciated area affected by the Ice Age. The disseminated gold deposits formed on the seafloor and occur within the Piedmont (foothills) of the southern Appalachians. The intense chemical weathering of the southeast tends to concentrate gold in soil, although erosion has removed the particulate gold and reconcentrated it into placer deposits. The gold comes from an active placer submarine hydrothermal vent deposit with an age of mineralization of 570 My. The data supporting the mean near-surface residency are provided in Table 13.4 and excludes any time spent at the seawater/sediment interface following initial gold deposition. Alternatively, episodic burial of the gold in the active stream channels is also discounted.

As with the other samples discussed above, we measured the masses of the North Carolina samples. Since these samples were not in the convenient nugget form that we had with the previous samples, the table reflects this information. First the Monkey Bottom/Furnace Mine sample was not created into a sample and was never run (see

Table 13.5: Masses of the North Carolina samples by run.

Sample		Mass [gm]
Golden Valley	Nugget 1	$0.3818 \pm 0.0001$
	Nugget 2	$0.2990 \pm 0.0001$
	Nugget 3	$0.2543 \pm 0.0001$
	Nugget 4	$0.2292 \pm 0.0001$
	Nugget 5	$0.2247 \pm 0.0001$
	Nugget 6	$0.1791 \pm 0.0001$
	Total	$1.5681 \pm 0.0001$
	Au4	$0.3811 \pm 0.0001$
	Au5	$0.1951 \pm 0.0001$
Black Run Creek	Nugget 1	$0.5940 \pm 0.0001$
	Nugget 2	$0.3692 \pm 0.0001$
	Nugget 3	$0.3580 \pm 0.0001$
	Nugget 4	$0.1264 \pm 0.0001$
	Total	$1.4476 \pm 0.0001$
	Au4	$0.3774 \pm 0.0001$
Furnace Mine	Nugget 1	$0.9113 \pm 0.0001$
	Nugget 2	$0.1950 \pm 0.0001$
	Nugget 3	$0.1491 \pm 0.0001$
	Nugget 4	$0.1323 \pm 0.0001$
	Nugget 5	$0.1042 \pm 0.0001$
	Nugget 4	$0.0829 \pm 0.0001$
	Total	$1.5830 \pm 0.0001$

Table 13.5). This was because of the difficulty in packing this sample into the copper cathodes.

In AMS we usually deal with samples that are in their powder form, so packing them into the copper cathode comes at relatively little effort. However, packing a nugget (which is metal) into metal cathode with smooth surfaces can be difficult. For

the nuggets described above, we were able to countersink the cathode causing a lip on the interior edge of the sample area. For a relatively rough nugget pounding it into the cathode allows a few of its edges to catch on this lip causing it to remain in the cathode. With the Golden Valley/McDowell City and Black Run Creek samples the nuggets were small enough that when we pounded them together in this counter-sunk cathode they could grab onto the ledge. While the Furnace Mine sample had several decent sized nuggets they were all very smooth and would not grab onto the lip. Since we already had two NC samples which were packing well, we decided to simply omit it from Run Au4. In Au5 we were pressed for time and as a result chose to run only the Golden Valley sample in order to decrease run times.

### **General Remarks**

Of the geological samples, those from Australia clearly have the longest near-surface residency. The hardest data to quantify are the erosion rates and the amount of gold initially lost to erosion, and have subsequent losses thereafter are of secondary concern. Australia's numbers are considerably lower than the other continents because of the arid climate and lack of topography.

The large standard deviations reflect the range of ages for the gold in any residual concentrate. The only way for us to get around this would be to either run a large number of samples or a homogenized composite sample.

While the model for estimating the near-surface residency discussed above is fairly simplistic, trying to make it more complex would undoubtedly run into the limitations of the geologic data. In each case the model was run for 100 time intervals, and the inputs are all based on current conditions instead of reflecting the climate over the past 10 million years.

### **13.3 Exotic Samples**

While our geological samples provide us with gold found near the Earth's surface with long cosmic ray exposure time we have also obtained a number of exotic samples that complete the collection. These samples give us long exposure times under unique conditions.

### 13.3.1 NASA's Long Duration Exposure Facility

Dr. Friedrich Hörz from NASA's Johnson Spaceflight Center has graciously provided samples which flew on the Long Duration Exposure Facility (LDEF) satellite (see Figure 13.3). LDEF was in Earth orbit for 69 months from 1984 to 1990 and was designed to provide long-term data on the space environment and its effects on space systems and operations. The 21,500 lb (9,772 kg) cylindrical spacecraft carried 57 experiments mounted in 86 trays about its periphery. LDEF, still one of the largest Shuttle-deployed payloads, was placed in orbit on April 7, 1984 by the Shuttle *Challenger*. LDEF was placed into a nearly circular orbit at an altitude of 275 nautical miles and at an inclination of 28.4 degrees. In order to protect the experiment trays from acceleration forces and contaminants from jet firings, LDEF attitude control was achieved with gravity gradient and inertial distribution to maintain three-axis stability in orbit. During its 32,422 Earth orbits, LDEF experienced one-half a solar cycle,

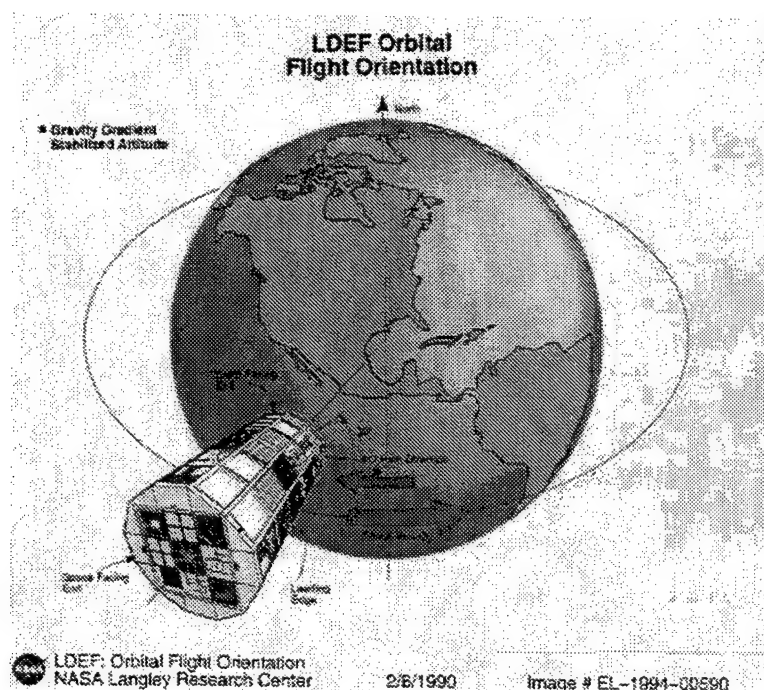


Figure 13.3: An artists conception of LDEF in orbit about the Earth. Our samples were from one panel which exposed gold the space environment aboard LDEF from 1984 to 1990. Image courtesy of NASA.

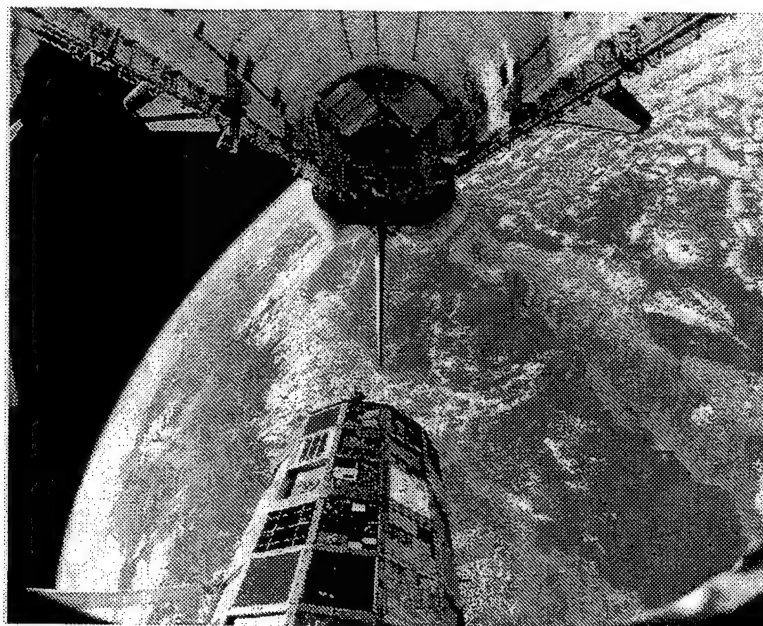


Figure 13.4: Picture of LDEF taken from the shuttle main cabin during its capture in 1990. Image courtesy of NASA.

as it was deployed during a solar minimum and retrieved at a solar maximum. LDEF was retrieved nearly 5.7 years later on January 11, 1990 by the Shuttle *Columbia* (see Figure 13.4 for an image taken during capture).

LDEF carried over 10,000 materials specimens as part of the Materials Special Investigation Group. While most of the gold exposed to the space environment has since been destroyed or analyzed, we were fortunate to find trays of gold used in the Meteoroid and Exposure Module. Gold foils were used, and their reaction to micrometeorite impacts was studied (a picture of the mounted gold foils is provided in Figure 13.5). However, much of the exposed gold foils were never impacted with meteoroids and it is this surplus of space exposed gold from which our samples are comprised. This gold was flown in Bay A, Row 3, Component # A0187-1, Surface A03E00E, Sub-surface 10266.33 of the NASA Long Duration Exposure Facility. For more information regarding the origin of these samples and the original LDEF experiment see the paper by Hörz *et al.* [186].

The LDEF spacecraft was a 14-faced (12 sides and two ends), open-grid structure on which a series of rectangular trays used for mounting experimental hardware were

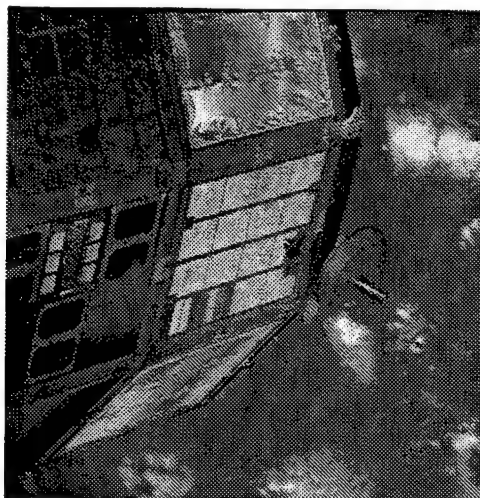


Figure 13.5: A picture of the gold foil used in our experiment while it was mounted on the LDEF satellite. Image courtesy of NASA.

attached. Bays A01-F12 held the larger, rectangular, peripheral experiment trays that housed 72 of the 86 experiments, while the remaining 14 experiments resided within square-shaped experiment trays on either the space-facing (eight bays) or Earth-facing ends (six bays) of the spacecraft. The larger peripheral trays possessed dimensions of 34" x 50" (86.4 x 127 cm), while the space-facing and Earth-facing end trays measured 34 in<sup>2</sup> (86.4 cm<sup>2</sup>); three depths (i.e., 3" [7.62 cm], 6" [15.24 cm], and 12" [30.48 cm]) of experiment trays were available. The typical experiment weight that could be accommodated by the experiment trays was 180 to 200 lbs (396 to 440 kg) for the peripheral and end trays, respectively.

The original numbering scheme for the spacecraft grid was established where components were identified using "Bay" and "Row" numbers (e.g., A03 identifies the experiment occupying Bay A and Row 3). Figure 13.6 is a diagram showing this labeling scheme (our gold came from A03).

The LDEF samples were analyzed during Runs Au4 and Au5. NASA provided us with  $3.9546 \pm 0.0002$  grams of gold exposed on LDEF. They also provided us with  $3.5955 \pm 0.0002$  grams of control gold which was gold that was from the same batch as the gold exposed on LDEF, but which was not exposed in space. This was an important check because although we did not run the control gold samples they would

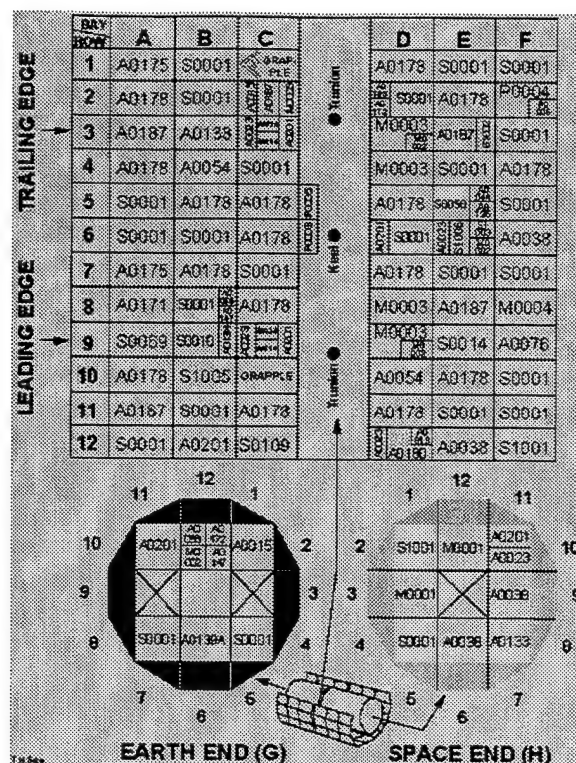


Figure 13.6: Schematic of LDEF showing the Bay and Row assignments along with the overall structure of the spacecraft. Our gold samples were housed on the trailing edge in Bay A Row 3. Image courtesy of NASA.

allow for a comparison if such a comparison needed to be performed. For example, if we had found an indication of SIMPs in the samples we could have compared the spectra of the LDEF exposed gold to the LDEF control gold. This would have allowed us to determine if the SIMP had in fact been captured while the sample was outside the Earth's atmosphere.

The exposed and control gold came in 2 pieces each (see Figure 13.7); the exposed gold was already labeled with the numbers 13 and 18 on two small round disks while the control gold, which we labeled as 1 and 2, were in the form of two thin squares. The measurements of the samples along with the masses of the samples used up during the runs is provided in Table 13.6.

All the experiment trays aboard LDEF were constructed of chromic-anodized 6061-T6 aluminum with the 6"- and 12"-deep trays utilizing 0.125" (3.175 mm) thick

Table 13.6: Masses of the LDEF samples by run. Two different types of samples were provided by NASA: exposed and control gold.

Sample	Quantity	Value
Exposed # 13	Mass	$1.9625 \pm 0.0001$ grams
	Diameter, $d_{13}$	1.585 cm
	Thickness, $t_{13}$	0.71 mm
	Run Au4 Mass	$0.2770 \pm 0.0001$ grams
	Run Au5 Mass	$0.2322 \pm 0.0001$ grams
Exposed # 18	Mass	$1.9921 \pm 0.0001$ grams
	Diameter, $d_{18}$	1.584 cm
	Thickness, $t_{18}$	0.69 mm
Control # 1	Mass	$1.7745 \pm 0.0001$ grams
	Length $l_1$	0.955 cm
	Width $w_1$	0.965 cm
	Thickness, $t_1$	1.03 mm
Control # 2	Mass	$1.8210 \pm 0.0001$ grams
	Length $l_2$	0.986 cm
	Width $w_2$	0.954 cm
	Thickness, $t_2$	1.04 mm



Figure 13.7: A picture of our LDEF samples. Their sizes are evident by referencing against the ruler.

aluminum, and the 3"-deep variety utilizing 0.0625" (1.5875 mm) thick aluminum. The experiment trays were then held within their respective bays by 1.9" x 5" x 0.18" (4.8 x 12.7 x 4.5 cm) thick, 6061-T6 chromic-anodized aluminum clamps with each clamp fastened to the spacecraft by three hex-head, 303 stainless steel bolts. Peripheral experiment trays utilized eight clamps to hold the tray in place, while end trays were affixed to the spacecraft by 12 clamps.

At first sight this information may seem irrelevant, but may have a large impact on whether the SIMPs could be captured by the 5 mm (0.03 inch) thick gold. Consider a beam containing  $N_0$  particles incident on a target material of thickness  $T$  containing  $n$  scattering centers per unit volume, each with a cross-sectional area  $\sigma$ . Any time an incident particle encounters one of the scattering centers in a thin slice,  $dT$ , of the target material it will be scattered. Thus the ratio of the number of scattered particles to the number of particles  $N$  incident on the thin slice will be the same as the ratio of the total area of the scattering centers to the area of the beam,  $A$ . Thus we have the relation,

$$\begin{aligned}
 \frac{\text{number of scattered particles}}{\text{number of incident particles}} &= \frac{\text{total area of scattering centers}}{\text{area of target}} \\
 &= \frac{\text{volume of target} \times n \times \sigma}{\text{area of target}} \\
 &= \frac{(AdT) \times n \times \sigma}{A} \\
 &= n\sigma dT.
 \end{aligned} \tag{13.1}$$

In other words

$$\frac{dN_{sc}}{N} = -\frac{dN}{N} = n\sigma dT \tag{13.2}$$

where the minus sign is used because an increase of scattered particles,  $dN_{sc}$ , corresponds to a decrease of the incident particles,  $-dN$ . Integrating the above expression gives

$$\begin{aligned}
-\int_{N_0}^{N_f} \frac{dN}{N} &= \int_0^T n\sigma dT \\
\Rightarrow -\ln \frac{N_f}{N_0} &= n\sigma T \\
\Rightarrow N_f &= N_0 e^{-n\sigma T}
\end{aligned} \tag{13.3}$$

with  $N_0$  and  $N_f$  the initial and final numbers of particles in the beam. The resulting number of scattered particles is then given by

$$N_{sc} = N_0 - N_f = N_0(1 - e^{-n\sigma_{SN}T}). \tag{13.4}$$

Using the SIMP nucleon interaction cross-section derived in the previous chapter,

$$\begin{aligned}
\sigma_{SN} &= \frac{0.4 \text{ mb}}{M_S [\text{GeV}]} \left( \frac{1 \times 10^{-3} \text{ b}}{1 \text{ mb}} \right) \left( \frac{1 \times 10^{-28} \text{ m}^2}{1 \text{ b}} \right) \\
&= \frac{4 \times 10^{32} \text{ m}^2}{M_S [\text{GeV}]},
\end{aligned} \tag{13.5}$$

gives an approximate evaluation of the fraction of SIMPs which interact with the Au nuclei in a foil of thickness  $T$ . For the LDEF samples  $T \approx 5 \text{ mm}$  and we may calculate the number of Au scattering centers as

$$\begin{aligned}
n_{Au} &= \left( \frac{6.02 \times 10^{26} \text{ nuclei/kmol}}{197 \text{ kg/kmol}} \right) (19.311 \text{ gm/cm}^3) \left( \frac{1 \text{ kg}}{1000 \text{ gm}} \right) \left( \frac{100 \text{ cm}}{1 \text{ m}} \right)^3 \\
&= 5.9 \times 10^{28} \text{ nuclei/m}^3
\end{aligned} \tag{13.6}$$

Inserting Eqs. (13.6) and (13.5) into Eq. (13.4) gives the result shown in Figure 13.8. If all the incident SIMPs were captured by gold nuclei this ratio would be  $N_{sc}/N_0 = 1$ . Here we see that for a 1 GeV SIMP only about  $1 \times 10^{-5}$  or 0.001% are captured by the a gold nucleus. For a 1 TeV (1,000 GeV) SIMP only about  $1 \times 10^{-8}$  are captured. The fraction of Au with a SIMP then depends on the flux of these SIMPs and the gold exposure time. Explicit calculations of this were performed in

the previous chapter for geological samples. As will be developed in the paragraphs below, a similar but more rigorous definition can be derived in parallel with that of the previous chapter, and with results which agree reasonably well with our simple model given here. Detailed calculations on neutron scattering (from which our simple model is derived) can be found in Chapter 3.2 of the text by DeBenedetti [187] along with explicit data for neutron scattering in Au provided in Refs. [188, 189].

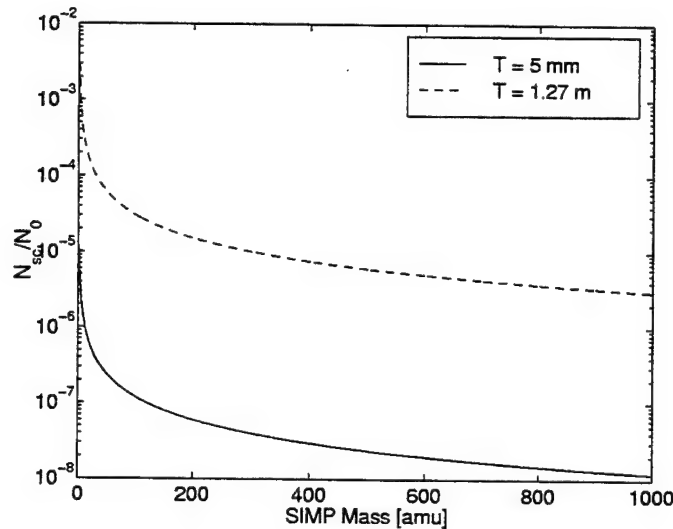


Figure 13.8: Result of simple model for nuclear scattering. This is a plot of Equation (13.4) for different SIMP masses which enter into the equation through our choice of the interaction cross-section. These calculations were performed assuming a foil thicknesses of 5 mm and 1.27 m which are the approximate thickness and width of our LDEF samples.

This of course is a very simple model and a more rigorous development can be derived using the discussion for the Dark Matter SIMP from the previous section. Here we set  $\tilde{A} = 197$  and  $\rho = 19.311 \text{ gm/cm}^2$  (the density of gold). Making these changes will transform Equation (12.12) into

$$\lambda_S = \frac{197^{1/3} m_{nuc}}{\rho \sigma_{SN} \left[ 1 - \left( \frac{M_S}{M_S + 197 m_{nuc}} \right)^2 \right]}. \quad (13.7)$$

This then can be used to determine the thickness needed to stop all the SIMPs. We

may then check our approximation by solving for the thickness required to obtain  $N_{sc}/N_0 = 1$ . These two are plotted together in Figure 13.9 and we notice that our rough approximation works well enough within the errors introduced by our assumptions. The approximation however is much easier to derive and understand because of its simplicity.

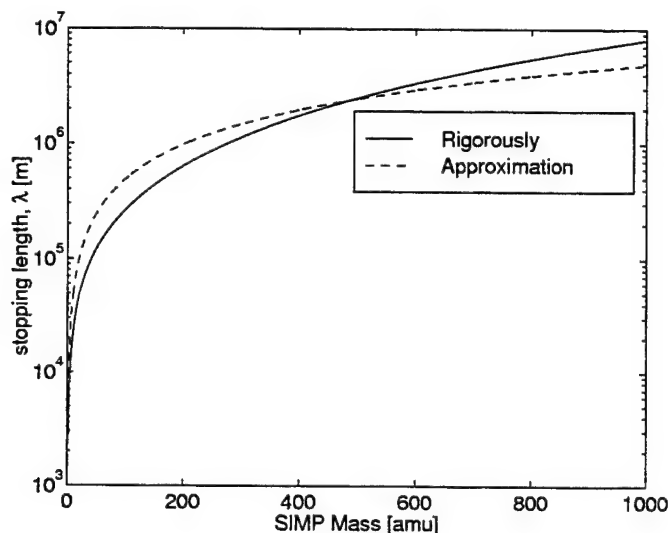


Figure 13.9: Distance required to stop 99% of SIMPs with an energy of 14.5 keV. Here we compare our approximate solution for the scattering to the more rigorous solution developed in the previous chapter.

We also notice the extremely large thickness of gold foil needed to completely stop a SIMP beam (or basically to have a 100% chance of a gold nucleus capturing a SIMP). Of course this is impractical; however, what this does tell us is that our approximation is reasonable and thus the estimate that 0.001% of SIMPs will be stopped in the 5 mm gold foil makes sense.

However this assumes the SIMP enters from the trailing edge of the spacecraft normal to the surface. Recall that the trays have a long side of 127 cm. If instead the SIMP enters the foil from the side it will see a 1.27 m thickness and would exhibit the properties displayed by the dashed line in Figure 13.8. We also notice that this time almost 1% of SIMPs would be stopped if they were incident along the long side of the tray.

We also must consider the situation where the SIMP enters through the leading edge of the spacecraft and must pass through the vehicle structure. In this case the structure will help to lower the SIMP energy closer to the that of thermal equilibrium so that a the gold in the foil does not have to do all the work to slow the particle down. In fact if the discussion of the previous chapter is correct and there exists a minimum mass which can absorb a SIMP we may also increase the probability of a SIMP capture.

What is important here is that for every SIMP mass scanned there is a finite possibility that a SIMP may be captured by the 5 mm thick Au foil flown aboard LDEF.

### 13.3.2 Relativistic Heavy Ion Collider Beam Dump

Dr. Sam Aronson of Brookhaven National Laboratory and Dr. Mike Bennett of the Los Alamos National Laboratory provided us with  $30.7171 \pm 0.0001$  grams of Au from the beam dump of the Relativistic Heavy Ion Collider (RHIC) at Brookhaven National Laboratory. Figure 13.10 is a picture of the gold which came in several thin strips. Since the samples were radioactive we had to undergo the required training through the Purdue University Radiological and Environmental Management office.

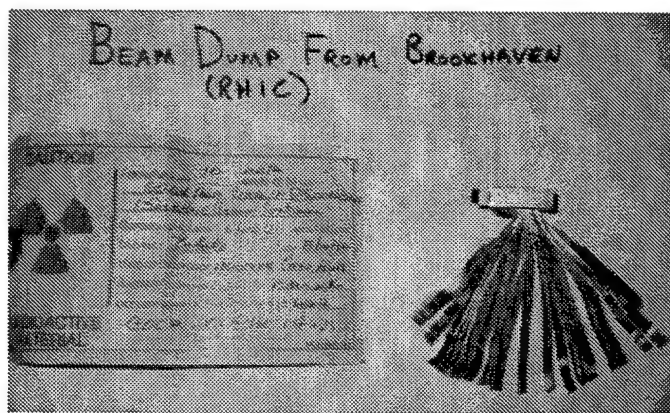


Figure 13.10: Picture of the RHIC samples including the radioactive tag which always accompanies the samples. Dr. Sam Aronson and the Brookhaven National Laboratory donated almost 31 grams of Au beam dump to this experiment.

Since PRIME Lab is a carbon and chlorine free environment, we needed to first perform swipe tests on the gold to make sure that it did not have abnormal quantities

of our measured radioisotopes. This analysis was performed by Dr. George Jackson, Ken Mueller, and Mary Ann Rounds. After passing these swipe tests the RHIC samples were able to be transferred down to PRIME Lab. In the interim they were stored in the Biomedical Lab (B23) in the basement of the Physics building.

In the 1993 experiment performed at RHIC, a gold beam with a flux of  $3.55 \times 10^{12}$  was incident upon the E878 Au strip target. The target which was a 30% interaction length target with a thickness of 0.616 cm. The thickness of the Au target is specified so that 22.5% of the incident Au beam interacts assuming a 6850 mb total inelastic Au+Au cross-section. Using this model the total flux of  $3.55 \times 10^{12}$  represents  $7.81 \times 10^{11}$  inelastic Au+Au interactions. The flux of incident Au ions was deposited predominantly in the center cm of the target with a negligible amount deposited near the edges.

### 13.3.3 Canyon Diablo Meteorite

Dr. Ephraim Fischbach obtained, as a gift, a 2995.6 gram iron (Fe) meteorite from Idella Marx (see Figure 13.11). The meteorite is a fragment of the much larger meteoroid which impacted the Earth at Canyon Diablo (Lat:  $35^{\circ} 3' N$ , Long:  $111^{\circ} 2' W$ ) in Arizona (see Figure 13.12). The meteorite is predominantly iron (92%) and nickel (7%) with only traces of other elements. While most of the meteor fragments were recovered in the vicinity of the crater, pieces have been found up to 10 miles away.

The meteoroid is estimated to have an original mass of 63,000 tons and would have been a sphere of with a diameter of more that 30 meters if it was traveling at 14.5 km/s. Most of this mass would have shock melted on impact and spread as an enormous expansion plume produced by gases released from the Colorado Plateau limestone in the Earth beneath the impact site. What was left was blasted into small bits (the largest single piece recovered weighing 639 kg). The typical meteorite is about 90% kamacite (which is an iron nickel alloy), 1–4% taenite and plessite, up to 8.5% toilitite (which is an iron sulfide sometimes mixed with graphite, daubreelite, chromite, or other base metal sulfides) which occurs as nodule up to 50 mm across.

The Canyon Diablo meteorite is a coarse octahedrite, Og, structural class meteorite with a Widmanstätten bandwidth of  $2.0 \pm 0.5$  mm. The Widmanstätten

bandwidth gives a measure of how hot the meteorite was, and how long it took to cool. Kamacite and taenite are minerals that compose the majority of iron meteorites and are formed by cooling of magma (molten material). In this case the magma is composed mostly of two elements Iron (Fe) and Nickel (Ni). As the magma cools, these elements begin to bond together. The true Widmanstatten structure forms by a diffusion-controlled nucleation that is slow, even on a geologic time scale [190]. In simpler terms, this means that it takes a long time to cool Fe and Ni, and even longer to bond them together. It is the amount of time for cooling that generates the size of the bands in the Widmanstatten structure. Since Ni would like to bond as soon as possible it begins to bond at a higher temperature. In fact, at about 1100° C Ni atomic structure is stable enough to allow bonding while the Fe, however, is still reluctant to bond. So as time passes more Ni atoms bond than Fe atoms bond. This continues until most of the Ni is gone from the melt resulting in bandwidths

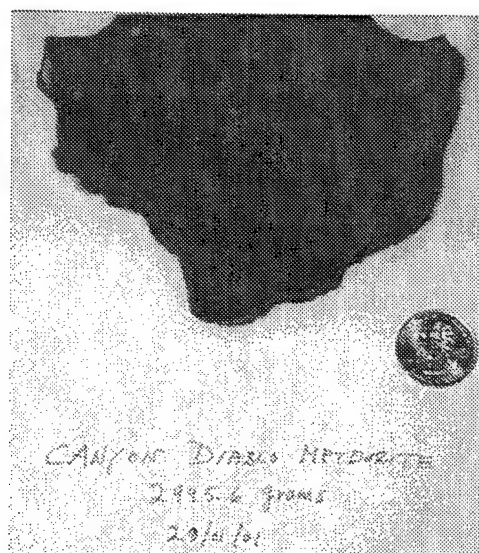


Figure 13.11: Picture of 3000 gram Canyon Diablo Meteorite donated by Mrs. Idella Marx. This fragment is a small piece retrieved from an approximately 60,000 ton meteorite which impacted the Earth near Winslow, AZ. However, since most of the meteor shock melted on impact, this fragment is considered rather large and is by far the sample with the highest monetary value since current rates are around \$0.70 per gram.



Figure 13.12: Picture of Canyon Diablo Meteor Crater. The crater is about 1.2 km across and 180 meters (570 feet) deep with a rim that rises 200 feet above the plain.

range from .006 mm to 3.1 mm. The Widmanstätten pattern is often used to verify a meteor's extra-terrestrial origin. For more information see the Handbook of Iron Meteorites by Vagn Buchwald [190].

What is important in our study is that the Canyon Diablo meteoroid spent an estimated 50 million years in interstellar space before impacting the Earth approximately 50 thousand years ago. Based on the simple expression for the penetration depth discussed in the preceding sections we notice that for a 1 GeV SIMP 10% may be captured while for a 1 TeV SIMP only 0.01% would be captured. This is about 4 orders of magnitude better than for the Au foils discussed in the previous section. Since our sample most likely came from close to the interior we slightly increase our chances of a SIMP captured by an Fe nucleus. Figure 13.13 gives the estimated fraction of SIMPs captured by the Fe atoms as a function of the SIMP mass assuming the number of Fe scattering centers is

$$\begin{aligned}
 n_{Fe} &= \left( \frac{6.02 \times 10^{26} \text{ nuclei/kmol}}{56 \text{ kg/kmol}} \right) (7.86 \text{ gm/cm}^3) \left( \frac{1 \text{ kg}}{1000 \text{ gm}} \right) \left( \frac{100 \text{ cm}}{1 \text{ m}} \right)^3 \\
 &= 8.4 \times 10^{28} \text{ nuclei/m}^3
 \end{aligned}
 \tag{13.8}$$

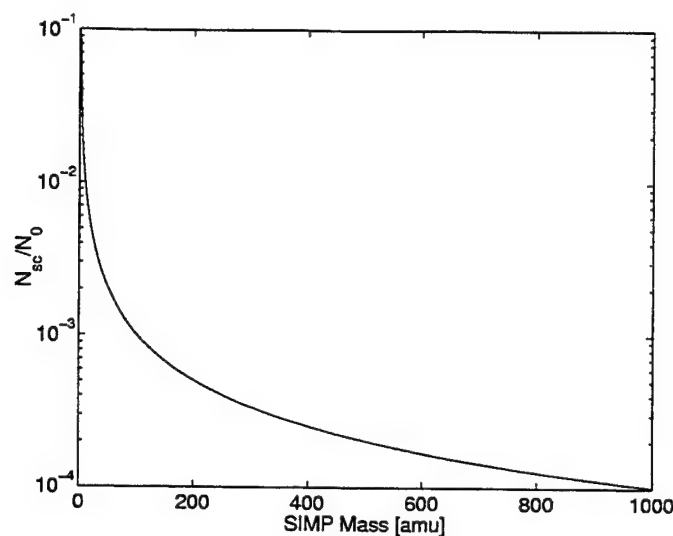


Figure 13.13: Result of simple model for nuclear scattering inside the Canyon Diablo meteorite. This is a plot of Equation (13.4) for different SIMP masses which enter into the equation through our choice of the interaction cross-section. These calculations were performed assuming a meteorite whose initial diameter was 30 meters.

Of course as mentioned before the fraction of Fe scattering centers is actually a function of the exposure time and actual interaction cross-section. However, this gives a reasonable estimate for the fraction of SIMPs stopped by the Fe in the meteorite.

## CHAPTER 14. EXPERIMENTAL RESULTS

### 14.1 Introduction

As in the Paronic Beryllium experiment a number of runs on the AMS were performed searching for heavy isotopes of gold. As is customary in these types of experiments, the initial runs are spent learning how to proceed and drawing up the procedures necessary for an efficient final run. As a result, the runs are cumulative and each run builds on earlier results. In the process, the data and our understanding improved as we overcame different obstacles associated with equipment limitations.

### 14.2 Run Au1, Dec 1999: Initial Tuning and Injector Magnet Scan

The objective of the first run was to accomplish two goals: First to tune Au to the Image Faraday cup just beyond the 90° analyzing magnet (see Figure 1.1), and to measure the transmission using both foil and gas stripping in a few different charge states. Second, we wanted to obtain a rough estimate of the amount of contaminants present in a typical sample.

Just like the Be runs we began with the appropriate scaling of the magnetic and electrostatic elements using the values of a known ion beam (denoted with a subscript 1 in the following equations). Although the relevant equations are provided in Chapter 1 and at the beginning of the Be Results chapter, we reproduce them here since they are at the heart of all the calculations used in the following runs. Recall that the magnetic elements scale according to the relation

$$B_2 = B_1 \left( \frac{q_1}{q_2} \sqrt{\frac{M_2 E_2}{M_1 E_1}} \right), \quad (14.1)$$

With  $B$  denoting the field setting of the magnet in question. The electrostatic field  $\mathcal{E}$  settings are given by

$$\mathcal{E}_2 = \mathcal{E}_1 \left( \frac{q_1 E_2}{q_2 E_1} \right) \quad (14.2)$$

In fact, while these are remarkably simple expressions the actual observed values are strikingly close to the predicted values. When searching for a particle which should not exist it is important this scaling of the parameters is well understood. We will discuss how we check and fine tune this scaling during the scan in later sections when it becomes more relevant.

The tune progressed slowly at first while we spent time with a problem with the software that controls the injector magnetic field setting. We finally went to manual control of the magnet since computer control was not necessary for this first run. We were able to predict the  $\text{Au}^-$  current based on data produced by Middleton [138]. With the Extractor at 8 kV and the Pre-Acc at 13 kV (resulting in a total injection energy of 21 keV) we obtained around 4.3  $\mu\text{A}$  of current in the injector Faraday cup. This was slightly lower than predicted, which may have been the result of a small sample surface coupled with a different sample type (we were using gold powder while Middleton used filings). In the first test of the magnetic scaling given in Eq. (14.1) above, we used the  $\text{Au}^-$  beam (with a  $B_{inj} = -0.47256$  T) to find the  $\text{Au}_2^-$  beam which came in exactly where it was expected. For example we expected the  $\text{Au}_2^-$  beam at  $B_{inj} = -0.66828$  T and we found 155 nA of beam at  $B_{inj} = -0.66824$  T. Of course from the equation we see that the field corresponding to a given mass depends on the injection energy. As a result, each run has different field settings for the Au beam.

Before we could put the Au beam through the machine we had to prepare the analyzing magnet. This was necessary because we were preparing to run the magnet to levels that the existing power supply would not be able to handle. Thus we had to cannibalize the switching magnet power supply, but had to leave the usual analyzing magnet power supply on standby so that the water which cools the magnet would continue to flow through the coils. The highest field we were able to obtain was -1.63 T (which is just shy of the -1.7 T we were aiming for).

We began looking for the beam with gas stripping. We held the gas pressure at  $4 \times 10^{-6}$  Torr, and proceeded to look for the  $q = +5$  beam. The pressure is measured

at the high end by an EMIS gauge. Since we do not have a pressure gauge inside the stripper we watch the vacuum increase on the high end. Originally we had difficulty finding the beam because of our inexperience with the high mass ion beams. We found what we believed to be the beam at 2.807 MV. With  $2.4 \mu\text{A}$  at the injector Faraday cup and 4.8 nA at the image Faraday cup this gave an efficiency (calculated from Eq. (1.14)) of 0.04%. We then went to  $q = +4$  and seemed to find a beam at 2.237 MV which gave a transmission of 0.004%. Since the transmissions were so low we decided to switch over and test the foil stripping.

At the same time we proceeded to higher charge states in hopes of finding higher efficiencies. At  $q = +6$  we found the obvious 1.2 nA beam at 3.820 MV, which with the slits in gave a transmission of 0.2%. Without the slits we get a larger beam current, but one that is nearly impossible to tune because of beam divergence from the foil. For example with GVM control we obtain an efficiency of 1.3%.

Another drawback to running the foils is that we consume them remarkably quickly, and we can even watch the beam current drop as the foil deteriorates. However, using the foils gives us good practice in the initial stages of the tune. After switching to several different charge states we were able to produce the efficiency results reported in Table 14.1.

It is important that we not misinterpret these results. The foil data are highly dependent upon the condition of the foil. To better illustrate this we note that for  $q = +7$  foil # 21 gave an  $\eta = 0.63\%$  while foil #22 gave  $\eta = 1.23\%$ . Since the foils did not last long enough to allow us to compare two beams with the same foil, these data are inconclusive. It is also important to note that the data are taken at different energies, and as we recall from Chapter 1, the efficiency is a function of the ion energy. Thus, it is difficult to draw any conclusions from these data other than the fact that the foils give a better efficiency than the gas.

What is important is that we were able to tune Au through to the image Faraday cup. However, in future tunes we had to learn to use the gas stripping, since it is impractical to use the foil for two main reasons. First their short lifetimes under the high mass beam means that we would go through half of our foils to complete an

Table 14.1: Stripper yield for several charge states using both gas and foil stripping. One may observe from these data that a foil stripper gives much higher efficiencies than the gas. The gas data were taken at a gas pressure of  $4 \times 10^{-6}$  Torr.

Charge State	Stripping Efficiency, $\eta$ [%]	
	Gas	Foil
+4	0.004	—
+5	0.04	1.07
+6	—	1.08
+7	—	1.23
+8	—	1.58
+9	—	1.41
+10	—	1.39

entire tune. Since the only way to replace the foils is to physically go into the tank, this is highly impractical. Second, if a foil were to break during a run at high mass we would have no way of detecting it until we reached a guide beam at which point we would have to redo that segment. This also is impractical and called for us to use gas stripping, even though the transmission efficiencies are significantly worse.

Before ending the run we performed two scans on lab gold using the injector magnet. We tuned the Au beam to the injector Faraday cup and proceeded to slowly increase the injector magnetic field noting each peak which arose above the background current. The first scan was between Au and Au<sub>2</sub>, and the results are provided in Figure 14.1.

We can transform the injector magnetic field setting into a mass and thus obtain the current at each mass assuming no doubly negative ions are produced by the source. As a very rough estimate of the fraction of SIMPs in Au, we then take the ratio of the background current to that of Au in the regions between the peaks to set the following limits on the presence of SIMPs in Au:

$$\frac{M X}{^{197}\text{Au}} < 2 \times 10^{-5}, \quad \text{for } 197 < M < 394 \text{ amu.} \quad (14.3)$$

We then changed the injector settings so that the maximum injector magnetic field corresponded to 1000 amu instead of the  $\text{Au}_2$  mass of 394 as done previously. As mentioned before, the lower field setting dictates a lower injection energy which we calculated to be at 9.07 keV for the high mass scan. This resulted in an Au beam setting of -0.30492 T with the maximum mass (of 1002 amu) bent at a magnetic field of -0.68774 T. The results from this scan are provided in Figure 14.2 with the final  $X/\text{Au}$  bound at

$$\frac{M X}{^{197}\text{Au}} < 7 \times 10^{-5}, \quad \text{for } 197 < M < 1002 \text{ amu} \quad (14.4)$$

Thus following the first Au run we verified that the experimental concept was possible with existing equipment. We successfully tuned Au through the machine to the

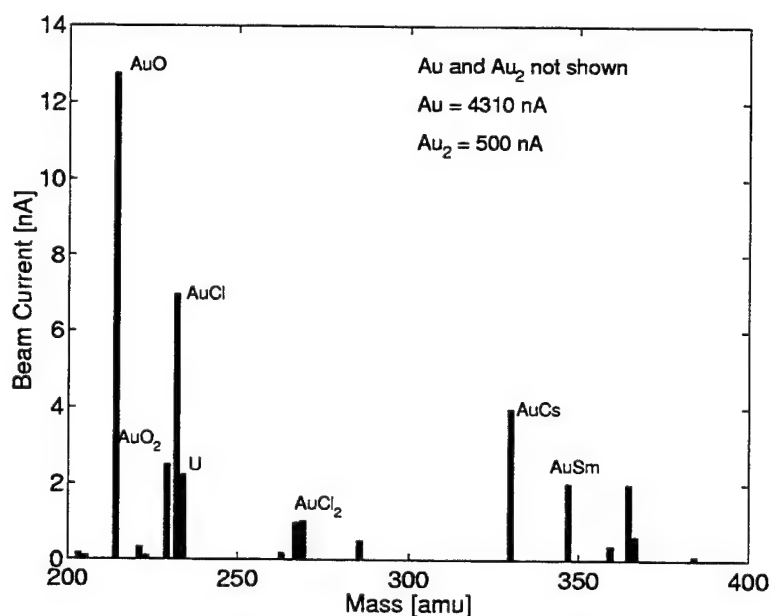


Figure 14.1: Results of the first scans from 197 to 394 amu. Each noticeable peak is labeled and most peaks were easily identified. Note the presence of AuSm which comes from the  $\text{Sm}_2\text{O}_3$  target used in the Be experiment noted earlier. The gold samples for this experiment were made with the same spatula and the contamination is clearly evident. Also notice the presence of Cl which was the isotope run directly before us.

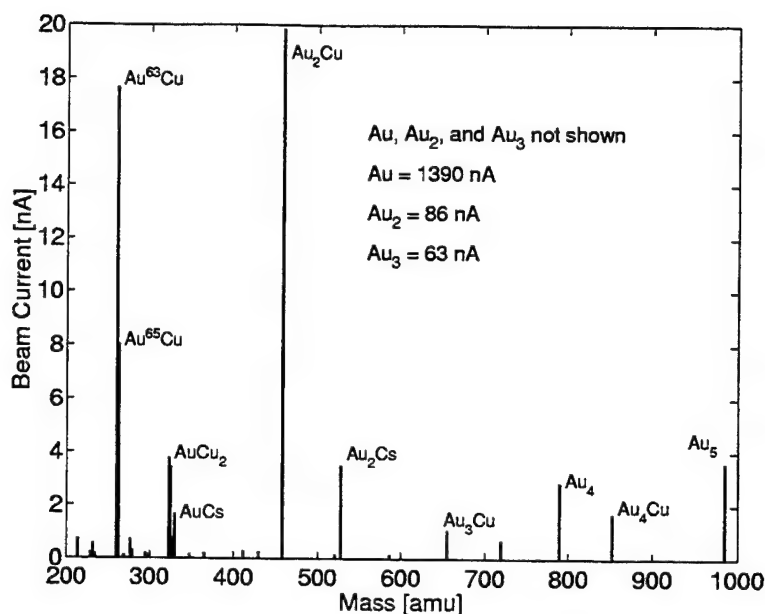


Figure 14.2: Results of the first scans from 197 to 1002 amu. Again each noticeable peak is labeled and most peaks were easily identified.

image Faraday cup and performed two scans which gave the amount of contaminants to expect along with a crude limit on the SIMP abundance in Au. Namely it gave us a result to improve upon since no experiments of this type had been performed.

### 14.3 Run Au2, July 2000: Mass scan from 200-350 amu

The objectives of this run were to tune Au to the detector, and to scan the lab and Australia gold up to the highest guide beam. Before we began we retook the stripping data acquired from the previous run because we felt that the data could be faulty. In fact the data from Au1 were deemed incorrect because the Walker power supply which was obtained from the switching magnet was not scaled properly, since the power supply settings were not changed when going to the different charge states. As a result these data were taken over and are given in Table 14.2.

Since we had already decided from the Run Au1 that foil stripping would not work we only tested it one time. Of course we observed almost a factor of 10 improvement in the beam, but decided to use gas stripping for the reasons discussed in the previous

Table 14.2: Reanalysis of stripper yield for several charge states using both gas and foil stripping. The gas data was taken at a gas pressure of  $2.5 \times 10^{-6}$  Torr. The difficulty of short foil lifetimes discussed in the previous section resulted in our choice to run with gas stripping.

Charge State	Terminal Voltage, $V_T$ [MV]	Stripping Efficiency, $\eta$ [%]	
		Gas	Foil
+4	1.988	0.5	—
+5	2.601	0.24	—
+6	3.217 (3.225)	0.17	1.2
+7	3.829	0.15	—
+8	4.447	0.10	—
+9	5.088	0.06	—

section. We also notice the curious effect that the terminal voltage is slightly higher for the foil stripping (denoted in parentheses in Table 14.2) which results from energy loss in the foil. We also see the trend that is predicted by the STRIP program, which is that the yield decreases with increasing charge state. This is because of the fact that the peak for each charge state is at a higher energy. Since we cannot operate at these higher energies, and are limited by the analyzing magnetic field, we are operating farther out on the tails of the asymmetric Gaussian discussed in Chapter 1. This accounts for the lower efficiencies.

We thus see the initial problem encountered: There is a tradeoff between transmission efficiency and mass. By this we mean that a high mass range will be accessed by running at a higher charge state, which follows from Eq. (1.9). A higher charge state will tolerate a higher initial energy, and this change in energy is what defines the mass range capable of being scanned with our machine. Thus we would like to run at the highest possible charge state. However, we see from Table 14.2 that the efficiency drops with increasing charge state. Thus we need to find a good compromise between the competing effects which permits us to run up to high masses, while still retaining a relatively high transmission efficiency. This approach will be modified in the final run which shifts the paradigm, but for the present we continue along with

Table 14.3: Evaluation of the optimal gas pressure. This data were taken at  $q = +6$  and  $V_T = 3.217$  MV. These data suggests we should try to run at a pressure of  $1 \times 10^{-6}$  Torr.

Pressure [Torr]	IMG FC [nA]	$\eta$ [%]
$2.5 \times 10^{-6}$	14	0.17
$1.5 \times 10^{-6}$	19	0.24
$8.7 \times 10^{-7}$	18	0.24
$6.0 \times 10^{-7}$	13	0.17

the development as described above.

Before continuing with the tune we needed to find the optimum pressure for the stripper gas. A brief study was performed at  $q = +6$  which determined the optimal gas pressure to tune with. The outcome from this study is provided in Table 14.3.

We also were running into the problem of currents which were not large enough in magnitude to tune all the way to the detector. Since this was our first time we needed a larger current and we thus settled on  $q = +7$  to perform the tune and initial mass scan. Unfortunately, we quickly encountered a new problem associated with the Transmission Quadrupole which is located in the beampipe between the Analyzing and Switching magnets. In fact, it was the next element in the tune beyond the image cup. Unfortunately, the power supply was unable to produce the current needed to run the magnets high enough to focus the beam. This problem was somewhat solved when we attached a power supply which could go up to 40 A, which is higher than the 30 A limit of the old one. However, this was still not enough, which meant that in order to continue with the tune we needed to reduce the ion energy by lowering the terminal voltage from 3.829 MV to 2.860 MV. After trying several different charge states ( $q = +6$  and  $q = +8$  both had similar results) we stayed with charge state  $+7$  and at least had a beam that could be focused by the Trans Quad. We then proceeded to tune the beam all the way to the detector. Unfortunately, we had to run at an Analyzing magnet field setting that was less than maximum. This dictated a lower beam energy and hence lower transmission efficiencies. However, a large amount of

Table 14.4: Tandem parameter settings following the tune on  $q = +7$ . Refer to Figure 1.1 to locate the different elements.

Stage	Setting	Value
Ion Source	Cathode =	50 %
	Extractor =	15 % = 0.15(40 kV) = 6 kV
	Pre-Acc =	17.5 kV
	Injection Energy =	0.0235 MeV
	INJ X/Y Steerers =	50%/50%
Low End	Au Injector B-field =	-0.47282 T
	INJ IMG Einzel Lens =	24.6%
	LEBL Einzel Lens =	24.2%
	Gridded Lens =	1.1%
	LE X/Y Steerers =	0.7%/-0.7%
Terminal	Stripping =	Gas @ $9.3 \times 10^{-7}$ Torr
	Charge State, $q =$	+7
	Terminal Voltage, $V_t =$	2.860 MV GVM
	Au Energy =	22.904 MeV
	LE Chain PS =	13 kV
High End	HE Chain PS =	13 kV
	ESQ A/B =	14.89%/16.43%
	Analyzing B-field =	-1.41550 T
	X/Y Steerers =	0, 10D
	Trans Quad A/B =	103.5%/98.94%
Final Transmission	BL Quad A/B =	46.33%/49.02%
	Switching B-field =	-0.91175 T
	Electrostatic Analyzer, ESA =	33.13 kV
	LE FC Current =	2.5 $\mu$ A
	Image FC Current =	8.4 nA
	Detector FC Current =	6.4 nA
	Complete Transmission, $\eta_{tot} =$	0.04 %

information was gained in this tune to the detector. The final tandem settings for the low energy  $q = +7$  beam are provided in Table 14.4.

In this run we decided to use  $\text{Au}_2\text{Cs}$  as our highest guide beam and thus had the intention of going up to a mass of 527 amu. This then dictated that our injection energy needed to drop from 24 keV to 17.4 keV which we accomplished by lowering the Pre-Acc voltage. This then required some tune adjustments all the way through the source. The final settings for the scan are given in Table 14.5.

Table 14.5: Tandem parameter settings following the tune on  $q = +7$ . These were the settings used for the first scan on the lab and Laverton gold. These are different from Table 14.4 because of the reduced injector energy which was dictated by the desire to reach a maximum mass of 527 amu. Refer to Figure 1.1 to locate the different elements.

Stage	Setting	Value
Ion Source	Cathode =	50 %
	Extractor =	15 % = 0.15(40 kV) = 6 kV
	Pre-Acc =	11.8 kV
	Injection Energy =	0.0174 MeV
	INJ X/Y Steerers =	50%/50%
Low End	Au Injector B-field =	-0.40672 T
	INJ IMG Einzel Lens =	24.6%
	LEBL Einzel Lens =	24.2%
	Gridded Lens =	1.1%
	LE X/Y Steerers =	0.7%/-0.7%
Terminal	Stripping =	Gas @ $9.8 \times 10^{-7}$ Torr
	Charge State, $q$ =	+7
	Terminal Voltage, $V_t$ =	2.858 MV GVM
	Au Energy =	22.904 MeV
	LE Chain PS =	13 kV
High End	HE Chain PS =	13 kV
	Au ESQ A/B =	14.79%/16.19%
	Analyzing B-field =	-1.41555 T
	X/Y Steerers =	2L, 16D
	Trans Quad A/B =	103.51%/98.94%
Final Transmission	BL Quad A/B =	47.52%/47.86%
	Switching B-field =	-0.91175 T
	Au ESA =	33.19 kV
	LE FC Current =	600 nA
	Image FC Current =	1.7 nA
	Detector FC Current =	1.3 nA
	Complete Transmission, $\eta_{tot}$ =	0.04 %

For the scan the step size which would guarantee overlap of the different steps was chosen to be 2 amu based on an estimation that the terminal voltage fluctuations were approximately 0.024 MV. If 1 amu  $\approx$  0.015 MV, 0.024 MV would correspond to roughly 2 amu steps. This would later prove to be overly conservative, and that much larger steps could be used, but for the first scan we needed a stepsize in which we would see clear overlap. We then proceeded with the scan which was originally designed to go all the way up to 527 amu, but which was abruptly halted when we failed to find

our  $\text{Au}^{+4}$  guide beam at the SIMP mass step of 345. We finally determined that the beam energy was insufficient to penetrate the window (the  $\text{Au}^{+4}$  beam had an energy of only 2.5 MeV). After several hours of changing the beam energy (which is not a trivial task since it involves scaling all the magnetic and electrostatic elements along the beamline appropriately), we determined that a 13 MeV beam was barely visible in the detector. However, before pursuing this point, we review the importance of guide beams (which were discussed in greater detail in Chapter 1).

Recall that counts observed in the detector are particles which satisfied all the constraining equations imposed by the different elements, but still are not uniquely selected since each count in the detector have the same  $M/q$ . Thus we obtain contaminating beams which are at the wrong energy but which get into the detector. As a result we may use a known beam in a lower charge state, say Au in  $q = +4$ , to test the tune for an X particle (which is a SIMP+Au) of mass 345 in  $q = +7$  since

$$\frac{M}{q} = \frac{197}{4} = \frac{345}{7}. \quad (14.5)$$

At low masses (masses close to Au) we get many contaminating guide beams which we then must identify or rule out. These guide beams, however, must create a molecule that will survive the trip around the injector magnet which is set for the higher mass. Thus we see a drop off in the contaminating guide beams as the mass increases, because it becomes increasingly difficult for an atom to create a negative ion of the needed molecule to get around the injector magnet. Since contaminating guide beams are so plentiful at low masses it is not necessary to identify all of them, as long as we can ensure that they could be some known atom and not the SIMP of interest. This resolution comes in the detector which permits us to measure the total energy of the incident ion. Thus while we may see several different contaminating beams in the detector, they show up as different peaks on the total energy spectrum produced by the detector<sup>1</sup>. Since we calibrate the detector with Au in  $q = +7$  we know the correspondence between the detector channel and the total energy, and thus may discern the charge state and mass of each peak observed in the detector. More

<sup>1</sup>For more information on how the detector accomplishes this feat see Chapter 1.

importantly, we know which channel and energy our X particle will come in at and thus may screen out the contaminating beams.

However, it is good to have some beams which we may predict in order to check to make sure that the AMS elements are still properly tuned. Thus we may use this  $M/q$  dependence to know when to expect a beam in a given channel. When that beam does not exist we may wonder about potential problems. It was precisely this observation that indicated the problem with the window. The energy required to penetrate the window was then determined by slowly changing the beam energy until the beam was seen. Luckily the  $q = +4$  beam was just above this energy which is what clued us onto this problem instead of suggesting tune problems.

The raw results (or the data prior to application of detector energy separation) of the beam in the ungated spectrum gives the number of background peaks for each mass step. For this first run most of the beams were identified and labeled as shown in Figures 14.3 and 14.4.

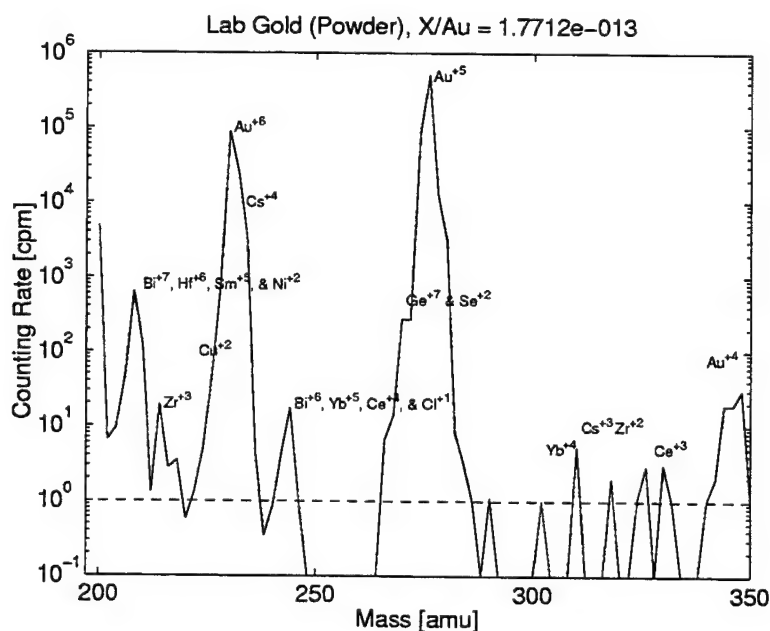


Figure 14.3: The scan on the laboratory gold before detector energy resolution constraints have been applied. Each noticeable peak is labeled and most peaks were easily identified.

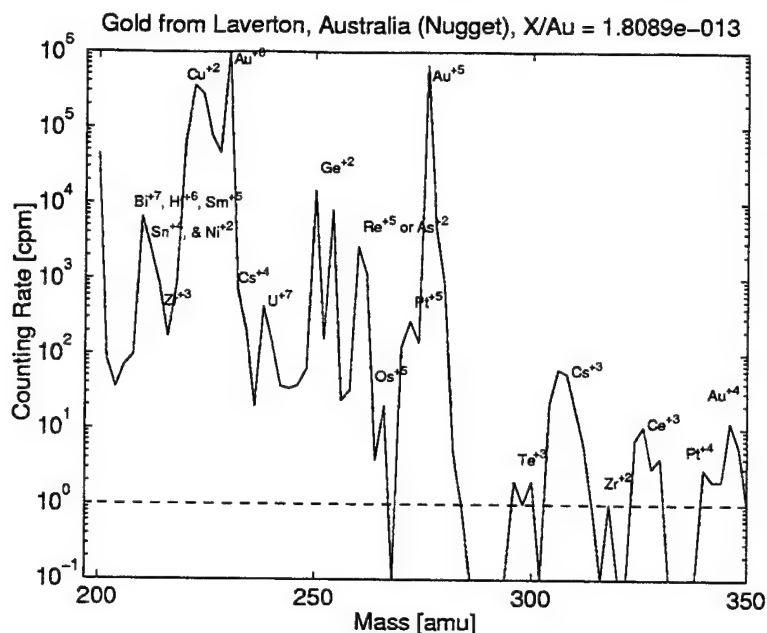


Figure 14.4: The scan on the gold from Laverton Australia before detector energy resolution constraints have been applied. Each noticeable peak is labeled and most peaks were easily identified.

The high levels of contamination are present because of the existence of several elemental surfaces which we intentionally introduced to the source so that these peaks would all be visible. All the beams shown here were intentionally introduced and used to check our guide beam concept with several beams other than just Au, Cu and Cs. The  $X/Au$  ratio reported at the top of the figures is the limit we would have set with this scan if the transmission efficiency was not a function of SIMP mass but rather was constant.

However the efficiency is a function of the SIMP mass, since as the mass increases the velocity of the ion decreases for a given energy. If we recall from the discussion on the stripper yield provided in Chapter 1, the stripping efficiency drops because of the averaging effect of the potential seen by the slower moving ion. Thus it was necessary to determine the stripper efficiency as a function of SIMP mass (which is really a dependence on velocity). This topic would be the focus of the next run Au3. Thus our limit would have to wait for better understanding of the stripper efficiencies dependence on SIMP mass.

Recall that we may distinguish between the energy of the beam entering the detector and the energy of the predicted  $X$  particle by noting that if the peak channel in the total energy spectrum of the GKS plot (the set of energy distribution histograms) matches that of the SIMP. It is this resolution that allows us to verify that none of the peaks shown in Figures 14.3 and 14.4 is actually a SIMP peak. This is because at each mass step we produce a plot of the number of counts as a function of the total energy (denoted in channels which correspond to voltages on the sum of the anode plates). Thus each point on the figures shown above reports the sum of all the channels. The peaks are then identified by observing this total energy spectrum and determining the channel of each peak. Before transforming the channels into the actual incident ion energy, we needed to calibrate the detector since the channel/energy relationship is a function of the detector gas pressure along with gains and other detector settings.

For this first run we determined the channel/energy relationship by putting  $\text{Au}^{+7}$  into the detector (with the image slits all the way in) in order to perform this calibration. Since we know the relationship is linear, we simply measure the channel corresponding to the known energy spectrum. Assuming that 0 volts (and thus channel 0) means that there is no beam, we then determined that it scales with the following relationship:

$$\begin{aligned}
 E &= \frac{E_{Au}}{Chan_{Au}} \text{ Channel} \\
 &= \frac{22.58 \text{ MeV}}{692 \text{ Channel}} \text{ Channel} \\
 &= (0.0326) \text{ MeV}
 \end{aligned}
 \tag{14.6}$$

where  $Chan_{Au}$  and  $E_{Au}$  were the channel and energy of the observed gold peak. Of course in subsequent runs this method was improved by taking several gold peaks at different energies in order to perform this calibration, but this worked well enough for this first run.

Using this equation the energy of a peak in the detector was then checked against the energy of a SIMP at each mass step. Throughout this entire scan, 200–350 amu,

there were no counts at the desired SIMP energy. So even though counts were arriving in the detector at many of the steps they were simply contamination and in many instances were used as “guide beams” (refer to earlier discussions for more details).

Before shutting down the machine we wanted to quickly perform some tests on the transmission quadrupole, since Tom Miller believed he had a way to detune the ES Quads in order to allow the Trans Quad to focus well enough to run at the higher energy. With the experience gained from one tune, we were better equipped to make adjustments. This study proved to work well since we were subsequently able to tune  $q = +7$ ,  $+8$ , and  $+9$  through to the detector with the analyzing magnet at full current. This was accomplished by first setting the Trans Quads to their maximum settings, and then tuning the other elements around them. This was a novel step in that it allowed us to move to the other charge states with the Analyzing magnet at its maximum field. Before moving on we found several of the guide beams that would be used for a possible  $q = +8$  and  $q = +9$  run.

#### 14.4 Run Au3, Oct 2000: Transmission Efficiency Studies

As mentioned at the conclusion of the previous section, the efficiency of the AMS in detecting heavy nuclei is directly related to the stripper yield for each charge state. This relationship is a Gaussian-like distribution centered on an optimal charge state and is determined by the properties of the stripping gas and the incident particle. In the region of this distribution in which our experiment was performed, increasing the charge state decreases the efficiency. Theoretical studies of such charge exchange, and the resulting equilibrium charge distributions have been analyzed for more than sixty years [33]. During the scan a more massive particle has a lower velocity and thus its yield in a given charge state decreases with increasing mass. It follows that the transmission efficiency  $\eta$  of the AMS is a function of the mass, and hence the final experimental limits on the abundance of heavy Au isotopes with mass  $M_X$  will also depend on  $M_X$ .

Since we know that the particle velocity and  $Z$  of the ion are the primary contributions to the stripping process we may model the X particle (which has the same  $Z = 79$  as Au for a neutral SIMP) by observing Au at low velocities. We then may curve fit the data to obtain the approximate functional form which then allows us to

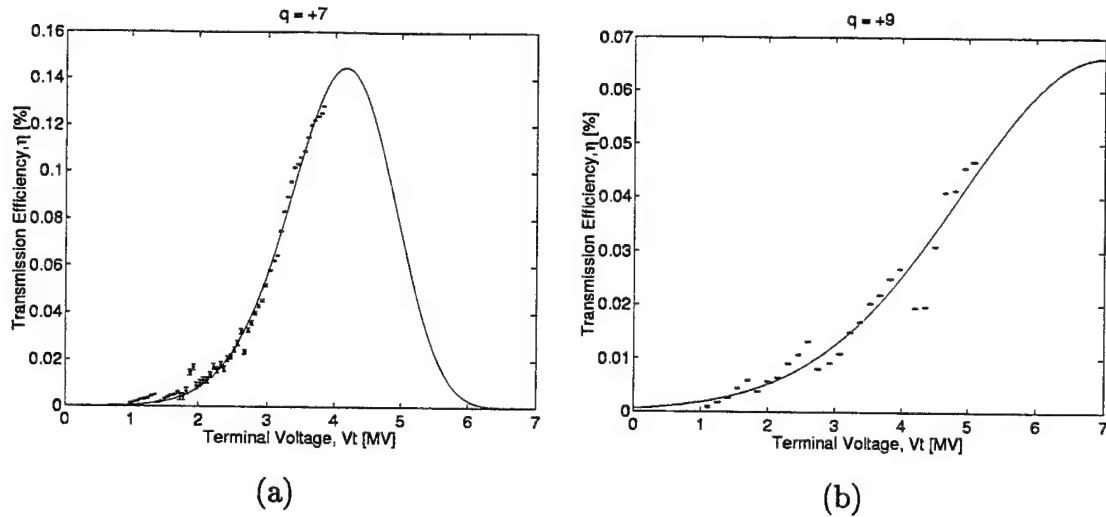


Figure 14.5: Raw data from transmission efficiency scan for (a)  $q = +7$  and (b)  $q = +9$ . Also included are the curve fitted asymmetric Gaussians which are predicted by [20].

estimate the stripping efficiency of the X particle. We thus took measurements of the transmission efficiency as a function of the terminal voltage for charge states  $q = +7$  and  $q = +9$  which resulted in the raw data given in Figure 14.5.

The data points shown on the plot have error bars whose values were determined using the typical rule for the product of two values ( $x$  and  $y$ ) whose systematic errors ( $\sigma_x$  and  $\sigma_y$ ) are known. This equation is given by

$$\sigma = \eta \sqrt{\left(\frac{\sigma_x}{x}\right)^2 + \left(\frac{\sigma_y}{y}\right)^2}. \quad (14.7)$$

The raw data were then curvefit with PAW (the same program we used to perform the linefit for the Be line calibration). The curves were fit to the general asymmetric Gaussian predicted by [20] and described by Equation (1.13). In the program we allowed 4 parameters ( $p_1$ ,  $p_2$ ,  $p_3$ , and  $p_4$ ) to be varied to optimize the curve to the data. This curve and the parameter definitions are given by

$$\eta = p_1 e^{\frac{p_2(V_t - p_3)^2}{1 + p_4(V_t - p_3)}} \quad (14.8)$$

The results from the PAW output for the different parameters are given in Table

14.6. From their definitions we see that  $p_1$  determines the amplitude of the curve, and  $p_3$  fixes the horizontal shift of the Gaussian, while  $p_4$  determines the degree of asymmetry while  $p_2$  determines how rapidly the curve drops off.

Table 14.6: Coefficients for the transmission efficiency curve fit for  $q = +7$  and  $q = +9$ . The definition of these parameters can be found in Equation (14.8). Notice that  $p_3$  is the horizontal shift of the Gaussian.

Charge State	$p_1$	$p_2$	$p_3$	$p_4$
+7	0.14	-0.82	4.165	-0.157
+9	0.066	-0.12	7.014	-0.028

It is important to note that when using PAW we are searching for the minimum in a 5-dimensional space consisting of the  $\chi^2$  for the distribution and the four parameters. As a result it is possible to lock onto a local minimum. However, we have begun by having the computer search for the minimum given the logical range for the parameters (e.g.,  $p_2, p_4 < 0$  and locating  $p_3$  based on our knowledge of the system from the STRIP program output). However, for our purposes we require the curve to be accurate in the regime of the tail. This ensures that however the curve behaves at the higher energies, our data will be collected on the low energy portions for which we have a reasonable estimate for the efficiency.

These raw data may then be applied to the scans by transforming the terminal voltage into the velocity and finally into the SIMP mass. This is performed for both charge states, and normalizing to the initial efficiency (which is what is done when applying it to the final result) we obtain the data given in Figure 14.6.

The transformation from the terminal voltage  $V_T$  for the Au test beam to the SIMP mass  $M$  is performed through a simple transformation using a lot of algebra. After some algebra we find,

$$\frac{1}{2}Mv^2 = V_T + E_p \quad (14.9)$$

where  $E_p$  is the injection energy. We then use the fact that the Au velocity is simulating a SIMP of the same velocity which results in two different terminal voltages

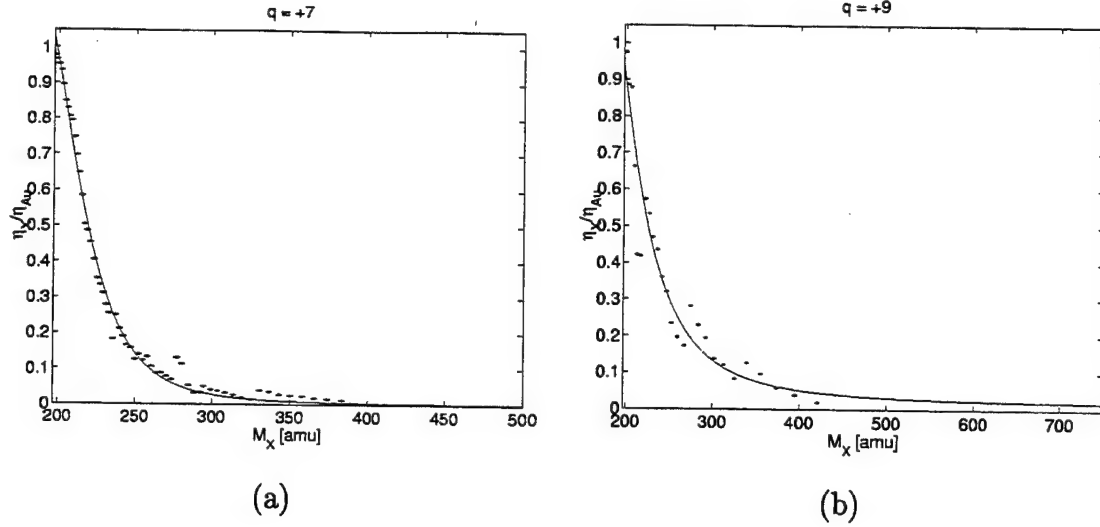


Figure 14.6: Dependence of the ratio of the transmission efficiencies  $\eta_X/\eta_{Au}$  on the  $X$  mass  $M_X$  for (a)  $q = +7$  and (b)  $q = +9$ . The dependence of  $\eta$  on  $M_X$  arises from its dependence on the particle velocity which is a function of  $M_X$ .

associated with the two different particles with the same velocity. Coupling this with the known equation for the magnetic components we are led to solving the following two equations for  $M_X$  and  $V_{TX}$ :

$$\frac{V_{TAu} + E_p}{M_{Au}} = \frac{V_{TX} + E_p}{M_X}$$

$$\frac{M_X E_X}{q^2} = \frac{M_{Au} E_0}{q^2} \quad (14.10)$$

which leads to the final result which transforms the experimental data given in terms of  $V_{TAu}$  into the SIMP mass,

$$M_X = \frac{M_{Au}[qE_p + \sqrt{q^2 E_p^2 + 4E_0(V_{tAu} + E_p)(1+q)}]}{2(V_{tAu} + E_p)(1+q)}. \quad (14.11)$$

Data on the charge state +9 were taken in anticipation of our next run which we planned to utilize in order to reach a higher maximum mass. Thus application of this study would have to wait until the next run.

However, the scan from Run Au2 was performed on  $q = +7$  and so this was the final ingredient needed to complete the limit set on SIMPs in Au for this scan. In Au2 we found  $I_{det} = (4.8 \pm 0.1)$  nA for the lab gold, and  $I_{det} = (4.7 \pm 0.1)$  nA for the Australian gold samples. As noted above, the ratio of the transmission efficiency for the massive isotope to that of gold,  $\eta_X/\eta_{Au}$ , was found to vary with mass as can be seen from Figure 14.6.

The scan performed on Au2 gave no indication of SIMPs in any of the predicted channels. However, obtaining zero counts had to be transferred into a meaningful result on the abundance of SIMPs in Au. The ratio of the number of hypothetical  ${}_{79}X$  particles (having a mass  $M_X$ ) to the number of  ${}_{79}\text{Au}^{197}$  atoms in the beam, or the SIMP abundance, is determined by the Au beam current  $I_{det}$  measured by the detector Faraday cup (located just in front of the detector window). Recall from Chapter 1 that we can express  $X/Au$  in terms of  $I_{det}$  and the charge state  $q$ ,

$$\frac{X}{Au} = (2.672 \times 10^{-12}) (-\ln \varepsilon_X) \frac{q}{I_{det}} \left( \frac{\eta_{Au}}{\eta_X} \right). \quad (14.12)$$

Here  $\varepsilon_X = (1 - \text{CL})$  where CL is the confidence limit, derived using standard Poisson statistics<sup>2</sup> [40] and  $\eta_{Au}$  ( $\eta_X$ ) is the transmission efficiency for detecting  ${}_{79}\text{Au}^{197}$  ( ${}_{79}X$ ). The results quoted here are at the 95% CL which corresponds to  $(-\ln \varepsilon_X) = 3.00$ . The numerical coefficient in Eq. (14.12) is obtained by noting that when  $q$  is measured in units of the electric charge  $[|e|]$ , and  $I_{det}$  is measured in nanoamps [nA] then

$$\frac{q [|e|] (1.602 \times 10^{-19} \text{ C}/|e|) (1 \text{ nA})}{I_{det} [\text{nA}] (1 \times 10^{-9} \text{ C/sec}) (60 \text{ sec})} = \frac{q [|e|] (2.672 \times 10^{-12} \text{ nA})}{I_{det} [\text{nA}]} \quad (14.13)$$

so that  $X/Au$  is dimensionless as expected.

This result from application of the efficiency curvefit (represented in Figure 14.6a) is then inserted into Eq. (14.12), and the result is plotted for  $q = +7$  in Figure 14.7. Table 14.7 exhibits the  $X/Au$  ratios for both the lab gold and Australia gold at each of the masses predicted by those theories whose range is covered by the present run. Notice that the limit weakens with increasing mass which is a result of the dropping

<sup>2</sup>See Chapter 1 for more information on Poisson Statistics.

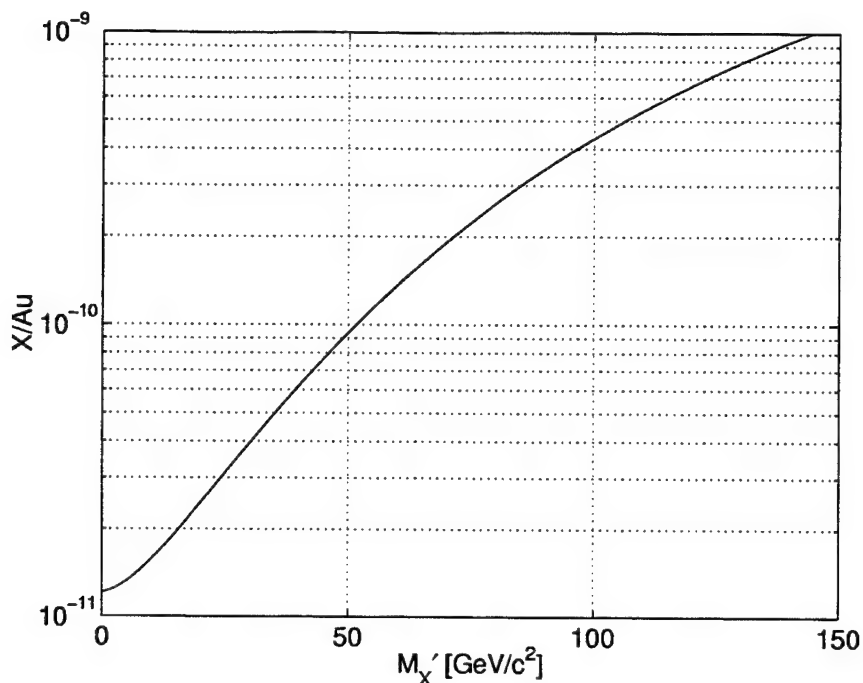


Figure 14.7: 95% confidence limits on the  $X/Au$  ratio in Equation (14.12) as a function of  $M'_X$  in  $\text{GeV}/c^2$ , obtained from the Australia gold sample. As can be seen from Table 14.7, the results for the samples of lab gold and Australian gold are virtually identical.

stripping efficiency. Since this is the first limit on SIMPs bound to heavy nuclei it is difficult to compare this result with other experiments.

However, we may display the constraints emerging from this scan on Table II of Ref. [6] by identifying the regions excluded by the present experiment. The boxed values in our Table 14.8 represent those entries for which the abundance of SIMPs in gold should have been large enough for SIMPs to have been seen by our AMS search had they been present. Thus we see that even from this first run we were able to constrain regions in the SIMP mass/cross-section phase space.

#### 14.5 Run Au4, January 2001: Mass Scan from 200-688 amu, All Samples

In Run Au2 the window caused us to end the run prematurely since the beam did not possess sufficient energy to penetrate into the detector. As a result, this limited the maximum mass to 350 amu. It was natural to try to get to ever higher masses

Table 14.7: Summary of X/Au ratios for the effective SIMP mass  $M'_X$  in  $\text{GeV}/c^2$ . We define  $M'_X \equiv M_X - M_{Au} = M_S - |E_B|$  where  $|E_B|$  is the magnitude of the binding energy of the SIMP to the Au nucleus. See text for further discussion.

Sample	$M'_X$ [ $\text{GeV}/c^2$ ]			
	3	50	100	144
Lab	$< 1.2 \times 10^{-11}$	$< 9.6 \times 10^{-11}$	$< 4.2 \times 10^{-10}$	$< 4.2 \times 10^{-10}$
Australia	$< 1.3 \times 10^{-11}$	$< 1.0 \times 10^{-10}$	$< 4.3 \times 10^{-10}$	$< 4.4 \times 10^{-10}$

and in this light we decided to switch to a higher charge state which allowed us to reach a higher maximum mass. The highest energy guide beam that was observed was at 13 MeV. Thus with this constraint we were again going to be limited by the window energy; however, by switching to a higher charge state we push the mass up for a given minimum energy (recall that  $ME/q^2$  is constant).

The novel aspect of this run was the inclusion of all our unknown samples. Since the stripper efficiency data for  $q = +9$  had already been taken, all that was needed was to actually run the samples. This time eight samples were mounted on the sample wheel (see Figure 14.8 for a picture of the samples) and each was rotated into the Cs beam at each mass step. As in Run Au2, the run time for each sample was limited to 1 minute at each mass step which served to both prolong sample lifetimes while minimizing the total run time.

The samples were pounded into the cathodes and loaded into the sample positions listed in Table 14.9. Notice that we now include data on an iron meteorite sample, which has long exposure times, along with the Au samples. In this particular case we then are looking for anomalous Fe nuclei instead of Au nuclei. Since the tune is for a particular mass and charge state, the AMS does not care about what the host nucleus is, provided we know a priori how it behaves in the stripper. This will be discussed in greater detail later in the section. We proceed to analyze the data for the Au first.

Table 14.8:  $M_X$  (vertical) in units of  $\text{GeV}/c^2$  versus  $\sigma_{SN}$  (horizontal) in units of mb. Table entries give the predicted values of  $-\log_{10}(X/\text{Au})$  obtained from Ref. [6]. These predictions are obtained under the approximation [7, 6]  $\sigma_{SN}^2 \sim \sigma_{SS}\sigma_{NN}$ , which is used to determine the cosmic S abundance. Such baryonic SIMPs fail to saturate halo dark matter for  $\sigma_{SN} > 10^{-3}$  mb. The entries in boxes are excluded by the present experimental results at the 95% confidence level. For the sake of comparison to Ref. [6] we assume here that  $M'_X \approx M_S$ .

$M_X$ ( $\text{GeV}/c^2$ )	$\sigma_{SN}$ (mb)									
	.0005	.0015	.0042	0.012	0.032	0.09	0.25	0.69	1.9	5.3
2.7								5.9	7.9	8.3
4.3							5.7	7.7	8.1	11.1
7.1						5.5	7.5	7.9	10.9	12.1
12					5.6	7.6	8.1	8.5	12.2	12.7
19					7.5	7.9	8.3	11.3	12.5	12.9
31				7.4	7.8	8.2	8.6	12.4	12.8	13.2
50			5.7	7.7	8.1	8.5	11.5	12.7	13.1	13.6
81		5.7	7.7	8.1	8.5	8.9	11.9	13.1	13.5	14.0
132	5.7	7.7	8.1	8.5	8.9	9.3	12.2	13.5	13.9	14.3
220	6.0	8.0	8.4	8.9	9.3	9.7	12.6	13.9	14.3	14.7

While Run Au2 went off without a hitch (discounting the window problem), this run was a completely different story. Right from the start we were plagued with tank sparks (about 4 per day all at relatively low  $V_T$ ). We also ran into a puzzling problem. The breaker in the sub-basement tripped off unexpectedly which let up the two cryopumps in the beam pipe between the analyzing and switching magnets. After regenerating the cryos (which takes a little over half a day), we realized that this was the first time the analyzing magnet power supply had been run up to maximum since the addition of the cryopump to the aforementioned beamline. In fact with the magnet power supply at maximum we were drawing 104 A from a 100 A circuit

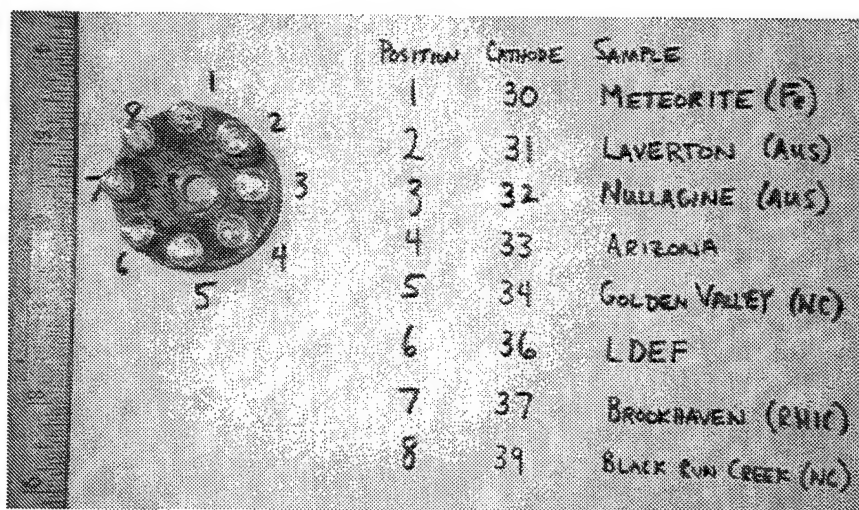


Figure 14.8: Photograph of the sample wheel before the run began. This picture gives a good representation of how the samples are loaded as well as showing their sizes.

breaker. As a result we needed to switch the Danfysik power supply (which runs the analyzing magnet) to another circuit breaker. This took the better portion of a day to resolve. Thus we began a week long run which should have been completed in two days.

In order to make the procedure simpler we decided to add the diverter, which is a mechanism that is designed to protect the detector from beams with high counting rates. In Run Au2, this protection was achieved by the operator who inserted the attenuator and detector faraday cups before crashproofing the computer. After checking the rate on the scope and the red interference meter on the electronics stack, the operator would then uncrashproof the computer and remove the attenuator and detector cups. Unfortunately this was a very cumbersome procedure that was rarely needed and which introduced several possibilities to give an erroneous null result. This is because the computer does not control the detector Faraday cup, and hence if left in by accident it would block the beam from getting into the detector. Likewise crashproofing the computer means that we remove the incoming counts by disconnecting the BNC connector leading from the ADCs (analog to digital converters) which process the signal from the detector. Like the detector Faraday cup, this would result in a null result since the computer would not actually be receiving data from the

Table 14.9: Sample positions on wheel along with the respective holder numbers (which are stamped on the back of the cathodes).

Position	Nuclei	Sample	Holder Number
1	Fe	Meteorite (Canyon Diablo)	30
2	Au	Laverton (Australia)	31
3	Au	Nullagine (Australia)	32
4	Au	Arizona (Gold Basin)	33
5	Au	North Carolina (Golden Valley)	34
6	Au	LDEF (NASA, Disk 13)	36
7	Au	RHIC (Brookhaven National Lab)	37
8	Au	North Carolina (Black Run Creek)	39

detector. The only way to catch such an operator error would be to fail to find an expected guide beam, which is why guide beams are so vital to this experiment.

The diverter works in conjunction with the  $\Delta E_1$  plate by steering the beam away from the detector for 500 ms when high counting rates are present. For low counting rates the diverter has a relatively small effect since the time separation between ions is greater than the 500 ms diverter (beam off) time. The diverter is used regularly in AMS and we would usually simply turn it on and start using it. However, some simple software modifications had been made which prompted us to test the diverter to make sure it was working properly. In the process of testing the diverter we discovered an even bigger problem. At the beginning of the tests it appeared that the diverter was not working properly because we were seeing large fluctuations in the counting rate. We soon determined that the fluctuations existed even in the absence of the diverter, which pointed us to an undiscovered problem.

The problem is quite simple to explain: from one data point to the next we were obtaining beam currents which were inconsistent by over a factor of 2. This is quite substantial and thus gave us a hint it was coming from something that was happening to the beam between the cataloging of each data point. After two days of searching

through the beam we narrowed the problem to the injector Faraday cup. For a reason that was then unknown, the Faraday cup going into and out of the beam caused the tune to change resulting in the observed fluctuations in the counting rates. Since we could not find a way to prevent the injector cup from going in and out we manually removed its computer control. Unfortunately, this prevented us from rotating the sample wheel. After a prolonged discussion of the behavior of the injector Faraday cup, it was determined that although the cup was getting completely removed from the beam it was retracting to a slightly different location each time. If the cup were uncharged this would not be a problem; however, in front of the cup is a bias plate (see Figure 14.9) which is just slightly negatively charged (at -300 V). This is so that particles that try to bounce out of the cup will see the small electric field produced by the bias and get pushed back in when it is inserted into the beamline. This helps produce an accurate measure of the beam current.

When the cup retracts out of the beam it blocks the electric field lines from the bias. Even though this small asymmetric electric field steers the beam by a small amount, steerers further down the beamline may correct for this assuming that it remains constant. With the cup retracting to a different spot each time, the asymmetry of the bias field seen by the beam changes, thus resulting in slightly different steering by the bias. In normal AMS operations the beam injection energies are high enough that this perturbation caused by the inconsistencies associated with the cup position are relatively small (although they do cause a noticeable effect when trying to obtain 1% precision). In our previous Au runs we also were running at injection energies which were relatively insensitive to this steering.

However, in order to achieve ever higher masses we had to lower the injection energy (down to 7.5 keV). Thus we finally crossed the threshold into the regime where the cup bias was significantly steering the low energy beam. Once this was realized, the problem was readily fixed by simply turning off the bias, which then resulted in consistent data, and allowed us to verify that the diverter was indeed working properly.

Fixing this problem was not only beneficial to us but also helpful to PRIME Lab, since it may be a major contributing factor to what had been a difficulty in

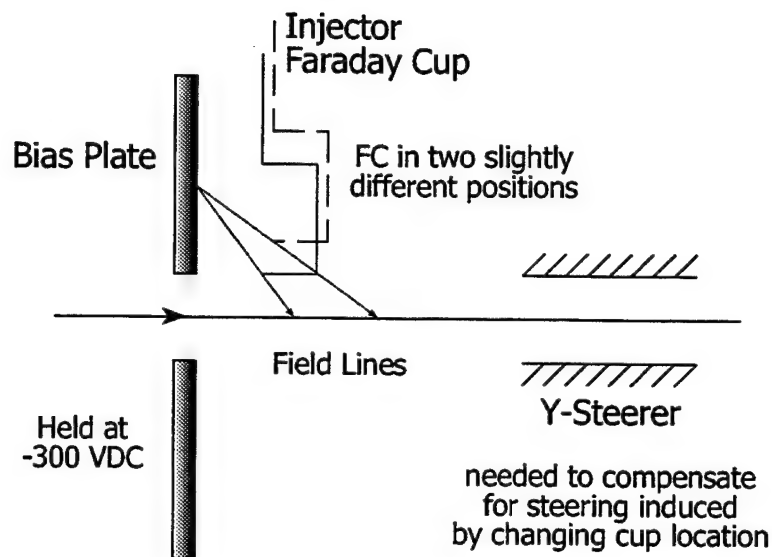


Figure 14.9: Schematic of bias plate and injector Faraday cup. Each time the cup is inserted into the beam it retracts to a slightly different position between the negatively charged bias plate. The cup then blocks a slightly different fraction of the electric field lines emanating from the plate, thus creating an asymmetric electric field which changes slightly each time the cup is inserted. This had the effect of steering our low energy beam and caused current fluctuations greater than a factor of 2. The problem was solved by removing the bias electric field.

obtaining high precision results. If so it should reduce run times by allowing the desired precision to be reached in fewer sequences. Once we had this problem solved we were able to actually begin taking data. The final tandem settings are provided in Table 14.11.

Once the tune was adjusted following the solution of the injector cup problem we were ready to proceed with the detector calibration. This time we used the  $\text{Au}^{+9}$  and  $\text{Au}^{+8}$  beam peaks to determine the calibration line relating the channel to the energy. The data for the energies and channels from these two data points is given in Table 14.10 and resulted in the following calibration of the detector

$$E = (0.0496) \text{ Channel} + 4.546 \quad (14.14)$$

where  $E$  is a function of the observed channel and is reported in MeV.

Table 14.10: Measured parameters used to calibrate the detector.

Beam	Channel	Energy [MeV]
Au <sup>+9</sup>	930	50.7075
Au <sup>+8</sup>	711	39.8371

Data analysis of Run Au2 showed that the 2 amu stepsize was overly conservative since we were able to realize guide beams approximately 3–5 mass steps before we were centered on them which occurred because the width of the beam was actually 3–5 times as wide as the 2 amu stepsize we were using. As a result, we determined the stepsize based on the width of the Au beam. This study was performed by slowly changing the terminal voltage while watching the current in the detector Faraday cup. This then defined the width of the beam and the steps were then scaled so that they overlapped at full-width half maximum all along the scan. This overlap was checked by finding a guide beam (Au<sup>+5</sup>) which fell exactly halfway in between two steps (steps at masses 351 and 359 amu). The width of the beam is shown in Figure 14.10.

Finally we were ready to actually take the data. Throughout the run the beam currents for each of the different samples were monitored so that later we would be able to factor their drift into the final result. This also allowed us to monitor whether the samples were being consumed, and if we needed to touch up the tune at the ion source. To take these data the settings all needed to be taken back up to the original Au beam (or basically back to mass 197) which meant the terminal voltage, ES Quads, ESA, and Injector magnet all had to be run back to Au<sup>+9</sup>. While the ES Quads and ESA are manual settings dialed into the potentiometers (pots) by the operator, the terminal voltage needed to be slowly adjusted up and down while keeping the corona current and balance as constant as possible. The injector magnetic field setting was set using the computer to relay the command and determine the appropriate power supply setting. Plots of the currents as a function of mass are given in Figure 14.11.

The figure shows all of the samples following the same general trend, as they all decrease slowly. The dashed lines represent the curve fit through the data points

Table 14.11: Tandem parameter settings following the tune on  $q = +9$ . Refer to Figure 1.1 to locate the different elements.

Stage	Setting	Value
Ion Source	Cathode =	30 %
	Extractor =	3.0 kV
	Pre-Acc =	4.5 kV
	Injection Energy =	0.0075 MeV
	1st/2nd Einzel Lens =	2.3%/2.1%
	INJ IMG X/Y Steerers =	49.0%/48.9%
	Au Injector B-field =	-0.27066 T
Low End	INJ IMG Einzel Lens =	7.2%
	LEBL Einzel Lens =	6.8%
	Gridded Lens =	2.0%
	LE X/Y Steerers =	2.7%/-7.8%
Terminal	Stripping =	Gas @ $9.8 \times 10^{-7}$ Torr
	Charge State, $q$ =	+9
	Terminal Voltage, $V_t$ =	5.070 MV GVM
	Au Energy =	50.7075 MeV
	Corona Current =	23 $\mu$ A
	Points =	13.0 inches
High End	Au ESQ A/B =	24.75%/27.62%
	Analyzing B-field =	-1.63000 T
	Trans Quad A/B =	105.21%/88.78%
	BL Quad A/B =	54.06%/52.78%
	Au ESA =	57.55%
Detector	Gas Pressure =	25.01 Torr
Final Transmission	INJ FC Current =	673
	LE FC Current =	610 nA
	HE FC Current =	970 nA
	Image FC Current =	2.5 nA
	SM FC Current =	1.8 nA
	Detector FC Current =	1.6 nA
	Complete Transmission, $\eta_{tot}$ =	0.03 %

and was used to represent the current as a continuous function of mass (really an indication of time) that is eventually used to evaluate the SIMP abundance limit in each sample. We will delay discussion of the Fe data until later in the section.

As before, no counts were detected in the SIMP channels. This time we also looked at a range of possible SIMP channels which took account of possible errors in the detector calibration. The width of channels observed was equal to  $2 \times$  the full width at half maximum of the gold peak (which turned out to be roughly 56 channels). Once the high end of the SIMP peak channel window dropped below channel 500 the

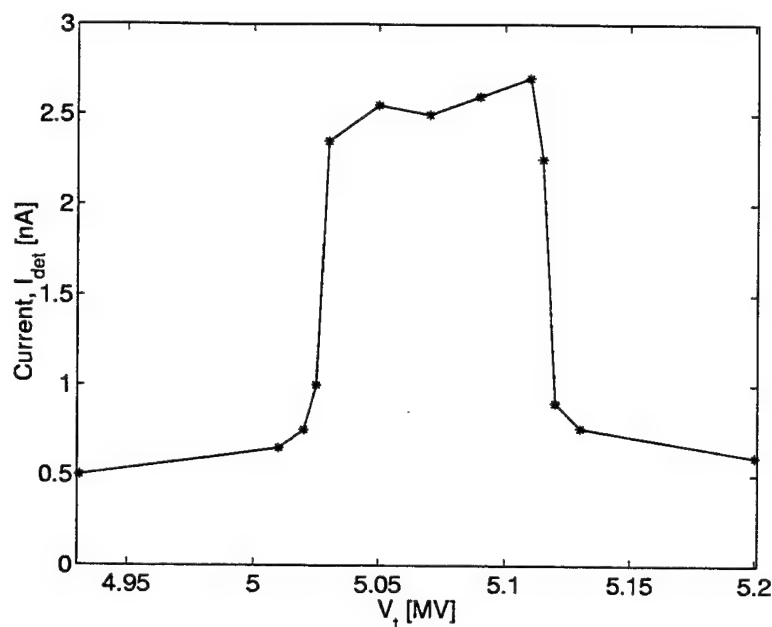


Figure 14.10: Beam profile as measured in the detector Faraday cup. This profile allowed us to determine the optimal stepsize to ensure overlap between steps while simultaneously preventing redundancy of the data points.

gain was increased by a factor of 2 so that we would obtain better peak resolution and not have all the peaks pushed against the lower left of the GKS plot of the energy histograms. The factor of two was then tested to make sure that a guide beam peak scaled appropriately. When the gain is changed in this manner it simply means that the counts are distributed over every 2 channels instead of over every channel, and this has the effect of making the peaks easier to distinguish when looking at the whole spectrum. Of course the line calibration moves in a characteristic way so as to still be valid.

The final results after fitting a curve through the  $q = +9$  data of Run Au3 to the raw results (which include the currents shown in Figure 14.11), and inserting into Equation (14.12) gives the results provided in Figure 14.12.

To compare the previous results (those of Run Au2) to those obtained in the current run we consider Figure 14.13. The  $q = +7$  data end at 350 amu because of the limitation produced by the window. This same limitation is what prevented the

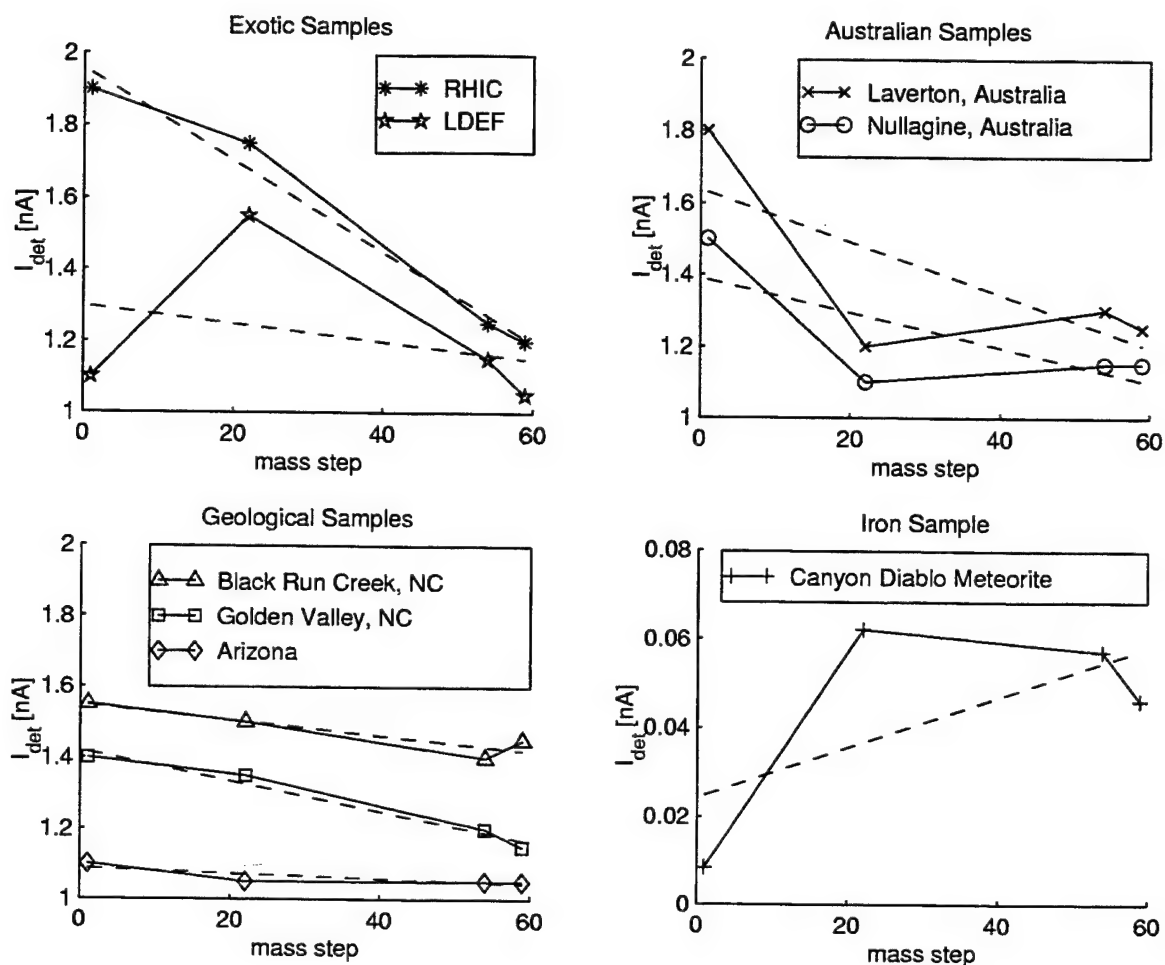


Figure 14.11: Sample currents measured in the detector Faraday cup. These data are used to calculate the  $X/Au$  limit for each sample. The Fe data were used only to monitor the sample consumption since the Fe current is needed to evaluate  $X/Au$ .

$q = +9$  data from going even higher. Recall that the energy necessary to penetrate the window in Run Au2 was 12.9 MeV; this time the energy needed was measured at 14.5 MeV which stopped us short of our anticipated maximum mass. This window problem was our biggest limitation as we will discuss below. It is important to note a feature which is clearly evident in Figure 14.13, that is the observation that for each mass there is an optimum charge state at which to run. For example, the  $q = +7$  data gives a better limit below masses of  $\approx 290$  amu, while the  $q = +9$  data gives a

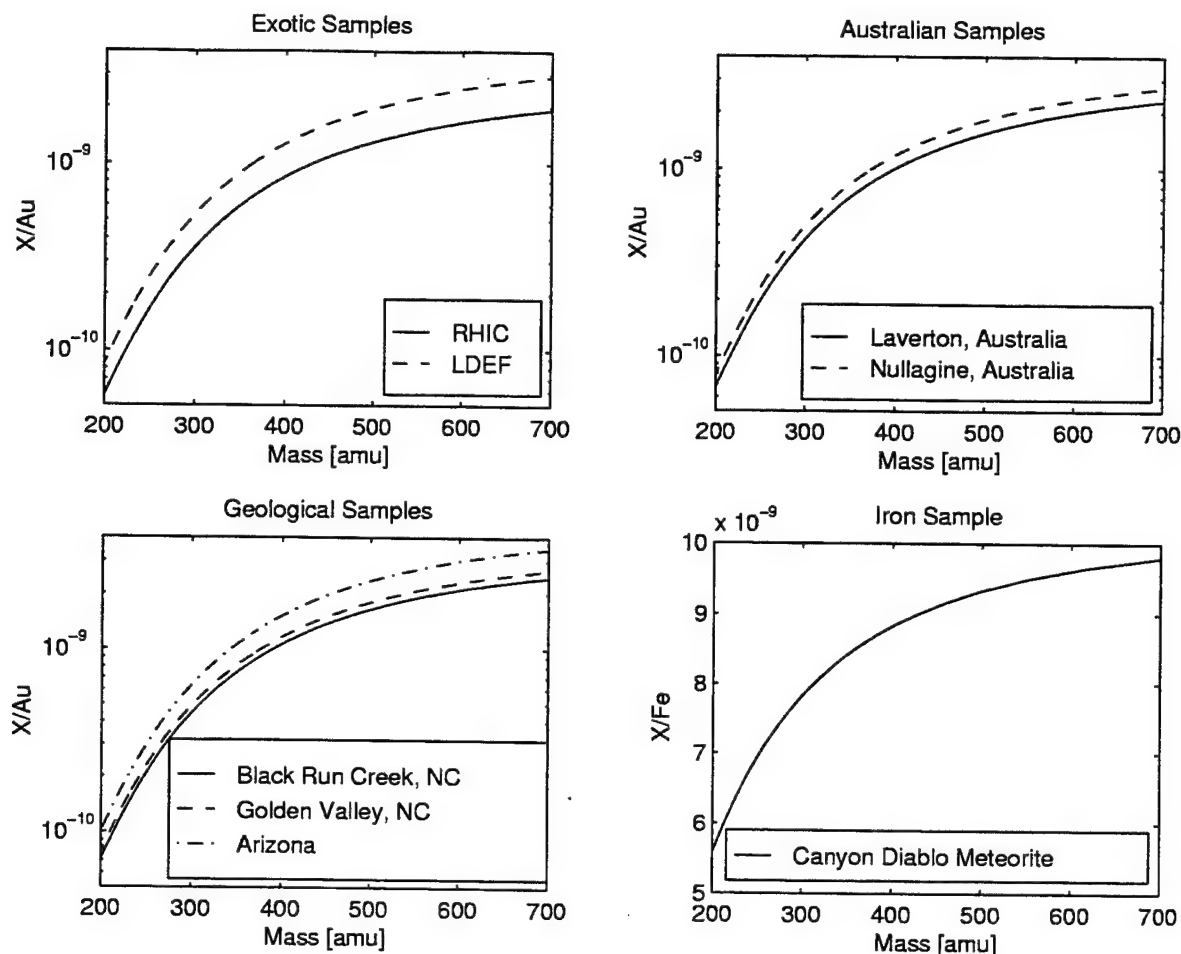


Figure 14.12: The final results of the  $q = +9$  run on all eight samples. The data for the Fe Meteorite will be discussed in the following pages.

better limit above. This provides some insight into how we may set limits on higher masses. By performing the scan at a charge state which gives the best efficiency – and whose energy is greater than that necessary to penetrate the window – for a given mass gives us the best possible limit. This concept will be derived and implemented for the final Au run and is an outgrowth of the results shown in Figure 14.13.

As previously noted, we also ran the iron meteorite sample during this run. This run was performed sequentially with the Au run since the massive particle doesn't care what  $Z$  it has. Of course its stripping efficiency cannot be predicted by the Au data but, we were fortunate enough to be given just enough time to complete an

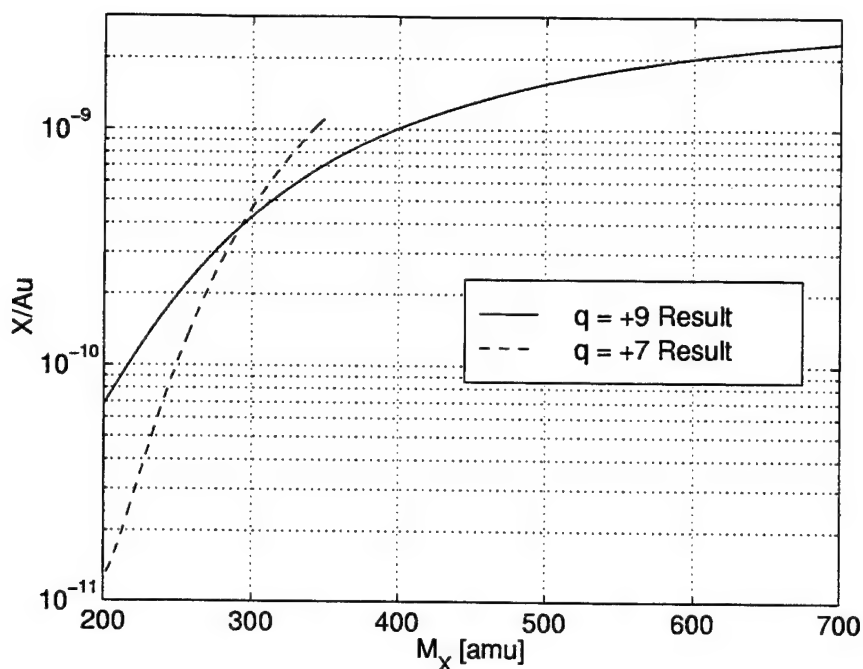


Figure 14.13: A comparison of the results for the Laverton data taken during Runs Au2 and Au4. Here we get a glimpse of the tradeoff from one charge state to another. The charge state +7 data gives slightly better limits between 197 and 290; however at 290 the limits from charge state +9 data become more stringent and extend our mass range up to 688 amu. This corresponds to an effective SIMP mass of 491 amu.

efficiency scan for  $\text{Fe}^{+9}$ . This was not a trivial task but involved a fresh new tune on Fe which we had never done before. As such it was like performing Run Au1 but with Fe. Of course, by now we had experience finding and tuning high mass beams, so the tune did progress slightly faster than the original Au tune. The results of the raw data from the efficiency scan are given in Figure 14.14.

The curve fit through the experimental data in Figure 14.14 was again performed with PAW. Again the data were fit with a curve whose general functional form obeys that of Equation (14.8) and the values for the coefficients are given in Table 14.12.

These results were then inserted into Equation (14.12) along with the current information (after being normalized to the Fe current produced by the sample) to

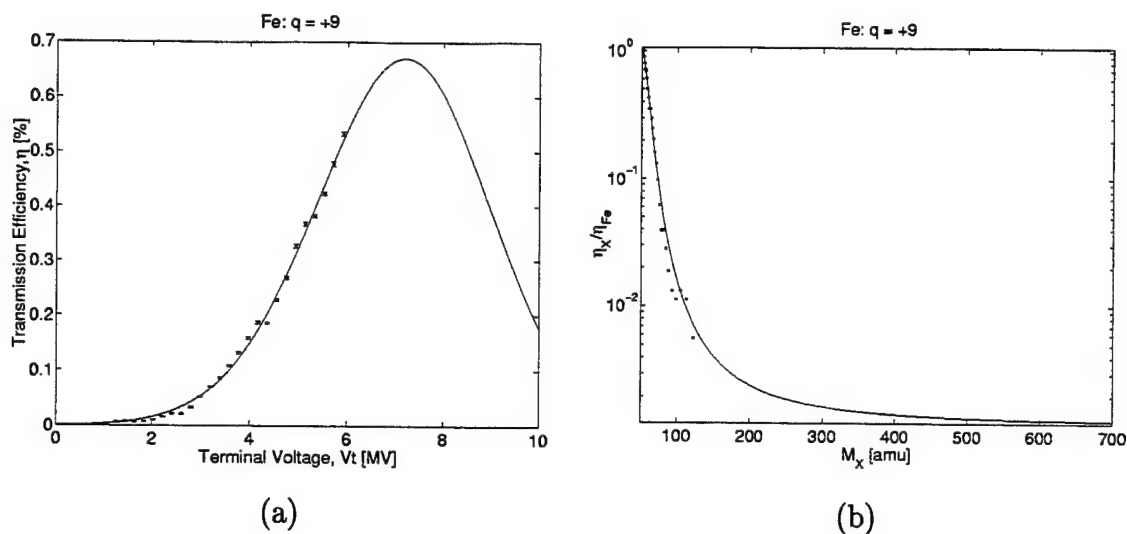


Figure 14.14: (a) The raw data from the efficiency scan on  $\text{Fe}^{+9}$  and (b) the normalized efficiency as a function of total mass.

Table 14.12: Coefficients for the transmission efficiency curve fit for Fe in charge state +9. The definition of these parameters can be found in Equation (14.8). Notice that  $p_3$  is the horizontal shift of the Gaussian.

Charge State	$p_1$	$p_2$	$p_3$	$p_4$
+9	0.67	-0.16	7.207	-0.026

produce the result shown in Figure 14.12. Notice that for the Au SIMP the scan translates into a SIMP effective mass of 3–491 amu. Here we define the effective SIMP mass to be  $M'_X \equiv M_X - M_{Au} = M_S - |E_B|$  where  $|E_B|$  is the magnitude of the binding energy of the SIMP to the Au nucleus. In contrast, for the Fe sample the same scan translates into a SIMP mass range of 144–632 amu. Which means that for Fe we have data going up to higher SIMP masses than the results obtained from the Au. This difference is simply the difference in the masses of Fe and Au (which is 141 amu).

Following this run we had set the stage for utilizing the variational charge state method which would optimize the efficiency while also permitting us to obtain the highest possible mass.

#### 14.6 Run Au5, May 2001: Final Mass Scan 200-1777 amu

The previous two runs (Au2 and Au4) ended because of beam energy limitations due to the detector window. With this in mind we had two options to reach higher masses. First we could try to find a thinner window. The existing window is  $2.5\ \mu\text{m}$  thick and is made from Mylar which has a nominal chemical formula  $\text{H}_8\text{C}_{10}\text{O}_4$ . The Stopping Range of Ions in Matter (SRIM) program offered by IBM-Research and written by James Ziegler predicts that an Au ion must have a minimum energy of greater than 9.12 MeV to penetrate a  $2.5\ \mu\text{m}$  thick Mylar film. In the previous two runs we determined that beams with minimum energies of 12.9 MeV and 14.5 MeV were visible above the noise region of the ADCs. Thus within the errors of the experiment we could say that the predictions made by the SRIM program are reliable. However, they may be slightly generous since SRIM is unable to compensate for machining tolerances associated with the inevitable nonuniformities in mylar thickness. This is important because we were able to locate and purchase a new film manufactured by Chemplex which is  $1.5\ \mu\text{m}$  thick. This film was made from Ultra-Polyester and has the same chemical formula as Mylar since the materials are related. The SRIM program predicts that an Au beam needs a minimum energy of 5.21 MeV to penetrate the  $1.5\ \mu\text{m}$  thick ultra-polyester film. This suggests (assuming a constant scaling) that an Au beam of around 7.8 MeV would be needed to be seen above the ADC noise. This is an optimistic result since this would raise the maximum mass limit in  $q = +9$  from 688 amu to 1275 amu. However, the drawback is that the new window would need to be inserted and tested, with no guarantees that it would be strong enough to withstand the pressures of the detector. Running such tests would take at least a day to perform if not more depending on any unforeseen problems.

Another way to circumvent this problem is to introduce higher charge states which allow higher energy beams to be selected with the high end magnetic elements. In this method, the lowest possible charge state with an energy greater than the window cutoff energy would be used to search for SIMPs. This method meant that we would be able to reach high masses (up to 1775 amu in  $q = +14$ ) with the existing window. In this search we would thus use certain charge states to scan at particular masses. Because of time limitations this was chosen as our best course of action since we

increased the mass window at the cost of efficiency. Of course the best scenario would have been to combine the two: insert the new window *and* use the variational charge state method.

During Run Au5 we implemented this variational method by selectively taking data points as the terminal voltage and other electrostatic elements were slowly decreased. When data for more than one charge state were available at a given terminal voltage, the injector magnet field was changed accordingly to correspond to the masses of each charge state. Since we recall that  $M/q$  is constant this made life simple and the ES Quads and ESA only needed to be adjusted enough so as to shift their  $E/q$  so that the constant  $M/q$  condition was then satisfied. Table 14.13 gives the mass ranges for each charge state and shows the general flow of data accumulation during the run.

The maximum obtainable mass for a given charge state was determined by keeping track of the energy. Thus once the energy dropped below the window cutoff energy we would switch to a higher charge state and the mass scan was then picked up at the appropriate mass and continued until this condition was again satisfied.

Of course this method relied on our ability to perform transmission efficiency scans on each of the charge states in question. Thus while we already have data on  $q = +7$  and  $q = +9$  which we acquired during Run Au3, we needed the data on  $q = +5, +6, +8, +10, +11, +12, +13, +14$ . This is a large undertaking because of the rigor and tedium associated with changing all the settings as the energy is decreased. The efficiency scans were all done using the same method as that described in Run Au3 where the stripper efficiency was measured from the LE FC to the IMG FC. The point of interest is not necessarily the absolute magnitude of the efficiency but rather the behavior of the efficiency as the energy is reduced, since it is normalized to the Au efficiency. The number of data points taken to create the curvefit was generally kept greater than ten when possible. Again time was a big factor and at several of the intermediate charge states (6, 8, and 10) only ten data points were taken. However, the  $q = +5$  and  $q = +12$  data both had significantly more data points so that we could obtain nice fits for the extremal charge states. Our data for  $q = +13$  and

Table 14.13: Outline of the variational charge state method which was implemented in Run Au5. Table entries are the mass in amu scanned at each terminal voltage whose units are in MV. Notice that the data wraps to the right column due to the large quantity of points. As a result the  $q = +10$  data had to be broken up. This table actually defines an entire phase space with the values shown here corresponding to those actually used in the run.

Charge State						Charge State						
$V_t$	5	6	7	8	9	10	$V_t$	10	11	12	13	14
2.828		225					1.361	825	916			
2.773		229					1.331	844	936			
2.718		234					1.301	863	957			
2.665		238					1.272	883	979	1076		
2.613		243					1.244	903	1002	1101		
2.561	201	248					1.215		1025	1126		
2.510	205	253					1.187		1049	1153		
2.461	209	258					1.159		1075	1181	1287	
2.412	213	263					1.132			1209	1318	
2.364	218	269					1.104			1239	1350	
2.318	222	274	327				1.078			1270	1384	1498
2.272		280	333				1.051			1302	1419	1536
2.228		285	340				1.024				1456	1576
2.184		291	347				0.998				1494	1617
2.141		297	353				0.972					1660
2.099		303	361				0.947					1705
2.058		309	368				0.921					1752
2.017		315	375									
1.977		321	383	444								
1.938			390	453								
1.900			398	462								
1.862			406	472								
1.825			415	481								
1.788			423	491								
1.752			432	501	571							
1.717			441	512	583							
1.682				522	595							
1.648				533	607							
1.614				544	620							
1.581				556	633							
1.548				567	646	726						
1.516					660	741						
1.484					674	757						
1.453					689	773						
1.422					704	790						
1.391					719	807						

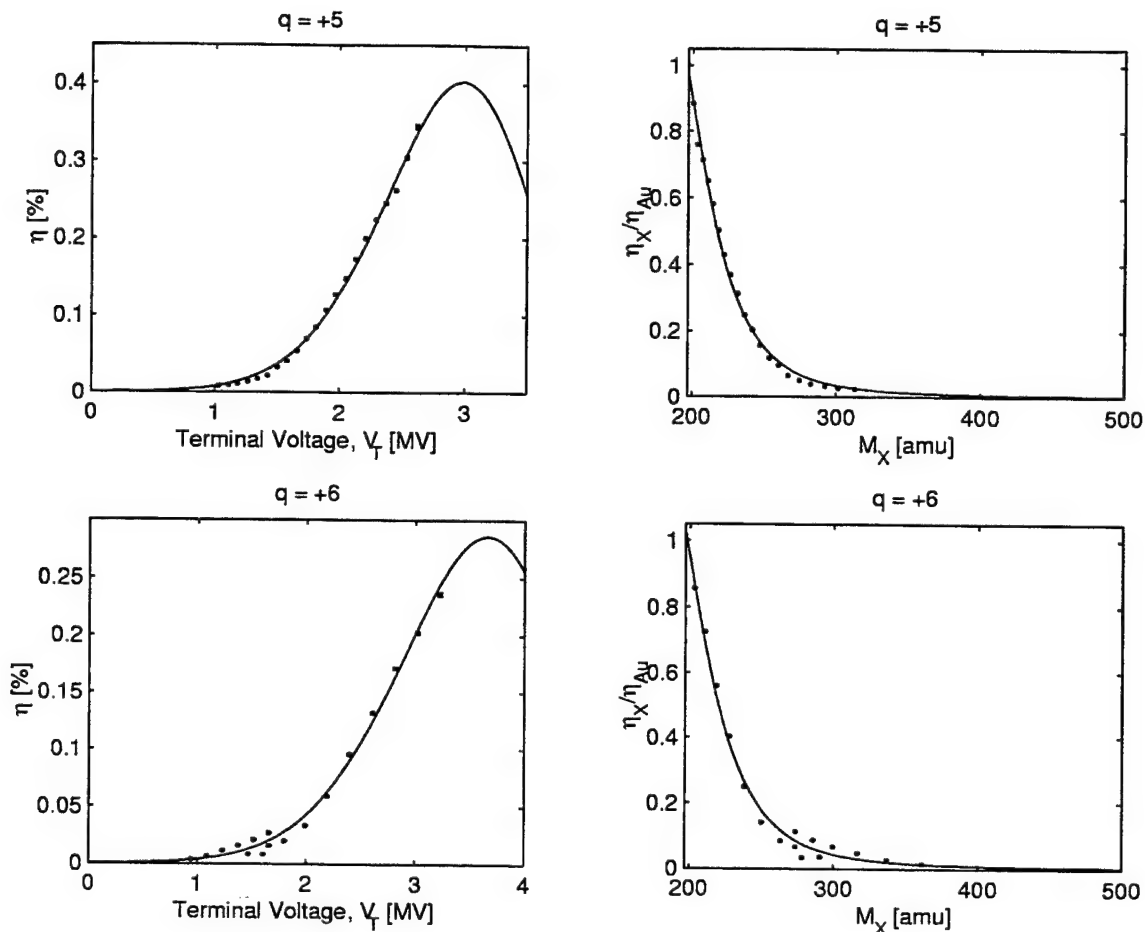


Figure 14.15: Stripper efficiency data for charge states  $q = +5$  and  $q = +6$ . Notice that the scales are not the same for each plot.

$q = +14$  are limited. As the charge state increased we moved further down onto the tails of the Gaussian distribution. For charge states +5 through +12 we were able to at least begin with the analyzing magnet at its maximum setting thus obtaining the best possible data given the magnet restrictions. For charge states +13 and +14 we had to adjust the analyzing magnet and terminal voltage since the magnet could not even bend Au in this charge state at the optimal settings. Thus the data for +13 and +14 are not optimized due to magnet constraints.

We are also clearly on the flat portion of the tail of the Gaussian as the current began to approach the background rate. For both  $q = +13$  and  $q = +14$  the Au

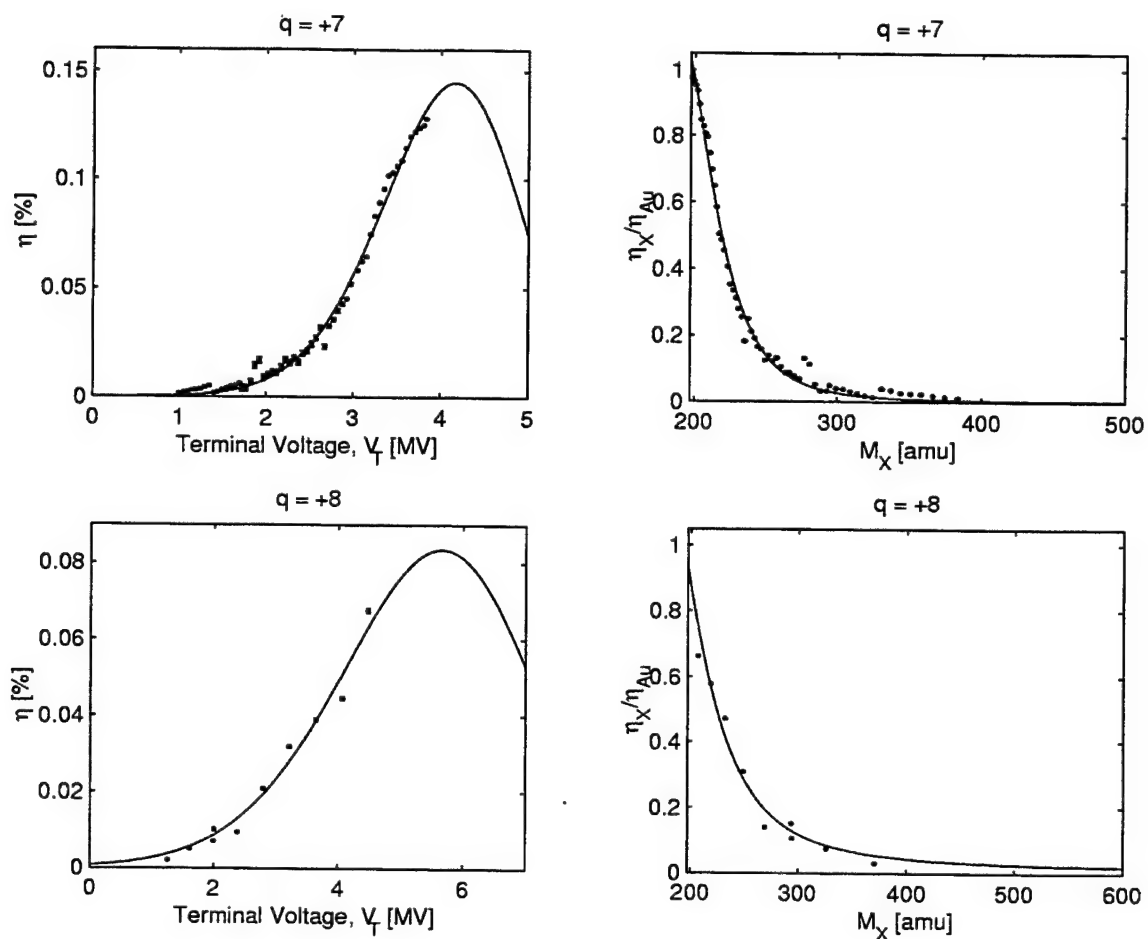


Figure 14.16: Stripper efficiency data for charge states  $q = +7$  and  $q = +8$ . Notice that the scales are not the same for each plot. The  $q = +8$  data are new while the  $q = +7$  were taken during Run Au3. They are included together here so that the progression with increasing charge states can be visualized.

beams were found above background. However, because of the low initial beam current we were unable to get the ten desired data points taking us down to the minimum terminal voltage. In both cases the current dropped to background before the ten data points could be taken. Also the lack of Gaussian-like structure to the data (since we are fitting a Gaussian to data that looks more like a line) produces a result which is seemingly uncharacteristic when compared to the other charge states.

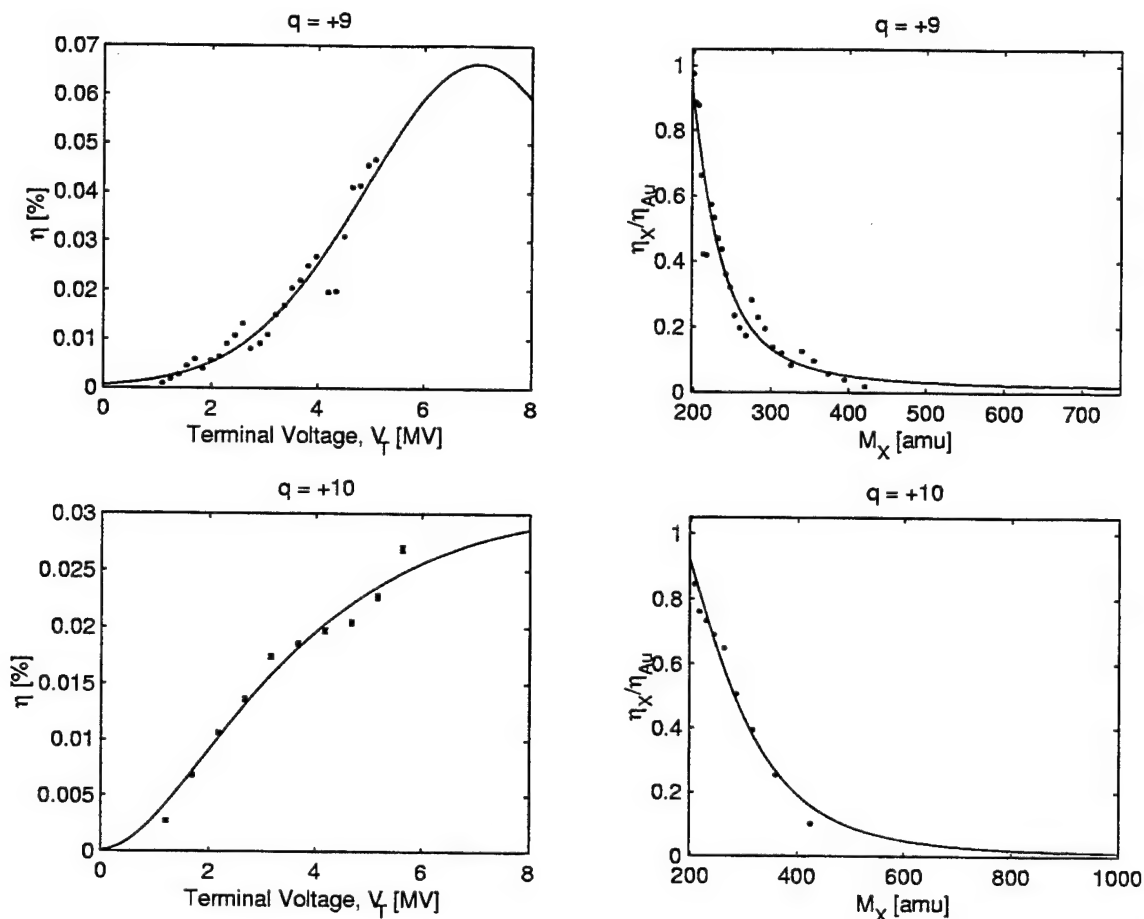


Figure 14.17: Stripper efficiency data for charge states  $q = +9$  and  $q = +10$ . Again the  $q = +10$  data are new while the  $q = +9$  were taken during Run Au3. They are included together here so that the progression with increasing charge states can be visualized. Also notice that compared to the previous figure for charge states +7 and +8, the peaks have shifted to the right while the data have come from further into the tail of the peak. Also notice the decrease in amplitude.

However, recall that the SIMP search is operating in this very same energy region, and that the overall structure of the Gaussian peak is not as important as the behavior in the tails. These data, while a difficult curve fit, are the best that can be achieved within the apparatus limitations. Again, we reiterate the importance of the curve

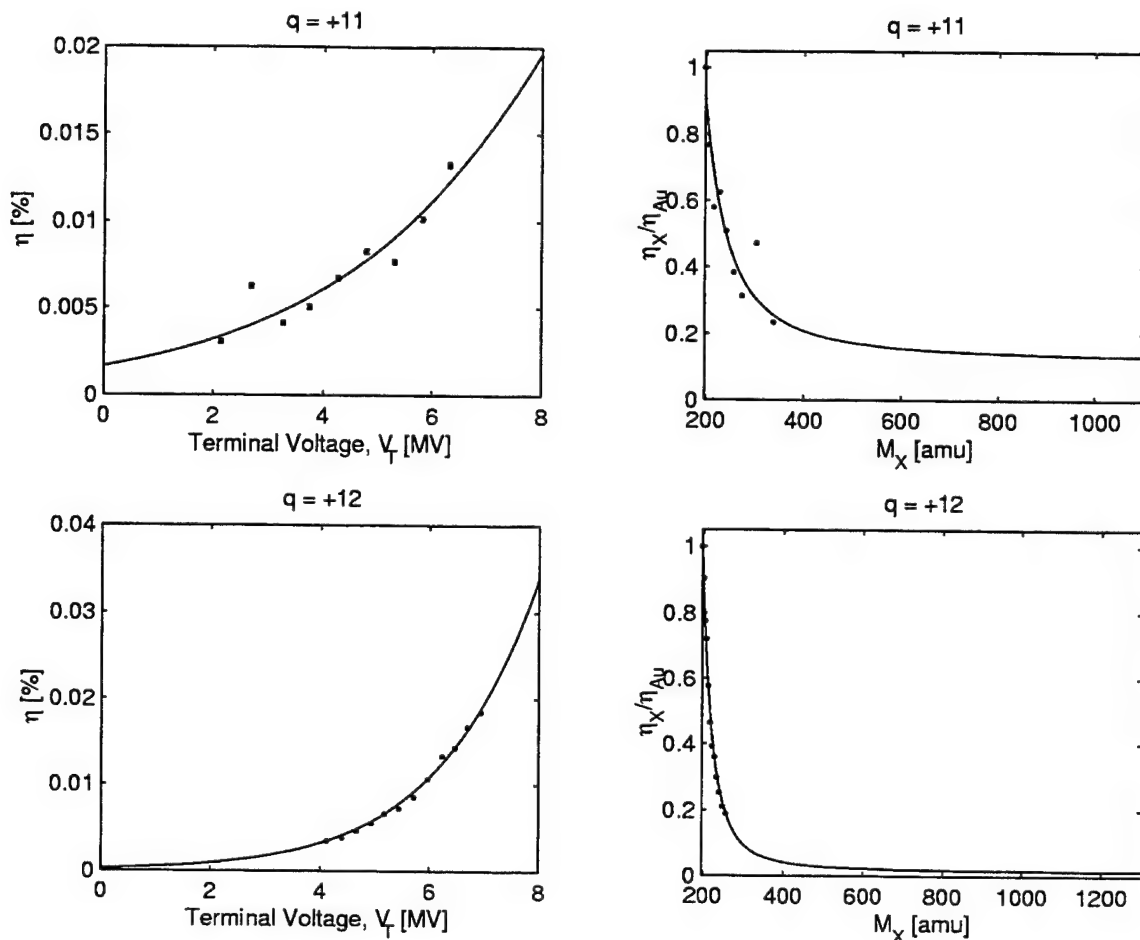


Figure 14.18: Stripper efficiency data for charge states  $q = +11$  and  $q = +12$ .

which represents the data in the region where the data were taken. The fits all follow this trend.

The axes of the figures are fixed so that the mass ranges in which they are applied may be emphasized. For example, since charge state +5 was used from 200–222 amu (see Table 14.13) the axes on the +5  $\eta_X/\eta_{Au}$  plot in Figure 14.15 were extended all the way out to 1775 amu, since much of the structure would be lost in the magnification.

As with the  $q = +7$ ,  $+9$ , and Fe data we again fit the data, with the help of PAW, to a curve whose form is that of an asymmetric Gaussian given in Equation (14.8). The values of the different coefficients for each charge state are provided in Table 14.14.

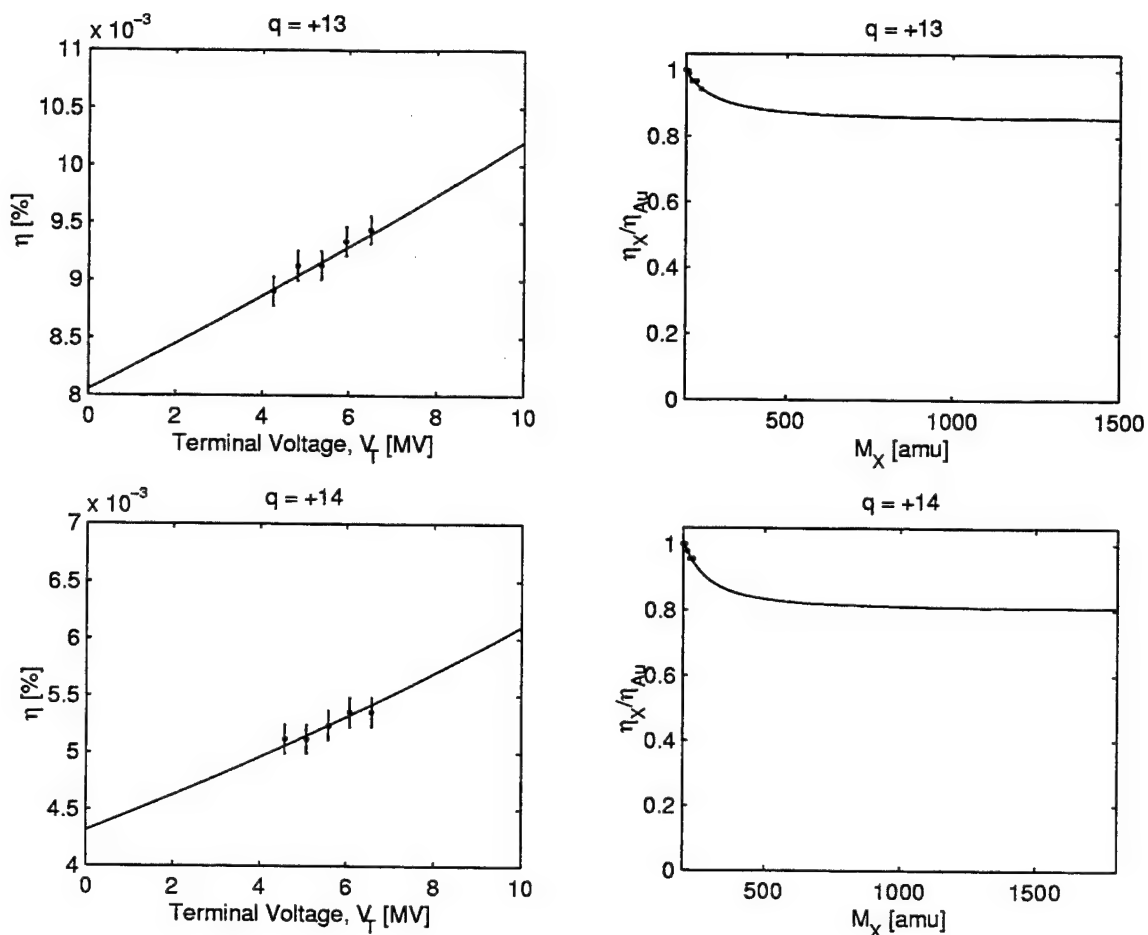


Figure 14.19: Stripper efficiency data for charge states  $q = +13$  and  $q = +14$ . Notice that the data are clearly on the flattened portion of the tail and as a result change very little with increasing mass.

There are several trends which we would expect to observe in the data after examining the predictions made by the STRIP program. In this high mass regime the program becomes unreliable in correctly predicting the efficiency behavior, and is what prompted these studies. For Au the STRIP program predicts that the efficiencies of the different charge states will behave as shown in Figure 1.9. From this output we would expect that the peak would shift to higher energies with increasing charge state while simultaneously decreasing in amplitude. After inspection of Table 14.14 we see that in general the peak location (dictated by  $p_3$ ) is shifting to higher energies

Table 14.14: Coefficients for the transmission efficiency curve fits through the experimental data plotted in Figures 14.15–14.19. The definition of these parameters can be found in Equation (14.8). Notice that  $p_3$  is the horizontal shift of the Gaussian.

Charge State	$p_1$	$p_2$	$p_3$	$p_4$
+5	0.40	-1.46	2.98	-0.24
+6	0.29	-0.89	3.66	-0.17
+7	0.14	-0.82	4.17	-0.16
+8	0.083	-0.22	5.66	-0.083
+9	0.066	-0.12	7.01	-0.028
+10	0.030	-0.0036	10.93	+0.085
+11	0.064	-0.045	14.87	-0.12
+12	0.36	-0.12	14.34	-0.18
+13	0.018	-0.0026	39.91	-0.10
+14	0.020	-0.0042	50.14	-0.12

(with the exception that  $q = +11$  and  $q = +12$  are about the same) along with the decrease in the amplitude (which is dictated by  $p_1$ ; again  $q = +12$  seems to be a little off the trend). Again we reiterate that the tail is the region of the curve we are interested in, which fortunately is where our data exist and forces a better fit. To emulate Figure 1.9 produced by the STRIP program, we produced a plot of our data for the energies we dealt with during our run (see Figure 14.20).

Finally, it is important to reiterate that PAW's final fit depends on the input data provided by the user. As the user we input the sign of the constants along with rough order of magnitude values, and allow PAW to find a local minimum in the 5-dimensional phase space discussed above. PAW searches until a local minimum is found. For example, even though we expect that  $q = +10$  should have  $p_4 < 0$ , PAW was unable to locate a minimum based on the data. The resulting curve fit was the one that fit the data best, a result that we could confirm visually. The high peak values of charge states +13 and +14 are also a result of no apparent local minimum with a peak in the region we would expect (namely,  $|p_3|$  around 15–20). However, the behavior at low energies is what is important in this study.

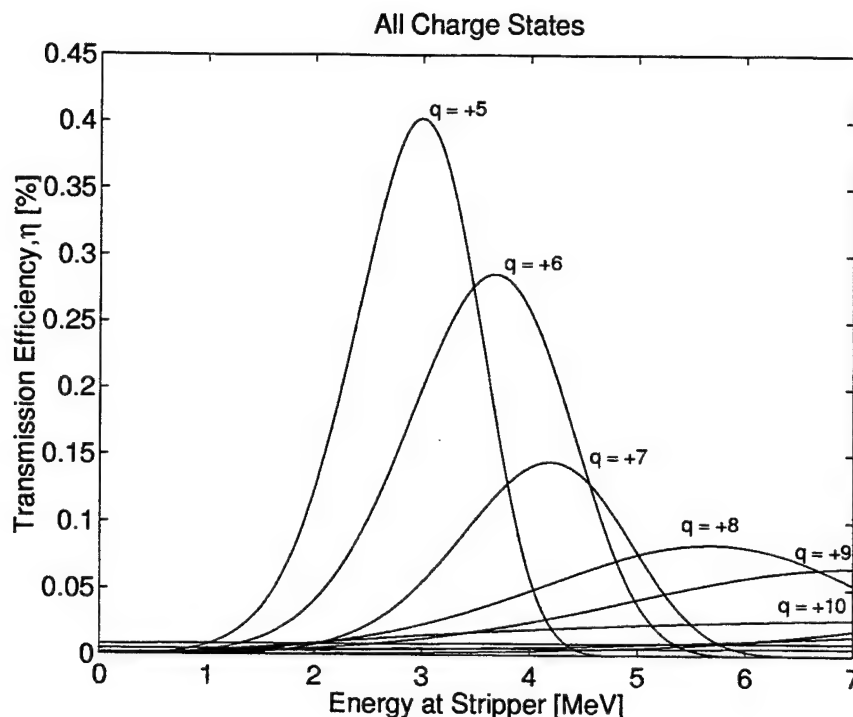


Figure 14.20: Stripper efficiency as a function of energy for the charge states +5 to +14. This is an analogous plot to the output generated by the STRIP program which is given in Figure 1.9. Notice the flatness of the curves in the low energy region for the higher charge states.

With the efficiency scans finished we were ready to proceed to take the actual data. However, there were still a few issues to deal with. As with previous runs it was necessary to calibrate the detector. This time we wished to use Upperset 3 of the GKS plot of the energy spectra in which we gated out all tails from other peaks (we discuss this in greater detail below). We had to calibrate the energy spectrum on each of the different plates along with the total energy spectrum. The same concept as before was used to calibrate the detector down to energies just above the window cutoff energy. This was done by running the  $q = +7$  beam at three different energies and noting the channel for the Au peak. The results from this are provided in Table 14.15. The data points were then curve fit with lines via the method of least squares with the resulting energy/channel relationships shown in Figure 14.21.

Table 14.15: The energies and channels of the Au peak on each detector plate.

Beam Energy $E_b$ [MeV]	Detector Plate Channel			
	$\Delta E_1$	$\Delta E_2$	$\Delta E_3$	Total $E$
22.9	459	375	387	852
20.0	408	345	334	714
16.8	336	303	83	522
$Channel = (c_1)E_b + c_2$				
$c_1$	20.22	11.83	50.37	54.24
$c_2$	-1.59	105.3	-734.96	-384

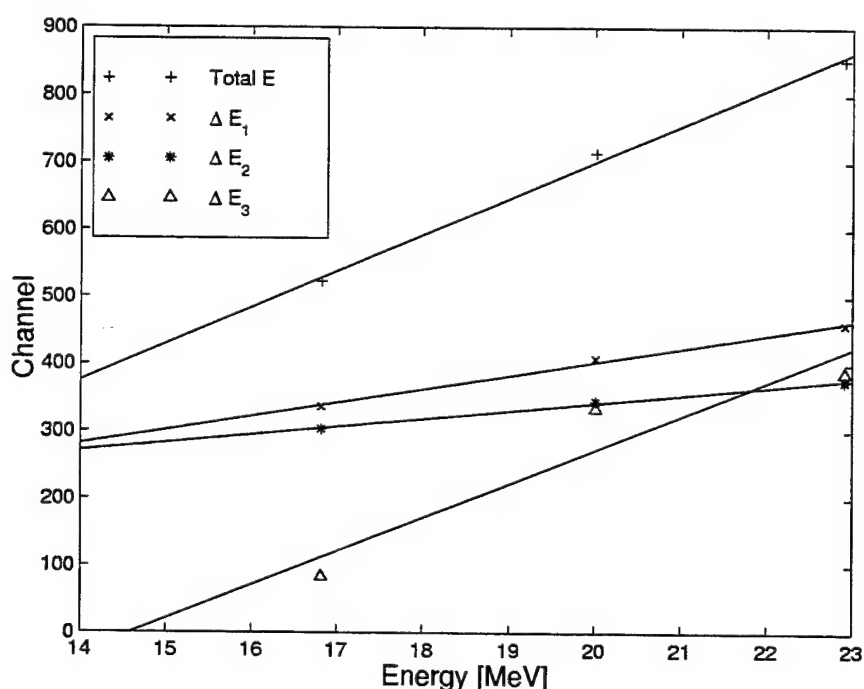


Figure 14.21: Calibration of the detector energy plates. The raw data and equations for the various fit lines can be found in Table 14.15.

As before, the width of allowed SIMP region was gated by a window that was twice the full width at half maximum for the Au peak. Notice that the  $\Delta E_3$  plate data goes to zero before 13.7 MeV (the calculated window cutoff energy for this run

using the  $q = +7$  beam). To see if this is relevant to our data we need to understand how Upperset 3 is used to gate out unwanted tails.

Recall that our detector allows for energy resolution between different beams. Because of the limits of the experimental apparatus and the natural fluctuations in the terminal voltage, it is possible for a particle to enter the detector with an energy slightly higher or lower than the value we are set at. While most of the particles will come in at the desired energy we see a spread in the peak as a result. (Some of the peak spread is also due to the circumstance that the window does not remove a uniform amount of energy from each particle.) Thus when a large contamination peak is nearby it may have tails that wash over into our SIMP region causing an increased background at that mass step. However, our detector actually has greater capabilities than we originally realized.

The detector also has the capability of  $Z$  resolution between two particles of the same energy. This arises from the same basic physics that we discussed in the stripper section. When an atom penetrates into a medium it quickly establishes a charge exchange process as the beam and the medium interact. This process is governed by several factors of which the energy and  $Z$  are the most important. Since we are discussing  $Z$  resolution we will assume that two particles enter with the same energy (if they had different energies we would be able to differentiate them based on the energy resolution means discussed before). These two particles will each interact differently with the surrounding medium (which in our case is propane gas). More importantly, they will lose their energy at different rates and thus will penetrate to different depths in the detector while still depositing the same total energy. While it would be difficult to determine an exact penetration depth into the detector, we can determine the fraction of the total energy deposited on each anode plate. This is precisely why we have several anode plates on the detector diagram given in Figure 1.11.

If we begin by calibrating these fractions with an Au beam we will know how the energy should be deposited on each plate for a SIMP whose  $Z = 79$  as for Au. When data are taken at a particular mass step we may have the GKS plot the data with three different constraints being exercised which we saved as information

sets called Upperset U, Upperset 1, and Upperset 3. In Upperset U (the Ungated spectra), we include every count that reaches the detector. As a result, we only obtain energy resolution. Upperset 1, which are the data we have reported to the PF3-2 table output, includes the energy resolution but includes only those counts that fall within the SIMP window, thereby neglecting the contaminating guide beams. Finally, Upperset 3 is the most sophisticated and was only used in the rare instance that a tail caused a rise in the background of the Upperset 1 result. In Upperset 3 the only counts that are reported are those that fall within predetermined energy windows, or gates set on each separate plate, along with the total energy spectrum. (Recall that the gates were twice the width at half maximum of the Au peak.) This is easier to see by an example.

If a particle enters the detector and has an energy which falls within the gates placed on the total energy spectrum, and it also has an energy which falls within the gates on the  $\Delta E_2$  and  $\Delta E_3$  plates then the point is plotted on the  $\Delta E_1$  gate display. If this point then is also within gates of  $\Delta E_1$  it is considered a valid count. One can think of this as verifying that the count whose energy is within the gates set for the SIMP deposited the fraction of its energy on each plate that is consistent with a particle whose  $Z = 79$ . Otherwise it would have deposited either more or less energy on one of the plates resulting in a rejection of the point based on  $Z$  resolution. This principle was only used to analyze the data at 6 mass steps, which shows how rarely this technique was needed in the run. Four of the six times it was to remove an unwanted tail, while the final two times were to resolve  $^{209}\text{Bi}$  and  $^{204}\text{Tl}$  (thallium is a common contaminant for AMS iodine runs) from the expected SIMP location.

Thus since Upperset 3 was used only a few times at higher energies, the fact that its curve fit went below zero before reaching the window cutoff energy was not a factor. Had we seen evidence for a SIMP and had needed to use Upperset 3 to verify the SIMP at energies low enough that zero was within the width of the  $\Delta E_3$  gates, we would have removed the the gates on the  $\Delta E_3$  spectrum and only exercised the constraints imposed by the  $\Delta E_1$ ,  $\Delta E_2$ , and total energy gates. This is because the SIMP could still be within the  $\Delta E_3$  gates but not have been seen because it didn't penetrate deep enough to register a signal on the  $\Delta E_3$  plate.

As in the previous run, the terminal voltage step size was dictated by the width of the Au beam. This time however, we took several beam widths as a function of the terminal voltage so that we would be able to better simulate the correct beam width and modify the steps appropriately throughout the scan. This beam width determination was performed using the four primary guide beams which are given in Table 14.16. The fit through these data which allowed us to determine the actual stepsize is given in Figure 14.23 and appears to be quadratic. The reason for the quadratic nature is not immediately apparent: the ratio  $\Delta V_T/V_T$  seems to be  $\approx 0.02$  for each charge state suggesting a linear fit would also have worked. However, the

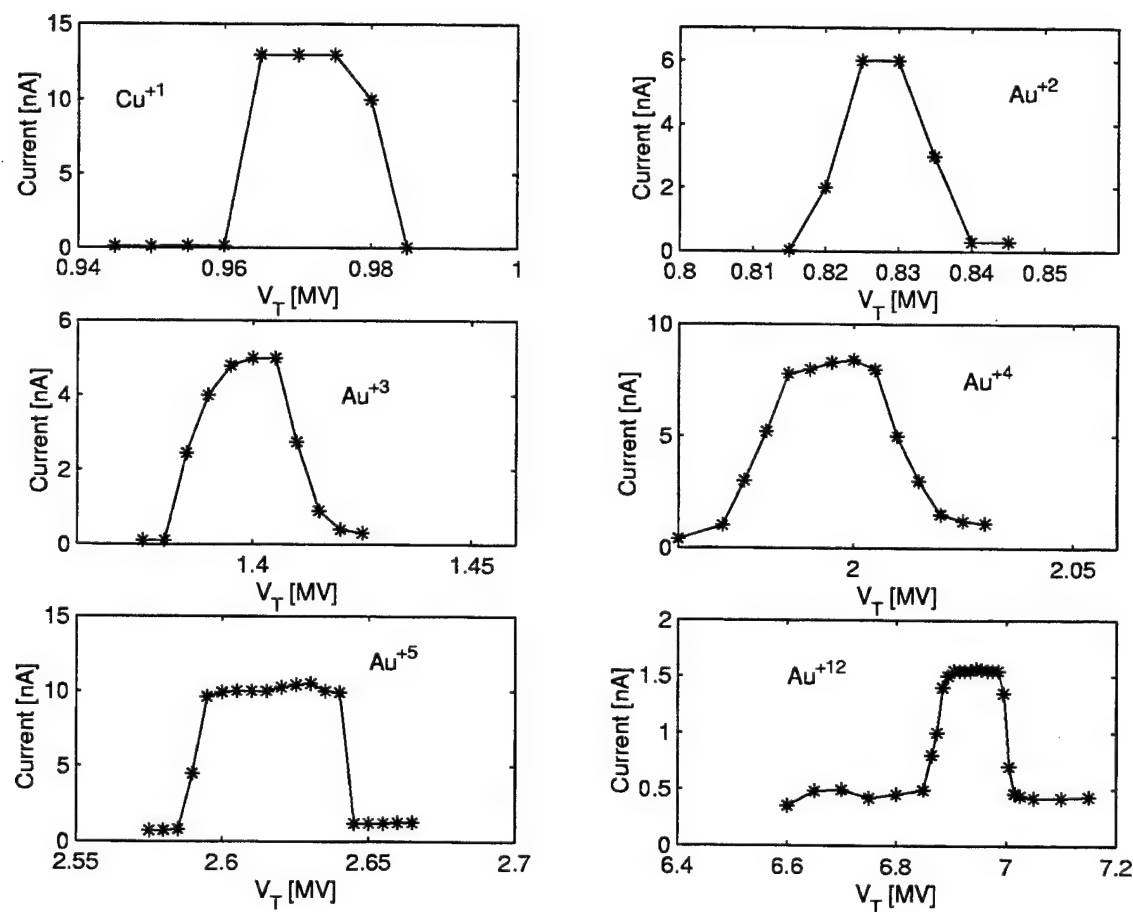


Figure 14.22: Beam profiles for the guide beams listed in Table 14.16. The data in the final column of the table was obtained from these plots.

higher order curve fit the lower end data better, and since we would be running at the lower terminal voltages it was used to determine the stepsize.

Table 14.16: Run Au5 Guide Beams. These were used to adjust and verify the tune throughout the scan. We also used them to determine the terminal voltage stepsize needed to ensure the half maximum overlap of sequential steps.

Guide Beam	$V_T$ [MV]	Energy [MeV]	$\Delta V_T$ [MV]
Au <sup>+12</sup>	6.945	90.30	0.155
Au <sup>+9</sup>	5.070	50.71	0.095
Au <sup>+5</sup>	2.613	15.69	0.052
Au <sup>+4</sup>	1.995	9.99	0.04
Au <sup>+3</sup>	1.397	5.60	0.03
Cu <sup>+1</sup>	0.972	1.96	0.025
Au <sup>+2</sup>	0.828	2.50	0.025

After all the preparatory work was completed, we were ready to actually take data. With the exception of a complete power failure when we were about 85% complete, the run went smoothly. At each mass shown in Table 14.13 data were taken for only five of the nine samples due to time constraints: RHIC, LDEF, Laverton, AZ, and Golden Valley, NC. Since the Laverton and Nullagine samples both came from the same general locations, we assumed that any exposure in one also happened in the other. The same went for the North Carolina samples and was the result of an effort to minimize the total run time. Thus for each mass above we took data for the five samples. In the end no evidence for SIMPs was found. Again the currents were monitored to obtain their variation as a function of time. However, in this run they can only be used to determine if the sample had been consumed, since we would have had to monitor the currents in every charge state each time (which calls for significant changes in the tandem settings) resulting in impractically long run times. Instead their charge state +5 currents were monitored, and their final currents in each charge state were measured at the end of the run, thus providing us with a

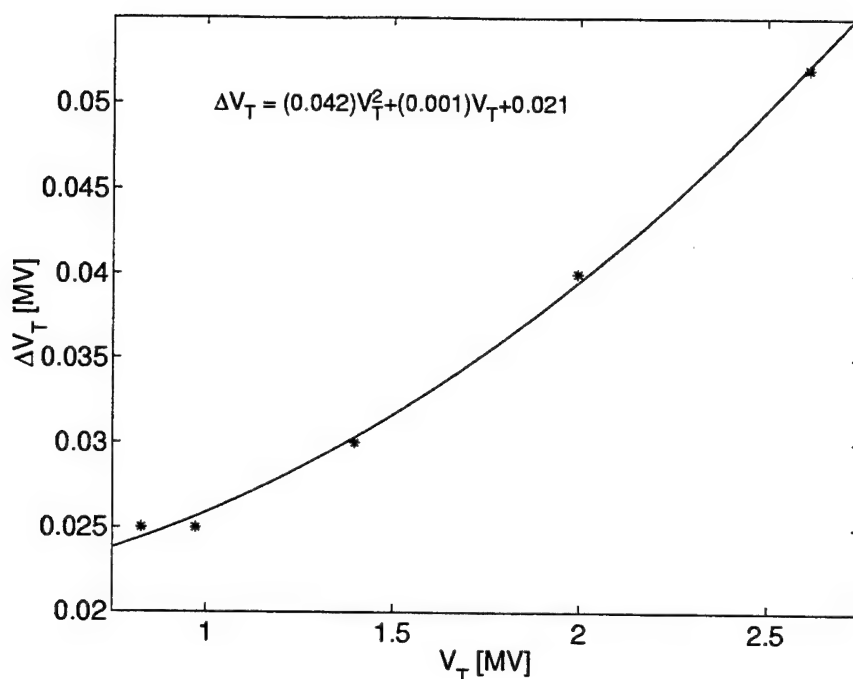


Figure 14.23: Stepsize dependence on terminal voltage. Only the portion of the curve relevant to our scan is given here, while the raw data for the higher  $V_T$  data may be found in Table 14.16.

conservative estimate, since currents generally decrease with time. Finally we arrive at the experimental results for the 5 samples. The limits on SIMPs in the samples are given in Figure 14.24.

There are several important issues to discuss about this data. The steps in the curve denote the transition to the next higher charge state as denoted in Table 14.13. It is important to note that the steps also increase in size as we increase the charge state. This effect comes from the poorer efficiency along with the lower beam currents which exist at the higher charge states. The flatness of the curve at high masses is indicative of the fact that we are dealing with the flattened portion of the tail. Thus in this result we lose the characteristic shape most prominently displayed in Figure 14.7. We see a deterioration of this in the result reported in Figure 14.12.

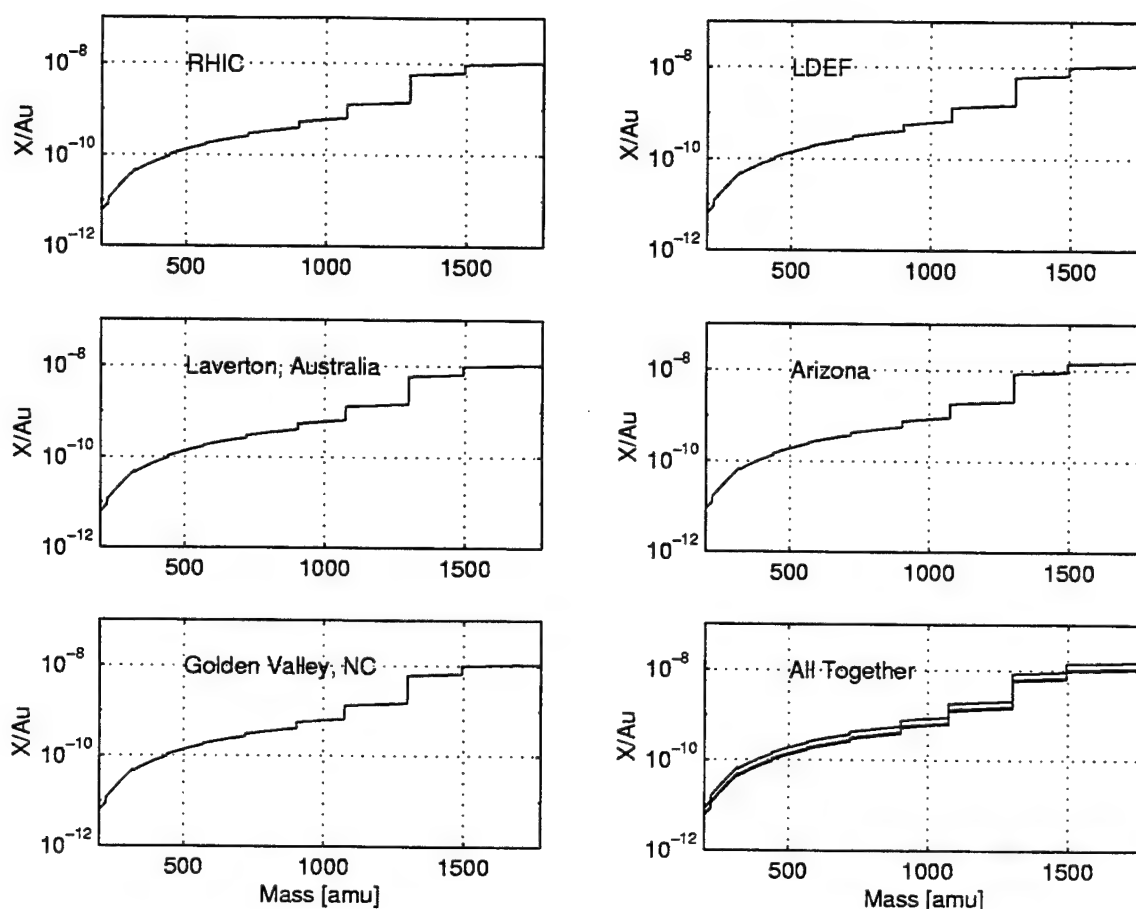


Figure 14.24: The  $X/Au$  ratios for the 5 different samples. These results effectively search for a 1.48 TeV SIMP. From the bottom right figure we see that they all have very similar limits, their differences result from slightly different beam currents. Notice that the AZ sample produced the lowest beam currents which is reflected by its poorer limit. The small steps in the curve denote the transition to the next higher charge state as indicated in Table 14.13. The steps also increase in size as we increase the charge state which comes from the poorer efficiency along with the lower beam currents.

## 14.7 Conclusions

Following the experimental results provided in the preceding sections we are able to draw several conclusions regarding strongly interacting massive particles bound to

gold and iron nuclei. Before discussing the impact of these data on the theoretical motivations of the previous chapters, we draw the following direct conclusions from our data:

1. *Au SIMP Limits* - We discuss the limits placed on each of our gold samples.

From Table 14.17 we see that with each run we increased the highest mass while also decreasing the limit at the low mass (by going to a lower charge state). Thus we see that we are able to constrain a 1.5 TeV SIMP to an abundance of less than 10 ppb in Au.

Table 14.17: Final experimental results broken down by Sample showing the Run and limit set in the indicated mass range.

Sample	Run	Low Mass [GeV/c <sup>2</sup> ]	$X/Au$	High Mass [GeV/c <sup>2</sup> ]	$X/Au$
RHIC	Au4	3	$5.4 \times 10^{-11}$	461.5	$1.9 \times 10^{-9}$
	Au5	3	$6.2 \times 10^{-12}$	1483	$1.0 \times 10^{-8}$
LDEF	Au4	3	$7.9 \times 10^{-11}$	461.5	$2.9 \times 10^{-9}$
	Au5	3	$6.6 \times 10^{-12}$	1483	$1.1 \times 10^{-8}$
Laverton	Au2	3	$1.2 \times 10^{-11}$	143.8	$7.1 \times 10^{-10}$
	Au4	3	$6.4 \times 10^{-11}$	461.5	$2.3 \times 10^{-9}$
	Au5	3	$6.3 \times 10^{-12}$	1483	$1.1 \times 10^{-8}$
Nullagine	Au4	3	$7.5 \times 10^{-11}$	461.5	$2.7 \times 10^{-9}$
Arizona	Au4	3	$9.4 \times 10^{-11}$	461.5	$3.4 \times 10^{-9}$
	Au5	3	$8.9 \times 10^{-12}$	1483	$1.5 \times 10^{-8}$
Golden Valley, NC	Au4	3	$7.3 \times 10^{-11}$	461.5	$2.6 \times 10^{-9}$
	Au5	3	$6.5 \times 10^{-12}$	1483	$1.1 \times 10^{-8}$
Black Creek, NC	Au4	3	$6.6 \times 10^{-11}$	461.5	$2.4 \times 10^{-9}$

2. *Fe SIMP Limits* - In Run Au4 we also collected data on the Canyon Diablo meteorite. Because of the lower nuclear mass this translated into a higher effective SIMP mass than the Au data for that run. It also allowed us to test

for SIMPs in another nucleus. The Fe data set limits on  $X/Fe$  better than  $9.7 \times 10^{-9}$  for a 594 GeV SIMP with the most stringent limit being  $5.6 \times 10^{-9}$  for a 135 GeV SIMP.

3. *Heavy Ion Stripping* - We have also performed a detailed analysis of heavy ion stripping with Ar and have data for several different charge states. For Au we have data on charge states +5 to +14 while for Fe we have data for charge state +9. This experience with heavy ions may be useful if future nuclear or particle physics experiments are run again on the AMS facility at PRIME Lab. The fact that we were able to see  $Au^{+14}$  is significant, as our machine has never run such high masses in extreme charge states.
4. *AMS Operations* - Our use of guide beams, coupled with our ability to extend each accelerator element to its limits, has allowed us to utilize the full extent of the tandem's operational phase space. We now know the maximum fields for the magnets, and we can ensure that they are attainable without any modifications. We have also isolated the Trans Quads as the limiting factors for high energy, low charge state beams.
5. *AMS Problems/Solutions* - In addition we have solved several AMS problems. First, and most importantly, we found the problem with the Injector Cup Bias steering the beam a different amount depending on the final position of the cup. We also solved the minor problem of drawing too much current on the sub-basement circuit breaker which may have been encountered in the subsequent iodine run. We also have supplied PRIME Lab with a new optional window which was never used for our experiment. However, if applied to AMS operations this should reduce energy peak widths due to less energy loss in the thinner window.

We also are able to draw several indirect conclusions which relate to the theories discussed in Chapter 11. To begin with, our results may only be applied to these theories if SIMPs do bind to gold (or iron) nuclei. The current theoretical framework for such binding is given for Au in the paper by Mohapatra, Olness, Stroynowski,

and Teplitz [5]. While this derivation was originally motivated by the possibility of a Dark Matter SIMP, it may be applied to the other motivations as well.

From our results we may reproduce the Table II of Ref. [5], with our final results from runs Au4 and Au5 now included. The addition of this table allows us to see the impact of our final run data on previously published work.

Table 14.18:  $M_X$  (vertical) in units of  $\text{GeV}/c^2$  versus  $\sigma_{SN}$  (horizontal) in units of mb. Table entries give the predicted values of  $-\log_{10}(X/\text{Au})$  obtained from Ref. [6]. These predictions are obtained under the approximation [7, 6]  $\sigma_{SN}^2 \sim \sigma_{\bar{S}S}\sigma_{NN}$ , which is used to determine the cosmic S abundance. Such baryonic SIMPs fail to saturate halo dark matter for  $\sigma_{SN} > 10^{-3}$  mb. The entries in boxes are excluded by the present experimental results at the 95% confidence level. For the sake of comparison to Ref. [6] we assume here that  $M'_X \approx M_S$ .

$M_X$ ( $\text{GeV}/c^2$ )	$\sigma_{SN}$ (mb)									
	.0005	.0015	.0042	0.012	0.032	0.09	0.25	0.69	1.9	5.3
2.7								5.9	7.9	8.3
4.3							5.7	7.7	8.1	11.1
7.1						5.5	7.5	7.9	10.9	12.1
12					5.6	7.6	8.1	8.5	12.2	12.7
19					7.5	7.9	8.3	11.3	12.5	12.9
31				7.4	7.8	8.2	8.6	12.4	12.8	13.2
50			5.7	7.7	8.1	8.5	11.5	12.7	13.1	13.6
81		5.7	7.7	8.1	8.5	8.9	11.9	13.1	13.5	14.0
132	5.7	7.7	8.1	8.5	8.9	9.3	12.2	13.5	13.9	14.3
220	6.0	8.0	8.4	8.9	9.3	9.7	12.6	13.9	14.3	14.7
350	6.4	8.4	8.8	9.3	9.7	10.1	13.8	14.3	14.7	15.1
570	8.4	8.8	9.2	9.7	10.1	10.5	14.3	14.7	15.1	15.5
930	8.9	9.3	9.7	10.1	10.5	10.9	14.7	15.1	15.5	16.0

The empty spaces to the left represent regions of the  $M_S - \sigma$  phase space where a SIMP will not bind to an Au nucleus (recall our minimum  $A$  requirement shown in Figure 12.1). For the most conservative case scenario (in which  $\sigma_{S\bar{S}} \approx 3 \times 10^{-13}$  barn) SIMP binding does not occur in Au until the SIMP's mass is greater than 80 GeV. In the other cross-section models binding occurs earlier, resulting in the observed cutoff at  $M_S^2 \sigma_{SN} \approx 5 \text{ mb GeV}^2$ . We also note that the decreasing fraction with increasing interaction cross-section is consistent with the abundance  $Y_\infty$  behavior predicted by Kolb and Turner [154] that  $Y_\infty \approx 1/(M_S \sigma_{S\bar{S}})$ .

We may use the analysis outlined in Sections 11.2 and 12.2 to actually calculate a bound on the SIMP contribution to the cosmological density parameter. To remain consistent with the previous analysis, the cosmological density parameter is computed using the two different models for the  $S - N$  cross section given in Equation (12.7). If we then assume that the massive SIMP had an abundance just below the detection limit of the experiment, we provide the constraint on  $\Omega$  shown in Figure 14.25.

This is a truly astonishing result and states that from our results we may conclude that a SIMP of mass  $M_S < 10 \text{ GeV}$  cannot solely be used to explain  $\Omega = 1$ . However, SIMPs whose masses are in the range  $10 < M_S < 1480 \text{ GeV}$  could still saturate the cosmic density with a high enough abundance to allow the density parameter to be unity, while still going undetected by our experiment. Thus our experiment has ruled out low mass SIMPs as an explanation to this theoretically desired result.

The value  $\Omega = 1$  is heavily favored both for theoretical and aesthetic reasons. One characteristic feature of the Universe is the isotropy of the Cosmic Background Radiation (CBR) [155, 154, 166]. This observation was difficult to explain until the introduction of inflation [191, 192] which postulates that there was a period in the early stages of the Universe in which the stress-energy was dominated by vacuum energy. During this short phase the Universe underwent exponential expansion by a repulsive scalar field until the decay of the false vacuum. Inflation is very attractive because of its ability to describe the isotropy of CBR, and also because it generates primordial density perturbations that are similar to those observed in galaxy formation. Most importantly to this discussion is that inflation requires that  $\Omega = 1$ .

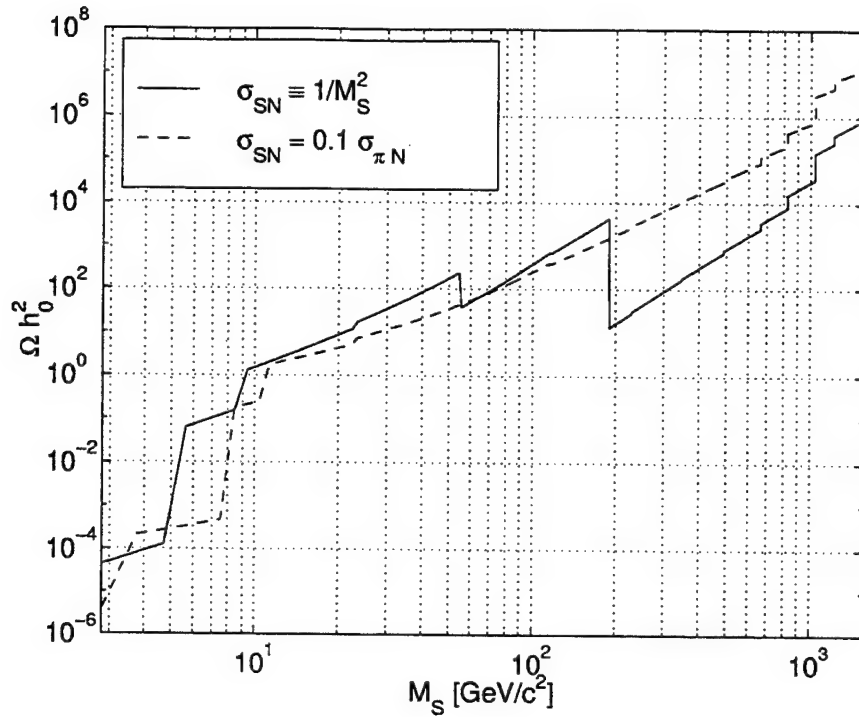


Figure 14.25: Limits placed on the SIMP contribution to the cosmological density parameter  $\Omega$ . The small increasing jumps mirror the changes in charge state in the  $X/Au$  data observed in Figure 14.24. The decreasing jumps observed in the  $\sigma_{SN} \equiv 1/M_S^2$  limit are from the shift of  $A_{min}$  from the second to first row of Table 12.1.

We also believe  $\Omega$  is unity because it is the only value that does not change rapidly as the Universe expands. Since it is measured to be within an order of magnitude of unity today, then it must have been  $1 \pm 10^{-60}$  at the Planck time (see Figure 11.5) [166, 17, 154]. Thus  $\Omega = 1$  is the natural value, and if not unity, will diverge rapidly from the present value, which would suggest that we live at a rather unique moment in the history of the Universe.

To recapitulate the discussion of Chapter 11, our experiment investigated the possibility that the theoretically predicted relic particles are strongly interacting. The allowable mass ranges of such strongly interacting massive particles (SIMPs) are then constrained by the experiment which provides the limits on  $\Omega$  shown in Figure

14.25. These limits are a function of the SIMP mass and  $S - N$  interaction cross section (of which two of the most likely cases were reported). The important result is that for a certain mass range the SIMP data (like the neutrino contribution) a result of  $\Omega = 1$  is consistent with the experimental results, and a SIMP could exist in a high enough abundance for  $\Omega$  to be unity and still have gone undetected by the experiment. More summaries of other SIMP constraints are provided by Starkman *et al.* [4]. This may be compared to the other factors contributing to the total cosmological density parameter.

From the luminosity measurements we find that the fraction of the critical density directly associated with luminous sources is

$$\Omega_{LUM} \simeq 0.01, \quad (14.15)$$

which means that luminous mass represents only 1% of the critical density.

The inclusion of baryonic dark matter in the form of MACHOs and interstellar gas contribute an additional order of magnitude to give a value similar to that obtained from primordial nucleosynthesis,

$$\Omega_B \leq 0.16. \quad (14.16)$$

This is a much larger contribution than that derived from luminosity measurements, but still falls short of the aesthetically desired  $\Omega = 1$ .

We also have observations from dynamical methods which indicate that the matter that clusters with bright galaxies on distance scales of 10-30 Mpc contributes

$$\Omega_{Cluster} \simeq 0.2 \pm 0.1 \quad (14.17)$$

We also have shown that the difference between  $\Omega = 1$  and the values given for baryonic dark matter may be explained if the neutrinos had an average mass of only 8 eV, which is not yet ruled out by experiment, as seen from the limits on the neutrino masses given in Eq. (11.45). The density parameter is thus limited by the neutrino masses via Eq. (11.44), and is bounded from current experimental results to be

$$\Omega_\nu h_0^2 \leq 1.97 \times 10^5. \quad (14.18)$$

Thus, from the experimental results  $\Omega = 1$  is still allowed and massive neutrinos are a legitimate solution to the dark matter problem.

It is also possible to construct, from nucleosynthesis, dark matter which is non-baryonic. These to-be discovered relic particles are predicted by several theories beyond the standard model including the widely championed supersymmetry (SUSY). Because of the theoretical aesthetics of supersymmetry many believe it will be shown to be evident shortly. However, since it is a badly broken symmetry, evidence of SUSY may have escaped detection in high energy accelerators. In SUSY the superpartners will all decay into regular particles and the lightest supersymmetric particle is predicted to be stable if  $R$ -parity is conserved ( $R$ -parity is the labeling of  $R = +1$  for particles and  $R = -1$  for superparticles).

Weakly interacting massive particles (WIMPs) may provide the necessary contribution to solve the dark matter problem and raise  $\Omega$  to unity. As of yet no WIMPs have been found, which suggests through theoretical analysis to a WIMP contribution of

$$\Omega_{\text{WIMP}} \geq \frac{M_X^2}{(300 \text{ TeV})^2 h_0^2} \quad (14.19)$$

Thus SIMPs of masses  $> 10 \text{ GeV}$  are still viable candidates which would allow  $\Omega = 1$ , but as seen from the previous discussion will compete with the other contributing factors to achieve this goal.

## LIST OF REFERENCES

## LIST OF REFERENCES

- [1] Particle Data Group. *European Physical Journal C*, 15:1, 2000.
- [2] Frederick K. Lutgens and Edward J. Tarbuck. *The Atmosphere*. Prentice Hall, Inc., 1992.
- [3] John N. Bahcall and Jeremiah P. Ostriker. *Unsolved Problems in Astrophysics*. Princeton University Press, 1997.
- [4] G.D. Starkman, A. Gould, R. Esmailzadeh, and S. Dimopoulos. *Phys. Rev. D*, 41:3594–3603, 1990.
- [5] R. N. Mohapatra, F. Olness, R. Stroynowski, and V. L. Teplitz. *Physical Review D*, 60(115013):1–5, 1999.
- [6] R. N. Mohapatra. *et. al.*, *Physical Review D*, 60(115013):1–5, 1999.
- [7] R. N. Mohapatra and V. L. Teplitz. *Physical Review Letters*, 81(15):3079–3082, 1998.
- [8] U. Amaldi, W. de Boer, and H. Furstenau. *Physics Letters B*, 260:447–455, 1992.
- [9] G.W.F. Drake. *Physical Review A*, 39(2):897–899, 1989.
- [10] V. M. Novikov, A. A. Pomansky, T. Faestermann, H. Gail, A. Gillitzer, G. Korschinek, D. Muller, R. Scheuer, and E. Nolte. *Physics Letters B*, 240:227–231, 1990.
- [11] E. Nolte, Th. Faestermann, H. Gail, A. Gillitzer, G. Korschinek, D. Muller, R. Scheuer, V. M. Novikov, A. A. Pomansky, D. Miljanic, A. Ljubičić, and Logan B. A. *Nuclear Instruments and Methods in Physics Research B*, 52:563–567, 1990.
- [12] E. Nolte, T. Faestermann, A. Gillitzer, G. Korschinek, D. Muller, V. M. Novikov, A. A. Pomansky, A. Ljubičić, and D. Miljanic. *Zeitschrift fur Physik A - Hadrons and Nuclei*, 340:411–413, 1991.
- [13] E. Nolte, T. Brunner, T. Faestermann, A. Gillitzer, G. Korschinek, D. Muller, B. Schneck, D. Welselka, V. M. Novikov, A. A. Pomansky, A. Ljubičić, D. Miljanic, and H. Vonach. *J. Phys. G: Nucl. Part. Phys.*, 17:S355–S362, 1991.
- [14] John B. Russel. *General Chemistry*. McGraw-Hill, Inc., 1992.
- [15] D. Hayes. *U.S. Geological Survey: Minerals Yearbook*, 36:1–8, 1998.
- [16] E. Fischbach, T. Kirsten, and O. A. Schaeffer. *Physical Review Letters*, 20(18):1012–1014, 1968.
- [17] P.D.B. Collins, A.D. Martin, and Squires E.J. *Particle Physics and Cosmology*. John Wiley & Sons, Inc., 1989.
- [18] AGASA Collaboration, M. Takeda, N. Hayashida, K. Honda, N. Inoue, K. Kadota, F. Kakimoto, K. Kamata, S. Kawaguchi, Y. Kawasaki, N. Kawasumi, H. Kitamura, E. Kusano, Y. Matsubara, Y. Murakami, M. Nagano,

- D. Nishikawa, H. Ohoka, N. Sakaki, M. Sasaki, K. Shinozaki, N. Souma, M. Teshima, R. Torii, I. Tsushima, Y. Uchihori, T. Yamamoto, S. Yoshida, and H. Yoshi. *Astrophysical Journal*, 522:225–227, 1999.
- [19] AGASA Collaboration, M. Takeda, N. Hayashida, K. Honda, N. Inoue, K. Kadota, F. Kakimoto, K. Kamata, S. Kawaguchi, Y. Kawasaki, N. Kawasumi, E. Kusano, Y. Matsubara, Y. Murakami, M. Nagano, D. Nishikawa, H. Ohoka, S. Osone, N. Sakaki, M. Sasaki, K. Shinozaki, N. Souma, M. Teshima, R. Torii, I. Tsushima, Y. Uchihori, T. Yamamoto, S. Yoshida, and H. Yoshi. *Astrophysical Journal*, 522:225–227, 1999.
- [20] R.O. Sayer. *Revue De Physique Appliquées*, 12:1543–1546, 1977.
- [21] Raymond A. Serway. *Physics for Scientists and Engineers*. Saunders College Publishing, 1992.
- [22] John R. Reitz, Frederick J. Milford, and Robert W. Christy. *Foundations of Electromagnetic Theory*. Addison-Wesley Publishing Company, 1993.
- [23] Mark A. Heald and Jerry B. Marion. *Classical Electromagnetic Radiation*. Saunders College Publishing, 1995.
- [24] David J. Griffiths. *Introduction to Electrodynamics*. Prentice-Hall, Inc., 1999.
- [25] John D. Jackson. *Classical Electrodynamics*. John Wiley & Sons, Inc., 1999.
- [26] Claudio Tuniz, John R. Bird, David Fink, and Gregory F. Herzog. *Accelerator Mass Spectrometry: Ultrasensitive Analysis for Global Science*. CRC Press LLC, 1998.
- [27] Mario Conte and William W. MacKay. *An Introduction to the Physics of Particle Accelerators*. World Scientific Publishing Co. Pte. Ltd., 1991.
- [28] Shyn-Yuan Lee. *Accelerator Physics*. World Scientific Publishing Co. Pte. Ltd., 1999.
- [29] Helmut Wiedemann. *Particle Accelerator Physics I: Basic Principles and Linear Beam Dynamics*. Springer Publishing Company, 1999.
- [30] Helmut Wiedemann. *Particle Accelerator Physics II: Nonlinear and Higher Order Beam Dynamics*. Springer Publishing Company, 1999.
- [31] National Electrostatics Corporation. *Instruction Manual for Operation and Service of FN Charging Conversion System*. 1993.
- [32] N. Bohr and J. Lindhard. *Kgl. Danske Videnskab. Selskab, Mat.-Fys. Medd.*, 28:7, 1954.
- [33] H. D. Betz. *Reviews of Modern Physics*, 44:465–539, 1972.
- [34] D. L. Knies and D. Elmore. *Nuclear Instrument and Methods in Physics Research B*, 92:134–137, 1994.
- [35] R. Middleton, D. Juenemann, and J. Klein. *Nuclear Instruments and Methods in Physics Research B*, 93:39–51, 1994.
- [36] T.E. Litherland. *Phil. Trans. R. Soc. London A*, 323:5, 1987.
- [37] J.K. Nørskov and B.L. Lundqvist. *Physical Review B*, 19:5661, 1979.
- [38] Jay L. Devore. *Probability and Statistics for Engineering and the Sciences*. Brooks/Cole Publishing Company, 1995.
- [39] Byron P. Roe. *Probability and Statistics in Experimental Physics*. Springer-Verlag New York, Inc., 1992.

- [40] Particle Data Group. *Physical Review D*, 54:1, 1996.
- [41] W. D. Myers and W. J. Swiatecki. *Nuclear Physics*, 81:1, 1966.
- [42] S. Wolfram. *Physics Letters B*, 82(1):65–68, 1979.
- [43] C. B. Dover, T. K. Gaisser, and G. Steigman. *Physical Review Letters*, 42:1117–1120, 1979.
- [44] I. Antoniadis and K. Benakli. *Physics Letters B*, 295:219–224, 1992.
- [45] D. Elmore, P.W. Kubik, T. Hemmick, R. Teng, H. Kagan, P. Haas, R.N. Boyd, R. Turner, D. Nitz, D. Ciampa, S.L. Olsen, T. Gentile, and T. Haelen. *Nuclear Instruments and Methods in Physics Research B*, 10/11:738–742, 1985.
- [46] R.G. Milner, B.H. Cooper, K.H. Chang, K. Wilson, J. Labrenz, and R.D. McKeeown. *Physical Review D*, 36(1):37–43, 1987.
- [47] J.N. Bahcall, R.N. Davis Jr., and L. Wolfenstein. *Nature*, 334:487–493, 1988.
- [48] J.N. Bahcall and R.K. Ulrich. *Reviews of Modern Physics*, 60:297–372, 1988.
- [49] E.L. Fireman, A.E. Litherland, and J.K. Rowley. *Nuclear Instrument and Methods in Physics Research B*, 29:387, 1987.
- [50] W. Lucha and et. al. *Nucl. Part. Phys.*, 16:155, 1986.
- [51] K.W. Allen. *Nuclear Instruments and Methods*, 186:479–482, 1981.
- [52] David J. Griffiths. *Introduction to Elementary Particles*. John Wiley & Sons, Inc., 1987.
- [53] Gordon Kane. *Modern Elementary Particle Physics*. Perseus Books Publishing, L.L.C., 1993.
- [54] Donald H. Perkins. *Introduction to High Energy Physics*. Cambridge University Press, 2000.
- [55] John Gribbin. *In Search of Schrodinger's Cat: Quantum Physics and Reality*. Bantam Doubleday Dell Publishing Group, Inc., 1984.
- [56] D.B. Lichtenberg and S.P. Rosen. *Developments in the Quark Theory of Hadrons*. Nonantum: Hadronic Press, 1980.
- [57] Amit Goswami. *Quantum Mechanics*. Wm. C. Brown Publishers, 1997.
- [58] David J. Griffiths. *Introduction to Quantum Mechanics*. Prentice-Hall, Inc., 1995.
- [59] Jun John Sakurai. *Modern Quantum Mechanics*. Addison-Wesley Publishing Company, Inc., 1994.
- [60] Claude Itzykson and Jean-Bernard Zuber. *Quantum Field Theory*. McGraw-Hill Inc., 1980.
- [61] Robin Ticciati. *Quantum Field Theory for Mathematicians*. Cambridge University Press, 1999.
- [62] Steven Weinberg. *The Quantum Theory of Fields I: Foundations*. Cambridge University Press, 1995.
- [63] Steven Weinberg. *The Quantum Theory of Fields II: Modern Applications*. Cambridge University Press, 1996.
- [64] Steven Weinberg. *The Quantum Theory of Fields III: Supersymmetry*. Cambridge University Press, 2000.

- [65] Yoshio Ohnuki and Susumu Kamefuchi. *Quantum Field Theory and Parastatistics*. University of Tokyo Press, 1982.
- [66] Michael A. Morrison, Thomas L. Estle, and Neal F. Lane. *Quantum States of Atoms, Molecules, and Solids*. Prentice-Hall, Inc., 1976.
- [67] Richard E. Wilde and Surjit Singh. *Statistical Mechanics: Fundamentals and Modern Applications*. John Wiley & Sons, Inc., 1998.
- [68] George D.J. Phillies. *Elementary Lectures in Statistical Mechanics*. Springer-Verlag New York, Inc., 2000.
- [69] R.D. Amado and H. Primakoff. *Physical Review C*, 22(3):1338–1340, 1980.
- [70] Richard P. Feynman, Robert B. Leighton, and Matthew Sands. *The Feynman Lectures on Physics: Volume III*. Addison-Wesley Publishing Company, 1965.
- [71] Ian Duck and E.C.G. Sudarshan. *Pauli and the Spin-Statistics Theorem*. World Scientific Publishing Co. Pte. Ltd., 1997.
- [72] John A. Peacock. *Cosmological Physics*. Cambridge University Press, 1999.
- [73] Maurice Jacob. *Supersymmetry and Supergravity*. Elsevier Science Publishers, 1986.
- [74] H.J.W. Muller-Kirsten and A. Wiedemann. *Supersymmetry: An Introduction with Conceptual and Computational Details*. World Scientific Publishing Co. Pte. Ltd., 1987.
- [75] M.J. Duff. *The World in Eleven Dimensions: Supergravity, Supermembranes and M-theory*. Institute of Physics Publishing Ltd, 1999.
- [76] Michio Kaku. *Introduction to Superstrings and M-Theory*. Springer-Verlag New York, Inc., 1999.
- [77] Gordon Kane. *Supersymmetry: Unveiling the Ultimate Laws of Nature*. Perseus Books Publishing, L.L.C., 2000.
- [78] S. Raby. *Physics Letters B*, 422:158–162, 1998.
- [79] A. Metz, J. Jolie, G. Graw, R. Hertenberger, J. Groger, C. Gunther, N. Warr, and Y. Eisermann. *Physical Review Letters*, 83(8):1542–1545, 1999.
- [80] Robert C. Hilborn, Guglielmo M. Tino, and (ed.). *Spin-Statistics Connection and Commutation Relations: Experimental Tests and Theoretical Implications*. American Institute of Physics, 2000.
- [81] W. Pauli. *Z. Phys.*, 31:765–783, 1925.
- [82] L. B. Okun'. *JETP Lett.*, 46(11):529–532, 1987.
- [83] O. W. Greenberg and R. N. Mohapatra. *Physical Review Letters*, 59(22):2507–2510, 1987.
- [84] H. S. Green. *Physical Review*, 90(2):270–273, 1953.
- [85] A. Yu. Ignat'ev and V. A. Kuz'min. *Sov. J. Nucl. Phys.*, 46(3):444–446, 1987.
- [86] O.W. Greenberg and A.M. Messiah. *Physical Review B*, 138(5):1155, 1965.
- [87] A. B. Govorkov. *Theor. Math. Phys.*, 54:234, 1983.
- [88] O. W. Greenberg and R. N. Mohapatra. *Physical Review Letters*, 62(7):712–714, 1989.
- [89] R. N. Mohapatra. *Physics Letters B*, 242:407–411, 1990.

- [90] O. W. Greenberg. *Physical Review Letters*, 64:705, 1990.
- [91] O. W. Greenberg. *Physical Review D*, 43(12):4111–4120, 1991.
- [92] K. Fredenhagen. *Commun. Math. Phys.*, 79:141, 1981.
- [93] N. Langer, A. Deutschmann, S. Wellstein, and P. Hoflich. *Astronomy and Astrophysics*, 362:1046–1064, 2000.
- [94] D. Koester. *Astrophysical Journal*, 322:852, 1987.
- [95] H. Schmidt. *Astronomy and Astrophysics*, 311:852–857, 1996.
- [96] J.L. Provencal, H.L. Shipman, E. Hog, and P. Thejll. *Astrophysical Journal*, 494:759–767, 1998.
- [97] F. Brachwitz, D.J. Dean, W.R. Hix, K. Iwamoto, K. Langanke, G. Martinez-Pinedo, K. Nomoto, M.R. Strayer, F. Thielemann, and H. Umeda. *Astrophysical Journal*, 536:934–947, 2000.
- [98] R. Plaga. *Zeitschrift fur Physik A - Atomic Nuclei*, 333:397–403, 1989.
- [99] Donald D. Clayton. *Principles of Stellar Evolution and Nucleosynthesis*. University of Chicago Press, Ltd., 1983.
- [100] V. Rahal and A. Campa. *Physical Review A*, 38(7):3728–3731, 1988.
- [101] Daniel V. Schroeder. *An Introduction to Thermal Physics*. Addison Wesley Longman, 2000.
- [102] Peter T. Landsberg. *Thermodynamics and Statistical Physics*. Dover Publications Inc., 1990.
- [103] C. Wolf. *International Journal of Theoretical Physics*, 36(3):625–634, 1997.
- [104] Y.S. Wu. *Physical Review Letters*, 73:922, 1994.
- [105] D. Kelleher. *Bull. Am. Phys. Soc.*, 33:998, 1988.
- [106] K. Akama, H. Terazawa, and M. Yasuè. *Physical Review Letters*, 68(12):1826–1829, 1992.
- [107] L.C. Biedenharn, P. Truini, and H. van Dam. *J. Phys. A: Math. Gen.*, 22:L67–L71, 1989.
- [108] O. W. Greenberg and R. N. Mohapatra. *Physical Review D*, 39(7):2032–2038, 1989.
- [109] Dennis Krause, 2001. (Private Communication).
- [110] M. Goldhaber and G. S. Scharff-Goldhaber. *Physical Review*, 73:1472–1473, 1948.
- [111] E. Ramberg and G. A. Snow. *Physics Letters B*, 238:438–441, 1990.
- [112] F. Reines and H. W. Sobel. *Physical Review Letters*, 32(17):954, 1974.
- [113] M.K. Moe and F. Reines. *Physical Review*, 140:B992, 1965.
- [114] B. A. Logan and Ljubičić. *Physical Review C*, 20(5):1957–1958, 1979.
- [115] T. Kishimoto, T. Shibata, M. Imamura, S. Shibata, and Y. Uwamino. *J. Phys. G*, 18:443–448, 1992.
- [116] H. Ejiri and H. Toki. *Physics Letters B*, 306:218–223, 1993.
- [117] R. Bernabei, P. Belli, F. Montecchia, M. De Sanctis, W. Di Nicolantonio, A. Incicchitti, D. Prosperi, C. Bacci, C.J. Dai, L.K. Ding, H.H. Kuang, and J.M. Ma. *Physics Letters B*, 408:439–444, 1997.

- [118] Y. Suzuki, Y. Fukuda, K.S. Hirata, K. Inoue, T. Ishida, T. Kajita, K. Kihara, M. Nakahata, K. Nakamura, A. Sakai, N. Sato, Y. Totsuka, M. Mori, Y. Oyama, A. Suzuki, K. Takahashi, M. Yamada, M. Koshihara, K. Nishijima, T. Kajumura, T. Suda, A.T. Suzuki, K. Miyano, H. Miyata, H. Takei, E. Kodera, Y. Nagashima, M. Takita, H. Yokoyama, K. Kaneyuki, Y. Takeuchi, T. Tanimori, and H. Ejiri. *Physics Letters B*, 311:357–361, 1993.
- [119] R. Arnold, C. Augier, J. Baker, A. Barabash, D. Blum, V. Brudanin, A.J. Caffrey, J.E. Campagne, E. Caurier, D. Dassie, V. Egorov, T. Filipova, R. Gurriaran, J.L. Guyonnet, F. Hubert, Ph. Hubert, S. Jullian, O. Kochetov, I. Kisel, V.N. Kornoukhov, V. Kovalenko, D. Lalanne, F. Lapanche, F. Laccia, I. Linck, C. Longuemare, Ch. Marquet, F. Mauger, H.W. Nicholson, I. Pilugin, F. Piquemal, J-L. Reyss, X. Sarazin, F. Scheibling, J. Suhonen, C.S. Sutton, G. Szklarz, V. Timkin, R. Torres, V.I. Tretyak, V. Umatov, I. Vanyushin, A. Vareille, Yu. Vasilyev, and Ts. Vylov. *European Physical Journal A*, 6:361–366, 1999.
- [120] D. Kekez, A. Ljubičić, and B.A. Logan. *Nature*, 348:224, 1990.
- [121] V.N. Gavrin, A.Yu. Ignatiev, and V.A. Kuzmin. *Physics Letters B*, 206(2):343–345, 1988.
- [122] V.M. Novikov and A.A. Pomanskii. *JETP Letters*, 49(2):81–83, 1989.
- [123] V.M. Novikov, E. Nolte, and A.A. Pomanskii. *JETP Letters*, 51(1):1–3, 1990.
- [124] A. S. Barabash, V. N. Kornoukhov, Yu. M. Tsipenyuk, and B. A. Chapyzhnikov. *JETP Letters*, 68(2):112–116, 1998.
- [125] Yu.M. Tsipenyuk, A.S. Barabash, V.N. Kornoukhov, and B.A. Chapyzhnikov. *Radiat. Phys. Chem.*, 51(4–6):507–511, 1998.
- [126] O. W. Greenberg. *Physica (Amsterdam)*, 180A:419, 1992.
- [127] K. Deilamian, J. D. Gillaspay, and D. E. Kelleher. *Physical Review Letters*, 74(24):4787–4790, 1995.
- [128] R.C. Hillborn. *Bull. Am. Phys. Soc.*, 35:982, 1990.
- [129] G.M. Tino. *Nuovo Cimento Soc. Ital. Fis.*, 16D:523, 1994.
- [130] G. de Angelis, G. Gagliardi, L. Gianfrani, and G.M. Tino. *Physical Review Letters*, 76(16):2840–2843, 1996.
- [131] R.C. Hillborn and C.L. Yuca. *Physical Review Letters*, 76(16):2844–2847, 1996.
- [132] G. Modugno, M. Inguscio, and G.M. Tino. *Physical Review Letters*, 81(22):4790–4793, 1998.
- [133] D. Mazzotti, P. Cancio, G. Guisfredi, M. Inguscio, and P. De Natale. *Physical Review Letters*, 86(10):1919–1922, 2001.
- [134] C.C. Gerry and R.C. Hilborn. *Physical Review A*, 55(6):4126–4130, 1997.
- [135] D. DeMille, D. Budker, N. Derr, and E. Deveney. *Physical Review Letters*, 83(20):3978–3981, 1999.
- [136] C.J. Bowers, D. Budker, E.D. Commins, D. DeMille, S.J. Freedman, A.-T. Nguyen, S.-Q. Shang, and M. Zolotarev. *Physical Review A*, 53:3103, 1996.
- [137] M.H. Thoma and E. Nolte. *Physics Letters B*, 291:484–487, 1992.
- [138] R. Middleton. *A Negative-Ion Cookbook*. University of Pennsylvania Preprint, 1990.

- [139] James S. Monroe and Reed Wicander. *Physical Geology: Exploring the Earth*. West Publishing Company, 1992.
- [140] S. Dimopoulos, D. Eichler, R. Esmailzadeh, and G. D. Starkman. *Physical Review D*, 41(8):2388–2397, 1990.
- [141] E. Nardi and E. Roulet. *Physics Letters B*, 245(1):105–110, 1990.
- [142] R. S. Chivukula, A. G. Cohen, S. Dimopoulos, and T. P. Walker. *Physical Review Letters*, 65(8):957–959, 1990.
- [143] R. N. Mohapatra and S. Nandi. *Physical Review Letters*, 79(2):181–184, 1997.
- [144] S. Raby. *Physical Review D*, 56(5):2852–2860, 1997.
- [145] Z. Chacko, B. Dutta, R. N. Mohapatra, and S. Nandi. *Physical Review D*, 56(9):5466–5474, 1997.
- [146] R. N. Mohapatra and S. Nussinov. *Physical Review D*, 57(3):1940–1946, 1998.
- [147] V. Berezhinsky and M. Kachelrieß. *Physics Letters B*, 422:163–170, 1998.
- [148] D. O. Caldwell and R. N. Mohapatra. *Physical Review D*, 48(7):3259–3263, 1993.
- [149] R. Foot and R. R. Volkas. *Physical Review D*, 52(11):6595–6606, 1995.
- [150] Z. G. Berezhiani and R. N. Mohapatra. *Physical Review D*, 52(11):6607–6611, 1995.
- [151] V. S. Berezhinskiĭ and B. L. Ioffe. *Sov. Phys. JETP*, 63(5):920–925, 1986.
- [152] D. J. H. Chung, G. R. Farrar, and E. W. Kolb. *Physical Review D*, 57(8):4606–4613, 1998.
- [153] I. F. M. Albuquerque, G. R. Farrar, and E. W. Kolb. *Physical Review D*, 59(015021):1–12, 1998.
- [154] E. W. Kolb and M. Turner. *The Early Universe*. Addison-Wesley, 1990.
- [155] Malcom S. Longair. *High Energy Astrophysics Volume 2: Stars, the Galaxy and the interstellar medium*. Cambridge University Press, 1994.
- [156] Steven Weinberg. *Gravitation and Cosmology: Principles and Applications of the General Theory of Relativity*. John Wiley & Sons, Inc., 1972.
- [157] Malcom S. Longair. *High Energy Astrophysics Volume 1: Particles, photons and their detection*. Cambridge University Press, 1992.
- [158] F. Schweizer, J. H. Van Gorkom, and P. Seitzer. *Astrophysics Journal*, 338:770–788, 1989.
- [159] B. Paczynski. *Astrophysical Journal*, 304:1–5, 1986.
- [160] B. Paczynski. *Astrophysical Journal*, 371:L63–L67, 1991.
- [161] C. Alcock, C. W. Akerlof, R. A. Allsman, T. S. Axelrod, D. P. Bennett, S. Chan, K. H. Cook, K. C. Freeman, K. Griest, S. L. Marshall, H. S. Park, S. Perlmutter, B. A. Peterson, M. R. Pratt, P. J. Quinn, A. W. Rodgers, C. W. Stubbs, and W. Sutherland. *Nature*, 365:621–623, 1993.
- [162] E. Aubourg, P. Bareyre, S. Brehin, M. Gros, M. Lachieze-Rey, B. Laurent, E. Lesquoy, E. Magneville, A. Milsztajn, L. Moscoso, F. Queinnec, J. Rich, M. Spiro, L. Vigroux, S. Zylberajch, R. Ansari, F. Cavalier, M. Moniez, J.-P. Beaulieu, R. Ferlet, Ph. Grison, A. Vidal-Madjar, J. Guibert, O. Moreau, F. Tajahmady, E. Maurice, L. Prevot, and C. Gry. *Nature*, 365:623–625, 1993.

- [163] A. Udalski, M. Szymanski, J. Kaluzny, M. Kubiak, M. Mateo, and W. Krzeminski. *Astrophysical Journal*, 426:L69–L72, 1994.
- [164] C. Alcock, R.A. Allsman, T.S. Axelrod, D.P. Bennett, K.H. Cook, K.C. Freeman, K. Griest, J.A. Guern, M.J. Lehner, S.L. Marshall, H-S. Park, S. Perlmutter, B.A. Peterson, M.R. Pratt, P.J. Quinn, A.W. Rodgers, C.W. Stubbs, and W. Sutherland. *Physical Review Letters*, 74(15):2867–2871, 1995.
- [165] C. Alcock, R.A. Allsman, T.S. Axelrod, D.P. Bennett, K.H. Cook, K.C. Freeman, K. Griest, S.L. Marshall, S. Perlmutter, B.A. Peterson, M.R. Pratt, P.J. Quinn, A.W. Rodgers, C.W. Stubbs, and W. Sutherland. *Astrophysical Journal*, 445:133–139, 1995.
- [166] G. Jungman, M. Kamionkowski, and K. Griest. *Physics Reports*, 5:195–376, 1996.
- [167] S. Tremaine and J.E. Gunn. *Physical Review Letters*, 42:407–410, 1979.
- [168] T. K. Hemmick, D. Elmore, T. Gentile, P. W. Kubick, S. L. Olsen, D. Ciampa, D. Nitz, H. Kagan, P. Haas, P. F. Smith, B. B. McInteer, and J. Bigeleisen. *Physical Review D*, 41(7):2074–2080, 1990.
- [169] K. Greisen. *Physical Review Letters*, 16:748, 1966.
- [170] G. T. Zatsepin and V. A. Kuźmin. *Zh. Eksp. Teor. Fiz.*, 4:114, 1966.
- [171] A. A. Watson. *Nucl. Phys. B (Proc Suppl.)*, 22B:116, 1991.
- [172] V. A. Rubakov. *Physics - Uspekhi*, 42(12):1193–1203, 1999.
- [173] P. Bhattacharjee and G. Sigl. *Physics Reports*, 327:109–247, 2000.
- [174] A. Mafi and S. Raby. *Physical Review D*, 62:035003, 2000.
- [175] A. Mafi and S. Raby. *Physical Review D*, 63:055010, 2001.
- [176] G.R. Farrar. *Physical Review Letters*, 76:4111, 1996.
- [177] S. Barr, D. Chang, and G. Senjanović. *Physical Review Letters*, 67(20):2765–2768, 1991.
- [178] R. Middleton, R. W. Zurmuhle, J. Klein, and R. V. Kollarits. *Physical Review Letters*, 43(6):429–431, 1979.
- [179] D. Oliver. (Private Communication).
- [180] D.E. Granger, J.W. Kirchner, and R. Finkel. *The Journal of Geology*, 104:249–257, 1996.
- [181] D.E. Granger, D. Fabel, and A.N. Palmer. *Geological Society of America Bulletin*, 113(7):825–836, 2001.
- [182] G. Brent Dalrymple. *The Age of the Earth*. Stanford University Press, 1991.
- [183] P. Bierman and J. Turner. *Quaternary Research*, 44:378–382, 1995.
- [184] D. Javorsek II, D. Elmore, E. Fischbach, T. Miller, D. Oliver, and V. Teplitz. *Physical Review D*, 64:012005, 2001.
- [185] M.J. Pavich, L. Brown, J.N. Valette-Silver, J. Klein, and R. Middleton. *Geology*, 13:39–41, 1925.
- [186] F. Horz, R.P. Bernhard, J. Warren, T.H. See, D.E. Brownlee, M.R. Lurance, S. Messenger, and R. Peterson. *LDEF - 69 Months in Space: First LDEF Post-Retrieval Symposium, NASA Conference Publication*, 3134:487–501, 1991.

- [187] Sergio DeBenedetti. *Nuclear Interactions*. John Wiley & Sons, Inc., 1964.
- [188] Murrey D. Goldberg, Said F. Mughabghab, Surendra N. Purohit, Benjamin A. Magurno, and Victoria M. May. *Neutron Cross Sections Volume IIC, Z = 61 to 87, BNL 325*. Brookhaven National Laboratory Associated Universities, Inc., 1966.
- [189] D.I. Garber and R.R. Kinsey. *Neutron Cross Sections Volume II, Curves, BNL 325*. Brookhaven National Laboratory Associated Universities, Inc., 1976.
- [190] Vagn Buchwald. *Handbook of Iron Meteorites*. University of California Press, 1975.
- [191] A.H. Guth. *Physical Review D*, 23:347–356, 1981.
- [192] Alan H. Guth. *The Inflationary Universe*. Addison-Wesley Longman, Inc., 1997.

VITA

## VITA

Daniel Javorsek II was born on 24 January 1977 in San Diego, California. After graduating from Liberty High School of Colorado Springs, Colorado in 1995 he attended Purdue University in West Lafayette, Indiana. In 1999 he graduated with highest distinction, receiving a B.S. in Aeronautical and Astronautical Engineering. He was awarded the Fredrick N. Andrews Doctoral Fellowship and the Dr. Theodore von Kármán Fellowship for graduate study in Nuclear Astrophysics. He was also commissioned as an Air Force Second Lieutenant and was accepted to the Civilian Institution Scholarship/Fellowship/Grant Program governed by the Air Force Institute of Technology. This assignment was authorized as casual status awaiting class 03-02 of Euro-NATO Joint Jet Pilot Training.

While pursuing his Ph.D. in nuclear astrophysics he continued research in spacecraft attitude dynamics with Professor James Longuski of the Department of Aeronautics and Astronautics. This research resulted in a practical modification to rocket engines called the Velocity Precision-pointing Enhancement System (VPES) for which he and Professor Longuski have filed U.S. Patent Application Number 09/635,225.